Investigation into Contact Resistance and Damage of Metal Contacts used in RF-MEMS Switches

DISSERTATION

Kevin W. Gilbert, Lieutenant Colonel, USAF

AFIT/DS/ENY/09-J03

DEPARTMENT OF THE AIR FORCE
AIR UNIVERSITY

AIR FORCE INSTITUTE OF TECHNOLOGY

Wright-Patterson Air Force Base, Ohio

AFIT/DS/ENY/09-J03

Investigation into Contact Resistance and Damage of Metal Contacts used in RF-MEMS Switches

DISSERTATION

Presented to the Faculty

Graduate School of Engineering and Management

Air Force Institute of Technology

Air University

Air Education and Training Command

In Partial Fulfillment of the Requirements for the

Degree of Doctor of Philosophy

Kevin W. Gilbert, B.S.M.E., M.S.M.E., P.E.

Lieutenant Colonel, USAF

September 2009

AFIT/DS/ENY/09-J03

Investigation into Contact Resistance and Damage of Metal Contacts used in RF-MEMS Switches

Kevin W. Gilbert, B.S.M.E., M.S.M.E., P.E.
Lieutenant Colonel, USAF

Approved:

Dr. Shankar Mall (Chairman)	date
Dr. Jonathan Black (Member)	date
Maj. LaVern Starman, PhD (Member)	date
Dr. Michael Heil (Member)	date
Dr. Kevin Leedy (Member)	date

Accepted:

Dr. M.U. Thomas Dean, Graduate School of Engineering and Management	Date

AFIT/DS/ENY/09-J03

Abstract

This research effort examines the physical and electrical processes involved in lifecycle failure of Microelectromechanical (MEMS) Radio-Frequency (RF) cantilever beam ohmic contact switches. The development of better and more reliable RF components is critical to the future improvement of space-based and airborne USAF RF systems. Power and weight are expensive and any devices which offer reduction in power needs or weight will enable revolutionary improvement in next generation systems. RF MEMS switches offer several advantages over conventional solid-state switches: lower power required, smaller size, less weight, and lower insertion loss. However, current MEMS ohmic contact switches lack the reliable lifetimes needed for use in military applications. Complete details of microcontact performance are difficult to measure and have not been previously reported. Data of contact parameters, failure and characteristics of failure over the lifetime are sparse. The objective of this study was to fill this gap by designing and constructing a novel experimental setup to provide new insight into microcontact behavior by testing three contact materials. Gold, Au5%Ru and Au-4%V_2O_5 were all tested as contact switch materials.

This study developed and proved an automated method to simulate the action of MEMS contact switches. A custom silicon cantilever with an integrated contact bump was designed and fabricated in order to avoid the significant effort involved in process redesign required when contact materials are changed in actual MEMS switches. A nanoindenter was integrated with a custom designed sample tray and precise positioning devices. An automated test method was developed to control the test apparatus and acquire data. Test cases were run to verify measurements and system capability.

The performance of gold, gold-ruthenium alloy and gold-vanadium oxide dispersion strengthened alloy contacts were tested in laboratory air conditions. Contact

resistance, pull-off force, the contact force required for stable ohmic contact (referred to as threshold force), the deformation required between contact surfaces to achieve stable ohmic contact (referred to as threshold distance), contact unloading stiffness, contact interference and energy absorbed by the contacts were all measured over their lifetime. Time-dependent deformation was detected in all three materials tested. No dependence of these parameters on contact bump shape was found. Gold had the shortest tested lifetime, with Au5%Ru performing about four-times better than gold. Au-4%V_2O_5, the dispersion strengthened material developed at Lehigh University, showed the most promise as a contact material of the materials tested with the longest-life contact lasting more than 15.5×10^6 cycles. Evidence of contact heating during cycling was noted in all materials tested and was most evident in the Au-4%V_2O_5 contacts. However, material hardness was not proportional to contact lifetime.

There was considerable variation in the lifetime of each material as seen in practical applications of MEMS switches. Failure characteristics were similar over certain ranges of the lifetime in each contact material. Short-life contacts commonly showed higher early pull-off force, lower initial threshold force and lower initial threshold distance when compared to long-life contacts. These results suggest the existence of a higher level of initial surface contamination on contacts which demonstrated a longer lifetime. Short-life contacts also showed evidence of early contact smoothening. Longer-life contacts showed evidence of brittle separation while the short-life contacts showed evidence of ductile separation. Ductile separation was more common in gold, whereas brittle separation was more common in the harder materials. Harder materials delayed and minimized damage to the contact surface.

The experimental apparatus demonstrated its usefulness as an efficient method to test various candidate contact materials and provide insight into contact failure. The experimental apparatus as designed and built is capable of simulating microswitches and producing data on contact behavior. This ability to test candidate materials and understand their behavior in simulated microswitch conditions offers the first step of an empirical contact material selection technique.

Acknowledgements

I would like to thank my advisor, Dr. Shankar Mall, for his assistance and advice during this project. I would also like to thank the members of my committee who were also very helpful during my research work. Several AFIT technicians were crucial to my success during development of the experimental design, including Randy Miller, Jason Vangel, Dan Ryan, Barry Page, Bill Trop, and Sean Miller. I would like to thank Rick Patton for his help with the SEM. Maj. Glenn Kading deserves thanks for proving significant help in development of masks for cantilever beam manufacture as do 1Lt Dan Denninghof and 2Lt Ginny Miller for their assistance with the AFRL SEM and in the AFRL cleanroom. Dr. Volodomyr Sabelkin also assisted me in completing the experimental portion of my work and I am grateful for his help. I would also like to thank Dr. Lei Chen, Northeastern University, especially for his invaluable assistance at the beginning stages of my work and consultation during my research, as well as his professors Drs. McGruer and Adams. Professor R.P. Vinci from Lehigh University also provided sputtering of samples for testing and coordinated XPS testing.

Several people at the Air Force Research Lab Sensors Directorate were also extremely helpful. Dr. Becky Cortez assisted me in the cleanroom and provided a place to store my samples without which I would have been dead in the water. Dr. Bill Siskaninetz helped sort out operation of the MJB-3 Mask Aligner, so that I could proceed with fabrication. Bob Fitch and Paul Cassity were extremely helpful in working with me to create the recipe which would eventually successfully fabricate contact bumps. Dr. Jack Ebel was extremely helpful with ideas and discussion when I ran into roadblocks. Dr. Kevin Leedy was extremely helpful with contacts to Northeastern University and Lehigh University as well as getting me the necessary cleanroom access and performing the necessary sputtering. Larry Callahan made the project possible with his skill in manipulating and dicing small items and his facility

with the wire bonder. Dr. Tom Dalrymple fabricated my cantilever mount plates and ensured I had a steady supply.

MTS Nanoinstruments (now Agilent Technologies) personnel were extremely helpful and supportive during my experimental development work. My experiment as conceived could not have been built without their help. Jenny Hay, Kermit Parks, Lee Spencer, and Pierre Morel, among others, all were helpful. Bryan Crawford, in particular, provided key assistance. His patience and time spent training and assisting me in programming test methods were fundamental to the project's success. David Rego, Jeff North and Jaye Jillson, engineers at Physik Instrumente Inc. (PI), were also very patient and helpful in answering my questions and assisting with repairs.

Thanks also to my BARFmates, and members of the class of DS-07S who helped me out with occasional text editing and made the process sometimes bearable. Particular thanks go to LtCol Tim Jorris who taught me LaTeX with the assistance of LtCol David Irvin, LtCol David Marsh who helped format code for presentation in the appendix, and LtCol Justin Green and Capt Ted Kim who were always willing to discuss ideas.

If I have inadvertently forgotten someone, I apologize. There were clearly many people without whose help I could not have accomplished this project. For their help, I am extremely grateful.

Last but not least, I would like to thank my parents and my wife and daughter without whose support this effort would not have been possible.

Kevin W. Gilbert

Table of Contents

List of Figures

List of Tables

Investigation into Contact Resistance and Damage of Metal Contacts used in RF-MEMS Switches

I. Introduction

Radio-Frequency (RF) Microelectromechanical Systems (MEMS) cantilever beam metal-to-metal ohmic contact switches are an area of significant current research, some of which has occurred at the Air Force Institute of Technology (e.g. [46, 122, 133, 134, 166]) and Air Force Research Laboratory (e.g. [65, 144, 146]). Development of high-performing and reliable MEMS switches offer potential for improvement in applications as varied as cell phones, phase shifters, automated test equipment, and phased array radar [159, 203, 231]. RF switches are necessary in all communication and tracking systems [256]. MEMS switches and relays have the potential to replace traditional solid state devices and interest in MEMS switches has increased, primarily due to demonstrated device performance [65,139,171,202]. An example of a successful electrostatic RF MEMS switch and its geometry is shown in Figure 1.1. Electrostatic switches are the most successful MEMS switches to date, so most of the background information describes this type of switch actuation [241]. Advances in RF switching technology will enable future Department of Defense and Air Force systems like space radar. However, the lifetime, reliability and power carrying capacity of RF MEMS switches currently limit their use and widespread application [75, 137, 192, 241].

1.1 Motivation

RF MEMS Switches offer significant advantages for many applications. RF MEMS Switches are smaller, use less power, have lower insertion loss and could reduce system weight, when compared to traditional solid state switches [82, 159, 202, 231]. These characteristics of RF MEMS Switches offer significant promise for space and airborne RF applications [30, 95]. Micro-satellites are of significant interest currently,

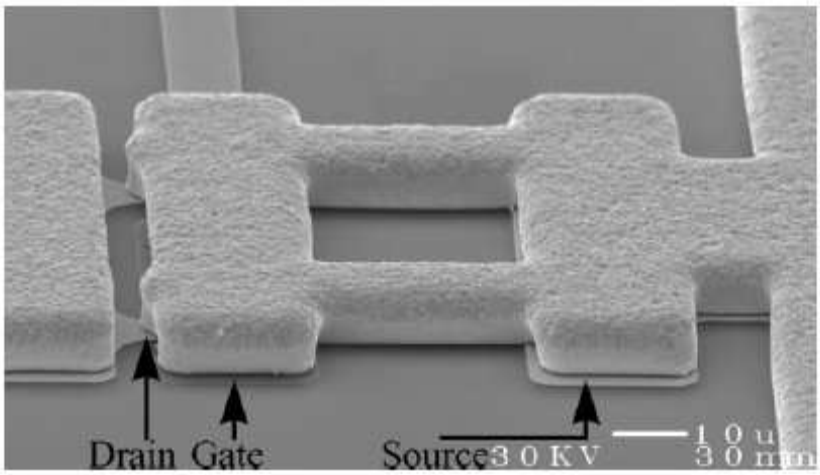

Figure 1.1: Example of a cantilever beam RF MEMS ohmic contact switch [163].[1]

for the operational advantages they could offer [82, 112]. These small satellites could have many applications, including reconnaissance, intelligence gathering, space control, space situational awareness and space force enhancement [112]. Operational micro-satellites would offer significant enhancements to current capabilities in intelligence, satellite clusters and quick reaction operationally responsive space (ORS) systems (e.g. rapidly launched, inexpensive, disposable satellites for tactical use by a theater combatant commander) [112]. Advances in MEMS will enable reduction in traditional satellite weight and power requirements as well [82]. This offers advantages of its own as the cost of launch is driven by the weight of the satellite [82].

1.2 Background

Significant amounts of research have been reported in the area of RF MEMS devices and miniaturization. This includes design and development of MEMS Switches for use in RF devices. RF MEMS ohmic contact switches are commercially available and reported "lifetime" results are increasing each year [80]. However, little data exists on the variability of lifetime results and very little reliability data has been

[1]Reprinted from Sensors and Actuators A, Vol 93. Sumit Majumder, N.E. McGruer, George G. Adams, P.M. Zavracky, Richard H. Morrison and Jacqueline Krim. "Study of contacts in an electrostatically actuated microswitch," pp19-26, Copyright 2001, with permission from Elsevier.

published [171]. The data which has been published shows large variability in lifetime testing and usually only includes "hero" results [65]. Also, there are currently no analyses or models which can predict or estimate contact performance as a function of switch cycles or which enable the characterization of switch lifetime performance and behavior. There exists very little experimental data upon which to base model development.

There are two basic types of MEMS Switches – metal-metal contact (or ohmic) switches and capacitive type switches. Capacitive switches typically operate in the 6-120 Gigahertz (GHz) range, while ohmic contact switches typically operate from DC - 60 GHz [202]. Much research is being reported on extending the life of capacitive switches, but not much is reported in the area of life-extension for ohmic contact switches. MIT Lincoln Laboratories (Lexington, MA) and MEMTronics (Richardson, TX) have developed long life capacitive switch designs. Radant MEMS reports a long lifetime RF MEMS ohmic contact switch, however, few details have been published describing the engineering and analysis which increased the reported lifetime of this switch far past any others available [160, 161].

The causes for failure in ohmic contact switches all seem to be related to the contact and contact metal used for the ohmic contact. Contact adhesion failure, which occurs when the restoring force of a switch is no longer able to open the contact, (e.g. the switch remains stuck shut), and a significant rise in switch contact resistance are the two most common contact failure types [37]. The mechanics of the contact and the contact material choice are interwoven with the failure mechanisms.

1.2.1 Lifetime & Reliability. There have been published reports on the extension of MEMS switch lifetimes, including Radant MEMS contact switches with a "lifetime" of 10 billion cycles [160] which has recently increased to a reported 900 billion cycles [80], and MIT Lincoln Laboratory capacitive switches with lifetimes of up to 10 Billion cycles [203], and capacitive switches from MEMTronics Corporation of 100 Billion cycles [80]. However, even though companies are shipping commercial

RF MEMS switches, the issues of reliability and lifetime remain among the critical issues holding back widespread use of these devices [75, 181, 237]. The requirement for lifetime performance of RF switches in radar and other systems is reliable, predictable operation up to several hundred billion cycles [181, 203]. These switches will not be implemented on a wide scale in defense systems until the predictability and reliability of their lifetime performance is significantly increased.

1.2.2 Actuation Voltage. One barrier to widespread implementation and commercial use of MEMS switches has been that the actuation voltage (e.g. pull-down voltage) is very high, on the order of 40-120 V [159]. This is due to the competing requirements of cantilever beam designs to have a high enough spring constant to open the switch after the pull-down voltage is released, and at the same time, have enough contact force to ensure a good electrical contact at the contacts. With this level of actuation voltage, based on a design using a contact material other than gold, electrostatic MEMS switches usually operate at a contact force of 200 μN and have a contact resistance of 3 Ω [159]. Contact forces used in MEMS switches range from 50 μN - 2mN [202]. However, recently reported results from Lee, et al. proposed a design which requires low voltage operation of only 2.5 V using piezoelectric actuation [140]. They used gold contacts, however, they do not report contact forces, contact evolution, lifetime or reliability of the switch.

1.2.3 Contact Theory. The investigation of contact mechanics is important to the study of MEMS switches. The physical contact between two bodies is required for switch operation, and the mechanics of this contact plays a strong role in the eventual degradation or failure of the electrical characteristics of the switch. The study of macro switch contacts is applicable in some ways to the micro scale. The deformation during mechanical contact of the micro-switch is described as either elastic, plastic, or elastic-plastic. The contact mechanics of macro switch contacts has been studied for many years. Holm's work is the background for many studies of electrical contacts, and Slade's book is the current encyclopedic work on electrical contacts [103, 230].

The transport of electrons through a contact is described as diffusive, ballistic, or quasi-ballistic depending upon the size of the effective contact radius [3]. Ziad performed some initial work analyzing contacts in-between macro size and micro size scales. The contact diameters studied in his work were 100 μm, 200 μm and 500 μm respectively [268]. Majumder developed a clean metal contact resistance model and compared resistance results over switch cycles for gold-on-gold microswitches [163]. Majumder also extended the contact model and successfully compared it to experimental results [161, 165].

Contact resistance can be modeled based on either single or multiple asperity models. Majumder developed a multiple asperity model which appears to agree with experimental results using the Northeastern University DC-contact micro-switch [165]. He uses a single asperity model as an upper bound on the contact resistance. Northeastern University (NEU) researchers are among the leaders in the field of MEMS switches and the study of MEMS contacts. Majumder's research into contact resistance and adhesion was accomplished at Northeastern [160, 161].

Much work has been done on single contact resistance studies, for example Pruitt who used cantilevers of various stiffnesses to compare resistance at low contact force to Hertzian elastic contact theory [198] and Ziad [268], but only a few such as Majumder, Chen, Mihailovich, and Gregori have focused on contact evolution [39, 93, 161, 174]. The study presented here is focused toward extending understanding of micro-contact behavior and the evolution of contacts by developing a new experimental technique as well as baseline micro-contact data.

1.2.4 Switching Conditions. The evolution of electrical contacts as they are switched is different between hot-switching and cold-switching. Hot-switching is defined as the making and breaking of electrical contact while current is being passed through the contact, and cold-switching is defined as making and breaking of the mechanical contact while current is not flowing. Patton and Zabinski studied the failure mechanisms of direct current MEMS switches under hot-switching conditions by using

a micro adhesion apparatus [189]. They compared "low current" of 1-10 μA to "high current" of 1-10 mA in laboratory air and found that the "current had a profound effect on deformation mechanisms, adhesion, contact resistance (R), and reliability/-durability" of the contacts [189]. They found that "asperity melting, slightly lower R, near zero adhesion, poor durability and switch shorting by nanowire formation were present at high current", while "asperity creep, slightly higher resistance, switching induced adhesion and switch bouncing were present at low current" [189]. Patton, Eapen and Zabinski also have studied the lubrication of micro-switch contacts at 200 μN load and 1 μA current [190]. However, the apparatus used for this research was on a simulated contact larger than the size actually used in micro-switches. The apparatus developed by Patton and Zabinski used a contact material coated 1.6 mm diameter stainless steel ball as a contact which is much larger than contacts commonly used in RF MEMS switches [189].

Generally, the lifetime of MEMS switches are significantly longer under cold-switching conditions and switch manufacturers usually report their switch lifetimes tested while cold-switching. Researchers have also reported on the transfer of material between contact surfaces. Hyman's work on gold contacts shows an example of material transfer in a microcontact having a current of 10 mA with 200-500 μN contact force [107, 108].

1.2.5 Contact Wear & Mechanics. There is still a need for a fundamental understanding of microscale mechanics including adhesion, friction, wear and the role of surface contamination and environment on operating devices [21]. Researchers also point out that metallurgy and mechanics of contact materials at the micro-scale need further study [250]. One specific area which needs further study is the phenomena of contact wear. Wear is caused by the contact of rough surfaces, and one characteristic of wear is its unpredictability [71]. Wear and/or abrasion of metal contacts could be a contributing factor in the evolution of contact performance over time. Fretting may also be a factor in contacts which change over time. Fretting is the result of

microscopic relative motions of parts while they are in contact [227]. Strain hardening of contacts due to plastic deformation could also be a contributing factor. The author is unaware of studies reporting on contact wear or experimental results showing strain hardening of contacts in micro-switches.

1.2.6 Contact Material. The choice of contact metal is an important design characteristic of MEMS ohmic contact switches, but few studies have investigated contact metals other than gold for use in micro-switches. The majority of work on MEMS contact switches has used gold as the contact metal for its excellent conductivity, low hardness, and resistance to the formation of oxide layers (e.g. [61,62,107,115,138,140,161,163,173,189,190,252,253]). Schimkat and Varadan, et al. recommended that gold is not an appropriate microrelay contact metal due to its high adherence [217,247]. However, most current research relies on a non-scientific "build and bust" approach to contact material selection and testing.

Thus, one area open for research is in the understanding of mechanics of microcontact and the influence of material properties on contact behavior over contact lifetime. Sharma performed work on adhesion of electrical contacts in macro-switches and determined the effect of physical and material properties of the contact material on adhesion of bulk metals in 1974 [224]. This was early research suggesting alloying could be used to customize metal contact material properties in order to find the best possible properties for use in a given switch design [224]. However, little experimental data or analysis exists on behavior of microcontacts as they are cycled or on the effect of material properties on contact behavior. Contact metals chosen for use in a micro-switch design should have a low contact resistance and a high resistance to wear. Basic material properties have been measured, but no method of systematic scientific testing of contact metals comparing their performance in a switch-like setup and relating the results to their material properties has been reported.

The ideal contact material should have minimum resistivity but maximum hardness. These should be selected based on the switching conditions expected in a specific

design. Lower resistivity of the contact material reduces the insertion loss of the contact and higher hardness is related to higher wear resistance and lower adhesion forces in the contact. Ideally, the alloying should be such that the hardness (and wear resistance) of a material be increased without a corresponding increase in resistivity. The desired trend of properties is shown in Figure 1.2. However, other factors may dictate the specific alloying and microstructure such as the susceptibility to adhesion, the surface energy of the material, and the relative resistance of the microstructure to contamination. Materials of non-regular lattice structure having a high elastic modulus, high melting point, low work hardening coefficient, and high recrystallization temperature have reduced contact adhesion in macro-switches [224].

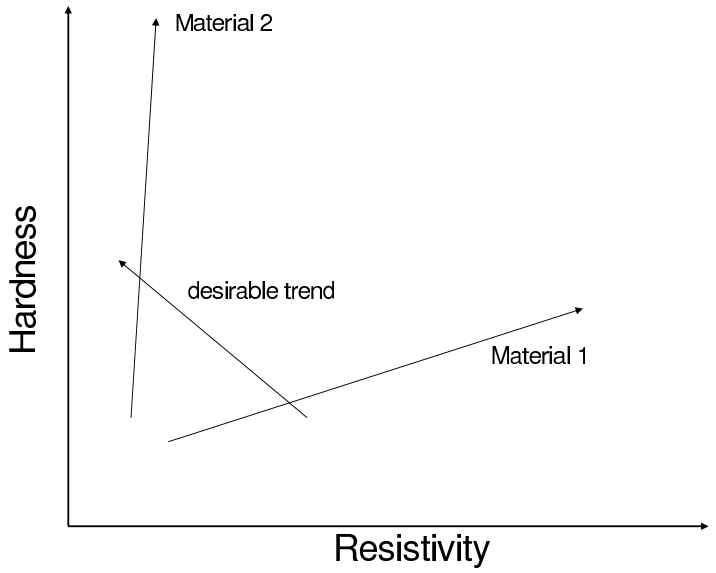

Figure 1.2: Nominal representation of desired material property relationships of hardness and resistivity for micro-contact materials.

Optimal RF MEMS switch design requires proper selection of contact metal and an understanding of the phenomena that affect the contact over its life and contribute to switch failure. While the main types of failure in these switches are known, a poor understanding of the physical mechanisms that limit cycling lifetimes in ohmic contact switches exists. Previous experimental work shows that many-cycle failure occurs at

the metal contacts, although details about these failures are sparse (e.g [202]). Key questions surround the dominant mechanisms contributing to contact failure and how these failure mechanisms evolve with cycle number. The author was unable to locate a study addressing these issues. Such work is critical to the continued improvement of MEMS ohmic switch reliability, especially under demanding operational conditions such as hot switching and high signal powers. Studies focusing on contact metals other than gold are limited. Information on the behavior of microcontacts in microswitches and the relationship to material properties of the contact metal would be of great benefit to switch designers.

The present study addresses these issues and demonstrates a systematic experimental method with which to study microcontact mechanics and which could be used to evaluate candidate contact materials. The present study also reports test data for three materials using this method.

1.2.7 Experimental Methods. Microcantilever beam mechanics and behavior were experimentally investigated as early as 1979 [196]. Nanoindentation equipment has been used by various researchers to study cantilever beam bending and mechanics of microcantilever beams as early as 1988 [104, 127, 249, 254, 255], for microstructure adhesion as early as 1992 [167], as well as the hysteresis of microcantilever adhesion [48, 120], device spring constants [31], and fatigue of nanoscale structures [148]. Nanoindenters have also been used by multiple researchers to characterize virgin MEMS switches [46, 66, 67, 143, 184, 221] and to measure switch spring constants and evolution of adhesive forces in MEMS switches [93].

Chen at NEU developed an experimental method to simulate ohmic contact switches with the use of a cantilever installed in a scanning probe microscope [39]. This experimental design allowed the comparison of contact materials without complete switch fabrication process redesign for the first time and was the first step toward systematic understanding of micro-contact mechanics and material influences. Chen's experimental setup nullified contact sliding and allowed direct observation of

displacement of the cantilever, however contact forces and adhesion forces were determined based on calculated cantilever stiffness. This work is described in more detail in Appendix E.

The experimental work reported in the literature to date has not combined the direct measurement of contact forces with correlated data collection of electrical contact performance. Reported work to date using instrumented nanoindenters did not have the ability to simultaneously measure electrical and mechanical characteristics of microcontacts. Thus, detailed and correlated experimental methods and data useful in systematically investigating microcontact performance behavior is sparse or non-existent.

1.3 Problem Statement

The lack of experimental data on microcontact performance has led to the current non-scientific practice "build and bust" approach to contact material selection. Therefore, the objectives of this dissertation are two-fold. First, to develop a realistic test facility without going through the entire switch fabrication process while gathering all necessary data to understand contact performance during typical MEMS switch operation (e.g. contact loads, wear patterns, possible contamination growth as a function of cycles, etc.). Second, this dissertation demonstrates this test facility by conducting tests on three possible contact materials of differing microstructure. A large contribution of this research is the ability to produce significant data needed for microcontact analysis and the development of this data for three contact materials. Third, this study developed data on the types of adhesive failures which occur during microcontact cycling.

1.3.1 Research Objectives. This research provides a scientific based experimental method for analyzing performance of contact switch materials in a systematic manner. This research also deepens the understanding of the failure mechanisms of MEMS ohmic contact switches and specifically provides MEMS design engineers

with knowledge of possible contact metal choices for use in switch design. The overall goal was to experimentally investigate the parameters of microcontact mechanics. The ability to develop data for various candidate contact materials will also provide switch designers a method to develop performance information useful in selection of contact materials for their specific application of interest.

Thin films of three contact metals and simulated MEMS micro-switches in the form of a micro-cantilever beam fabricated of silicon with a contact bump and coated with the contact metal were tested to generate experimental data and characterize the effects of contact metallurgy, contact wear/fretting, changes in contact morphology, and change in contact resistance due to cycling. This research accomplishes measurements of contact performance which are not reported so far in the literature.

1.3.2 Material Selection. This study was not intended to select or demonstrate the perfect contact material for use in MEMS switches. However, this research was aimed to develop and demonstrate an experimental method and generate data for screening criteria, screening tests, selection criteria and tests for developing and choosing contact materials for use in MEMS switches. The development of experimental methods and selection tests such as this will lead to a systematic method for material selection in this important field of engineering development.

Another purpose was to demonstrate the effect of hardness (and wear resistance) on contact performance. Alloys were chosen with differing microstructure, hardness and resistivity in order to provide a range of empirical data and show trends, including the tradeoff between hardness and contact resistance. It was expected that differences in contact wear would be seen which could be explained by changes in contact hardness. Gold was chosen as the standard baseline contact material. Two specific alloys chosen in this study were Gold 5% Ruthenium (at%) and Gold-Vanadium Oxide (Au-4%V_2O_5 (at%)), and they were selected due to the advantages offered by their respective microstructure. The contact metals were sputtered on the underside of test cantilevers using a Denton vacuum discovery 18 DC magnetron sputtering system with

a base vacuum of 1.4×10^{-6} Pa at AFRL to a thickness of 300 nm. The Au-4%V_2O_5 films were deposited at Lehigh University using the same method as described in [9].

Precipitate and dispersion strengthening are able to increase material hardness, increase wear resistance, reduce contact adhesion, and offer more possibilities for material development and choices for switch designers when compared to solid solution strengthening. Chen performed experimental studies at NEU showing that Au5%Ru, Au10%Ru and Au10%Pt perform well [37]. The Au5%Ru was shown to have a smaller pull-off force than Au10%Pt [36, 37]. Increasing pull-off force is indicative of higher contact adhesion and likely has a negative effect on contact lifetime. Another factor is that alloying Ru into Au changes the d-band electron structure in gold reducing surface reactivity and thus the likelihood of contamination developing during cycling [37]. The reduced likelihood of contamination and lowered contact adhesion led to the choice of Au5%Ru as the second contact material in the present study.

Lehigh University recently developed a dispersion strengthened material which shows promise as a MEMS scale contact metal [8]. This material has not been incorporated in a MEMS switch, and thus offered an opportunity to investigate its contact performance. The results from Au-4%V_2O_5 testing demonstrated the utility of the experiment in quickly integrating newly fabricated contact materials without the need to accomplish a full switch fabrication design.

This research focused on developing baseline performance of gold microcontacts and a promising alloy of gold and ruthenium as well as comparison to a promising gold-vanadium oxide alloy developed at Lehigh University. Work on material properties of these and other alloys has been accomplished at AFIT, NEU and Lehigh [8, 36, 142].

1.4 Experimental Setup Overview

The research was accomplished by simulating MEMS contact switches with the use of a custom designed silicon cantilever beam fabricated with a contact bump. An

example of the type of cantilever and bump used during this research is shown in Figure 1.3.

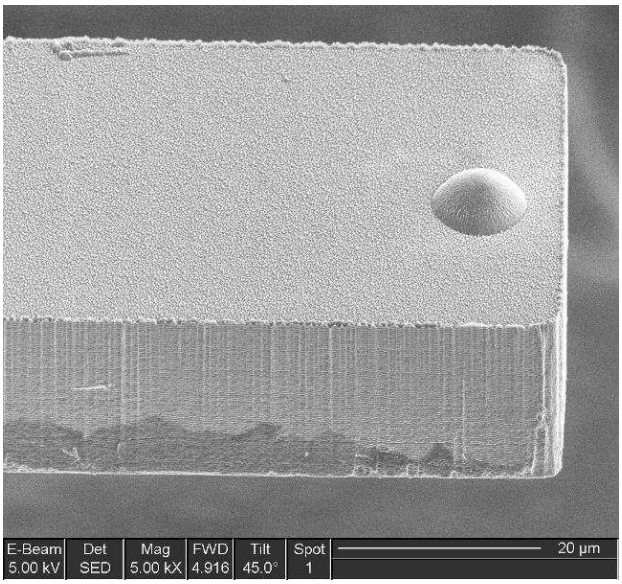

Figure 1.3: Image of a custom designed cantilever and fabricated bump used in testing.

The experiment developed in this research was designed to simulate the action of a MEMS-scale switch. The basic geometry of the test setup is shown in Figure 1.4. A cantilever beam was set up to contact a flat piece of silicon coated with a conductive metal layer. This simulated switch was mechanically cycled by a piezoelectric transducer (PZT). The resistance through the simulated switch was measured using a four-wire measurement technique. This technique provides measurement of the resistance change in the simulated switch over time as it cycles. Three different contact metals were tested. Test alloys were chosen to demonstrate the effectivity of the experimental setup and to develop insight into the relationship of the properties of contact materials to the performance of micro-contacts.

1.5 Layout of Dissertation

First, chapter 2 describes the current state of MEMS contact switch research, including a brief overview of contact theory. Then chapter 3 gives an overview of engi-

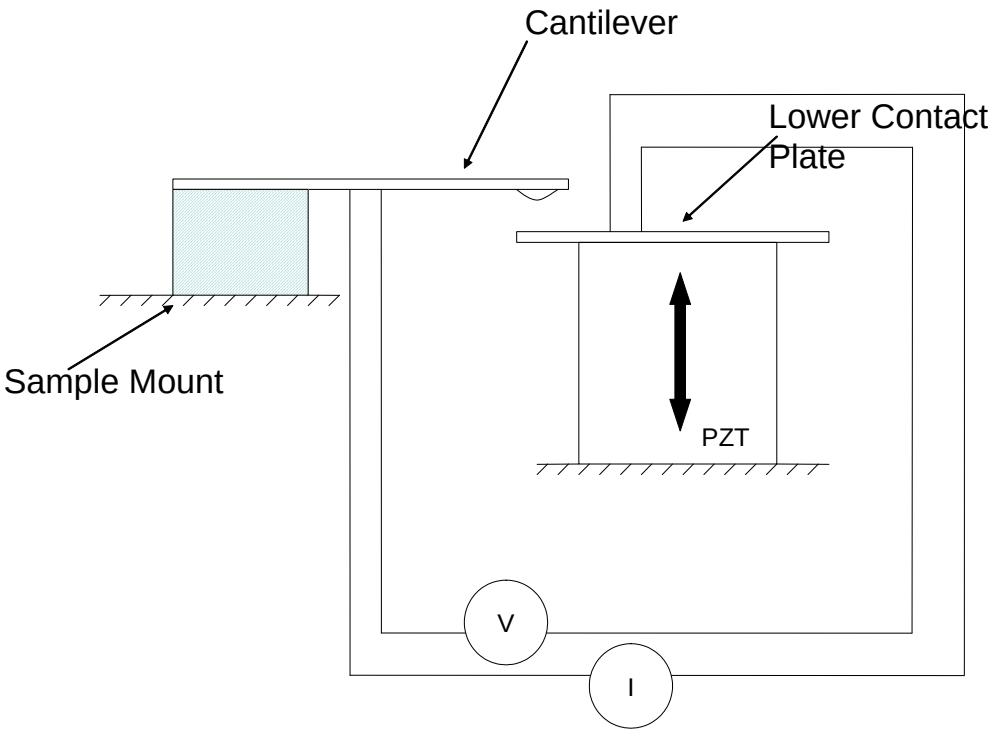

Figure 1.4: Basic concept diagram of simulation of a micro-switch using a micro-cantilever and how the 4-wire resistance measurement was set up.

neering material selection and shows where this research fits in the material selection process. Chapter 4 describes the design and fabrication of custom test cantilevers. Chapter 5 discusses the experimental design and setup, while Chapter 6 discusses the procedure used in testing. Chapter 7 discusses the capabilities of the setup and demonstrates its utility. Chapter 8, 9 and 10 discuss gold, Au5%Ru and Au-4%V_2O_5 results respectively. Chapter 11 summarizes the research accomplished and recommends future work. Appendices provide a description of the test device fabrication development, the bump etching technique developed for this work, the process follower used in cantilever processing, instructions on setup of the experimental apparatus, a summary of research performed at Northeastern University, a short description of RF device performance measurement, categorization of Au-V_2O_5 failure types and the TestWorks test method developed for use in this study.

II. Background on MEMS Contact Switches

This chapter describes the benefits and status of research into MEMS switches, including a brief overview of contact mechanics theory. Typical MEMS switches and their operation are described, as well as current applications of RF MEMS Switches. The current state of MEMS switch lifetime and reliability are discussed, followed by other characteristics of MEMS ohmic contact switches, including power handling capability and actuation voltage. DC and RF testing are compared and basic contact mechanics theory and its current state in the area of micro-size contacts are reviewed along with current models of contact. Contact wear is discussed, as well as the state of research on development of contaminant films in micro-scale contacts. The main types of contact failure in MEMS ohmic contact switches are reviewed and discussed. Also, types of MEMS switches will be discussed.

2.1 Types of MEMS Switches

There are two basic types of MEMS Switches: Metal (or ohmic) contact and capacitive. Figure 1.1 shows a typical metal contact switch developed and used at Northeastern University and Radant MEMS for several studies [161, 163, 165]. Figure 2.1 and Figure 2.2 show examples of capacitive type switches. Metal contact, also called ohmic contact, switches provide a low resistance when in contact and high resistance when open. Capacitive switches change capacitance from low to very high when closed. Ohmic contact switches operate primarily in the RF signal frequency range of DC-60 GHz while capacitive switches are generally most effective in the 10-120 GHz signal range [202]. "Capacitive switches can handle more RF power than metal contact switches and are the preferred switch for applications requiring 100-500 mW of RF power" [202]. However, metal contact switches are the only switch of choice for applications operating at less than 6 GHz [202]. The present research is focused on the mechanics of microcontact in the metal contact type switch.

There are two basic ways in which MEMS switches can be implemented in a circuit: series or shunt. Series switches pass a signal when closed and block the signal

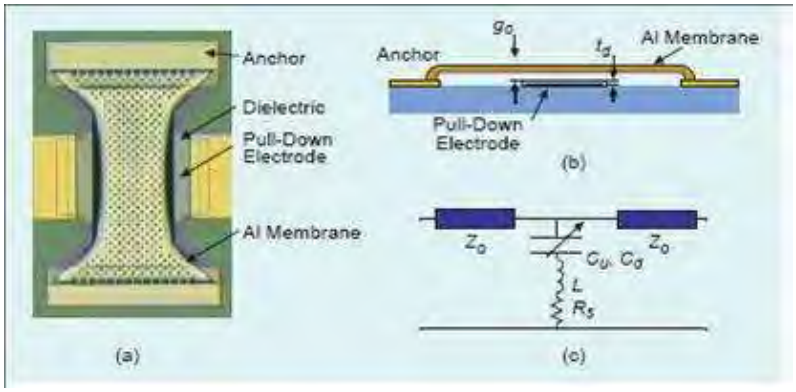

Figure 2.1: Capacitive RF MEMS switch. This is the Raytheon MEMS capacitive shunt switch: (a) top view, (b) cross-sectional view and (c) electrical model [203]. ©2001 IEEE.

when open. Shunt switches are implemented such that the signal is passed while the switch is open, but is shunted to ground when the switch is closed [203]. For example, a capacitive shunt switch provides very high capacitance to ground and no effect to the signal when in the up-state, but when actuated provides low capacitance to ground, generating a short circuit and high isolation of the signal [203]. Thus, the capacitive shunt switch varies the impedance on the signal when opened and closed, passing RF energy when open and shunting it to ground when closed [203]. The main causes of failure in capacitive switches are dielectric charging and contact adhesion failure [203]. One method used to extend the lifetime of switches, both capacitive and metal contact, is encapsulation to prevent contamination and control the environment in which the switch operates [146, 166, 202]. An example of thin-film encapsulation developed by AFRL protecting a switch is shown in Figure 2.2.

Switches can also be categorized by their actuation method. Switches can be electrostatically, magnetically, thermally or piezoelectrically actuated [202]. They can be normally closed or normally open. That is, they are closed until actuated open, or they are open and actuated closed. Electrostatic switches are designed with a contact pad below a movable membrane, cantilever, or doubly supported beam, sometimes called a "bridge" [202, 247]. When a potential difference is put across the actuation pad to the beam, the electrostatic force pulls the beam into contact. The voltage

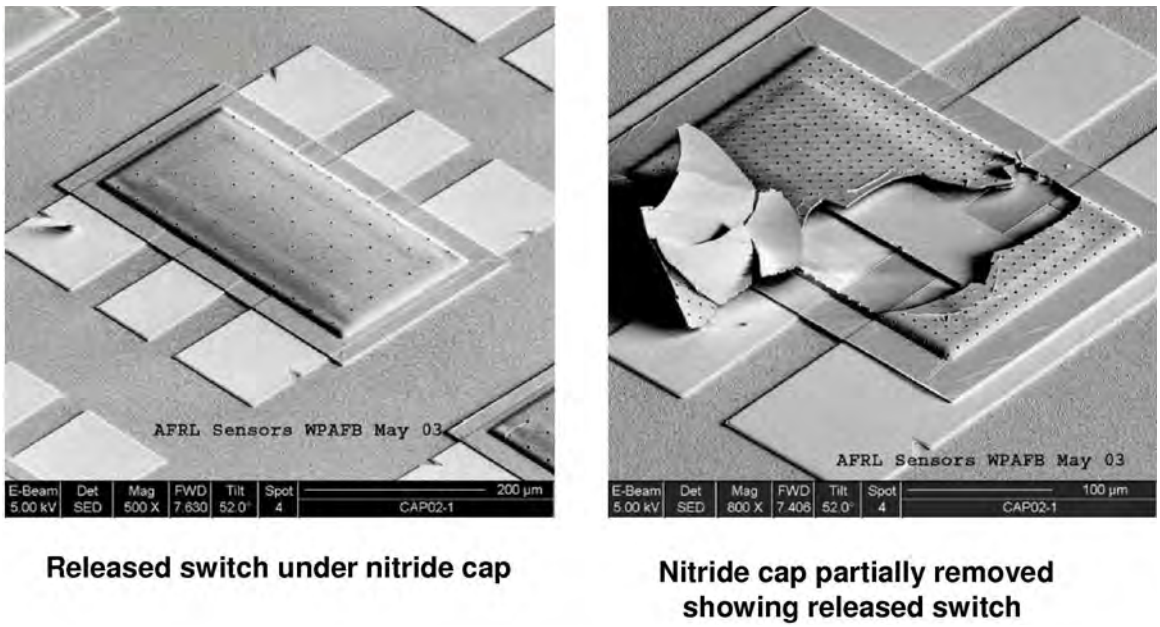

Figure 2.2: Thin-film encapsulated capacitive RF MEMS switch developed by AFRL [64].

applied depends on the design and can be just a few volts, but is more commonly on the order of 20-80 V [202]. The applied voltage can be designed to provide the contact force acting on the electrical contact and the voltage applied can be designed to reduce bounce and improve the speed of switch closure [29]. Electrostatic switches are currently the most successful and most common [202, 203, 241, 247].

MEMS switches have been designed as single-pole single throw (SPST) and single-pole double throw (SPDT) configurations [202]. SPST switches can be thought of as simple on/off switches and SPDT switches can be thought of as simple changeover switches [257]. There are significant benefits of continuing research into MEMS switches and improving their performance and reliability. The use and benefits of MEMS switches are described in the next section.

2.2 Benefits of MEMS Switches

MEMS switches have been widely touted as offering significant advantages to RF engineers and developers for applications as widely varying as space radar and cell

Table 2.1: Side-by-side comparison of performance indicators of RF MEMS switches compared to traditional solid-state devices [202].

Parameter	RF MEMS	PIN	FET
Voltage (V)	20-80	3-5	3-5
Current (mA)	0	3-20	0
Power Consumption (mW)	0.05-0.1	5-100	0.05-0.1
Switching Time	1-300 μs	1-100 ns	1-100 ns
Up capacitance (series) (C_{up}) (fF)	1-6	40-80	70-140
Rs (series) (Ω)	0.5-2	2-4	4-6
Cutoff frequency (THz)	20-80	1-4	0.5-2
Isolation (1-10 GHz)	Very High	High	Medium
Isolation (10-40 GHz)	Very High	Medium	Low
Isolation (60-100 GHz)	High	Medium	None
Loss (1-100 GHz) (dB)	0.05-0.2	0.3-1.2	0.4-2.5
Power Handling (W)	<1	<10	<10

phones. MEMS switches have better isolation, lower insertion loss, use less power, show better linearity and are lighter weight than corresponding solid-state switching devices, such as PIN diodes and field effect transistors [247]. Table 2.1 shows a side by side comparison of solid state devices to MEMS switches in several measures of performance for RF systems [202].

This table shows that the two areas where MEMS switches don't compare well are in the voltage required for actuation and power handling capability. In electrostatic switch design, generally the pull in voltage is a trade with the restoring force of the switch. Many designers use a very stiff cantilever or doubly supported beam in order to provide a large pull-off force to avoid adhesion failures. Stiffer beams and higher pull-off forces translate to a higher actuation voltage. The designer must trade pull-off force with actuation voltage. The necessary high voltage can be developed in a system by designing a method to increase the operating voltage when employing this type of electrostatically actuated switch. The benefit of the electrostatically actuated switch type is that the power required to operate the switch is very low.

Power handling is an area of interest to current researchers as well, however many RF applications do not require more than 1 W power [84]. Research into contact physics and contact materials may also provide a better understanding and a method to improve power handling through MEMS switches. The large electric field through very small contacts is a very stressing environment in which the contact material must survive. Further research on microcontact mechanics and contact material behavior while passing current would be extremely valuable for switch designers.

One example of a benefit of MEMS switches has been shown in the success of an Air Force Small Business Innovative Research project with Radant MEMS. The Air Force and other Department of Defense components require light, low power electronically steerable antennas (ESA) and MEMS switch technology offers significant improvements over current systems. The Air Force Research Lab and Radant MEMS recently developed and tested a demonstration 0.4 m^2 ESA showing that it is feasible to build RF antennas using MEMS switch technology [200, 214]. The Radant X-band antenna contains 25,000 MEMS devices, electronically steers 120 degrees and operates over a 1 GHz bandwidth [200, 214]. This antenna replaced a standard antenna and saved weight and power when compared with conventional active ESAs [200, 214]. The array is shown in Figure 2.3. However, for an antenna such as this to realize its full potential, the issues of lifetime and reliability of MEMS switches need to be addressed.

2.3 Lifetime & Reliability of MEMS Switches

Reliability and the reliable lifetime of MEMS switches has been the weak point of the technology to date. Switches exist and have been reported which have successfully lasted for as many as 900 billion cycles, but the lifetime of the most successful switch in a batch is not a valid measure of reliability. This type of reporting is sometimes called reporting of "Hero" results and occurs in the literature [65]. Reliability is more correctly defined as the probability that any given switch will not fail in a given number of cycles [63]. For successful use in space and defense applications, RF

Figure 2.3: Radant MEMS 0.4 m^2 demonstration Electronically Steerable Antenna in Radant's Antenna Test Chamber. It contains 25,000 MEMS devices and operates over 1 GHz bandwidth at X-band. Image reproduced from [214].

switches which survive after several hundred billion cycles with an extremely high probability are needed [181, 203]. Researchers believe that capacitive and metal contact switches can be improved to meet this need with "advances in contact metallurgy, thermal analysis, high-quality dielectric materials, stress control, and mechanical design" [202]. The present study developed and utilized an experimental method to investigate microcontact mechanics and performance as a step in addressing these needs.

However, the current state of switch design and processing parameters are not well enough known so that switch designers and manufacturers are able to accurately predict which switches among a given lot are going to be the longest lasting. For example, TeraVicta was one of two companies, the other being Radant MEMS, producing high-quality commercial RF MEMS switches. TeraVicta's published reliability data,

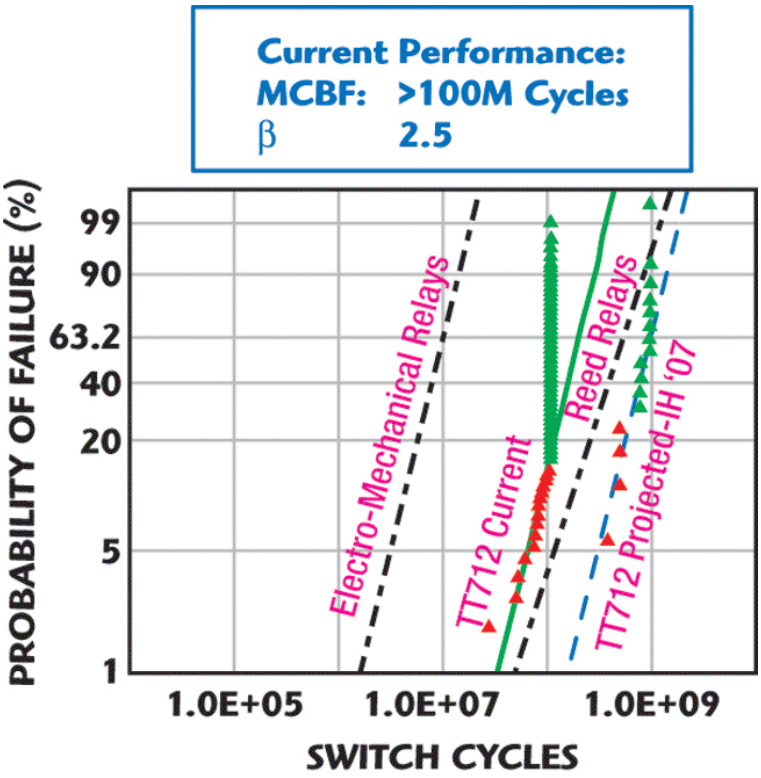

Figure 2.4: Published lifetime reliability of TeraVicta commercial MEMS switches. This is a Weibull plot of test data and uses Mean Cycles Between Failures (MCBF) as this is a more valid measure for switch lifetime than Mean Time Between Failures (MTBF) [171]. Reprinted with permission of Microwave Journal.

shown in Figure 2.4, shows that the Mean Cycles Between Failure (MCBF) numbers for their current commercial switch have a high reliability (approx 1% or less probability of failure) to 150 million cycles [171]. However, note that TeraVicta has since gone out of business. It is important to understand that a certain switch design may produce switches which operate to more than 700 billion cycles, such as reported by Radant MEMS [200], but there is no indication of distribution of successful switches within a lot. Recently, Radant MEMS switches were reported as having a mean cycles-to-failure lifetime of 430 billion cycles [181]. The scatter of lifetime results for the sets of switches reported by these researchers is also very broad. When reading literature, the reader must note how the number is presented in order to understand the actual reliable lifetime that is being presented and to understand where the possibilities for research and improvement of understanding in the field exist.

The study presented here provides information to MEMS switch researchers and designers on contact damage and lifecycle evolution useful in designing and understanding the behavior of MEMS metal contact switches. A background of published lifetime and reliability studies of MEMS switches is described next.

RF MEMS reliability has been studied by many researchers, including DeNatale, Mihailovich, DeWolf, and others [50, 51, 174]. DeNatale focused on reliability limiting mechanisms that can impact RF MEMS devices with an emphasis on issues relevant to switch cycling lifetimes. He reported that contact degradation effects can be mitigated through selection of contact materials, but the work didn't offer a description of how to select contact materials for an optimum reliability and switch lifetime extension [174]. DeWolf focused on methods of performing reliability testing of MEMS [52]. Patton and Zabinski have studied failure mechanisms in both ohmic contact and capacitive MEMS switches, both focusing on adhesion failures in the gold-gold switches [188–190].

Since that time, there have been published reports of the extension of MEMS switch lifetimes, including Radant MEMS contact switches with from up to 10 billion cycles [160] to 900 billion [80], MIT Lincoln Laboratories capacitive switches with lifetimes of up to 10 billion cycles [203], and lifetimes up to 100 billion cycles for MEMTronics capacitive switches [80]. As of June 2007, two companies were producing commercial MEMS Switches [79]. However, even though companies are shipping commercial RF MEMS switches and MEMS switches have been used in technology demonstration projects such as the Air Force Small Business Innovative Research (SBIR) program, reliability and lifetime remain among the critical issues for widespread use of these devices [75].

2.4 Contact Material

The majority of work on MEMS contact switches has used gold as the contact metal for its excellent conductivity, low hardness, and resistance to the formation of oxide layers, even though Schimkat and Varadan, et al. recommended that gold

is not an appropriate microrelay contact metal due to its high adherence [217, 247]. Many researchers have published work on MEMS contact switches using gold as a contact metal [61, 62, 107, 115, 140, 161, 163, 173, 189, 190, 252, 253]. Schimkat, Chen et al., Lee et al., Kwon et al. and Randall performed research on other contact materials [36, 137, 142, 201, 217]. Schimkat looked at Au, AuNi5 (5% Ni) and Rh in his test setup. His contacts were small, although they don't appear to have been at the microscale and the contact forces in his work ranged from micro-Newtons to 10 mN [216]. Researchers at Bell Labs as early as 1974 were looking into contact material properties and alloys to reduce contact adhesion problems in electrical contacts [224]. Hyman tested contacts with gold, rhenium, and palladium flash coated contacts [108]. Coutu fabricated, tested and presented eight lifetime resistance test results for microswitches with metal alloys as contact materials, two switch designs with each of four materials, one test for each switch design/contact material combination [43, 45, 46]. Coutu excluded materials other than solid-solution alloys and developed a method which focuses solely on solid-solution alloys as contact materials [43, 45–47], primarily due to ease of fabrication [10]. The most advanced work published to date on contact metals and metal alloys for MEMS switches was performed at AFIT and NEU [36, 142]. Kwon, et al. looked at dissimilar contact materials in an attempt to increase the power handling capability of MEMS switches [137] and recommend dissimilar materials such as Au-to-Pt or Au-to-Ir over a solid-solution alloy of Au-6%Pt as "an effective method to enhance reliability" [137]. Randall used rhodium as a contact material to avoid sticking problems [201]. Bannuru, et al. and Williams, et al. developed dispersion strengthened thin films as potential MEMS contact materials. The most successful commercial switch uses "a thin layer of refractory metal deposited on the underside of the beam and on the drain, giving better stiction free lifetime than the more common gold contacts" [156]. This is important, because the thin film is used to provide a wear and adhesion resistant surface while maintaining use of gold as the cantilever structural material. This gives the switch design the benefit of the high performing contact material as well as the RF performance benefits of the gold cantilever. It is

also important to note that RF signals exhibit a skin effect, that is, the transmission of RF signals is limited to the surface layer of the transmission line. For example, a 1 GHz signal in gold is limited to approximately the top 2.5 μm [247]. It is suspected that the material choice plays a large role in the success of this design.

One area open for research is in the behavior of the contact as it is cycled and the influence of material properties on contact parameters. Previous research in the area of microcontacts has not analyzed the effect of material properties on lifetime contact switch performance. This research addresses these issues in an attempt to provide information useful to switch designers. The present research begins to systematize knowledge of microcontact mechanics and ohmic contact behavior, providing researchers further insight into the material properties necessary to improve switch designs. This was accomplished by the design and construction of an experimental method to directly compare contact behavior of different materials as well as conduct parameter measurement of three candidate contact materials.

2.5 Power Handling Capability

MEMS switches, due in part to their small size, have low power handling capability. Most reported RF MEMS switches are designed to handle only several hundred milliwatts [252]. Wang, et al. have reported a switch designed and fabricated to handle up to 10W RF power at a frequency of 8-12 GHz [252]. Their solution is to have a large, flat contact pad to minimize contact resistance and avoid ohmic heating due to a large signal current. However, they don't describe the contact surface in detail, and only describe the contact material as gold. Performance results, including lifetime reliability, for their switch is not yet reported. Lifetime switch tests are generally measured at a current of 20 mA or less, and the current is applied only during switch closure [159]. This is referred to as "cold-switching". There is clearly room for research into microcontact mechanics and material properties which could improve the current handling capability of micro-switches.

2.6 DC to RF Test Comparison

Insertion loss is a primary metric of RF switch performance. Insertion loss is a measure of the power loss introduced into a system roughly analagous to resistance in a DC circuit and is measured in negative dB. The formal definition of dB is: $dB = 10 \log \frac{P_{out}}{P_{in}}$ [84]. A lossless device would have an insertion loss of 0 dB and a device which completely attenuated the signal would have an insertion loss of -∞ dB [166]. The characteristic impedance of RF systems designed to optimize power is 50 Ω [84]. RF devices are designed to avoid impedance mismatches in the system. RF Switches are therefore designed to maintain 50 Ω through the switch [84]. Any additional resistance in the switch will cause insertion loss.

RF testing must verify the insertion loss and other performance characteristics of RF devices. However, Hyman determined that the microwave performance of a closed relay can be modeled as a simple resistor to a first order equivalent [106, 108]. The relay resistance is used to calculate the insertion loss of the relay assuming it is significantly less than the impedance of the RF input and output lines. The test equipment Hyman used had an input and output impedance of 50 Ω. Equation 2.1 shows the method to calculate insertion loss based on switch resistance (R_{relay}) and driving impedance (R_0) [108].

$$I.L. = 10 \log \left[1 + \left(\frac{R_{relay}}{R_0} \right) \right] \tag{2.1}$$

Equation 2.2 shows the simplified form for a 50-Ω system [108].

$$I.L.|_{R_{relay} << 50} = (0.087\ dB/\Omega) \times R_{relay} \tag{2.2}$$

Transmission of RF power is different than transmission of DC current. However, Hyman also showed that the RF power-handling of a micro-relay can be compared to the DC current handling of a micro-relay in terms of heat dissipation of the contact [108]. He found that the RF r.m.s. current level which caused relays to fail

was slightly lower than the DC current which caused identical devices to fail during hot-switching. Therefore, it was demonstrated that RF power handling capabilities were closely related to DC power handling capabilities [108].

The study presented here used a simple DC circuit setup to determine performance of various contact materials. The DC test setup was conceived due to the difficulty and expense of passing RF signals, as RF components cost significantly more than their equivalent DC components and the results of DC testing were shown by Hyman to be closely related to RF performance. The insertion loss of a switch utilizing a conductive thin film can be predicted by its DC contact resistance and the thermal behavior of the contact material can be estimated using DC current testing [38, 108], therefore DC testing is appropriate for the study performed. Other RF switch performance data is intimately related to switch design, so other test methods would me more appropriate for estimating those parameters. Appendix F includes a brief discussion of RF performance measurements.

2.7 Actuation Voltage

Another difficulty in widespread implementation and commercial use of MEMS switches has been that the actuation voltage (e.g. pull-down voltage) has been very high, on the order of 40-120 V. [159]. University of Illinois researchers reported designs with typical actuation voltages of 15-20 V [15]. Radant MEMS reports threshold voltage of 60V with contact overdrive of 100 V [156]. The different choices for driving voltage are due to the competing requirements of cantilever beam designs with high enough spring constant to open the switch after the pull-down voltage is released, and at the same time, enough contact force for a good electrical contact at the contact point. Different designs require different contact force and thus different driving voltage, which are usually relatively high and more than is generally available in current system circuit designs.

However, recently reported results from H.C. Lee, et al. propose a design which requires low voltage operation of only 2.5 V using piezoelectric actuation [140]. They

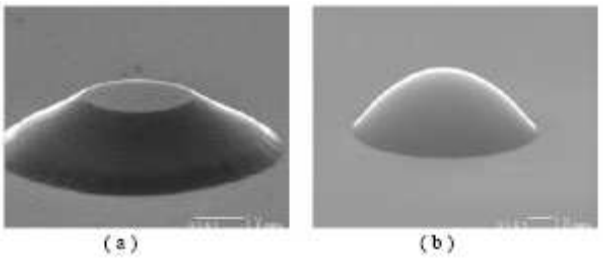

Figure 2.5: These are contact bumps used by Chen for testing at Northeastern University. (a) Flat-topped, (b) Hemispherical [37]. Reprinted with permission.

used gold contacts, however, they do not report contact evolution, lifetime, or reliability of the switch. Harder contact materials generally are expected to resist wear longer than relatively soft materials, but require a larger contact force to make good electrical contact. Effects of contact material choice in the design trade-off is clear, with harder contact materials requiring higher contact forces and thus possibly higher actuation voltages. The contact forces used in MEMS switches range from 50 μN - 2 mN [202].

2.8 Contact Bump Designs

Some researchers include the shape and design of the contact bumps used in their switches and tests, however many do not describe or show images of the contact bumps used in their switches(e.g. [106, 140, 175, 215, 252]). There does not seem to be a consensus on the best design for long lasting switches. For example, Chen used both rounded hemispherical and flat-topped bumps as shown in Figure 2.5. Another image of gold coated rounded bumps used at Northeastern is shown in Figure 2.6. Figures 2.7 and 2.8 show the switch and contact bump detail for an NEU developed switch. A rounded bump with a rough surface from [164] is shown in Figure 2.9.

Jensen also used a flat-topped bump, although his was square in shape [115]. It is shown in Figure 2.10. His bump is 1.18 μm high, and varied in size between 5 x 5 and 20 x 20 μm [115]. AFRL produced switches with flat tops and an edge surrounding them as shown in Figure 2.11 [63]. The fabrication technique was also altered slightly to produce some test switches with rounded bumps as shown in Figure

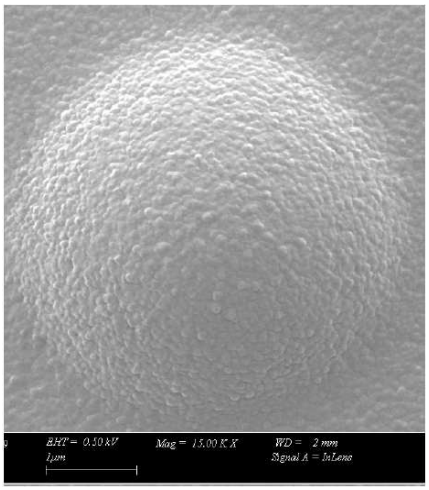

Figure 2.6: This is a gold coated contact bump used at Northeastern University for contact adherence tests. This is SiO_2 coated with 250nm of gold [170]. ©2006 IEEE.

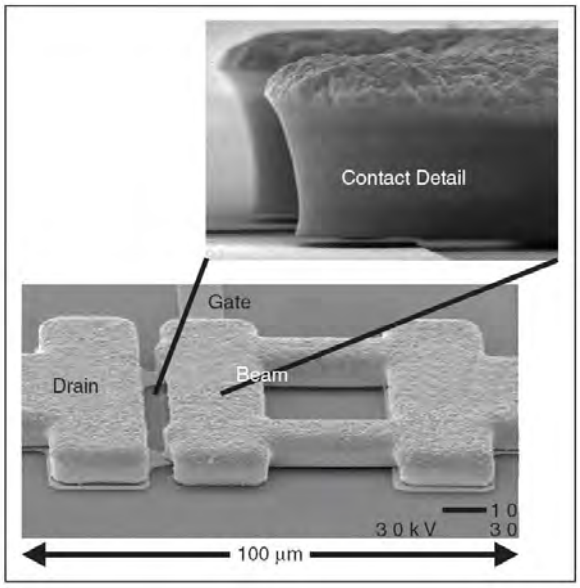

Figure 2.7: Contact detail image for Northeastern University developed switch [159, 162]. ©2003 IEEE.

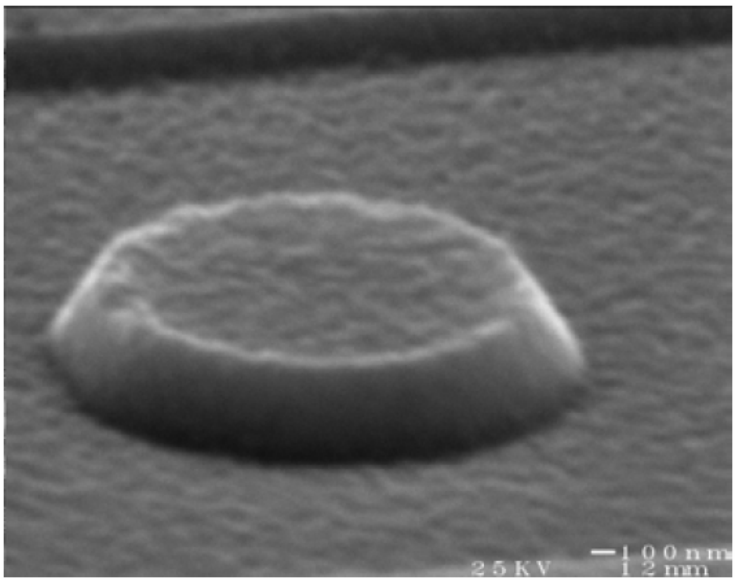

Figure 2.8: Contact bump image for Northeastern University developed switch shown in Figure 2.7 [159, 162]. ©2003 IEEE.

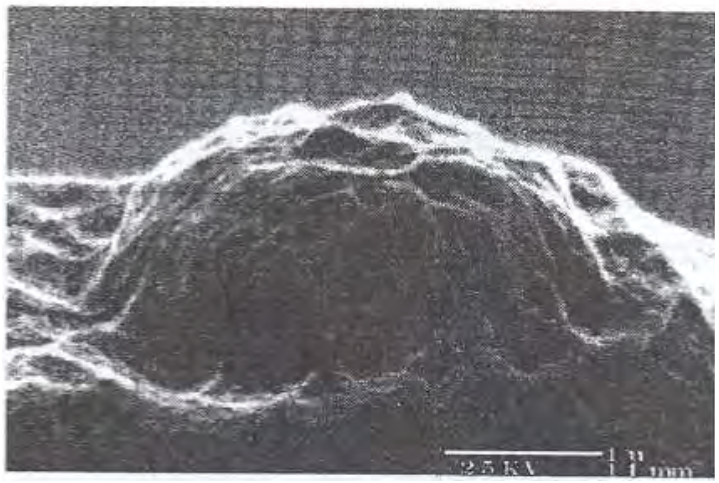

Figure 2.9: Rounded contact bump with rough surface [164, 202]. ©1997 IEEE.

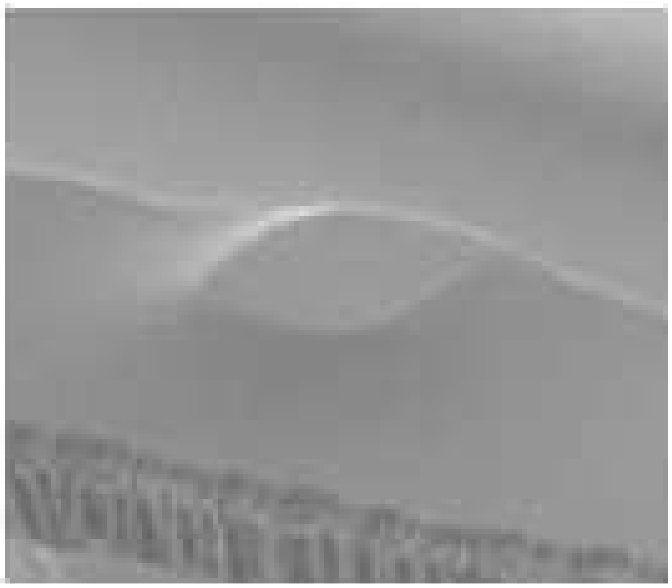

Figure 2.10: Flat Topped Contact Bump [115]. ©2005 IEEE.

2.12 [63]. No difference in performance was noted between the flat and the rounded AFRL bumps, although a specific study was not performed [63]. Gregori et al. used a nanoindenter on Rockwell Scientific RF MEMS contact switches [92,93]. The contact bump in their switches is rounded and is shown in Figure 2.13.

It is clear that there are a variety of shapes, sizes, and surface conditions of bumps being used in microswitches as well as in microcontact studies. It is difficult to compare the bumps and surfaces directly, as the scale of electron microscope images are not always shown and the surface is not always in focus enough to show the grain structure and roughness of the contact surfaces. None of the research cited here specifically compared performance between different contact bump shapes. Jensen [115] compared different sizes of the same shape and surface. There appears to be no comparisons of contact shape performance in the literature or any determinations of how the shape affects the lifetime characteristics of microswitches. However, if contact is in the plastic regime and contact area can be calculated using only material hardness and contact force as described in Section 2.9.4, contact bump design likely plays only a small role in microswitch performance. It is important to note that many researchers do not report contact information, which includes the size, shape

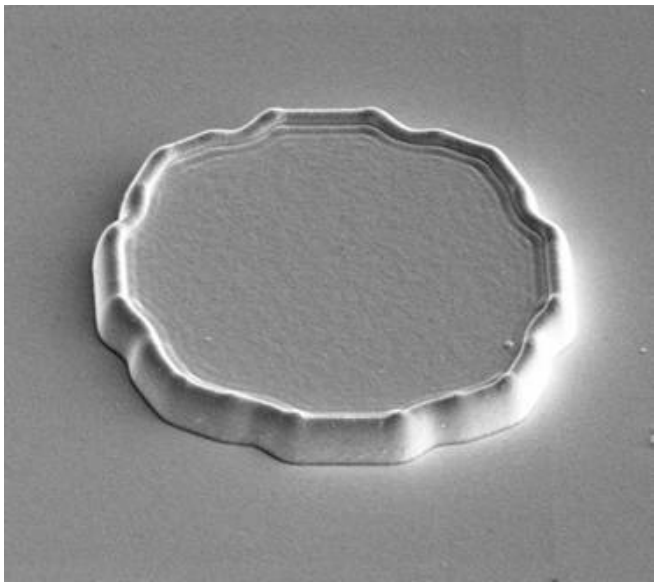

Figure 2.11: Flat Topped Contact Bump used by AFRL [63].

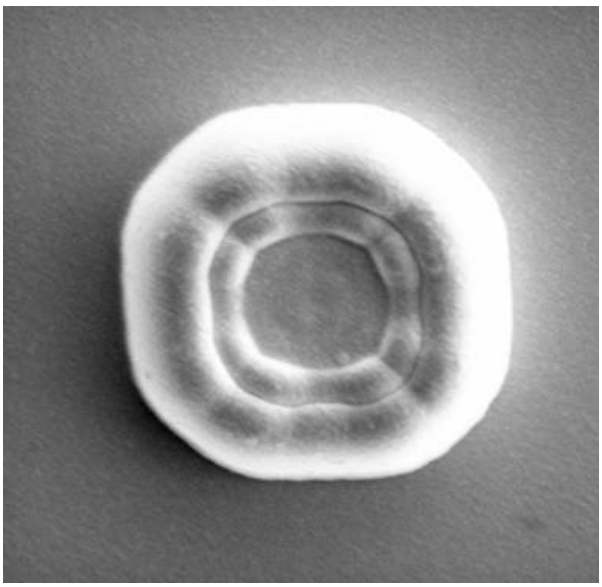

Figure 2.12: Rounded Contact Bump used by AFRL [63].

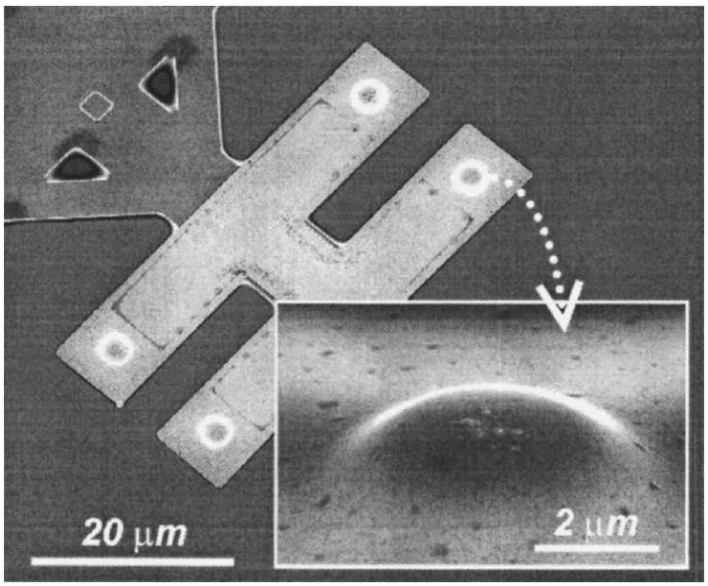

Figure 2.13: This is a Scanning Electron Microscope image of the lower side of a Rockwell Scientific RF-MEMS switch used by Gregori. Detail is shown in the inset with a tilt angle of 52° [92].[2]

and surface condition and other details of the contacts included in their switch designs (e.g. [15, 105, 139, 156, 183]). The next section describes some of the basic theory and work which has been done on contact mechanics theory in order to describe the mechanical and electrical behavior of microcontacts.

2.9 Contact Mechanics Theory

Contact mechanics is important to this study. The physical contact between two bodies is required for metal-contact switch operation, and the mechanics of this contact plays a strong role in the eventual degradation or failure of the electrical characteristics of the switch. The study of macro-switch contacts is applicable in some ways to the micro-scale. However, material properties scale with size. Generally, hardness has been found to be greater at the micro/nano scale while coefficients of friction and wear rates are smaller [20].

[2]Reprinted with permission from Applied Physics Letters, vol 87, no 15, "Mechanical creep as a life-limiting factor of radio frequency microswitches", G. Gregori and D.R. Clarke, Copyright 2005, American Institute of Physics

The mechanical contact of the micro-switch is described as either elastic, plastic, or elastic-plastic in the literature, depending on whether the local stresses are greater than the plastic yield point at the micro-mechanics level. The transport of electrons through the contact is either diffusive, ballistic, or quasi-ballistic [3], depending on the comparative size of the real contact area to the mean free path of electrons in the contact metal. The mean free path of electrons in most metals is 5-30 Å, depending on the energy of the electron [149]. Ziad performed some initial work analyzing contacts in between macro size and micro size scales. The contact diameters studied in that work were 100 μm, 200 μm and 500 μm respectively [268]. However, that research was done at a scale which is still larger than that of operative metal-contact micro-switches. Majumder developed a clean metal contact resistance model and compared resistance results over switch cycles for gold-on-gold microswitches [163]. Majumder also further developed the contact model and successfully compared it to experimental results [161, 165]. Majumder's research into contact resistance was accomplished at Northeastern [160, 161]. Northeastern University researchers developed the first methodology to simulate ohmic contact MEMS switches using an AFM setup with detached cantilevers contacting on a flat surface [39].

Contact resistance can be modeled based on either single or multiple asperity models. Majumder developed a multiple asperity model which appears to agree with experimental results using the NEU DC contact micro-switch [165]. He used a single asperity model as an upper bound on the contact resistance. Much work has been done on single contact resistance studies, for example Pruitt who used cantilevers of various stiffnesses to compare resistance at low contact force to Hertzian elastic contact theory [198] and Ziad [268] but only a few such as Majumder, Chen, and Mihailovich focused on contact evolution [37,163,174]. Researchers have also reported on the transfer of material between contact surfaces. Hyman's work on gold contacts shows an example of material transfer in a micro-contact from a current of 10 mA and 200-500 μN contact force [107, 108].

The evolution of electrical contacts is different under hot-switching and cold-switching conditions. Hot-switching is defined here as the making and breaking of electrical contact while current is being passed through the contact, and cold-switching is defined as making and breaking of the mechanical contact without current flowing. Generally, the lifetime of MEMS switches are significantly longer under cold-switching conditions and switch manufacturers generally report their switch lifetimes under cold-switching.

2.9.1 Hertzian Contact Model. The simplest contact theory is the Hertz theory of elastic contact. This theory assumes that the contact area must be small in comparison to the dimensions of each contacting body, and small in comparison to the relative radii of curvature of each of the contacting surfaces, in other words, that each solid can be considered to be an elastic half-space. The theory also requires that the strains in the contact region are sufficiently small such that the linear theory of elasticity may be applied. Hertzian contact also assumes that the surfaces are frictionless [119]. A commonly referenced case developed by Hertz is the contact of a sphere to a flat, which is similar to the contact envisioned in a contact switch. The following equations, presented in Johnson's classic work on contact mechanics [119], are developed from the Hertz theory for contact radius, compression, and maximum pressure.

$$a = \left(\frac{3PR}{4E^*}\right)^{\frac{1}{3}} \tag{2.3}$$

$$\delta = \frac{a^2}{R} = \left(\frac{9P^2}{16RE^{*2}}\right)^{\frac{1}{3}} \tag{2.4}$$

$$p_0 = \frac{3P}{2\pi a^2} = \left(\frac{6PE^{*2}}{\pi^3 R^2}\right)^{\frac{1}{3}} \tag{2.5}$$

where a is contact radius, δ is compression, p_0 is maximum contact pressure, P is contact load, R is relative radius of curvature, and E^* is given by:

$$\frac{1}{E^*} = \frac{1-{\nu_1}^2}{E_1} + \frac{1-{\nu_2}^2}{E_2} \tag{2.6}$$

where E_1 and E_2 are the moduli of elasticity and ν_1 and ν_2 are Poisson's ratio for the contacting materials. If both surfaces are curved, the relative radius of curvature can be calculated using:

$$\frac{1}{R} = \frac{1}{R_1} + \frac{1}{R_2} \tag{2.7}$$

The elastic contact force can alternately be calculated using Hertz contact theory, if the area of contact is known [262].

$$\Delta F_e = \frac{4E^* a^3}{3R} \tag{2.8}$$

The contact stresses can be calculated using the theory of elasticity, as accomplished by Timoshenko, Goodier and Johnson based on Hertz's theory [119,243]. One very interesting result of Hertz contact theory is that the maximum shear stress in the contact does not occur at the surface of the spherical contact, but below the surface. The maximum shear stress occurs at 0.48a (for $\nu = 0.3$) and is approximately $0.31p_0$ [119]. Thus, plastic yielding can be expected to initiate beneath the surface. This is an interesting result considering the many experimental studies showing material transfer between contacts.

Also, Hertz found that the maximum tensile stress in the flat surface occurs at the edge of the contact circle at the surface and is given by [70]:

$$\sigma_{max} = (1-2\nu)\frac{P}{2\pi a^2} \tag{2.9}$$

This stress acts in a radial direction on the flat outside the sphere and decreases as the inverse square of the distance away from the center of the contact [70].

The largest stress in the contact is the maximum compressive stress in the contact and is located at the center of the surface of contact (σ_z). The other two principal stresses at that same point are equal to $\frac{1}{2}(1+2\nu)\sigma_z$ [243]. Plastic yielding can be calculated using the von Mises criterion, shown in Equation 2.10 [103].

$$(\sigma_1-\sigma_2)^2+(\sigma_2-\sigma_3)^2+(\sigma_3-\sigma_1)^2=2S_y^2 \tag{2.10}$$

This theory predicts yielding occurs whenever the distortion energy in a unit volume equals the distortion energy in the same volume when uniaxially stressed to the yield point [227], in equation form this is $\sigma_{vm} \geq S_y$. The stress causing contact yielding below the surface can be shown based on the von Mises stress for the three dimensional state of stress as [227]:

$$\sigma_{vm}=[\frac{(\sigma_1-\sigma_2)^2+(\sigma_2-\sigma_3)^2+(\sigma_1-\sigma_3)^2}{2}]^{\frac{1}{2}} \tag{2.11}$$

In the case of contact, the three stresses σ_x, σ_y, σ_z are the principal stresses, σ_1, σ_2 and σ_3. Note that $\sigma_x=\sigma_y$ at the point of maximum shear stress, and that the shear stresses are $\sigma_{xz}=\sigma_{yz}=\frac{\sigma_x-\sigma_z}{2}=\frac{\sigma_y-\sigma_z}{2}$ Substituting these values into Equation 2.11 produces:

$$\sigma_{vm}=[\frac{(\sigma_y-\sigma_z)^2}{2}+\frac{(\sigma_x-\sigma_z)^2}{2}]^{\frac{1}{2}}=[(\sigma_x-\sigma_z)^2]^{\frac{1}{2}}=\sigma_x-\sigma_z \tag{2.12}$$

Thus, since $\sigma_{xz}=\frac{\sigma_x-\sigma_z}{2}$, we have that:

$$\sigma_{vm}=2\sigma_{xz} \tag{2.13}$$

and therefore, yielding will occur when $\frac{\sigma_{vm}}{2}=\sigma_{xz}\geq\frac{S_y}{2}$.

Plastic deformation is defined as a permanent change of relative positions between atoms or molecules in a material. This permanent change in crystal arrangement consists largely of group displacements in the lattice on planes of least resis-

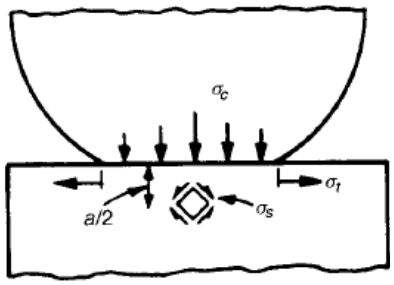

Figure 2.14: Schematic diagram of state of stress. Maximum shear location (σ_s) and maximum tensile stress locations σ_t, along with the compressive stress distribution (σ_c) are shown [5][3].

tance [266]. The maximum shear stress can be used to determine when plastic yielding begins, when the plastic zone appears and when the plastic field is fully developed. As noted above, the point of maximum shearing stress and the location of first yield is below the surface of the contact. Based on the von Mises yield criterion shown above, plastic deformation initiates at the location of maximum shearing stress when

$$\sigma_s > \frac{S_y}{2} \tag{2.14}$$

where σ_s is shear stress and S_y is the yield strength of the material. A diagram of the contact, with the state of stress is shown in Figure 2.14.

Therefore, since yielding initiates for materials with $\nu = 0.3$ when $0.48P_{ave} = 0.5S_y$, then

$$P_{ave} \approx 1.1S_y \tag{2.15}$$

that is, the mean pressure of the contact (P_{ave}) is approximately 1.1 times the yield strength of the material (S_y) [236]. The plastic zone is fully developed when the average contact pressure is approximately three times the yield strength of the material [5], thus when

$$P_{ave} \cong 3S_y \tag{2.16}$$

[3]This figure was published in *Materials Selection in Mechanical Design*, Michael F. Ashby, Butterworth Heinemann, p391, Copyright Elsevier 1999.

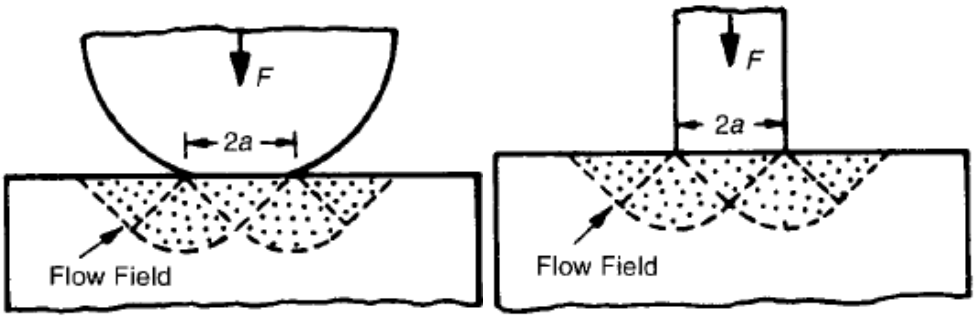

(a) Plastic flow field for hemispherical on flat contact [5]

(b) Plastic flow field for cylindrical flat punch contact [5]

Figure 2.15: Comparison of fully developed plastic flow fields for two types of contact.[4]

the shape of the approximate plastic flow field in this case when fully developed is shown in Figure 2.15(a) [5].

The shape of the plastic flow caused by a flat cylindrical punch is shown schematically in Figure 2.15(b). Some researchers have used flat-topped contacts, so this gives a qualitative feel for how the fully developed plastic flow compares to a hemispherical on flat contact.

Hertz contact theory is an excellent starting point for calculating contact areas, and has been used in calculating the contact of asperities in more detailed analyses of rough surface contact. However, in realistic contact situations, surface roughness and plasticity plays a very important role.

2.9.2 Surface Roughness [240, 270]. In Hertz contact theory, the surfaces are assumed smooth. In reality, however, all surfaces have some amount of roughness. In micro-scale contacts, this roughness can lead to a real contact area which varies significantly from the estimated Hertzian contact area. The actual contact area is of extreme importance in understanding and describing the electron transport through an electrical contact. This is due to the effect of ballistic electron transport through the contact area as described in [3, 118]. The measurement of surface texture and

[4]These figures were published in *Materials Selection in Mechanical Design*, Michael F. Ashby, Butterworth Heinemann, p391, Copyright Elsevier 1999.

the description of surface roughness is extremely complicated, and there are many methods used. Many methods used to measure surface roughness exist because there are a great number of applications for surface descriptions in many areas of engineering materials development. At least 24 national standards committees have assigned names and definitions for the parameters used to describe surface roughness [240]. The most common method of measuring surface roughness, particularly on the micro-scale is through the use of Root-Mean Squared variation.

Surface topography is divided into three main categories: form error, waviness, and surface roughness [240]. Form error is the deviation of the surface from its nominal shape. If the shape should be spherical, then the form error is its deviation from a perfect sphere. Waviness is defined as the wavelike component of the deviation from the nominal shape. This could be considered to be ripples in a flat surface. Roughness is the component of deviation from nominal which is made up of many randomly shaped asperities or undulations. The division of surface variation from nominal into these three categories is arbitrary, but is done based on the size of the sample and the analysis at hand [240].

The four basic variables of interest in analyzing surface roughness are the maximum deviation from centerline (Max R_a), arithmetic average deviation from centerline (R_a), Root Mean Squared (RMS) deviation from centerline (R_{RMS}), and maximum peak-to-valley distance (PV). The arithmetic average deviation from centerline can be seen in Figure 2.16 and the maximum peak-to-valley distance is shown in Figure 2.17. These variables can be measured in various ways, including the use of stylus profilometers, Atomic Force Microscopes, or interferometers, such as a Zygo.

It is important to note that an analyst must be careful in using only one of these parameters to describe a surface. For example, Figure 2.18 shows three different surfaces with the same maximum Peak-to-Valley measurement. However, the reader can easily see that the three represented surfaces have significantly different surface

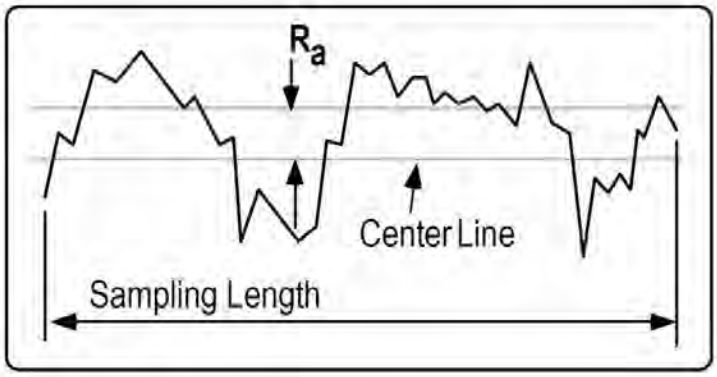

Figure 2.16: Arithmetic mean deviation from centerline factor for describing surface roughness. The max deviation from centerline could be easily selected [270]. Reproduced with permission from Zygo Corporation.

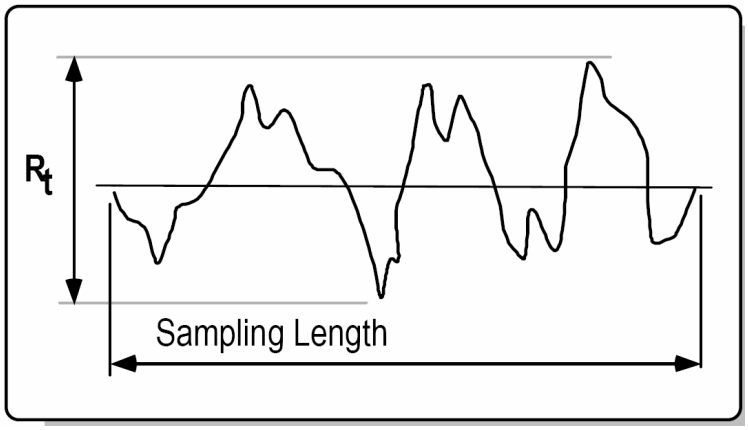

Figure 2.17: Maximum Peak-to-Valley distance used to describe surface roughness [270]. Reproduced with permission from Zygo Corporation.

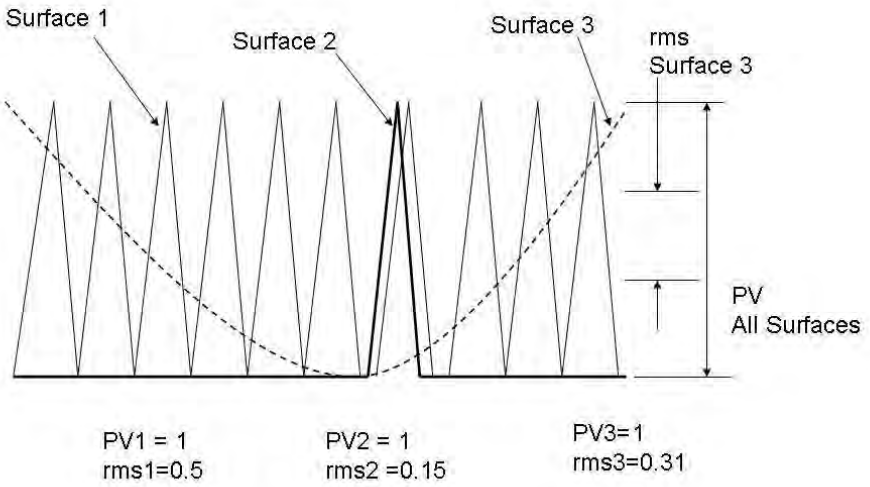

Figure 2.18: Very different surfaces showing same Peak-to-Valley measurement (based on [269]). Reproduced with permission from Zygo Corporation.

roughnesses. Note also that the RMS value is lowest for surface 2, the surface with only one protruding asperity.

Arithmetic average is calculated by the following formula, per ANSI/ASME standard [240]:

$$R_a = \frac{1}{L}\int_0^L |y| dx \tag{2.17}$$

where L is the sampling length, and y is the height relative to centerline. Root Mean Squared deviation from centerline is calculated by ANSI/ASME standard by the following formula [240]:

$$R_{RMS} = \left(\frac{1}{L}\int_0^L y^2 dx\right)^{1/2} \tag{2.18}$$

Generally, the RMS deviation can be used by itself to provide general knowledge of the roughness of a surface. This is the only roughness parameter described here which can be used in that manner, and it is the only measure of surface roughness which can be scale independent [18]. A general understanding of roughness is necessary in order to estimate actual contact area of two solid surfaces in contact.

2.9.3 Plasticity Index. The plasticity of a contact of rough surfaces was determined by Greenwood and Williamson through the use of a plasticity index [86]. This is given in Equation 2.19

$$\Psi = \frac{E'}{H}\sqrt{\frac{\sigma}{\beta}} \tag{2.19}$$

where E' is $\frac{E}{1-\nu^2}$ for mono-metallic contacts, H is hardness, σ is RMS roughness, which is the average height of the asperities, and β is the average radius of curvature of asperities on the surface.

If $\Psi < 0.6$ the contact is elastic and if $\Psi > 1$ the contact is fully plastic, without any dependence on material properties or magnitude of load [86]. These authors found that, except for especially smooth surfaces, the asperities and thus the contact flows plastically under the lightest loads. Other researchers have referenced and used this index as well (e.g [94, 110]).

For a gaussian distribution of surface roughness asperities, and if the mean height (σ) and radius of curvature (β) are known, the contact force (P) can be used to calculate the real elastic area of contact using Equation 2.20 [86, 110].

$$\frac{P}{A} = \frac{1}{4}E'\sqrt{\frac{\sigma}{\beta}} \tag{2.20}$$

thus

$$A_{actualelastic} = \frac{4P}{E'\sqrt{\frac{\sigma}{\beta}}} \tag{2.21}$$

Maugis [168] also reports an interesting result of Greenwood and Williamson's work. The ratio of plastically deformed asperities to elastically deformed asperities can be calculated using the plasticity index. The ratio of plastic contact is given in Equation 2.22 where η is the number of asperities in contact and η_p is the number of plastically deformed asperities [168].

$$\frac{\eta_p}{\eta} = exp(-\frac{1}{\Psi^2}) \tag{2.22}$$

The materials and surfaces used in the present research deform plastically based on this index. Ruthenium was the hardest material contemplated for testing in the present study which would therefore have been the least likely to experience plastic deformation. The material properties used in this sample calculation are E=292 GPa, H=15 GPa, and ν=0.3. The surface characteristics are estimated based on profilometer traces to have an RMS height (σ) of approximately 100 Å, and an asperity mean curvature of radius (β) maximum of 2 μm. Using Equation 2.19 this comes out to be $\Psi = 2.84$, which is clearly in the plastic range. Note that $\Psi > 1$ is the range of plastic deformation. The other materials in the present study are more likely to behave plastically than ruthenium so it can reasonably be assumed that all contacts in this study will be plastic and the contact area described in the next section will be applicable.

2.9.4 Contact Area for Plastic Contact. Hertzian contact theory provides a nominal contact area for any mechanical contact and assumes a smooth surface. However, the actual area of contact depends on the contact of asperities due to surface roughness. If the contact is plastic, a very simple, yet effective, calculation of actual area of contact is given by Slade [230]. Plastic contact area is given in Equation 2.23.

$$F_c = A_c H \tag{2.23}$$

where F_c is the contact force, A_c is the actual contact area, and H is the hardness of the contact material. This equation shows that the actual contact area does not depend on the contact size, but the force and hardness of the contact material.

This can be understood by using an example from Timsit given in [230] where two different size contacts made up of the same surface material are compared. Both contacts have the same surface roughness and therefore the same size and density

of surface asperities. If one contact is 10 times the size of the other, the number of asperities in contact would be n, where the number of asperities in contact in the larger case would be 10n. The average mechanical load on each asperity in the smaller case would be F/n, where the average mechanical load on each asperity in the larger case would be F/10n. If asperity deformation is fully plastic, the area of contact at each asperity in the smaller case would be ten times larger than the area of contact at each asperity in the larger case [230]. This leads to the same overall contact area for both size contacts [230]. Rebeiz states that this simple purely plastic hardness model can be used for contact forces equal to and larger than 200 μN and is expressed in Equation 2.24 [202].

$$A = \pi a^2 = \frac{F}{Hn} \tag{2.24}$$

Another method of calculating contact area, based on the tested resistance of a contact is by Jensen, et al. [115]. This is given by solving Equation 2.25 for the contact radius, a.

$$R_c = \gamma\left(\frac{\lambda}{a}\right) R_M + R_S = \frac{1 + 0.83(\frac{\lambda}{a})}{1 + 1.33(\frac{\lambda}{a})}\frac{\rho}{2a} + \frac{4\rho\lambda}{3\pi a^2} \tag{2.25}$$

where λ is the mean free path of electrons in the conductor, ρ is the electrical resistivity, R_M is the resistance due to lattice scattering (Maxwell spreading resistance) and R_S is the additional resistance due to boundary scattering in small constrictions, also called the Sharvin resistance. Jensen, et al. reported contact resistance tests using a contact which was square and flat in shape, with a height of 1.18 μm and lateral dimensions of 5x5 and 20x20 μm [115]. The contact surface was sputtered gold. They calculated the mean free path of electrons in gold as 38 nm, and using their lowest measured contact resistance of 0.5 Ω and the resistivity of gold of $3.6 \times 10^{-8}\ \Omega \cdot m$, they calculated the radius of true contact area as 51.8 nm using Equation 2.25 [115]. They estimated that the Young's Modulus of their gold film to be 50 $\pm$ 5 GPa, but did not provide an estimate or measurement of the gold film hardness.

2.9.5 Contact Resistance. When current flow is constricted by a reduced area, changing the streamlines of current flow, resistance increases. Many authors have treated this to derive the total constriction resistance of a contact. A particularly good development is given by Llewelyn-Jones in his 1957 text, *The Physics of Electrical Contacts* [153]. Total constriction resistance is shown in Equation 2.26 [103, 153, 230].

$$R = \frac{\rho}{2a} \tag{2.26}$$

where ρ is the resistivity of the contact metal and a is the radius of the actual contact area.

Rebeiz has a slightly different equation, given without derivation or citation in [202]. His formula for Maxwell spreading resistance, which he also calls constriction resistance, is given in Equation 2.27.

$$R = \frac{\rho}{\pi a} \tag{2.27}$$

The equation for constriction resistance is used when the contact area is comparatively large [202]. This would be when the area is larger than the mean free path of electrons in the material. When the radius of the contact becomes smaller than the electron mean free path and the transport becomes ballistic, the Swartjes relation is used [138], shown in 2.28.

$$R_s = \frac{4\rho l}{3\pi a^2} \tag{2.28}$$

where l is the electron mean free path, given as 36 nm for gold, 39 nm for copper, and 53 nm for silver [138]. Using both Equations 2.23 and 2.26, Holm developed a simple equation which predicts the minimum contact resistance for various contact materials, assuming clean surfaces [8, 103].

$$R_c = \frac{\rho}{2}\sqrt{\frac{H\pi}{F_c}} \tag{2.29}$$

where R_c is the contact resistance, ρ is the film resistivity, H is the material hardness and F_c is the contact force. This equation appears to underpredict contact resistance [8], often because of possible interposing contaminant films. Jensen used a combination of constriction resistance and ballistic resistance in calculating contact area based on the measured resistance in his experiment, as previously described in Section 2.9.4.

It is interesting to note that Equation 2.29 for contact resistance shows mathematically that with infinite contact force the contact resistance would be zero Ohms. This is shown mathematically in Equation 2.30.

$$\lim_{F_c \to \infty} R_c = \lim_{F_c \to \infty} \frac{\rho}{2} \sqrt{\frac{H\pi}{F_c}} = 0 \tag{2.30}$$

Equation 2.29 is clearly an excellent rule of thumb for calculating contact resistance, but does not completely capture contact behavior. It is clear that no matter how large the contact force is, with a material interface the contact resistance will not be zero. There is some limiting resistance based on the yield strength of the material and the contact area when the contact is fully plastically deformed. However, there is some contact force which produces a reliable, metallic contact depending on the contact material in use and the switch design.

The contact force used in a switch should be enough to reduce switch bounce and reliably produce low contact resistance. However, the contact force in a switch must be chosen such that it does not cause damage build up in the contact material and possible premature mechanical failure of the material. For reference, Peek and Wagar in their book *Switching Relay Design* report that a minimum contact force of 2 kilodynes (20 mN) is adequate to give contact resistance of less than 0.1 Ω in macro-switches [211]. Hyman reports that hundreds of μN of contact force are required for reliable fully metallic contacts in gold [107].

2.9.6 Sheet Resistance. Contact resistance measurements do not always measure only the resistance due to the interface between two conducting bodies. Sometimes parasitic resistances such as sheet resistance must be included. Sheet resistance is a measure of the electrical resistivity of a layer of conductive material. It is defined as the ratio of electrical resistivity to thickness ($R_s = \rho/t$) [111]. The value of sheet resistance is given in Ohms (Ω) or Ohms per square ($\Omega/\square$). Sheet resistance can be calculated for a thin-film of conductive metal. For example, if a thin-film of gold is 300 nm thick, the sheet resistance based on an electrical resistivity of ρ=3.6 $\mu\Omega cm$ would be 0.12 $\Omega/\square$. For a ruthenium thin film of 300nm thickness, with an electrical resistivity of 13.8 $\mu\Omega cm$, the sheet resistance would be 0.46 $\Omega/\square$. This calculated value matches relatively well with the value of 0.8 Ω measured across a piece of silicon coated with 300nm thick ruthenium using a multimeter. The additional 0.4 Ω was likely due to the resistance through two solder joints as the copper measurement wires were soldered to the surface of the ruthenium approximately 4 mm apart.

2.9.7 Contact Heating. Current through a contact heats the contact. The current passing through a constriction creates heat and the heat can only be removed by conduction through the bodies in contact [230]. The physical interface heats up at the contact asperity, or a-spot. This temperature can be related to the voltage drop across the contact by Equation 2.31:

$$V = 2[2\int_{T_1}^{T_m} \lambda\rho dT]^{\frac{1}{2}} \tag{2.31}$$

This equation yields the well-known form of the voltage-temperature relation shown in Equation 2.32 for contacts of a single contact material, assuming that the thermal conductance and electrical resistivity vary little with temperature [230].

$$T_m - T_1 = \frac{V^2}{8\lambda\rho} \tag{2.32}$$

The Wiedemann-Franz law can be used to remove the limitation of changes with temperature variation and calculate temperature changes in contacts made of more than one material. The Wiedemann-Franz Law states that the thermal conductivity and resistivity of metals vary such that the thermal conductivity, λ, and electrical resistivity, ρ, are related by the expression given in Equation 2.33 [103, 153, 230]

$$\lambda\rho = LT \tag{2.33}$$

where L is the Lorenz constant ($2.45 \times 10^{-8} \frac{V^2}{K^2}$) and T is the absolute temperature.

The two equations then yield the Voltage-Temperature relation which is independent of the materials in the contact. This is valid as long as the average a-spot diameter is larger than the mean free path of electrons in the contact material [230]. Assuming gold contacts and a current of 0.5 mA, as used in the present study, the temperature increase in the contacts tested is calculated as approximately 18-25 °C using the simplified Equation 2.34 assuming a contact resistance of 2.5-10 Ω.

$$V^2 = 4L({T_m}^2 - {T_1}^2) \tag{2.34}$$

Voltage generated heating can cause the contact material to soften, melt, and if high enough, to boil. It is important for micro-contact designers to ensure that the material chosen for MEMS switches do not encounter voltage/current combinations high enough to cause damage due to heat. The operating conditions for a switch may drive the designer to material with high enough softening and melting temperatures. Note that, generally the maximum temperature may be considered to occur at the physical interface of the contact [230]. However, in specific switch designs, the point of maximum temperature may not be located at the contact. Yan showed that in the switch design analyzed in [263] the highest temperature in the switch tested occurred in the thin-film drain trace 3-5 μm from the center of the contact. Also, Greenwood and Williamson reported that the rate of heat production in an electrical contact rises

Table 2.2: Comparison of thermal physical properties of various contact materials from Slade [230]. Values marked (est) are estimated for comparison as described in text and were added to data excerpted from [230].

Material	Softening Temp °C	Softening Voltage V	Melting Point °C	Melting Voltage Measured V	Melting Voltage Calculated V	Thermal Conductance W/(m K)	Boiling Temp °C
Gold	100	0.08	1063	0.43	0.42	297	2966
Platinum	540	0.25	1769	0.71	0.64	72	3850
Rhodium	655	0.14 (est)	1966		0.70	88	3900
Ruthenium	783 (est)	0.30 (est)	2350		0.81	105	4900
Vanadium	633 (est)	0.04 (est)	1900		0.68	29	3400

sharply at the edges of a circle of contact [85]. It can be expected that temperature effects, if any, in a contact will be initially manifested at the edges of the area of contact. Note that Yan [263] reports images showing ring-like structures indicating melting near the edge of the contact area.

Table 2.2 gives the softening temperature, softening voltage, melting point, thermal conductance and boiling point of bulk contact materials that are of interest to MEMS switch designers. The values are from Slade, and the entries marked (est) are estimated based on the softening temperature being approximately 1/3 of the melting temperature and by using Equation 2.32 to estimate the softening voltage [230]. However, Jensen reports that the softening temperature for gold is 65°C, which is significantly less than the gold bulk softening temperature of 100°C [115].

Resistivity of metals also change with temperature, and the change in resistivity for small perturbations of temperature can be characterized by Equation 2.35 [81].

$$\alpha = \frac{1}{\rho}\frac{\partial \rho}{\partial T} \tag{2.35}$$

where α is the temperature coefficient of resistivity and ρ is the resitivity. The temperature coefficient of resistivity for gold is given as 3.61×10^{-3}. For a simple estimate of the change in resistivity, approximating $\frac{\partial \rho}{\partial T}$ as $\Delta\rho/\Delta T$, Equation 2.36 can be used.

$$\Delta\rho = \alpha\rho\Delta T \tag{2.36}$$

For a temperature change of 20 degrees Celsius, the gold shows an increase in resistivity of approximately 7%. Equation 2.29 infers that this effect leads to a contact resistance increase of approximately 7%. Contact heating could be one of the causes of resistance increase which has been noted in some microswitch studies.

2.9.8 Contact Evolution. One area which needs further study is contact wear. Wear is caused by the contact of rough surfaces and the most important characteristic of wear is its unpredictability [71]. Wear and/or abrasion of metal contacts could be a contributing factor in the evolution of contact performance over time. Fretting may also be a factor in contact changes over time. Fretting is the result of microscopic motions of parts while they are in contact [227]. Strain hardening of contacts due to plastic deformation could also be a contributing factor. A literature search yielded no reports of experimental results showing strain hardening of contacts in micro-switches. Electric fields, the passage of electric current through contacts, and thermal effects created by electric current (joule heating) may also cause changes in the contact morphology.

Gally, Abnet, and Brown published a study called, "Investigation of Wear of Microelectromechanical Contacts" [74]. The experimental setup was slightly larger than typical MEMS device dimensions. The setup consisted of a 400 μm spherical tip coated with sputtered gold contacting a gold coated membrane. Their results showed failure at lower current densities and contact pressure than previous studies and are summarized in Table 2.3 [74]. Their study did not focus directly on mechanical wear, rather it was an analysis which looked more at the relationship between current density and contact pressure. It did not contain reference to the material properties of the contact materials used in the experiments that were compared. The researchers estimated the experimental contact area.

Table 2.3: Side-by-side comparison of current density and contact pressure for three micro-contact failure studies [74].

Investigator	Coatings	Current Density (A/m^2)	Contact Pressure (MPa)
Hyman, 1999	Sputtered Au, Electrodeposited Au	1.25 x 10^9	37.5
Majumder, 1998	Plated Au	1.25 x 10^9	25
Gally, 1999	Sputtered Au	22 x 10^6	0.025

The possible creation and rupture of contaminant films on electric contacts is another factor besides wear which is important in analysis of electric contact performance and change as the contacts are cycled. It is important to understand the basics of contaminant films, the process by which these films are disturbed by the passage of electric current, and the process by which contaminant films may be created during contact cycling. The next sections provide an overview of contaminant films and their behavior in electric contacts.

2.9.9 Contaminant Films & Fritting. Barriers to electrical contact, such as insulating or semi-insulating layers, are a common problem in all electrical connectors and contacts [259]. These films must be broken or penetrated in order to create spots of electrical contact [259]. It has been noted by previous researchers that contaminant films are present on all metals used for electrical contacts [103] and contaminant films are often cited as the reason that measured contact resistance differs from resistance predicted by theory. In his 1967 book on electrical contacts, Holm reported that, "The fact that water is adsorbed on solid surfaces that are exposed to humid air has been known for more than 100 years." [103] The type, thickness, and resistivity of contaminant films depends on the type of metal and the environment to which the metal is exposed [99, 103, 230]. Some metals form oxides while others adsorb elements from the environment [55]. Gold is a noble metal and does not form a surface oxide [103]. However, gold chemisorbs a monolayer of oxygen in air, as does every metal [103]. Silver is a common contact metal used in macro-sized contacts,

but forms a dark, resistive film of Ag_2S in air due to the very small amounts of sulfur in the atmosphere [103]. This film is easily ruptured in macro-size contacts but is difficult to rupture with low contact forces at the micro-scale [202]. Other metals form an oxide when exposed to the atmosphere. This process is commonly called tarnishing and the films become very highly resistive [103].

Mechanical means are not the only method to rupture these resistive contaminant films to allow electrical contact. Fritting, which is the electrical breakdown of a thin film when enough voltage is applied, is also used to damage insulating films [103]. Fritting actually generates contact spots, called a-spots by Holm, able to carry current "at a contact voltage below the melting voltage but above the softening voltage of the metal" [103]. Plastic yielding of the metal may also occur. This breakdown is called regular A-fritting. Another type of fritting is called B-fritting. B-fritting occurs when an a-spot already exists, and the conducting area is widened through the action of increasing current [103]. This can also involve plastic yielding [103].

These physical mechanisms of puncturing contaminant films have been utilized to clean electrical contacts [202]. Switches can be designed to take advantage of mechanical cleaning by wiping the contacts such that the contaminants are physically ruptured or displaced [103, 230]. Electrical contact cleaning, called Schaltreinigung by Schimkat, uses electric potential and the phenomenon of fritting to remove contamination during switch closure [103,216]. Sun has also reported that higher contact forces may suppress the growth of resistive films at contact spots [235].

Contaminants created during switch cycling are a possible cause of the failures described in the next sections. These films are sometimes described as "carbonaceous" [54, 123, 136, 174] and can inhibit contact resulting in high contact resistance leading to a high resistance contact failure [29].

2.9.10 Contact Activation/Contaminant Buildup During Cycling. The creation of a contaminant layer during micro-switch cycling has been hypothesized by many researchers. Germer, Smith, Hermance, Egan, Keefer and Gumley did initial

studies in the buildup of contaminants as part of Bell Telephone Laboratory studies into the failure of telephone switches [78, 101, 123]. "Contact activation" was first defined by Germer [78] as "the process of particle formation on d.c. relay contacts that gives an increase in the duration of the relay make and break arcs" [78,230]. The term "frictional polymer" was proposed by Hermance and Egan to describe an amorphous brownish organic deposit which formed on non-arcing palladium contacts [101]. Their analysis showed that the brown deposits resembled mixed polymers in their properties so they proposed the term "frictional polymer" [101]. Note the difference between the two descriptions. One occurred under arcing conditions, the other under non-arcing conditions requiring rubbing of contacts. The product of contact activation is described by Germer and Smith as "black soot" and "carbonaceous" whereas Hermance and Egan called the substance created on their contacts a "brown powder" as it was solid and brown in color. Germer refers to the "brown deposit" as closely related to the activation of relay contacts as the formation of polymerized layers of organic material upon contact surfaces as the result of friction. Germer also reports that carbon is produced on noble metals but not base metals in air, and that brown deposit was formed on vanadium, molybdenum, and tantalum but not on silver and sparingly on gold [78]. According to Holm, the dark-brown insulating powder is formed on contacts made of Palladium (Pd), Platinum (Pt), Ruthenium (Ru), Molybdenum (Mo), Tantalum (Ta) and Chromium (Cr), but Gold (Au) and Silver (Ag) do not catalyze this kind of reaction [103].

Other researchers have looked into this more recently. Hinohara looked at reed switches in the 20-70 mm length range with contacts made of rhodium. Similar to the phenomenon seen in micro-sized switches, the contact resistance of the reed switches tested increased as the switch was cycled at a low level load of 5 VDC and 100 μA. This resistance increase was due to the formation on the contact surface of a brownish reaction product. This research showed through surface analysis that this reaction product consisted of carbon [102]. The research reported that the contact resistance of deactivated rhodium contacts is stable over time. Also, Hinohara reported that an

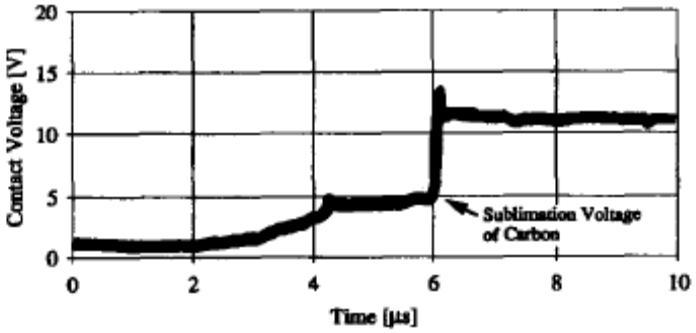

Figure 2.19: Contact Voltage during break: Gold contacts, 10 V, 100 mA, 0.05 N. This graph indicates creation of carbon contamination during an opening arc [179, 180].©1995 IEEE.

effective method to avoid the creation of this contamination is to provide an approximately 50 Å-thick rhodium oxide (Rh_2O_3) film [102]. It is important to note that "exposure to organic vapors without arcing will not result in activation" [230] which is a result from work done by Neufeld and Rieder on macro-relay switches, and "carbon is not formed on nonarcing contacts, even near a switching contact" [179]. Carbon has a resistivity of 10^{-4} Ω-m and a hardness (measurement technique not reported) of 5×10^8 N/m^2 [179], thus has significantly higher contact resistance than metallic contact materials.

Contact voltage versus time can indicate the activation process occurring in the contact. For example, in Figure 2.19 a voltage plateau at contact opening can be seen which was observed by Neufeld and Rieder before the contacts were contaminated by carbon. They observed a voltage plateau at the sublimation voltage of carbon for 2-20 μs just before arc ignition. Holm determined the sublimation voltage to be between 2.4 - 6.8 V where the variation is due to uncertainty of measurements used to calculate this value [179]. This result offers other researchers a method to determine when carbon contamination is taking place assuming the data collection rate is at least 500 kHz just prior to the event [180]. The boiling of a contact or creation of a metallic bridge arc can be indicated similarly by a voltage plateau upon contact break [180]. Figure 2.20 as measured by Neufeld and Rieder shows a plateau at the boiling voltage of gold.

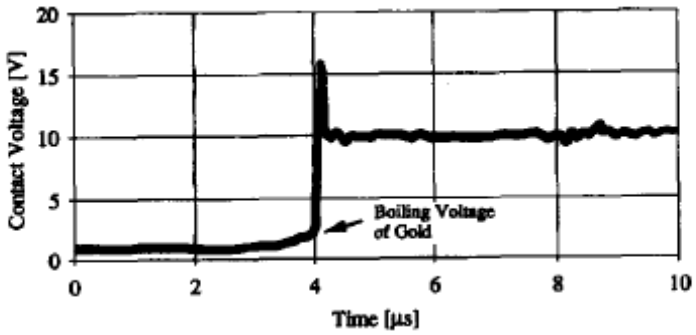

Figure 2.20: Contact Voltage during break: clean gold contacts, 10 V, 100 mA, 0.05 N. This graph indicates boiling of the gold contact immediately before an opening arc [180].©1995 IEEE.

According to Neufeld and Rieder, different types of contamination can be identified with the aid of easily applied measurement methods including measurement of contact voltage and resistance [180]:

- Particles cause a sudden increase of the contact resistance until they are suddenly removed again (if at all).
- Corrosion may cause infinite contact resistance values; current flow is established only by destruction of the corrosive layer; weakly semiconducting layers may be damaged by A-fritting at increasing voltage; B-fritting may occur at increasing current.
- Carbon causes a steady rise of the contact resistance over about three decades to constant values according to the constriction resistance of elementary carbon; no fritting process occurs; a 'contact voltage plateau' in the range of the 'sublimation voltage' of carbon appears during contact separation. ©1995 IEEE [180]

The contamination problem is difficult and requires further research in the area of micro-contacts to fully understand its mechanisms.

2.9.11 Electromigration [230]. Electromigration is defined as the transport of contact material across a bimetallic contact due to interdiffusion caused by the presence of an electrical current of high density [230]. The current study only investigates mono-metallic contacts, so the phenomenon of electromigration by definition did not affect the results. Additionally, in Slade [230], Timsit developed a theoretical calculation of the maximum intermetallic shift due to the action of direct current. The shift is calculated based on $y = vt$ where v is the velocity of the shift, and t is

time. The velocity is given as $v = eZ^*D\rho j/kT$, where e is the magnitude of the electronic charge, Z^* and D are the effective charge number and the diffusion coefficient of the diffusing species, ρ is the electrical resistivity of the diffusive host, j is the electrical current density, k is Boltzmann's constant, and T is absolute temperature. At T=200° C, Timsit calculated $v = 1.0 \times 10^{-22}$ joule-meter/sec (jms^{-1}). This means that the shift cannot exceed approximately 36 nm after 1000 hours of operation, which is negligible in comparison with intermetallics grown thermally in similar conditions [230]. Electromigration experiments were also accomplished in macro-contacts including aluminum/brass interfaces. The aluminum/brass experiments and Timsit's experience showed that intermetallics growth are sensitive to temperature and are not affected significantly by the presence of an electrical current [230].

2.9.12 Contact Arcing. Contact arcing is defined as the electrical discharge between electrodes of a contact which causes wearing away of the contact material [103]. Under certain conditions, contact material is transferred from one side of the contact to the other producing rapid wear and disfigurement of the contact [153]. Certain conditions must exist for the existence of an arc, and much research has been done in the past 50 years on arcing and its causes.

Paschen's law describes the conditions required for the electric breakdown of a gas-filled gap with a uniform electric field [103] during contact closure [230]. This empirical law states that the sparking or breakdown potential, V_s, is a function of the gas and the product δs where δ is the density of the gas and s is the gap width. The term δs is sometimes replaced by the term ps where s is in cm and p is pressure measured in Torr or atm [103]. The standard Paschen's curve shows a minimum breakdown voltage of V_s=300V and an upturn of the line when the quantity ps is less than 10^{-3} atm-cm [103]. Holm [103] reports experiments which show that at small gaps this is not the case and the breakdown voltage can be as low as 50V with observations of gaps down to 1000 Å. Breakdown voltage as predicted by Paschen's

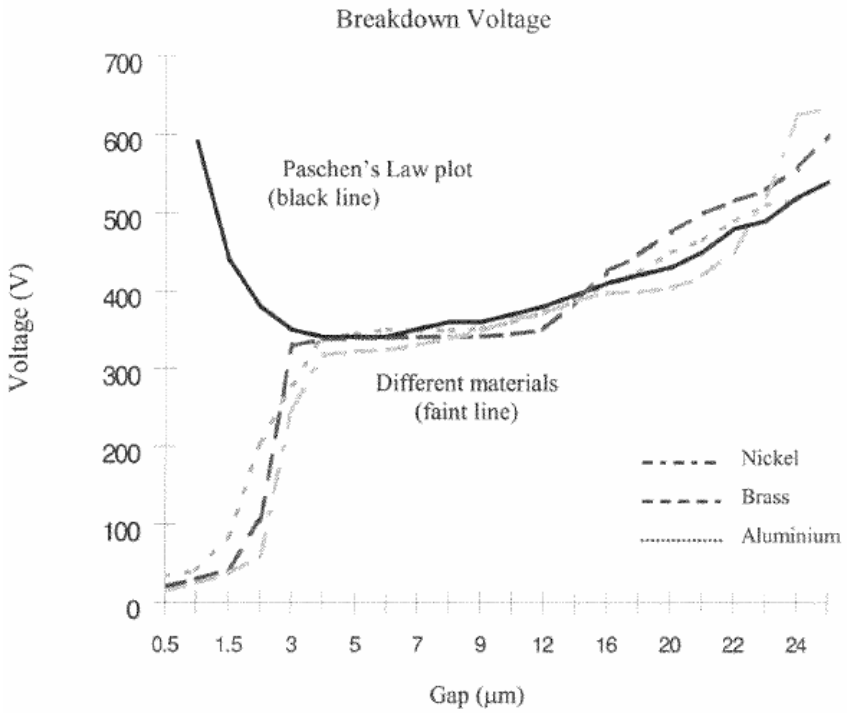

Figure 2.21: Breakdown field strength in air showing behavior at small gaps [244].[5]

Law is shown by the dark line in Figure 2.21. This is sometimes also called "Townsend arcing" because Townsend first explained the processes causing the arc [103].

More recent studies [53, 186, 244] have also shown that the breakdown voltage at smaller gaps is less than that predicted by Paschen's Law. Torres and Dhariwal [53, 244] have done work on various materials investigating very small gap distances. Figure 2.21 shows the variation of behavior from that predicted by Paschen's Law, but it also shows a breakdown voltage of approximately 20V at the gap distance of 0.5 μm and the curves are flattening at that point. Thus, there appears to be some minimum voltage where breakdown does not occur.

Arcing during contact opening also depends on the conditions being favorable for starting and sustaining the breakdown. A minimum voltage (U_{min}) and current

[5]Figure reproduced from *Nanotechnology*, vol 10, J-M Torres and R.S. Dhariwal, "Electric field breakdown at micrometre separations", pp102-107, Copyright 1999, with permission from Institute of Physics.

Table 2.4: Comparison of voltage minimum (U_{min}) and current minimum (I_{min}) for arcing in different contact materials compared to sum of ionization potential (V_i) and work function potential (U_ϕ) [230].

	V_i (volts)	U_ϕ (volts)	$V_i + U_\phi$ (volts)	U_{min} (volts)	I_{min} (clean) (amperes)
Au	9.22	4.90	14.12	12.5	0.35
Pd	8.33	4.97	13.30	14	0.8
Pt	8.96	4.60	13.56	14	0.9
Rh	7.70	4.57	12.27	13	0.35
C	11.27	4.60	15.87	20	0.01

(I_{min}) are required. The properties of the contact material drive these minimums and the arc initiates in a metal vapor from the contacts [230]. The arc requires that the voltage in the circuit at least corresponds to the work function voltage of the contact metal (U_ϕ) and the ionization potential of the gas (V_i). Thus, for an arc to occur, $U_{min} \geq V_i + U_\phi$ [230]. Slade [230] gives a table of values for various contact metals, partially reproduced here as Table 2.4. If a contact becomes activated, that is, contaminated with carbon deposits, the I_{min} decreases to a value associated with carbon contacts [230].

The behavior of minimum voltages and currents can be seen graphically in Figure 2.22 [230].This diagram shows that a switch operating below both the voltage minimum and the current minimum will not sustain an arc. The voltages and currents in the experimental design of the current research are well below those which cause extended arcing. No evidence of arcing was noted during tests run in this study.

2.9.13 Contact Adhesion. Contact adhesion is a complete field of study in itself. Significant work has been done on the mechanisms and theoretical understanding of adhesion. Static and dynamic friction impact many engineering devices, and understanding the adhesion of rough surfaces is intrinsic to understanding the operation of these devices. It is also important to understand the basics of adhesion when studying contact switches at both macro and micro scales. Several researchers have done work

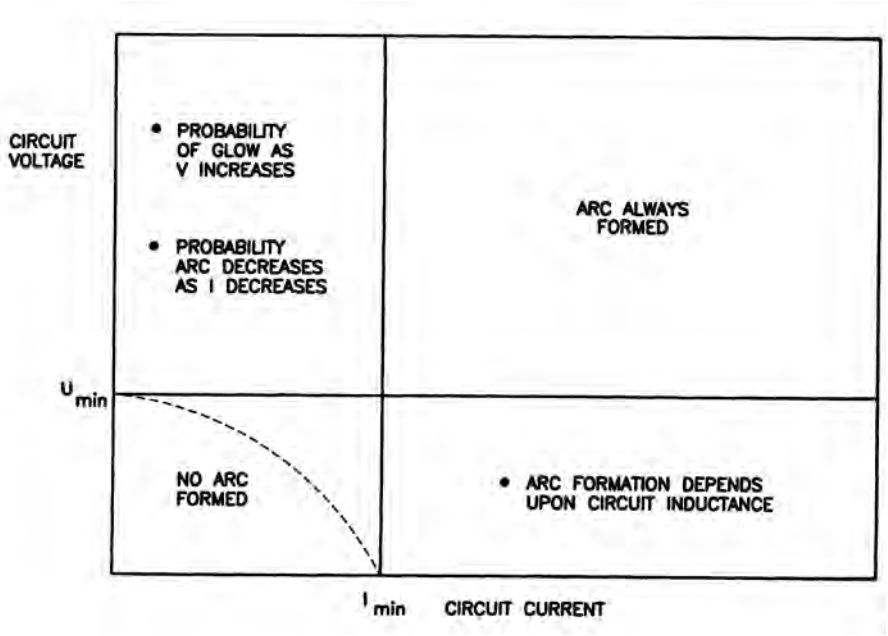

Figure 2.22: Conditions required to sustain an arc. Voltage is shown on the Y-axis and current is shown on the X-axis. Arcs are probable above and to the right of the dotted line shown in the "No Arc Formed" quadrant. No arcs will be formed below and to the left of the dotted line. [230][6].

in the area of microcontact adhesion [2,92,93,130,161,169,170,189]. Contact adhesion, or "stuck closed" failures, continue to be a limiting factor for MEMS switches [156]. Chang describes the adhesion of rough surfaces in detail [33]. An important result of the work on contact adhesion is the magnitude of the force required to pull the adhering surfaces apart. This is often called the "pull-off" force and can be calculated using Equation 2.37 [33]. This equation is based on the Derjaguin-Muller-Toporov (DMT) model which according to Chang is more applicable to metallic materials than the Johnson-Kendall-Roberts (JKR) model [33].

$$F_{po} = 2\pi R \Delta\gamma \tag{2.37}$$

where F_{po} is the pull-off force, R is the mean radius of asperity in contact and $\Delta\gamma$ is the surface energy of adhesion given by $\Delta\gamma = \gamma_1 + \gamma_2 - \gamma_{12}$ where γ_1 is the surface

[6]Reproduced with permission of TAYLOR & FRANCIS GROUP LLC from ELECTRICAL CONTACTS: PRINCIPLES AND APPLICATIONS by Paul G. Slade. Copyright 1999 by TAYLOR & FRANCIS GROUP LLC; permission conveyed through Copyright Clearance Center, Inc.

energy of material 1 and γ_2 is the surface energy of material 2 before contact and γ_{12} is the energy of the interface after contact [33]. The interfacial term γ_{12} is zero when the contacting materials are identical [37].

However, the JKR model is more appropriate for microcontact studies [37]. Adhesive force calculated similarly by the JKR model is given in Equation 2.38.

$$F_{po} = \frac{3}{2}\pi R\Delta\gamma \tag{2.38}$$

Equation 2.39 gives the Tabor parameter where w is the work of adhesion and z_0 is the equilibrium separation between atomic planes. JKR theory is more applicable when $\mu >> 1$ and DMT theory is more applicable when $\mu << 1$ [37, 96]. The Tabor parameter calculated for gold contacts used in this study is $\mu = 6.5$ and for Ru contacts is 6.3. Thus, JKR is more applicable for the contacts used in the present study.

$$\mu = \left(\frac{Rw^2}{E^{*2}z_0^3}\right)^{1/3} \tag{2.39}$$

Komvopoulos reports that "smooth micromachine surfaces exhibit a greater tendency for permanent interfacial adhesion" [131]. Chang concludes that the pull-off force for smooth surfaces is much higher than that for rough surfaces for a given surface energy of adhesion [33]. He defines smooth surfaces as surfaces with a plasticity index of $\psi = 0.5$ and rough surfaces as having a plasticity index of $\psi = 2.5$. He gives the example of $\Delta\gamma = 0.5 J/m^2$ as the surface energy of adhesion for contaminated surfaces [33]. Chen reports 1-3 J/m^2 as the range of surface energy for clean metal surfaces. [37]. Section 3.2.4 contains a description of surface energy and reports values of surface energy of possible microcontact materials obtained from the literature.

2.10 Contact Failure Modes

An understanding of the failure modes of MEMS contact switches is an important starting point for research dedicated to improvement of MEMS switch contact

lifetimes and reliability. Contacts fail in micro-switches in two ways: contact adhesion failure where the contacts remain stuck shut or through a sudden increase in contact resistance [37]. After a contact adhesion failure, the switch is no longer able to open and thus no longer capable of performing its designed function. After a significant increase in contact resistance, the characteristics of the system in which the switch operates are changed enough that the system no longer operates as designed because current no longer flows through the device.

2.10.1 Contact Adhesion Failure. Contact adhesion failure occurs when the metal contacts of the microswitch fail to open after a switch cycle. The contact fails to separate when the adhesion force between the contact surfaces is greater than the restoring force available in the switch design. Adhesion failure has been studied, especially for gold-gold contacts [39, 93, 117, 161, 173, 189, 190, 224]. Patton and Zabinski focused on adhesion force in both DC and Capacitive switches [188,190]. Chen performed analysis of adhesion in contact evolution and focused on the modes of separation of contacts and their role in contact evolution [37].

2.10.1.1 Types of Adhesion Failure. Contact adhesion failure can be caused by liquid-mediated adhesion (if the device is operated in a humid environment) or solid-solid adhesion. Contact adhesion failure is more likely in both cases if the surface roughness is low [261]. Mercado proposes a mechanical approach to provide enough restoring force to overcome adhesion at the contact surface [173]. Jensen, et al. proposes that the restoring force be as large as possible while the contact bump size be as small as possible [117]. Gregori, Mihailovich and DeNatale used a nanoindenter to investigate the mechanical response of actual Rockwell Scientific contact switches and to measure the adhesive force between gold contacts and how they changed as the switch was cycled [92, 93]. They conclude that the adhesion force of the contacts increase as the contact cycles. However, they were working only with load vs. displacement data and did not publish contact force vs. resistance

characteristics of the contacts or investigate contact materials or material property effects on their results.

Contact adhesion failure is even considered by some to be the primary failure mechanism for MEMS switches [156]. In some of the literature, the term "stiction" is used to describe all contact adhesion failures. However, there is no agreed upon definition of stiction [199]. "Stiction" includes high static friction and a sizable level of adhesion. Stiction technically requires a smooth surface and always requires a liquid film at the interface [199]. This study uses the more precise term "contact adhesion failure" unless the failure is known to have been caused by high static friction or high adhesion with a liquid film at the interface.

2.10.1.2 Role of Material Properties in Contact Adhesion. Maugis reported that adherence depends on the material parameters of Young's modulus, yield strength, and surface energy [169] while Sharma showed that materials of high hardness, hexagonal crystal structure, high melting point, high elastic modulus, low work hardening coefficient and high recrystallization temperature have low adhesion [224]. An interesting note is that some researchers [132, 202] claim that the adhesion force is higher between harder metals and lower between contacts made up of softer metals. They cite a mechanics of materials text by Courtney [42] but do not clearly explain the reasoning used to come to that conclusion. However, the text cited does not appear to conclude that harder metals show higher adherence. Analysis of the work by Chang [33] discussed in the previous section and the results of the experiment developed here indicate that the hypothesis that higher adherence forces are developed in harder contact materials is likely incorrect. Analysis performed at Northeastern University also shows that materials of higher hardness lead to less plastic yielding and smaller adherence forces [170].

Due to the significant failures caused by contact adherence and the fact that softer metals have a lower yield strength than harder metals, it can be concluded that, given the same surface roughness, softer metals exhibit higher adherence forces than

harder metals. The experiments performed in this study show direct measurement of adhesion force and direct comparison of soft contact materials to harder materials and the progression of adherence force as the contact is cycled. Note that Chen [37] is the first to compare materials in a microcontact directly by measuring adherence force indirectly using displacement and a known cantilever stiffness.

2.10.2 Resistance Increase. The second major failure mechanism for micromechanical contacts is the sudden increase in contact resistance attributed to the development of a highly resistive, possibly carbonaceous layer between the two metallic contacts. Several researchers, including Dickrell and Dugger at Sandia National Labs have looked into the growth of a resistive layer due to environmental contamination [54, 55]. The sudden growth of the resistive layer is remarked on in many studies, but Carton is one of the first to report on the elemental content of the resistive film in microcontacts [29]. It is likely that the processes involved in the sudden resistance increase in microswitches are very similar to the two mechanisms of contaminant film creation identified in macro switches: "frictional polymerization" and contact activation.

Recent work by Jensen, et al. shows that mechanical cycling alone is an important factor in contact resistance increase, and demonstrated that heating of the metal-to-metal contact reduces the contact resistance [115]. Other work by Jensen shows that gold contacts in a microswitch demonstrate contact softening at about 65°C [115]. A previous paper by Jensen, et al. suggested that strain hardening due to contact deformation and necking is responsible for some of the observed contact resistance increase due to cycling, but the later paper argues that the resistance increase is too high to be explained completely by strain hardening [114–116]. It is clear that the mechanisms of failure in MEMS switches are greatly affected by the mechanics of contact and contact material properties. Switch designers would be well served by analyzing the material selection processes used commonly by practicing engineers in

other fields, and developing the data and analysis to support a methodical material design and selection process.

2.11 Background Summary

The background described above provides knowledge of MEMS contact switches which is currently available. Many studies have investigated design and performance of MEMS switches for use in RF and other devices. Types of MEMS switches and their characteristics and potential benefits were discussed. A brief overview of contact mechanics and contact behavior as they relate to MEMS scale contacts was discussed. These studies include some work on various contact materials, but little experimental data on the parameters or mechanics of microcontact. This study addressed this lack of data by developing a method of testing microcontacts and measuring contact parameters of three representative contact materials. However, no work covers the details of how to judiciously compare and select contact materials based on microcontact material properties. The next chapter addresses material property based selection methodology in MEMS switch design and offers a starting point for further work.

III. Contact Switch Materials and Selection

One element of switch design in which there is significant room for research is the selection of contact materials based on their material properties. In the infancy of MEMS switches, the effect of materials and material properties on contact mechanics was poorly understood. Some research into small-scale contact mechanics has been reported, as previously discussed in Chapter II. However, development of experimental understanding of micro-contact behavior and a systematic material selection methodology is critical to understanding and extending the life and reliability of MEMS switches.

This chapter describes the basic process of selecting materials for engineering design, develops information on possible contact materials for use in MEMS contact switches and includes a brief overview of the metallurgy of some contact materials of interest. Material properties which are of interest to contact switch designers are discussed as well as how to adjust some of those properties. The materials selected for study of their contact properties during this research are also described.

3.1 Selection of Materials in Engineering Design [57]

The selection of materials for specific purposes is a key part of all engineering design. The process by which materials are selected for use is very similar for all engineering tasks. An excellent overview of the material selection process is given by Dieter in his text on Engineering Design [57]. Dieter's four steps in material selection are repeated here, along with a brief discussion based on his presentation [57]:

1. Analysis of the material requirements
2. Screening of the candidate materials
3. Selection of candidate materials
4. Development of design data [57]

Step 1 must be accomplished before any material selection for design takes place. A design engineer must seek to understand the environment in which the design will operate and the conditions the design will face. The design engineer must perform

analysis of which material properties are most critical for successful performance. For example, if a design will endure high cyclic tensile loading, the material chosen must have a high ultimate tensile strength as well as high resistance to fatigue. If the environment is corrosive, the material chosen must also have a high resistance to corrosion. The engineer should make a list of important material properties, and weigh the importance of each. At this stage, the performance of the material is important but not the specific microstructure of the materials under consideration.

The second step is to screen materials based on the expected operational environment and material requirements of the design. During this step, the design engineer will take the material properties required and screen candidate materials for these properties. For example, if fracture strength of materials are not known, a simple ratio of ultimate tensile strength to yield strength can be used to generate a list of candidate materials which likely have high fracture toughness. That is, the higher the ratio, the higher the expected resistance to fracture.

The third step in the process is the downselect to a smaller list of the best candidate materials for more serious consideration. This downselected list of candidate materials can then be tested to verify the fracture toughness and/or performance in a test similar to the expected operational environment. The most promising of these materials can then be the basis for a list of candidate materials appropriate for application to the final design selection.

The final step in the material selection process is the development of design data specific to the application and the contemplated materials. This step allows the design engineer to collect data on the actual performance of a material during its operational use or in operational testing or testing in a manner very similar to the operational environment that the material will experience. This data can be collected and analyzed either during the design of the engineering system or after it has initially been designed and produced. This step is also iterative, as data collected from actual

performance can be analyzed to improve material selection for the next generation of devices.

The present study was designed to provide data and support to all four steps in the engineering material selection process for micro-switch electrical contacts. Few published researchers describe the material properties necessary for a long-life switch. This is partially due to the fact that early researchers hypothesized that soft contact metals with low resistivity (e.g. gold) would perform better than harder metals due to the low contact forces available in micro-switches (e.g. [132]). However, the longest-lasting and most reliable micro-switch commercially available uses a hard contact metal, described as a "platinum-group metal" [160]. This material selection is believed to be based on the fact that the hardness of a material is related to the ability of the material to resist wear and avoid developing high adhesion forces. Therefore, it is hypothesized that harder contact metals delay damage due to contact wear and exhibit less contact adhesion. The present study tested effects of micro-contact cycling on three different contact metals with varying material properties to provide data helpful to switch designers in developing a method to screen contact materials for inclusion in micro-switch designs.

The present study also provides support to design engineers interested in developing a method to perform selection of candidate materials. The test apparatus designed and demonstrated for the first time in this research provides a method for micro-switch engineers to test lifetime performance of a small number of contact materials in a realistic, representative test facility before the work is done to integrate the candidate material into a switch design.

This test setup could also be used by switch designers to develop design data helpful to switch design. Switch designers could easily alter other variables besides contact material which could effect contact performance including contact morphology, film thickness, contact force, current, cycling rate, etc. A large compilation of

design performance data could be collected, organized and made available to switch designers using this test apparatus.

Dieter also suggests the following four questions whose answers determine the success of a materials selection process [57]:

1. Have performance requirements and service environments been properly and completely defined?
2. Is there a good correlation between the performance requirements and the material properties used in evaluating the candidate materials?
3. Has the relation between properties and their modification by subsequent manufacturing process been fully considered?
4. Is the material available in the shapes and configurations required and at an acceptable price? [57]

The study performed here is dedicated to developing further data to answer question 1 by experimentally measuring microcontact parameters, as well as to provide the starting point for correlating performance to material properties and in the development of processes to evaluate contact materials to answer question 2 in improving the material selection process used for contact material selection.

Significant work has been done in developing material properties and design data for structural materials such as high-strength steels, carbon-fiber composite materials and current work is being done in the area of ceramic-matrix composite materials for a variety of engineering uses. This kind of systematic data development and materials testing process has not yet been applied to the field of micro-electric contact materials selection. The first step in starting this kind of systematic material property development was to choose materials for testing in order to provide data useful for designers and engineers to understand the mechanics of microcontact and continue development of a systematic material selection process.

3.2 Material Properties of Interest

The material properties of interest to micro-switch designers are hardness, wear resistance, resistivity, corrosion & contamination resistance, modulus of elasticity,

yield strength, surface energy and melting point [224]. General bulk material properties for several metals of interest are shown in Table 3.1. This table shows why gold is of significant interest to switch designers. It is soft, and thus easily makes ohmic contact, requiring small contact forces from a switch design and also has a very low resistivity and thus develops very low contact resistance. However, gold does not exhibit high wear resistance and often develops high adhesive forces. It is clear that ruthenium and rhodium are much harder than the others. The melting point of ruthenium is also much higher than gold. Some researchers have hypothesized that part of the lifetime limits of contacts is caused by localized melting due to joule heating of the contacts, although recent work by Jensen, et al. suggests that existing contact theory significantly over-predicts contact heating at contact spots for MEMS microswitches [115]. Varadan reports that, "The surface morphology has a strong influence on stiction and is a serious problem in particular in metal-to-metal switches" [247].

Alloying a small amount of a harder metal with gold increases the alloy's hardness over pure gold, and therefore increases wear resistance. Also, the melting point of the alloy could be raised above the original melting point of gold with the addition of a metal with a higher melting point. For these reasons, the properties of rhodium and ruthenium make them very attractive options to alloy with gold to develop a possible high performing contact metal. The tradeoff would be an increase in electrical resistivity and possible increased susceptibility to contamination. The addition of Rh or Ru, both reactive metals, to gold would alter the nobility of gold and its electronic structure thus increasing the material surface reactivity. Systematic material analysis, based on experimental data similar to that produced in the present study, are necessary to determine if this trade-off could be of value to the MEMS switch designer.

Table 3.2 shows other bulk mechanical properties of contact metals of interest to switch designers. MEMS literature contains limited analysis of mechanical properties, especially important properties such as yield strength. Frequently, authors have estimated some properties by calculating yield strength by dividing tested material

Table 3.1: Side-by-side comparison of bulk material properties of some metals of possible interest for use in MEMS contact switches. Data from www.matweb.com [7]. Data marked [260] taken from www.webelements.com

Material	Hardness (Vickers)	Electrical Resistivity ($\mu\Omega$-cm)	Tensile Str. Ultimate (MPa)	Elastic Modulus (GPa)	Poisson's Ratio	Thermal Conduct. (W/m-K)	Melting Point (°C)
Gold	25	2.2	120	77.2	0.42	301	1064
Platinum	40	10.6	125-165	171	0.39	69.1	1769
Ruthenium	220	7.2	370	414	0.3 [260]	116	2310
Palladium	37	9.93	180	117	0.39	71.2	1552
Rhodium (annealed)	100	4.3	951	359	0.26 [260]	151	1960

hardness by three (e.g. [108,114,132]). This estimate ($S_y = H/3$) is applicable only to metals which show perfectly plastic behavior, such as strain hardened materials [236]. Not much analysis has been published specifically analyzing or describing the combination of material properties desirable in a contact switch, other than hardness and resistivity. An exception to this is Sharma who developed a list of desirable material properties for macro-switch contact material [224]. The yield strength of possible material choices and their relative ductile or brittle behavior could play a role in the longevity of contact material choices [37]. Gold is significantly more ductile than ruthenium, with a yield strength an order of magnitude smaller. Note that there are differences in the published properties from different sources, thus suggesting further research in this area could be useful.

Table 3.2: Bulk mechanical properties of precious metals in the annealed condition of possible interest for use in MEMS contact switches. Data from [213].

Metal	Hardness VHN(BHN) (MPa)	Ultimate Tensile Str σ_u, (MPa)	Yield Strength $\sigma_{0.2}$,(MPa)	Elongation (%)	Reduction of Area (%)
Gold	220-250	120-130	10-25	45-50	90-95
Platinum	390-420	120-160	60-80	40-50	95-100
Ruthenium	2000-3000	500-600	350-400	3-10	2-3
Palladium	380-460	180-200	50-70	25-35	80-85
Rhodium	1000-1300	400-560	70-100	8-15	20-25

It is also important to note that the material properties of thin-films and properties measured at the micro/nano-scale differ from measured bulk properties. Higher strengths in smaller volumes of material are consistently reported [91]. This has been hypothesized as being caused by the dislocation starved conditions which prevail in small volumes [88]. The hardness is greater on a nano-scale than that measured in the bulk material [20].

Care should be taken in comparing hardness values between differing test methods as the results can depend on the method used. Table 3.1 shows Vickers hardness, given in the typical Vickers units of kg/mm^2, as a comparison of bulk properties, but generally nanoindentation with a Berkovich tip is used for micro/nano-hardness property measurement, given in units of GPa. Measurement of the micro/nano-scale hardness has been accomplished at AFIT and reported by Lee et al. and Chen et al. [36, 142]. Table 3.3 shows material properties of thin films measured at the micro/nano-scale. A comparison of these results to the values given in Tables 3.1 and 3.2 demonstrates material behavior differences due to scale.

Table 3.3: Material properties of metal thin films of possible interest for use in MEMS contact switches. The thin films measured here were 300 nm, and the mechanical properties were measured by Berkovich tip nanoindentation at 24 nm depth to avoid substrate and indentation size effects. The resistivity was calculated from sheet resistance measured by a standard four-wire probe technique [36].

Material	Hardness (GPa)	Electrical Resistivity ($\mu\Omega$-cm)	Elastic Modulus (GPa)
Gold	1.04	3.6	86
Platinum	5.39	16.6	183
Rhodium	9.75	9.3	256
Ruthenium	15.28	13.8	295

It can be seen in Figure 3.1 that alloying gold with other platinum group metals increases the hardness moderately above the level of gold, but resistivity is also increased. Testing of these alloys is required to determine whether they offer in-

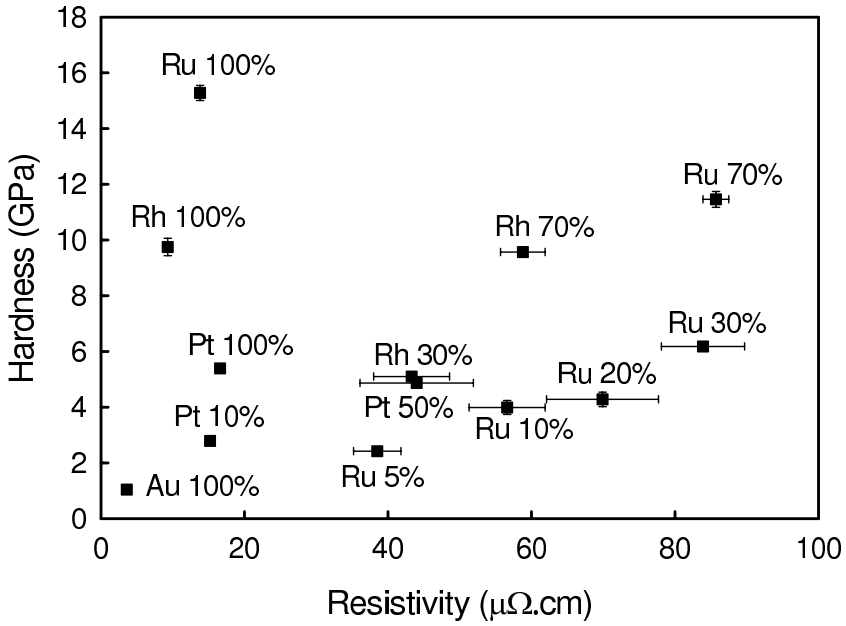

Figure 3.1: The hardness and resistivity of several metals and alloys considered for use as contact materials is presented here. The percentage amounts shown are the percent of that metal when alloyed with gold. 100% markings indicate a pure metal [36].[7]

creased micro-contact wear resistance and lifetime. In addition to providing insight into micro-contact behavior, the test apparatus developed during this study offers the ability to compare each material directly against the others in order to support micro-contact material selection.

The material properties of interest to micro-contact switch designers are described in more detail in the next sections. The definitions and importance of hardness, yield strength and surface energy to micro-contact mechanics are reviewed.

3.2.1 Material Hardness. Material hardness and the ability of materials to resist wear are linked. While there are many ways of measuring hardness, hardness is usually defined as the resistance to penetration [71] and can be used as an indi-

[7]Reprinted with permission from *Journal of Applied Physics*, 102(7), L. Chen, H. Lee, Z.J. Guo, K.W. Gilbert, S. Mall, K.D. Leedy, N.E. McGruer and G.G. Adams, "Contact resistance study of noble metals and alloy films using a scanning probe microscope test station", Copyright 2007, American Institute of Physics.

cator of the wear resistance of a material, including in MEMS devices. Hardness, as used in this dissertation unless otherwise noted, is the hardness measured through nanoindentation with the use of a pyramidal Berkovich indenter tip, using the Oliver-Pharr method [185, 197]. It should be noted that the sharpest Berkovich indenter tips have a radius of curvature at their points of 20-25 nm, thus any data taken using this method at less than 20-25 nm depth must be carefully analyzed because the Oliver-Pharr method depends on the validity of the tip's area coefficient. This tip area coefficient is only valid when the tip indents far enough into the surface for the area function to take effect. It should also be noted that measured hardness depends on the cone angle of the indenter tip used [228].

3.2.2 Methods of Increasing Material Hardness. Several methods exist to increase the hardness of a softer metal, such as gold, through the use of alloying: solid solution hardening, dispersion hardening, precipitate hardening or introduction of a second phase. Alloys of substitutional solid solutions exist when atoms of a second metal substitute in the crystal lattice for atoms of the original metal, and thus the material is in a single phase. Only a relatively small hardening effect can be produced by solid-solution hardening [56]. Thus, the ability to strengthen and/or harden materials using solid-solution strengthening is limited. This method of hardening is also limited to elements which have approximately the same physical atomic size and the same crystalline structure [56, 71]. Also, research by Hyun, et al. indicates that solid solution alloying in thin films of gold is not likely to add strength if elevated temperatures, such as could be experienced by contacts undergoing joule heating, are unavoidable [109]. Other researchers have noted that "solid solution hardening is not very effective at high temperatures" [258]. Coutu developed a method to select solid-solution hardened alloys, but did not perform comparative testing between solid-solution and other alloy types [46,47]. Yang, et al. compared gold, solid-solution Au-Ni, and two-phase gold-nickel alloys and found that the two-phase alloy yielded

a larger number of cycles to failure and a lower contact resistance when compared to the solid-solution alloy [265].

Two-phase or dispersion hardening and precipitate hardening offer significantly more choices and possibilities for hardening materials and increasing wear resistance. Finely dispersed second phase particles make the alloy "much more resistant to recrystallization and grain growth than single-phase alloys" [56]. In two or more phase materials, the softer background or continuous phase is usually called the matrix. Dispersion hardening occurs when a second phase of the material is dispersed in the microstructure but is not usually coherent with the matrix [56, 71]. Precipitate hardening is a process where the second phase is precipitated from a supersaturated solid solution in fine particles which are usually coherent with the matrix [56, 71]. The Au-Ru alloy considered here is a two-phase precipitate hardened material, whereas the Au-V_2O_5 researched by Bannuru, et al. is an example of a dispersion hardened material [8]. Note that Bannuru reports that dispersion strengthened Au-V_2O_5 shows less increase in resistivity and more promise as a contact material than solid solution Au-V [8]. Another example of a recently developed dispersion hardened alloy specifically developed for use as a MEMS electrical contact material is gold strengthened with zirconia nanoparticles [258]. Note that in macro-contacts, "The resistance of gold to mechanical wear is considerably improved on strengthening by a dispersion of oxide particles" [213].

3.2.3 Yield Strength (S_y). Ductile materials, including most metals, will plastically deform under a load without failure. The point at which strain on a material increases rapidly without a corresponding increase in stress is called the yield point [227]. Yield strength, sometimes indicated by S_y or Y, is the term used to indicate the yield stress when the yield point for a particular material is reached. The yield point is not always obvious from material test data, thus yield strength is often defined using the offset method, that is, defined by a specific permanent strain or set, usually 0.2% [227]. Yield strength can also be changed through material processing

such as cold-working. Yield strength and ultimate strength are often measured using standard tensile testing in bulk materials.

Material hardness and modulus of elasticity of thin films can easily be determined through the use of indentation testing. However, the determination of yield strength of thin films is difficult and is an area of continuing research. The most recent work in this area was done by Shim on extracting flow properties of silicon carbide by nanoindentation and finite element simulation [228]. The lack of data on yield strength of thin films has led to the use of simplifying assumptions in the literature dealing with behavior of microcontacts, mainly in the interchangeability of yield strength and material hardness. For example, the relations Y=0.35H, Y=0.354H, or H = 3Y, where H is the material hardness and Y is the yield strength of the material are often used in contact problems e.g. [33, 34].

Previous studies in this area often cite Tabor's work on the hardness of metals from 1951 [236]. However, Tabor's work assumed an ideal plastic material and he stated that no real metals are known to have these properties [236]. Also, the yield strength of engineering materials can be adjusted by processes such as cold working, tempering and annealing. Thus, this relation is a rough approximation but does not actually represent real material behavior unless the material is perfectly plastic and does not strain harden. This can clearly be demonstrated by randomly selecting common engineering materials for which yield strength and hardness are known. Table 3.4 demonstrates the possible errors using the oversimplification of the relationship Y=0.354H using material data from [227]. Table 3.2 also shows that the oversimplification of the relationship between hardness and yield strength does not necessarily apply to the precious metals contemplated for use as micro-contact materials.

A better relationship clearly showing the relationship between hardness (or the average pressure exerted by an indenter during a hardness test) and yield strength for materials which do not work-harden is given by Courtney, and is shown in Equation 3.1 [42].

Table 3.4: Comparison of known yield strength with yield strength calculated based on hardness (Y=0.354H). Hardness & measured yield strength data from [227].

Material	Brinell Hardness HB (kg/mm^2)	Brinell Hardness Converted (GPa)	Measured Yield Strength (MPa)	Estimated Yield Strength (MPa)	Error (%)
1030 Steel (annealed)	137	1.34	317	476	50%
2024-O Aluminum	47	0.46	76	163	115%
2024-T3 Aluminum	120	1.18	345	417	21%

$$\bar{p} = \frac{4F}{\pi d^2} \cong (2.5 - 3.0)S_y \tag{3.1}$$

where $\bar{p}$ is the average pressure exerted by an indenter, F is the force applied by the indenter, d is the diameter of a spherical indenter, and S_y is the yield strength of the material. This relationship is not exact, does not apply to materials which work-harden and should not be used to replace yield strength in contact mechanics calculations with hardness values, unless the relationship between yield strength and hardness is known for the specific material in use. Khan shows that reported yield strength of nanocrystalline copper varies over 100% [124]. Khan also concludes that "...the Tabor relation is not reliable for predicting the yield behavior of materials" [124].

It should be noted that the terms flow stress and yield stress are not interchangeable. The original relation as given by Tabor is $H = C_\Theta \cdot \sigma_f$ where C_Θ is the constraint factor and σ_f is the flow stress [228]. Note that this relationship applies only to rigid-plastic materials, e.g. where the ratio E/σ_y is very large [228].

A method to estimate yield strength of metals based on modulus of elasticity is found in Rabinowicz. For pure metals, $\sigma_y \approx 0.0025E$ and for alloys $\sigma_y \approx 0.0035E$ [199].

More accurate development of contact mechanics should include the yield strength of the materials to be used as contact materials, since most metals work-harden and

thus are not perfectly plastic [227]. Shim, et al. recently published a methodology which can be used to determine yield strength of thin films using a combination of nanoindentation and finite element analysis [228]. See Table 3.2 for comparisons of bulk material yield strength of possible microswitch contact materials. The ductility of the contact metal may also play an important role in contact longevity.

3.2.4 Surface Energy [199]. Surface energy is an intrinsic material property which is important in consideration of friction, wear and adhesional behavior of materials in physical contact [199]. Effects caused by surface energy are negligible at the macro scale, but at the scale of microcontacts, the effects due to surface energy should be considered [199]. Some researchers in the area of microcontacts have considered surface energy (e.g. [37]), but few have analyzed the surface energy properties of various possible contact materials and developed predictions of contact adhesion based on these properties. Finite element analysis of microcontacts including roughness, adhesion and plasticity was performed by Du at Northeastern University [59]. Note that surface energy considerations have only recently been applied to friction and wear problems in general [199].

Surface energy exists because atoms or molecules at the surface of a liquid or solid have more energy than similar atoms or molecules in the interior of a liquid or solid. Surface tension in liquids, capillary action, the formation of spherical drops and bubbles and meniscus formation are due to surface energy [199]. Note that the surface tension of a liquid measured in $dyne/cm$ has the same value as its surface free energy in erg/cm^2 [199].

The surface energy of a solid affects its mechanical properties. See Rabinowicz [199] for a simple derivation. Specifically of interest to MEMS switch designers is the relationship of surface energy to material hardness. A chart showing the close relationship based on surface energy and hardness data for elemental metals in Rabinowicz is shown on a log-log scale in Figure 3.2. Surface energy is related to the amount of work necessary to extend the existing surface area of a material. The

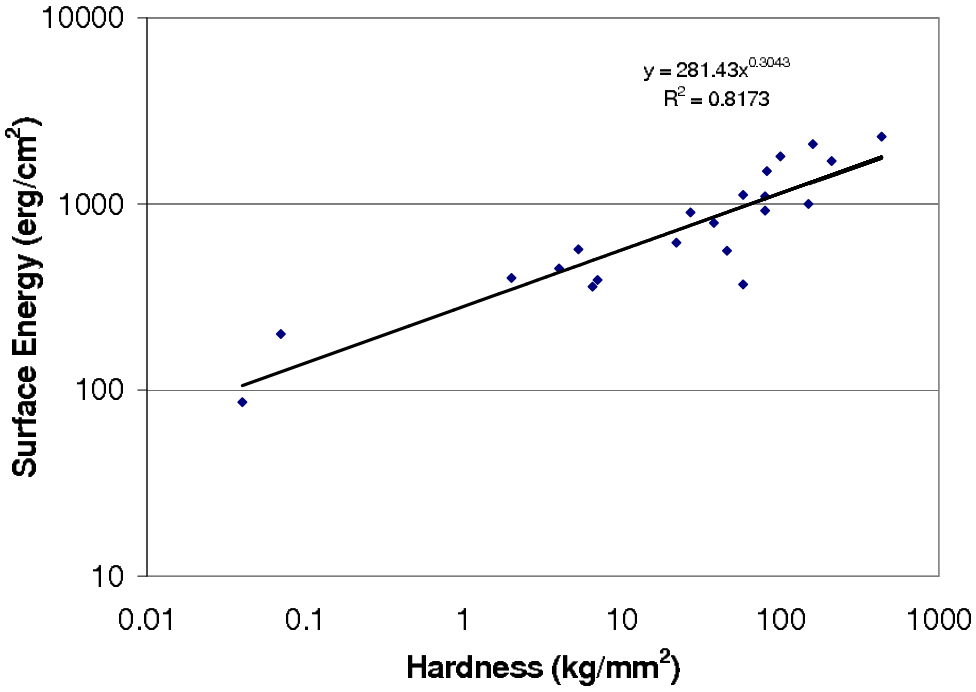

Figure 3.2: Surface energy of elemental metals as a function of hardness. Regression calculated using data given in [199].

surface energy of a contact material can be used in estimating the adhesive force in microcontacts as described previously. Data for contact metals of possible interest for use in microcontacts is given in Table 3.5. Materials with a low $\frac{\gamma}{H}$ ratio demonstrate lower adhesion [199]. Surface energy effects in contact problems are usually negligible, unless the ratio of $\frac{\gamma}{\sigma_y}$ is on the order of the radii of materials in contact [199]. This is the case for MEMS devices.

Yield strength and hardness, in addition to resistivity, wear resistance and modulus of elasticity, are important material properties to be considered when selecting electrical contact materials for MEMS switches. Knowledge of surface energy of the possible contact materials help the designer to investigate problems of contact adhesion. The next section suggests a possible quantitative material selection tool which would use the material properties described as a method of downselecting contact materials.

Table 3.5: Side-by-side comparison of surface energy properties of some metals of possible interest for use in MEMS contact switches. Surface energy data taken from Rabinowicz [199]. The surface energy values marked (est) [246] were calculated by Tyson [246]. Hardness values used were from [36]. [199, 246]

Material	Crystal Structure	Surface Energy γ (j/m^2)	γ/H $(j/(10^9 N))$
Gold	FCC	1.12	1.08
Platinum	FCC	1.80	0.33
Ruthenium	HCP	2.89 (est) [246]	0.19
Palladium	FCC	1.63 (est) [246]	
Rhodium	FCC	2.49 (est) [246]	0.26
Vanadium	BCC	2.28 (est) [246]	
Silver	FCC	0.920	

3.2.5 Material Index: Quantitative Material Selection Tool. Material selection is often done using quantitative tools such as a material index to select a few materials of interest for further study. According to Ashby, "A material index is a combination of material properties which characterizes the performance of a material in a given application" [5]. A simple example of a material index for a light tie bar would be $M = \sigma_f/\rho$ where σ_f is failure strength of the material and ρ is the material density [5]. As seen in the previous discussion, a contact material with high hardness to avoid wear, high melting temperature to avoid current induced heating damage, a low resistivity to reduce contact resistance and a low modulus of elasticity to facilitate elastic contact at low contact forces. Thus, the author proposes a material index for comparing contact materials using the relationship given in Equation 3.2.

$$M = \frac{HT_{melt}}{E\rho} \tag{3.2}$$

where H is contact material hardness, T_{melt} is the melting temperature, E is the modulus of elasticity, and ρ is electrical resistivity. The hardness and melting temperature are in the numerator because it is likely that the designers would want to maximize hardness and melting temperature. The resistivity is in the denominator because

resistivity should be minimized to ensure a low contact resistance. The modulus of elasticity would be minimized to ensure elastic contact at low contact force.

Using this quantitative comparison and the material data given in Section 3.3, for pure metals ruthenium receives the highest relative score at 8.9 with rhodium scoring 8.0. Platinum receives the lowest score according to this criterion at 3.1 with gold scoring 3.6. Note that this material index is simplified and doesn't include all properties which affect the contact performance of a material, including its susceptibility to becoming contaminated. The material properties of melting temperature and density were not available for the alloys, so they were not compared. This material index could be used as a starting point for possible contact material selection. However, it doesn't include the design tradeoffs of the contact force available in each particular switch design, so it may be impossible for a switch designer to completely optimize based on this material index. It is offered here as a starting point for systematic material selection, and to show the relative desirability of ruthenium as a contact material. The next section describes the selection of test materials used in the present study. Each of the contact metals of current interest is described in the next section, along with data on thin film material properties published by Chen, et al. [36].

3.3 Contact Materials of Interest

This section contains background information on precious metals of interest as contact materials, including bulk material properties as well as properties of thin films and some alloys of interest. Material data on gold, platinum, rhodium, ruthenium and the dispersion strengthened gold/vanadium oxide developed at Lehigh University are also presented.

3.3.1 Characteristics of Gold (Au). Gold (Au) has been chosen by most researchers and developers as a micro-contact metal due to its low hardness and resistance to the formation of oxide layers [103, 202]. Hannoe and Hosaka showed

that gold has a lower contact resistance in air than silver (Ag) or palladium (Pd) at very low contact force [97]. However, over time gold contacts implemented in a micro-switch have a tendency to stick closed and fail to open thus causing switch failure due to adhesion [4, 37]. This failure type has been analyzed by various researchers and the design trade-off to avoid adhesive failure is often to increase the stiffness of the cantilever and thus the available switch opening force (e.g. Mercado [173]). However, increasing the stiffness of the cantilever causes the required electrostatic force, and thus the actuation voltage required to close the switch to increase significantly.

3.3.2 Characteristics of Platinum (Pt). Platinum (Pt) is also a good conductor and is significantly harder than gold. However, platinum has a tendency to form a resistive layer when used as a contact metal. Its catalyzing ability is also hypothesized to cause local reactions creating a layer of resistive material [149]. There are a few published reports of the use of platinum (or platinum group metals) as a contact material [137, 160].

Platinum does not oxidize in air at any temperature, but corrodes in the presence of halogens, cyanides, sulfur and caustic alkalis [260]. Platinum is commonly used as a catalyst. Platinum also is known to absorb hydrogen, and gives it off at red heat [149]. On the macro scale, hydrogen and oxygen explode in the presence of platinum [149]. Material properties of gold and platinum alloys are given in Table 3.6.

3.3.3 Characteristics of Rhodium (Rh). Rhodium (Rh) is a platinum group metal which has a higher melting point and higher hardness than platinum, and is generally used as an alloying agent to harden platinum and palladium [260]. "Rhodium is used as an electrical contact material, as it has low resistivity and a low and stable contact resistance" [260]. Rhodium is highly resistant to corrosion and is sometimes used as a catalyst [149]. Material properties of rhodium and gold thin films are given in Table 3.7.

Table 3.6: Material properties of metal thin alloys of gold and platinum. The thin films measured here were 300 nm, and the mechanical properties were measured by Berkovich nanoindentation at 24 nm depth to avoid substrate and indentation size effects [36].

Material	Hardness (GPa)	Electrical Resistivity ($\mu\Omega$-cm)	Elastic Modulus (GPa)
Gold	1.04	3.6	86
Au-10%Pt	2.79	15.2	124
Au-50%Pt	5.1	47.2	155
Platinum	5.39	16.6	183

Table 3.7: Material properties of metal thin film alloys of gold and rhodium. The thin films measured here were 300 nm, and the mechanical properties were measured at 24 nm depth to avoid substrate and indentation size effects [36].

Material	Hardness (GPa)	Electrical Resistivity ($\mu\Omega$-cm)	Elastic Modulus (GPa)
Gold	1.04	3.6	86
Au-30%Rh	4.87	58.8	153
Au-70%Rh	9.57	44	217
Rhodium	9.75	9.3	256

3.3.4 Characteristics of Ruthenium (Ru). Ruthenium(Ru) is also a platinum group metal which is "a very effective hardener for platinum and palladium, and is alloyed with those metals to make severe wear resistant electrical contacts" [260]. Ruthenium does not oxidize in air, but tarnishes at 800°C [260]. Ruthenium oxide (RuO_2) is also conductive. Ruthenium is also a versatile catalyst [149]. Properties of ruthenium and gold alloy thin films are given in Table 3.8. Ruthenium has hexagonally close packed (HCP) crystal structure and has been shown to have a low coefficient of adhesion [225]. HCP materials are generally low in operative slip systems in shear, which decreases ductility and thus reduces adhesion [225].

Table 3.8: Material properties of metal thin film alloys of gold and ruthenium. The thin films measured here were 300 nm, and the mechanical properties were measured by Berkovich nanoindentation at 24 nm depth to avoid substrate and indentation size effects [36].

Material	Hardness (GPa)	Electrical Resistivity ($\mu\Omega$-cm)	Elastic Modulus (GPa)
Gold	1.04	3.6	86
Au-5%Ru	2.42	38.5	122
Au-10%Ru	3.99	56.5	137
Au-20%Ru	4.28	69.9	148
Au-30%Ru	6.18	87	154
Au-70%Ru	11.46	86	231
Ruthenium	15.28	13.8	295

3.3.5 Characteristics of Au-V_2O_5 [8]. Bannuru, et al. developed solid solution thin films of gold-vanadium (Au-V) and dispersion strengthened thin films of gold-vanadium oxide (Au-V_2O_5) for analysis as possible MEMS electrical contact materials. In [8], Bannuru, et al. report measured resistivity and hardness of eight combinations and conclude that the dispersion strengthened thin films offer more potential as MEMS contact materials due to reduced adhesion in contact tests and lower increase in resistivity when compared to solid solutions. In [10] Bannuru, et al. further demonstrate the value of the oxide dispersion strengthening approach to thin film microswitch applications. They report a first order estimation of the dispersed particle radius as 2.2 nm [10]. The grain size of the material was approximately 35 nm and the distance between particles for the Au-4%V_2O_5 was 12.7 nm [10]. The volume fraction of the V_2O_5 for the 4% (at) alloy is reported as 9.8%. A summary table of reported Au-V_2O_5 properties is given in Table 3.9.

Additional hardness testing on a Au-4%V_2O_5 thin film was accomplished during the present study using an MTS Nano Indenter XP^{TM}with a Berkovich tip. This testing determined the hardness of the Au-4%V_2O_5 to be 4.2 GPa and the modulus of elasticity to be approximately 175 GPa. The hardness result is very close to the

Table 3.9: Material properties of metal thin film alloys of gold and vanadium oxide from Bannuru, et al. [8]. The hardness was measured using a Hysitron Triboscope with a Berkovich tip.

Material	Hardness (GPa)	Electrical Resistivity ($\mu\Omega$-cm)
Gold	2.52	6.1
Au-2.3%V_2O_5	3.28	12.0
Au-4%V_2O_5	4.00	17.7

measurement reported in [8]. Note that the gold properties of hardness and resistivity differ between the gold deposited at AFRL and Lehigh, as reported in Tables 3.8 and 3.9 respectively. This is likely due to variations in the sputtering tools and process, including a difference in base pressure used. Note that Bannuru states that resistivity measurements reported in other studies vary widely [9].

3.4 Test Material Selection

The first essential step in material selection methodology for electric contacts in MEMS switches is to characterize the interrelationship between hardness and resistivity [142], and to experimentally determine how the relationship between these and other material properties affects the lifecycle performance of the contact material. The intention of this study was not to develop the optimal contact material for use in a MEMS switch, however the study did develop and demonstrate a new experimental method to compare contact materials directly and show the influence of hardness and resistivity on the lifecycle performance of contact metals as well as develop contact performance data on the tested materials.

Contact materials tested were selected to provide a range of hardness values and microstructures to give designers empirical data on the influence of material hardness on contact performance. The materials chosen for testing were a first step toward developing systematic screening testing and criteria, and selection testing and criteria for use by MEMS switch designers. The experiment designed and developed here

can be used to assist MEMS switch designers to make design trades based on these material properties.

Three different contact metals were chosen for testing: 100% gold, 95% gold/5% ruthenium and 96% gold/4% V_2O_5. Gold was chosen as a test metal to provide a baseline for this research as the majority of MEMS contact research has been done using gold as a contact material. Research by Chen, et al. shows that Au/Ru alloys perform extremely well in lifecycle tests [36]. During the cycling tests done by Chen, et al., only minor contact wear was observed in Au-5%Ru, Au-10%Ru, Au10%Pt and Rh [36]. Also, neither the Au-5%Ru nor the Au-10%Ru showed a sudden large increase in contact resistance during cycling but the Au-10%Ru did show a black contamination layer grown around the contact area [36]. The gold/ruthenium alloy of Au-5%Ru was chosen because its properties of hardness and resistivity have enough variance with gold such that the experimental data can be analyzed to see the effect of material properties on the performance of the contact metal. This binary alloy also demonstrated a reduced susceptibility to contamination due to reduced surface reactivity.

The material selection focused on promising alloys of gold and ruthenium which had a wide variation of hardness and resistivity. These are also two-phase materials, for which lifetime and performance data is sparse. The choice of alloys was based on material properties of hardness and resistivity. A plot of resistivity versus hardness of a variety of materials is shown in Figure 3.1. Baseline work on the properties of these and several other alloys has been reported by AFIT and NEU [36, 46, 142]. The selection of alloys for use in the present study was also based on the knowledge that small amounts of ruthenium will harden gold, providing a projected long-life and wear resistant electrical contact. Ruthenium is also of great interest in this research and for use as a MEMS contact metal because ruthenium oxide is also conductive and it has been reported that a layer of RuO_2 on top of Ru can substantially reduce contamination of a Ru contact [170].

Gold/Ruthenium alloys also show promise over other alloys with similar hardness and resistivity due to the possibility that they are less reactive and thus are less prone to contamination buildup. A first principle calculation suggests that alloying ruthenium with gold reduces the binding energy of oxygen to gold [37,83]. It has been hypothesized by Chen that because the alloyed Ruthenium shifts the d-band electron structure of the gold film, the surface reactivity changes and thus makes the contact material less susceptible to contamination [36, 37].

Au-4%V_2O_5 as developed by Lehigh University [8] was chosen to compare results of a dispersion strengthened material to the binary Au-5%Ru alloy. The gold-vanadium oxide is a new material developed for use in MEMS contact switches and data on micro-contact size performance and lifetime performance of this contact metal has not yet been published. Testing of this material demonstrated the effects of material properties on performance, and also is an illustration of the utility of this test setup and its ability to quickly test prospective contact materials.

Gold, gold/ruthenium and gold/V_2O_5 alloys were the contact metals chosen for use in this study given their material properties. The hardness of gold is easily increased through the addition of only moderate amounts of Ru. Bannuru et al. showed that dispersion strengthened Au-V_2O_5 is more promising than solid solution Au-V [8]. The engineering tradeoff due to alloying is the increase in electrical resistivity, but the wear resistance benefit due to increased hardness and possibly increased lifetime may outweigh the loss of resistivity.

3.5 Predicted Results

The harder materials were expected to perform better and last longer under the conditions of the test. The Au-V_2O_5 alloy was expected to show performance advantages over the other two materials tested. Damage and evolution of contact materials is expected to be a significant factor in the lifetime performance of micro-switch contacts. Harder materials with a higher yield strength were expected to accumulate less damage during testing and therefore exhibit longer lifetimes. Measurements of pull-off

force, contact interference, threshold force and threshold distance were all expected to vary inversely with hardness. However, use of harder materials will require tradeoffs in design and will generally cause an increase in contact resistance.

The hypotheses tested in this research were as follows:

1. The lifetime performance of gold is improved by alloying with ruthenium to increase its hardness.
2. The growth of resistive layers and/or failure of the contact is reduced by alloying as seen in [37].
3. The strain hardening of contacts is seen during the cycling tests.
4. The adhesion force (or pull-off force) is greatest for the softest metal and will decrease with hardness, unlike it is described in [132, 202].
5. The force required to make good electrical contact (defined as threshold force in this study) increases with cycling, as will the pull-off force required to separate the contact from the strike plate.

3.6 Summary

Materials selection is an important element of engineering design in any field of engineering. It is very important to develop systematic methods for these when designing devices for any function. This chapter described the basis for a detailed and systematic approach based on material properties to address microcontact mechanics and material selection. Researchers, with a few exceptions, have either mostly reported on gold due to its attractive properties or tested and recommended other materials without using a systematic analysis of material properties and material performance. Descriptions of several materials and their properties and description of the material properties which most affect microcontact performance were provided. The importance of developing realistic operationally representative testing capabilities to use in screening and selection of candidate materials in MEMS switch design was described.

This background suggests that further work is needed to understand and quantify the importance of each material property on micro-contact performance. Some of this future work will necessarily need to be experimental in order to directly compare the performance of various materials so that designers can understand the tradeoffs they must make when designing and fabricating switches. The next chapter describes the design and custom fabrication of test devices which were used in the research for simulating microswitches and developing contact data on different materials.

IV. Design and Non-planar Fabrication of Custom Test Cantilevers

This chapter describes the design work which went into developing test cantilevers used for this study, as well as the process developed for patterning and etching contact bumps onto non-planar, released silicon surfaces. Similar test devices were developed at Northeastern University, however their process used a standard planar bulk etching process to create contact bumps on micro-cantilevers [37]. This chapter describes the design of the cantilever used in the present study, initial fabrication efforts, the final fabrication chosen for the cantilever and the process used to produce contact bumps on the cantilevers. Cantilevers were used to simulate the contact action of MEMS switches instead of complete MEMS switches to reduce the development efforts necessary to change the test contact material. The test setup designed also offered a relatively simple method of analyzing contact surfaces after cycling without requiring switches to be opened, risking damage to the contact surfaces.

Cantilevers were designed using L-edit, and were fabricated using the Silicon-on-Insulator Multi User MEMS Processing System (SOIMUMPS) process by MEMSCAP (Research Triangle Park, NC). A contact mask containing 7.5 μm diameter dots corresponding to a location at one diameter distance from the end of each cantilever was designed and procured. MEMSCAP dies were mounted on silicon wafers, coated with 1818, and the dots patterned and exposed on a Karl Süss MJB3 contact mask aligner and then developed. The remaining photoresist dots were reflowed into hemispherical bumps. Then, the critical etch step using inductively coupled plasma/reactive ion etching (ICP/RIE) was accomplished at the Air Force Research Laboratory.

The design of cantilevers for use as test devices is described first, followed by a description of the effort to fabricate the cantilevers. The successful fabrication technique developed is described in this chapter, including difficulties faced in the fabrication and their solutions. Appendix B presents a description of the etch recipe development work accomplished while Appendix C gives the process follower developed for fabrication in the present study.

4.1 Cantilever Design

The cantilever test devices developed were a significant part of the experimental design. The cantilevers used at Northeastern University in their AFM based experiments had a stiffness of approximately 1.5×10^4 N/m [37]. However, that setup had much more precise vertical position measurement capability with the laser motion sensor built into the AFM than the nanoindenter based apparatus designed for the present study. Cantilevers designed for use in the setup created for the present study require less stiffness to generate realistic contact forces representative of those used in MEMS micro-switches. Typical MEMS switches use contact forces in the range 50-1000 μN [202, 247]. Cantilever beam stiffnesses in actual switch designs generally fall between 15-40 N/m, with the pull-off force available of 30-120 μN [202]. Note that thin layers of contact material on a silicon cantilever as tested here can represent the behavior of actual MEMS switches. This is due to two factors: First, some switches have a contact material thickness of approximately 500 nm, and second, due to the skin effect where RF current is carried mostly by the top layer of the conductor (e.g. the surface 2.5×10^6 m in gold carries all of a 1-GHz signal).

Several design iterations were required, but the final cantilever design was a cantilever with a stiffness of approximately 200 N/m, which would provide a 400 μN contact force at 2 μm of displacement. Figure 4.1 shows the top view of the cantilever design as fabricated. The test cantilever points to the left in the image and is shown attached to the mounting substrate which was large enough to be handled with tweezers. The side rails extending to the top and bottom of the image indicate that this cantilever has not yet been cut apart from the die. The design stiffness of the cantilevers had to be balanced with the need for a relatively handling tolerant design. The cantilevers as fabricated and mounted in this study did not have the physical protection and robustness of typical surface micromachined cantilevers fabricated on a substrate and were therefore much more challenging to handle without damage. Efforts made to fabricate the cantilever design are described in the next section.

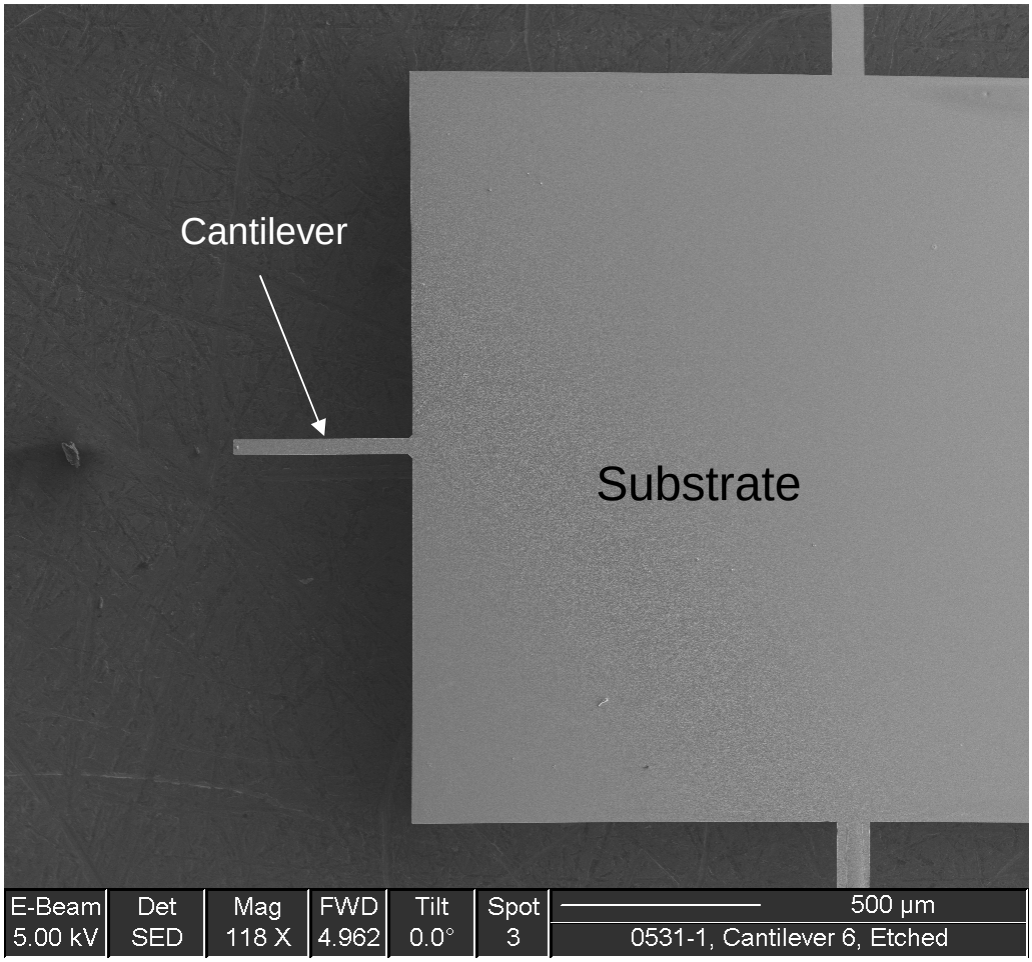

Figure 4.1: Scanning Electron Microscope micrograph at 118X showing final cantilever design as fabricated.

First, the attempt at bulk micromachining of devices is described, then the ultimately successful use of SOIMUMPS is described.

4.2 Cantilever Fabrication

Cantilever fabrication was a significant effort which required a large amount of development work. Design and development of the unique test devices was central to the research and on the critical path for project completion. The experimental setup could not be finalized and tested without fabricated specimens of the final version of the test cantilever. The first attempt was to model a bulk micromachining process after the Northeastern University process used on Silicon-on-Insulator wafers.

The next section describes this attempted bulk micromachining effort, followed by a description of the ultimately successful use of the SOIMUMPS process.

4.2.1 Bulk Micromachining Effort. Bulk micromachining of silicon is a simple process to describe. Wafers can be coated with photoresist, patterned, developed and then chemically wet etched with an etchant such as Tetra Methyl Ammonium Hydroxide (TMAH). This type of etching preferentially etches the $< 111 >$ plane of the silicon. Thus, an angle of 57.4° is created in areas not masked with SiO_2 [111]. Attempts to wet etch with TMAH were not successful.

An attempt was made to perform some of the process steps at the University of Dayton (UD), however the UD backside aligner did not have the attachments necessary to fit masks for use with 100 mm wafers. The bulk micromachining effort was abandoned due to the amount of time required to acquire, calibrate equipment and develop the process.

An alternative to fabricating cantilevers locally was selected. The method chosen was similar to the POLYMUMPS process which AFIT students commonly use for fabrication of MEMS devices. The process is called SOIMUMPS and is run by MEMSCAP in North Carolina. A description of the design and fabrication of cantilevers using this process follows.

4.2.2 SOIMUMPS. A design using the SOIMUMPS design rules and process was put together for fabrication of custom die with one dozen cantilevers per die. The development and research accomplished here demonstrate the viability of coating, patterning and bulk etching non-planar surfaces.

The basic process of SOIMUMPS fabrication begins with a researcher putting together a design which takes advantage of the common processing steps used and then sending the design electronically to MEMSCAP. SOIMUMPS uses standard steps described in the SOIMUMPS Design Handbook [176] which perform processing on Silicon on Insulator wafers with a device layer thickness of either 10 μm or 25 μm.

See the SOIMUMPS Design Handbook [176] for a detailed description of the steps in SOIMUMPS processing. The designer lays out the pattern for etching in each step on a 1 cm x 1 cm wafer segment. This design is repeated along with the designs of other SOIMUMPS users on each wafer being fabricated at MEMSCAP. The designer then receives 15 each 1 cm x 1 cm dies patterned to his specifications approximately three months later. The design die layout developed for this research is shown in Figure 4.2. Once the cantilever die were received, further processing was required in order to prepare them for use in testing and fully realize the test devices necessary for simulation of microswitch contacts.

The cantilevers as designed were 450 μm long x 40 μm wide x 25 μm thick attached to a substrate of dimensions 3.6 mm x 1.6 mm. The substrate is large enough to handle with tweezers. The sidewalls of the etch using SOIMUMPS are vertical and end up being relatively easy to grasp with tweezers. However, because the cantilever extends from the substrate without any protection after dicing, these test devices are much more difficult to handle both before and after mounting on the mount plate than other typical MEMS devices which can be mounted on microchips. The cantilevers used in this study were fragile, unprotected and required careful handling during mounting and experimental setup. This study also showed that with proper handling, setup, processing steps and experiment design, unusual micro devices such as these can be experimentally investigated.

4.3 Test Device Fabrication

The SOIMUMPS process successfully fabricated silicon cantilevers. However, these cantilevers needed a contact bump to simulate the contacts used in MEMS switches. The next step in the process was to develop a methodology by which standard MEMS processing techniques could be used on the non-continuous and non-planar die surface of the released cantilevers. The successful preparation and etch of contact bumps onto SOIMUMPS dies consisted of the following steps: (1) Mounting dies onto carrier wafers, (2) Processing mounted dies through photolithography, (3)

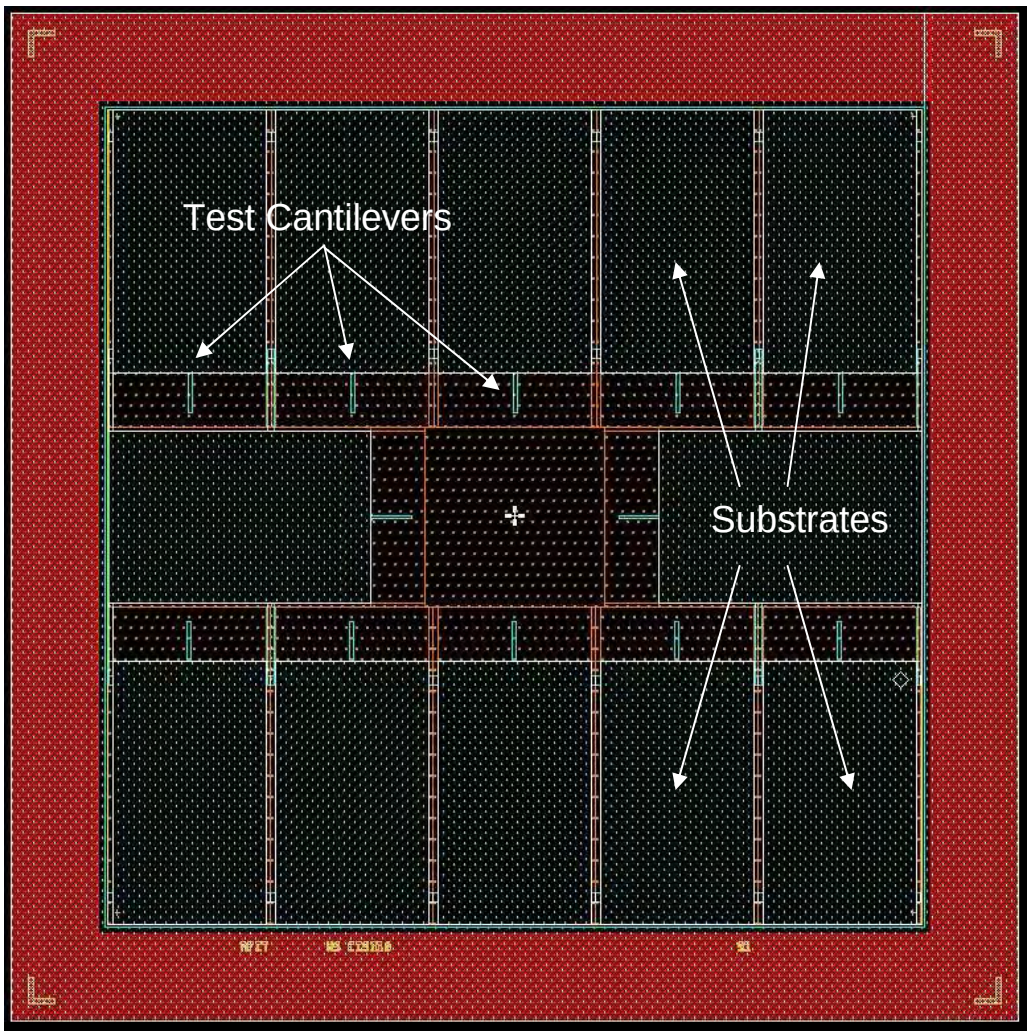

Figure 4.2: Top view of design developed for SOIMUMPS fabrication. Note that it contains 12 cantilevers over a large void on the inside of the die. The fabricated die were 1 cm squares. This diagram is a design proof received from MEMSCAP.

Etching bumps into cantilevers using RIE/ICP, (4) Demounting dies from carrier wafers, and (5) Dicing cantilevers apart. Each of these steps enabling successful fabrication is described in the following section. The efforts required to develop the processing technique for developing the test devices used in this study are described in Appendix A. The bump etching technique used for test device fabrication is given in Appendix B. The process follower developed for this process is given in Appendix C. An example of a test cantilever with etched bump is shown in Figure 4.3.

MEMSCAP fabricated die were mounted on 50 mm silicon wafers to facilitate handling and processing during bump fabrication. The die containing released cantilevers were adhered to the carrier wafers using 1818 photoresist. This allowed the die to be released after processing by soaking the carrier wafer in solvent. Mounting the die on carrier wafers also enabled the use of standard photolithography processing.

After mounting, the die were spin coated with 1818 photoresist for 30 seconds at 4000 rpm. An MJB3 contact mask aligner was used to pattern the contact bumps near the end of the cantilevers on the die. After exposure, the pattern was spin-developed which left a photoresist dot at the end of each cantilever. The wafer was then heated on a hotplate which caused the remaining photoresist to reflow into a hemispherical shape.

An ICP/RIE recipe was developed to etch the bump into the end of the cantilever and is described in Appendix B. After etching, the wafer was cleaned using a heated 1165 bath. This resulted in removal of residual photoresist as well as die separation from the carrier wafer. The die then consisted of twelve silicon cantilevers with a silicon contact bump near the end of each cantilever. Two examples of etched bumps are shown in Figures 4.3 and 4.4.

After etching and cleaning, each cantilever bump was imaged using a scanning electron microscope (SEM). After imaging, each die was diced using a Micro-Ace 3 Load Point Limited Series high-speed diamond saw by a skilled technician at AFRL.

4.3.1 Contact Material Coating . After the etched die were diced and cleaned, they were coated with the appropriate contact material at AFRL or Lehigh University. At AFRL, the contact material was deposited in a Denton Vacuum Discovery 18 DC magnetron sputtering system with a base vacuum of 1.4×10^{-6} Pa. The thickness of all coats was 300 nm and a chromium adhesion layer was used for the gold coat. The test samples coated at Lehigh University were prepared using DC magnetron sputtering with a thin titanium adhesion layer. The process gas used at Lehigh was argon at 4 mTorr and oxygen was added to the process stream at 0.1

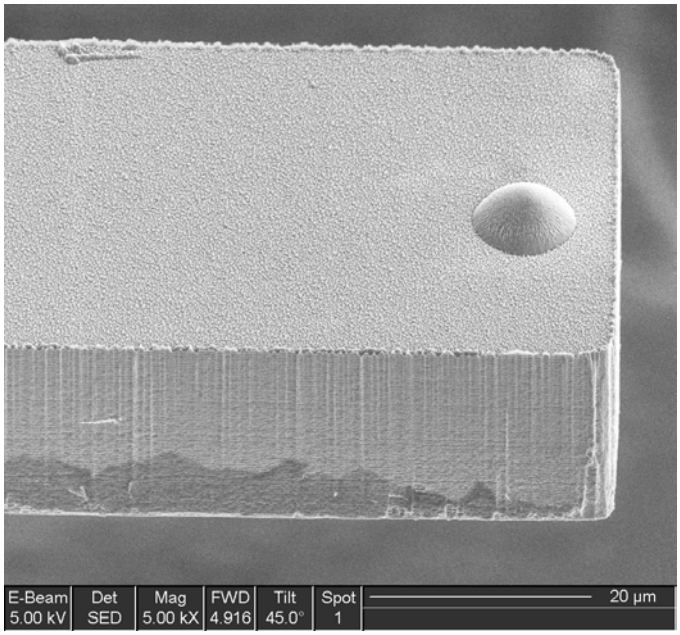

Figure 4.3: Close-up SEM micrograph of a sample 7.5 μm diameter rounded contact bump fabricated using 1818 for these experiments.

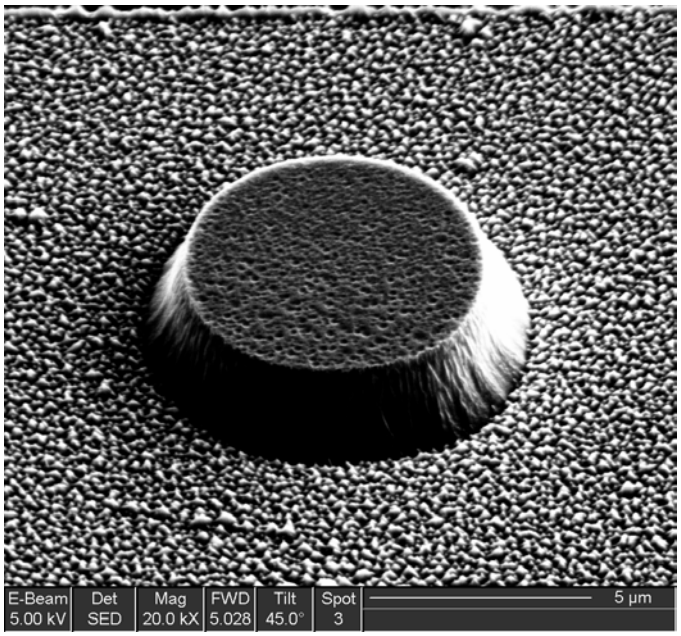

Figure 4.4: Close-up SEM micrograph of a sample 7.5 μm diameter flat-topped contact bump fabricated using 1818 for these experiments.

mTorr during deposition [8]. After coating, the contact bumps were again imaged using scanning electron microscopy.

4.4 Summary

Test devices were custom designed and fabricated for use in this study. Test cantilevers were used insead of actual MEMS switches to provide the ability to easily change the contact material of interest without requiring significant redesign of the switch fabrication process and to simplify post-cycling evaluation of contact surfaces. The use of cantilevers to simulate microcontact mechanics allows researchers to focus on the measurement of contact parameters and their relationship to material properties rather than process development. The development of test cantilevers reported here will simplify the processing and fabrication development needed for future use of the nanoindenter based test setup and future research into microcontact mechanics.

Design was done based on the SOIMUMPS process and a fabrication methodology was developed to mount dies, and coat, process and bulk etch non-planar surfaces (e.g. cantilevers mounted and released hanging over a void). The design and process development work was completed successfully fabricating silicon cantilevers with approximately 200 N/m stiffness with rounded or flat-topped bumps which were used to simulate the action of MEMS contact switches. The next chapter discusses the design of the apparatus used to mount and measure the performance of microcontacts using the test devices herein described.

V. Engineering Design, Development and Fabrication of Experimental Setup

This chapter describes the design work which went into developing, constructing and automating the tasks of this study. The sample tray design was the main enabling factor for the success of the test, and the overall experimental set-up used custom designed and commercially available components integrated with automation capability to develop a unique tool for generating test data and analyzing performance of contact materials used in MEMS contact switches. It should be noted that this study was not simply a task to make use of an existing tool or set of tools to produce experimental data on contact materials. The project required design, development and proof-of-concept work to design and build an apparatus within a set of constraints to enable experimental collection of micro-contact data. The design of this set-up was built around mounting and operating test devices to simulate operation of a MEMS ohmic contact switch and measure performance of MEMS' microcontacts. The experimental design enabled measurement of force vs. resistance, contact interference, change in contact stiffness due to cycling, threshold force and distance, as well as other contact parameters over the lifetime of test microcontacts.

The MTS Nano Indenter XP is a versatile and capable instrument. It is programmable and allows input and output of variables and data other than merely force and displacement of the indenter head. The present study used capabilities of the system which were not previously exercised. The use of the National Instruments Data Acquisition (NIDAQ) system including modules which output current and acquire the resulting voltage measurements and then utilizing the measurements to calculate change in resistance have not been previously accomplished. This set-up offers a possibility for commercialization opportunities to MTS Nanoinstruments for expanding the operational range and use of their instruments.

5.1 Setup Design

Design, fabrication and installation of the test fixture inside the MTS Nano Indenter required the design of a mounting system for a micro-cantilever, a method to control three-axis alignment of the cantilever and the lower contact, and the design and fabrication of a new sample tray to enable the test setup to fit inside the nanoindenter and maintain clearance between the test sample and microprobe tip. It was also necessary to simultaneously ensure the cantilever was within the 2 mm working range of the microprobe. Tests were performed using a custom modified MTS Nano Indenter system using the XP nanomechanical actuating transducer, TestWorks Explorer^{TM}software, NIDAQ TestWorks Channel Manager and a phase-lock amplifier for continuous stiffness measurement.

The test set-up simulates the action of MEMS contact switches by using a silicon cantilever beam with a contact bump on the end, as previously described. To simulate a switch, the cantilever beam contacts a flat piece of silicon (strike plate) coated with a conductive metal layer. This simulated switch is mechanically cycled by a strike plate attached to the top of a piezoelectric transducer (PZT). The resistance through the simulated switch is measured using a four-wire measurement technique. This measurement shows the resistance change in the simulated switch as it is being cycled. Different contact metals and alloys can easily be installed in this experimental setup in order to demonstrate and compare the relative performance of differing contact materials. An overview schematic of the test setup is shown in Figure 5.1.

The contact is cycled by raising the strike plate into contact and displacing the cantilever end by a given distance at a prescribed frequency for a specified number of cycles. Then the cycling is stopped and the contact resistance is measured by raising the strike plate and holding it in contact at a preset displacement. The strike plate is then lowered for an out of contact resistance measurement. The contact force and resistance characteristics are then measured by the nanoindenter. The microprobe tip was an extended shaft cube corner tip. This tip was chosen to avoid physical contact

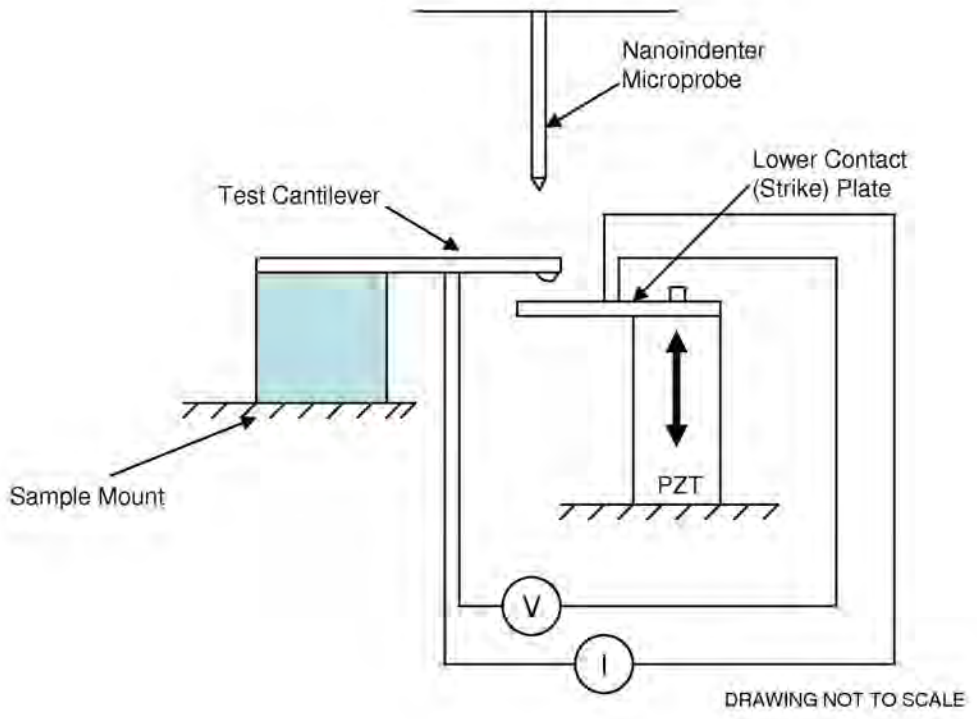

Figure 5.1: Overview schematic of relative geometry of experimental apparatus.

between the tip and any of the experimental setup and to provide extremely accurate indent positioning. The MTS Nano Indenter was used in load controlled mode and has a load resolution of 50 nN and a displacement resolution of 0.01 nm.

The most critical item for success of the present study was also the one which had to be designed and fabricated before any other steps in the experimental development could be taken, i.e. a method of mounting small micro-cantilevers inside the limited working space of the nanoindenter was required. Specifications of the available space were obtained from MTS Nanoinstruments and several design iterations pursued. Ultimately, a machined block of aluminum was designed to replace the standard sample tray to mount the set-up inside the MTS Nano Indenter XP. This design was dependent on the size of the motion control devices chosen to position the test cantilever and the strike plate to simulate the action of a micro-switch. Research into commercial positioning devices and their performance characteristics was required, resulting in selection of appropriate micro-control stages, both manual and computer controlled as well as a small piezotransducer (PZT) stack which was intended for use

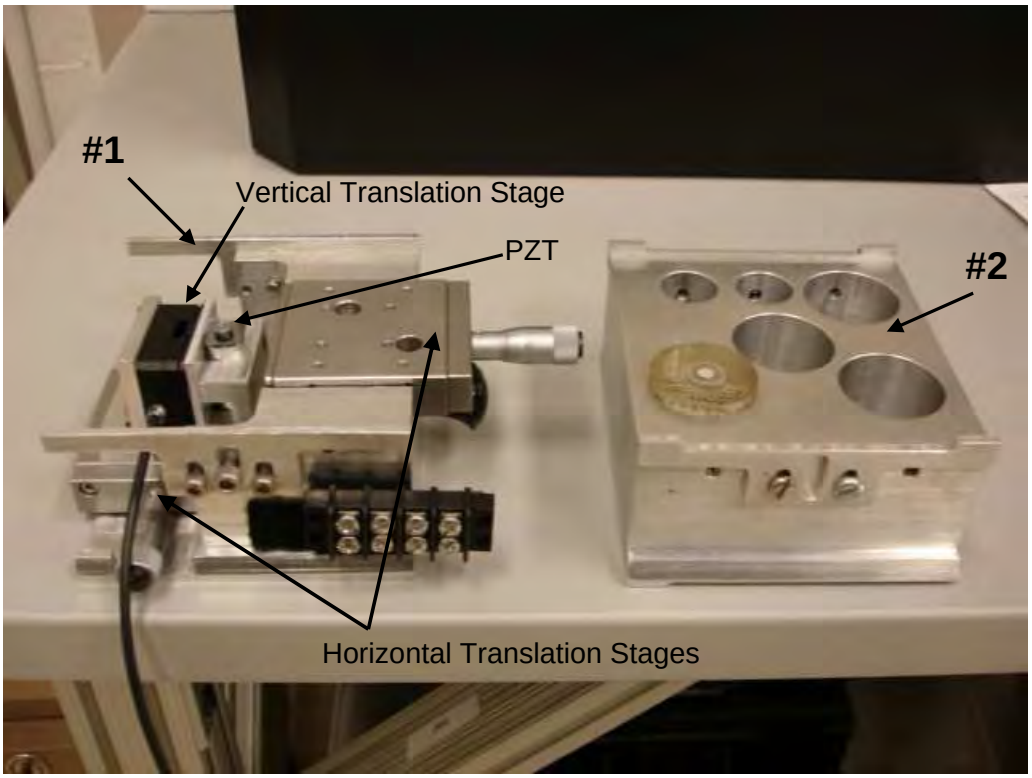

Figure 5.2: New sample tray (#1) designed to fit in the constrained space in the MTS Nanoindenter compared with the original (#2).

to cycle the simulated switch at a rate higher than the rate available from the indenter head. Devices from Physik Instrumente (PI) were chosen as the best option for size and automated control capability. The physical dimensions of these devices based on engineering drawings were used in laying out the design of the sample tray. Therefore, the design process was iterative and required to develop a successful apparatus geometry and control/positioning system.

5.1.1 Novel Sample Tray. The experimental set-up is based on a sample tray designed to fit in the space available in the working area of the MTS Nano Indenter XP. This sample tray (#1), shown in Figure 5.2, which was designed by the author and fabricated specifically to make this experiment possible, is shown next to the standard MTS sample tray (#2) used for thin-film materials nanoindentation testing in Figure 5.2. The design of the sample tray assembly to fit in the limited space within the

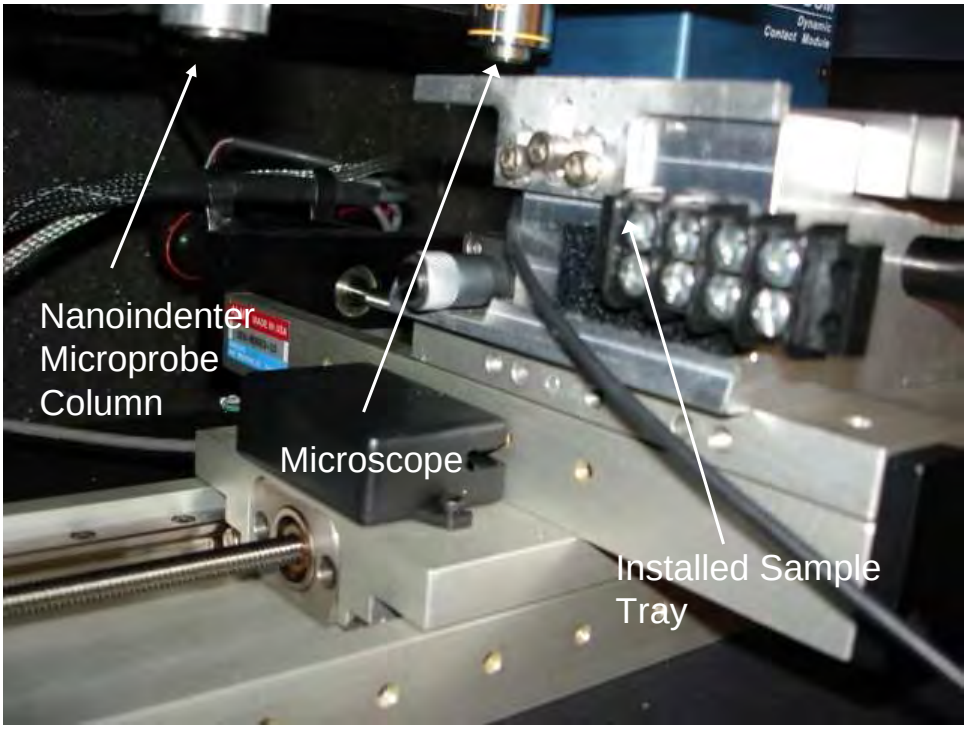

Figure 5.3: Side view of how the new sample tray fits in the constrained space in the MTS Nanoindenter.

MTS Nanoindenter XP was critical. The vertical limitation is 57.15 mm (2-1/4 in.) total. Any part of the experiment extending above the side rails on the sample tray could come in contact with the indenter head. If this happened, the indenter shaft could be damaged causing significant harm to the instrument. The fit of the newly designed sample tray in the limited space is shown in Figures 5.3 and Figure 5.4. The indenter head has a total travel range of 1.5 mm so the design required exact vertical placing of the cantilever near the middle of the head travel range such that the head would have clearance and yet enough remaining travel to actuate the simulated switch during testing. This sample tray was designed successfully within the constraints for this study and the set-up fit in the working space inside the nanoindenter.

Further, the setup is designed such that the user has 3 degrees-of-freedom control to align the cantilever with the flat conductive plate using the microscope built into the Nanoindenter XP. There is a vertical stage attached to a Piezoelectric Transducer (PZT) which raises the strike plate into contact with the cantilever. Contact is

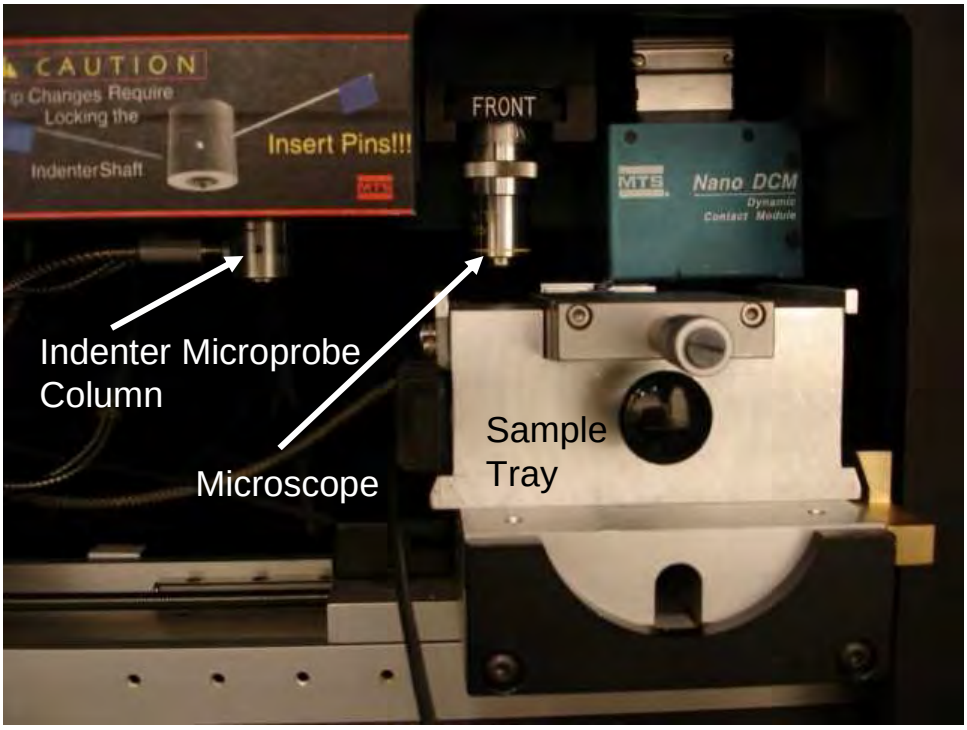

Figure 5.4: Front view of how the new sample tray fits in the constrained space in the MTS Nanoindenter.

detected when the four-wire resistance measurement first shows a resistance. This process is automated within the TestWorks test method developed and was programmed with the assistance of the Nano Instruments Innovation Center. The test method is a set of instructions, or test segments, used to automate experiments and data collection. Note that the capability to run the MTS Nano Indenter XP manually does not exist. The test method developed for this study is given in Appendix H.

The test method was developed such that TestWorks reads an input channel which shows voltage change across the four-wire setup and calculates the resistance across the simulated switch. The control logic in the test method looks for a change in resistance and compares it with a preset value to determine if the plate is in contact with the contact bump on the cantilever. If the plate comes into contact with the cantilever, the resistance value drops significantly below 80 Ω. The criterion which automatically determines that the bottom plate is in contact can be adjusted within the test method. The test method changes the voltage controlling the displacement

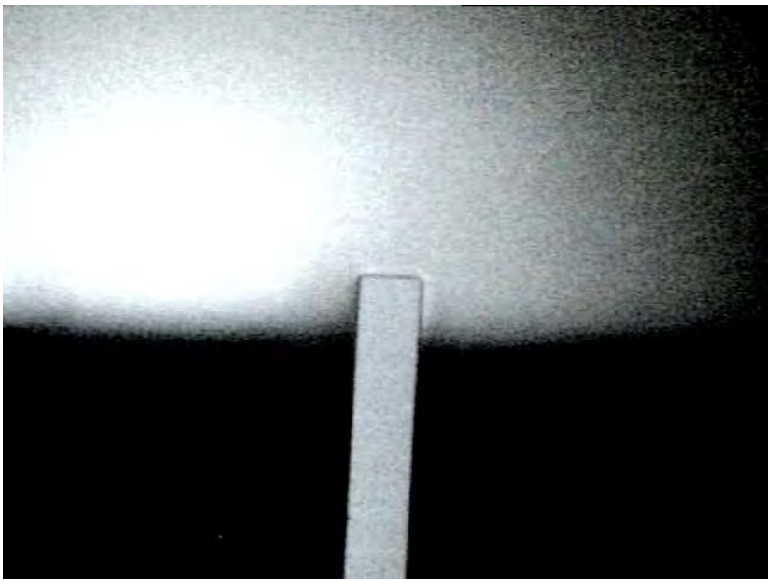

Figure 5.5: Top view from the microscope built into the nanoindenter. This is the view used when using the micrometer and vertical stage in setting up the alignment before the experimental runs. Note that the strike plate is out of focus because it is below the cantilever.

of the PZT by a very small value, and then measures the resistance change. The exact point of contact is calculated by slightly increasing the voltage applied to the PZT in steps of 0.001 V, which equates to a displacement of nominally 1.5 nm. The PZT device (Physik Instrumente (PI) P-841) is capable of fast translation, up to a maximum of 15 μm to within $\pm$10 nm. This device was used to cycle the contact with a prescribed displacement. The contact force was calculated using this displacement and the stiffness of the cantilever.

Figure 5.5 shows a test cantilever (450 μm length) in alignment with a strike plate. The strike plate is made of silicon coated with the contact metal under investigation, with a laser-cut hole which allows mechanical attachment to the PZT. The bottom contact strike plate has an approximate stiffness of 21,000 N/m installed and dimensions of approximately 12mm x 19mm. A photograph of a closeup of the experimental alignment is shown in Figure 5.6. The first iteration of bottom plate design was 12mm x 12mm. However, the bottom strike plate size was changed to ensure that the column protecting the nanoindenter head would have enough horizontal

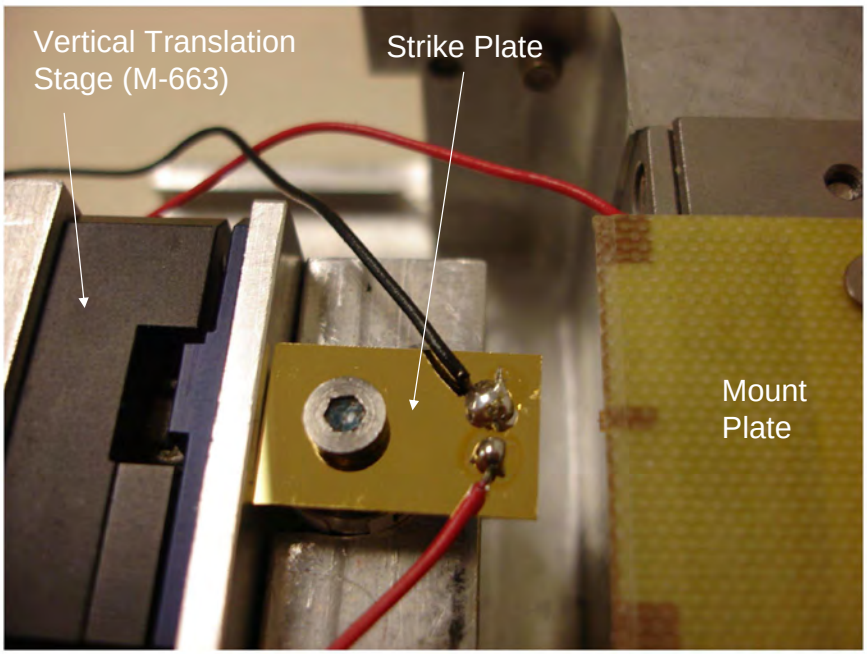

Figure 5.6: Experimental set-up alignment. Note that the strike plate design changed to a longer plate to ensure no lateral interference with the indenter column during indentation.

clearance to avoid interference when the cantilever was actuated by the microprobe. The dimensions of the redesigned bottom contact plate is shown in Figure 5.7.

5.1.2 Mount Plate. Design of the mount plate for the micro-cantilevers was another critical step. A method of mounting the test cantilevers which would allow for electrical connections and the use of the four-wire resistance measurement technique was needed. The solution was to use FR4 printed board material, with gold solder pads and traces to a center cantilever mount location. These conductive paths were 100 μin nickel and 50 μin gold. This design provided a location to wax mount the cantilever and to wire bond the conductive side of the cantilever to electrical conductive paths on the mount plate. These conductive traces were connected to conductive pads large enough to allow soldering of wires for the current input and voltage measurement loops. The use of cantilevers required wirebonding out of plane by a skilled technician, which was an untried operation prior to this design. The ability to wire-bond out of plane was the most important step to mount the cantilever on

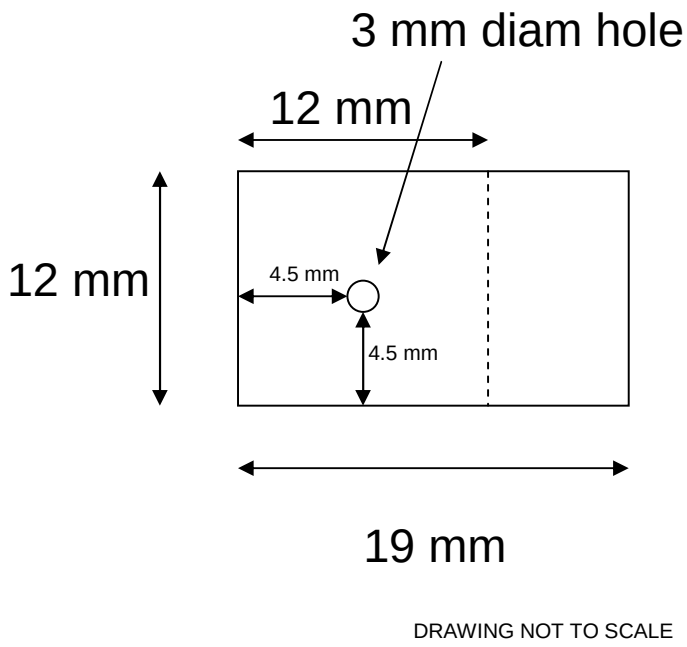

Figure 5.7: Dimensions of the redesigned contact strike plate to ensure lateral clearance around the indenter column. They were laser cut from 75 mm (3") silicon wafers by Mound Laser in Miamisburg, OH. The hole is to enable use of a 3 mm diameter mechanical fastener to attach the strike plate to the PZT.

the mount plate face up, and then turn the mount plate upside down for installation on the manual micro-translation stage to position the cantilever over the strike plate. A NEU cantilever wire-bonded on a mount plate is shown in Figure 5.8.

The thickness of the printed circuit board mount plate was also an issue. The plate needed to be stiff enough to not affect test results, but still place the cantilever within the operating range of the nanoindenter. A plate thickness of 0.762 mm (0.030") was used, which required beveling of the cantilever mounting edge to reduce the edge thickness and avoid interference with the microprobe tip. The tight tolerances required to make this setup work affected the choice of microprobe tip for use in the experiment, as will be described in the next section.

The size of the mount plate was based on the size of the manual micro-translation stage (PI M-105) chosen to move the test cantilever into the test position. Four 3-mm holes were drilled and countersunk in the mount plate to facilitate mechanical fastening of M3x4 fastener holes available on the translation stage. These holes in

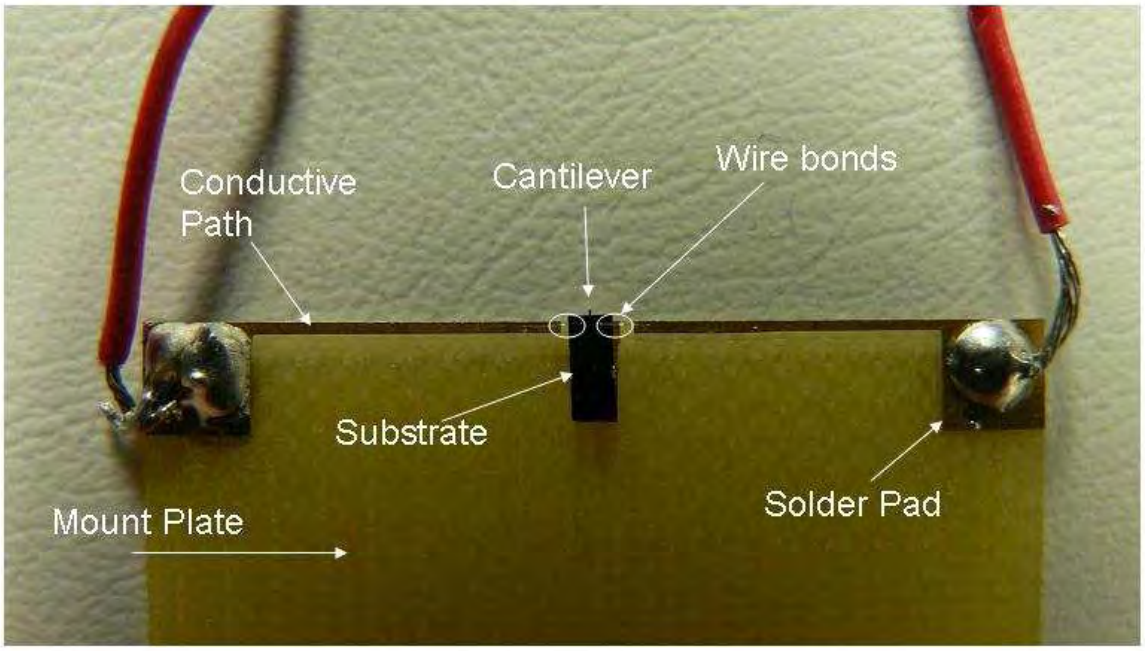

Figure 5.8: Top view close-up image of cantilever mounted on custom designed mount plate.

the mount plate were countersunk as much as possible in order to reduce the height of the mechanical fasteners to avoid the possibility of the screw heads colliding with the microprobe tip during tray motion and imparting lateral forces on the indenter column. M3x4 phillips head fasteners were required to attach the mount plate to the micro-translation stage. These fasteners were customized by machining away the material under the head such that the screw head was flat to minimize the height of the fastener heads above the mount plate. This was done to avoid accidental interference with the indenter head during motion of the sample tray inside the nanoindenter. The layout of the mount plate design is shown in Figure 5.9.

5.1.3 Cantilever Beams. In order to develop contact force regimes similar to that of actual MEMS switches, a cantilever 450 microns in length was designed. The beams were 40 microns in width and 25 microns thick. The calculated stiffness of these cantilevers was nominally 200 N/m. The contact forces easily available with this test apparatus using these test devices was therefore approximately 200 μN to 1 mN. This estimated force range is based on displacements of 1 to 5 μm [144]. Note that

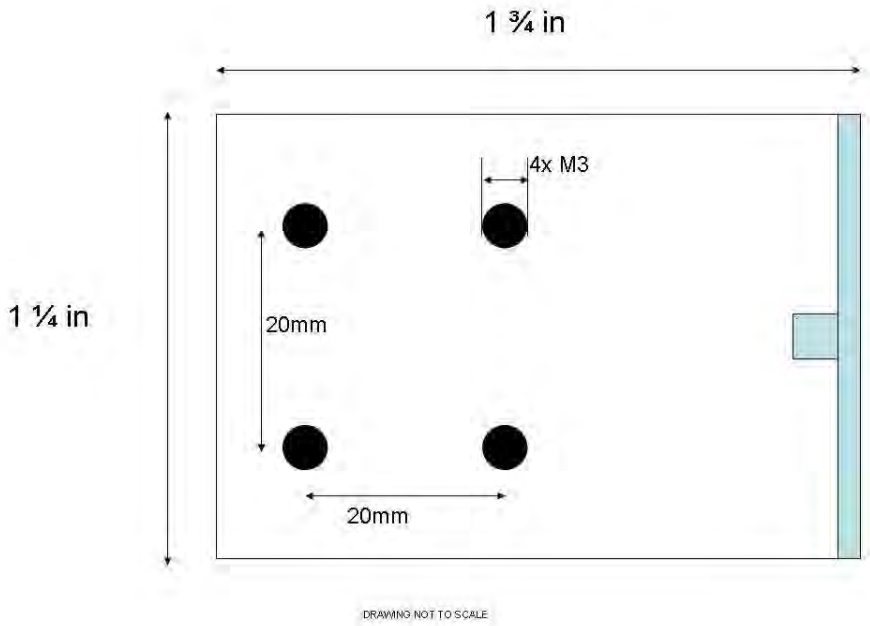

Figure 5.9: Top view of mount plate fabricated out of FR4 printed circuit board material with gold bond pads and traces for four-wire resistance connections. Designed to attach to top of M-105 micro-translation stage.

this displacement range is the range of actual MEMS switch displacements given by Leedy, et al. in [144]. The nanoindenter setup is capable of applying contact forces up to 10 mN, but contact forces of 400 μN were used for this study. This force could be reduced by using a cantilever of smaller stiffness as a test device. The cantilevers were micromachined out of a Silicon on Insulator (SOI) wafer, and included contact bumps at one diameter distance from the cantilever tips. Die containing flat cantilevers were fabricated by MEMSCAP (Research Triangle Park, NC) using the SOIMUMPS process. The contact bump was fabricated at AFIT and AFRL. A dot was patterned on the end of each cantilever using photoresist, reflowed to round the photoresist, and then ICP/RIE etched at AFRL. The bump size was approximately 7.5 microns in diameter as shown in Figure 5.10. Each cantilever and contact bump were sputter coated with the contact material to be tested. The design and fabrication of the custom cantilevers used in this study were previously described in detail in Chapter IV.

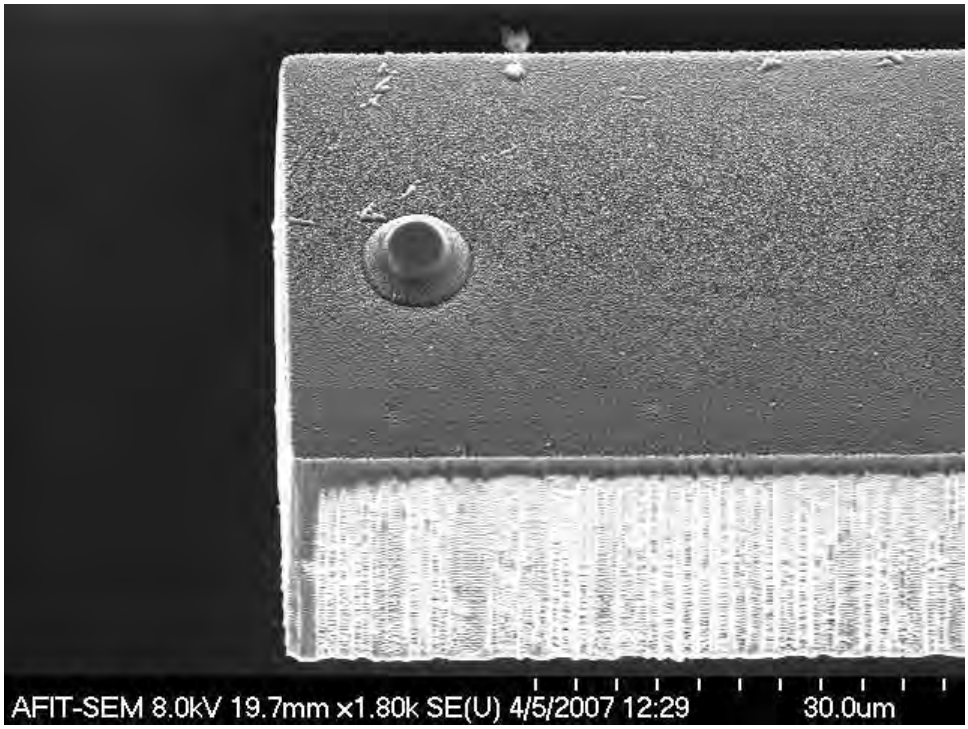

Figure 5.10: Sample 7.5 μm diameter contact bump fabricated for these experiments. The height is approximately 1.8 μm.

5.1.4 Microprobe Tip. During the first attempt at experimental setup using 120 μm long cantilevers fabricated at NEU, data was produced that showed higher contact forces required for low and stable electrical contact than is typical for MEMS switches. These results are shown in Figure 5.11. The threshold contact force of 8 mN measured when the microprobe applied load to the cantilever was far too high when compared to the much lower force normally required for gold micro-contacts to be in stable electrical contact. Microscopic analysis of the contact surface also showed that electrical contact was not occurring just at the contact bump. However, after engineering analysis of the mount plate and cantilever dimensions along with the dimensions of the indenter head and tip assembly, it was determined that these results were caused by interference between the indenter head and the mount plate. This problem caused by lack of clearance can be seen graphically in the drawing shown in Figure 5.12.

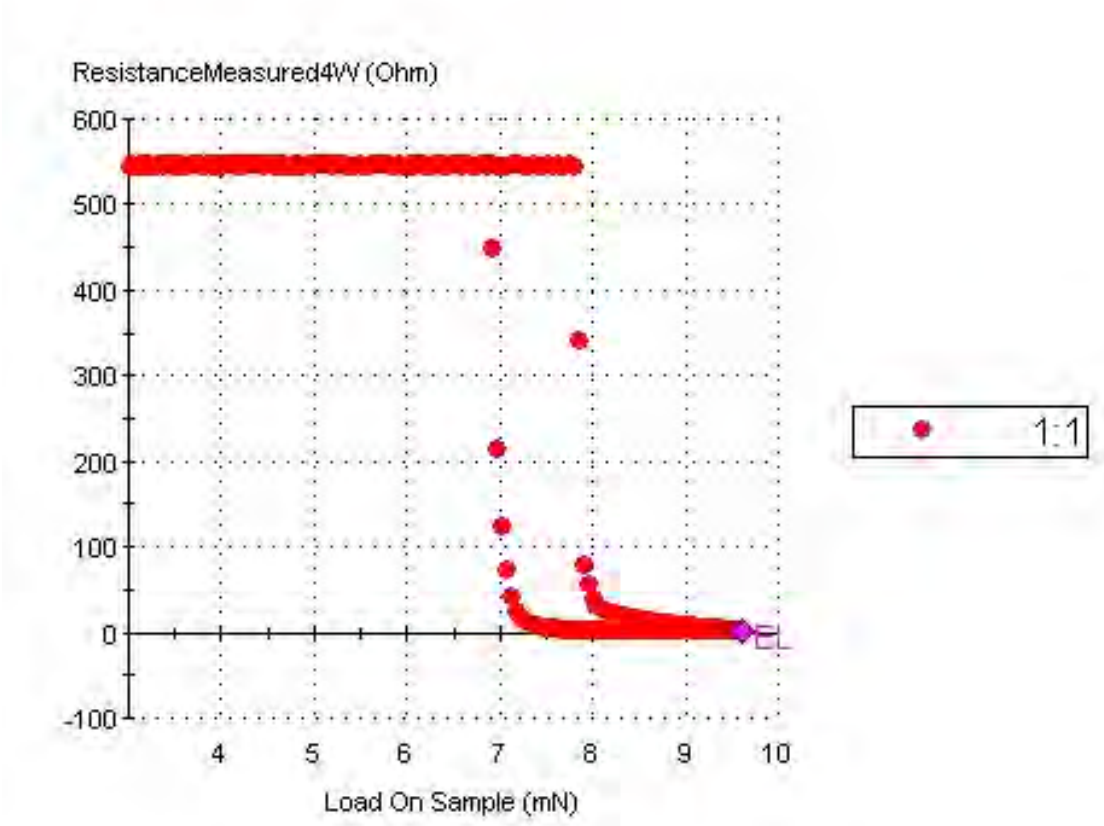

Figure 5.11: Output from the MTS Nanoindenter XP showing erroneous force levels due to interference between the indenter head and mount plate. These results are from a contact test of a gold-gold contact on a cantilever with stiffness of approximately 10^4 N/m fabricated at Northeastern University.

The solution to this problem was to choose a microprobe tip to avoid lateral contact with the support structure. A tip with a small conical angle and, if possible, an extended shaft was needed. The best available tip at AFIT for the experiment was a 25 μm radius spherical tip with a 90 degree conical angle. Unfortunately, this tip would have interfered with the mount plate. A dimensional check showed that the conical angle needed to be 60 degrees or less but even with a 60 degree conical angle, the clearance available was very small. The equivalent conical angle of a cube-corner tip is 35.3 degrees, which is the smallest effective conical angle available. MTS Nanoinstruments loaned an extended shaft cube-corner tip with a shaft 0.5 mm longer than standard tips for use in this study. The combination of extended shaft and small equivalent conical angle ensured no further interference between the microprobe and mounting hardware. The cantilever contact bump acted as the top contact during

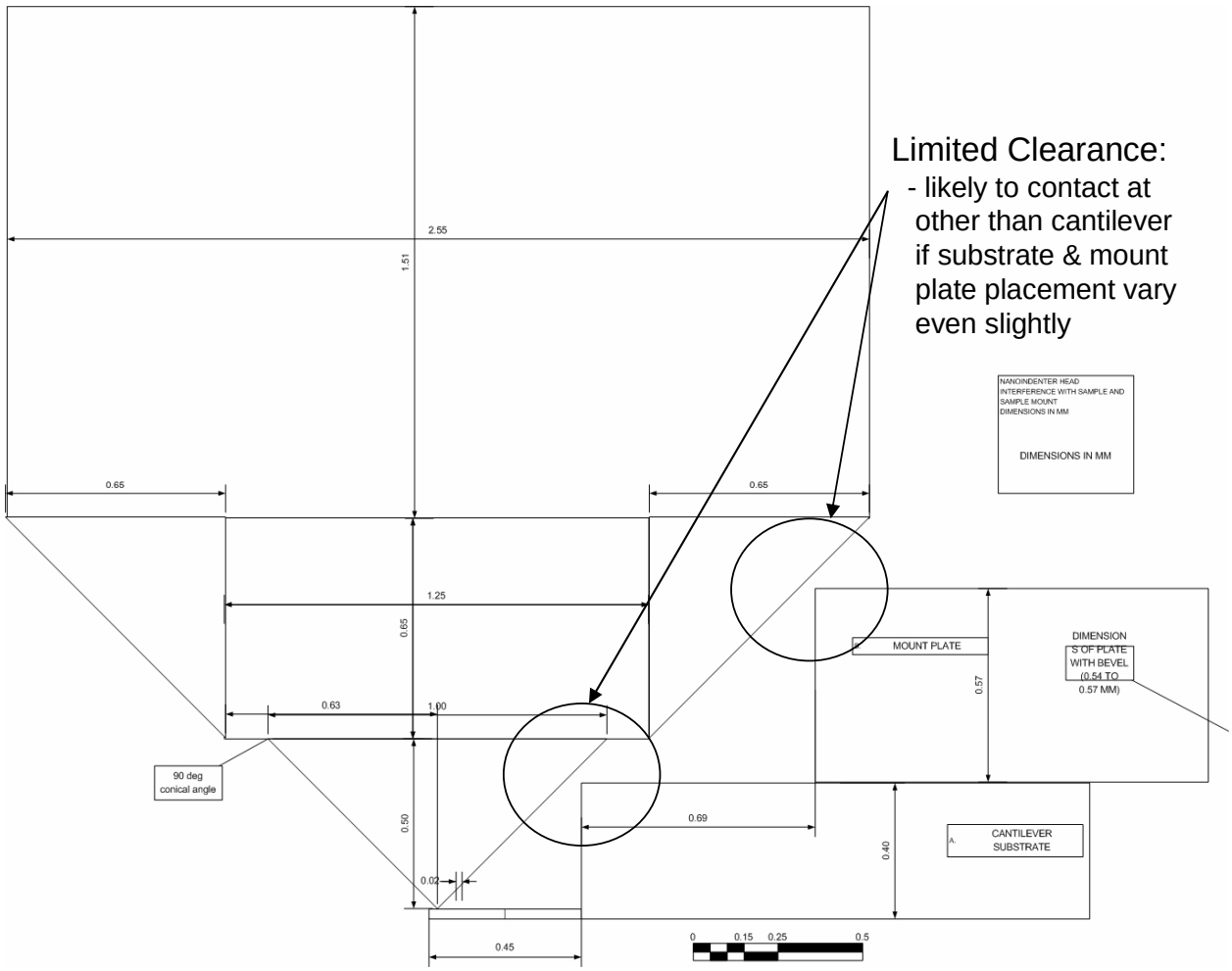

Figure 5.12: Scale drawing showing possible interference of indenter tip with 90 degree conical angle and head assembly with mount plate and test cantilever as mounted for testing.

cycling. The next critical design component was the method by which the bottom contact would be simulated.

5.1.5 Strike Plate. The strike plate (bottom contact) needed to be removable as well as mountable on top of the cycling PZT. A plate fabricated from a silicon wafer coated with the contact metal of interest was chosen for its similarity to the coatings and conduction paths available in real MEMS switch devices. The dimensions were determined from the PZT and the method of mounting and raising the PZT with a vertical translation stage and the space available in the new sample tray. At first, the dimensions chosen were 12 mm x 12 mm. Once the original strike plate wafers were received, they were installed in the experimental setup. However, upon inspection of the setup inside the nanoindenter it was clear that the fastener head attaching the strike plate to the PZT would interfere with the protective sheath around the indenter head assembly. The dimensions were changed to 12 mm x 19 mm to extend the contact point further from the fastener head. These final design dimensions are shown in Figure 5.7.

The method of fastening the strike plate to the PZT was also problematic. It needed to be removable, yet offer a stiff mounting method. The top of the PZT had a pre-fabricated screw hole and adhesive fastening was not easily removable, so mechanical fastening was chosen. However, a 3 mm diameter hole was needed in the silicon piece to fit the appropriate size fastener. Standard drilling techniques do not work in silicon, because it is an extremely brittle material and subject to fracture. Laser cutting was chosen as an appropriate method to cut fastener holes and a design was sent to Mound Laser and Photonics Center (MLPC) in Miamisburg, OH. They were able to laser cut precision holes in the silicon and cut the silicon pieces to size. However, upon inspection of the contact edge of the strike plates thus fabricated it was noted that the laser cutting caused heat damage and material contamination just at the edge of the strike plates in the locations where contact testing was planned. Therefore, it was decided that Mound Laser would only cut the fastener holes in an

appropriate pattern on the silicon wafers. The silicon wafers were then cleaved to strike plate size at AFRL. A diagram showing the size of a 75 mm wafer with the holes to be cut and an outline of the strike plates to be diced from the cut 75 mm wafer is given in Figure 5.13. The strike plates as designed and fabricated were then coated with the appropriate contact metal to a thickness of 300 nm using the same methodology as that used to coat the test cantilevers described in Section 4.3.1.

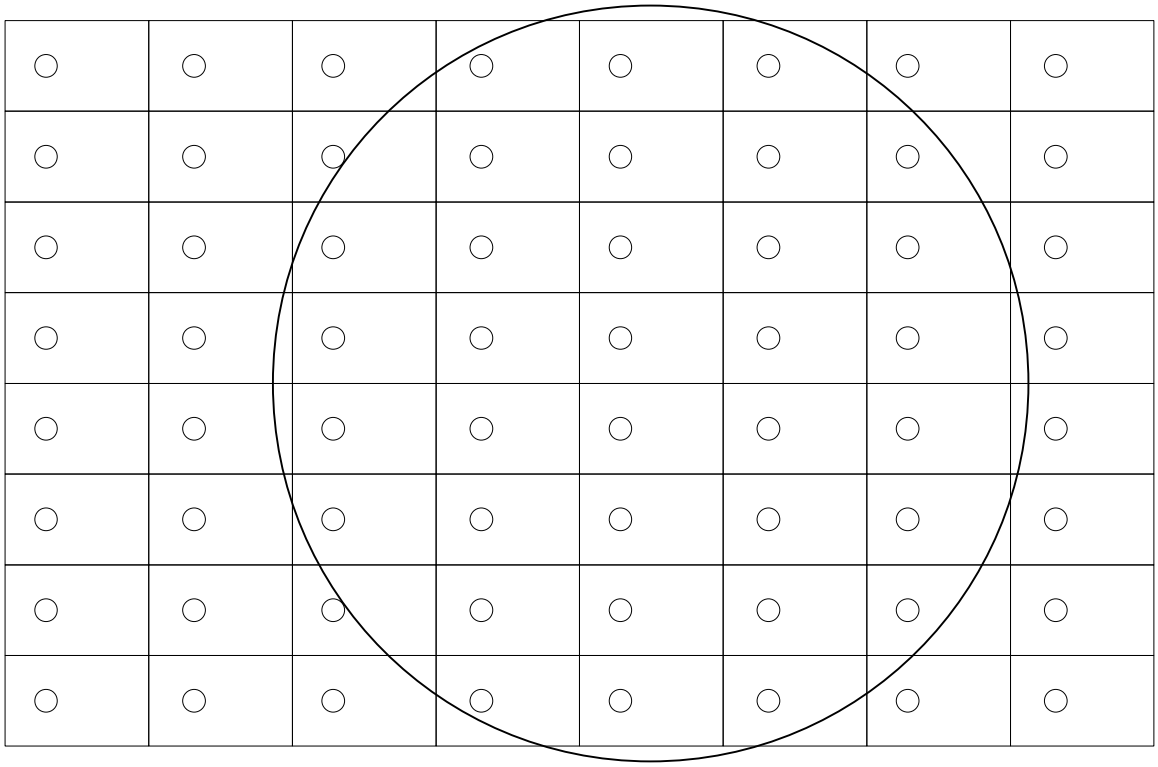

Figure 5.13: Scale drawing showing holes to be drilled in 75 mm silicon wafer for fabrication of strike plates.

5.1.5.1 Strike Plate Mounting. It was also noted that the use of a metallic fastener had a small risk of inadvertently introducing a small amount of current inside the PZT stack if the insulation around the fastener hole on the top of the PZT failed. Research was done to find an appropriate non-conductive fastener replacement. Only one 3 mm diameter non-conductive fastener was identified. These

fasteners were too long and the heads were very thick, which when introduced into the test setup caused interference with a bolt protruding from the rear of the protective sheath around the indenter shaft. The shafts of the non-conductive fasteners were then cut down to length, the heads ground down and a slot cut in the fastener heads at the AFIT Model Fabrication Facility. All tests were accomplished with strike plates mechanically fastened to the PZT with custom non-conductive fasteners.

5.2 Cycling Control

The intention of the original experiment design was to cycle the test cantilevers as fast as possible, to enable many cycles to be put on a contact quickly with as little testing time as possible. The ability of the indenter head to cycle the cantilever fast is limited. Therefore, a piezo device capable of precise higher frequency motion was chosen to provide cyclic contact motion. This device needed to be physically small and light enough ($\ll$100g) to be lifted by the stage used for vertical translation to roughly position the strike plate in the vicinity of the contact point. The Physik Instrumente P-841 fit the need. However, it is only controllable with either PI software or LabView. TestWorks is not capable of communicating with LabView or the PI software. Fortunately, the P-841 can be controlled by using an analog input mode with an analog input of 0-10 V. A time varying input voltage can therefore be used to cycle the PZT. Precise control of the displacement of the strike plate is enabled by the use of the P-841.

5.2.1 Frequency Control Limitation. Unfortunately, the PI controller limits the response of the PZT to approximately 100 Hz maximum without any attenuation of the signal. This was determined by monitoring the control voltage driving the PZT on an oscilloscope simultaneously with the signal from the SENSOR MONITOR output on the E-665 controller which monitors PZT motion. At 100 Hz, it can be seen that the amplitude of the signal is not decreased whereas at higher frequencies the frequency of the signal is maintained but the amplitude of PZT motion is decreased

due to limitations in response time of the P-841. Therefore, all cycling testing was accomplished at 100 Hz.

5.2.2 Digital Switch. The test arrangement required that the P-841 be stationary for part of the test, stable at two different locations (in contact and out of contact) and also to cycle at a frequency. This required two different voltage sources to control the motion of the PZT at different times. The first source was necessary to provide steady calibrated inputs during device actuation with the microprobe and in and out of contact measurements. The second source providing varying voltage was necessary to control the cycling. Use of two external voltage sources required a method to alternate between the two sources of control voltages at appropriate times during the test.

The problem was solved with the use of a digital switch and digital output from TestWorks running the nanoindenter. The digital switch controlled whether the voltage input to the E-665 was from the function generator or the constant output voltage from the National Instruments voltage output module. TestWorks was programmed to send a digital high or digital low signal out through a digital output line. This logic was controlled within the test method in TestWorks and will be described later. The digital switch was powered by a DC power source. When the switch received a digital high signal, the signal from the function generator was sent to the E-665 and the contact was cycled. When the digital low signal was received, the E-665 received the constant voltage from the SCC-AO10 voltage output device and the strike plate was positioned to one of three locations: out of contact with a gap of two microns, just in contact, or in contact deflecting the cantilever tip two microns.

5.3 Contact Alignment

Alignment of contact in three-dimensions to a sub-micron tolerance was an important part of overall system design. Alignment was accomplished through the integration of small form and fit micro-translation components into the sample tray

design. Accurate horizontal, lateral and vertical positioning of the cantilever and strike plate to ensure proper contact and simulate the switching action was required. The positioning control designed for this set-up is described in the following sections.

5.3.1 Vertical Placement Control. The vertical placement of the strike plate was critical in each test. The P-841 had a maximum displacement of 15 μm, so another method to raise the strike plate close to the location of the fixed cantilever was needed. No vertical translation stage with sub-micron accuracy was found to be commercially available. However, PI manufactures a horizontal translation stage which, when placed on its side, fit within the 57.15 mm (2-1/4") height requirement. This stage was chosen also due to its capability to lift up to 100g mass. The P-841 weighs 20g. An aluminum plate and bracket combination was specially designed to attach to the M-663 in order to mount and lift the P-841/Strike Plate assembly. The combined weight of the aluminum bracket design was calculated to be 35 g and thus the P-841/bracket assembly was within the weight limit of the M-663. However, a test showed that the cable connecting the P-841 to its controller needed to be supported otherwise the weight limit of the M-663 was surpassed and the vertical rough positioning stage was unable to operate.

The M-663 can not be controlled from within TestWorks using existing input/output channels. It must be controlled using PI software which came with the system. At the time of purchase, it was unknown whether the software controlling the M-663 could run simultaneously with TestWorks. Note that TestWorks and LabView software compete for computer resources and can not be run on the same computer platform simultaneously. However, tests showed that the PI software controller would successfully run while Test Works was running. This issue could have caused the experimental project to fail if the two software packages were incompatible.

The M-663 normally operates a calibration/self-check to run the stage out to the extreme limits of motion on both sides of the center of the stage before it will operate. This feature is not documented in the literature which came with the stage or its

associated controller (the PI C-865). However, the command "RON 10" entered into the PI command window turns off the calibration/self-check and only enables relative movement of the stage. After that, only the "Move Relative" (MVR) command will successfully command the stage to move. The syntax for this command is "MVR 1X" where X is the distance in millimeters for the stage to move, and can be either positive or negative depending on direction of desired motion. The user must be extremely careful not to drive the stage to its limit or into the ground while commanding relative movement. If the stage is driven too high, it could impact the microscope or the indenter shaft in the nanoindenter before it reaches its limit. Moreover, if driven into the ground, the stage will overheat and burn out the motor as the stage uses closed loop control and will continue to try to reach its commanded position even if it is physically hindered from doing so. The M-663 stage minimum incremental motion is 0.1 μm and its travel range is 20mm. Its maximum push/pull force is 1 N and its maximum holding force is 2 N. Therefore, the stage is strong enough to reach its required vertical position and hold the PZT steady during testing.

5.3.2 Horizontal and Lateral Positioning Control. Vertical translation and positioning is achieved using the P-841 and M-663 combination. However, horizontal and lateral translation of the setup was also necessary in setting up the simulated microswitch. The cantilever is mounted to the mount plate as described previously in Section 5.1.2. The mount plate is then mechanically attached to a M-105 translation stage with crossed roller bearings. The M-105 is a mechanical stage which has an 18mm travel range and a minimum incremental motion of 1 μm. It has M3x4 fastener holes in the top which were used to attach the specially designed mount plate described in Section 5.1.2. The M-105 is 15.5 mm tall. One M-105 was chosen for horizontal travel to extend the cantilever out over the strike plate and one M-105 was chosen as the base for the M-663/P-841 assembly which provides for lateral movement of the strike plate to enable the user to find the best possible contact site for simulated switch testing.

The design of the sample tray depended upon the size of these horizontal and lateral stages and their maximum travel range. The location and installation design of the M-663 and P-841 combination were dependent on the location and maximum range of the horizontal travel stage. The selection and procurement of the stages were required prior to sample tray fabrication for verification that design drawings and clearances were correct. The use of small, accurate vertical, horizontal and lateral translation stages enable three-dimensional sub-micron positioning and alignment needed for testing and locating the contact point accurately. Note that the experimental apparatus offers the user precise three-axis control of the parameters of the contact experiment performed.

5.3.3 Sample Tray Guide Rail. The use of a lateral translation stage of the type M-105 required redesign and replacement of the left side sample tray guide rail due to the length of the drive handle. The mechanical drive handle is 36.1 mm long and the entire stage is 97.1 mm long. This meant that the handle extended beyond the base of the sample tray in order to keep it centered and maintain maximum control over lateral placement of the strike plate. The height requirement of the entire assembly required that the handle could not be mounted above the level of the guide rail. Therefore, the left side guide rail was removed and a copy machined out of brass with approximately 25 mm (1") cut off the end to allow the sample tray to be placed on the nanoindenter X-Y stage first, followed by installation of the newly designed guide rail to ensure the sample tray was secured to the nanoindenter X-Y stage. The redesigned sample tray guide rail is shown on the bottom of Figure 5.14 with aluminum brackets attached and is shown next to the original guide rail for comparison.

5.4 Four-Wire Resistance Measurement

A main measure for an electrical contact is the resistance through the contact. One possible failure of MEMS switches is the sudden increase in contact resistance as

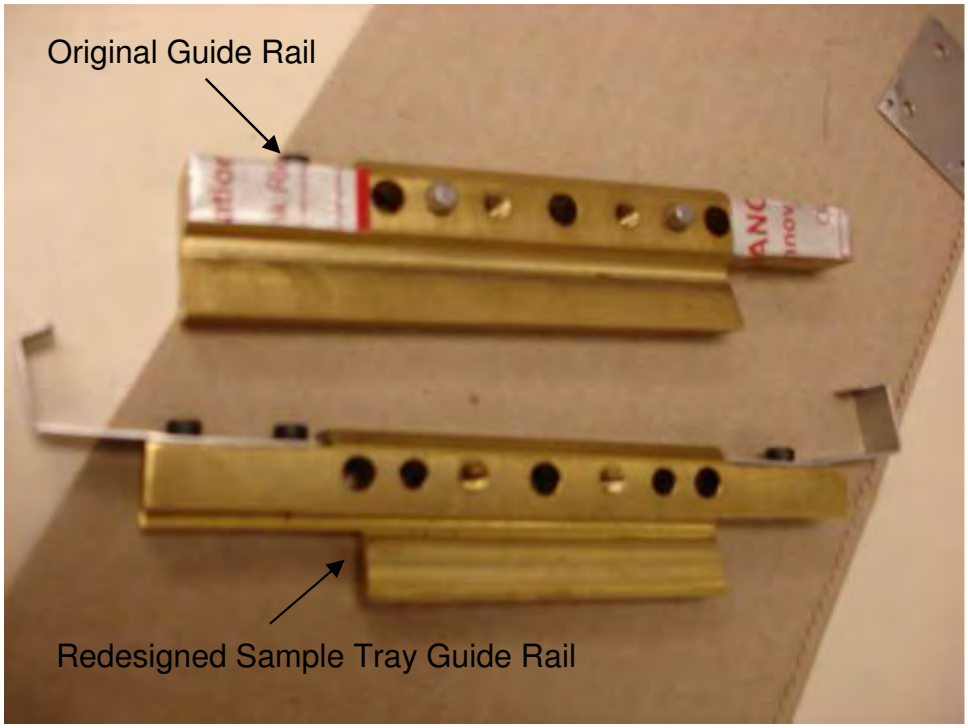

Figure 5.14: Sample tray guide rail (below with aluminum brackets attached) designed and fabricated for current study compared to standard guide rail.

the switch is cycled. A four-wire resistance measurement was set up as shown in Figure 5.15 to track resistance changes through the "simulated" switch during cycling. The applied current used in tests run during this study was 0.5 mA. This test current was chosen to fall within the range typically used in micro-contact testing. Test currents chosen typically fall between 100 μA and 1 mA (e.g. [37, 189]. Note that MEMS switches are designed mostly for low-power applications in the range of 0.1-1 mW of RF power (1.5-4 mA DC or RF current) [202]. The current was provided by a National Instruments NI SCC-C020 constant current source which is a module plugged into one of the output ports of the NI SC-2345 signal conditioning digital/analog input/output board. Note that an 80 Ω compliance resistor was connected to complete the circuit when the cantilever was not in contact. This was done to ensure that a high potential difference did not occur across the contact when contact was made during the hot-switching tests.

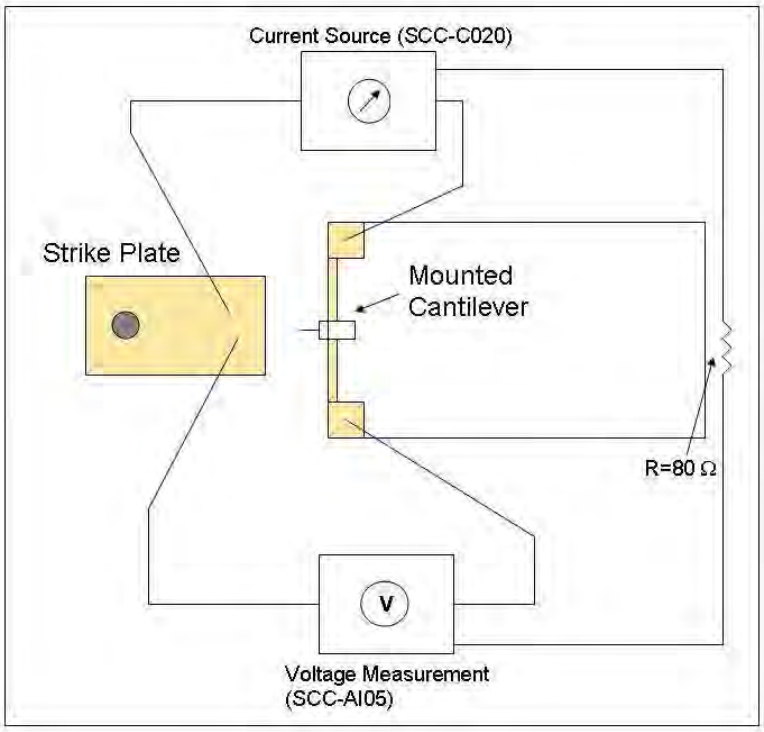

Figure 5.15: Schematic of four-wire resistance measurement set-up. Wires were soldered to the strike plate and on gold connector pads on the sample holder.

5.4.1 Sheet Resistance. A brief analysis of sheet resistance contributions to measured resistance is required because the current traveled for a short distance on the strike plate through a thin film of the contact metal being studied. There was also a small component due to the gold connector strips on the mount plate. Sheet resistance is generally defined as $R_s = (\rho/t)$, where ρ and t are resistivity and sheet thickness, respectively [111]. Using the resistivity values given in Table 5.1, the sheet resistance for a gold bottom plate of 300 nm thickness was calculated as 0.13 $\Omega/\square$. This value is approximately 5-10% of the resistance measured during gold contact testing. The sheet resistance value for a Au-5%Ru bottom contact plate was calculated as 1.28 $\Omega/\square$. This was also around 10% of the measured resistance through a Au-5%Ru contact metal simulated switch. The calculated sheet resistance of the 50 μin thick gold strips on the mount plate is 0.03 $\Omega/\square$. The gold on the mount plates is deposited on top of 100 μin Nickel, so the sheet resistance component is actually less than that. The calculated sheet resistance for materials used in this study are shown

Table 5.1: Sheet Resistance calculated for materials used in experiment.

Material	Electrical Resistivity ($\mu\Omega$-cm)	Thickness (nm)	Sheet Resistance ($\Omega/\square$)
Gold	3.6	300	0.12
Au-5%Ru	38.5	300	1.28
Au-4%V_2O_5	17.7	300	0.59

in Table 5.1. The mount plate contributes an insignificant amount of resistance to the test setup. While the calculated sheet resistance of the strike plate is not negligible, it is not large. The contact resistance also contains components of parasitic resistance through the solder joints, wirebond joints, and terminal strip. These components were all constant between tests of the same contact metal. The change in measured resistance due to changes at the contact is of most interest for this study and the sheet resistance was constant between tests of the same contact metal. Therefore, sheet resistance was not a factor influencing resistance results.

5.4.2 Paschen's Law and Breakdown Voltage. Electric field breakdown might occur during the tests of this simulated micro-switch just as it might occur during the operation of an actual MEMS contact switch. The breakdown of electric fields during switch operation would cause an electric discharge and damage the contact. At large scales, Paschen's law states that breakdown voltage is a simple function of the product of gas pressure and electrode spacing when the switch is in a gas environment [53]. However, very little information is published on discharge at micro-scales and the theory is not well understood [244]. Torres, Dhariwal, and Ono have done experimental work in this area and published some helpful data [53, 186, 244]. Strong, et. al. have done more recent work in this area [234]. Figure 2.21 shows the air gap results for three contact metals down to 0.5 μm. One interesting result contrary to Paschen's law prediction is that electric breakdown appears to become more likely as the gap gets smaller.

The breakdown voltage level shown in Figure 2.21 at 0.5 μm ranges from approximately 20 V to 35 V. The maximum voltage expected during tests in this study was 0.04 V when 0.5 mA of current was used. The breakdown voltage for metals measured by Torres and Dhariwal and Strong, et. al. is much greater than the maximum expected voltage across the simulated switch designed here, therefore arcing due to breakdown voltage was not expected. If arcing did occur, it would likely occur in an operational switch design with similar gap sizes as well. Switches and contacts will need to be designed to survive this type of discharge if it occurs. No evidence of arcing was noted during the study.

5.5 Measurement Setup

The uniqueness of this experimental design is also due to its ability to combine mechanical measurements of contact force and displacement with electrical measurements of contact performance. A very important part of this experimental arrangement is the ability of the user to exactly locate the point of contact and measure contact force directly and simultaneously with resistance. Control of a current source and voltage measurement were needed, as well as the ability of the TestWorks control software to communicate with all external devices.

The "NIDAQ option" (National Instruments Data Acquisition) on the MTS Nano Indenter XP system allows import and export of digital and analog signals to any external systems which can handle them. The normal NIDAQ option uses a BNC panel for connections with external sources and devices. However, that panel did not offer the capabilities needed for the present study. The standard panel did not include a method for producing a constant current which was necessary for the four-wire resistance measurement. The National Instruments signal conditioning panels offered modular capability for selection of input and output modules. An SC-2345 panel which offers two export channels and multiple input channels was chosen. National Instruments voltage output module (SCC-VO10) was chosen to control voltage output from 0-10V, along with a current output module (SCC-CO20) to output low constant

Table 5.2: Quantitative comparison of test method complexity based on size. Note that the test method developed for this study is much larger and more complex than standard methods used for material testing.

Test Method	Test Segments	Channels	Formulas	Inputs
XP Basic Load, Displacement & Time	26	13	13	30
XP Basic Hardness, Modulus & Tip Calibration	31	24	30	42
XP CSM Standard Hardness, Modulus & Tip Cal	39	30	42	48
Method Developed for this Study	126	56	100	71

current, and voltage input modules SCC-AI05 and SCC-AI03 to measure voltage. This signal conditioning device plugs into the standard connector cable offered by MTS in the NIDAQ option and can be controlled by TestWorks software. However, the standard BNC panel only reads input in differential mode whereas the signal conditioning panel and devices require non-referenced single ended (NRSE) measurements. The selection of the appropriate measurement technique must be done both in the MTS system configuration management software as well as in the National Instruments Measurement and Automation (MAX) software. Otherwise, erroneous input measurements will result and the system will not operate properly.

5.6 Test Method Programming

The test method is the set of instructions, or test segments, used to control and execute a test. Measurement devices were limited to those with the capability of integration with TestWorks. No test method for any similar test existed and hence this experiment as envisioned was accomplished by developing a new test method. A comparison of relative complexity between existing test methods and the test method developed for this study is shown in Table 5.2. Note that test segments are the line-by-line instructions used to command the system, channels are the real-time data collection variables, formulas are calculations which can be used multiple times in a test method, and inputs are the data needed by the test method. MTS Nanoinstruments developed an Application Note around the programming, customization and use of the instrument developed during this study. The test method has the capability

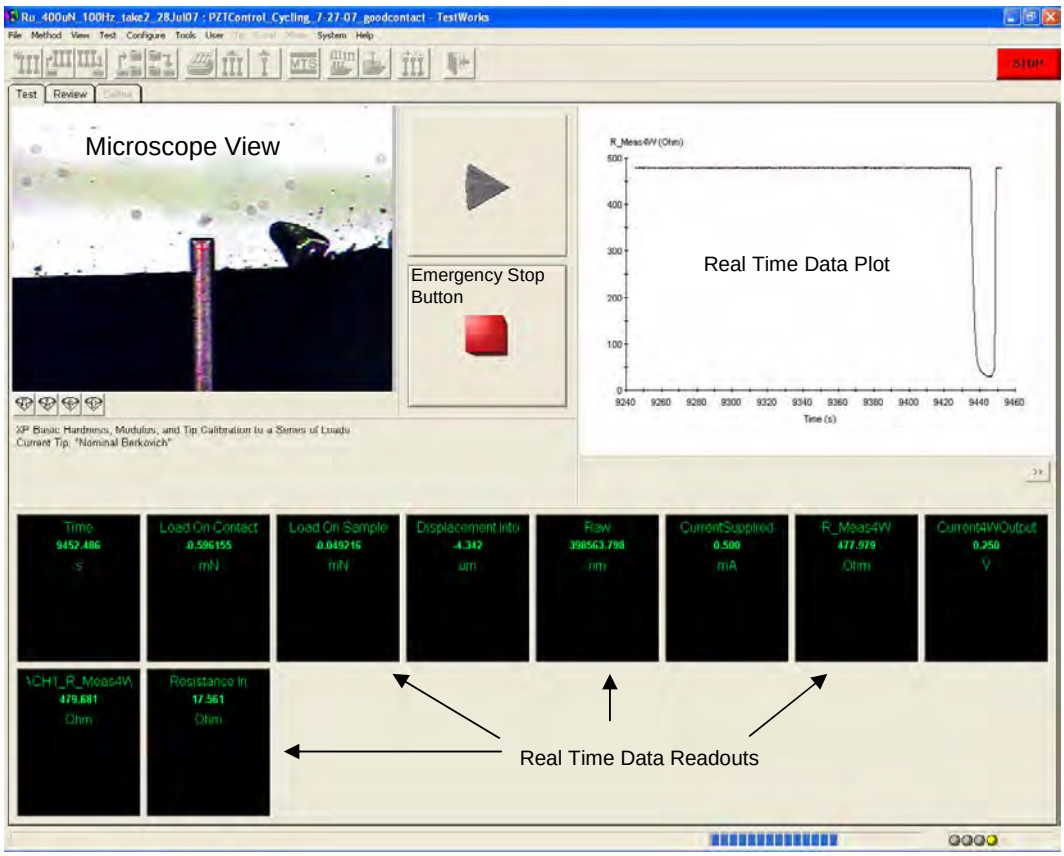

Figure 5.16: Example of output from the MTS Nanoindenter XP when running Test Method programmed for this research. The graph shown in this figure indicated contact resistance vs. time. Reproduced with Permission, Agilent Technologies, Inc.

of monitoring results in real-time, as shown in Figure 5.16. Figure 5.16 also shows the overhead microscope view used to align the cantilever and strike plate. Note that the large dark feature to the right of the cantilever is a chip at the edge of the strike plate. This image shows how the user can avoid visibly contaminated or unsuitable contact locations on the strike plate. This contact measurement capability can be used to directly measure changes in adhesion force over time as well as directly measure the change in force required to develop stable electrical contact. An experimental flow implemented by the test method is described in the next chapter.

5.7 Summary

The development of an experimental apparatus and automated method to use an MTS Nano Indenter XP to develop microcontact test data using micro-size cantilevers simulating microswitches was described. The experimental apparatus and test method developed for this study have the ability to produce data on contact material performance over the lifetime of micro sized electrical contacts. Difficulties faced during the design process are described and design decisions made are elaborated. Issues that future users will face while operating this apparatus are also outlined. The solution of these problems required understanding the interaction of each component within the system, and some components could only be tested serially after others were designed, fabricated, and troubleshooting completed. This test setup is unique and required hardware design and fabrication as well as test method programming. Design constraints were met in order to develop useful data involving simultaneously measuring contact force and electrical performance directly. It should be noted that due to the complexity of the setup and the need to have data accurately correlated with time, automation of the experiment was necessary and the study would not have been possible otherwise. The experimental development in this study expanded the capabilities of an existing material testing instrument and provided technology transfer and an increased capability to the commercial sector. The experimental procedure and test variables exercised in this study will be described in the next chapter.

VI. Experimental Procedure

This chapter describes in detail the experimental procedure and methodology used to test simulated MEMS contact switches. First, the general method used to control the experiment is described, along with the test variables and conditions. Then the experimental steps, test automation and data collection are described.

6.1 General Description

A schematic of the test setup utilizing the nanoindenter was shown previously in Figure 5.1 and is repeated here in Figure 6.1. The test was controlled through the use of MTS TestWorks software. The electrical setup and control connections are illustrated in Figure 6.2. A test method was written to automatically provide the current input through the simulated microswitch, the voltage output to control the location of the PZT/bottom contact plate, and a digital signal to control the signal used for cycling. The test method controlled the data acquisition system, which read the voltage measured from the four-wire resistance test, and calculated the contact resistance and open resistance. A compliance resistor with a resistance of 80 Ω was installed across the voltage measurement inputs. This was done to avoid building up a significant potential difference across the contact switch and avoid arcing.

6.2 Test Conditions & Variables

Table 6.1 shows a summary of variables and test conditions used in this study. Many variations of these variables are possible with the apparatus and test method developed here. However, testing was focused on the test conditions offering the most promise.

6.2.1 Choice of Contact Metals. Contact metals tested consisted of gold as a baseline as well as an alloy of gold/5% (Au5%Ru) ruthenium and a dispersion strengthened alloy of gold/4%vanadium oxide (Au-4%V_2O_5). According to Chen, et al. [36], the relationship between hardness and contact resistance of gold ruthenium alloys is linear. Au5%Ru was chosen due to its binary microstructure, hardness and

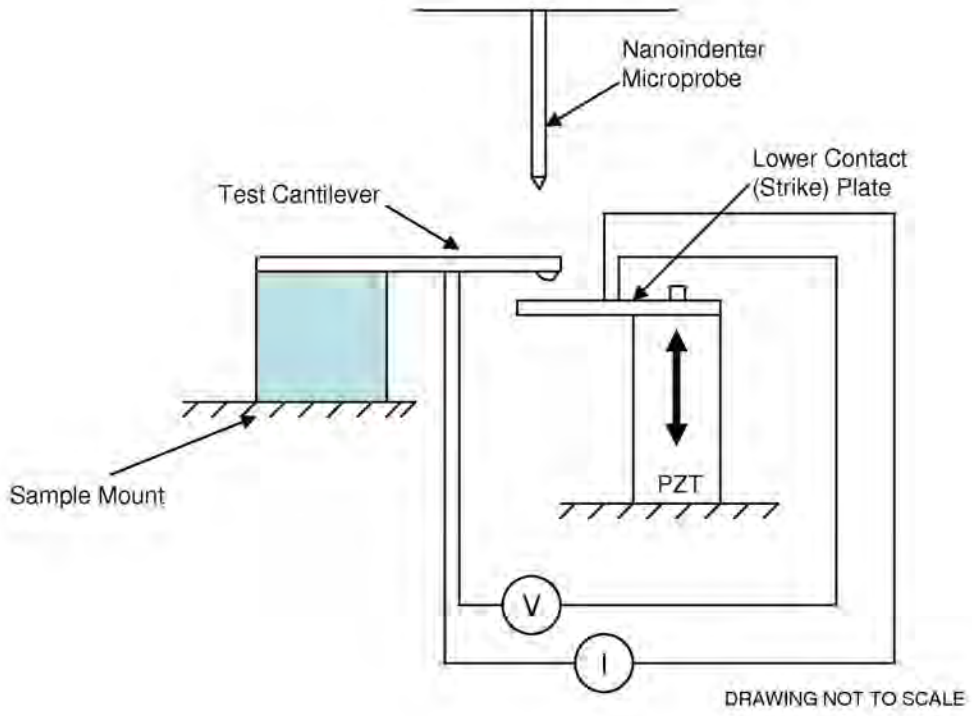

Figure 6.1: Overview schematic of relative geometry of experimental apparatus.

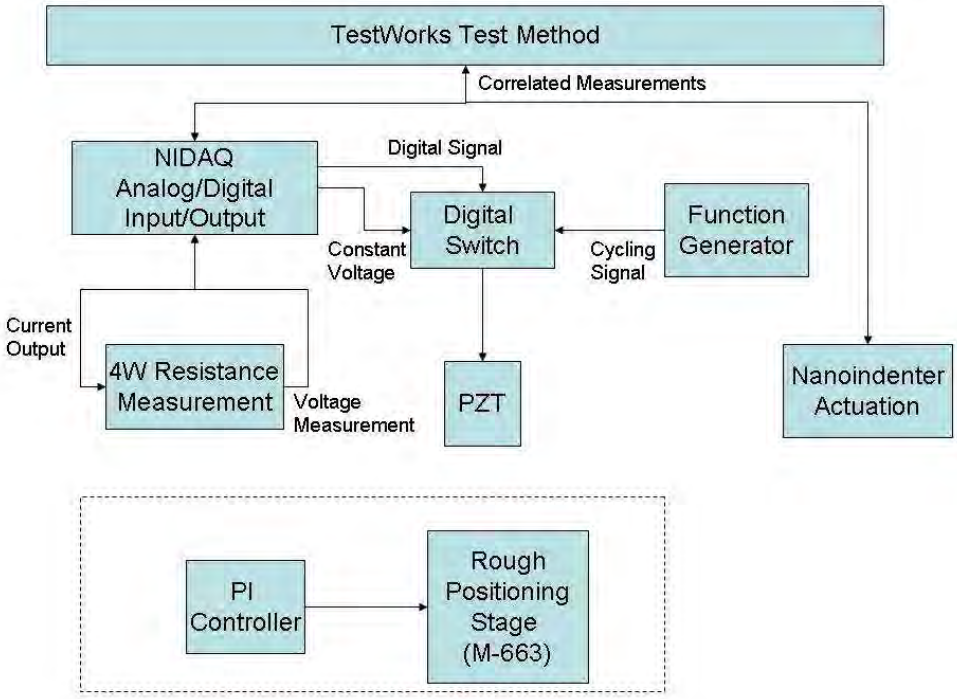

Figure 6.2: Basic block diagram of how the experiment was controlled using MTS TestWorks and the integrated National Instruments digital and analog input and output devices.

Table 6.1: Test variables and conditions in current study.

Contact Materials	Au, Au05%Ru, Au-4%V_2O_5
Cycling Displacement	2 μm
Cycling Contact Force	400 μN
Frequency	100 Hz
Environment	Lab Air
Test Current	0.5 mA
Switching	Hot-Switched

performance in previous studies [37]. The third material tested was Au-4%V_2O_5. This material was developed at Lehigh University (Bethlehem, PA) and could offer potential advantages for increasing the lifetime of MEMS switch contacts [8]. The upper and lower contacts were the same metal in each test. The metals tested consisted of 300 nm sputtered thin film coatings on a silicon bump at the end of a custom designed and fabricated silicon cantilever.

6.2.2 Cycling Displacement/Force. The contact force used in this research was 400 μN, which is at the upper limit of forces used in MEMS cantilever beam contact switches. Typical contact forces in MEMS switches range from 50-1000 μN [202]. Northeastern University used a contact force of 200 μN in their AFM-based testing [37]. The cycling force on the cantilevers was calculated based on the displacement at the end of the cantilever during cycling and the stiffness of the cantilever. The cantilevers used in the present study had a stiffness of approximately 200 N/m, and with a cycling displacement of 2 μm, F=kx gives the contact force due to cantilever beam bending as 400 μN. Note that MEMS switches typically are designed with a contact distance in the range of 1-5 μm [144], with 1-2 μm a very common design choice. Also note that typical MEMS switches have a cantilever beam stiffness of 15-40 N/m, with a mechanical restoring force of 30-120 μN [202].

6.2.3 Contact Gap. The contact gap chosen for the study was 2 μm, in order to replicate the gap used in actual devices. Also, it was shown by Hyman and also reported by Varadan that the contact gap in an ohmic contact switch is the

parameter which determines RF isolation performance, and that the isolation is only marginally improved at gaps larger than 2 μm [107, 247].

6.2.4 Nanoindenter Contact Force. The forces imposed by the nanoindenter ranged from 0 to 400 μN loaded linearly at a rate of 50 μN/sec in order to ensure the force measurement did not affect the results of the experiment. The microprobe applied the maximum 400 μN of force during each measurement. The contact force was measured after detection of the location of contact between the cantilever and base plate. The tip used in this experiment was an extended shaft cube corner tip. This microprobe was chosen to best avoid interference with the experimental apparatus and was the best option for the present 40 μm wide cantilever.

6.2.5 Failure Criteria. The failure criteria used for contact cycling was based on the in-contact and out-of-contact resistance measurements. The contact was defined as failed during the experiment when either the in-contact resistance was greater than 40 Ω or the out-of-contact resistance was less than 40 Ω in order to detect changes to the expected in-contact and out-of-contact resistance behavior of the "simulated" switch. A high in contact resistance indicated a high resistance type failure, and a low out of contact resistance indicated a contact adhesion type failure. In all test cases where the resistance increased to failure, the increase was significant. There would be no difference in results if a different value of resistance was used as a control variable. The test was stopped when one of these types of failure occurred.

6.2.6 Number of Cycles. Most tests were run until the failure criteria were met. Each cantilever and plate combination were removed at the end of the test for analysis. Because there was no way to ensure contact at the same location if the cantilever and strike plate were removed and reinstalled, the same contact could not be re-used to gather further data. A few tests were stopped before failure to analyze contact surface changes before failure.

6.2.7 Current Levels. All test were run at 0.5 mA (500 μA) current to develop results at a level to complement previously developed data and was within the operational range of RF MEMS switches. For comparison, Northeastern University researchers used current of 200 μA and 1 mA in testing to cover a range of current levels possible in a microswitch operation [37, 39]. The low current was chosen in the range of previous work and to ensure that the current level didn't destroy the contacts under test. Note that MEMS switches are mostly designed for low-power applications (0.1-1 mW RF power or 1.5-4 mA DC or RF current) [202].

6.2.8 Hot- vs. Cold-Switching. The performance of MEMS switches varies between hot-switching, where the contact is made or broken while current is flowing, and cold-switching, where contact is only made and broken when the current flow has stopped. This research investigated the effects of hot-switching, as hot-switching is the more demanding operational environment. However, most MEMS switch research has been done while cold-switching contacts. Rebeiz reports that hot-switching and cold-switching result in nearly the same lifetime results when tests are run at low RF or DC currents ($<$ 4 mA) [202]. Cold-switching testing would require significant additional effort programming the MTS Nanoindenter XP and would also require a slower cycling rate due to response time of the Nanoindenter XP system and attached peripherals. The XP is capable of performing these tests, so the test method could be modified and tests could be repeated with cold-switching for future research.

6.2.9 Cycling Frequency. The cycling frequency used during this test was 100 Hz. The testing was limited due to the response of the PZT and its associated controller. This cycling frequency is in the range of other tests, as shown in Table 6.2, and is in the range of actual in-use switching frequency of 1-300 Hz as reported by Maciel [155]. Future research could run further tests at other cycling frequencies. Higher test cycling frequencies would enable testing to more quickly reach the useful lifetimes of operational MEMS switches.

6.2.10 Environmental Control. All testing accomplished during this research was done in laboratory air. However, studies and experience have shown that switches cycled in ambient conditions are more susceptible to growth of high-resistance contamination on the contact than switches hermetically sealed or in a non-reactive gas atmosphere, such as nitrogen. In order to mitigate the issue with contamination, the test cantilevers were fabricated in a cleanroom environment, and were stored in a drybox until they were ready for testing, except while being mounted on sample mount plates.

Development of an inert gas atmosphere for cycling will require a redesign of the test setup. The nitrogen environment could be created through the use of a low flowrate of gaseous nitrogen over the contact area during the entire cycling test for each cantilever. This may be sufficient to keep organic contaminants from the environment away from the contact surface to minimize the creation of a resistive frictional polymer film. Future research should include tests in an inert or reducing environment.

6.2.11 Measurement Interval. The measurement interval used for testing ranged from resistance and microprobe measurements every 10,000 cycles to measurements every 250,000 cycles for the long lasting Lehigh contact material (Au-4%V_2O_5). Many tests were run with measurements every 10,000 cycles in order to gather enough data on the early life of the other two contact materials to capture changes in contact behavior at the very beginning of contact life. The larger measurement intervals were chosen for the Au-4%V_2O_5 tests because of memory limitations of the computer system used in data collection. The larger intervals allowed data collection during the lifetime of the long-lasting Au-4%V_2O_5 material without prematurely ending the tests due to memory full errors. The next section describes the procedure used in each experiment, including the method for setting the contact gap and the test flow used for all experiments.

Table 6.2: Comparison of various test parameters used in MEMS switch testing. Note that the only statistical results shown in this table are from [181]. Only the results for gold testing from this study are included.

Researcher	Date	Test Cycling Rate	DC Current or RF Power	Switching Type	Reported Switch Lifetime	Contact Material
Rebeiz&Muldavin [203]	2001	1-10 kHz	1-5 mW	Cold	50-500$\times 10^6$	not reported
Becher, et al. [15]	2002	10 Hz	not reported	Hot-Cold	1.3$\times 10^6$-3$\times 10^8$	not reported
Majumder [159]	2003	not reported	$\leq$20mA	Hot-Cold	10^7-10^{10}	platinum group
Tazzoli, et al. [239]	2007	1kHz	1 mW	Hot	20,000-> 10^6	gold
Chen [37]	2007	0.5 & 300 Hz	200 μA & 1 mA	Cold	10^8	gold
Newman, et al. [181]	2008	20 kHz	20 dBm (0.1 W)	Cold	Mean 430$\times 10^9$	platinum group
Gilbert	2008	100 Hz	0.5 mA	Hot	20,000-2$\times 10^6$	gold

6.3 Experimental Procedure Flow

The experimental flow for hot-switching is shown in Figure 6.3. The first step of each test is to carefully bring the cantilever and plate into contact. Measurement of resistance was used to determine physical contact of strike plate to cantilever. This was done by first bringing the plate and cantilever into focus through the microscope to verify that each was at the same vertical position in the setup, and that the cantilever was aligned with a promising contact location. The M-663 positioning stage upon which the PZT and strike plate are located was lowered at least 50 μm to ensure enough clearance to slide the cantilever forward without interference. The end of the cantilever was placed slightly over the plate location to ensure contact with the bump when the plate was raised. The M-663 was then raised in very small increments using separate PI controller software until a resistance less than the compliance resistance was measured. The M-663 positioning Z-stage was then backed off by 2 μm to ensure the desired contact gap. During each experiment, the contact gap was checked by using the manual control available on the PI controller to displace the PZT. If the contact gap was verified, the automated gap setting routine was started.

The automated gap setting routine was implemented in the test method written for this study. The voltage controlling the PZT and therefore the location of the baseplate was incremented by a small amount, nominally 1 mV which corresponds to one-axis PZT motion of 1.5 nm. This incremental control voltage increase was nested inside a control loop while the program was measuring contact resistance. The PZT was raised until the NIDAQ input/output detected a resistance less than a given

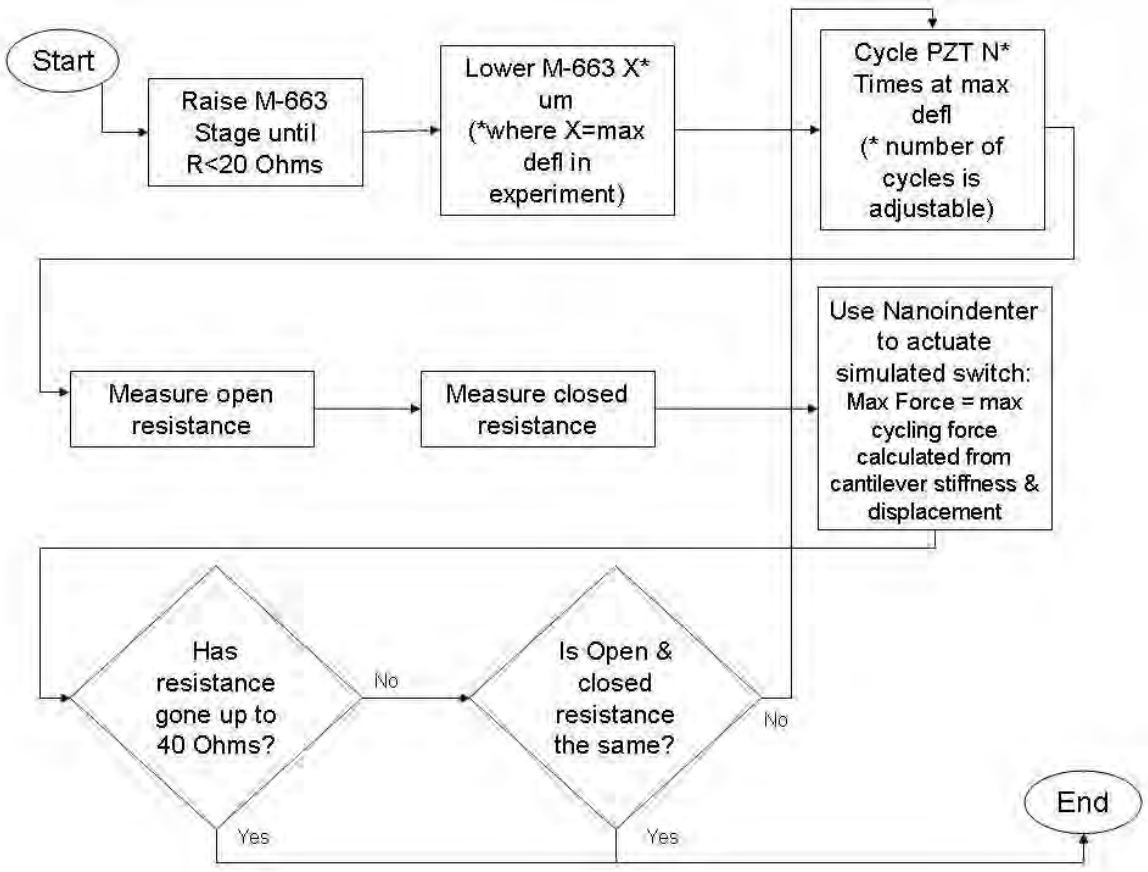

Figure 6.3: Simplified experimental flow for hot switching tests.

contact resistance value of 20 Ω. This defined the location of where the strike plate contacted the cantilever to within 1.5 nm. Then the PZT, and thus the strike plate, were withdrawn a set distance equal to the displacement gap used during the test. The displacement gap used during this study was 2 μm, which corresponded to a cycling force of 400 μN.

After initial contact was made, the test measured "just-in-contact" resistance, that is, resistance when the strike plate was located at the position where initial contact was detected. Then, the PZT was displaced to +2μm to apply the contact force of 400 μN and the first "in-contact resistance" was measured. The PZT was then dropped 4 μm and the first "out-of-contact" resistance was measured.

The first microprobe measurement was then performed, to gather initial data for the contact under test before any cycling occurred. After the microprobe measurement was complete, the contact was cycled for a set interval using a 100 Hz signal input to the PZT. When the cycling interval was complete, the in-contact and out-of-contact resistances were measured again. If the resistance measurements did not meet the failure criteria, the microprobe measurement was run again. This loop was continued until the contact resistance measurements met the failure criteria. The steps required to set up and run an experiment are given in Appendix D.

Multiple tests were run with the same sets of variables to ensure repeatability of test results. More tests were run with gold contact material than other contact materials in order to establish a microcontact performance baseline. The test details and results are presented in the results chapter for each of the contact materials tested. The next section describes the data collection and experimental automation used in the experiment.

6.4 Data Collection & Experimental Automation

Each experiment was controlled with the use of MTS TestWorks software. The software is extremely flexible. The nanoindenter, as well as analog and digital input and output, can be controlled with the use of TestWorks. Unique test methods were developed to exploit the flexibility, utility and precision measurement capabilities of the MTS Nanoindenter XP. TestWorks allowed control of the PZT, the National Instruments (NI) SCC-C020 current source, the NI SCC-AO10 voltage output source, as well as the NI voltage measurement modules used. TestWorks is thus capable of reading in data other than the typical force and displacement data it generates during normal indentation material testing. The experiment developed for the present study did more than use existing capabilities of the instruments involved. MTS Nanoinstruments improved the TestWorks software to enable the test setup designed and developed for the present work by adding an ability to output data for multiple test

loops within the same test to enable additional data analysis. The present study would have been unsuccessful without this upgrade.

TestWorks was programmed to measure force, displacement, voltage, and current as well as to calculate several other contact related data. TestWorks was also programmed to accurately locate the surface of the cantilever and the point of contact with the bottom electrode to within approximately ± 50 nm. The force applied to the contact after mechanical detection of switch contact was limited to 400 μN, so the maximum force applied to the switch during each test was controlled in order to minimize any effect that testing would have on results. Previous work with nanoindenters and MEMS switches only were able to estimate the point of contact and the electrical data was not precisely correlated to the force application [143].

The data collected from the four-wire measurement during each test consisted of the input current level, which is a controlled constant current, from two of the probes and the voltage measurement across the switch contact from the other two probes. These data points were taken at regular intervals (every N cycles) during opening and closing of the contact and used to calculate the resistance at those instances. Unfortunately, parasitic resistances including the sheet resistance of the bottom contact plate and the solder/wire joints were included in the measurements. However, changes in the measured resistance during testing were all due to change in the contact resistance. No changes in parasitic resistances occurred during testing.

With this measurement setup, it was easy to determine if contacts were stuck together when the resistance value did not change from the open measurement to the closed measurement. Thus, the system provided the number of cycles when an adhesion failure occurred or when a large sudden increase in contact resistance occurred to within the size of the measurement interval (±N cycles). At that instant, the cycling of the PZT was programmed to stop and the nanoindenter automatically conducted the measurement whereby the nanoindenter microprobe tip contacted the cantilever and pushed it into contact with the strike plate. The nanoindenter measured force

and displacement and read in the data to be used for resistance measurement simultaneously.

The experimental flows described here were programmed using MTS TestWorks software. Experimental control as well as hardware was developed incrementally during this study.

6.5 Benefits of New Experiment Design & Procedure

This experiment involving simulation of switches was developed specifically to provide engineers with the ability to track morphology changes as the lifecycle of the contact progresses while measuring multiple contact parameters. The difficulty of breaking open a cycled MEMS switch and the possibility of contamination or damage during that process is avoided with the use of this test set-up. Also, few researchers have investigated contact morphology changes on both contact surfaces during cycling.

This experimental set-up offers a method to test different contact metals side by side with minimum fabrication effort. This new capability will reduce/remove variables in switch design and fabrication and will allow materials engineers the ability to quickly test new alloys or conductive materials contemplated for use in MEMS switches before going through the time-consuming and expensive effort of determining switch fabrication techniques incorporating new and untried materials. New materials can easily be deposited by a variety of methods on the custom cantilevers and quickly tested. Further, this experiment can be used to investigate multiple variables which affect contact switch and contact material performance. Frequency of cycling, contact force, switch environment, current level, cold-switching and other variables can be tested using this test apparatus and procedure.

6.6 Summary

There are many different variables and operational conditions which could be tested using the apparatus and test method developed for the MTS Nano Indenter

XP. The present research was focused on three different kinds of metal thin-films (Au, Au5%Ru and Au-4%V_2O_5), with a cycling contact force of 400 μN, in a very demanding test environment for MEMS switches. The tests were run hot-switched in laboratory air at 100 Hz switching speed with a current of 0.5 mA. The use of these test variables provide information about the test metals to switch designers, and validate the experimental setup as a basic scientific and systematic tool for developing contact performance data and a judicious method of comparing contact materials for use in RF MEMS switches. The next chapter provides proof-of-concept results developed from the use of this experimental setup and demonstrates the capabilities of the test apparatus.

VII. Experimental Results

This chapter gives results and data from the experimental set-up showing its validity, and demonstrates measurements and data available through the use of this setup. This chapter describes the measurement capabilities offered by the apparatus, presents proof-of-concept and preliminary test results demonstrating the basic operation. Specific measurements available using the setup are described with examples. The chapter ends with a complete description of a sample test of a gold microcontact simulated switch.

7.1 Experimental Capabilities

This experimental set-up measured resistance performance of simulated microswitches, force vs. resistance curves as the simulated switch cycled, and was able to indicate contact adhesion failure as well as failure by resistance increase. It was also able to directly measure the contact adhesion of microcontacts as they cycle. Threshold force, the force required to obtain stable ohmic contact, was also precisely measurable using this test setup providing data on contact behavior. The interference between the contact bump and the lower contact plate was also measurable in this set-up. The threshold distance, defined as the interference required for stable ohmic contact, was also measurable with this setup. The strain-hardening or work hardening of contacts has been hypothesized, but not tested. This setup also enables measurement of changes in the stiffness of the contact material and thus is able to indicate whether work hardening of the contact occurred. Before and after cycling images of contacts demonstrating contact morphology change are key indicators of physical changes during cycling. This experimental setup also enabled these images to be easily obtained. Few researchers have shown contact morphology changes and fewer still have investigated contact damage on both the upper and lower contact sites.

The ability to directly measure contact force vs. resistance characteristics over lifetime as a contact cycles in addition to the changes in contact adhesion is a new

capability, and produces data which has not been published. This chapter describes sample results of proof-of-concept tests which were accomplished as well as data developed showing the physics of microcontacts, which demonstrates the utility of this experimental design. In the following chapters, the results of tests on different contact materials are reported and discussed. The behavior of the materials selected for testing are also compared to each other. In order to demonstrate the utility of this experimental method, first proof-of-concept tests demonstrating basic operation are presented, followed by detailed description of a test demonstrating successful integration, control and data collection.

7.2 Proof of Concept Test Results

An incremental development approach was taken in the development of the test design. As this type of mechanical cycling approach had never been attempted, a subset of the experimental design was run to see if the approach was feasible. First, the setup was placed under a microscope for alignment, connected to an external multimeter and a function generator was used to provide direct input to control the PZT. Then, after the experiment was integrated into the Nano Indenter XP, two tests were run to verify the input/output and control algorithms as well as the automated data collection developed in the test method.

7.2.1 Preliminary Setup Test. The objectives of the preliminary test were: (1) to verify that proper alignment of the cantilever and contact plate could be achieved with a microscope capable of only top-view, (2) that the gap between upper and lower contacts could be set using a decrease in resistance as the contact trigger, (3) that the contact resistance was on the order of predictions and other microcontact test data, (4) that the PZT could be controlled accurately using an external voltage source, and (5) that the two expected failure mechanisms (sudden resistance increase and contact adhesion) could be correctly detected using four-wire resistance techniques.

The preliminary experimental setup used LabView to control a digital multimeter and read data directly into the computer. This was a first step in experimental development, accomplished because it was simpler than integrating the NIDAQ system into the nanoindenter. A function generator was used to provide direct voltage input to the PZT controller to cycle the base plate and the open and closed contact resistance results were measured every cycle. The newly designed sample tray and mounting system was used, but was not integrated with the nanoindenter for this preliminary setup test. The test was run with NEU cantilevers having a stiffness of $1.5x10^4$ N/m coated with 300 nm of gold, using a displacement of 2 μm and therefore a nominal contact force of 30 mN. The test was run at 1 Hz and the open and closed resistances were measured at every cycle. Note that this test was done while hot-switching, and no shunt resistor was included in the test circuit to avoid the buildup of electric potential.

The closed resistance results of this test are shown in Figure 7.1. The closed resistance of approximately 0.5 Ω are reasonable and very close to the value of 0.5 Ω predicted by the Holm equation for gold contacts at a contact force of 400 μN. This figure does not indicate any kind of failure. However, this simulated switch failed in contact adhesion after approximately 25,000 cycles. The conclusion that this was a contact adhesion failure was made based on a review of the open resistance data. The adhesion occurred in the cycle when the open resistance was no longer infinite. This is clearly seen in Figure 7.2 which shows the resistance values for the "open" state of the simulated switch. Thus, the experimental setup was able to detect adhesion failures, although this preliminary setup was unable to automatically stop after the adhesive failure condition occurred.

The data collected for the final experimental setup described in Chapters V and VI did not measure open and closed resistance for every cycle as for this proof-of-concept case. However, cycling data was taken for open and closed resistance at intervals varying from every 10,000 to every 250,000 cycles during the actual tests.

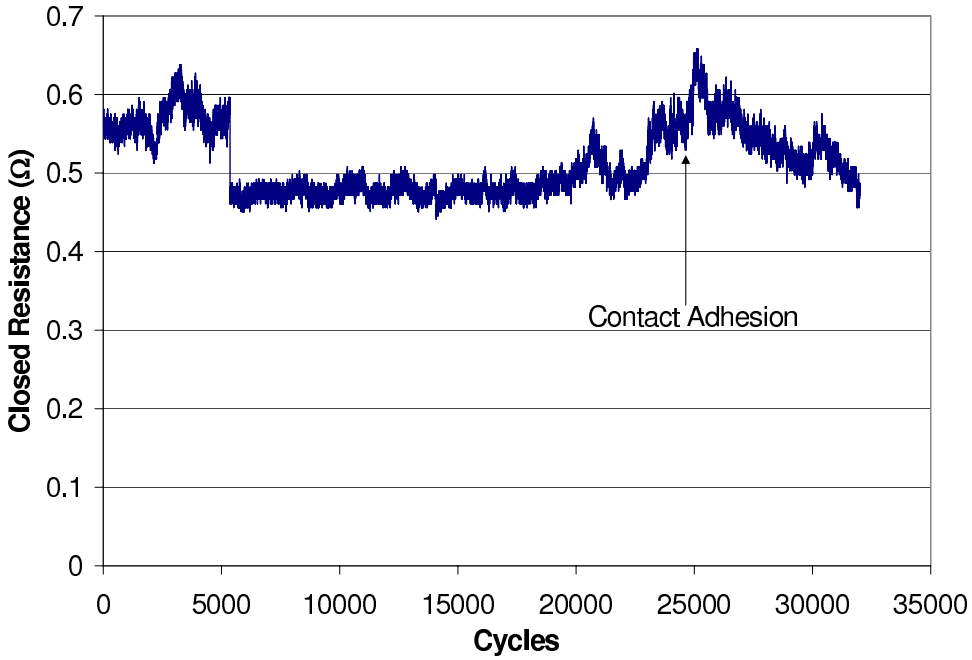

Figure 7.1: Simulated switch resistance results during cycling from a proof-of-concept resistance test of the PZT cycling experimental design. Data was taken by a digital multimeter and output to LabView running on a desktop computer. Test was cycled at 1 Hz with 1 mA of current at 400 μN contact force. The 0.1 Ω drop in resistance at 5000 cycles is likely due to fritting of contaminants on the contact surface.

This preliminary setup test successfully met all the test objectives outlined. The proof of concept was validated. Horizontal alignment was shown to be possible using the available microscope, indications showed that the vertical alignment and contact gap was correctly set at 2 μm, the contact resistance was reasonable, and control of the PZT was achieved using an external function generator.

Post-test review of the data showed that contact failure occurred in adhesion, but the test was not capable of automatically stopping. The test could have detected a sudden increase in contact resistance, but the test was unlikely to stop automatically if that occurred. The possibilities offered by the test setup were demonstrated. However, it was clear that manual testing with a setup like this would provide little value to engineers interested in investigating material performance in microcontacts. The next section describes the cycling only tests accomplished to demonstrate the

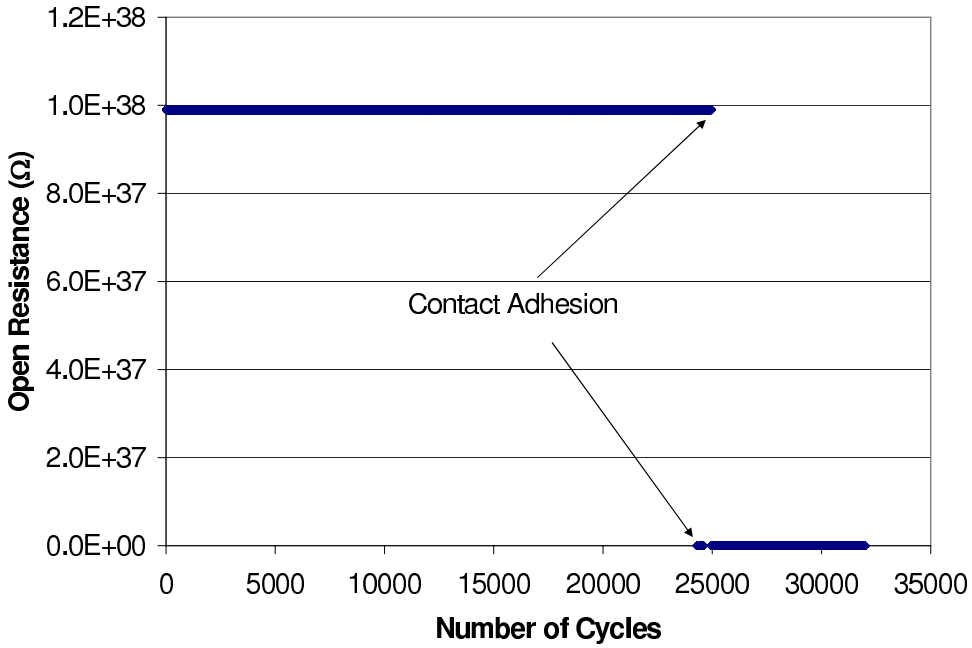

Figure 7.2: Simulated switch resistance results during cycling from a proof-of-concept resistance test of the PZT cycling experimental design. This chart shows "open" resistance values during a 1 Hz cycling rate test with 1 mA current. The cycle when the simulated switch no longer opened can clearly be seen.

feasibility of controlling the test automatically. The automatic test control developed included automatic detection of failure criteria, importing test measurements to ensure simultaneous data collection using the custom developed test method in TestWorks and integration of data acquisition modules with the MTS Nano Indenter.

7.2.2 Cycling Only Tests. The objectives of the cycling only tests were to demonstrate the routine developed to automatically set the contact gap using voltage output to the PZT, the control logic in the Test Method developed for this test, the TestWorks based control of the PZT using a digital switch to select either a constant voltage control or the time-varying voltage from a function generator, the detection of contact failure, and the insensitivity of contact performance to varying measurement intervals.

These cycling only tests were set up inside the nanoindenter using the experimental fixtures and gold coated NEU cantilevers, as in the first proof of concept test.

The PZT was controlled using TestWorks, and the four wire resistance measurement was set up using National Instruments devices controlled through TestWorks. The hardware and software control logic of the final test was used, except no indentation using the Nanoindenter head was commanded. Two hot-switched tests were run with a constant current of 0.5 mA. The first had a measurement interval of every 1,000 cycles and the second had a measurement interval of every 20,000 cycles. That is, the cantilevers were cycled at 100 Hz and stopped every 1,000 or 20,000 cycles respectively so that the in-contact and out-of-contact resistance could be measured. The nominal contact cycling force in these tests was also 30 mN. The results of the tests are shown in Figure 7.3. The contact failure of these two tests occurred within the scatter band. This result shows that the measurement interval does not affect the results. One failure occurred at 110,000 cycles and the other occurred at 113,000. The resistance of both of these switches went high at failure.

7.3 Contact Analysis

It is important that the contact occur at the bump and not elsewhere on the cantilever. Cycling only testing was accomplished using cantilever beams fabricated at Northeastern University. These tests showed that measurements could be made using the setup and that the contact occurred at the bump, even though it was only approximately 1 μm tall.

7.3.1 Bottom Contact Image. One feature of this experiment is the ease with which the morphology change on both contact surfaces can be analyzed. The simplicity of removing the contacts for post-cycling surface analysis was validated during the initial cycling only testing. The images shown here in Figures 7.4 and 7.5 are the results from that test. Figure 7.4 shows the bottom contact area on the strike plate from one of the tests run on NEU fabricated cantilevers. The impression of the upper contact can clearly be seen. No contamination appears to be present. The contact force used in this test was approximately 30 mN and the contact survived

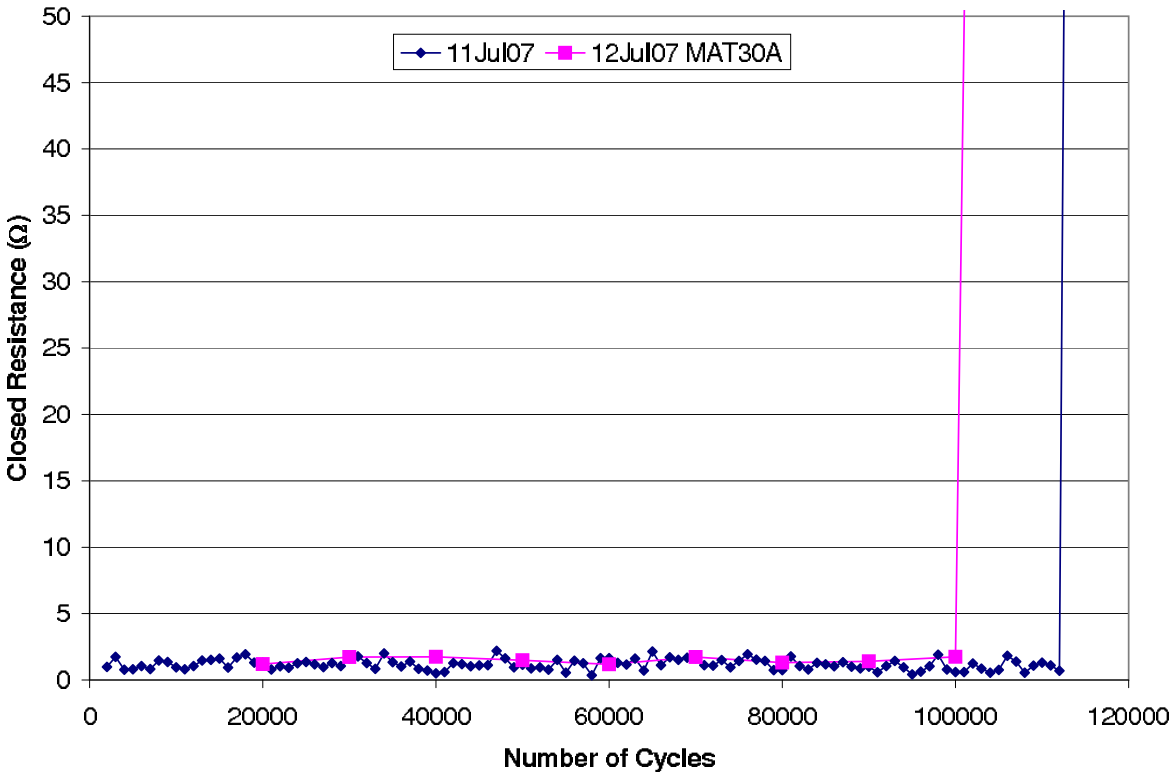

Figure 7.3: Simulated switch resistance results during cycling without indent using test setup and measurements through MTS Nanoindenter XP.

110,000 cycles. This contact was hot-switched with a current of 0.5 mA and run on the test setup without actuation by the microprobe.

7.3.2 Contact Bump Image. Figure 7.5 shows the contact bump on the cantilever. The shape of the morphology change can clearly be seen and compared with the lower strike plate contact shown in Figure 7.4. Figure 7.6 shows the end of the cantilever used in this test which indicates that contact only occurred at the contact bump. Contact only at the contact bump shows that the experimental design and alignment was good enough to ensure that the microcontact cycling experienced in MEMS switches was mechanically replicated. The rounded bumps fabricated on NEU cantilevers were shorter, and thus a more demanding contact alignment scenario than the taller bumps fabricated for AFIT testing. Note that the high resistance failure measured during the test on this contact appears to have been caused by severe

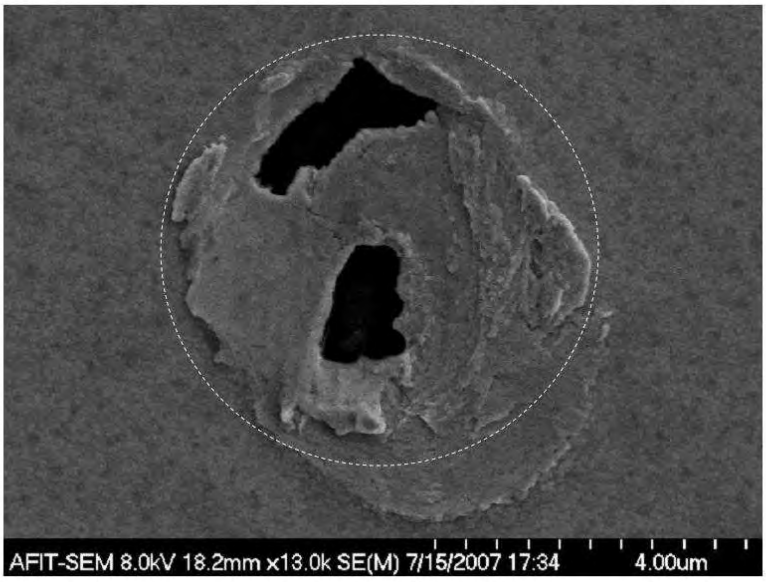

Figure 7.4: Example of bottom contact location after cycling. These results are from a contact test of a gold-gold contact on a cantilever with stiffness of approximately 10^4 N/m fabricated at Northeastern University with a contact force of 30mN and failed at 110,000 cycles. The dotted line indicates the approximate circle of contact. This is the contact location for the bump shown in Figure 7.5

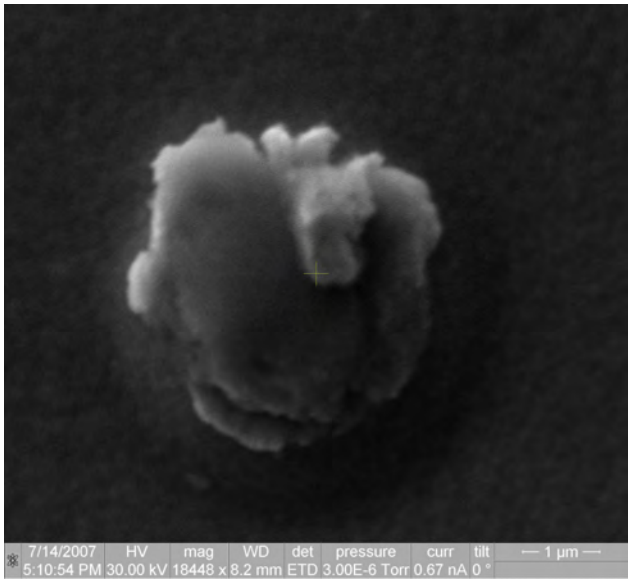

Figure 7.5: Example of bump contact after cycling. It can be seen that material from the lower contact adhered to the contact bump at failure. These results are from the contact test of a gold-gold contact on an NEU fabricated cantilever with current 0.5 mA and contact force of 30 mN which failed at 110,000 cycles. The strike plate contact area from this test is shown in Figure 7.4

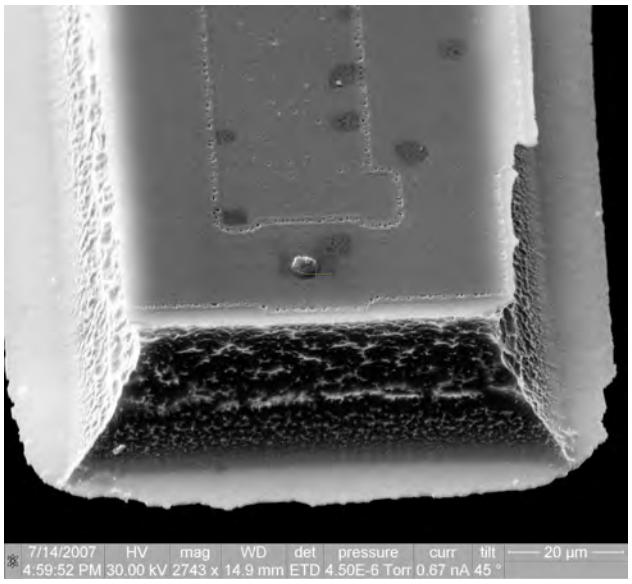

Figure 7.6: Contact bump of NEU cantilever after 110,000 cycles at 30mN. Shows that contact occurred only at contact bump. A close-up view of the contact bump on this test device is shown in Figure 7.5

damage to the contact film and not the creation of a high resistance contaminant layer.

During the experimental design, it was important to ensure arcing did not occur and analyze the possibility of contact arcing and how it might affect test results. The next section shows an example of arc damage in a contact similar to those used in tests, and discusses Paschen's curve as extended for small contact gaps of the size used in this study.

7.3.3 Arcing Damage. Arcing is always a possibility when opening and closing electrical switches while a potential difference exists across the contacts. This possibility was anticipated, so it was hypothesized that images of known arcing on contacts similar in size and material to those tested would be helpful in determining if arcing occurred during a test. One test cantilever was subjected to arcing and an example of damage caused by arcing at the contact is shown in Figures 7.7 and 7.8. Arcing during tests run for this study was not expected due to the low voltage between contact surfaces and the small contact gap. Paschen's Law and other research into

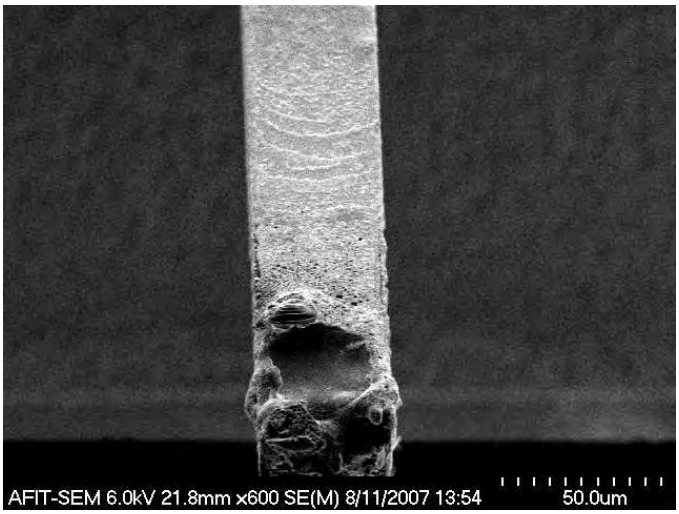

Figure 7.7: Example of arc damage to a gold coated cantilever/bump surface produced in test setup. Charge buildup was greater than 5 V. Image was taken at an angle of 45 degrees.

this behavior at small contact gaps did not predict the formation of arcs in the present setup.

A gold coated cantilever was installed in the test setup without a compliance resistor, and a charge of at least 5 V was allowed to build across the contact. The strike plate was slowly brought up to contact the cantilever bump. A bright flash was seen in the microscope display and electrical contact was not possible after discharge of the spark. The damage to the cantilever caused during this arc event is shown in Figure 7.7 and the damage to the strike plate is shown in Figure 7.8. The purpose of this test was to demonstrate the effect of arcing and the result in this test setup. Material on the cantilever was clearly vaporized and the contact area on the strike plate shows significant melting, material flow and spatter. No similar results were seen in any of the tests run when the potential difference across the contact was controlled with a compliance resistor, therefore it was concluded that arcing did not occur during the tests run in this study.

The types of failures expected during testing were either a sudden increase of resistance (failure open) or a contact adhesion failure (failure closed). The experi-

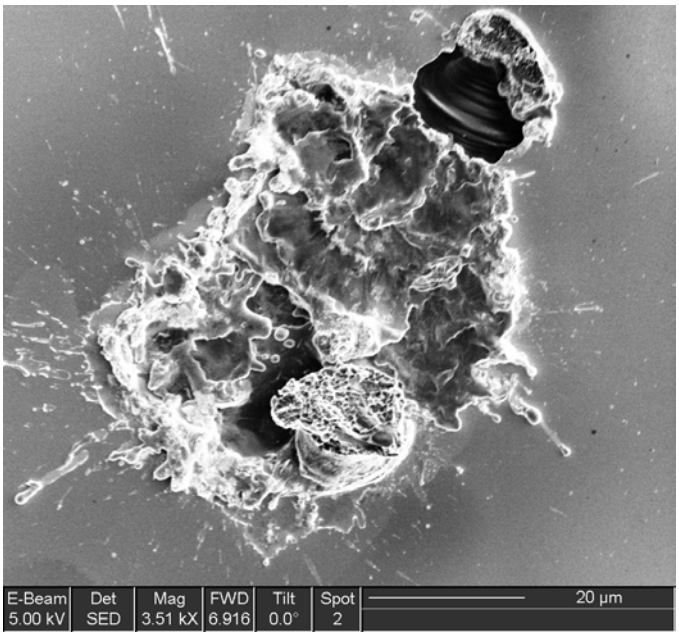

Figure 7.8: Example of arc damage to a gold surface produced in test setup. Charge buildup was greater than 5 V.

mental setup was designed to capture both cases and stop automatically when either one was detected. The following sections describe these results and the failures.

7.3.4 Resistance Increase. It was expected that resistance through simulated switches would stay constant for a certain number of cycles, and then increase dramatically, likely almost asymptotically. This type of failure is generally described as being caused by contact contamination in the literature and was expected to be more common in contact materials other than gold. However, adhesive failure of the contacts was the most common failure mode experienced by all materials tested in this study. It was expected that the resistance increase during cycling of gold-ruthenium alloys would be significant due to contamination on the contacts and that the majority of Au5%Ru contacts would fail with sudden increase in resistance. However, it was noted during testing that a few high resistance failures occurred. SEM examination of high resistance failed contacts showed that the adhesion of the thin film and its separation from the contact bump actually caused the high resistance failures.

7.3.5 Contact Adhesion Failure. Contact adhesion failure is probably the most common failure mechanism of micro-contacts in MEMS contact switches. This type of failure was predicted to be more common in gold-gold contact tests. It was expected that the majority of tests would fail in this manner. It was also expected that few, if any, Au5%Ru contacts would exhibit contact adhesion failures during testing. The criteria used to detect contact adhesion failure is described in Section 6.2.5 and the ability to measure contact adhesion failure is described and demonstrated in Sections 7.2.1 and 7.4.3.

7.4 Measurement Capabilities

A typical test measured resistance performance through contact force vs. resistance curves during cycling and was able to indicate contact adhesion failure or high resistance failure. The apparatus was also able to determine contact adhesion of the microcontacts as they were being cycled by direct measurement of pull-off force. The measurement of pull-off force is a measurement of the force required to break physical contact of the contacting surfaces. This was accomplished by analyzing nanoindenter force, displacement and resistance data channels. The force required to obtain stable ohmic contact, called threshold force in this study, is also measurable using this test setup providing another useful insight into contact behavior. This section demonstrates the aforementioned measurement capabilities of the test setup and provides a few example results. One technique required for success of this setup was the automatic surface locator. The cycling and measurement of contact behavior throughout the lifecycle of the contact would not have been possible without a successful automatic surface detection method.

7.4.1 Surface Locator Technique. An important step necessary for the success of the experiment was a method to first determine the point of contact between the microprobe and the cantilever, then to determine the point of contact when the cantilever was pushed into contact with the strike plate. The cycling and accurate

measurement of contact behavior throughout the lifecycle of the contact required an automatic surface detection method.

The surface locator technique employed in this experimental setup automatically detected contact between the microprobe and the cantilever as well as between the cantilever and strike plate. Precise determination of contact between the microprobe and the cantilever and then the cantilever and the strike plate was determined dynamically using the continuous stiffness measurement (CSM) technique. The CSM (a phase-lock amplifier) was used to examine the evolution of stiffness as the microprobe engaged the cantilever and deflected it into contact with the bottom plate. The CSM technique is described by Oliver and Pharr in [185]. This was accomplished by inducing an oscillation in the microprobe of $\pm$ 50 nm and monitoring the harmonic stiffness channel. When a change in harmonic stiffness occurred, surface contact was detected. A representative example of surface contact detection is shown in Figure 7.9.

The marker PS, in Figure 7.9, shows the point of contact of the microprobe with the cantilever, when the contact stiffness first increases and the marker PP shows the point where the cantilever is pushed into contact with the strike plate. Note the increases in harmonic stiffness at each point, clearly indicating contact. The harmonic displacement of the microprobe is turned off after contact with the strike plate is detected, so loading of the contact occurs without harmonic displacement. Note also that the accuracy of the surface locator was increased by post-processing. That is, the point identifying surface contact can be adjusted in the TestWorks output data to correctly mark the point at which harmonic stiffness changes. The harmonic contact stiffness plot clearly shows when contact with the plate is achieved, so adjustment of the contact point and recalculation of test data resulted in plate contact location with high accuracy. In the next few sections, measurements and data available from the experiment are described and examples of acquired data are presented. These descriptions and examples will be followed by the results of a sample test. Load-displacement data, pull-off (or adhesive) force, contact stiffness, contact interference,

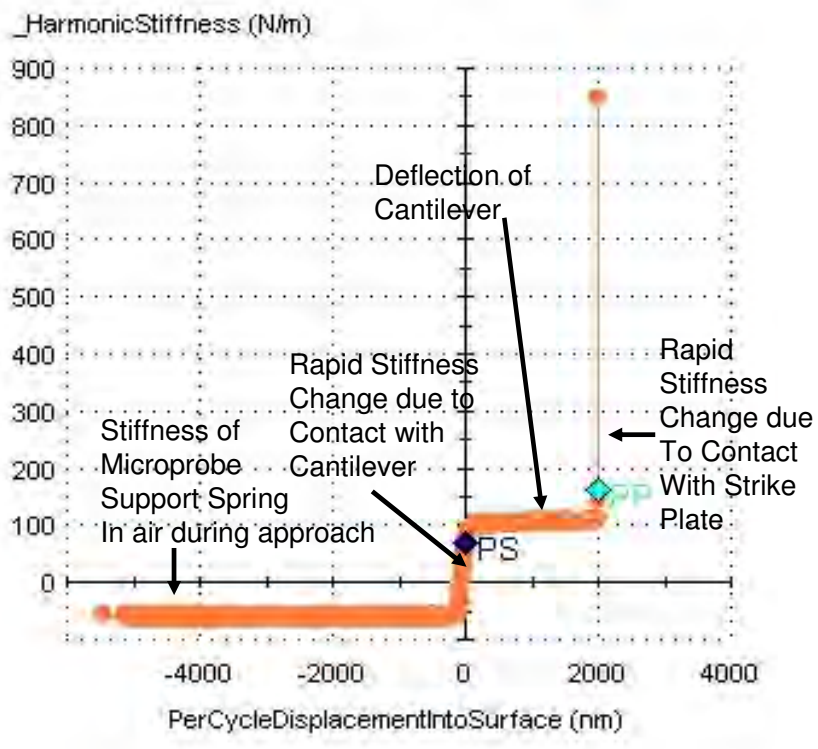

Figure 7.9: Example of results showing accuracy of surface detection routine in Test Method developed for this research. The marker PS shows contact with the cantilever and the marker PP shows contact between the cantilever contact bump and the strike plate.

energy absorbed by contact materials, the force vs. resistance results, threshold force and distance, and contact bump evolution are all described.

7.4.2 Load vs. Displacement Results. The basic measurements performed by a nanoindenter are the load on the microprobe and its displacement. Figure 7.10 shows a typical force-displacement curve for one microprobe actuation measurement in the contact segment of a test. This data shows the expected linear deflection of the cantilever and contact with the strike plate. The initial linear portion shown in the figure from the point marked "1" to the point marked "2", is the cantilever bending due to the load applied by the microprobe. Point 1 in Figure 7.10 is the point of initial contact between the microprobe and cantilever and corresponds to PS in Figure 7.9, and point 2 is the point of contact between the cantilever and the strike plate and corresponds to PP in Figure 7.9. The second linear portion (point 2 - point EL) of the

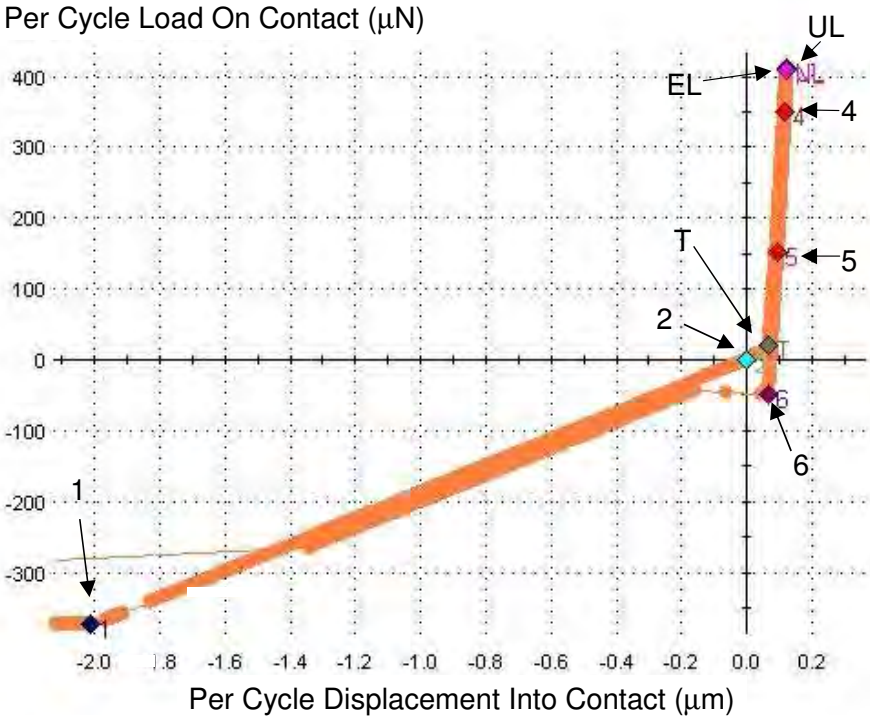

Figure 7.10: Example of load displacement output from the MTS Nano Indenter XP each time the indenter head actuated the cantilever simulated switch.

curve starting at point 2 is the loading path of the contact from the point where the surfaces come into contact up to maximum applied load. Deformation of the contact at maximum load, also called contact interference, can be calculated by taking the difference in "Per Cycle Displacement into Contact" between points 2 and EL. The unloading curve (point UL - point 6) is also seen in Figure 7.10.

7.4.3 Contact Resistance and Failure Detection. The in-contact and out-of-contact resistance were measured after each cycling interval. Contact failure was identified based solely on the resistance measurements as described in Section 6.2.5. If the in-contact resistance was measured high, as shown in Figure 7.11, the failure was a high resistance fail. If the contact resistance was measured very close to the in-contact resistance, as shown in Figure 7.12, the failure was an adhesive failure where the contact failed to open, that is, the contact remained stuck closed.

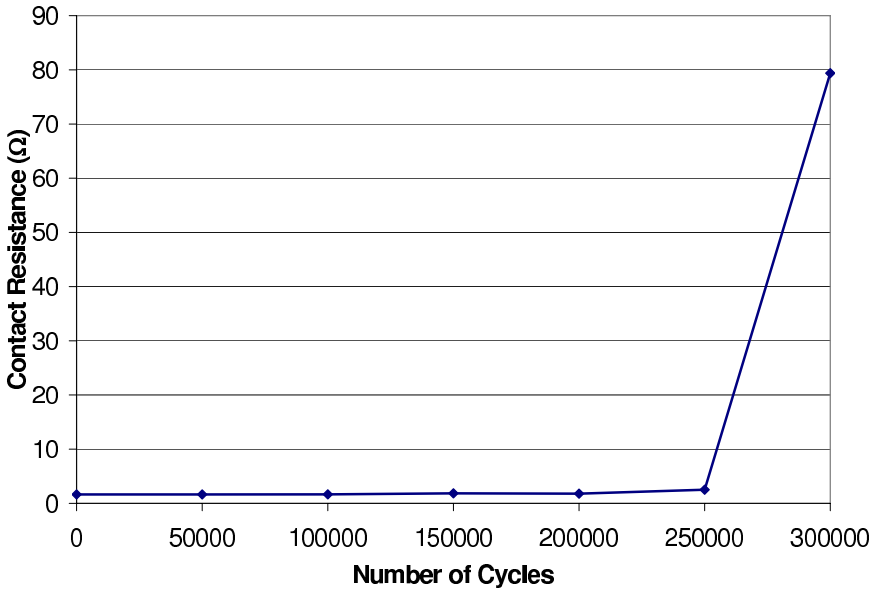

Figure 7.11: Example of in-contact resistance measurements from a test indicating high resistance failure of contact. This is typical of high resistance failures experienced during testing

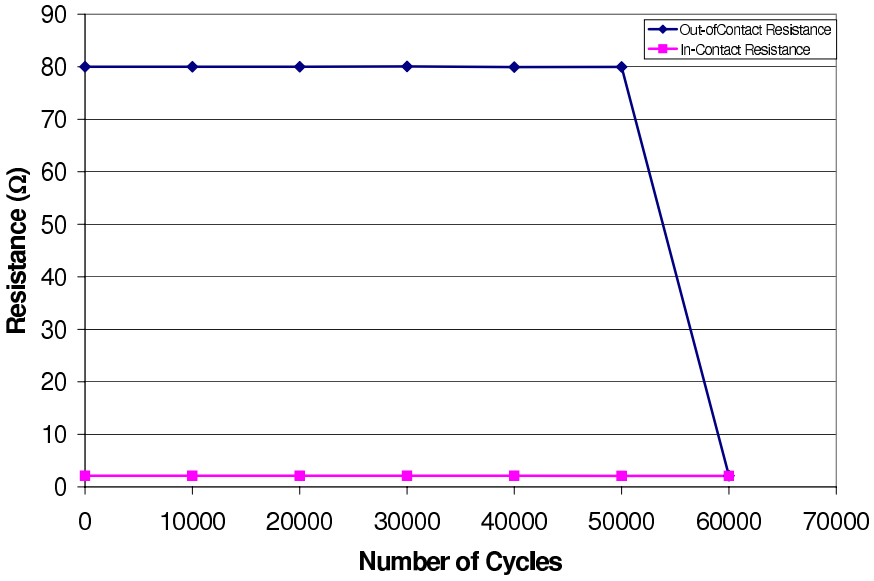

Figure 7.12: Example of adhesive failure determination using in-contact and out-of-contact resistance measurements. Note that out-of-contact measurement is very close to the in-contact measurement. This is a clear indication that the contact failed to open after application of the simulated switch restoring force. This is typical of adhesive failures experienced during testing.

7.4.4 Pull-Off Force. There is an adhesion force between contacts which has been noted by previous researchers [39]. This force causes hysteresis in the actuation of MEMS switches, and is the distance between the X-axis and the point labeled "6" on the unloading curve in Figure 7.10. The pull-off force is the force on the contact required to break the adhesive bonds created during contact loading and is a measure of the adhesive force between contact surfaces. Pull-off force is the measure of contact adhesion used throughout this study. The microprobe in all tests unloaded at a rate of 50 μN/sec. The change in pull-off force during each test can be tracked to show changes in adhesion over contact lifetime.

7.4.5 Contact Unloading Stiffness. This experimental setup also permits the investigation of possible stiffness changes in the contact material. The stiffness change in contacts as they cycle has not been reported, as far as the author is aware. The method for detecting stiffness changes uses the unloading portion of the load-displacement curve. The absolute value of the contact stiffness was not measured during this experiment, as the frame stiffness of the experimental setup was not determined. However, the changes in contact stiffness can be tracked because the only change in the stiffness during each experiment will be the change in contact material stiffness. The stiffness was measured by calculating the unloading slope between two points (labeled "4" and "5" in Figure 7.10) for each indenter measurement. These points 4 and 5 were chosen to capture the linear slope during unloading in order to capture only elastic stiffness and exclude the plasticity effects during initial unloading and contact separation. However, this stiffness measurement is not able to separate the component of stiffness due to the frame stiffness of the experimental setup. Therefore, in order to compare results between tests, the contact unloading stiffness measurement was normalized by the initial unloading stiffness measurement taken before cycling of the contact occurred. The normalized contact unloading stiffness was then used to generate data on contact stiffness changes during each test.

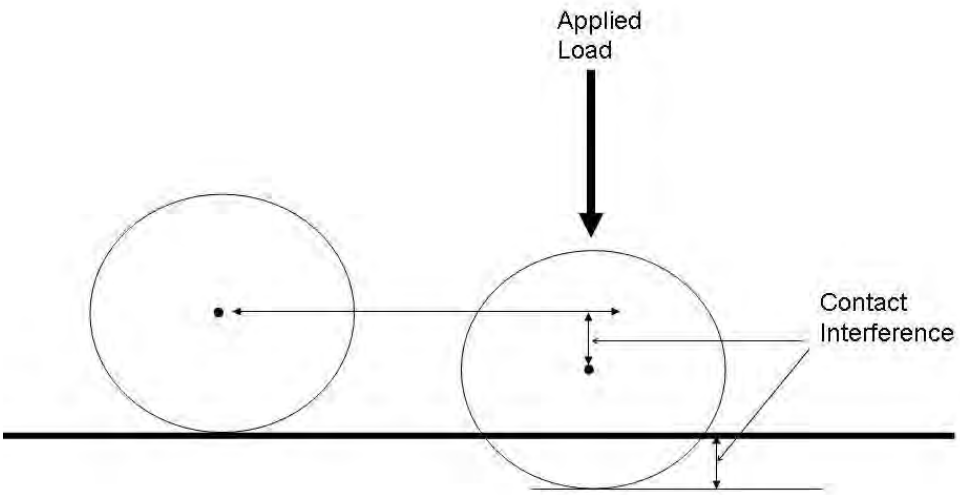

Figure 7.13: Simplified schematic demonstrating contact interference. The figure on the left shows a rounded contact bump just in contact and the figure on the right shows contact interference at maximum contact force. Note that the relative distances involved are exaggerated.

7.4.6 Contact Interference. Contact interference is defined as the deformation or compression distance when two solid surfaces are pressed together. A simplified schematic demonstrating the definition of contact interference used in this study is shown in Figure 7.13. Contact interference is calculated by taking the displacement difference between the plate contact point and the point of maximum load. This distance is measured between the location of plate contact (labeled "2") and the location at end of loading (labeled "EL"), which can be seen in Figure 7.10. The change in this "displacement into contact" can also be shown over the life of the contact.

7.4.7 Time Dependent Behavior. Another interesting facet of the contact behavior noted during this study was the existence of time-dependent behavior during contact loading, very similar to creep. During each test, a five second hold was programmed between the end of active loading and the unloading of the microprobe. There should have been no displacement during this hold time. However, in every case a small deformation occurred under the constant load. Gregori and Clarke suggested that creep in gold microcontacts occurs under load, and that creep is a factor in development of adhesive forces between the contacts [92]. They also cite unpublished

gold film indentation "companion studies" which confirmed that creep does occur at room temperature. Room temperature creep in gold thin films has also been investigated by Leseman [147]. Bannuru reports that time dependent plastic deformation in thin films is a cause of concern and that thin films are prone to creep even at room temperature and below the yield stress [9].

This behavior is likely due to the small size of the contacts, and the nature of the thin film contact. It is hypothesized that dislocations are created during cycling. Researchers have noted that dislocation motion dominates in thin films [109]. Researchers have also hypothesized that the high strengths which prevail in small volumes are associated with dislocation starved conditions that cause nucleation of dislocations to dominate plastic resistance [91]. The primary mechanism of plasticity on the nanometer scale is also hypothesized to be the nucleation of dislocations [88]. Because the area of contact is so small and the instrument used in this study is very sensitive, the dislocation motion due to creep may be detectable by nanometer scale tip displacement whereas in larger contacts or larger metallic materials using less sensitive measurement tools dislocation motion on the order of nanometers would be undetectable. Also, current is flowing during the test, thus the contact may be heating due to current flow through the constriction. This heating could cause softening of the contact material as the device is maintained in contact under load. Note that thin film softening temperature has been shown to be lower than that for bulk materials [115] and that rates of some creep mechanisms increase with smaller grain sizes [9].

7.4.8 Energy Absorbed by Contact Materials. MTS TestWorks offers the ability to perform calculations on the energy absorbed by the material being indented. The area under the load-displacement curve is the amount of energy absorbed by a specimen. This quantity was measured and automatically calculated during each actuation of the contact by the microprobe. This calculation gives a measure of the

amount of plastic deformation during each contact actuation. These results are given in units of N·mm.

7.4.9 Force vs. Resistance. Force vs. resistance curves at different intervals during the cycling can be developed using this experimental setup. This data is developed using nanoindenter force measurements automatically combined with the calculated resistance through the simulated switch. The experimental setup provides these curves. One such example is shown in Figure 7.14. This curve shows the measured resistance during a microprobe actuation. Arrows in the diagram show the direction of the loading and unloading path. Threshold force based on the threshold point and pull-off force based on the pull-off point can be determined from this graph. Note that this force vs. resistance data can only be collected by resistance measurement during hot-switching tests. This curve clearly shows the hysteresis involved in metallic contact and the adhesion which occurs in the micro-contact. Such information can be developed with this setup over the lifetime of microcontacts.

7.4.10 Threshold Force and Distance. Another measurement which can be made based on the force vs. resistance curve is the determination of the force necessary to cause metallic contact in microcontacts. This is referred to as threshold force in this study. Threshold force is analogous to the result called "force required for low and stable contact resistance" in other studies [174]. The compression distance, or interference, required for stable electrical contact can also be measured. This quantity is called threshold distance in this study. A schematic of a general force vs resistance curve for an electrical contact is shown in Figure 7.15 and demonstrates the definition of the threshold point and threshold force. The threshold point can be described as the point where quasimetallic contact transitions to metallic contact between the surfaces. The marker "T" in Figures 7.10 and 7.14 shows the threshold point for actual test data. Threshold force is the force applied to the contact after the contact surfaces physically touch up to the threshold point when the contact resistance is stable and approaching a stable value. Threshold distance is based on the distance

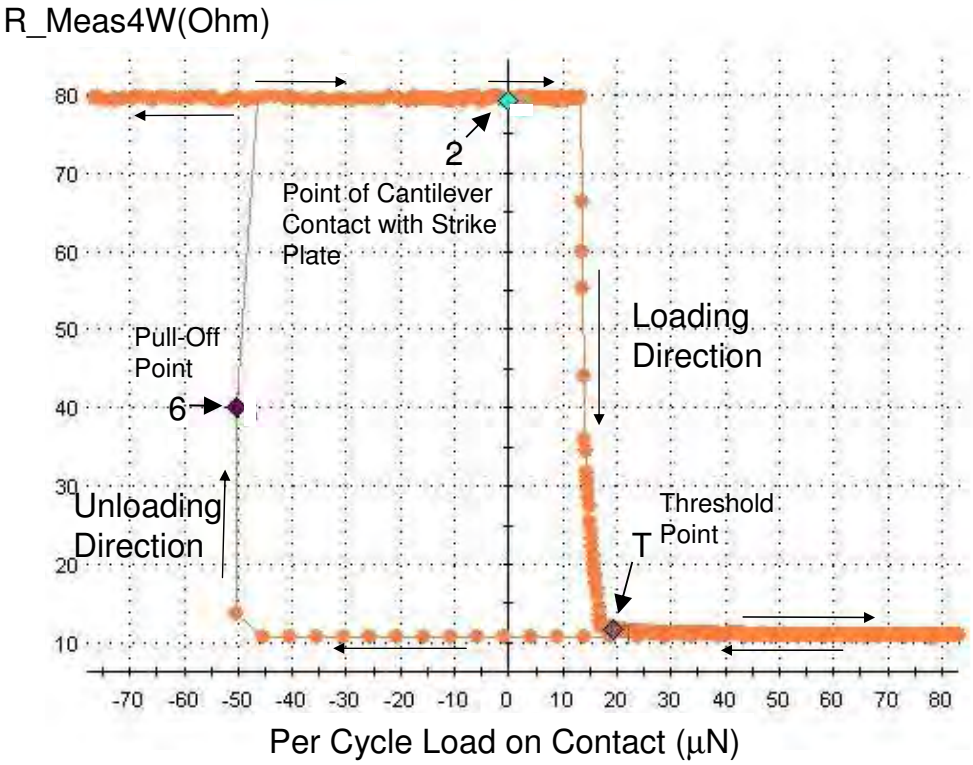

Figure 7.14: Example of output from the MTS Nanoindenter XP when connected to the four-wire resistance test setup through the NIDAQ system. These results are from a contact test of a contact on a cantilever with stiffness of approximately 200 N/m. Arrows in the diagram show the direction of the loading and unloading path.

between plate contact and the threshold point and can also be thought of as the contact interference required for stable ohmic contact.

7.4.11 Contact Bump Evolution. The contacts used in this experiment are either rounded or flat bumps, similar to the one shown in Figure 5.10 and are similar to those reported in other microcontact and MEMS switch studies. The experimental setup allows the contact bump to be removed and examined in a Scanning Electron Microscope (SEM). This flexibility allows analysis and a better understanding of the processes occurring at the contact during cycling. It also allows comparison of morphology changes between contact metals in comparable environments. The easily removable cantilever test setup design also allows chemical analysis of any material created or deposited during the cycling. This could be accomplished using Auger or

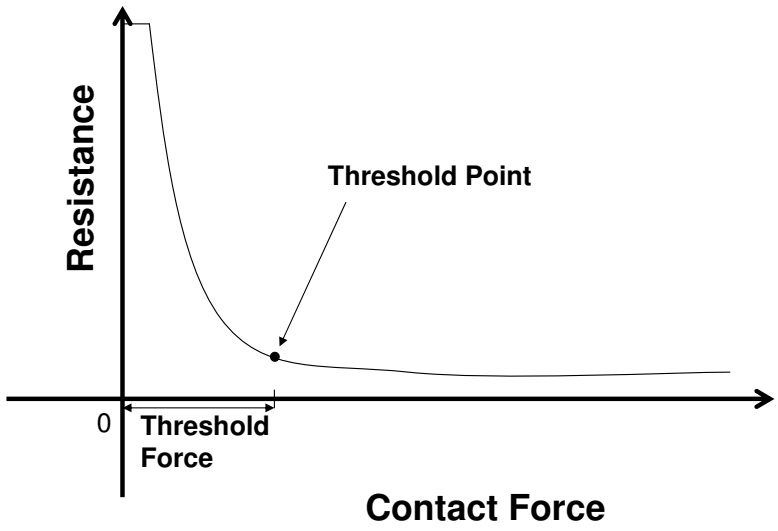

Figure 7.15: Schematic demonstrating definition of threshold point and threshold force. Threshold force is the force after which increasing force results in stable and constant contact resistance.

X-Ray Photoelectron Spectroscopy (XPS). The area of contact can also be investigated using SEM imagery to estimate the contact area of the simulated switches in this research. The results available for an example test run on a gold-gold contact is given next. This example demonstrates the data available from each test.

7.5 Sample Gold Adhesive Failure Results

This section presents sample results obtained from the experimental setup. One set of test results is given here to demonstrate the capability of this apparatus. This involved a test of a rounded contact bump coated with 300 nm of gold which failed in adhesion between 50,000 and 60,000 contact cycles. Note that the data plots show data only up to 50,000 cycles because the failure was indicated by the resistance measurement at 60,000 cycles, and no measurements were made after failure was detected. Contact resistance and nanoindenter measurements were taken every 10,000 cycles. Plots of measured contact resistance, pull-off force, threshold force and threshold displacement, as well as measures of contact interference, time dependent behavior observed and change in contact stiffness are shown here.

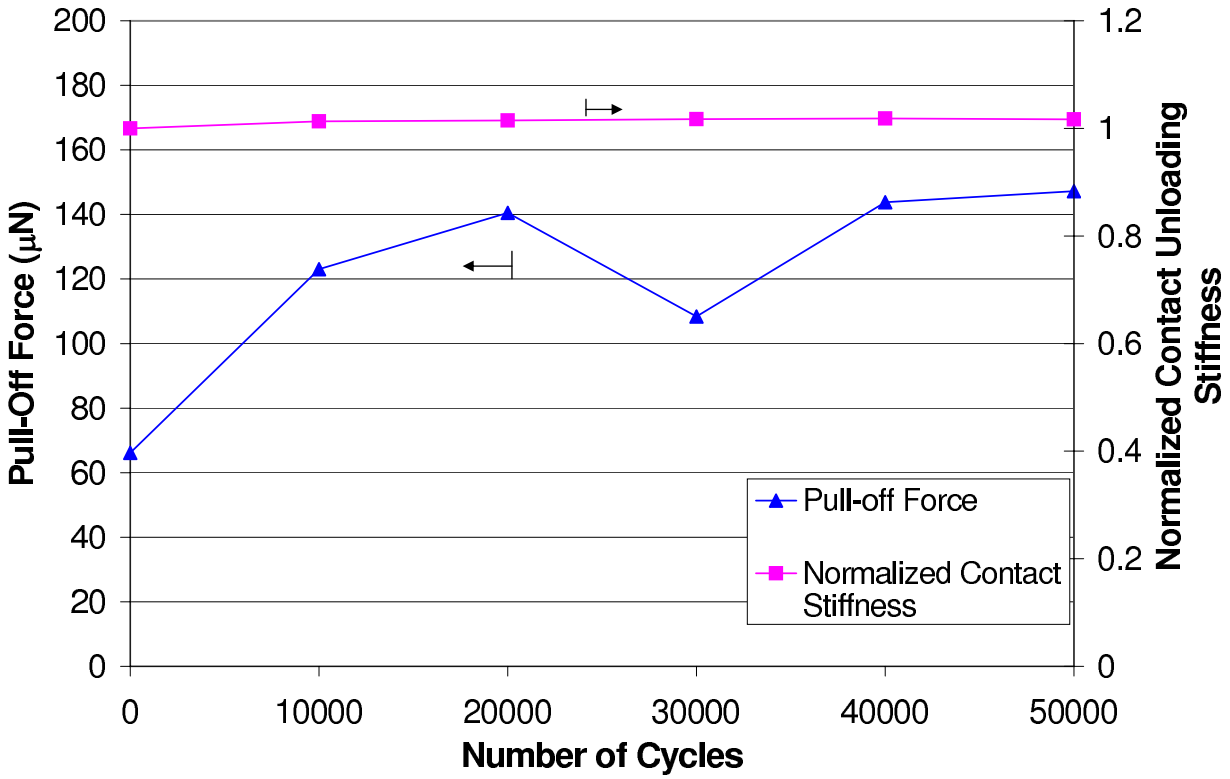

Figure 7.16: Sample gold contact adhesion failure pull-off and normalized change in contact stiffness results during 60,000 cycle gold adhesive contact failure. No data was takend at 60,000 cycles after adhesion failure was detected.

The pull-off force measured every 10,000 cycles in the sample experiment is shown in Figure 7.16. These values are much larger than the results given by Gregori, et. al. in [93] because the contact force, and therefore the contact area, was significantly larger in the present test. Note that Gregori, et. al. used a contact force of 25 μN with a contact diameter of approximately 2 μm [93]. The slight drop in pull-off force at 30,000 cycles is likely due to contamination increase or a surface roughness increase due to material transfer or plastic deformation. The contact unloading stiffness change for the sample test is also shown in Figure 7.16. There is less than 2% increase in contact stiffness after the first contact, and then the contact stiffness stays constant. Note that the stiffness was normalized by the initial stiffness measurement made before cycling occurred. There is no evidence of significant strain hardening in this test as demonstrated by the slope of the contact unloading stiffness curve in

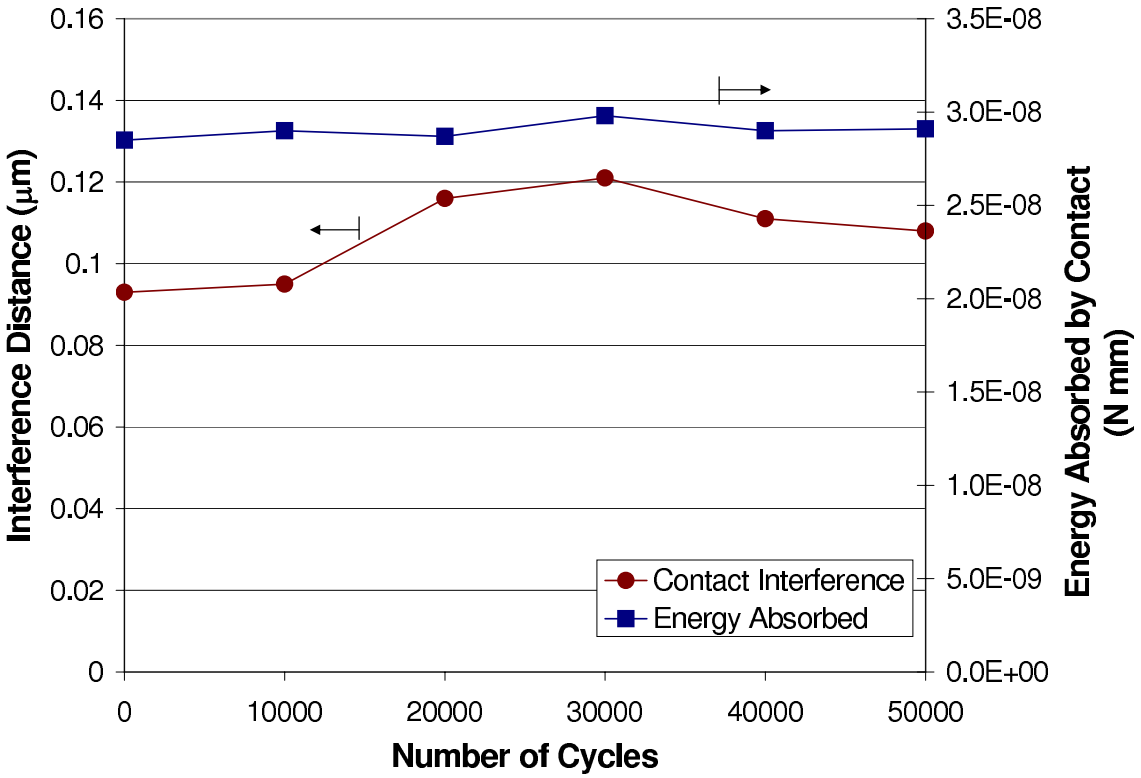

Figure 7.17: Contact interference (deformation) and energy absorbed during the 60,000 cycle gold contact adhesive failure. No data was taken at 60,000 cycles after adhesion failure was detected.

Figure 7.16. The contact interference, or deformation of the contact during loading, in this test is shown in Figure 7.17. The interference during this test increases then decreases slightly. This probably indicates that damage was occurring in the contact during cycling and may be accumulating gradually.

The energy absorbed during each measured interval in this test showed an upward trend during cycling from 2.84 to about 2.9×10^{-8} N·mm, and is shown in Figure 7.17. This indicates that the total plastic deformation in the contact does not occur in the first contact cycle, but that plastic deformation continues throughout the life of the contact and damage may be cumulative.

The time dependent displacement indicating possible creep behavior in this contact is shown in Figure 7.18. The displacement measured during the 5 second hold stays relatively constant through the short life of this contact at just less than 4

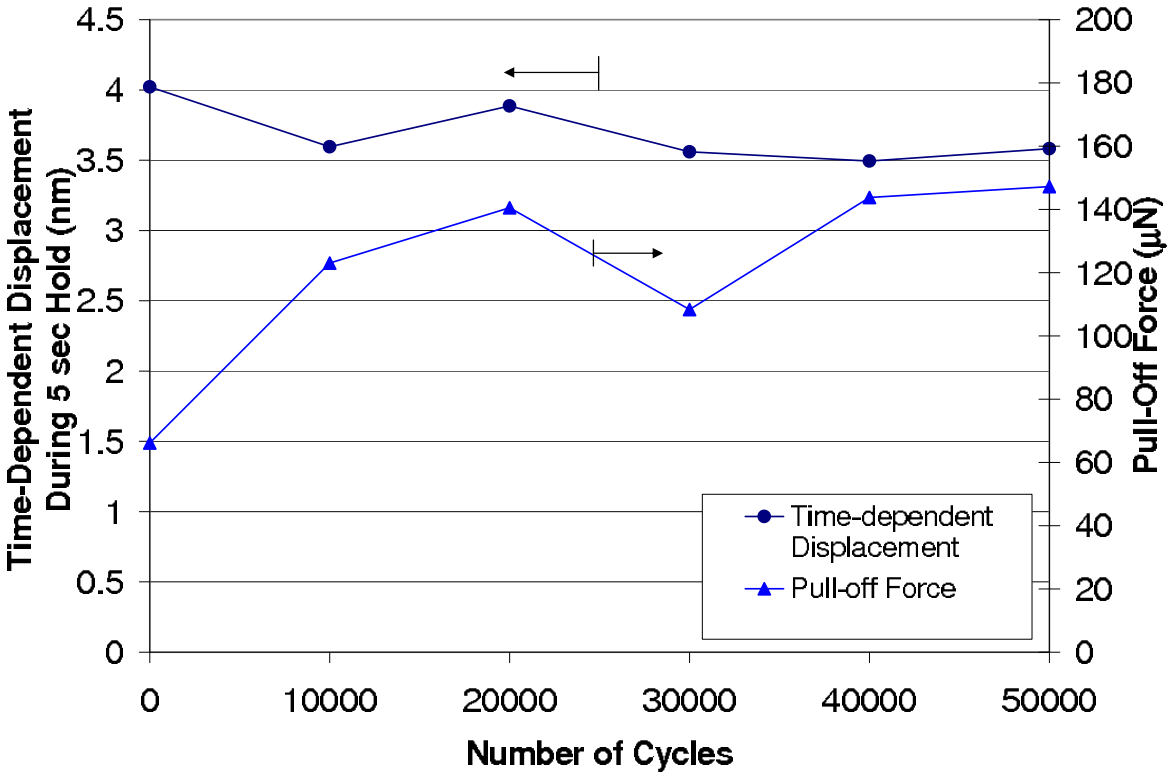

Figure 7.18: Time dependent contact deformation (creep) compared to pull-off force between end of active loading and start of unloading (5 sec).

nm. The time-dependent deformation behavior is shown with pull-off force in Figure 7.18. The time-dependent deformation stays relatively constant between 3.5-4.0 nm during the test, while the pull-off force increases from around 70 μN to 150 μN just before failure.

The threshold force and displacement for this test are shown in Figure 7.19. These results show that the threshold force is relatively constant at about 7-9 μN and the threshold displacement is relatively constant between 60 - 80 nm. This shows that during this test the electrical characteristics of the gold contact layer did not change significantly. This test used a gold coated rounded bump which had a relatively rough surface. An SEM image of the contact bump before cycling is shown in Figure 7.20. The contact experienced an adhesive failure between 50,000 and 60,000 cycles and the contact bump after testing is shown in Figure 7.21. A comparison of

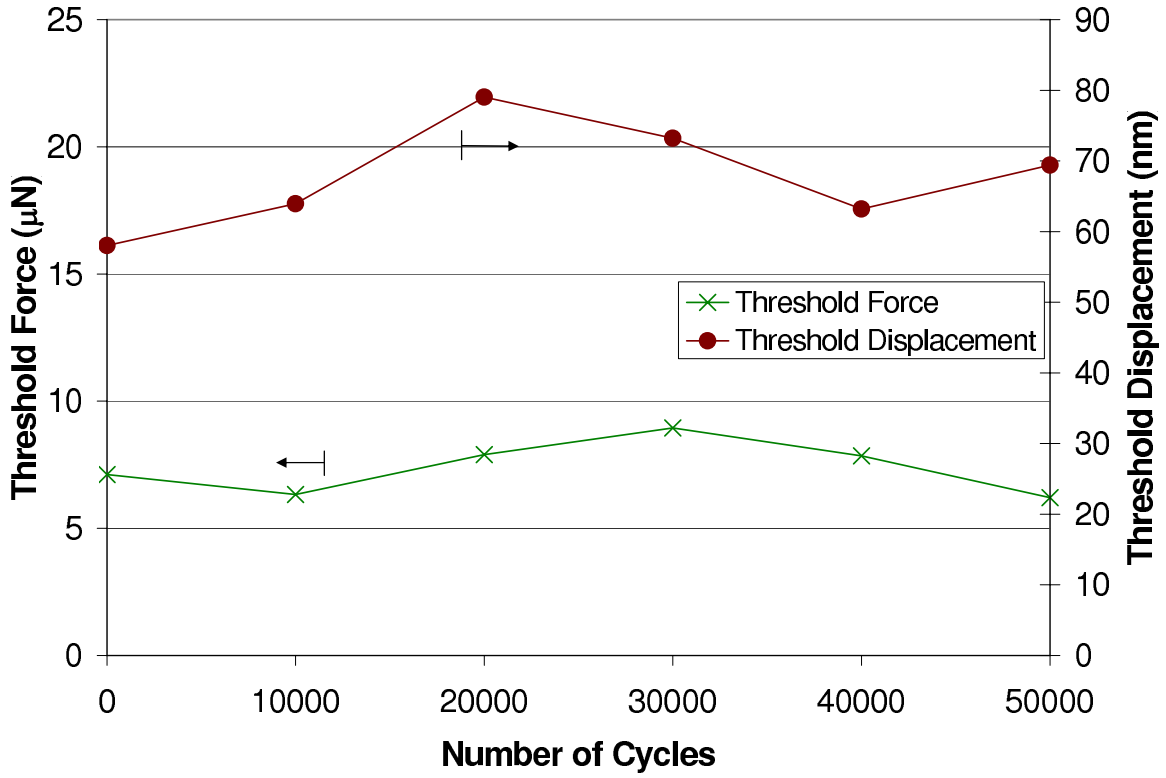

Figure 7.19: Threshold force and threshold displacement required to ensure ohmic contact with gold microcontacts during 60,000 cycle test. Test ended in adhesive failure of contact and no data was collected at 60,000 cycles after adhesion failure was detected.

these images shows that the surface of the bump was smoothed during cycling, which likely contributed to the early adhesion failure. The deformed material is clearly the location where the adhesion occurred, and it was pulled apart when the strike plate was removed at the end of the contact test. The pull-off appears to be ductile rupture of the gold film, and separation did not occur on the plane of contact.

Figure 7.22 shows a higher magnification image of the bottom contact location on the strike plate. The shape of the adhered portion from the contact bump can be clearly seen on the strike plate. Little contamination appears to be present. The image in Figure 7.22 shows the gold strike plate surface, which appears to be unchanged in the area around the contact spot other than the area of material transfer. This indicates that the smoothening effect mostly occurred in the bump surface. The gold on the contact bump was likely smoothed during cycling and the smoother contact

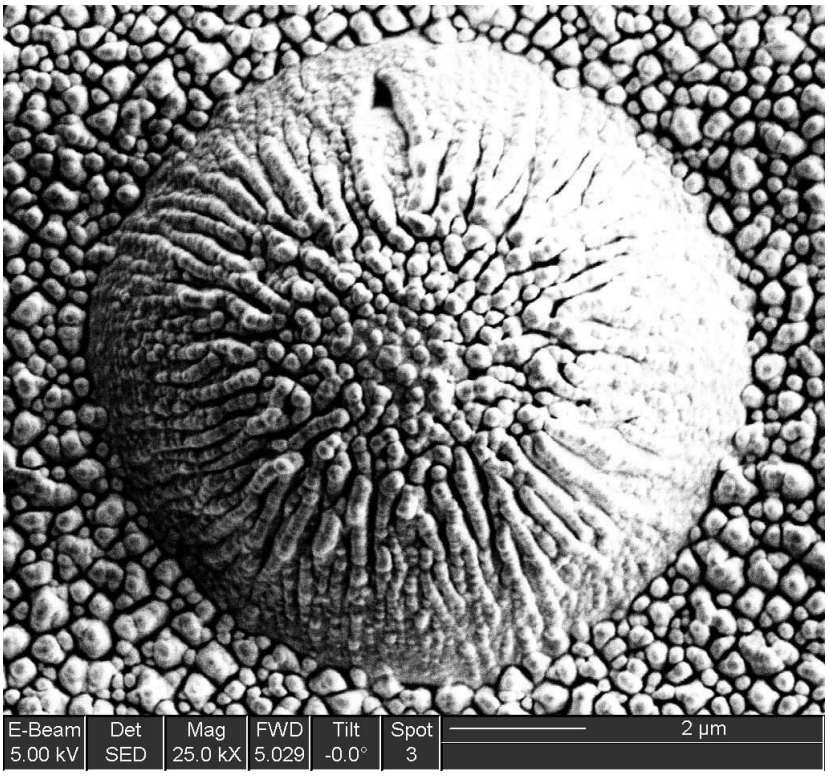

Figure 7.20: Gold coated bump before cycling test.

surface caused an increase in surface adhesion. This adhesion force then exceeded the 400 μN available restoring force. Ductile separation occurred at a plane other than the initial contact surface, as evidenced by the remaining material on the lower contact surface indicating that the adhesion at the surface layer was stronger than that at a possible pre-existing flaw or subsurface damage in the contact material.

This is just one example of a test which was accomplished during this research and demonstrates the data available for each test. Multiple tests were run on each contact material investigated. The next section provides a synopsis of all tests accomplished. Specific results for each material will be given in following chapters.

7.6 Overview of Accomplished Testing

Several tests were run on each contact material. More tests were run on gold-gold contacts than the others to develop a better baseline of data for comparison.

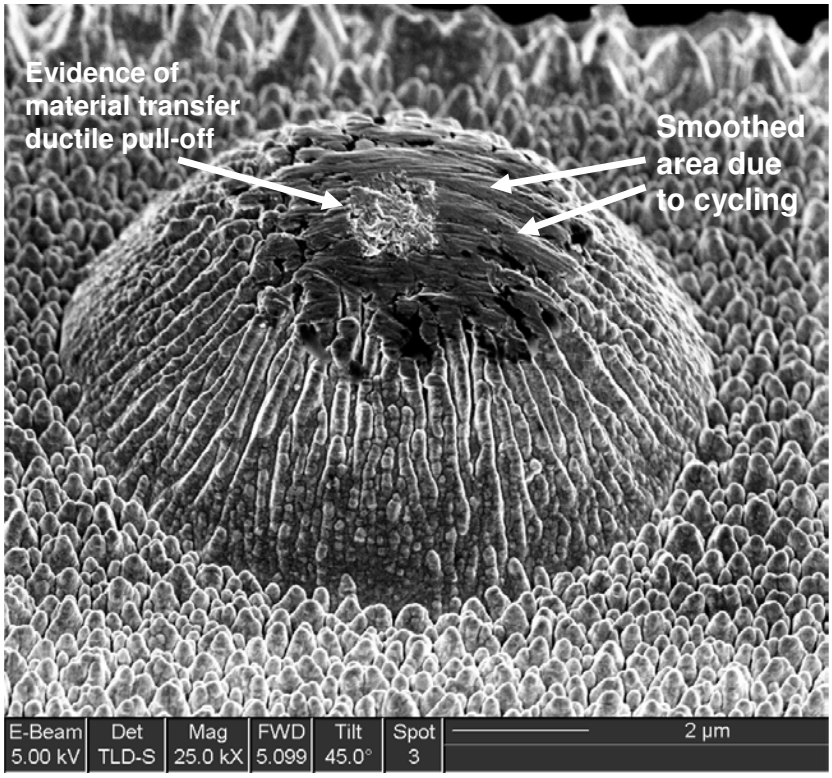

Figure 7.21: Gold coated bump after cycling test. Note smoothed portion of surface and evidence of necking and material transfer indicating ductile pull-off.

Almost all tests were run until contact failure to characterize the lifecycle behavior of the contacts. Table 7.1 shows a synopsis of tests accomplished during this research. Some tests were affected by memory limitations in the test computer, and thus did not collect data all the way to failure. The memory overload caused the responsiveness of the test apparatus to degrade which led to a time lag in commands sent to the instruments (e.g. End of Loading). This time lag caused the microprobe to overload contacts under test which shortened the life of some contacts. These tests produced valid data up until the point of memory overload. However, this did affect the length of some cycling tests. This problem was mitigated by the addition of memory to the computer and increasing the size of the measurement interval used during subsequent tests.

Only tests which cycled without overload are included in the lifecycle results. Overloading of contacts caused premature failure in several tests. Therefore, data

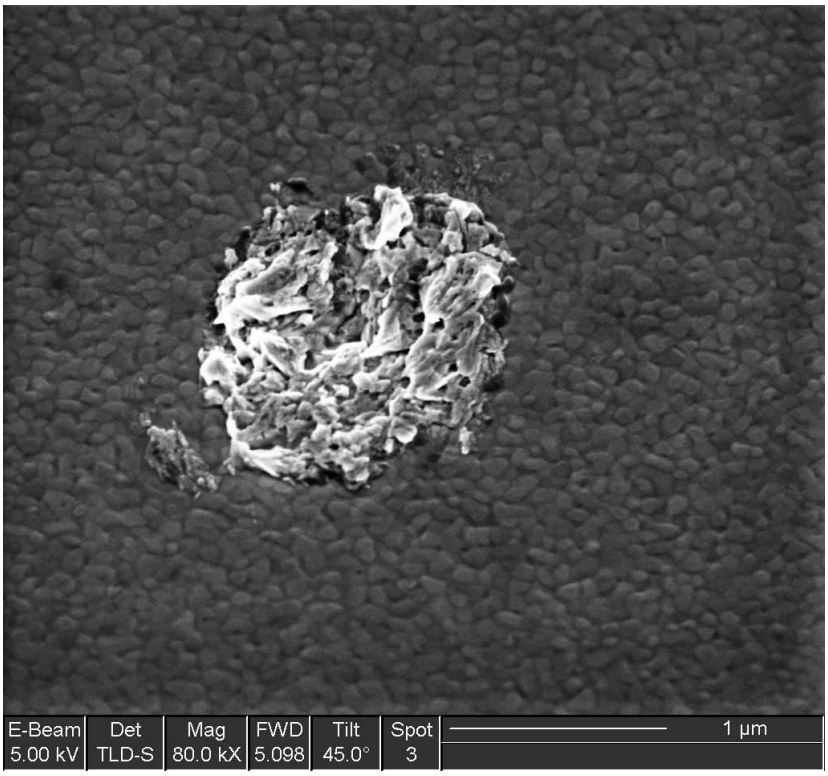

Figure 7.22: Gold coated bottom contact surface after 60,000 cycles and adhesive failure. Note evidence of ductile pull-off.

gathered after maximum contact load was erroneously increased are suspect. On the other hand, data gathered during the early life of all the contacts before the overloads occurred are valid. Thus, average cycling results in the following chapters are given up to 250,000 or 300,000 cycles because most data developed during this study was over the first 300,000 cycles of contact life. This early life behavior provides an excellent baseline contact performance. Behavior early in contact life is also very interesting because any trends noticed could be used to develop infant mortality screening tests. Data beyond 250,000 cycles was also collected for each contact material to investigate the long-term behavior of the contacts.

Table 7.1 shows the number of lifetime failure tests accomplished for each material studied which will be discussed in detail in following chapters. All failures were adhesive in nature. Some of the contacts failed to open. The remaining failed contacts showed an increase in resistance at the end of life, however SEM examination showed

Table 7.1: Micro-contact summary of this study.

Contact Material	Number of Tests Accomplished	Number Tests Until Failure	Failure Range (# Cycles)	Failure Mean (# Cycles)	Test Maximum (# Cycles)
Gold	27	17	10,000 - 2.35×10^6	495,000	2.35×10^6
Au5%Ru	12	6	70,000 - 6.25×10^6	2.18×10^6	6.25×10^6
Au-4%V_2O_5	6	3	20,000 - $> 15.5 \times 10^6$	$> 4.85 \times 10^6$	$> 15.5 \times 10^6$

that the contact film had peeled away in those cases. There was no indication that a layer of contaminant created or deposited during cycling caused any high resistance (or open) failures for the three contact materials studied.

7.7 Chapter Summary

This chapter described the measurement capabilities of the set-up as designed and built, and gave in-depth results from a representative sample test. An overview of a typical test was given. Details on testing done on each contact material are given in each of the next three chapters. Several tests were run on gold, and the results from gold testing will be reported in the next chapter.

VIII. Gold Contact Measurements

This chapter presents results of testing on gold-gold contacts. The tests were conducted using the setup and method described in the previous chapters. First, all test results on gold are summarized. Then, the failures are categorized and discussed. Following chapters discuss measurements and results of the other two contact materials tested.

8.1 Contact Lifetime and Failure Analysis

Gold is a very common microcontact material used by many microswitch designers. A significant result of the combined force and electrical measurements of the gold contacts in this research is that the threshold force required for stable ohmic contact is on the order of 10-25 μN, not in the hundreds of micronewtons as described by previous studies (e.g. [108] which did not measure contact force directly). Twenty-six tests were run on gold contacts. Eighteen of these were successfully run to failure and one test was stopped before failure occurred to analyze a pre-failure contact surface. Another test was run without current to observe any critical differences in behavior with and without current. All tests were run with 400 μN contact force, with the exception of one test run using a contact force of 200 μN.

Gold contacts lasted from 10,000 cycles to 2.3×10^6 cycles when tested to failure. The majority of failures were clearly adhesive failures (switch failed closed) with a few high resistance failures (failed open). Upon examination of contact surfaces after the testing, it was clear that even the high resistance measurement (open) failures in two tests were caused by adhesion of the contact film to the lower contact surface. Therefore, 18 out of 26 tests failed in adhesion, with eight tests failing early due to the increase of indent force caused by computer memory problems (See Section 7.6). These premature failures due to overload were not used to calculate lifetime averages or grouped among the lifecycle failures. The failures were grouped in three categories: short-life failures (Type I) between 10,000 $\sim$ 70,000 cycles, mid-life failures (Type II) roughly between 190,000-500,000 cycles, and longer life failures (Type III) at $> 1\times10^6$

Table 8.1: Test summary of gold contacts tested to failure. None of these contacts failed due to overload.

Contact ID	Contact Material	Contact Force (μN)	Initial Contact Resistance (Ω)	Failure Type	Number of Cycles to Failure (# Cycles)
0303-4_6	Gold	400	2.127	Adhesion	10,000
0210-2_3	Gold	200	1.472	Adhesion	10,000
0602-2_1(G)	Gold	400	2.707	Adhesion	10,000
0303-1_6	Gold	400	1.650	Adhesion	20,000
0602-1_12(D)	Gold	400	3.534	Adhesion	30,000
0801-1_6	Gold	400	0.972	Adhesion	50,000
0303-4_7	Gold	400	2.132	Adhesion	60,000
0801-3_1	Gold	400	2.053	Adhesion	70,000
0210-3_1	Gold	400	1.452	Adhesion (film torn)	190,000
0602-2_8(B)	Gold	400	2.451	Adhesion (film torn)	200,000
0801-1_12	Gold	400	1.646	High Resistance(film torn)	300,000
0602-2_11(E)	Gold	400	2.751	Adhesion (film torn)	440,000
1101-2_6	Gold	400	1.804	Adhesion (film torn)	500,000
0210-3_3	Gold	400	1.602	Adhesion (film torn)	500,000
0602-1_2(E)	Gold	400	2.253	High Resistance (film torn)	500,000
0801-1_7	Gold	400	1.585	No Failure	stopped at 550,000
0602-2_12(F)	Gold	400	2.470	Adhesion	1.06×10^6
0210-3_2	Gold	400	1.472	Adhesion	1.16×10^6
0602-3_8	Gold	400	2.171	Adhesion	2.35×10^6

cycles. The variation in cycles to failure is not surprising, as manufactured switches also show significant scatter in cycles to failure [65, 80, 171], and further, the tests accomplished in this study were run in lab air with little environmental control.

All shorter lifetime tests showed evidence of ductile separation, i.e. the adhesive bond created between the upper and lower contact surfaces caused failure at a location other than the contact interface. After ductile separation, ductile necks or signs of material transfer are always detected [37]. Two examples of short-life contacts are shown in the series of Figures 8.1, 8.2, 8.3 and 8.4, 8.5 which are adhesive failures after 10,000 cycles and 20,000 cycles respectively. The pre-cycling contact images for these are shown in Figures 8.1 and 8.4 respectively. The bottom contact surface shows material transfer due to adhesive forces. This can be clearly seen in the bottom contact of sample 0303-4_6 in Figure 8.3.

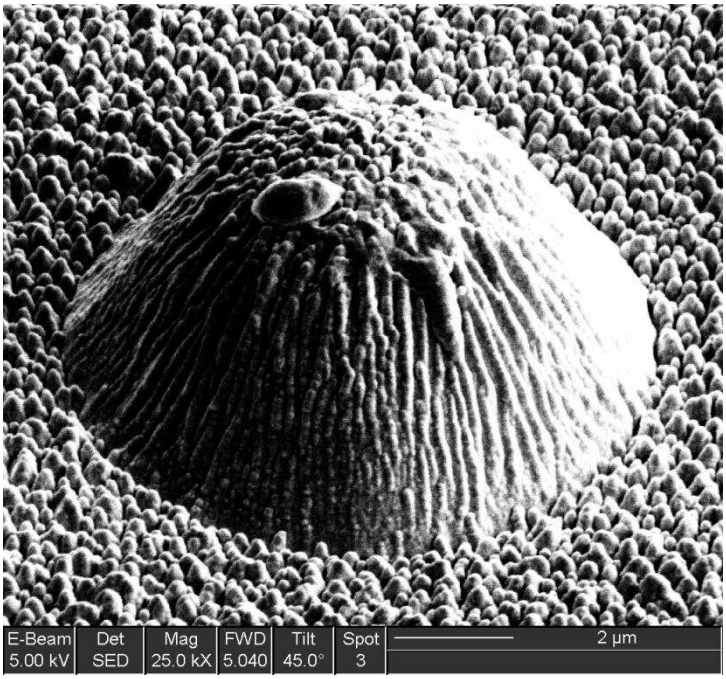

Figure 8.1: Gold coated bump (0303-4_6) contact surface before cycling.

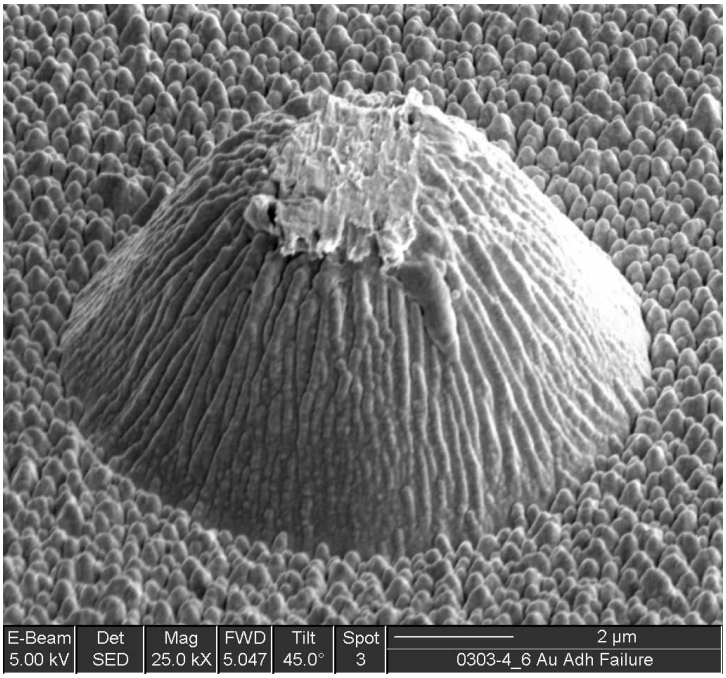

Figure 8.2: Gold coated bump (0303-4_6) contact surface after 10,000 cycles and adhesive failure.

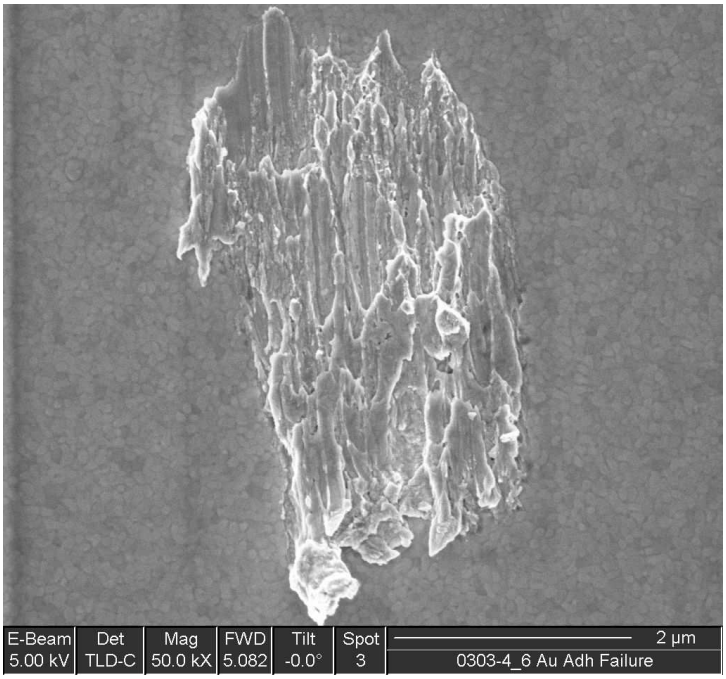

Figure 8.3: Gold coated bottom contact surface (0303-4_6)after 10,000 cycles and adhesive failure.

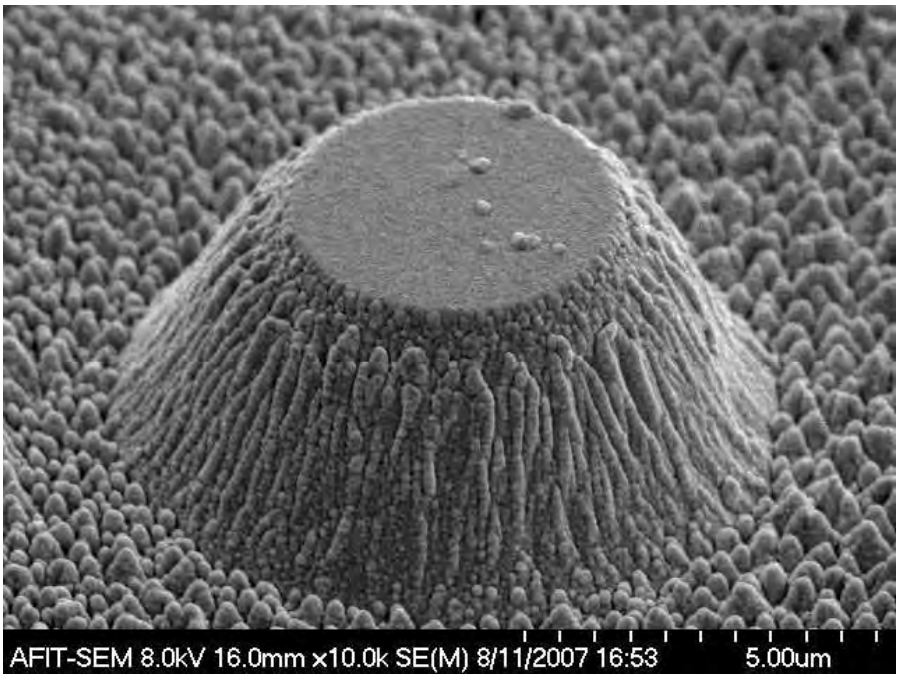

Figure 8.4: Gold coated bump(0602-1_12(D)) before cycling.

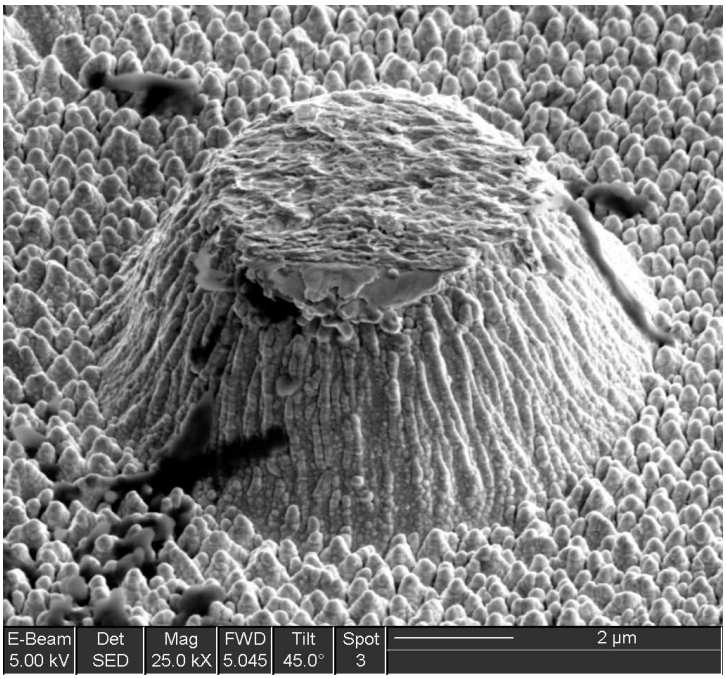

Figure 8.5: Gold coated bump (0602-1_12(D)) after adhesive failure at 20,000 cycles.

The mid-lifetime contacts (190,000-500,000 cycles) failed again due to adhesion and exhibited contact film delamination. That is, the contact film separated from the contact bump and adhered to the lower strike plate. There were two types of this failure exhibited during testing. The first one was when the switch failed closed and the contact separated at the end of test, the contact film stayed attached to the lower strike plate. The second type occurred when the 400 μN restoring force was applied by the cantilever during cycling and the film separated from the contact bump. This second type led to a high resistance failure in the next indent measurement cycle. An example of thin film failure is shown in the series of Figures 8.6, 8.7 and 8.8, with the pre-cycling image shown in Figure 8.6. Kwon reports a similar failure mode in testing of a simulated switch coated with thin film conductive test material, describing that "the surface of several samples was peeled off." [137]. An example similar to this is given by Tazzoli, et. al. in [238] where the contact bumps were completely delaminated or destroyed causing high resistance failures. This type of failure either indicates that subsurface damage developed during cycling or that the adhesive force

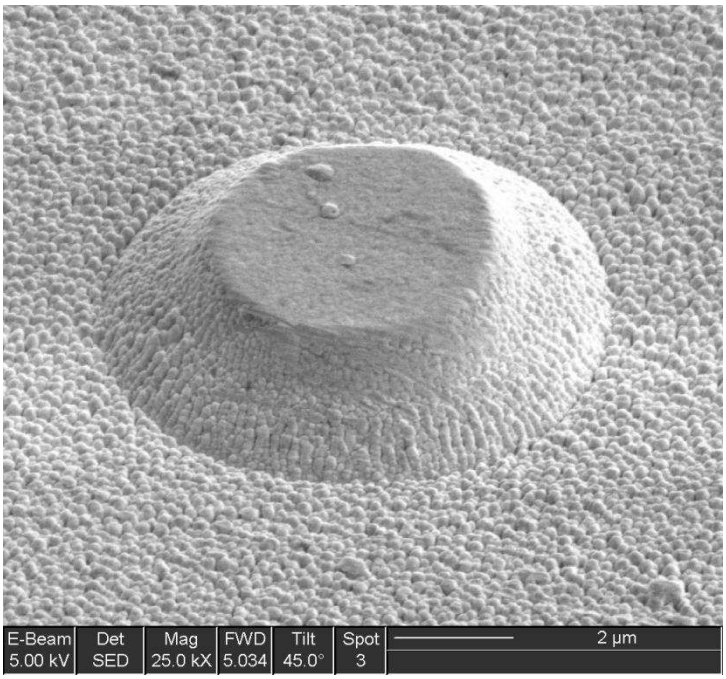

Figure 8.6: Gold coated contact surface (1101-2_6) before cycling.

between contact surfaces became larger than the adhesive force attaching the thin film to the substrate. Note that the sputtering process for gold included an initial adhesion layer of 10 nm of chromium on the silicon. It is also important to note that all silicon cantilevers were cleaned with a 10 minute piranha etch before coating. The piranha etch consisted of H_2SO_4:H_2O_2=2:1, then a deionized water rinse and an N_2 dry followed by a 2 minute 50 W plasma clean.

Only one of the three longer lifetime gold contact ($> 1 \times 10^6$ cycles) surfaces was successfully examined just after adhesive failure. This failure surface showed much less deformation than the short-life Type I ductile failure surfaces. The contact surfaces resulting from this longer running test showed a small amount of material transferred to the contact bump surface and a circular shaped lower contact surface which included an area visibly smoothed due to cycling. An example of a long-lifetime contact is shown before cycling in Figure 8.9 and after more than 2×10^6 cycles in Figure 8.10. Note the thin lamellar (platelike) features in the transferred material which can be identified by their lighter color in the SEM image. This transferred

Figure 8.7: Gold coated contact surface (1101-2_6) after 500,000 cycles and adhesive failure. Contact film separated and adhered to lower contact surface.

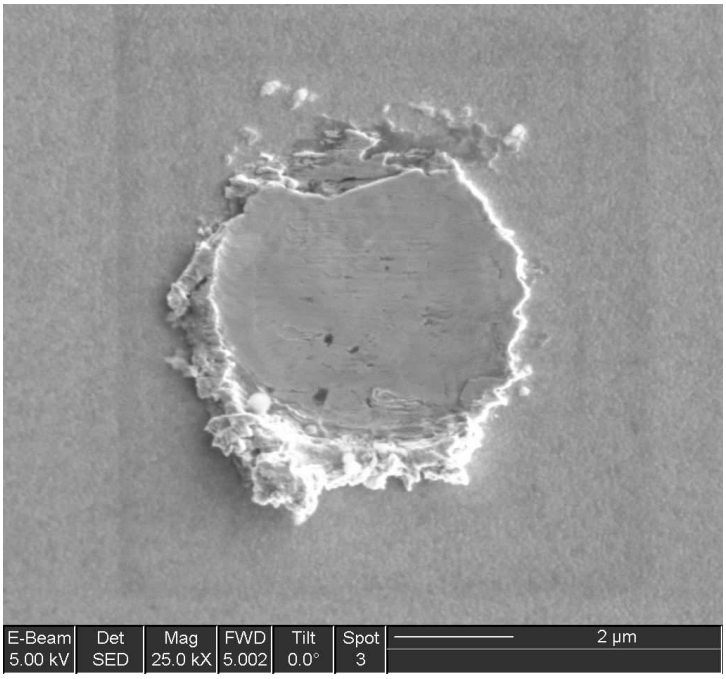

Figure 8.8: Mid-Lifetime Contact film separated from contact bump (1101-2_6) and adhered to bottom surface. This was 500,000 cycle adhesive failure.

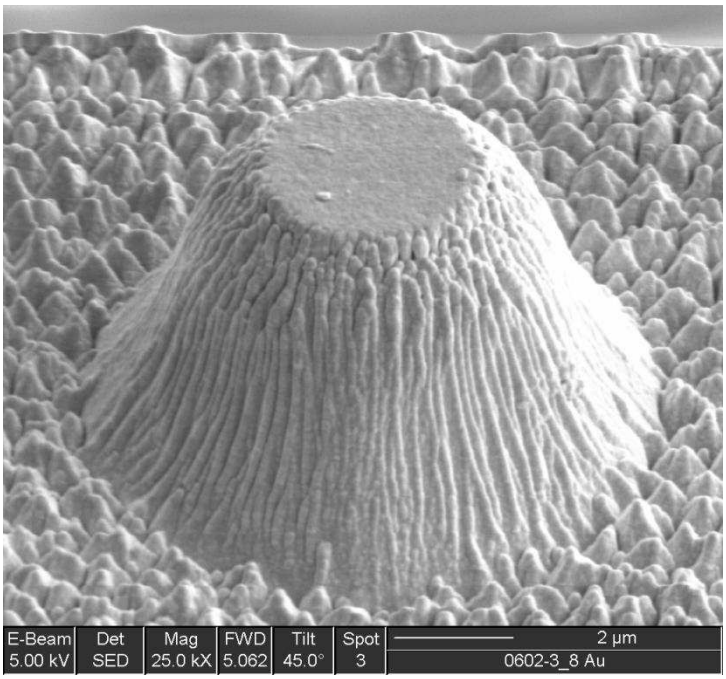

Figure 8.9: Gold coated contact surface (0602-3_8) before cycling. This bump failed in adhesion after 2.35×10^6 cycles.

material can be matched to the smoothed areas on the bottom contact image shown in Figure 8.11. This contact surface suggests brittle contact separation, which can be identified by plastically flattened features on the surface of the contact [37]. Note that brittle fracture surfaces have a bright, granular appearance, due to reflection from the flat cleavage surfaces which also suggests brittle separation [56]. The bottom contact location also showed a black annular ring around the contact area which indicates contamination of the contact and possible heating of the contact material at the edge of the contact area. The existence of contamination on the contact surface could explain why some contacts last longer than others. Note that contamination on contact interfaces reduces the adhesive force between surfaces [33]. This is because contamination on the interface reduces the surface energy and thus the adhesive force. Contamination will also reduce the likelihood of lattice matching of like materials when brought into contact. While high resistance contamination is not desired on contact surfaces, small amounts of non-resistive contamination may be beneficial in reducing adhesion [103].

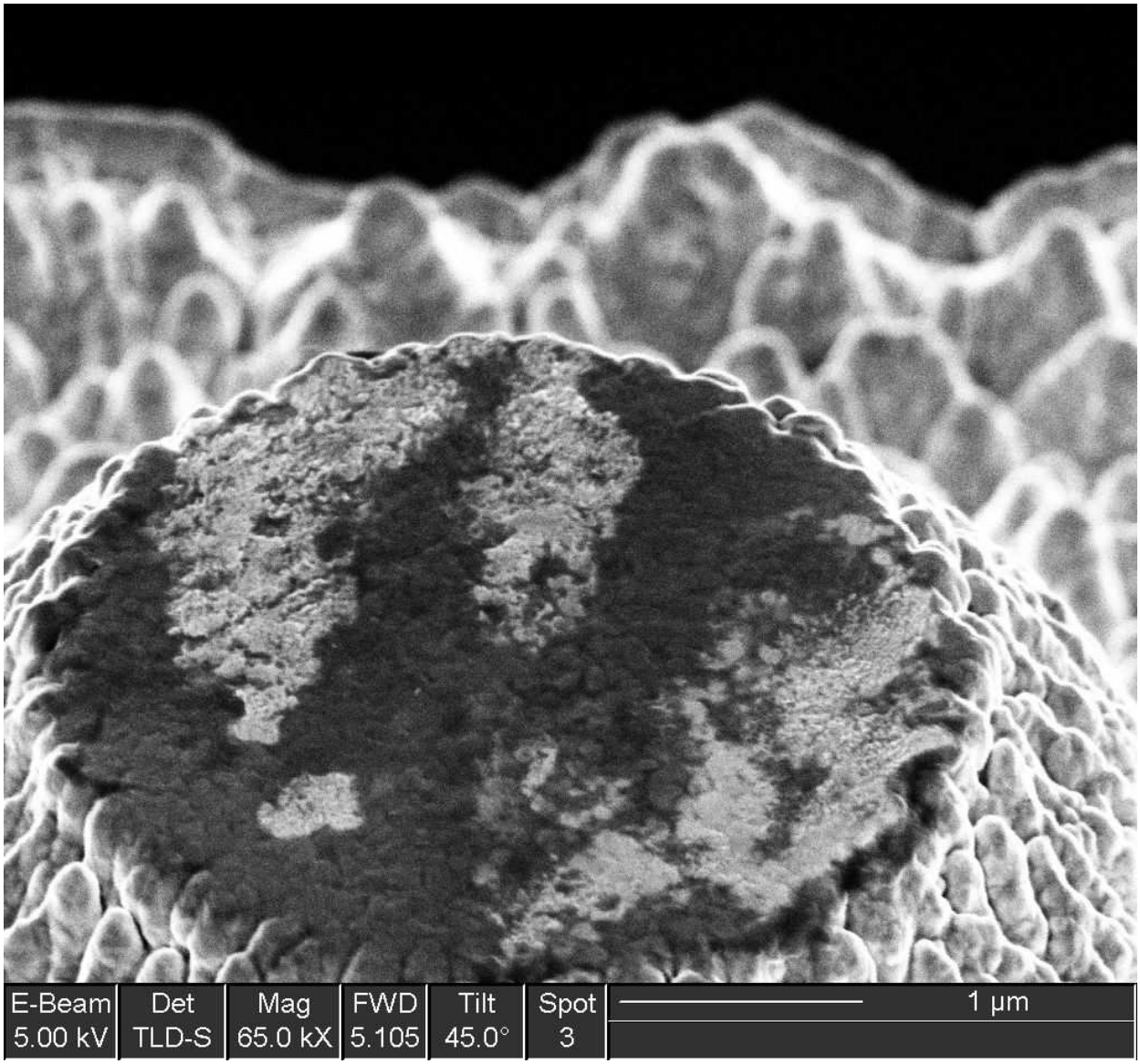

Figure 8.10: Gold coated contact surface (0602-3_8) after 2.35×10^6 cycles and adhesive failure shown at 45 degree tilt. Note thin lamellar features.

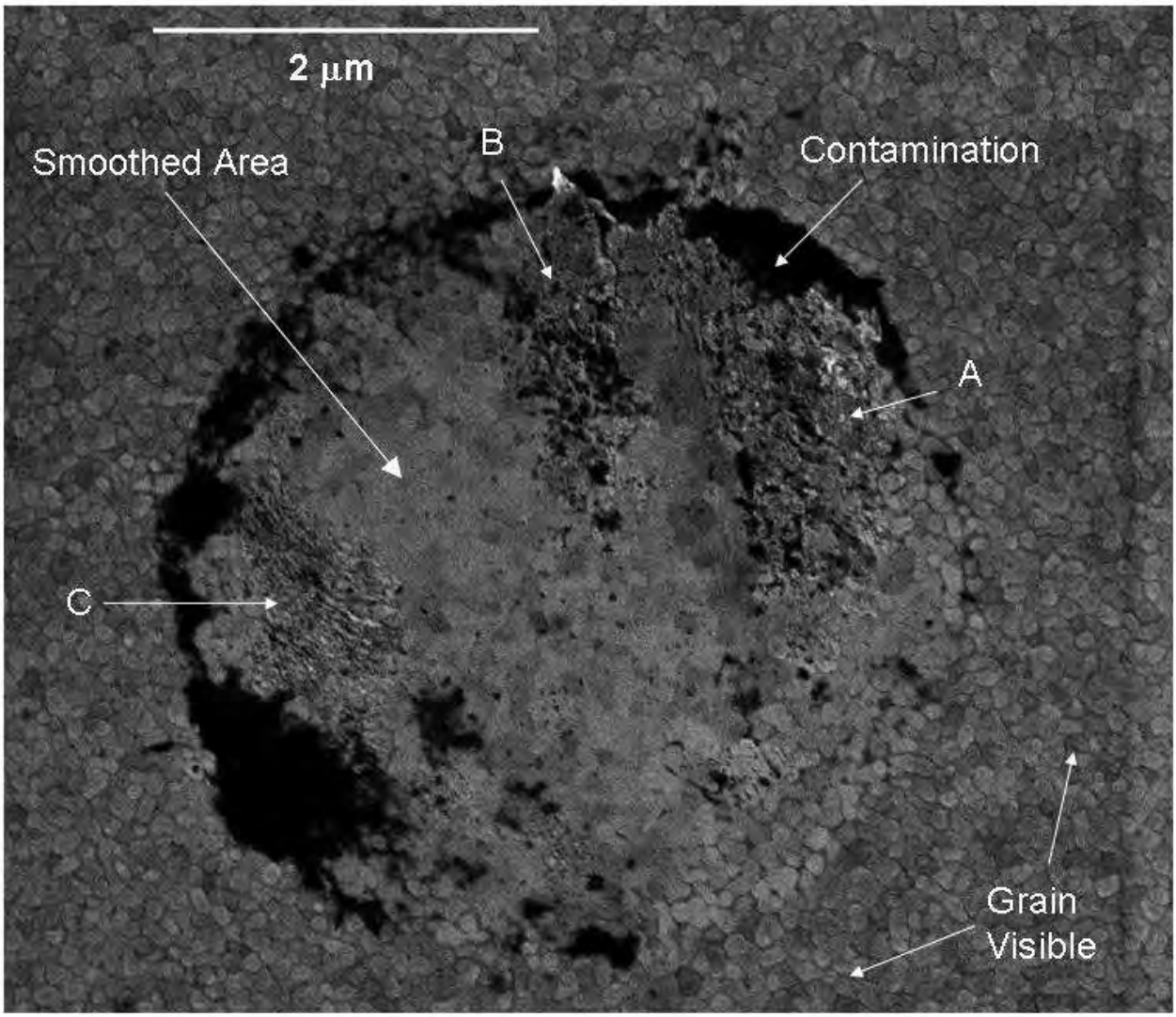

Figure 8.11: Gold coated bottom contact surface (0602-3_8) after 2.35×10^6 cycles and adhesive failure. Note smoothing of surface in contact area and dark annular ring indicating development of contact contamination. Grain size is estimated at 20-40 nm.

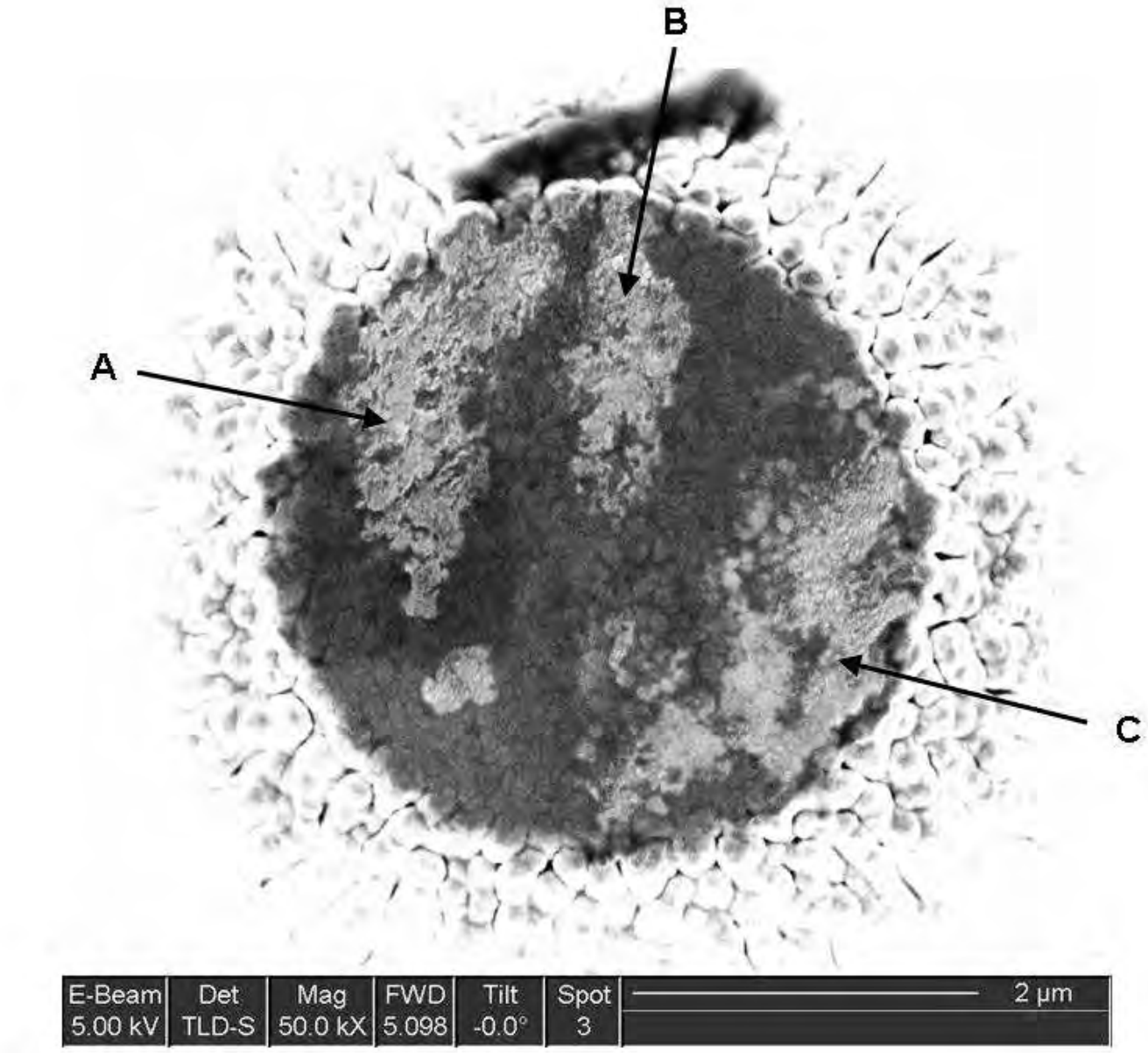

Figure 8.12: Gold coated top contact surface (0602-3_8) after 2.35×10^6 cycles and adhesive failure. Note that annotated brighter areas match marked rough areas in Figure 8.11.

8.1.1 No Current Test. One test was run without current in an attempt to ascertain what effects the 0.5 mA current had on gold contact behavior. Two contact cycles with current were necessary in the test in order to find the contact location and set the contact gap. After that, no current was used during testing. Therefore, the difference between this test and the others is that there was no current flowing during contact switching and therefore it is an example of contact cycling with no influence of electrical current on the contact morphology change experienced during repetitive force application. Because no current was run during this test, this contact did not experience electrical failure similar to the other contact tests run during this study. The test was run in order to investigate what the surface changes would be without electrical current and was stopped after 360,000 cycles. The precycling contact bump used for this test is shown in Figure 8.13 and the images of the contact surfaces after cycling are shown in Figures 8.14 and 8.15. Note that the top and bottom contact surfaces for the no current test show evidence of ductile necking. Additionally, there is a dark substance on both top and bottom contact surfaces which is evidence of contact contamination caused during cycling. The existence of contamination on this surface indicates electrical current is not necessary for contamination to be created or deposited on the contact surfaces. Note also that the shape of the surface damage/transferred material is not rounded as seen in the short-life contact results (e.g. Figure 8.5). The angular shaped surface damage in the no current test may indicate that the heating of the contact during hot-switching may lead to softening of the material which causes a more rounded appearance of the surface damage features. More tests should be run without current to verify these preliminary results.

8.1.2 200 μN Contact Force Test. One test was run at a contact force of 200 μN to study contact force related effects. A pull off force of 400 μN was still used in this test. Note that all other tests were accomplished using a contact force of 400 μN. The 200 μN test failed in adhesion after 10,000 cycles, and thus few measurements during this test were gathered. The results don't appear to be any different than

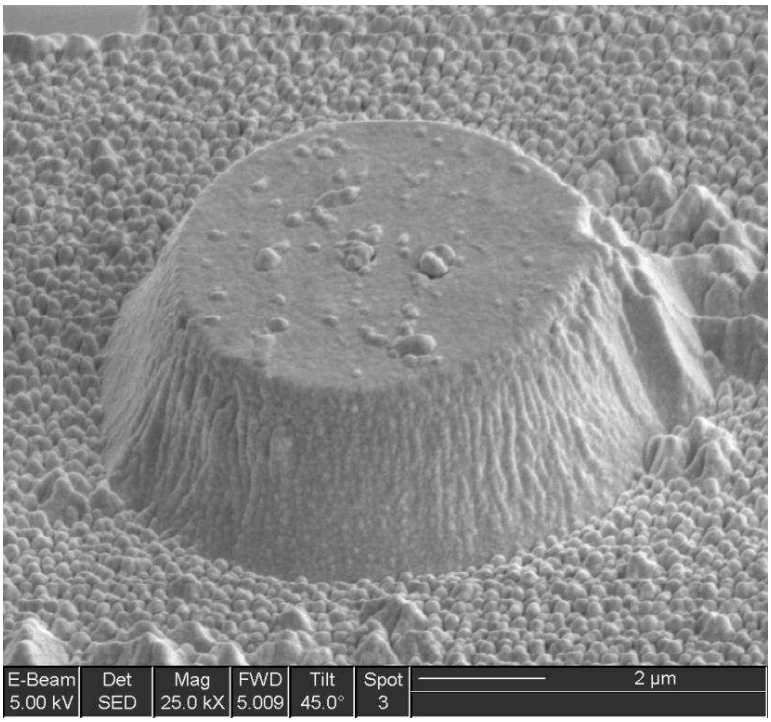

Figure 8.13: Gold coated contact surface before 360,000 cycle no current test.

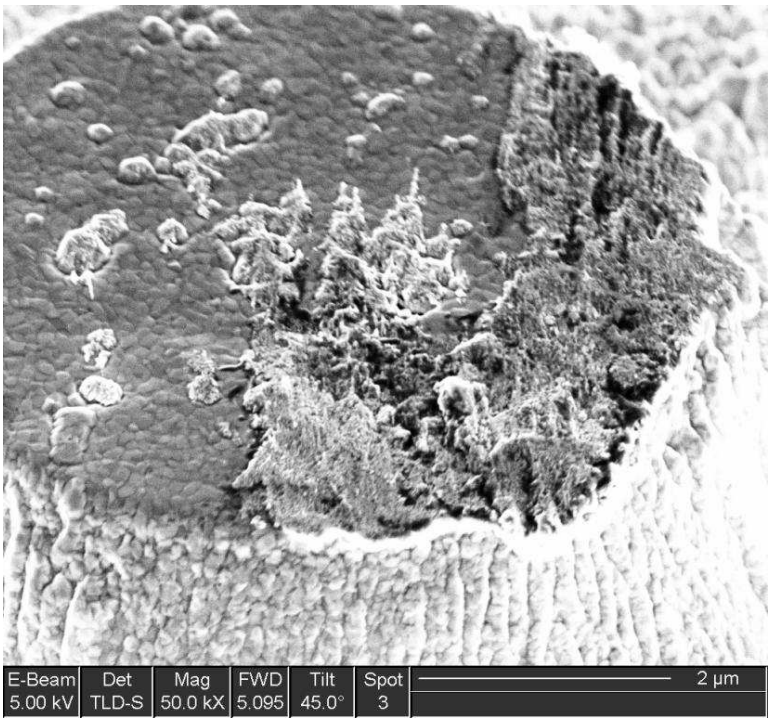

Figure 8.14: Gold coated contact surface after 360,000 cycle no current test. The image is set at a high magnification in order to better show surface features caused by no current cycling. Dark areas of contact indicate contact contamination.

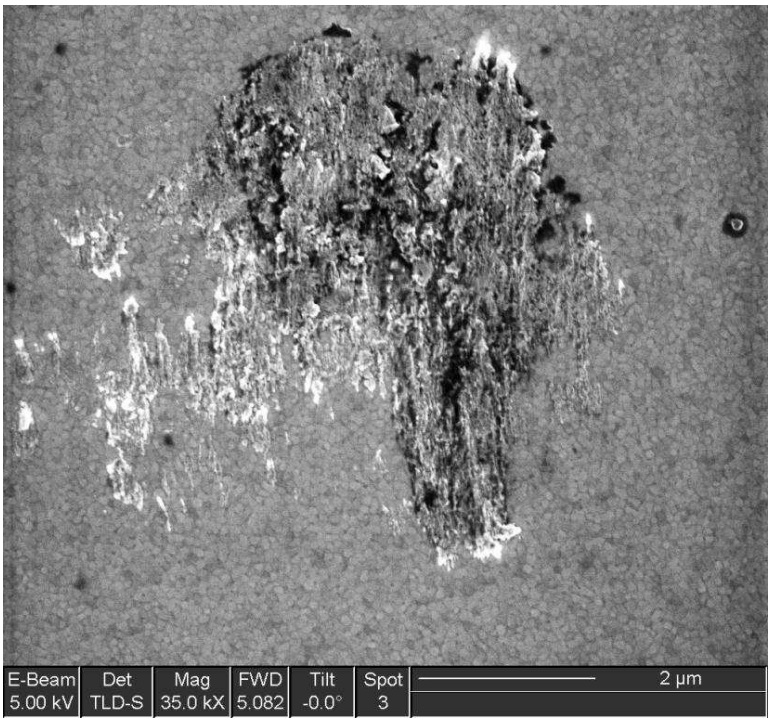

Figure 8.15: Gold coated bottom contact surface after 360,000 cycle no current test. Dark areas indicate presence of contact contamination.

the results from short-lifetime 400 μN contact force (Type I failure) tests, other than the contact interference in this test was 0.05 μm which is approximately 0.04 μm less than the average results for 400 μN contact testing. This is expected, with half the applied contact force resulting in roughly half the magnitude of contact interference.

The contact bump before cycling is shown in Figure 8.16 and the after cycling images can be seen in Figures 8.17 and 8.18. The top and bottom surfaces after cycling show clear indications of ductile pull-off. The contact surfaces indicate that the contact bump was not perfectly flat against the strike plate. There is no visible contamination in the region of the failure surface and it is clear that the failure did not occur at the initial contact interface. The characteristics of this failure surface match those from the 400 μN short-lifetime Type I contact tests. The contact force change did not affect the short lifetime failure characteristics, or the changes in the contact surface leading to adhesion failure of the gold contacts.

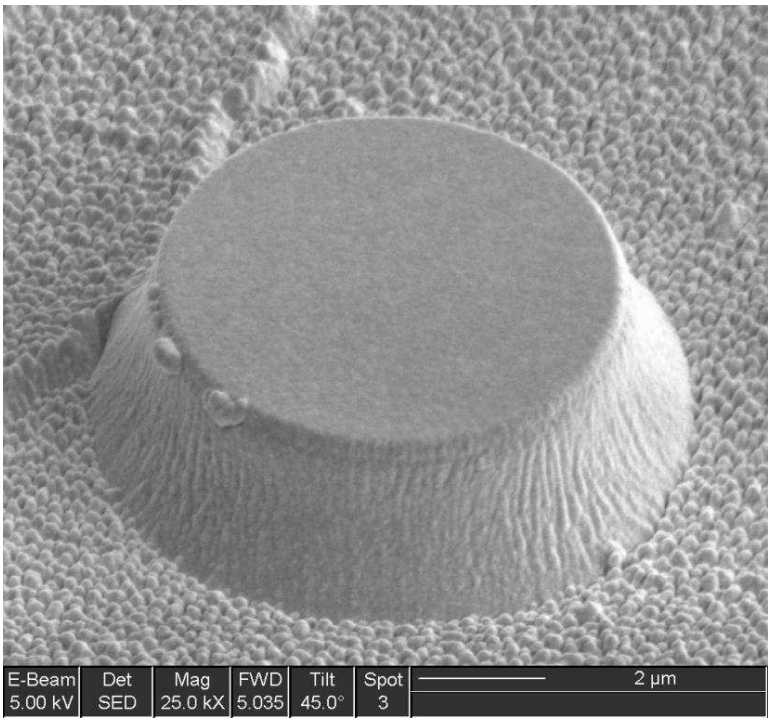

Figure 8.16: Gold coated contact surface before 200 μN cycling test.

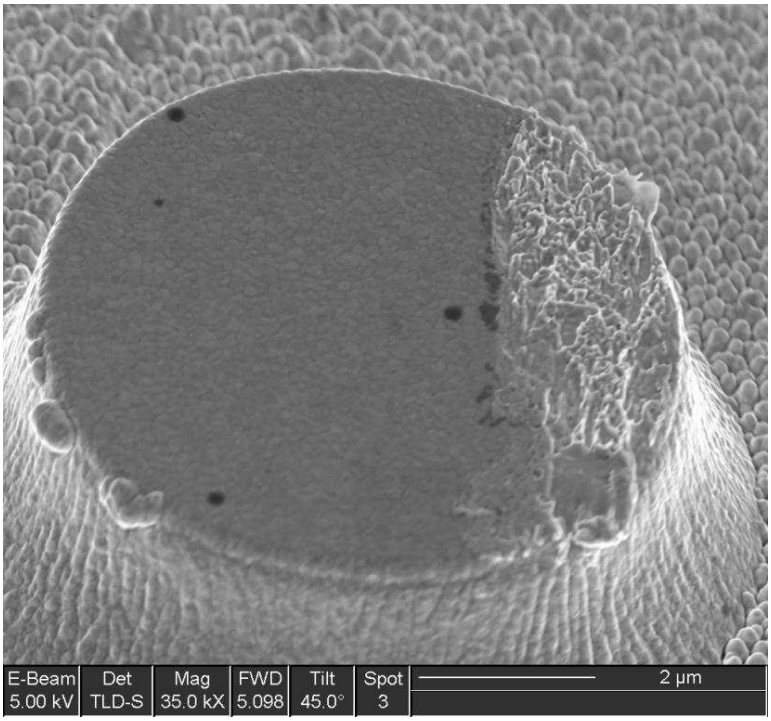

Figure 8.17: Gold coated contact surface after 10,000 cycle adhesive failure during 200 μN test. Note ductile pull-off characteristics.

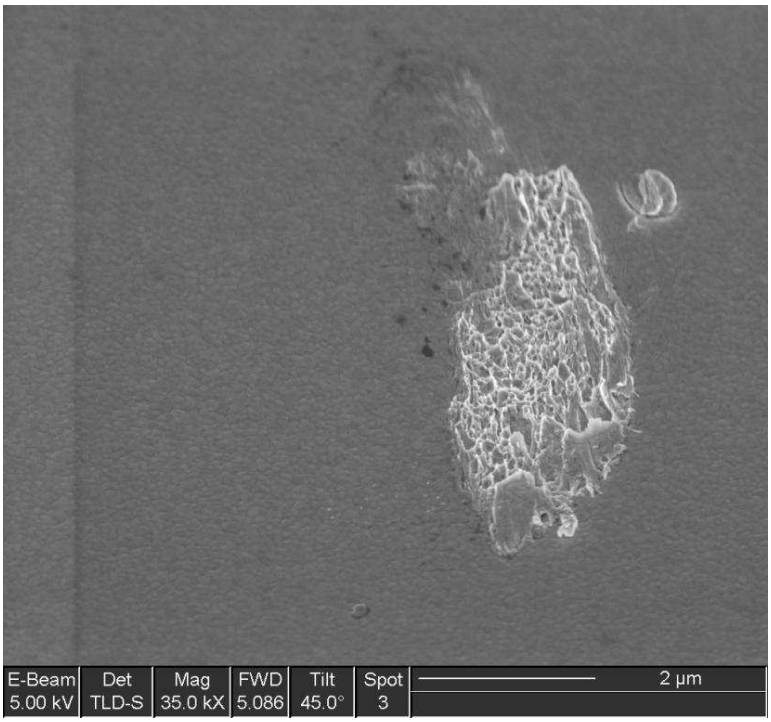

Figure 8.18: Gold coated bottom contact surface after 10,000 cycle adhesive failure during 200 μN test. Note ductile pull-off characteristics.

8.1.3 Failure Summary. Three categories of failures were indicated by the testing accomplished on gold contacts in this study and are described in Table 8.2. Type I failures were short-lifetime failures and all indicated ductile failure surface characteristics. Type II failures all occurred between 190,000 and 500,000 cycles where the contact film separated from the contact bump. Two of these mid-life failures were indicated by a sudden increase in contact resistance. Thus, not every sudden increase in contact resistance is indicative of growth of a high-resistance contaminant film. Therefore, contact switch researchers should investigate high resistance failures in order to conclusively determine the cause of the sudden increase in resistance. The thin film failures indicated either subsurface damage was being developed during cycling or the adhesive force between contact surfaces became larger than the adhesive force attaching the thin film to the substrate. Unfortunately, this thin film failure precluded investigation of the failure surfaces themselves. Examination of the contact surfaces is required for conclusive analysis of failure modes. Longer life contact sur-

Table 8.2: Description of failure types demonstrated and categorized in this study. Lifetimes are given for demonstrated values in respective materials.

Failure Type	Description	Material Demonstrated	Lifetime (# Cycles)
I	Ductile characteristics	Au	10,000-70,000
II	Contact film failure	Au	200,000-500,000
III	Brittle separation, smoothed surfaces and contamination formation	Au	$> 10^6$

faces were categorized as Type III failures, which were indicated by smoothed surfaces and characteristics of brittle separation. This type of contact and contact separation is desirable to ensure longer lasting contacts, as hypothesized by Chen [37].

The following sections describe measurements obtained on gold contacts using the nanoindenter based test apparatus designed and built for this research. Each section presents the behavior of gold microcontacts and shows the average behavior of gold microcontacts tested. The error bars correspond to one standard deviation. First, contact resistance will be discussed, then contact adhesion, threshold force and distance, strain hardening, contact interference, time dependent behavior, plastic deformation and contact damage progression will be discussed. Note that average results are presented up to 250,000 or 300,000 cycles. This is because the majority of data gathered during this study was in the early period of contact life. Not enough data points were gathered beyond this period of contact lifetime to provide statistically significant behavior. This information is of significant interest to switch designers, as the development of an "infant mortality" screening test based on contact behavior would be extremely valuable for use in improving contact switch reliability.

8.2 Contact Resistance

The average contact resistance for gold tests before cycling was 2.1 Ω. The average standard deviation for all resistance data points was 0.6 Ω. The range of measured contact resistances for gold contacts were 0.972-3.534 Ω. Contact resistance estimated based on a contact force of 400 μN using the Holm equation (Equation

2.29) for gold contacts is 0.5 Ω. The contact resistance in each test was higher than contact resistance calculated based on contact force due to parasitic resistances from the test setup. The resistance varied from test to test when compared to each other due to the difference in parasitic resistance through the solder joints and wire bonds. There was also 0.5 Ω parasitic resistance from each of the terminal strips connecting the measurement probe wires to the data acquisition lines. The contact resistance was practically constant during cycling in each test until failure. A graph showing contact resistance trends during testing is shown in Figure 8.19. The error bars show one standard deviation above and below the average value. The contact resistance measured during a representative long-term test is shown in Figure 8.20. Note that the in-contact resistance stayed practically constant during the entire test. The measured contact resistance did not change at the point of adhesion failure. Detection of contact adhesion failure using in-contact and out-of-contact resistance was described in Section 7.3.5 and is shown graphically for a gold contact test in Figure 8.21. The criteria used to detect contact adhesion failure is described in Section 6.2.5 and the ability to measure contact adhesion failure is described and demonstrated in Sections 7.2.1 and 7.4.3.

8.3 Contact Adhesion

All test failures in gold contacts, except those caused by contact force overloads, were due to adhesion. The cycling caused an increase in pull-off force between the contact surfaces. This study used pull-off force as a measure of adhesion between contact surfaces and the terms are occasionally used interchangeably because the effect of adhesion is to require a pull-off force of some magnitude to separate contacting surfaces. Figure 8.22 shows the average pull-off force for gold contacts tested. The pull-off force measured in this research showed an increase after 20,000-30,000 cycles, then the measured pull-off force gradually reduced to roughly 50 μN. This increase in pull-off force early in cycling matches the incidence of several adhesive failures around this time in the experiments at 10,000, 20,000 and 30,000 cycles. The downward trend

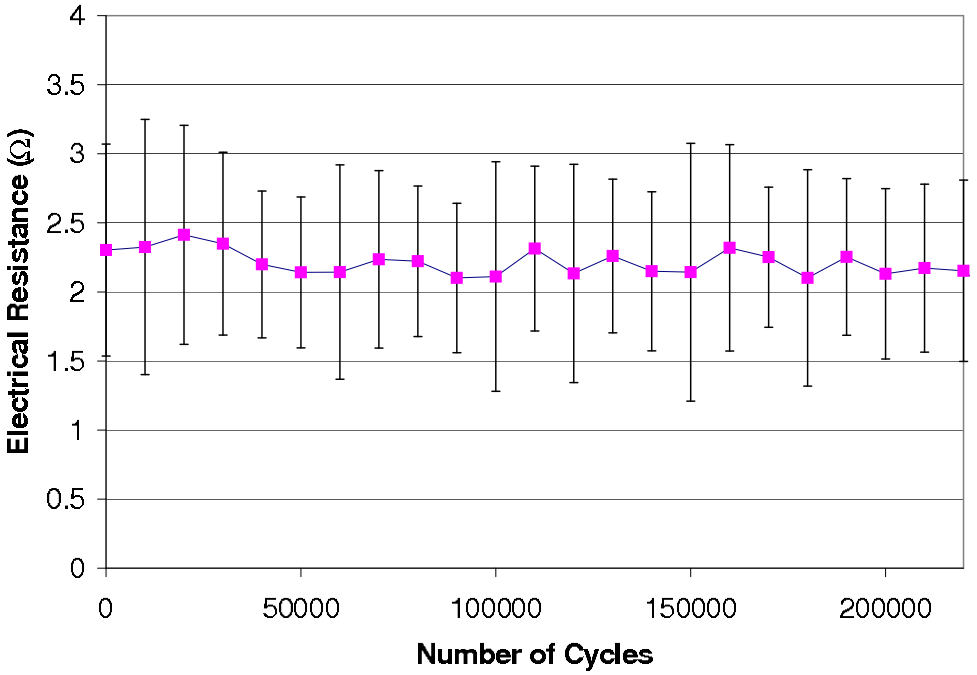

Figure 8.19: Average contact resistance of tested gold contacts during cycling. Error bars show one standard deviation.

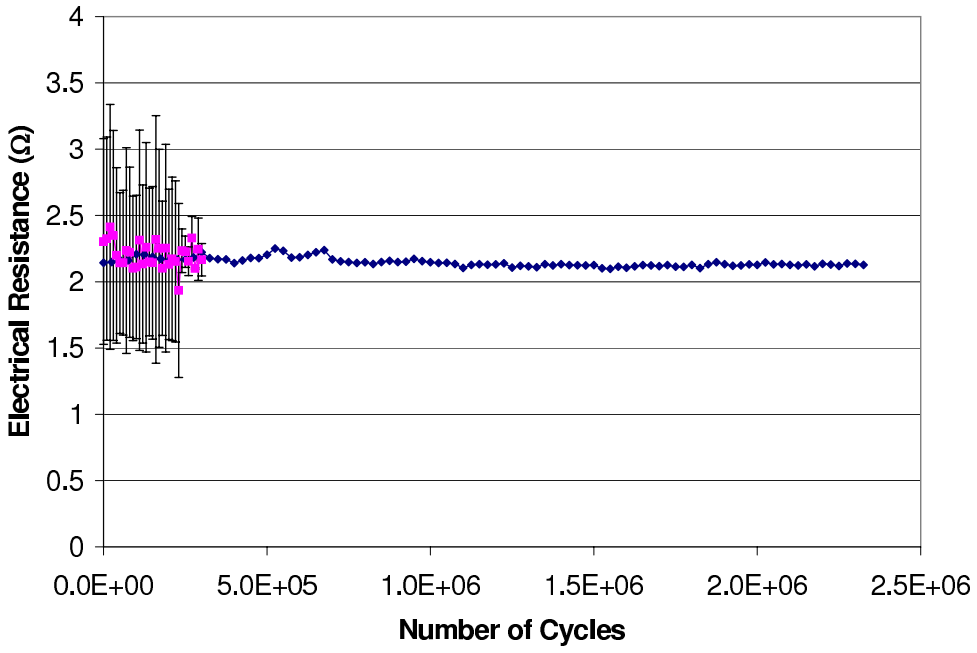

Figure 8.20: Representative in-contact resistance measurements for long-term gold contact test compared to average of gold test results (previously shown in Figure 8.19). Note that long term example falls right at the all-test average for contact resistance. See Section 8.11 for a comparison of measured resistances between short-, mid-, and long-life failures.

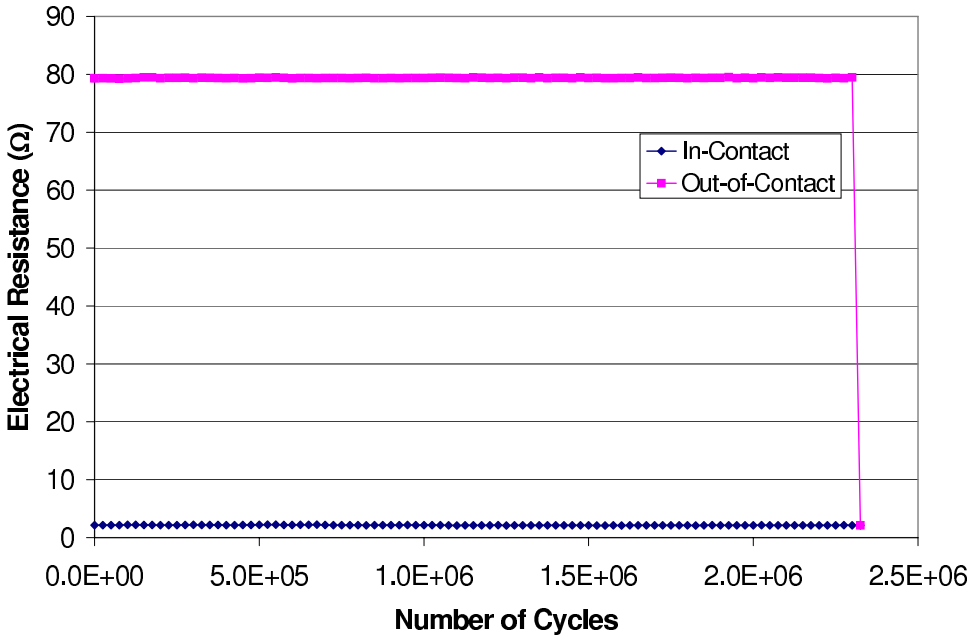

Figure 8.21: Long-term test example showing adhesive failure at 2.35×10^6 cycles. Note that this indicates that restoring force of cantilever was unable to pull contact surfaces apart, thus the adhesive force was greater than the restoring force(400μN in this test).

of the average pull-off force is attributed to the early failure in adhesion of short-life contacts with high initial pull-off force. These short-life contacts fail early likely due to smoothening and low levels of contamination on the surface causing an increase in adhesion and stop contributing to the pull-off average after failure. The mid- and long-life contacts exhibit lower initial pull-off force so the average is lower when only mid- and long-life contacts are cycling and included in the calculation. Note that the contacts which have lower adhesion early in life seem to last longer. See Section 8.11.1 for a comparison of pull-off force results between short- and long-life contacts.

The average pull-off force magnitude of 50 μN is roughly twice the predicted adhesive force of 21 μN between clean gold contacts based on the JKR theory of adhesion given in Equation 2.37. It is possible that this theory of adhesion under-predicts adhesion on microcontacts as it only takes surface energy and contact size into account. It is likely that the fritting effect due to the hot-switching kept the gold contacts relatively free of contaminants. However, there was variability in pull-off

force from measurement to measurement on the same contact, and sudden increases in adhesion were not necessarily predictable due to environmental factors, possibly such as humidity levels in the lab air. Also, the fritting effect or mechanical wiping may have caused the amount of contamination present on the contact to change from measurement to measurement, therefore affecting the resulting adhesion and thus the measured pull-off force. An example of the long-term trend of measured pull-off force during cycling is shown in Figure 8.23. This shows several spikes in pull-off force during cycling and the contact failed in adhesion as the measured pull-off was showing a downward trend. This indicates that the growth in adhesive force near failure is sudden or occurs at a faster rate than the measurement interval used in the test. The measurement of pull-off force was kept at a constant rate of 50 μN/sec during the testing based on the unloading rate of the microprobe. This constant rate of pull-off measurement may have missed measurement of an increase in pull-off force at high surface separation rates. Pull-off force may be rate dependent as suggested by Chen in [37] and this effect should be tested in further work. The unloading rate of the microprobe is controlled via programmable input in the automated test method developed for this study.

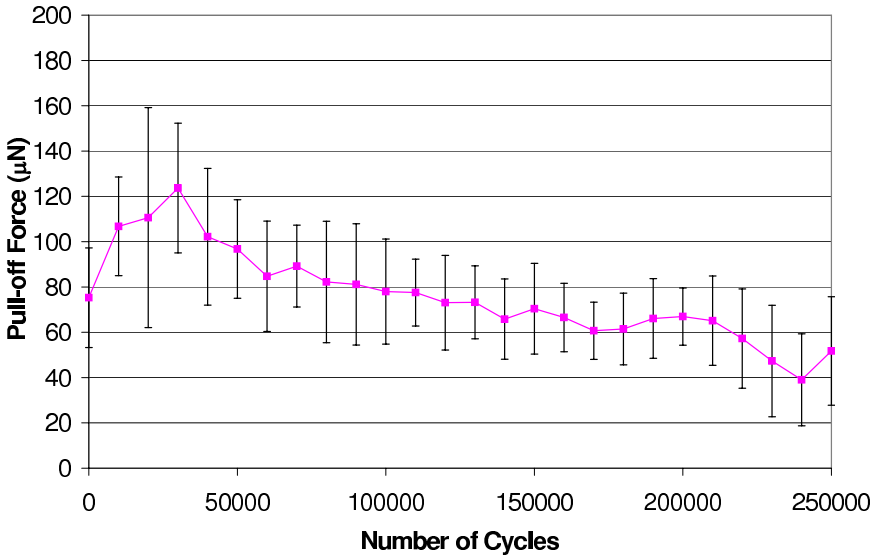

Figure 8.22: Average pull-off force measured during nanoindenter unloading of gold contacts. Unloading rate was 50 μN/sec. Note that this chart does not show instances of adhesive failure, but is intended to show the average trends in gold contact tests.

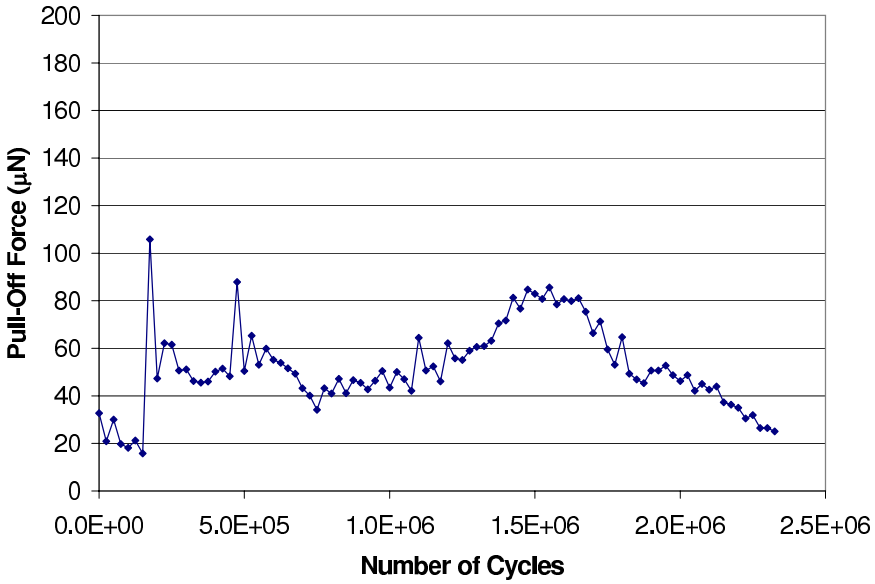

Figure 8.23: Example of long-term gold pull-off force trend during cycling. Note that because there is no measured large increase in pull-off force at the time of contact adhesive failure, this chart indicates that either the growth in adhesive force near failure is sudden or occurs at a rate faster than the measurement interval used in this test. Also note that large changes in adhesion occur during cycling as shown by the large increase at approximately 2×10^5 cycles

8.4 Threshold Force and Distance

The force required to make metallic, stable electrical contact using the gold contacts tested here was in the range of 10 to 25 μN. This is shown graphically in Figure 8.24. This result matches that reported by Hyman, who measured fully metallic conduction between gold contacts when 20-60 μN contact load was applied [107]. However, Hyman only measured threshold force for 60 load/unload cycles. The long term threshold force trend after the first few cycles was relatively constant as well. A long term example of the threshold force trend is shown in Figure 8.25. Note that this example shows a very high initial threshold force, then a drop. The threshold force through the rest of the life of the contact stays relatively constant. The high initial threshold force could indicate contamination of the gold contact at the beginning of the test. Mechanical cycling and fritting likely removed the contamination from the surface, allowing easier ohmic contact.

The threshold distance for gold contacts was approximately 70-75 nm. This value was relatively constant during cycling. There was a relatively large standard deviation in the threshold distance, this is likely due to a thin layer of contaminant deposited from the lab air environment. Figure 8.26 shows the average trend in threshold distance as the gold contacts cycle. An example of the long-term threshold distance trend in gold contact cycling is shown in Figure 8.27. This figure shows a decrease in threshold distance with cycling, possibly due to smoothening of the contact surface.

8.5 Contact Strain Hardening

The contact unloading stiffness of each gold contact was measured at the measurement interval of each test. The stiffness was calculated from the unloading slope after each microprobe loading cycle to 400 μN. The results were normalized by the first unloading stiffness measured in each test. This was done in order to remove the effect of the experimental frame stiffness from the results. The relative change in stiffness of the contact is the important measurement, not the absolute stiffness of the

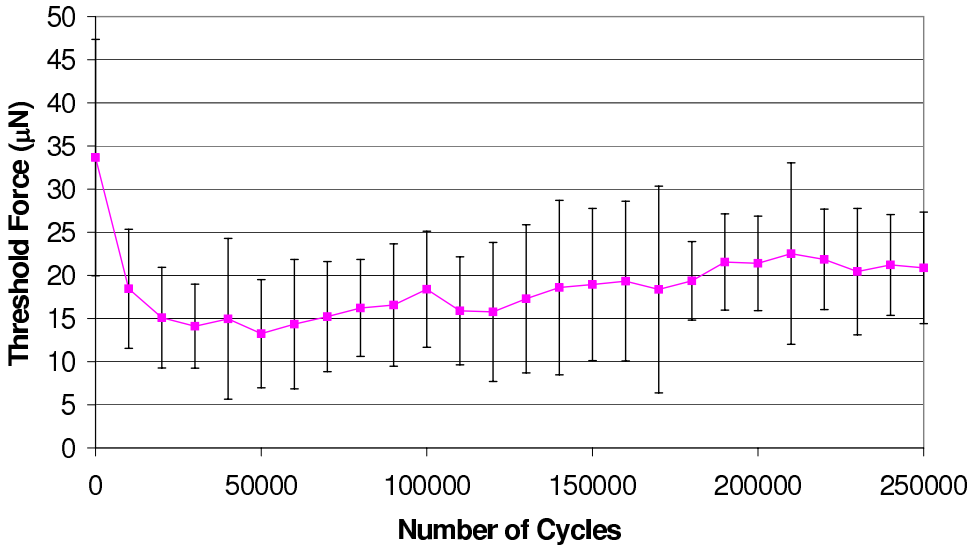

Figure 8.24: Average Threshold Force required to push gold contacts into ohmic contact.

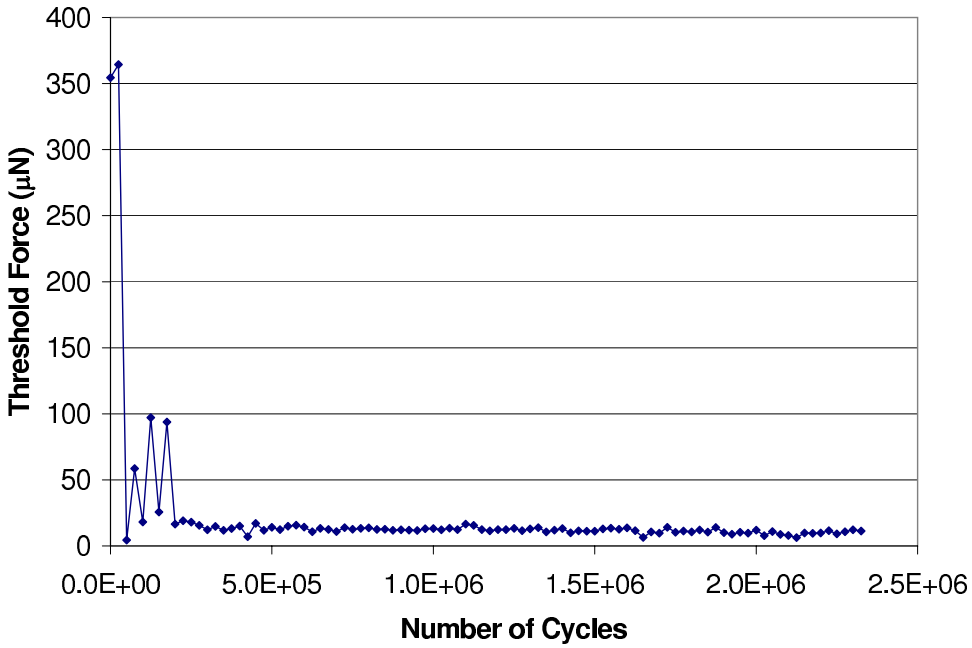

Figure 8.25: Example of gold long-term threshold force trend. The high initial threshold force is common to the longest lasting gold contact tests.

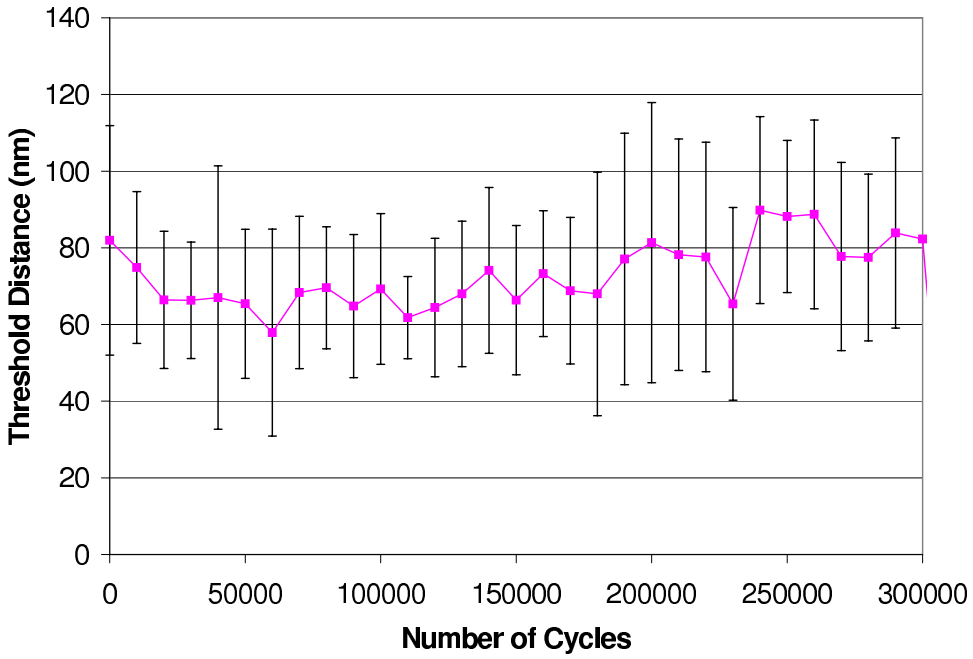

Figure 8.26: Average Threshold Distance required to push gold contacts into ohmic contact.

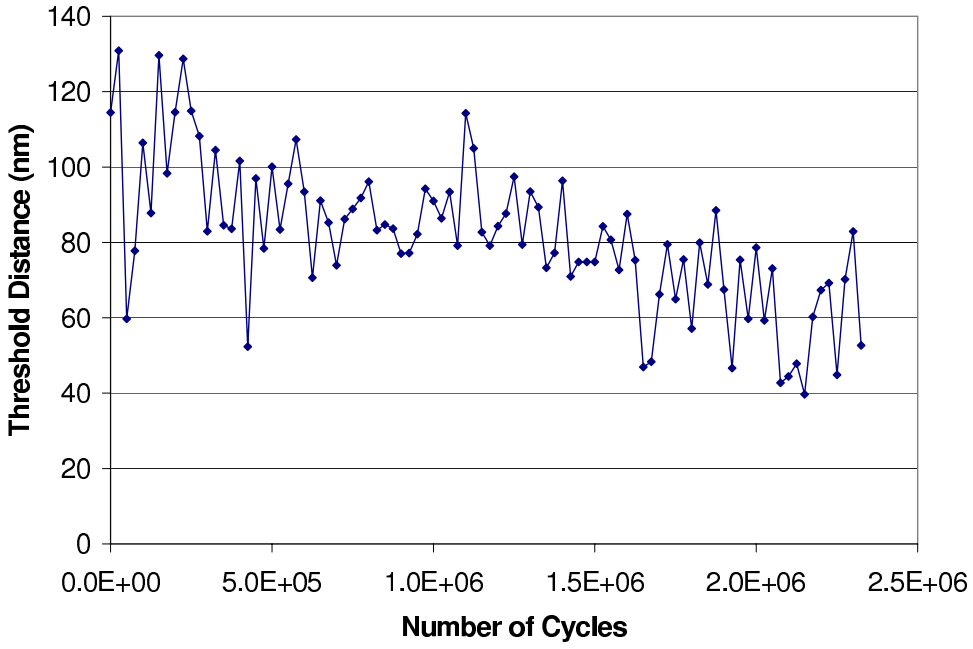

Figure 8.27: Example of gold long-term threshold distance trend. Note that the threshold distance is decreasing as the contact cycles.

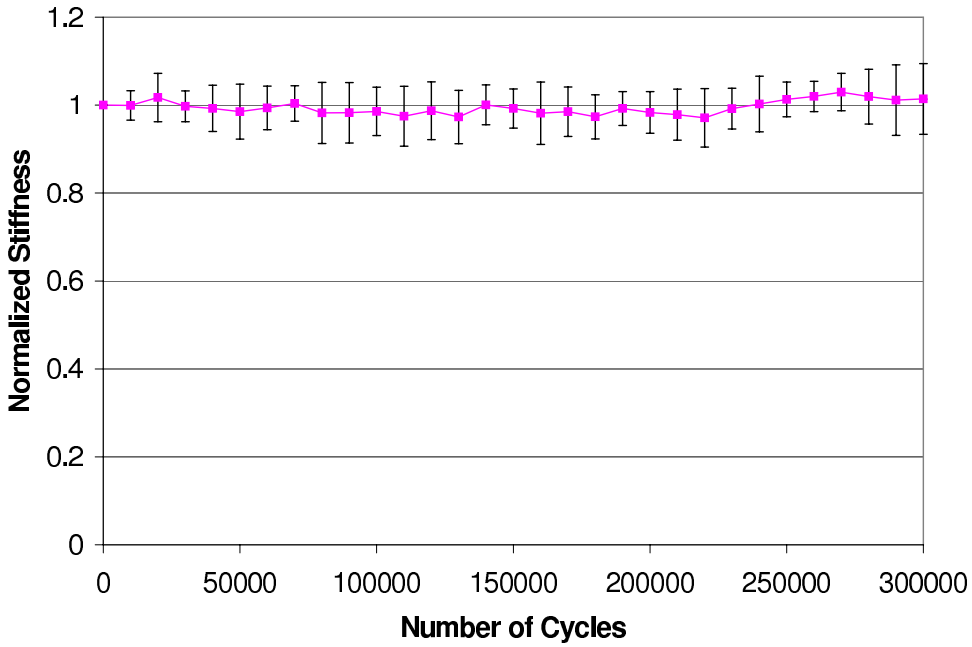

Figure 8.28: Average Contact Stiffness normalized by the first measurement in each test showing stiffness trends during gold contact testing.

contact. Average results for gold testing is shown in Figure 8.28. On average, there appears to be no strain hardening occurring during cycling. The standard deviation indicates that up to 10% strain hardening in the contact may be occurring during some tests, while not in others. This suggests that opposing mechanisms may be influencing contact behavior. That is, plastic deformation leading to strain hardening may be occurring while competing with an annealing effect due to contact heating or softening. A long term example shown in Figure 8.29 shows a small amount of strain hardening ($\sim 4\%$).

8.6 Contact Interference

The deformation of the contact bump and flat surface when they come into contact, also called contact interference, is measurable with the present set-up. This deformation was measured at each measurement interval and the average trend is shown in Figure 8.30. Note that all contact interference measurements were corrected for deformation caused by the microprobe on the top of the silicon cantilever during

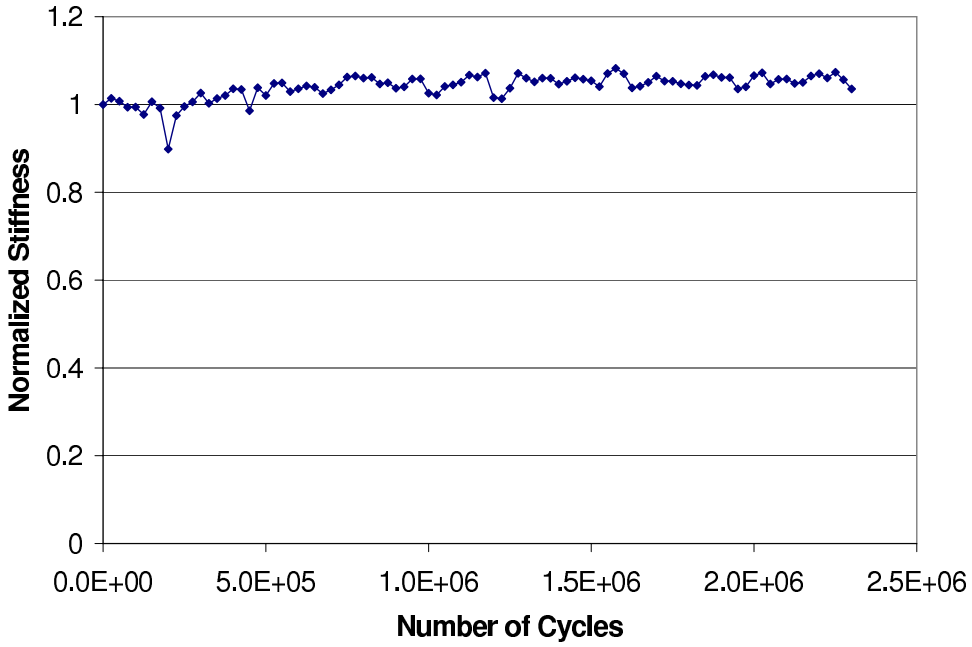

Figure 8.29: Normalized stiffness trend for long term test on gold contact. This test appears to have experienced a small amount of strain hardening.

actuation. Measurements accomplished on static microprobe tests on silicon showed that the microprobe deformed the silicon surface. This deformation was 60 nm, thus 60 nm was subtracted from each raw interference measurement to correct for this deformation.

Du developed a finite element model and used it to predict contact interference, including plasticity and contact adhesion effects, and compared results with two other models [59]. Extending those predictions to 400 μN contact force gives an estimate ranging from 45 to 60 nm contact interference in gold. These predictions show that the measurements made here are reasonable. Note that these measurements have been adjusted by subtracting the estimated amount of deformation caused by microprobe tip application of force to the top of the cantilever from the uncorrected interference measurement. This deformation was estimated as 60 nm based on a test run using a basic load displacement method with a load of 400 μN on a sample of test cantilever material. The interference measured in gold contacts settled out at approximately 90 nm as the test cycled. The difference between predicted and measured result is

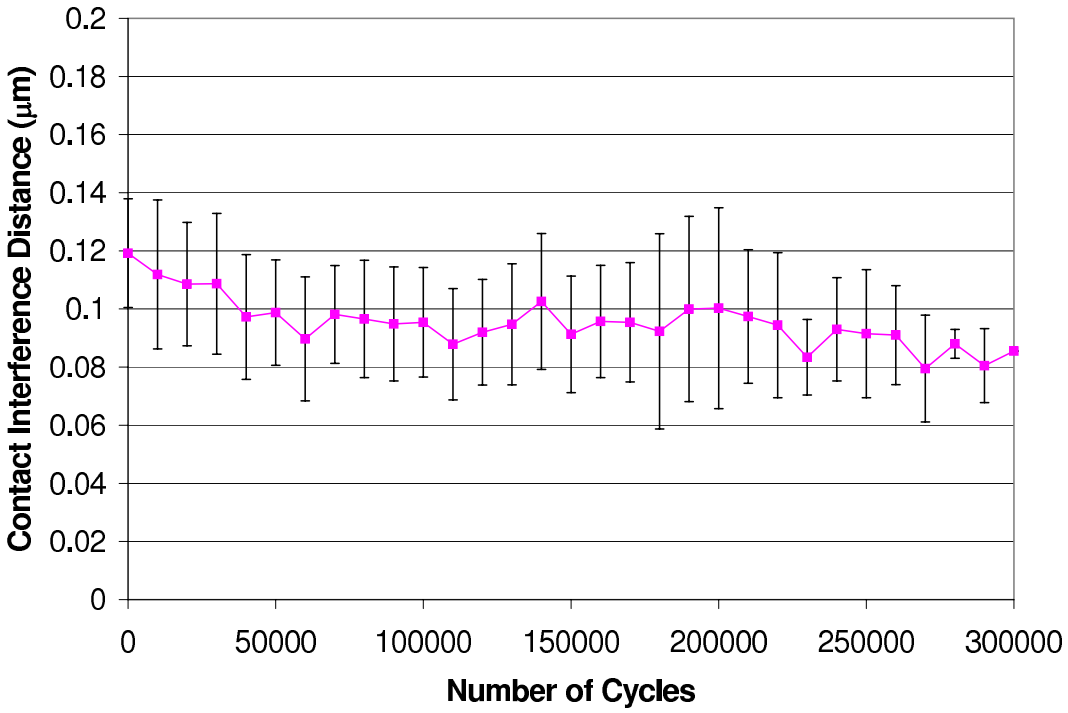

Figure 8.30: Average contact interference (deformation) on contact load of 400 μN measured during gold contact testing.

explained by the occurrence of additional plastic deformation not accounted for in the models and possible additional uncorrected deformation in the top of the cantilever caused by contact with the nanoindenter microprobe tip.

8.7 Time Dependent Behavior

One facet of the contact behavior noted during this study was the existence of time-dependent behavior during contact loading. Creep is defined as, "Permanent strain that increases as a function of time under stress" [71]. Normally, creep is associated with constant load applied for a long duration at an elevated temperature. During this testing, the compressive stress on the contact was maintained only a short time. During testing, a five second hold was programmed between the end of active loading and the unloading of the nanoindenter tip. There should have been no displacement during this hold time. However, in every case a small deformation occurred under constant load during the hold period. This was measured and the

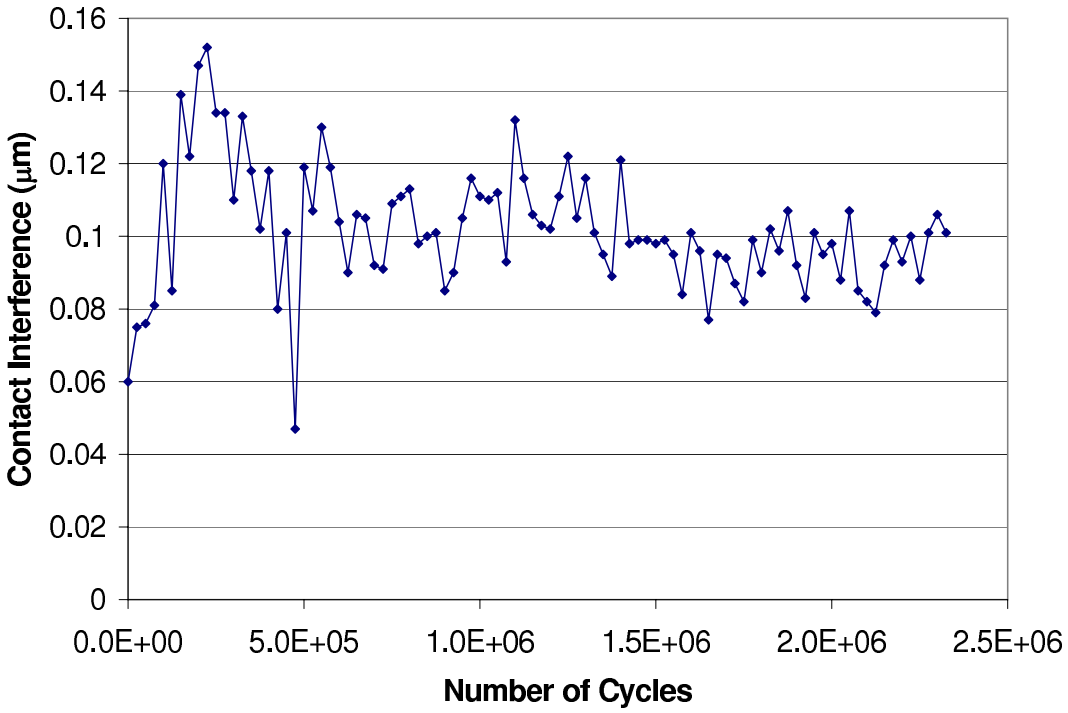

Figure 8.31: Gold long term contact interference (deformation) example during cycling test with contact load of 400 μN.

average is shown for gold contacts in Figure 8.32 which stabilizes at approximately 2 nm after 100,000 cycles. An example of the time dependent results for a long-term test is shown in Figure 8.33. The long-term test also shows a rough average of about 2 nm and increases slightly after 1.75×10^6 cycles. It is not clear if this time-dependent deformation is accurately described as "creep".

This behavior is possibly due to contact heating from current passing through the contact. The softening temperature of gold is lower at the micro-scale when compared to bulk softening temperature [115] and images of contact surfaces during this study indicate that melting or softening of contacts may occur. The small amount of time-dependent deformation could also be due to a soft interposing material on the contact surfaces which exhibits viscoelastic properties.

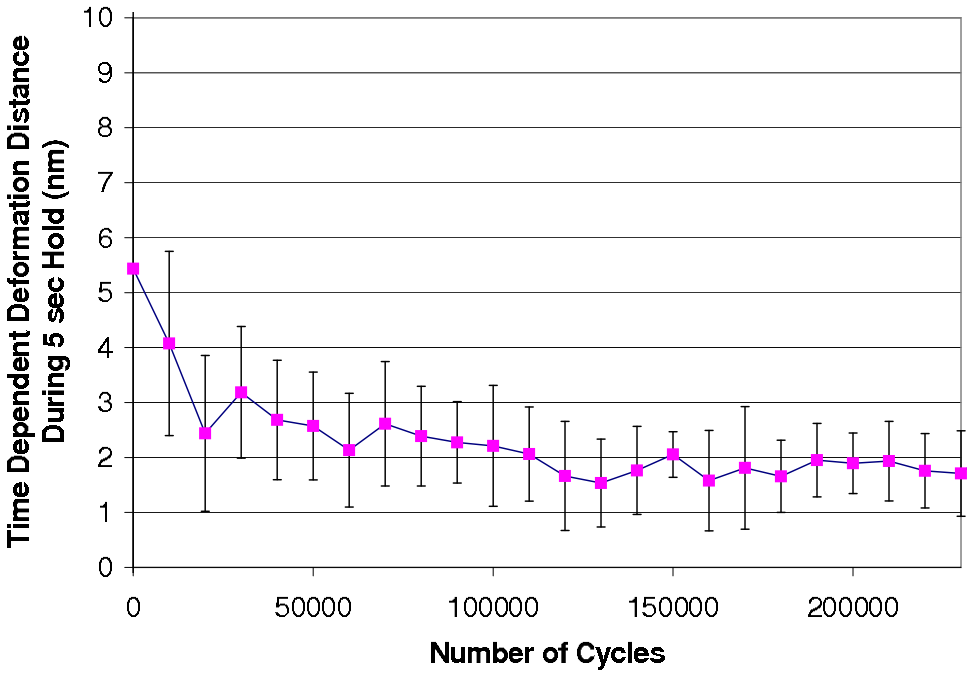

Figure 8.32: Average time-dependent contact deformation for gold contacts tested during 5 second constant load hold at 400 μN. This behavior appears very much like creep. Deformation occurs under constant load but for short time periods.

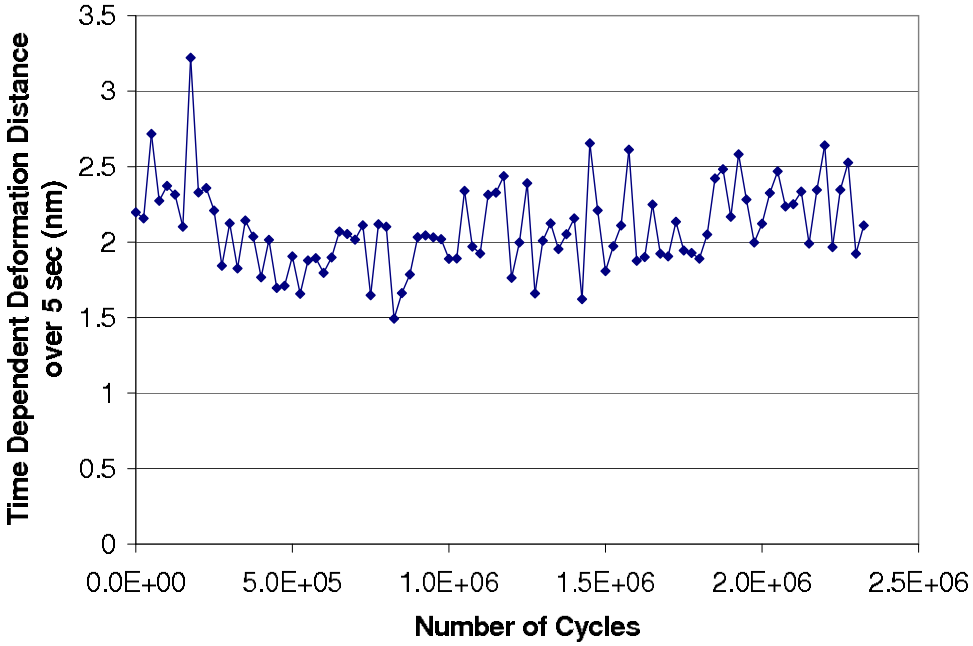

Figure 8.33: Gold long-term time-dependent contact deformation single-test example during 5 second constant load hold at 400 μN.

8.8 Plastic Deformation

Both elastic and plastic deformation occur during every contact load cycle. The slope of the loading portion of the contact cycle contains both elastic and plastic components, whereas the unloading slope shows the elastic component. One method to show the plastic component of the load cycle is to measure the energy absorbed during contact. The MTS Nanoindenter and TestWorks have the ability to calculate the energy absorbed by the contact. This ability was used during the gold contact testing to see how the plastic deformation of the contact changes as the contact cycles. Figure 8.34 shows the average of energy absorbed during gold contact cycling testing. This shows that slightly more plastic deformation occurs during the beginning of the contact life and then it is fairly constant later. An example of plastic deformation in a long lasting test is shown in Figure 8.35. The long-life contact example also shows an increase in plastic deformation early in contact life followed by a fairly constant value. The early energy absorbed may indicate the generation of dislocations in the contact material due to cycling. A dislocation is defined as, "A collection of point defects that results in a line defect." [71] As a material is stressed "into the region of plastic strain, slip takes place on the favorably oriented planes, producing dislocations and their movement." [71] The early increase in the plastic deformation in the contact may show that for a contact to last longer dislocations must be created early in the life of the contact, possibly causing strain hardening.

8.9 Contact Evolution

The failure of gold contacts appeared to be affected by adhesive wear of the contact. Rabinowicz defines wear as consisting of the removal of material from the surface of one contacting body as a result of interaction with another contacting body [199]. Adhesive wear is defined by Rabinowicz as the most common type of wear which "exists whenever one solid material is slid over the surface of another or is pressed against it." [199]. Rabinowicz further describes the mechanism of adhesive wear such that when two surfaces are brought together and separated, the "attractive

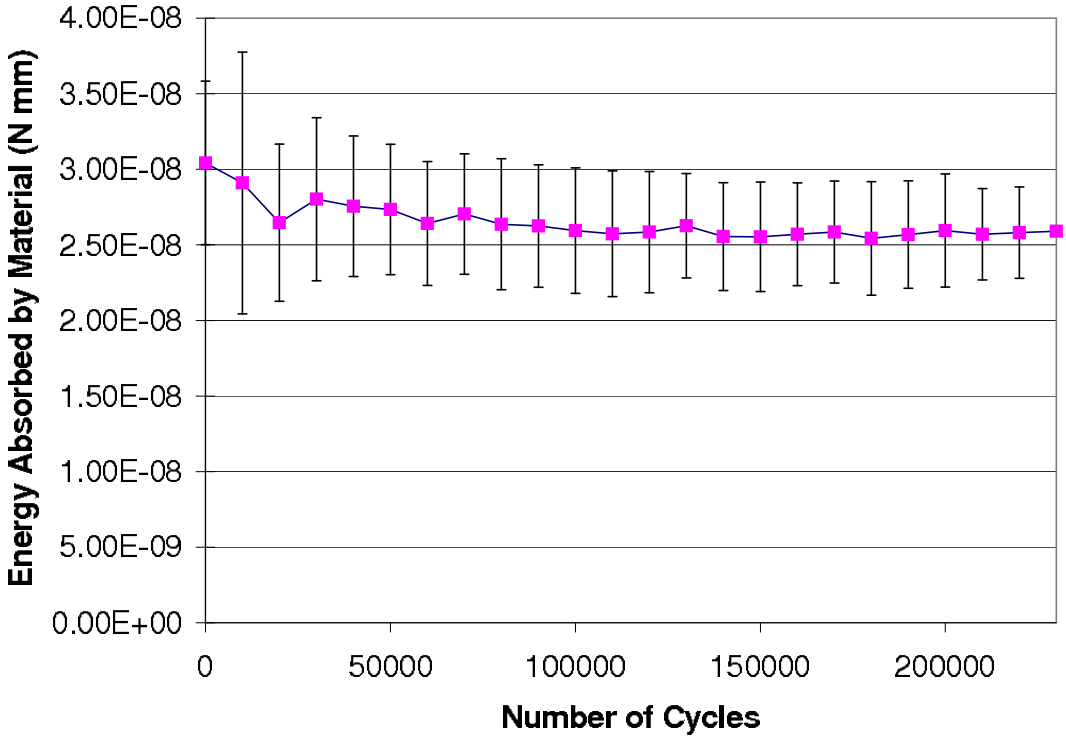

Figure 8.34: Average energy absorbed by gold contacts during cycling testing indicating amount of plastic deformation occurring on the gold contacts.

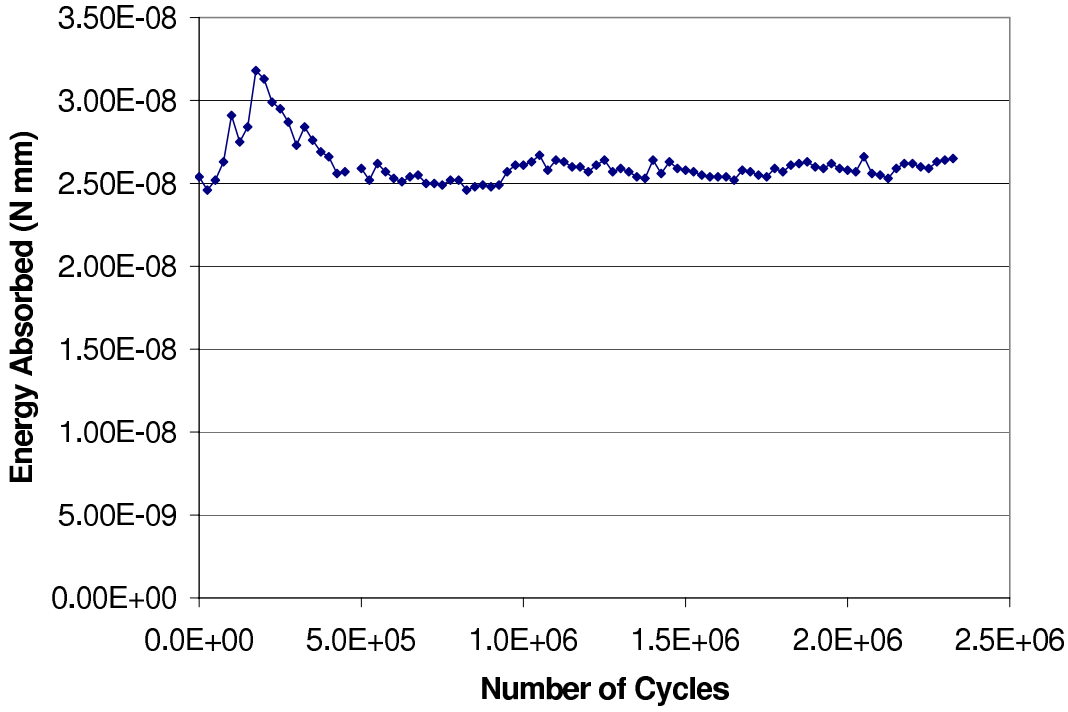

Figure 8.35: Long-term example of energy absorbed by a gold contact during cycling testing indicating amount of plastic deformation occurring.

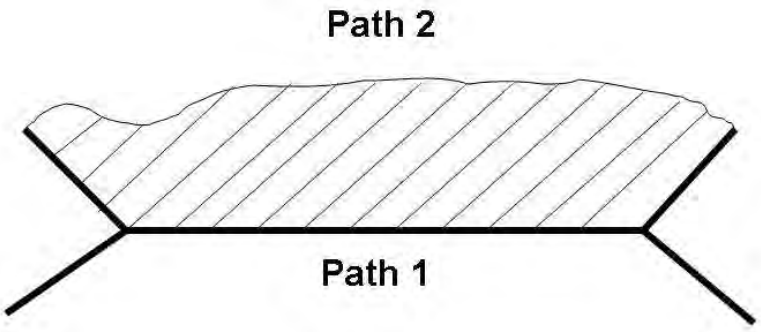

Figure 8.36: Diagram showing junction between two solid materials and mechanism of adhesive wear. If the strength of the junction is higher than the strength inside the bulk of either material, the separation of the junction will occur along Path 2, thus causing material transfer or creation of a wear particle [199][8].

forces act in such a way as to attempt to pull material from one surface on to the other" [199]. Rabinowicz also notes that, "the removal of material takes the form of small particles, which are usually transferred to the other surface but may come off in loose form" [199]. Figure 8.36 shows a junction between two solid materials. If the junction separates on the original interface, shown by Path 1, no material will be transferred. However, if the strength of the junction is greater than the strength away from the surface of the bulk material, the junction will separate along the most opportune path, here represented by Path 2 [199].

One test was stopped after 550,000 cycles but before contact failure in order to analyze the evolution in the contact surface due to cycling. This contact after 550,000 cycles shows indications that adhesive wear is occurring. Figure 8.37 shows the contact before cycling. Figure 8.38 shows the top contact surface after the test. Lamellar (Platelike) formations on the contact surface point to material transfer having occurred between contact surfaces. Figure 8.40 also shows clear evidence of material transfer having occurred from the bottom contact to the top. Cracks in the surface of the top contact are visible, thus pointing to possible incipient creation of a wear fragment or further material transfer. The incipient material transfer could be lead-

[8]From Rabinowicz, Friction and Wear of Materials, Second Edition, Copyright 1995, John Wiley & Sons Inc, reproduced by permission of John Wiley & Sons, Inc.

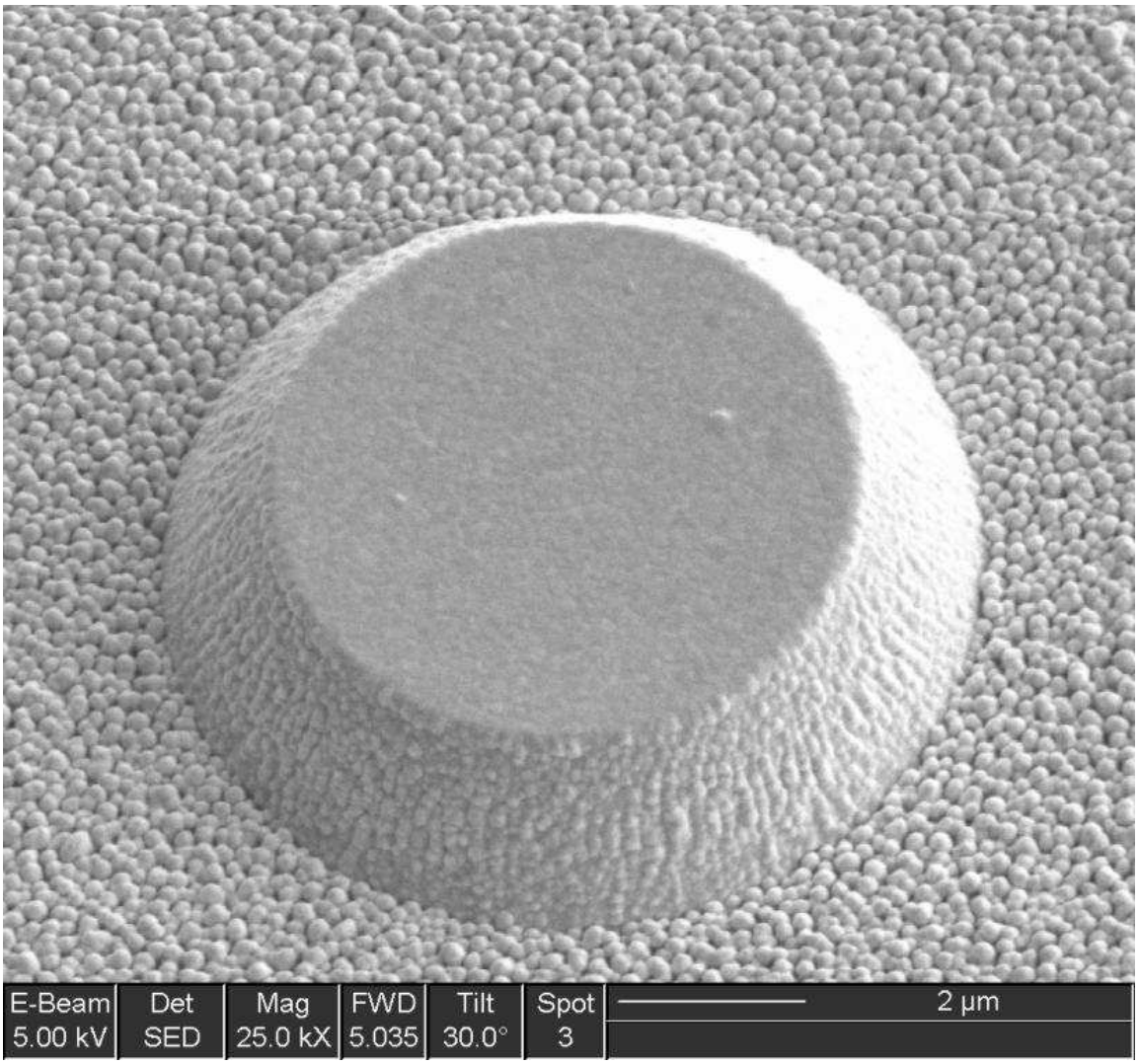

Figure 8.37: Gold coated contact bump surface before 550,000 cycle test.

ing to an increase in the adhesive force between the contact surfaces or indicating that the adhesive force between the contact surfaces is increasing. Changes in the contact surfaces can be seen in both Figures 8.38 and 8.39. Note that the annular ring around the contact area contains droplet shaped features which may indicate melting or softening of contact material at the edge of the contact circle. Recall that heat production rises sharply at the edge of the circular area in electrical contact [86]. This heating at the edge of the area of contact could lead to localized softening and melting as seen here.

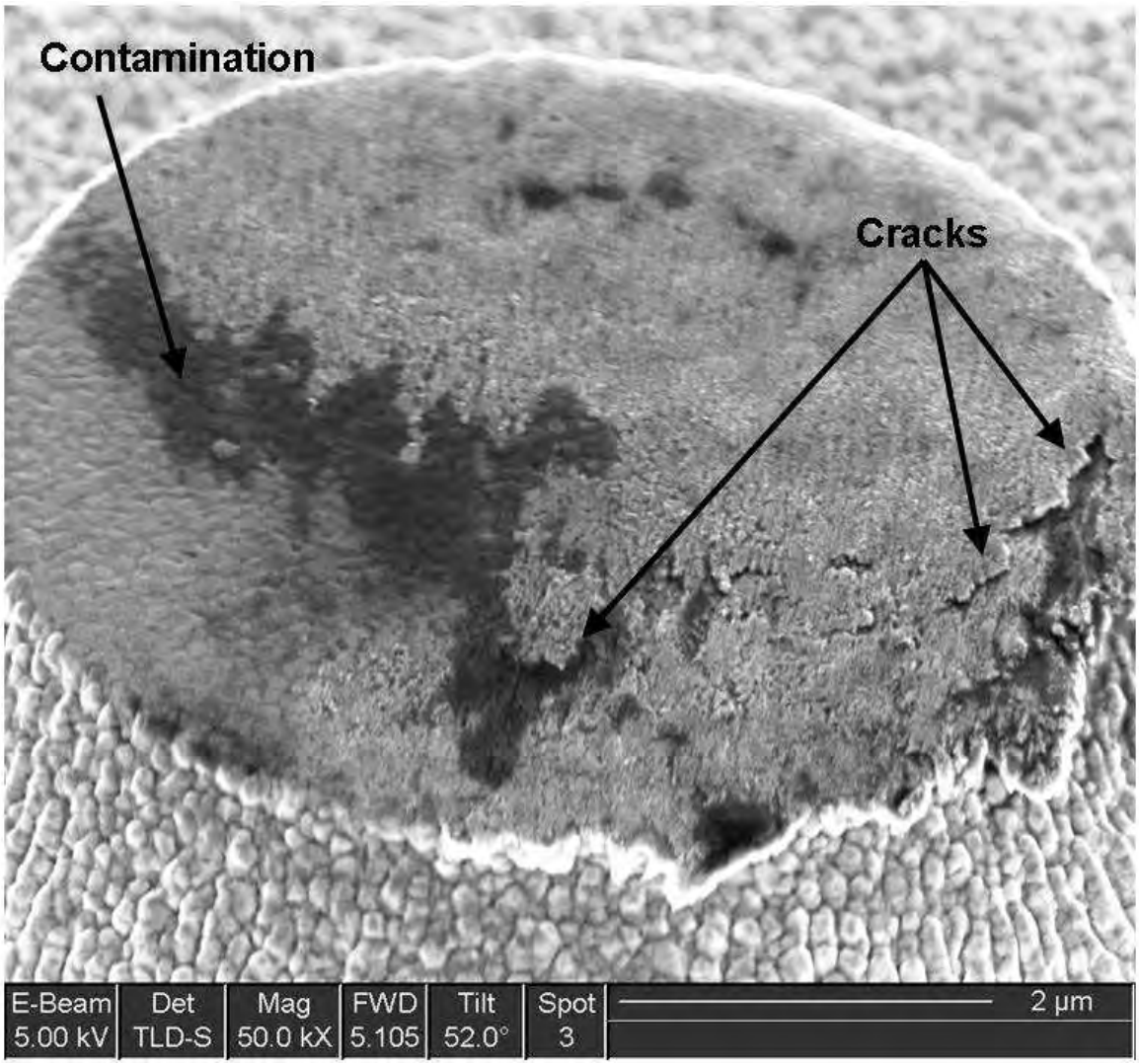

Figure 8.38: Gold coated top contact surface after 550,000 cycles without failure. Note surface changes in contact area and beginning of dark layer indicating contamination. Note also surface crack initiation and appearance of material transfer, as well as lamellar appearance at crack locations.

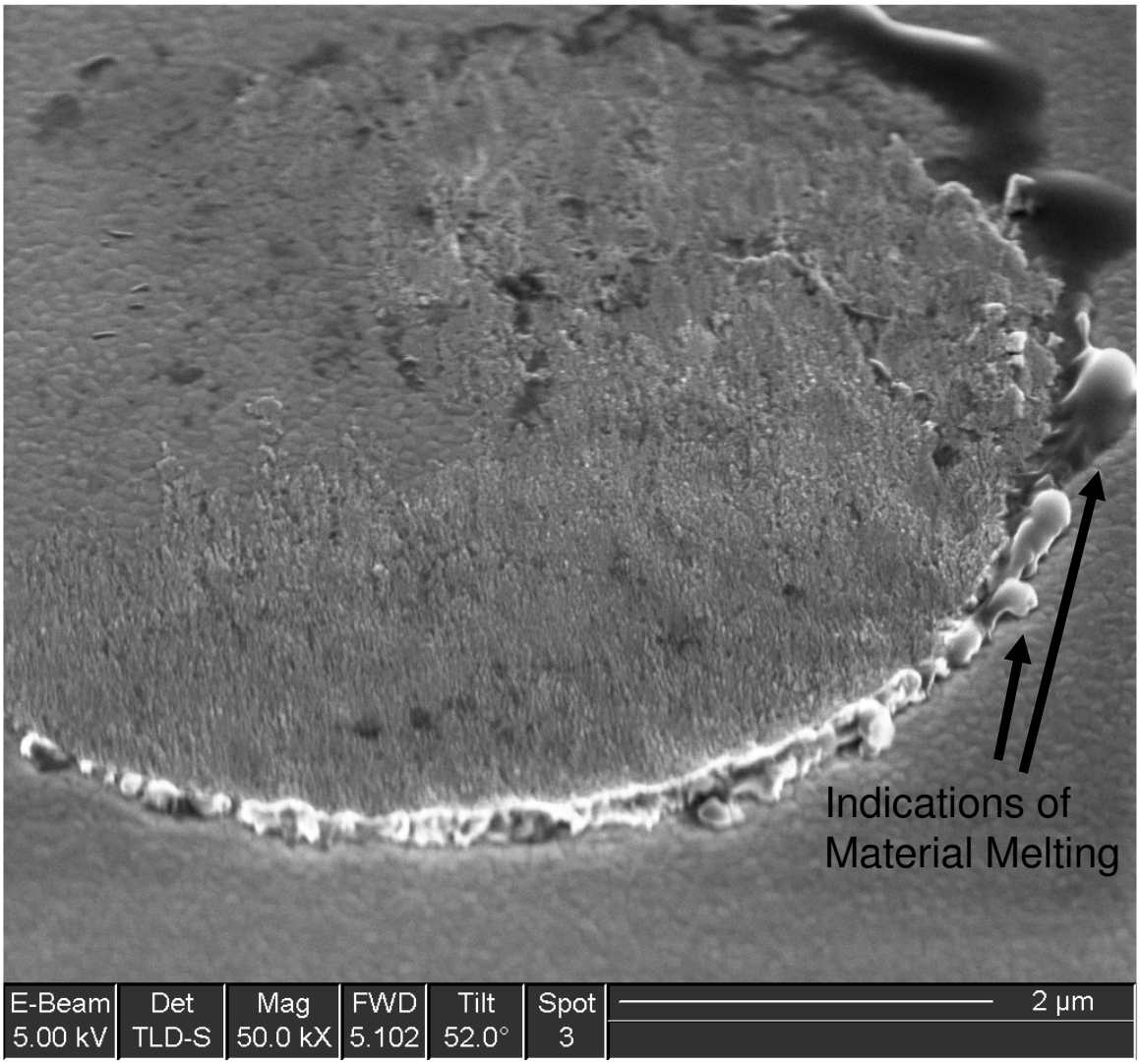

Figure 8.39: Gold coated bottom contact surface after 550,000 cycles without failure. Note surface changes in contact area and beginning of annular ring indicating contamination and possible softening or melting at edge of contact area.

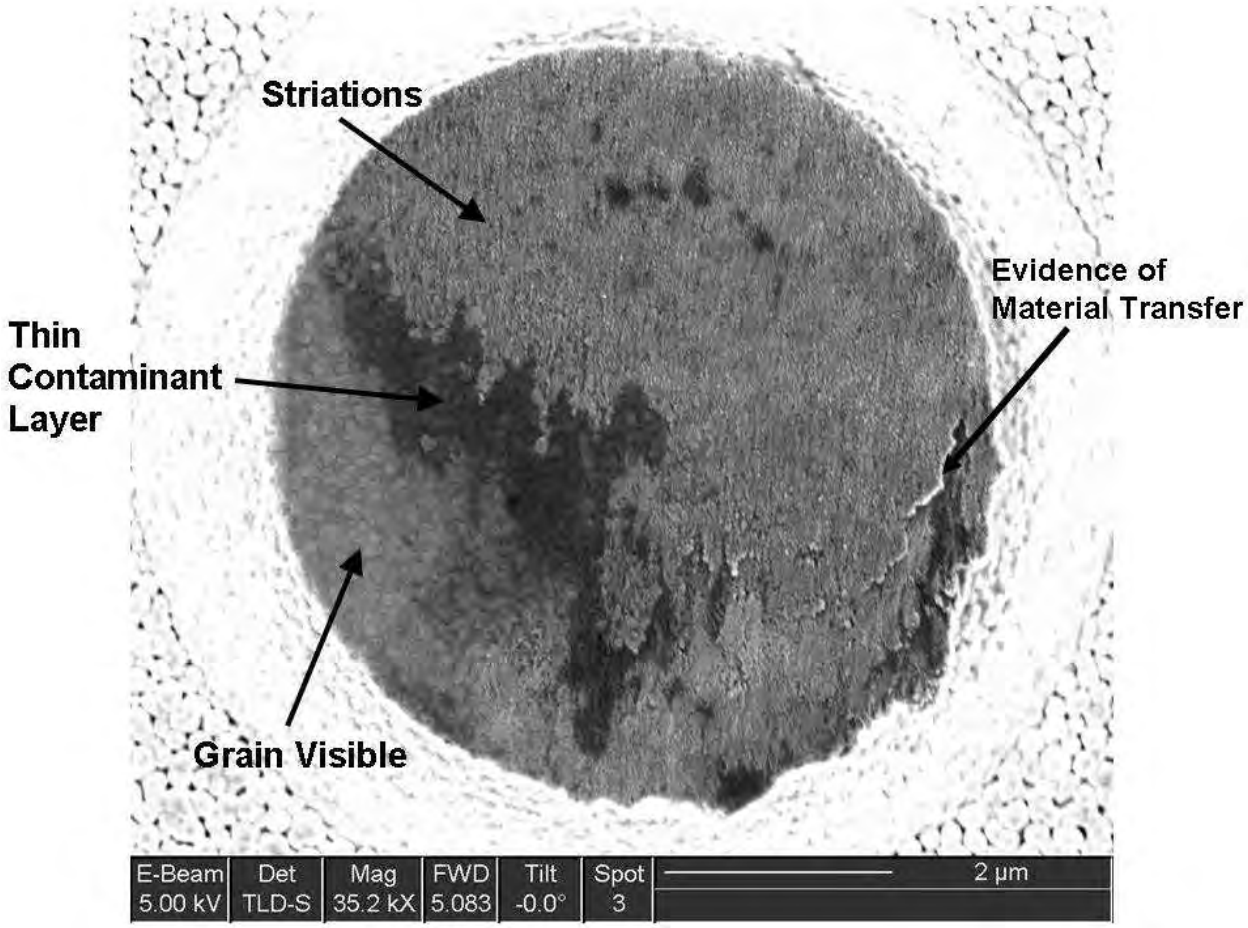

Figure 8.40: Topview of gold coated top contact surface after 550,000 cycles without failure. Note evidence of material transfer and thin contaminant layer. Striations appear on surface as well.

8.10 Contact Shape

There was no evidence that contact shape affected contact results. This result is reasonable if the contact is fully plastic, where the contact behavior is dominated by contact material properties and contact force rather than contact shape. This result matches the result reported in [115] showing no differences in contact resistance between contact bumps of varying size. Note also that Hyman concludes, "electrode surface damage for micrometallic contacts is dominated by nm-depth material properties rather than by electrode morphology" [107]. The only noticeable trend for shape of gold contacts was that all three rounded contacts tested failed in adhesion at 60,000 cycles or less. The contact shapes and sizes are given in Table 8.3. There is no apparent correlation in this set of data between contact bump size and contact lifetime. However, further testing should be accomplished to provide additional data on effect of contact shape.

8.11 Failure Type Categorization and Measurement

As previously discussed in this chapter, the adhesive failures of gold-gold contacts during this study can be categorized in three groups based on test lifetime and type of failure. Measured test results were sorted and averaged based on lifetime categories. Some of the measured quantities show slight differences between lifetime categories. The data plots are shown in this section without error bars for clarity. The upper and lower error bars overlapped in most cases, so definitive conclusions can not be made. However, trends in some areas were demonstrated and are discussed here. Generalized descriptions comparing the results qualitatively are given in Table 8.4. The measurements which show a difference are given in the following sections. However, no predictive factors were found such that contact life for an individual contact could be made before cycling. There is no such predictive ability, even with the state-of-the-art MEMS switches on the market today. Also, as discussed in Section 2.3, it should be noted that even the most advanced switches show significant variability in lifetime [65, 171]. The results presented here are the first to segregate failure by

Table 8.3: Test summary of shapes and sizes of gold contacts tested to failure. Contact bumps described as "Flat" are flat-topped bumps. Contact diameter and height were measured using SEM topview and off-axis SEM images.

Contact ID	Contact Shape	Contact Diameter (μm)	Contact Bump Height (μm)	Initial Contact Resistance (Ω)	Failure Type	Number of Cycles to Failure (# Cycles)
0303-4_6	Round	10.1	4.3	2.127	Adhesion	10,000
0210-2_3(200 μN)	Flat	6.5	2.0	1.472	Adhesion	10,000
0602-2_1(G)	Round	9.2	3.2	2.707	Adhesion	10,000
0303-1_6	Flat	6.6	1.4	1.650	Adhesion	20,000
0602-1_12(D)	Flat	4.2	3.2	3.534	Adhesion	30,000
0801-1_6	Flat	8.9	1.5	0.972	Adhesion	50,000
0303-4_7	Round	9.8	3.5	2.132	Adhesion	60,000
0801-3_1	Flat	5.4	1.8	2.053	Adhesion	70,000
0210-3_1	Flat	6.0	2.7	1.452	Adhesion (film torn)	190,000
0602-2_8(B)	Flat	2.9	3.4	2.451	Adhesion (film torn)	200,000
0801-1_12	Flat	6.5	1.6	1.646	High Resistance (film torn)	300,000
0602-2_11(E)	Flat	3.2	3.5	2.751	Adhesion (film torn)	440,000
1101-2_6	Flat	5.0	1.9	1.804	Adhesion (film torn)	500,000
0210-3_3	Flat	8.0	2.1	1.602	Adhesion (film torn)	500,000
0602-1_2(E)	Flat	3.3	3.3	2.253	High Resistance (film torn)	500,000
0801-1_7	Flat	6.2	1.7	1.585	No Failure	stopped at 550,000
0602-2_12(F)	Flat	4.2	3.4	2.470	Adhesion	1.06×10^6
0210-3_2	Flat	8.0	2.1	1.472	Adhesion	1.16×10^6
0602-3_8	Flat	3.8	4.5	2.171	Adhesion	2.35×10^6

lifetime groups and analyze measurements made on contacts including pull-off force, threshold force and distance, time-dependent deformation and energy absorbed in order to characterize failure type behavior differences.

8.11.1 Pull-Off Force. The measured pull-off force is clearly expected to show a difference between contacts with different lifetime failures. The earliest group of adhesive failures (Type I) shows the highest initial pull-off force, as expected. Both other types of failures show an initial increase in pull-off force magnitude and then decrease. The longest lasting contacts showed the least pull-off force increase. The pull-off force for Type III failures show a slightly increasing trend later over time. This can be seen in Figure 8.41. These results indicated that if the pull-off force increases early, the damage to the contact increases and thus the lifetime of the contact is decreased. Lower initial pull-off indicates longer life, and slower increase in pull-off force indicates longer life. The differences between the evolution of contact adhesion is likely due to environmental factors as well as specific makeup of contact surfaces. These include initial levels of surface contamination as well as quality and roughness of the thin film on the contacts under test. More research is needed to determine

Table 8.4: Qualitative comparison of measured results indicating differences between three categories of lifetime failures. Long-life failure results are used as the reference. ↑ = higher initial value; ↗ = slightly higher initial value; ↓ = lower initial value; ↘ = slightly lower initial value; → = similar value

Measured Result	Long-life Type III (brittle)	Mid-life Type II (thin film)	Short-life Type I (ductile)
Resistance	Baseline	→	→
Pull-off Force	Baseline	↗	↑
Threshold Force	Baseline	↓	↓
Threshold Distance	Baseline	↘	↓
Interference	Baseline	→	↓
Creep	Baseline	↑	↑
Energy Absorbed	Baseline	↑	→

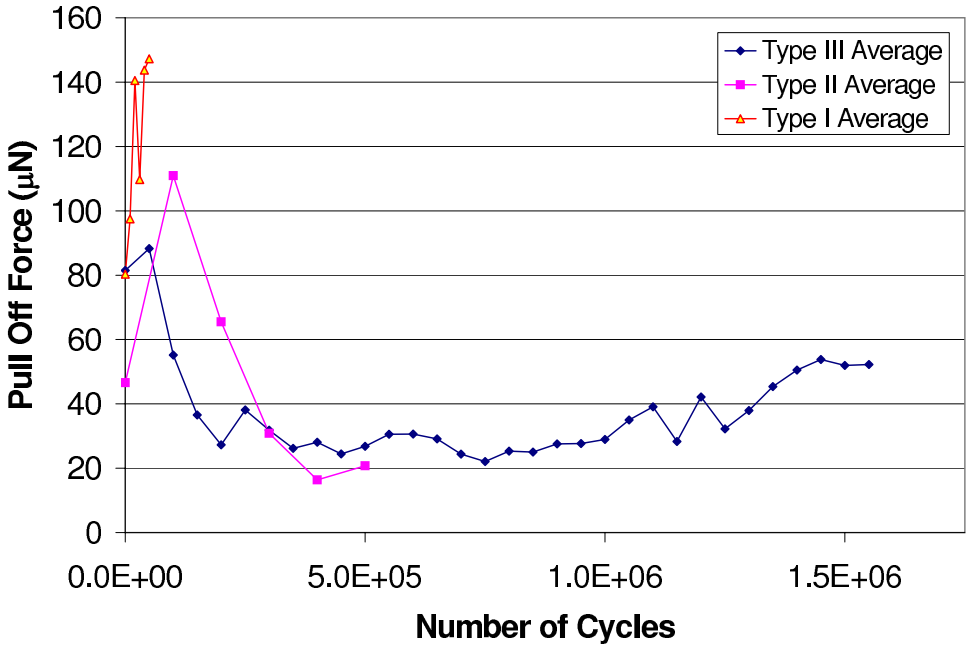

Figure 8.41: Average pull-off force comparison between lifetime failure categories. Note that the Type I failure shows highest early average pull-off force, as expected while other two categories peak and drop to a lower steady value.

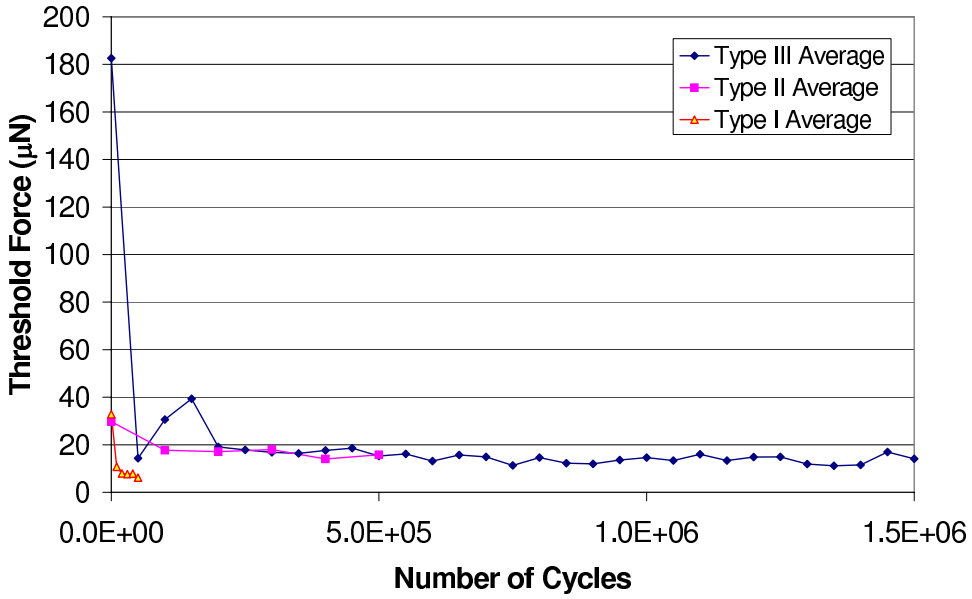

Figure 8.42: Average threshold force comparison between lifetime failure categories. Note that average threshold force for Type I early lifetime failure starts lower and is least value. Also, note that Type III longest lifetime shows high initial average threshold force.

the best method to delay the increase in pull-off force and thus contact adhesion, extending the life of microcontacts.

8.11.2 Threshold Force & Distance. One result when the tests were analyzed by lifetime categories is shown in Figure 8.42. Note that the longest lasting contacts have the highest average initial threshold force, and therefore can be the most difficult to get into initial ohmic contact. The longest lasting contacts also showed a second peak in average threshold force. This may indicate more contamination on the contacts at the start of testing or more contamination created during the initial stages of testing. The short- and mid- lifetime results (Type I and II) started at around the same level of average threshold force. The short-life (Type I) contacts decreased measured average threshold force quickly. This quick decrease in Type I threshold force may indicate intimate initial contact requiring less external force to ensure low resistance through the contact. This quick decrease and low initial threshold force

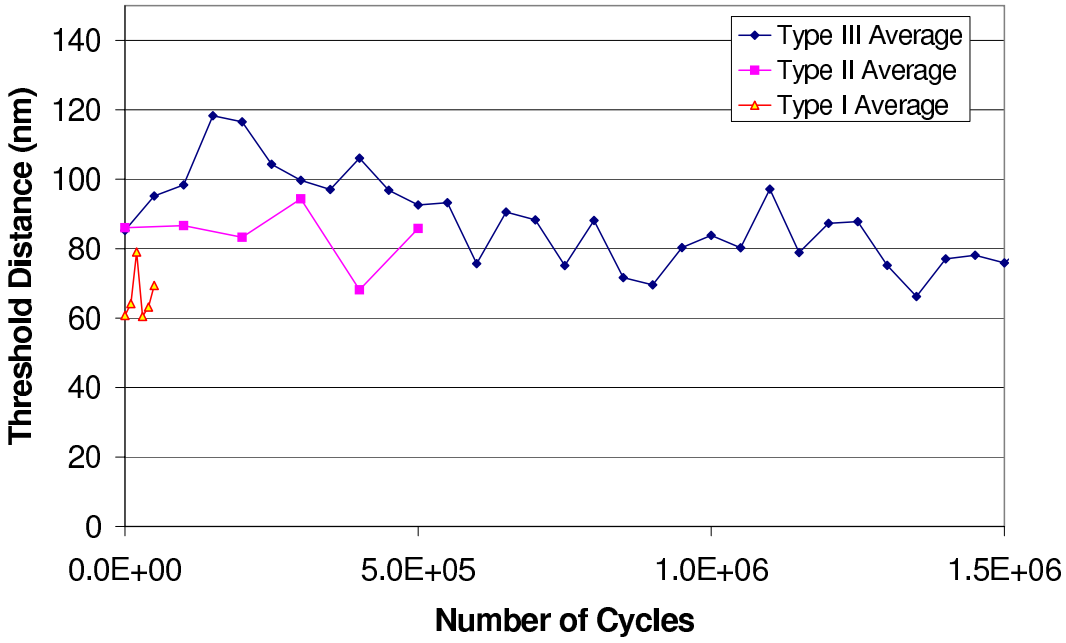

Figure 8.43: Average threshold distance comparison between lifetime failure categories. Note that threshold distance for Type 1 early failure is least.

may also indicate a cleaner or smoother inital contact surface at the start of testing, leading to higher adhesion forces.

The shortest lifetime (Type I) contacts also have a lower initial average threshold distance when compared to the longer life Type II and Type III contacts as seen in Figure 8.43. This also may indicate easier ohmic contact and possibly a cleaner or smoother contact in the beginning of shorter lifetime tests. The Type III long lifetime contacts also show a small increase early in the contact life similar to that shown in the threshold force results. The Type III threshold distance results also decrease slowly over time, possibly indicating smoothening of the contact which would therefore increase contact adhesion.

8.11.3 Time Dependent Behavior. The largest initial average creep behavior was in the Type II contacts and the lowest was in the Type III category contacts, as shown in Figure 8.44. The average time-dependent deformation in Type III longer lifetime contacts increased slightly, then dropped to a constant level below that of the Type II contacts. The Type I contacts average time-dependent behavior was in be-

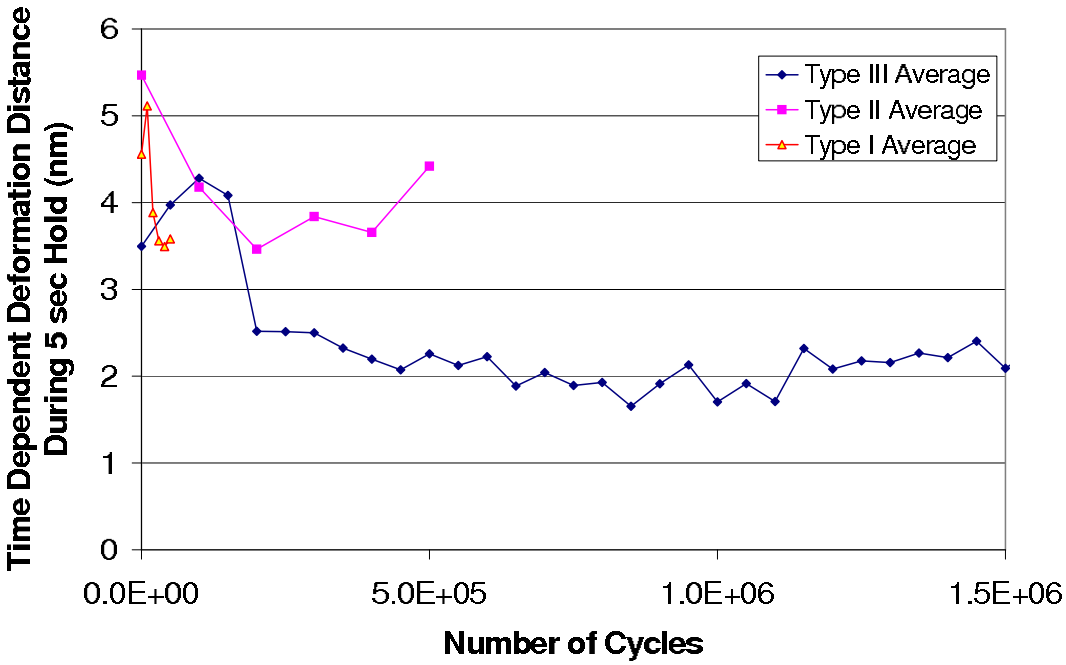

Figure 8.44: Average time dependent deformation ('Creep') comparison between lifetime failure categories. Note that the longest life (Type III) failure starts with the lowest creep and then shows decrease to steady value.

tween the Type II and Type III results. The time dependent deformation in the Type I contacts started high and dropped quickly, perhaps indicating rapid smoothening leading to increased adhesion and early failure. The long life average showing lower creep indicates that low levels of creep are beneficial in extending contact life. The initial condition of the contact thin film may play a role in lengthening the life of the contact. The slight increase of time-dependent deformation in the Type III contacts may indicate creation of dislocations which then reduce the time-dependent deformation later in the life, protecting the surface from smoothening effects and contact failure.

8.11.4 Energy Absorbed. The energy absorbed by the contacts is a measure of plastic deformation and the averages of the three failure categories are compared in Figure 8.45. Keeping in mind that the overlap of error bars preclude definitive conclusions, note that Type I and Type III contacts demonstrated similar results until Type I failures occurred. The Type II average energy absorbed was a constant

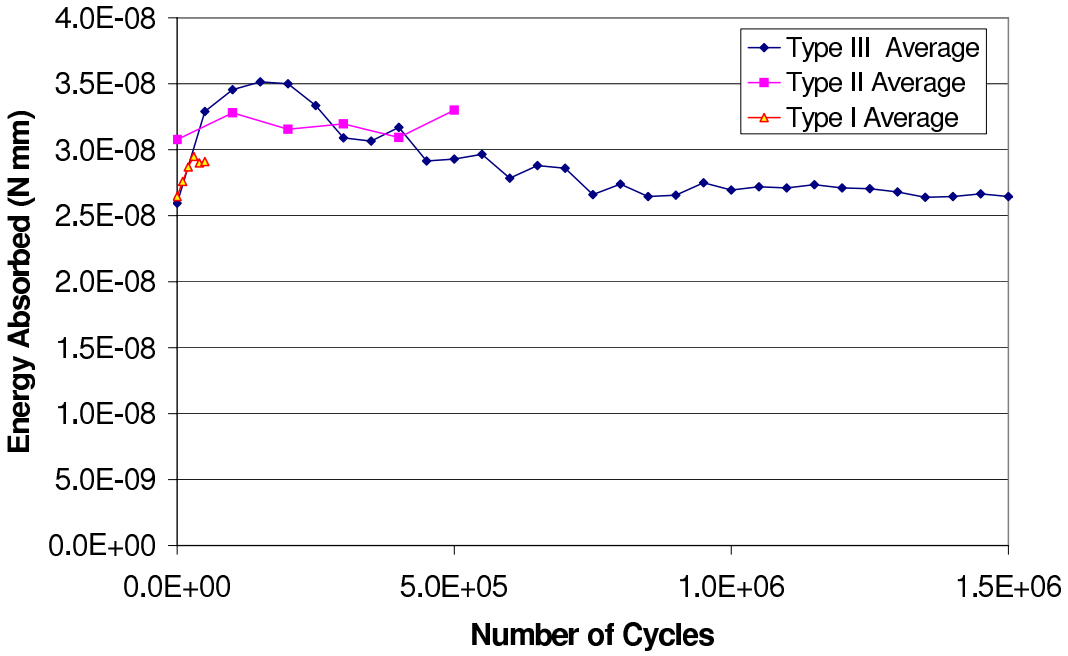

Figure 8.45: Average energy absorbed comparison between lifetime failure categories. Note that Type I and Type III failures look very similar at the beginning, while Type II failure average energy absorbed starts higher and stays relatively constant to failure.

value starting higher initially than the Type I and Type III measurements. The Type III data increased initially and then stabilized at a level slightly above the initial measurements of energy absorbed. The Type I and III contacts both showed an increase in plastic deformation during initial cycling. There is no way to tell the difference between them based on this measurement until the Type I contacts fail. The Type II contacts show a constant level of plastic deformation from initial cycling until failure. These results may indicate that in the Type III contacts, an initial level of dislocation barrier creation is necessary to reduce plastic deformation and smoothening, therefore slowing the increase of adhesive forces. Note that the time dependent behavior results for Type III contacts are similar to the plastic deformation results described here, with an initial increase then slow decrease as the contact cycles. Further research is needed to fully understand this mechanism and how to control plastic deformation on the contact surface to increase contact lifetime.

8.12 Summary of Gold Results

Gold is a commonly used microcontact material due to its attractive material properties and ease of fabrication. However, few detailed studies of performance of gold microcontacts have been accomplished. This chapter presented measurements of gold microcontact performance which have not previously been reported such as contact interference, contact stiffness change/strain hardening, threshold distance, time-dependent deformation and measures of plastic deformation. Adhesive failure was the main failure mechanism in the tests accomplished here, as expected for soft gold contacts. Note that gold contacts frequently fail by adhesion [128]. The adhesive failure lifetimes of the gold contacts determined in this study fell into three categories: short-life (or infant mortality) failure exhibiting ductile surface characteristics (Type I), mid-life failure demonstrating thin film separation (Type II), and long-life lifetime failure showing brittle surface separation (Type III). Each showed different failure characteristics. The Type I short-life failures were identifiable by the ductile adhesion surface features suggesting ductile pull-off dominated the cycling events. The mid-life failures showed the contact thin film adhering to the lower contact strike plate suggesting subsurface damage during cycling or contact adhesive force greater than the thin film-substrate adhesion. The long-life failure showed visible smoothening on the bottom contact area, physically flattened features and separation very close to the contact interface suggesting brittle separation during cycling.

The force required to generate ohmic contact, defined as threshold force, was determined to be approximately 10-25 μN. Ohmic, or metallic, contact is defined here as contact where the resistance between surfaces becomes low and stable, that is, when the transition from quasi-metallic to metallic conduction occurs. The pull-off force, contact interference, contact strain hardening, and energy absorbed by the contact were also measured. Average pull-off force values were of the same order as expected values based on JKR theory. Pull-off force measurements did not show a strong prediction of imminent adhesive failure. This may be due to the sudden increase of adhesion at the end of life or the possible rate dependence of pull-off

force measurement. Contact strain hardening as indicated by normalized stiffness measurements did not occur in every gold test. There may be competing effects of strain hardening and annealing occurring in the contact during cycling. Contact interference measured was two-times greater than a prediction based on previous analytic work [59]. The difference was ascribed to plasticity effects not included in the analysis or uncorrected deformation on the top of the cantilever due to microprobe loading. Time-dependent behavior of the contact material was also observed. This behavior was highest at the beginning of tests and then settled down to a constant value over the life of the contact. This is likely due to contact heating of the material caused by electric current passing through the contact constriction.

The measurement results were also categorized and analyzed by grouping similar lifetime failures together. Measured contact performance data for Type I (shorter lifetime), Type II (mid-life), and Type III (longer life) results were correlated, averaged and plotted to show differences based on lifetime. For gold, pull-off force, threshold force and distance, time-dependent behavior and energy absorbed all showed differences based on lifetime categories. Type I early life adhesive failures showed larger initial pull-off forces than the other two types. This indicates higher initial adhesion leading to the early failure of Type I contacts. The longest lasting Type III failures showed the largest initial threshold force when compared to the other two categories while demonstrating the smallest initial time dependent deformation. These results indicate that initial surface condition (e.g. roughness and contamination level) may be very important to ultimate contact lifetime. It is possible that dislocation barriers were created during early cycling of Type III long-life contacts which reduced time-dependent deformation and plastic deformation of the surface, reducing surface smoothening and therefore slowing the growth of contact adhesion. The Type II mid-life failures showed constant energy absorbed by the contact which indicated different plastic deformation behavior when compared to the others. There may have been sub-surface damage in these contacts which led to thin film delamination failure when the adhesion between contact surfaces increased.

No method to predict the lifetime of a specific contact prior to cycling was found. Environmental factors such as surface contamination and slight changes in the number and location of dislocations in the contact thin film likely affected the results and performance of the contacts. It appeared that the rate of smoothening of the contact surfaces affected the lifetime, with surfaces which took longer to become smooth lasting longer. Wide scatter in lifetime results is also seen among manufactured MEMS switches on the market today [65, 171]. Further research into the failure mechanisms and behavior of microcontacts is needed to specifically and quantitatively determine the factors leading to contact lifetimes in order to develop a predictive capability. The next chapters will discuss other materials tested and the measurements accomplished and will compare results to the gold results given here.

IX. Gold-Ruthenium Alloy Contact Measurements

This chapter presents results of testing on gold-ruthenium alloy contacts (Au5%Ru). The tests were conducted using the setup and method described in previous chapters. First, all tests run on Au5%Ru are summarized. Then, the failures are categorized and discussed. Trends, measurements and results for Au5%Ru tests are presented, analyzed and compared to gold-gold testing results.

9.1 Contact Lifetime and Failure Analysis

Au5%Ru was chosen as a contact material because of the two-phase nature of its microstructure and value as a useful contact material. Two phase materials were of interest due to their higher wear resistance, lower adhesion, and better high temperature performance when compared to single-phase alloys. Previous research has also indicated that Au5%Ru has potential as a contact material due to the reduction in contaminant creation during cycling when compared to pure ruthenium [37]. Table 9.1 gives an overview of testing accomplished on Au5%Ru contacts during this study. Twelve tests were accomplished with this contact material. Six tests were run to contact failure and one test was stopped before contact failure in order to examine its pre-failure contact surface. All tests were run with 400 μN contact force and failed in contact adhesion mode. One test was also run with no current to measure results and to attempt to isolate current effects. One test was run in a "cycling only" mode while only measuring contact resistance without actuation of the simulated switch by use of the nanoindenter microprobe. Five tests failed early due to computer memory overload, as described previously in Section 7.6.

The lifetime tests of the Au5%Ru contacts can be divided into two categories: shorter life adhesive failures ($< 210,000$ cycles) and longer lifetime adhesive failures ($> 6 \times 10^6$ cycles). Fewer Au5%Ru tests were run than baseline gold tests, but some trends did emerge. The shorter lifetime results showed smoothening of the contact surfaces and less overall contamination was evident on the contacts than in the longer lifetime tests. The longer lifetime tests showed wear fragments and an annular ring of

Table 9.1: Test summary of Au5%Ru micro-contact testing.

Contact ID	Contact Material	Contact Force (μN)	Initial Contact Resistance (Ω)	Failure Type	Number of Cycles to Failure (# Cycles)
0210-3_12	Au5%Ru	400	NA	Adhesion	70,000 (no current)
0801-3_8	Au5%Ru	400	10.7	No Fail	stopped at 80,000
0210-3_7	Au5%Ru	400	10.7	Adhesion	130,000
0210-3_11	Au5%Ru	400	10.5	Adhesion	140,000
0801-1_1	Au5%Ru	400	9.9	Adhesion	210,000
0602-2_3(I)	Au5%Ru	400	13.2	Adhesion	6.25×10^6
0602-2_4(J)	Au5%Ru	400	12.3	Adhesion	6.29×10^6
0801-3_9	Au5%Ru	NA	10.7	Overload	NA
0801-1_5	Au5%Ru	NA	9.2	Overload	NA
0210-3_8	Au5%Ru	NA	11.2	Overload	NA
0210-3_10	Au5%Ru	NA	11.4	Overload	NA
0602-2_2(H)	Au5%Ru	NA	15.1	Overload	NA

a dark substance which appears to be a contaminant. Initial surface roughness of the contacts may have played a role in contact lifetime differences. The surfaces which were smoother before cycling appear to have failed earlier than surfaces which had higher initial surface roughness. The initial surface roughnesses are different due to slight differences in processing and etching of the silicon cantilevers. The uncontrolled lab-air testing environment and the amount of contaminant on the contact may have also played a role. Contaminant on contact surfaces due to adsorption from the environment likely reduced adhesion during cycling thus avoiding early contact failure. There were no cases of the contact film separating from the surface of the contact bump and adhering to the bottom contact strike plate. This is likely due to the higher yield strength of the Au5%Ru material and a lesser likelihood of subsurface damage in the material during cycling. However, actual MEMS switches show a broad range of lifetimes in testing so a variation in lifetime results is expected [65, 171].

An example of the shorter lifetime adhesive failure contact surface is shown in Figures 9.1, 9.2 and 9.3, with the image of the contact bump before testing shown in Figure 9.1. The image of the bump after cycling is shown in Figure 9.2 and the bottom contact surface on the strike plate is shown in Figure 9.3. The contact shows

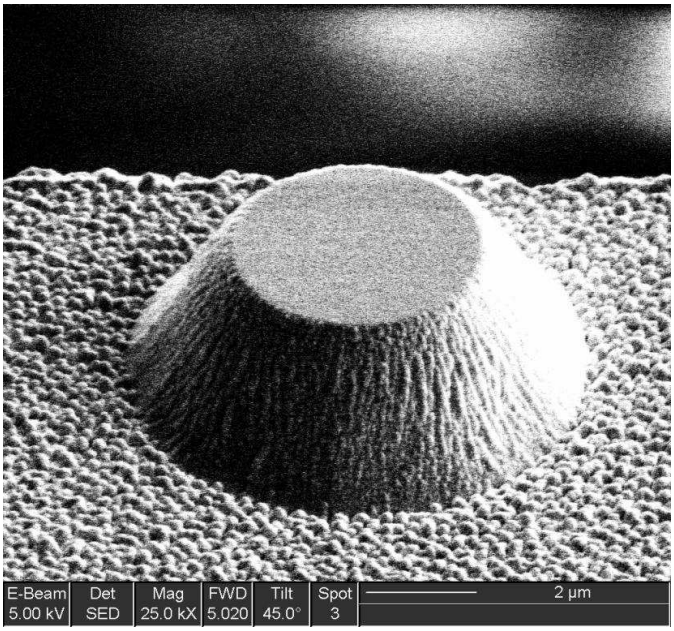

Figure 9.1: Au5%Ru contact bump (0210-3_7) before testing. The after test image is shown in Figure 9.2

a smoothing effect, there appears to be evidence of grain growth and a small amount of contamination in an annular ring around the contact area is visible and can be seen in Figure 9.3. The contact likely failed due to the smoothening of the contact area and the resultant increase in adhesion. The low amount of contamination also likely helped increase the adhesion force. Note that it is well established that contamination on metal contacting surfaces reduces the adhesion between the surfaces (e.g. [19,199]). This failure surface is most similar to the Type III failures described in gold contacts in the previous chapter. This shorter lifetime Au5%Ru contact failure will therefore be described as a Type IIIB failure.

An example of the Au5%Ru longer lifetime adhesive failure contact surfaces is shown in Figures 9.4, 9.5 and 9.6, with the precycling image of the bump tested shown in Figure 9.4, the bump after cycling in Figure 9.5 and the strike plate in Figure 9.6. The contact bump and contact area on the strike plate show an annular ring of contamination and wear debris surrounding the contact location and platelike wear features on the strike plate. Wear debris is visible because harder materials are

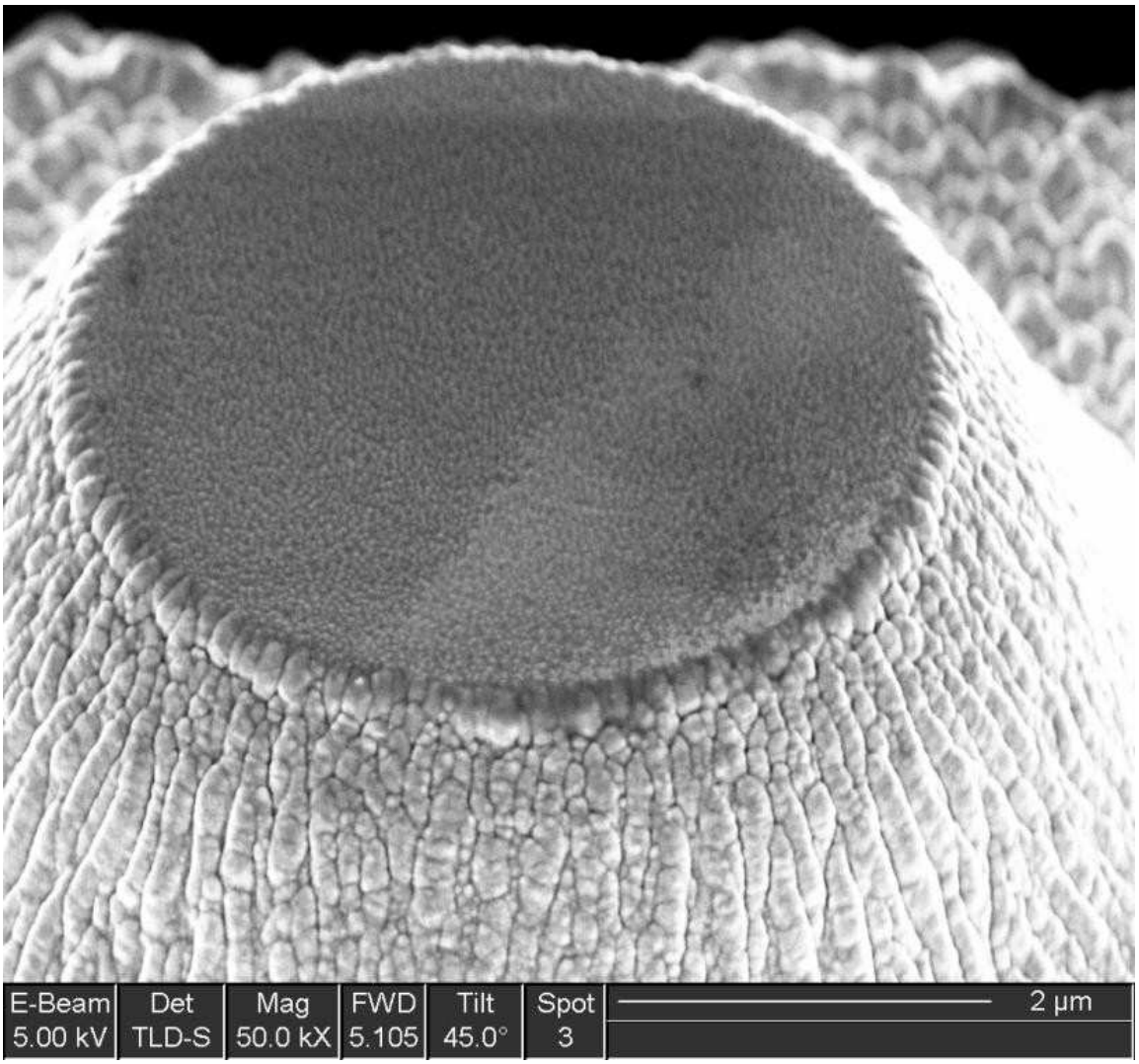

Figure 9.2: Au5%Ru contact bump (0210-3_7) which failed in adhesion after 140,000 cycles. Very little wear or deformation is visible.

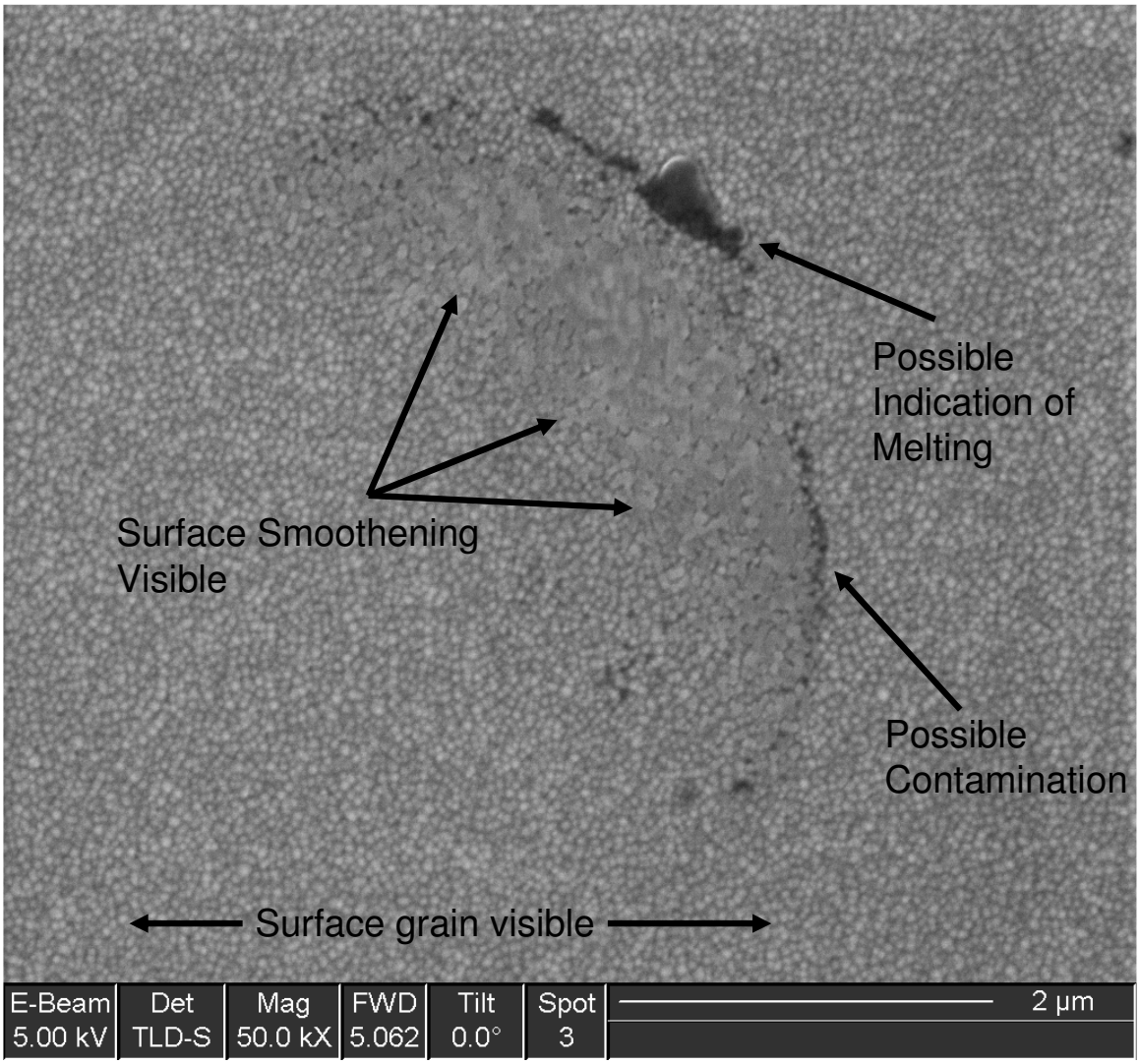

Figure 9.3: Au5%Ru contact location on strike plate (0210-3_7) which failed in adhesion after 140,000 cycles. Smoothed metal and a small amount of contamination is visible, with possible indication of melting on the edge of the contact area.

Table 9.2: Description of Au5%Ru failure types demonstrated and categorized in this study. Lifetimes are given for demonstrated values in respective materials.

Failure Type	Description	Material Demonstrated	Lifetime (# Cycles)
IIIB	Brittle separation, smoothed surfaces	Au5%Ru	130,000-210,000
IV	Worn down bump, wear fragments	Au5%Ru	$\sim 6 \times 10^6$

more likely to show brittle fracture mechanisms such as separation of wear debris rather than ductile necking. This contact also survived many more cycles than any of the gold contacts tested. This failure surface is completely different than the previous failures analyzed in gold contacts and thus will be described as a Type IV failure. The contact surface does not show ductile necking or other ductile separation features. Therefore, it appears that the longer-lived Au5%Ru contacts experienced continued brittle separation. The brittle nature of separation could explain why some contacts such as this one have longer lifetimes. Brittle and ductile separation characteristics are described in [37]. Brittle separation is preferable to ductile separation as there is less surface damage associated with brittle separation. The presence of contamination on the contact also could reduce cycling adhesive force and therefore increase the life of the contact under test. Note that while large amounts of resistive contamination is detrimental to switch operation, it has been established that small amounts of contamination can reduce friction and adhesion of contacts [103]. As Holm stated in his classic work, "Films on contacts create an electric resistance that can cause failure in contact applications. On the other hand, contact films diminish both cold welding and friction and therefore are desirable in many cases providing they do not harm the desired electric performance." [103]

9.1.1 No Current Test. One test was run with a Au5%Ru contact without current to analyze the effect of current on contact results. The test was run for 440,000 cycles, however, a contact adhesion failure was detected in the results after 70,000 cycles. After 70,000 cycles the contact did not experience further cycling because it failed to open and moved with the strike plate. This was determined by

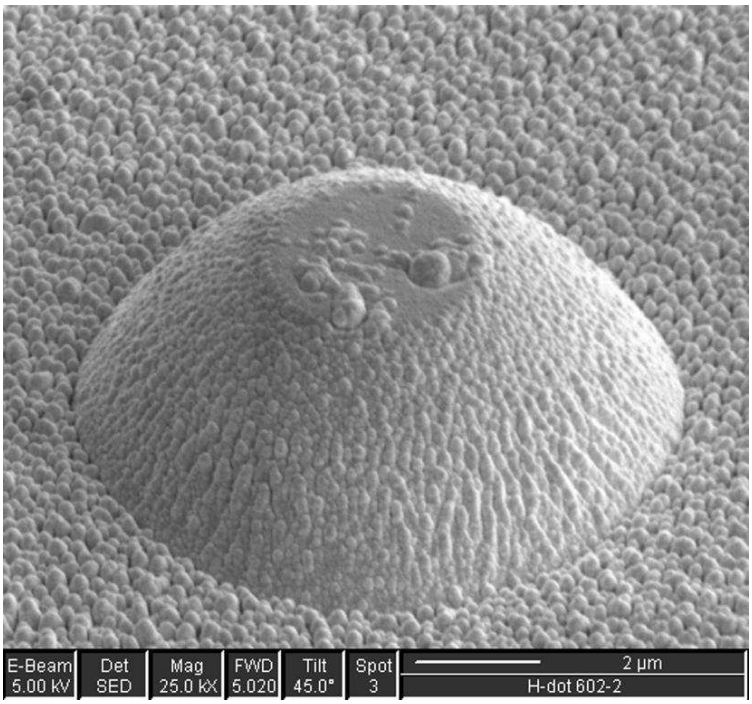

Figure 9.4: Au5%Ru contact bump before testing where it failed in adhesion after 6×10^6 cycles. Note rougher surface when compared to Figure 9.1

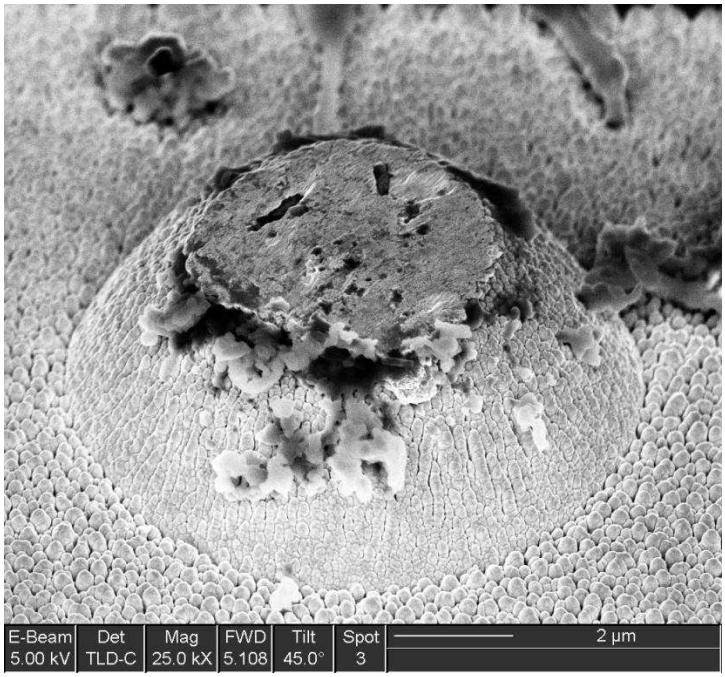

Figure 9.5: Au5%Ru contact bump which failed in adhesion after 6×10^6 cycles. Contamination and presence of wear fragments are visible. This contact survived many more cycles than long-lived gold contacts and harder materials are more likely to show brittle failure mechanisms.

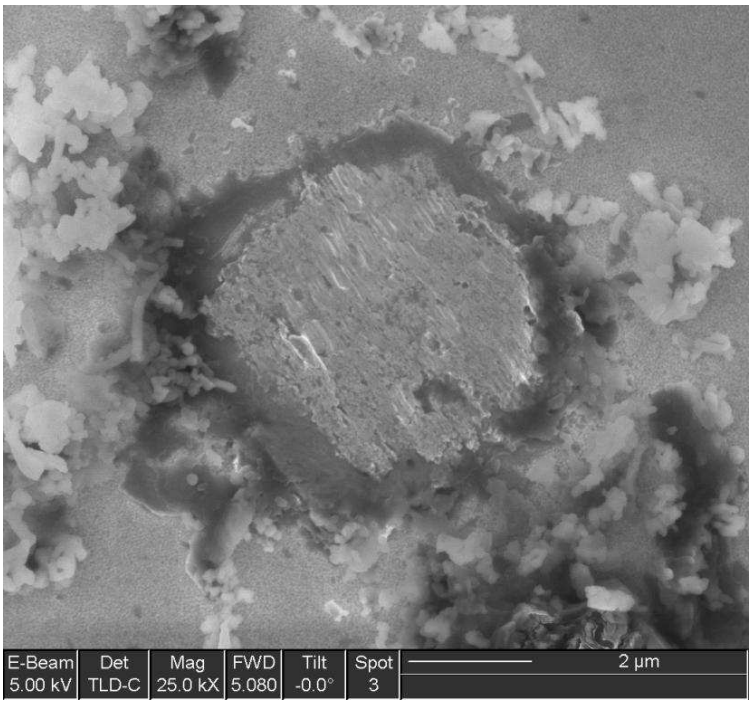

Figure 9.6: Au5%Ru bottom contact location on strike plate which failed in adhesion after 6×10^6 cycles. Contamination and wear debris are visible.

analyzing the test data which showed that there was no distance between detection of the cantilever and the strike plate at 70,000 cycles into the test. This contact failed in adhesion, possibly due to contact smoothening. The contact bump before cycling is shown in Figure 9.7. After cycling images of the contact are shown in Figures 9.8 and 9.9. There appears to be very little deformation in these images, and a small amount of black contamination. The appearance of contamination in this test suggests that electric current is not a necessary condition for the contact to become contaminated during cycling and that electric current is not a necessary condition for adhesion failure of the contact. Therefore, while current may play a role in adhesive failures of micro-contacts, mechanical behavior of the contact surface is an important factor in contact adhesion growth and therefore contact lifetime.

9.1.2 Reduced Contamination Compared to Pure Ruthenium. A test on a pure ruthenium contact was also accomplished in lab air in order to compare results to the gold-ruthenium alloy tested. The tests were initially run with 400 μN contact

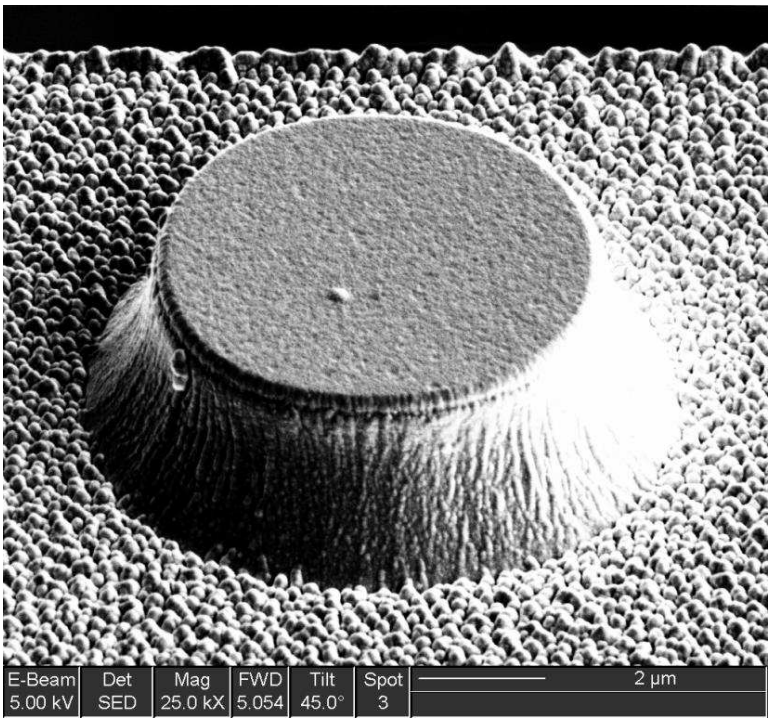

Figure 9.7: Au5%Ru coated contact bump before 70,000 cycle adhesion failure during no current test.

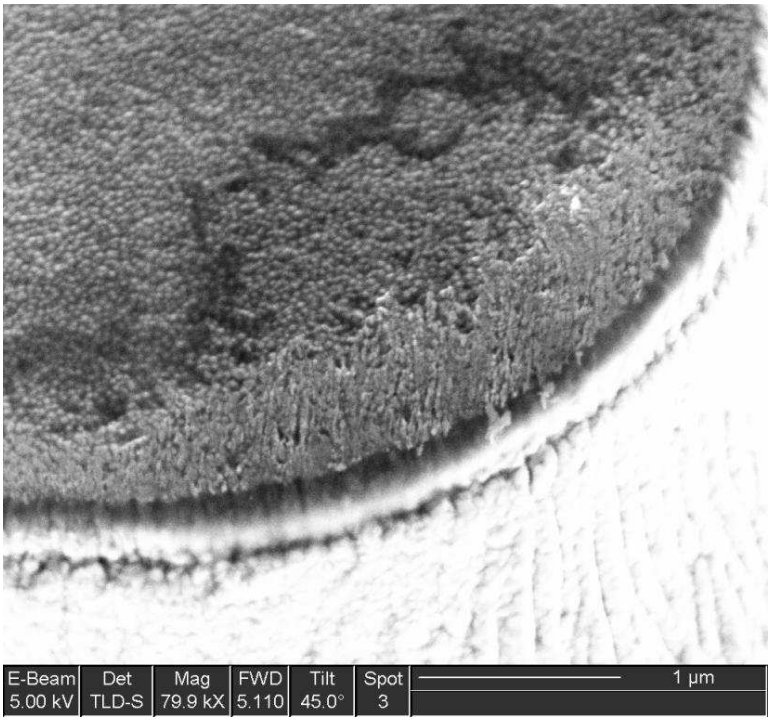

Figure 9.8: Au5%Ru coated contact bump after 70,000 cycle adhesion failure during no current test.

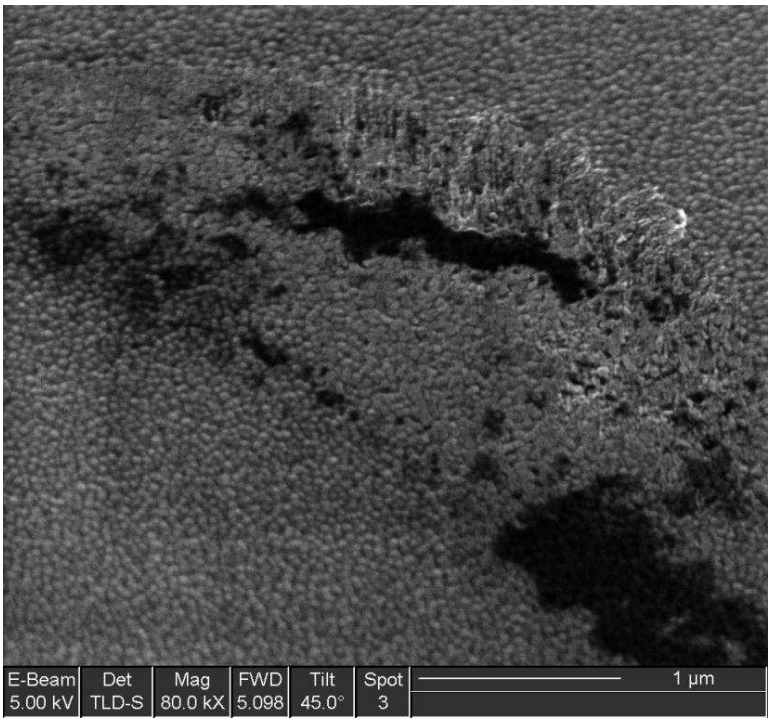

Figure 9.9: Au5%Ru coated contact surface on strike plate after 70,000 cycle adhesion failure during no current test. Shows that current is not necessary for contamination to occur.

force, in exactly the same manner as other testing done during this study. The contact resistance through the ruthenium-ruthenium contacts was approximately 20 Ω which was much higher than all other tests. As expected, this contact created a large amount of contamination during cycling. In fact, so much contamination was created that the contact resistance was clearly affected by excessive contamination. Other measurements were affected by the contamination, including threshold force and distance and contact adhesion. The microprobe was not able to push the simulated switch into electrical contact during every measurement using only a contact force of 400 μN. However, images of Ru contacts tested did prove valuable in determining that the cause of the test issues was contamination creation on the contacts. Figure 9.10 shows the ruthenium coated contact before cycling. The cantilever was broken during testing so no after cycling image is available. Figure 9.11 shows the bottom contact after 1.2 $\times 10^6$ cycles and high resistance failure. Figure 9.12 shows contaminant on the bottom contact after 500,000 cycles. These images show the large amount of contam-

ination created during cycling in laboratory air with ruthenium-ruthenium contact pairs and explains why the 400 μN microprobe contact load was unable to push the cantilever into electrical contact. It is unlikely that melting is indicated in this image, as the melting point of ruthenium is significantly higher than that of gold (2310 °C vs. 1064 °C for bulk material). This contaminant is possibly the "carbonaceous" compound or "frictional polymer" described in previous research [29, 78, 101].

One test was run with a constant 400 μN cycling contact load and a routine was written for the nanoindenter which automatically increased the microprobe load on the contact up to a maximum of 20 mN in order to provide enough contact force to ensure electrical contact through the large amount of contamination created. This was done in order to see how much more contact force would be required to push the ruthenium into electrical contact after contamination had formed on the contact and what the effect on contact evolution would be. Figure 9.13 shows the contact contamination caused during a test with up to 20 mN contact load. The circular contact area can clearly be seen. Also, in order to determine where the contaminant was being created and whether the Ru contact bump was being damaged, several cycling tests were run using the same Ru coated cantilever moved to virgin locations on the strike plate after each high resistance failure. That is, the contact was run to failure, then the cantilever was moved to a new location on the strike plate and the test was repeated. The measured contact resistance results from these three tests using the same cantilever on three different contact locations is shown in Figure 9.14. The third test was not run to failure. It is believed that the contaminant was mostly generated on the lower contact surface because successive tests using the same cantilever moved to a different location on the ruthenium strike plate were able to generate the same contact resistance as if both contacts were new. This can be seen in Figure 9.14. Note that the compliance resistor used for the pure ruthenium tests was 540 Ω. The Au5%Ru clearly has a smaller contamination problem than that experienced by pure ruthenium contacts. Further testing on ruthenium contacts was not pursued because

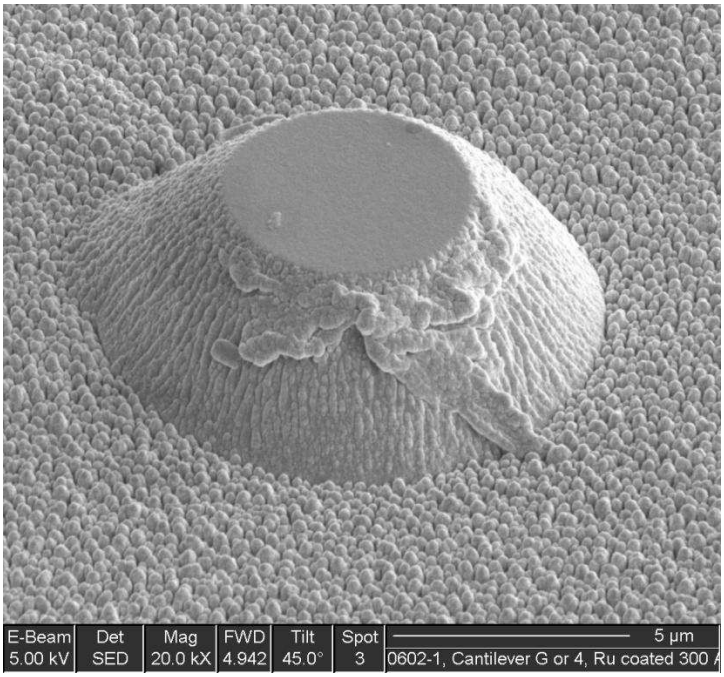

Figure 9.10: Ru coated contact bump before cycling testing.

of the high measured contact resistance and significant contamination of the contacts in lab air.

The alloying of ruthenium with gold increased contact material hardness and reduced contamination on the contacts during cycling when compared to results of pure ruthenium contacts. At the same time, the levels of contact contamination from environmental sources of the gold-ruthenium alloy was increased when compared to pure gold contacts. The higher hardness and resistance to wear of Au5%Ru due to its two-phase microstructure explain why the Au5%Ru material lasted longer than gold on average during the study. The separation of the Au5%Ru-Au5%Ru contacts is also more likely to be in a brittle mode as well. The tradeoff with these advantages when compared to gold, however, is an increase in contact resistance as discussed next.

9.2 Contact Resistance

The contact resistance during Au5%Ru tests ranged from 9.5-11 Ω and the average resistance was 10.8 Ω. Au5%Ru contact resistance with a contact force of 400

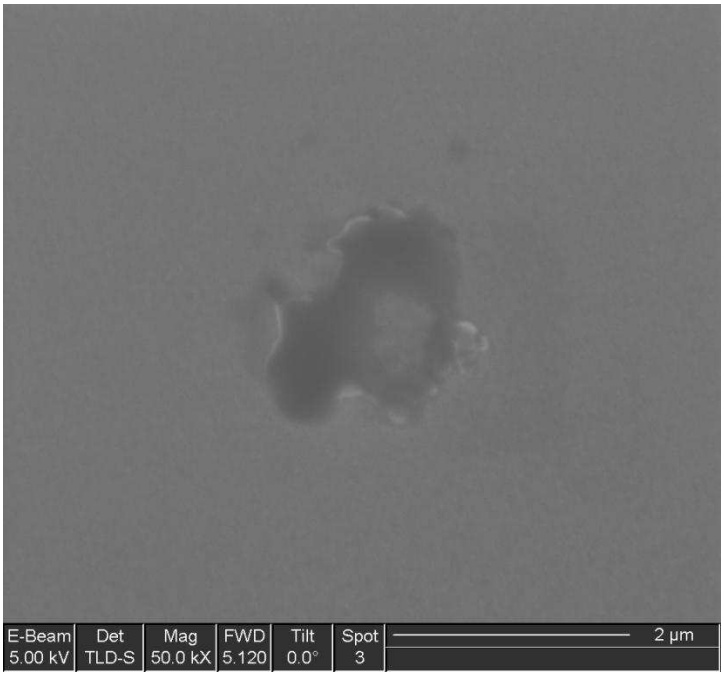

Figure 9.11: Ru coated strike plate showing contamination due to 1.2 $\times 10^6$ contact cycles at 400 μN contact load. This is test 0602-1_4 Test 1 shown in Figure 9.14 and was run to high resistance failure. The amount and appearance of contamination was similar between Tests 1 and 2.

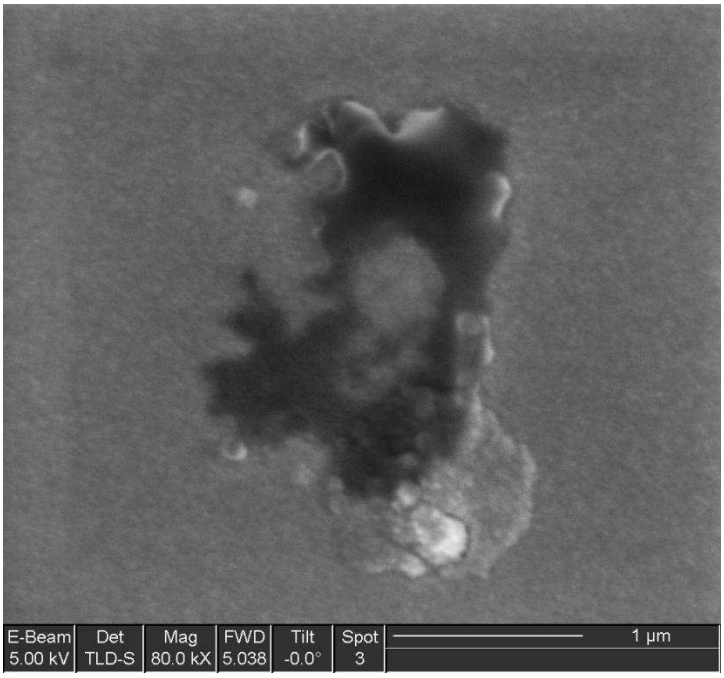

Figure 9.12: Ru coated strike plate showing contamination due to 500,000 contact cycles at 400 μN contact load. This is test 0602-1_4 Test 3 shown in Figure 9.14 and was not run to failure.

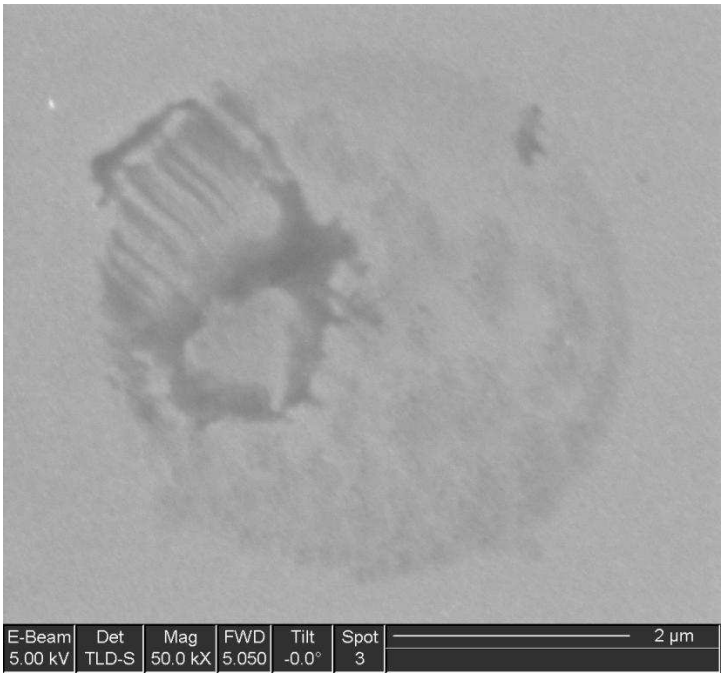

Figure 9.13: Ru coated strike plate showing contamination during cycling at 400 μN with approximately 20 mN microprobe actuation load.

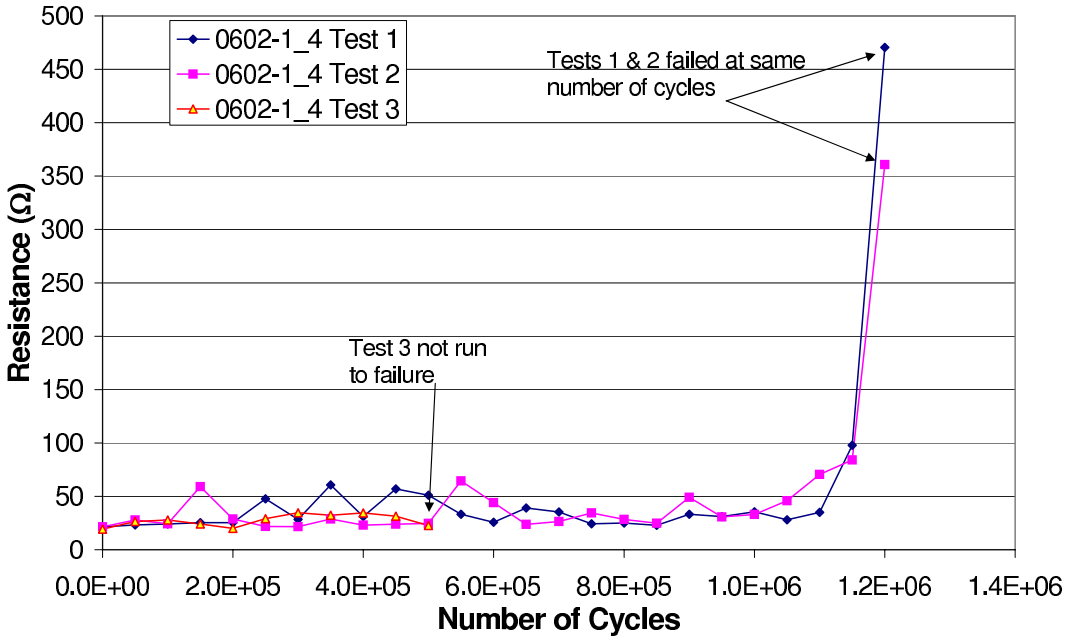

Figure 9.14: Contact resistance measured for three tests of ruthenium contact. The same contact bump was used on each of three different strike plate locations to generate this data. Note that contact resistance was reducued when failed cantilever was moved to a clean strike plate location and run again.

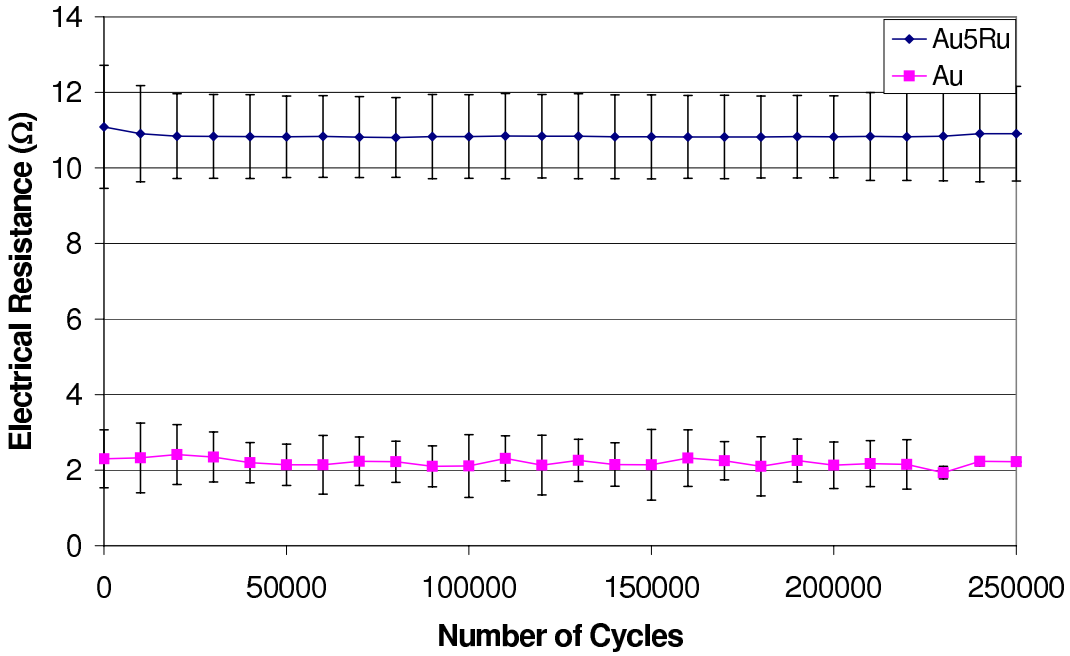

Figure 9.15: Average resistance measured during nanoindenter testing Au5%Ru contacts compared to average gold results.

μN is estimated at 8.4 Ω using the Holm equation (Equation 2.29). The measured contact resistance is higher than predicted because it included parasitic resistances such as losses in wirebonds, solder joints, and the terminal strip. It may also contain a component due to surface contamination. However, the only changes to the setup during measurement occurred at the contact, so changes in contact resistance were detectable. The resistance measured during Au5%Ru tests was significantly higher than the resistance measured during the gold-gold contact testing. This is due to the higher resistivity and hardness of the Au5%Ru material, as well as the higher parasitic resistance created during wirebonding and soldering to the Au5%Ru material. A comparison between the contact resistances measured for gold and Au5%Ru is shown in Figure 9.15. A comparison of resistance from two long-term tests of gold and Au5%Ru is shown in Figure 9.16. These results demonstrate the resistivity differences and therefore contact resistance differences between the two materials.

The contact resistance measured during testing generally decreases with cycling. This can be clearly seen in the resistance measurements shown in Figure 9.17 which

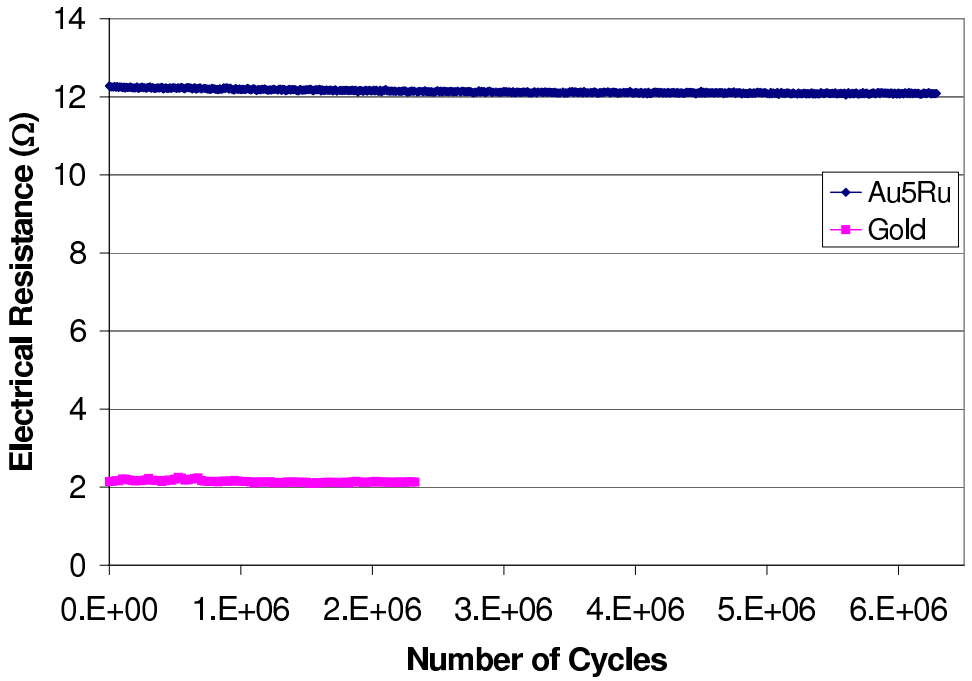

Figure 9.16: Measured contact resistance compared between one long-term Au5%Ru test and one long-term gold test.

were taken during the "cycling only" test done on one of the Au5%Ru contacts. Microprobe actuation of the simulated switch was not used during this test but this is a good example of resistance measurements obtained during a long-term alloy test. The resistance shows a slight reduction, and appears to be approaching a minimum value asymptotically when the contact fails in adhesion at 6.29×10^6 cycles. This result is consistent with previous studies which have noted that the contact resistance in MEMS switches decreases with repeated switching [9, 27, 92, 115]. This indicates that the simulated switch behavior in this study exhibits similar behavior to switches tested in other studies. This reduction in resistance effect is attributed to a small increase in contact area due to plastic deformation (e.g. [9]). This effect could also be caused by a temperature increase at the contact spot sufficient to cause annealing of dislocations in the contact material, thus reducing contact resistance through contact softening [115].

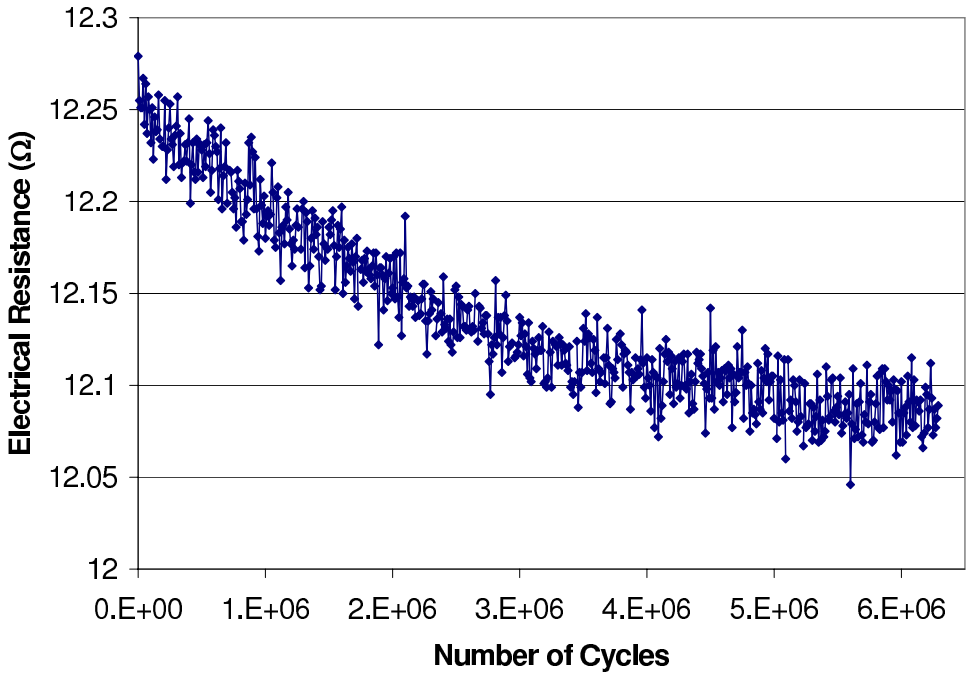

Figure 9.17: Measured contact resistance during one long term Au5%Ru cycling only test. This result shows the downward trend of measured resistance as the contact cycles. Resistance was measured every 10,000 cycles and microprobe actuation was not used.

9.3 Contact Adhesion

Detection of contact adhesion failure using in-contact and out-of-contact resistance was described in Section 7.3.5 and is shown graphically for a gold contact test in Figure 8.21 and a Au5%Ru contact test in Figure 9.18. The criteria used to detect contact adhesion failure is described in Section 6.2.5 and the ability of this test apparatus to automatically detect contact adhesion failure is described and demonstrated in Sections 7.2.1, 7.4.3 and 8.3. All complete Au5%Ru tests failed in adhesion. Figure 9.19 shows the lower average pull-off force measured for the Au5%Ru contacts compared to results for gold pull-off forces. This result shows that harder materials do not have a higher adhesive force as stated in [132] and [202]. This result indicates harder metals may have lower self-adherence when compared with softer metals. All six of the Au5%Ru tests successfully run to failure ended in adhesive failure, with an average lifetime of 2.2×10^6. This indicates that harder contact metals are desirable

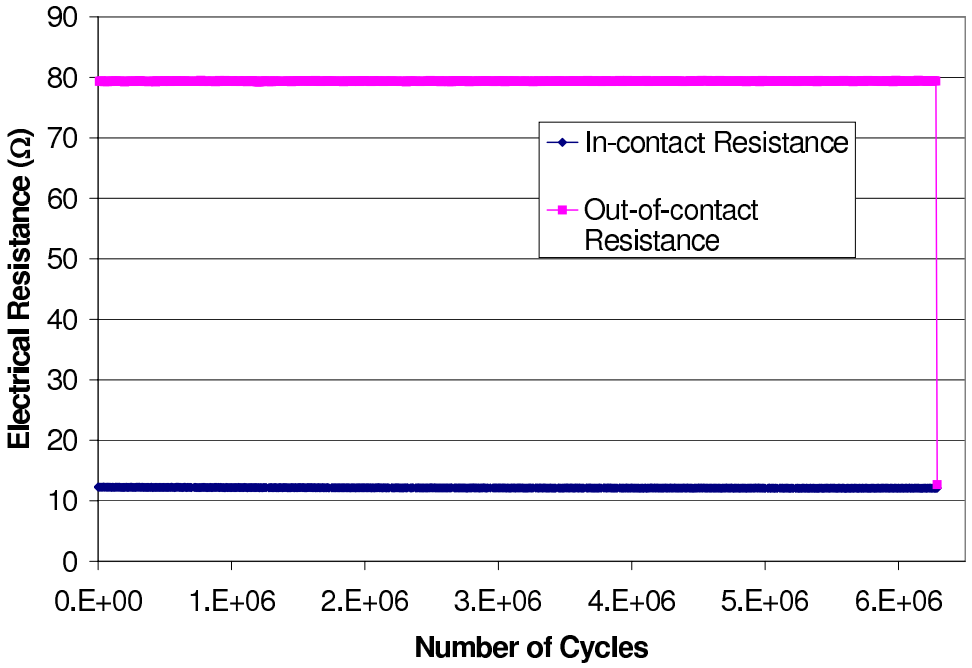

Figure 9.18: Long-term test example showing adhesive failure at 6.29×10^6 cycles. Note that this indicates that restoring force of cantilever was unable to pull contact surfaces apart, thus the adhesive force was greater than the restoring force(400μN in this test).

as MEMS contact materials to reduce contact adhesion, as well as to reduce damage to contact surfaces due to cycling.

The average pull-off forces measured during the cycling experiments run on Au5%Ru contact material were approximately 25 μN. The pull-off values stayed relatively constant during the first 250,000 cycles. However, contacts which failed in adhesion did generally show a slight upward trend in pull-off force in the measurements prior to adhesive failure. This can be seen by the Au5%Ru line in Figure 9.20 which is a long-term test result. The lack of a large increase in pull-off force just before failure likely indicates that there is a sudden increase in adhesion which occurs more rapidly than the measurement interval used in testing. The measurement of pull-off force may also be rate sensitive. Pull-off was measured at a rate of 50 μN/s in all cases. Note that the pull-off force in this long-term test is lower than the average pull-off force shown in Figure 9.19. The lower pull-off force in the long-term test explains why this contact exhibited a long lifetime before adhesive failure. Lower pull-off forces

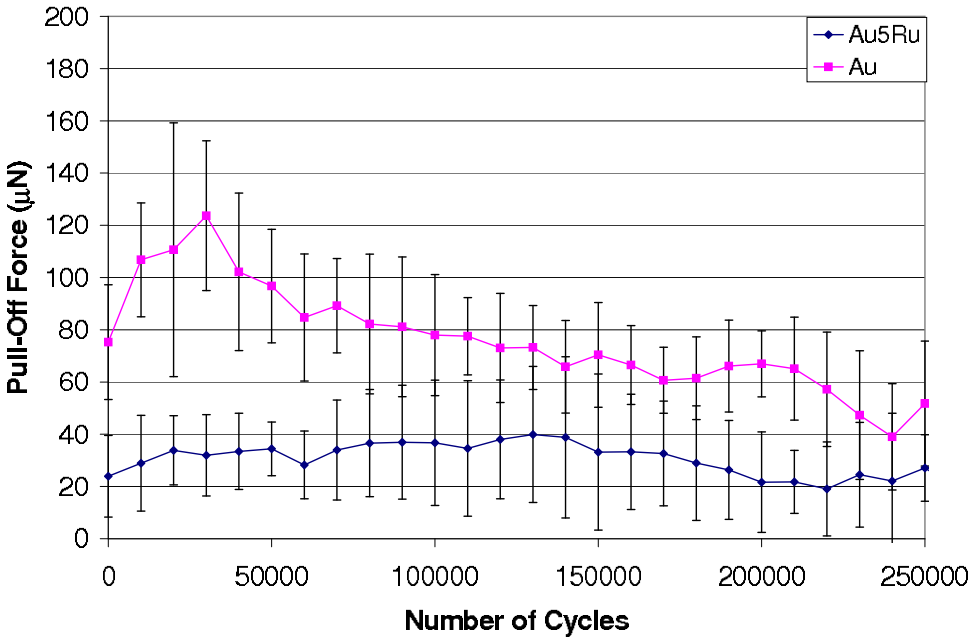

Figure 9.19: Average pull-off force measured during nanoindenter unloading of Au5%Ru contacts. Unloading rate was 50 μN/sec.

directly relate to less contact surface damage. Also note that the Au5%Ru long-term pull-off forces are lower in magnitude than a comparable long-term gold test.

9.4 Threshold Force and Distance

The threshold force required to push the Au5%Ru bumps into ohmic contact was higher when compared to the threshold force required for gold contacts as shown in Figures 9.21 and 9.22. This result is as expected, because it is clear that a harder metal would require higher contact force to cause enough deformation to ensure ohmic contact. The average threshold force value for Au5%Ru contacts centers around approximately 100 μN. However, the Au5%Ru showed significant variability in the threshold force. This can be seen by the error bars in Figure 9.21 and the large variability between subsequent measurements in Figure 9.22. Note that the negative error bars were not included in the plot for clarity. The error bars indicate one standard deviation in value from the mean for each data point measured. The larger deviations in Au5%Ru when compared to the relatively small deviations in gold are attributed

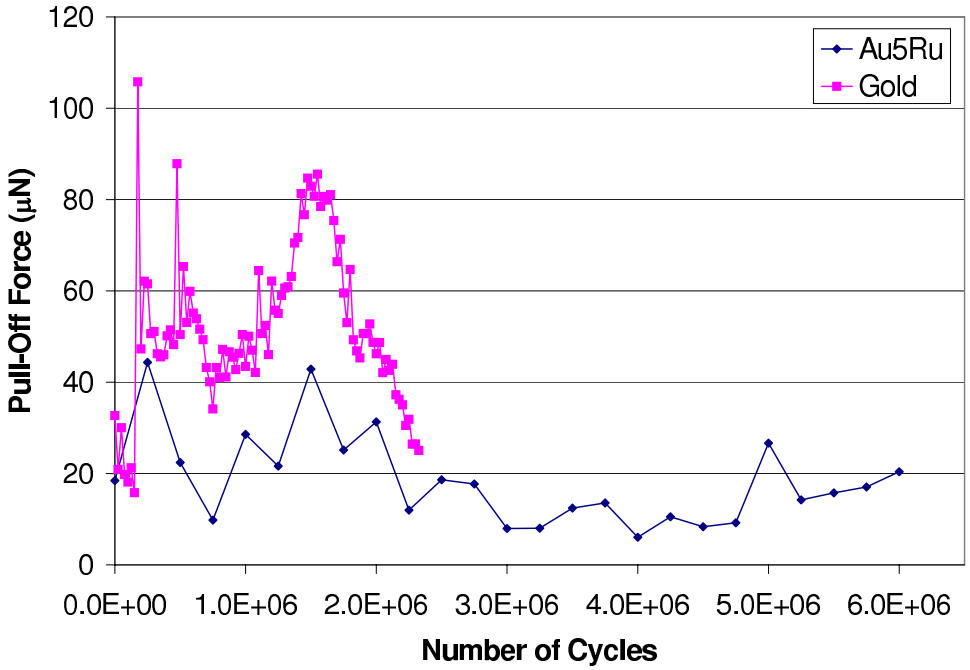

Figure 9.20: Example of long-term Au5%Ru and gold pull-off force trends during cycling. Note that because there is no measured large increase in pull-off force at the time of contact adhesive failure, this chart indicates that either the growth in adhesive force near failure is sudden or occurs at a rate faster than the measurement interval used in this test.

to the contamination occurring on the surface during contact. More contamination is created on Au5%Ru contacts than gold because of ruthenium's reactivity, even when mixed with gold. The Au5%Ru alloy has a higher reactivity than gold due to an incomplete d-band electron structure, when compared to the fully filled d-band structure in gold. The partially filled d-band structure makes it easier for the material to adsorb molecules from the air. See Chen for a description of the D-Band theory of Hammer and Norskov [37]. The higher reactivity of Au5%Ru will make it more prone to become contaminated while cycling in lab air when compared to pure gold. The large deviation in threshold force and threshold distance is due to the varying conditions in lab air, including deviations in temperature and humidity which could have a large effect on surface contamination. Fritting of the surfaces due to hot-switching could also play a role in the variation of threshold force between measurements.

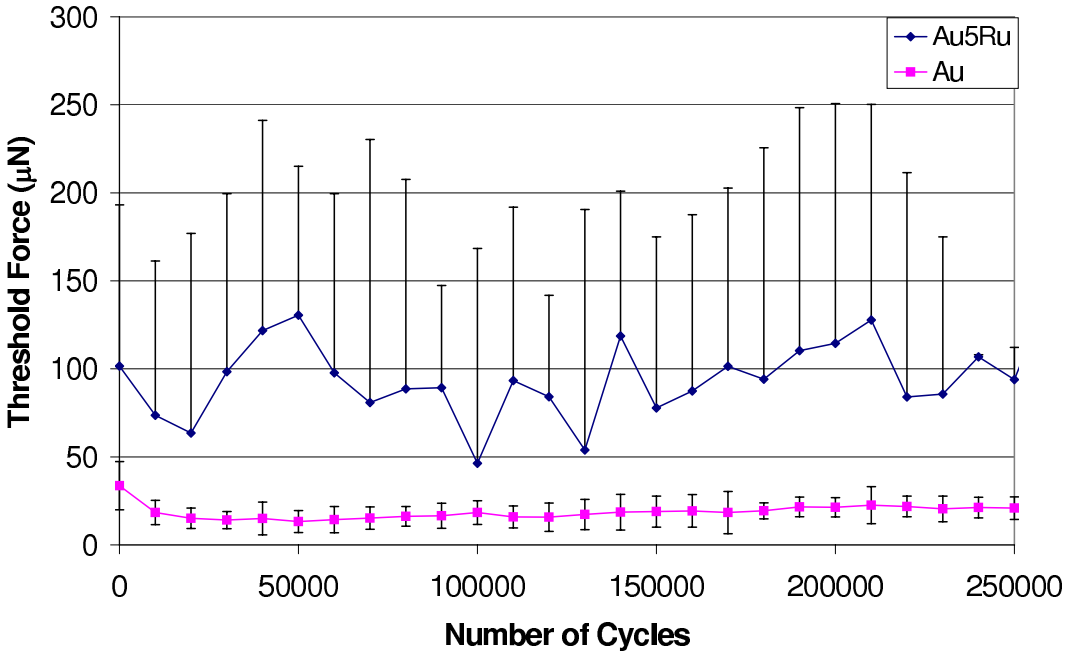

Figure 9.21: Average threshold force measured during nanoindenter loading of Au5%Ru contacts. Note that negative error bars for Au5%Ru are not shown for clarity.

The contact deformation (or interference) required for ohmic contact after the point of contact between the plate and the contact bump, defined as threshold distance, is not as variable as the threshold force. Also, the average threshold distance measured for the first 250,000 cycles of testing is similar between Au and Au5%Ru contacts as shown in Figure 9.23. This indicates that the physical proximity required between surfaces for stable electrical contact is constant between materials. The relative stiffness of the contact materials is evident in that more contact force is required to deform the Au5%Ru contact surface when compared to the contact force required to deform gold that same distance. The long-term threshold distance for Au5%Ru is also quite variable as shown in Figure 9.24 which indicates that changes to Au5%Ru contact surfaces occurred. This analysis is supported by Figures 9.5 and 9.6 which show contact wear processes changing the contact surfaces were at work in the long-term Au5%Ru test.

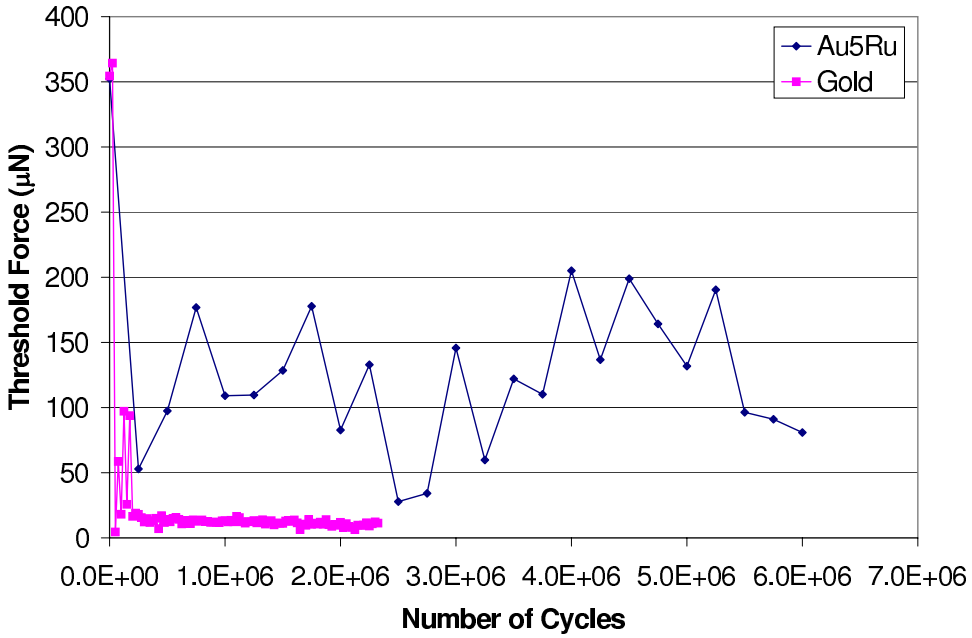

Figure 9.22: Example of Au5%Ru long-term threshold force trend compared to gold.

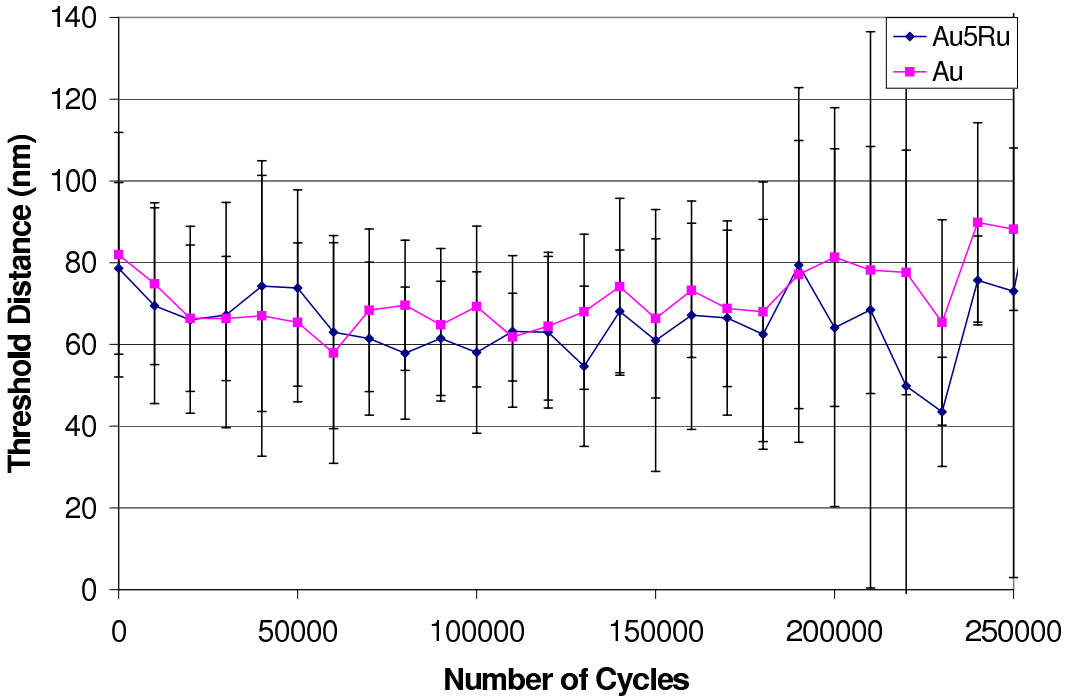

Figure 9.23: Average threshold distance measured during nanoindenter loading of Au5%Ru contacts.

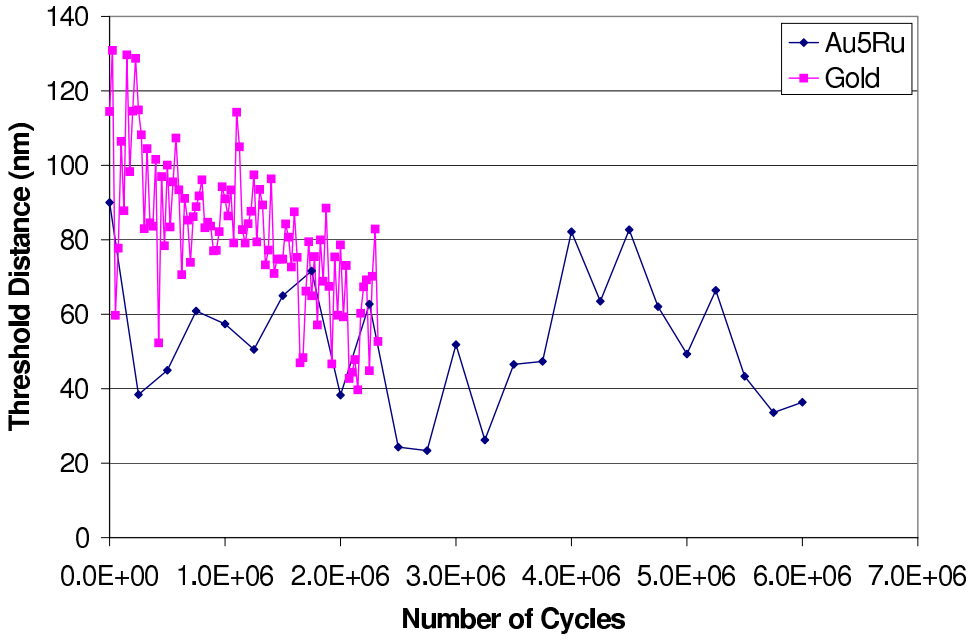

Figure 9.24: Example of Au5%Ru compared to gold long-term threshold distance trend. Note that the threshold distance is decreasing as the contact cycles.

9.5 Contact Hardening

It is possible that the properties of the contact material could change during cycling. One possible effect of cycling on the contact may be strain hardening of the contact material due to plastic deformation caused by impact and/or loading. The slope of the contact unloading curve was calculated during each microprobe measurement. The measurements taken during microprobe actuations during each test were normalized by the first stiffness measurement during that test. The average normalized stiffness trends of both gold and Au5%Ru contacts during cycling are shown in Figure 9.25. The results for Au5%Ru are very similar to the results for testing of gold contacts. There is little difference between results for harder and softer materials. The average strain hardening results are not conclusive. There are possibly competitive mechanisms of strain hardening and annealing due to contact heating at work.

One example of a long-term Au5%Ru test is shown in Figure 9.26 compared to a long-term gold test. The Au5%Ru test in this case does show contact softening. This

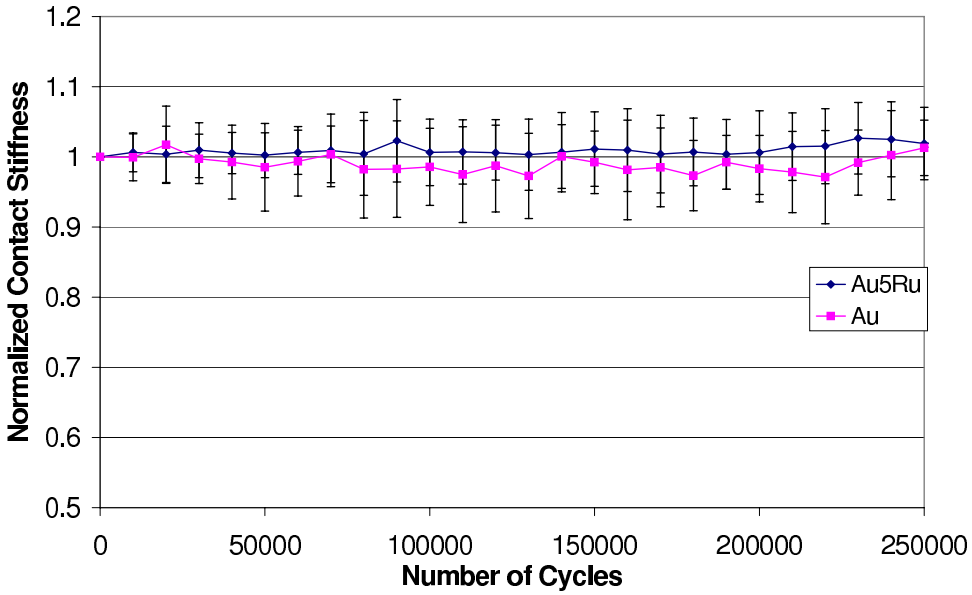

Figure 9.25: Average normalized contact stiffness change measured during nanoindenter loading of Au5%Ru contacts. Normalized by the first stiffness measurement of each test.

result suggests contact damage occurring to the contact under test, which matches the result indicated in the images of this contact showing wear debris and damage to the surface in Figures 9.5 and 9.6. It could also indicate contact heating.

9.6 Contact Interference

The average contact interference, or penetration, of Au5%Ru stays relatively constant at approximately 0.05 μm as the contacts cycle. This is almost half of the average interference for gold-gold contacts as can be seen in Figure 9.27. This result is due to the fact that gold is a softer metal than Au5%Ru and it is expected that Au5%Ru would deform less under the same contact load. Note that all contact interference measurements in this study were corrected for deformation caused on the top of the silicon cantilever by the microprobe. Displacement of 60 nm was subtracted from each interference measurement to correct for this deformation.

One example of the contact interference for a long-term Au5%Ru test compared to a gold long-term test is shown in Figure 9.28. The Au5%Ru long-term test shows

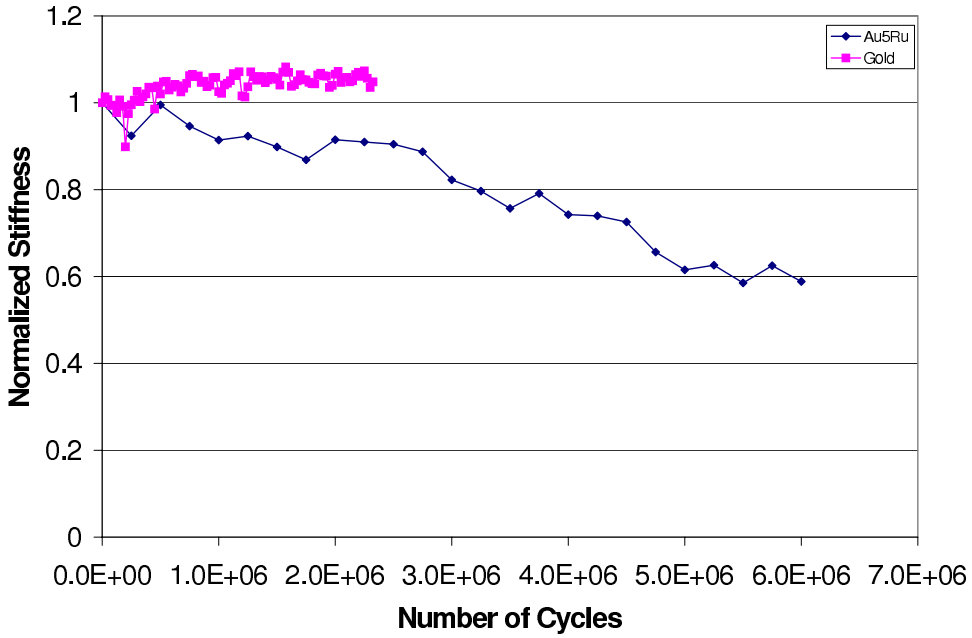

Figure 9.26: Normalized stiffness trend for an example long term test on Au5%Ru compared to an example gold test. This gold appears to have experienced a small amount of strain hardening while the Au5%Ru appears to have softened.

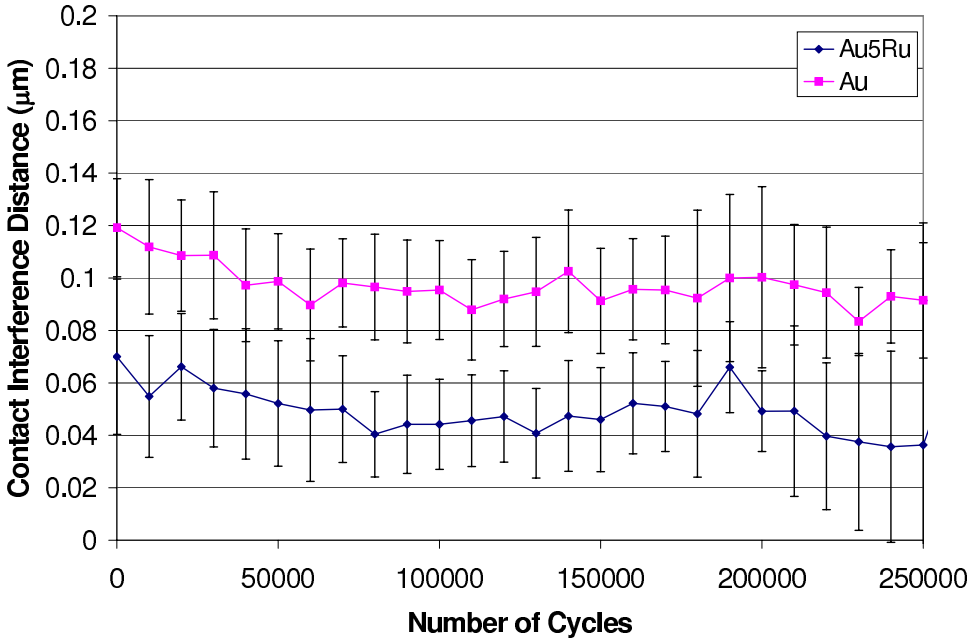

Figure 9.27: Average contact interference (or penetration) during contact cycling comparing Au to Au5%Ru. Results are consistent with the higher hardness of the Au5%Ru material.

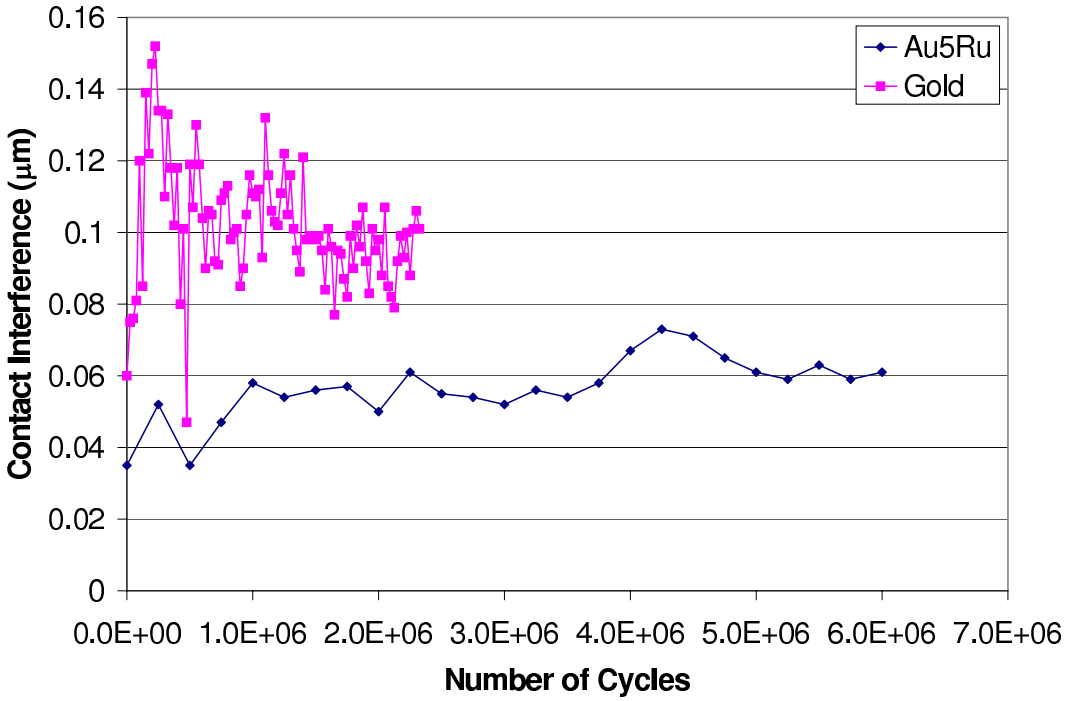

Figure 9.28: Au5%Ru long term contact interference (deformation) example compared to gold test during cycling with contact load of 400 μN.

a slight increase in contact interference as the contact cycles. This is likely due to plastic flattening of the contact surface which can be seen in Figure 9.5. This increase in interference demonstrates increased plastic deformation and contact softening, possibly due to contact heating or damage generation on and under the surface of the contact film leading to increased contact deformation as the contact cycles.

9.7 Time Dependent Behavior

Au5%Ru also showed time dependent behavior when in contact under load similar to the results seen with gold contacts. A comparison of the average time dependent deformation during the five second load hold in Au5%Ru contacts is shown in Figure 9.29. Time-dependent deformation in the beginning of the test is higher in the gold contacts than Au5%Ru. However, the time-dependent deformation in gold and Au5%Ru contact testing after approximately 20,000 cycles appears to be within the scatter band. This behavior is unexpected, as these metals are not normally visco-

elastic. The higher time dependent behavior in gold during the beginning of testing is likely due to the softness of gold and the relative ease with which dislocations can move in the contact area. Once barriers to dislocation motion are created, the time dependent motion slows. Time dependent behavior in Au5%Ru is similar to the behavior seen in gold, except that Au5%Ru does not show as much of an initial decrease when compared to gold. This is likely due to the increased hardness of Au5%Ru and existing barriers to dislocation motion in the two-phase material. Additionally, contact heating during the five second load hold while passing current may cause elevated temperature in the contact interface leading to a thermal environment where viscoelastic effects could occur. An example of time-dependent deformation in a long-life Au5%Ru test compared to a long-life gold test is shown in Figure 9.30. This figure shows that the long-term time-dependent deformation in Au5%Ru may show a moderately increasing trend through the end of life. This may be due to continued softening of the contact material due to heating or may be demonstrating deformation due to fracture and/or creation and displacement of wear fragments during the load hold period.

9.8 Plastic Deformation

The average energy absorbed by Au5%Ru contacts is shown in Figure 9.31 compared to the result for gold contacts. Energy absorbed by Au5%Ru does not appear to be significantly different than the energy absorbed by gold contacts in this test setup. Results of both contact materials are within the scatter band. There appears to be a slight reduction after approximately 20,000 cycles but the amount of energy absorbed through the testing appears to stay consistent. The work done on both contact materials during cycling appears to be the same. However, gold does show a larger drop after the first few cycles possibly indicating more plastic deformation during the initial stages of cycling. A comparison of examples of long-term behavior of Au and Au5%Ru contacts is shown in Figure 9.32. This figure shows that the energy absorbed in the Au5%Ru sample increases steadily as it cycles,

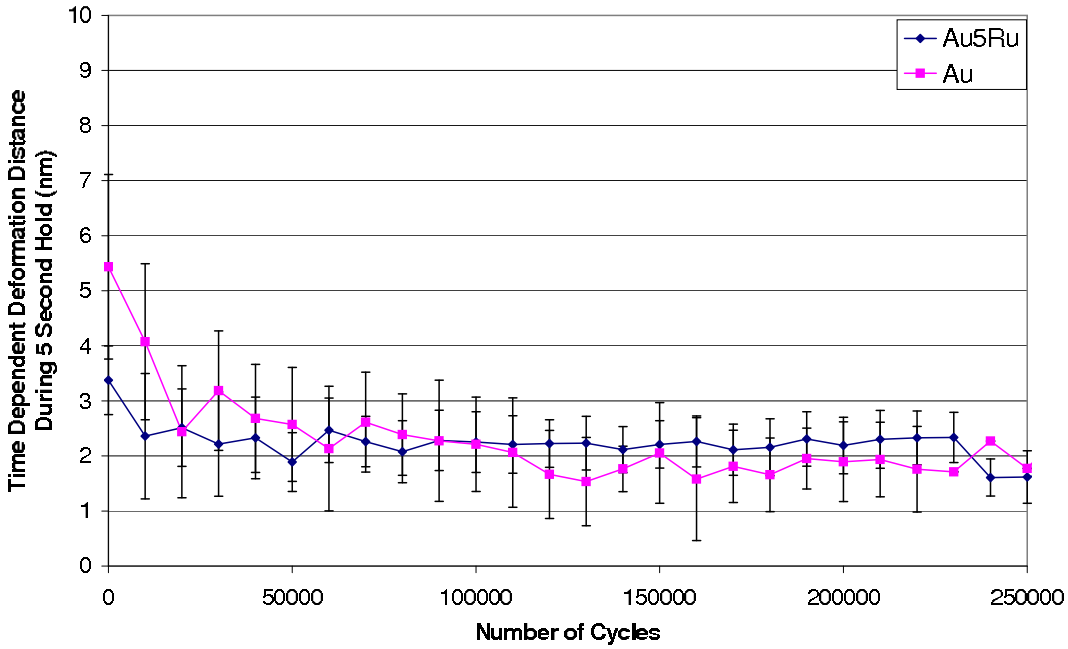

Figure 9.29: Average contact penetration time-dependent deformation during five second hold at 400 μN. Au compared to Au5%Ru. Results are consistent with the higher hardness of the Au5%Ru material.

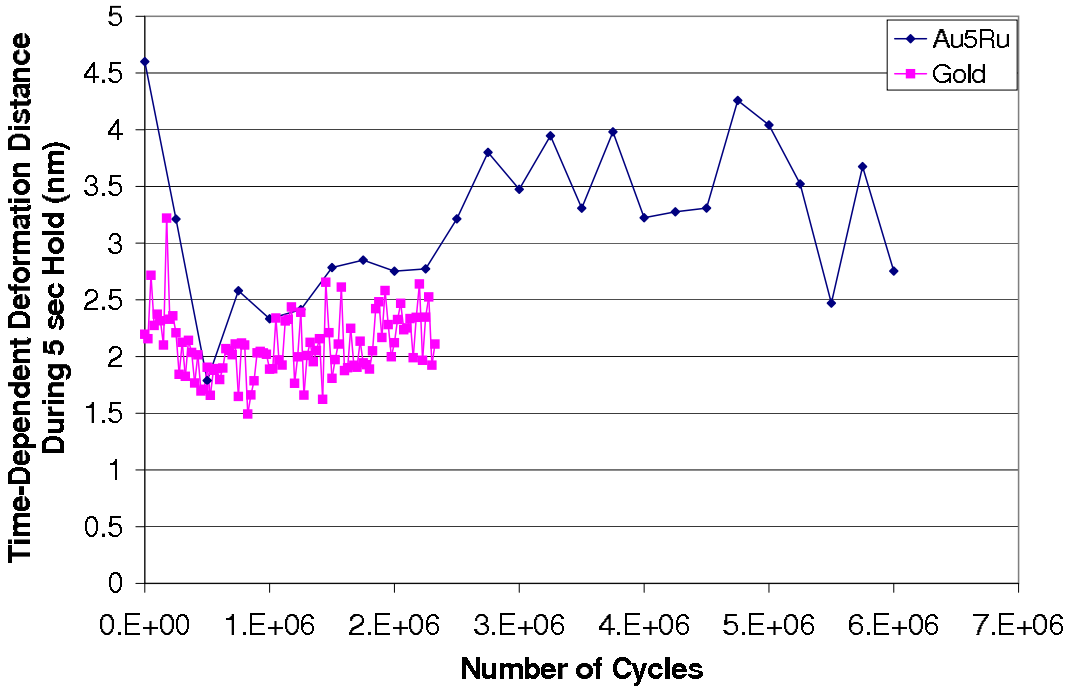

Figure 9.30: Au5%Ru long-term time-dependent contact deformation example compared to gold long-term test example during 5 second constant load hold at 400 μN.

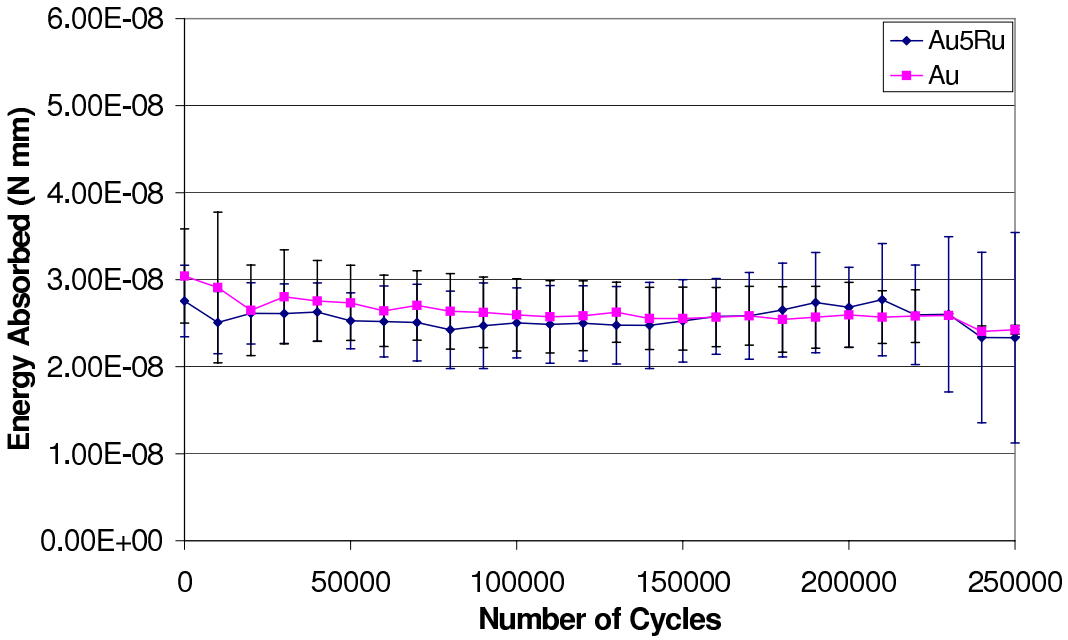

Figure 9.31: Average contact energy absorbed (or work done on contact) during measured actuation. Gold and Au5%Ru energy absorbed appear to be very similar during first 250,000 cycles.

indicating a steady increase in plastic deformation and damage to the contact. This is likely due to softening experienced during cycling, caused either by contact heating or progressing fatigue and surface wear in the contact material. The long-term gold result appears to show an increase in plastic deformation near the beginning of contact life, then have relatively consistent plastic deformation through the end of life whereas the long-term Au5%Ru test appears to show a stable beginning and have a steadily increasing rate of plastic deformation. This can be attributed to a possible slight strain hardening process in the gold test, whereas the Au5%Ru demonstrates a contact damage process which removes material from the contact surface. There may be discontinuities within the Au5%Ru material which act as initiation points for surface fracture due to locations of the second phase material.

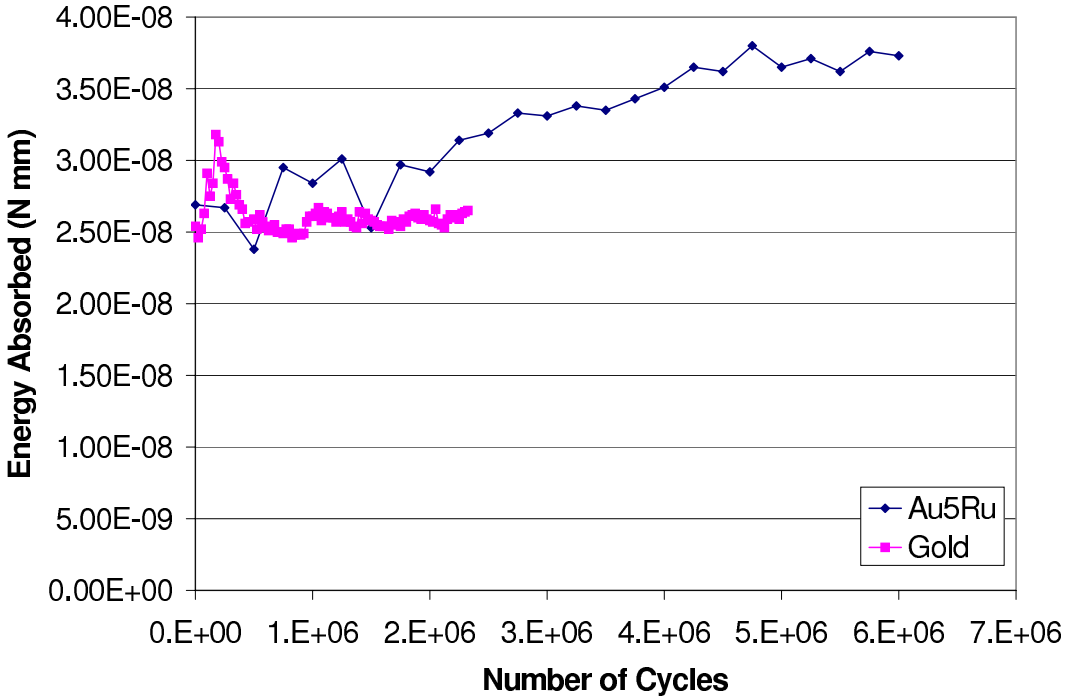

Figure 9.32: Long-term example of energy absorbed by a Au5%Ru compared to gold contact example during cycling testing. The energy absorbed indicates amount of plastic deformation occurring.

9.9 Contact Evolution

An example of a Au5%Ru contact which was cycled for 80,000 cycles but did not fail is shown in Figures 9.33, 9.34 and 9.35. Figure 9.33 is an SEM image of the bump before cycling, Figure 9.34 is an image of the bump after 80,000 cycles and Figure 9.35 is an image of the strike plate contact location after cycling. There is little evidence of damage on the contact bump, although some smoothing can be seen in Figure 9.34. The pattern of contact wear may indicate that the contact between surfaces was not perfectly flat. The strike plate contact region shows a small amount of material transfer and development of some contact contamination in an annular ring around the contact location. The Au5%Ru contacts demonstrated different contact evolution when compared to gold contacts. The gold contacts demonstrated material transfer but did not appear to generate a significant amount of debris like the Au5%Ru long-life contacts. This is likely due to the ductile nature of the gold contact separation and the brittle nature of the Au5%Ru separation. The gold was

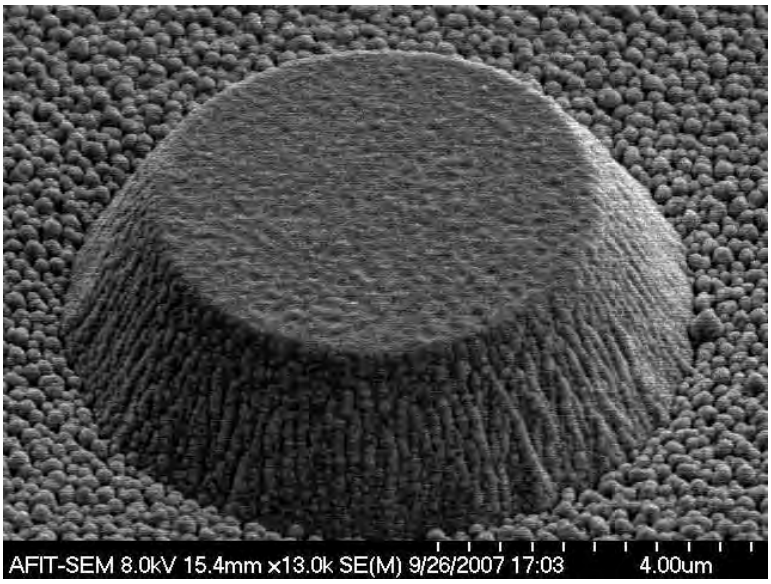

Figure 9.33: Au5%Ru contact bump before cycling. This contact was used in the Au5%Ru contact evolution test and underwent 80,000 cycles but did not fail.

more likely to separate at other than the contact interface while the Au5%Ru was more likely to separate at the contact interface. Both gold and Au5%Ru also demonstrated smoothening due to repeated contact, but the gold surface smoothed with fewer contact cycles due to its reduced hardness compared to Au5%Ru. Both contact materials demonstrated indications of possible contact heating, including both behavior and images of apparent contact melting at the edge of contact area.

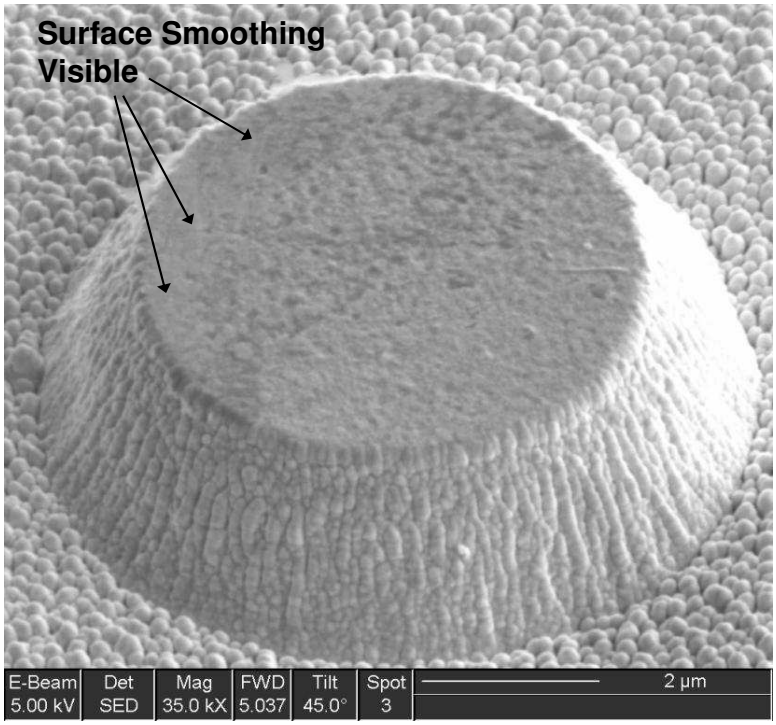

Figure 9.34: Au5%Ru contact bump which was stopped without failure after 80,000 cycles. Some surface smoothing due to cycling can be seen in the upper left hand quadrant of the contact.

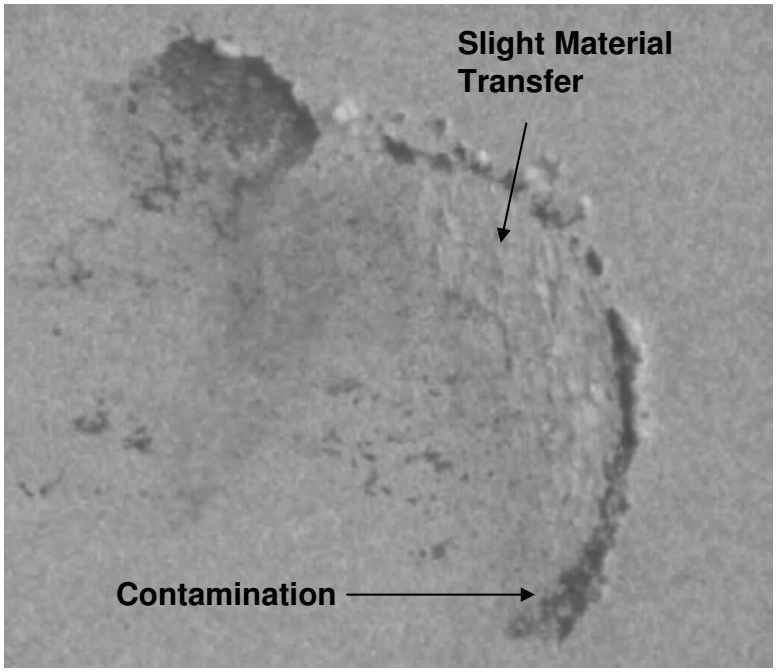

Figure 9.35: Au5%Ru contact plate which was stopped without failure after 80,000 cycles. Note some material transfer/contact damage and an annular ring of contamination is visible.

9.10 Contact Bump Shape

Table 9.3 gives the shape and diameter of Au5%Ru contact bumps used in this study along with their lifetime results. There is no indication in this data set that bump shape affected test measurements. Additionally, there is one example which indicates that bump shape does not significantly affect contact surface damage. This can be seen by comparing the before and after images of two long lifetime Au5%Ru tests with different contact bump shapes. One contact bump was flat-topped and the other was rounded. The pre-test images of the two differently shaped contact bumps are shown respectively in Figures 9.4 and 9.36, yet the after images in Figures 9.5 and 9.37 show that very similar processes were active during cycling. The different bump shapes demonstrated a similar number of cycles to adhesive failure (6.25×10^6 vs. 6.29×10^6). The after cycling image for the bottom contact area of the flat-topped bump can be seen in Figure 9.6 and the bottom contact area after image for the rounded bump is shown in Figure 9.38. The images from the rounded contact results don't show as much wear debris as the other long life Au5%Ru contact shown, however, wear debris is still visible in the rounded bump images. The missing wear debris on the rounded contact sample could be due to handling of the contacts after removal from the experimental setup. This result also supports the conclusion that contact behavior measurement using the microprobe does not affect test results. More testing should be done to further investigate effects of contact shape on microcontact lifetime performance.

Table 9.3: Test summary of shapes and sizes of Au5%Ru contacts tested to failure. Contact bumps described as "Flat" are flat-topped bumps. Contact diameter and height were measured/calculated using topview and off-axis SEM images.

Contact ID	Contact Shape	Contact Diameter (μm)	Contact Bump Height (μm)	Initial Contact Resistance (Ω)	Failure Type	Number of Cycles to Failure (# Cycles)
0210-3_12	Flat	6.8	2.1	NA	Adhesion	70,000 (no current)
0801-3_8	Flat	6.6	1.8	10.7	No Fail	stopped at 80,000
0210-3_7	Flat	6	2.5	10.7	Adhesion	130,000
0210-3_11	Flat	7	2.1	10.5	Adhesion	140,000
0801-1_1	Flat	6.2	1.7	9.9	Adhesion	210,000
0602-2_3(I)	Flat	3.5	3.3	13.2	Adhesion	6.25×10^6
0602-2_4(J)	Rounded	8	3.2	12.3	Adhesion	6.29×10^6
0801-3_9	Flat	6.3	1.8	10.7	Overload	NA
0801-1_5	Flat	6.2	1.7	9.2	Overload	NA
0210-3_8	Flat	6	2.3	11.2	Overload	NA
0210-3_10	Flat	7	2.1	11.4	Overload	NA
0602-2_2(H)	Flat	3.2	3.4	15.1	Overload	NA

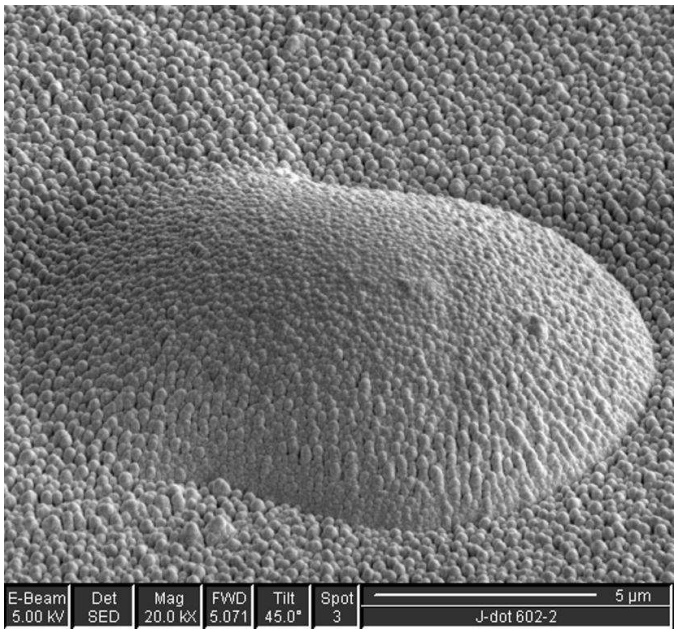

Figure 9.36: Au5%Ru rounded contact bump before testing. Contact failed in adhesion after 6.29×10^6 cycles.

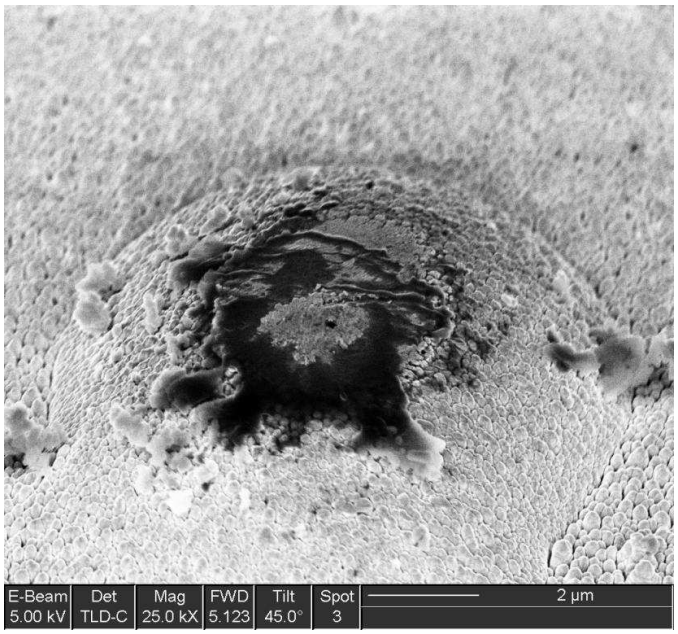

Figure 9.37: Au5%Ru rounded contact bump which failed in adhesion after 6.29×10^6 cycles. The resulting bump wear pattern is similar to the long life flat-topped bump shown in Figure 9.5

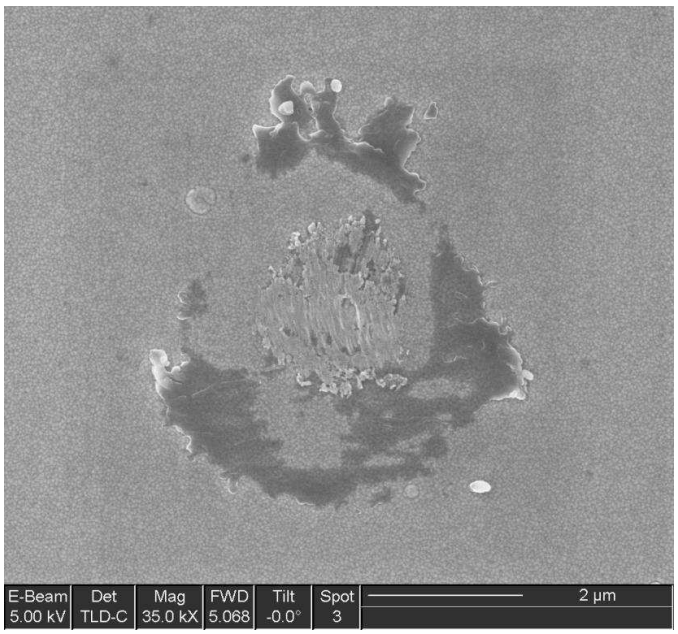

Figure 9.38: Au5%Ru bottom contact wear location for rounded contact bump which failed in adhesion after 6.29×10^6 cycles. The resulting wear pattern is similar to the long life flat-topped bump shown in Figure 9.6

9.11 Failure Type Categorization and Measurement

As previously discussed in this chapter, the adhesive failures of Au5%Ru-Au5%Ru contacts during this study can be divided into two categories based on test lifetime and failure characteristics. Au5%Ru contacts demonstrate a failure where the contacts show smoothing and have a flat separation surface, whose appearance is similar to the Type III failure described in gold. The similar appearing failure in Au5%Ru contacts is described as a Type IIIB failure, even though the lifetime of the Type III failure in gold was determined to be $> 1 \times 10^6$ cycles. Type IIIB failures in Au5Ru occurred at roughly 200,000 to 500,000 cycles under the test conditions used in this study. The difference in lifetime results between these two results is due to the different materials used. The gold was softer and more surface contamination than average for gold likely caused a reduction in adhesion to occur extending the Type III gold lifetime. The Au5%Ru in Type IIIB failures showed less contamination than average for Au5%Ru contacts leading to increased adhesion and adhesion failure. Testing occurred in a lab air environment so slight variations in humidity or other ambient variables could have resulted in varying levels of contamination before or during testing. The longest lasting failure surfaces in Au5%Ru contacts appeared very different than other failed contacts of this study with significant visible wear. This type of failure is categorized as Type IV and an example can be seen in Figure 9.37. The Type IV contacts showed wear debris, some contamination, and a clearly worn contact surface. The long-life Type IV failure occurred in Au5%Ru contacts at roughly 6×10^6 cycles in the test conditions used in this study.

The results were sorted by lifetime and averaged. The Type IV data is from a sample Au5%Ru long-lifetime test. The results demonstrate that some of the measured quantities showed differences between lifetime categories. General descriptions comparing the results qualitatively is given in Table 9.4. However, no method was detected which could predict the lifetime of a specific contact before cycling. There is currently a wide variation in contact lifetimes, even from the highest performing commercial switches [65, 171] and there is no in depth discussion of specific failure

Table 9.4: Qualitative comparison of results indicating differences between two categories of lifetime adhesive failures in Au5%Ru contacts. ↑ = higher initial value; ↓ = lower initial value

Measured Result	Long-life Type IV (worn surface)	Shorter-life Type IIIB (brittle)
Resistance	Baseline	↓
Pull-off Force	Baseline	↑
Threshold Force	Baseline	↓
Threshold Distance	Baseline	↓
Interference	Baseline	↓
Creep	Baseline	↓
Energy Absorbed	Baseline	↓

mechanisms in the literature. The measurements performed during this study which show a difference between contact failure types are described in the following sections.

9.11.1 Contact Resistance. The Type IIIB shorter lifetime failures demonstrate a lower contact resistance than the long-life results in Au5%Ru. Measured contact resistance for these two types of failures are compared in Figures 9.39 and 9.40 and likely indicate a lower level of contact contamination on the Type IIIB surfaces, which increases contact adhesion and therefore accelerates the accumulation of contact damage thus reducing the life of the contact. The images of the Type IIIB failure surfaces shown in Figures 9.1, 9.2 and 9.3 support this hypothesis.

9.11.2 Pull-Off Force. The measured pull-off force trend is expected to show a difference between contacts which exhibit different lifetimes. Higher early adhesive forces are expected in shorter lifetime contacts and the development of early adhesive forces likely leads to contact damage and development of adhesive forces high enough to cause adhesion failure. These results are shown in Figures 9.41 where the Au5%Ru Type IIIB shorter lifetime average pull-off results are compared to an average of all Au5%Ru pull-off test results and Figure 9.42 where the Type IIIB average is compared to a representative Type IV long-life test. The shorter-life adhesive failures in Au5%Ru contacts (Type IIIB) shows higher initial pull-off force, as expected and as

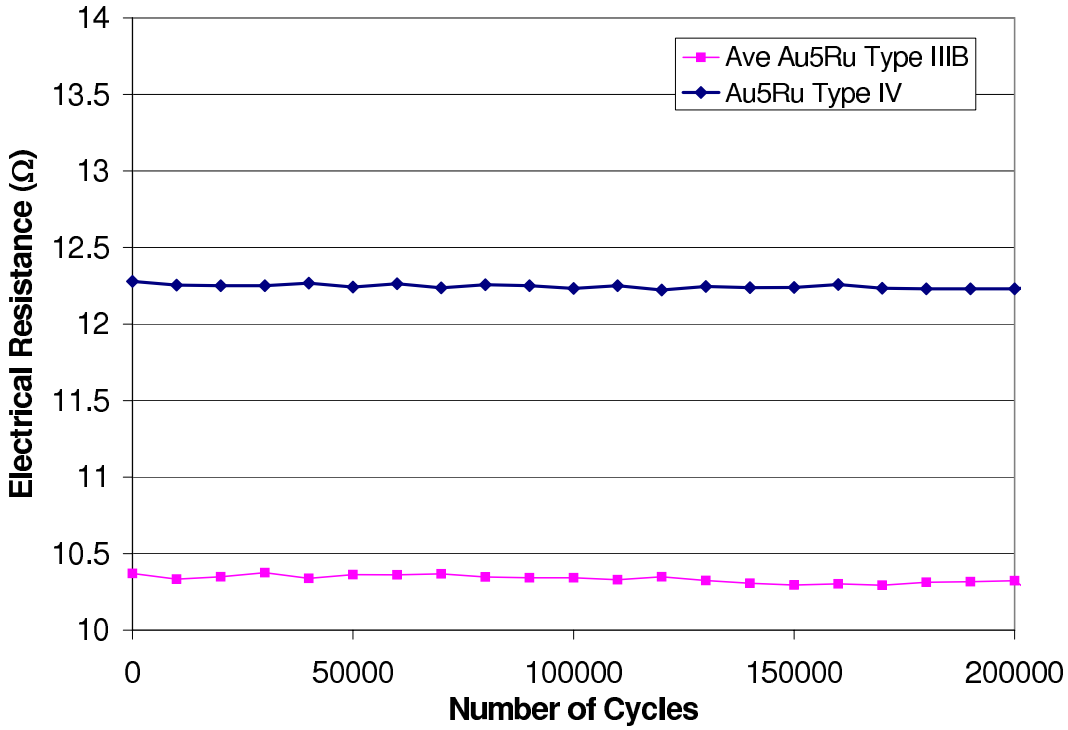

Figure 9.39: Average resistance results for Au5%Ru Type IIIB Failures.

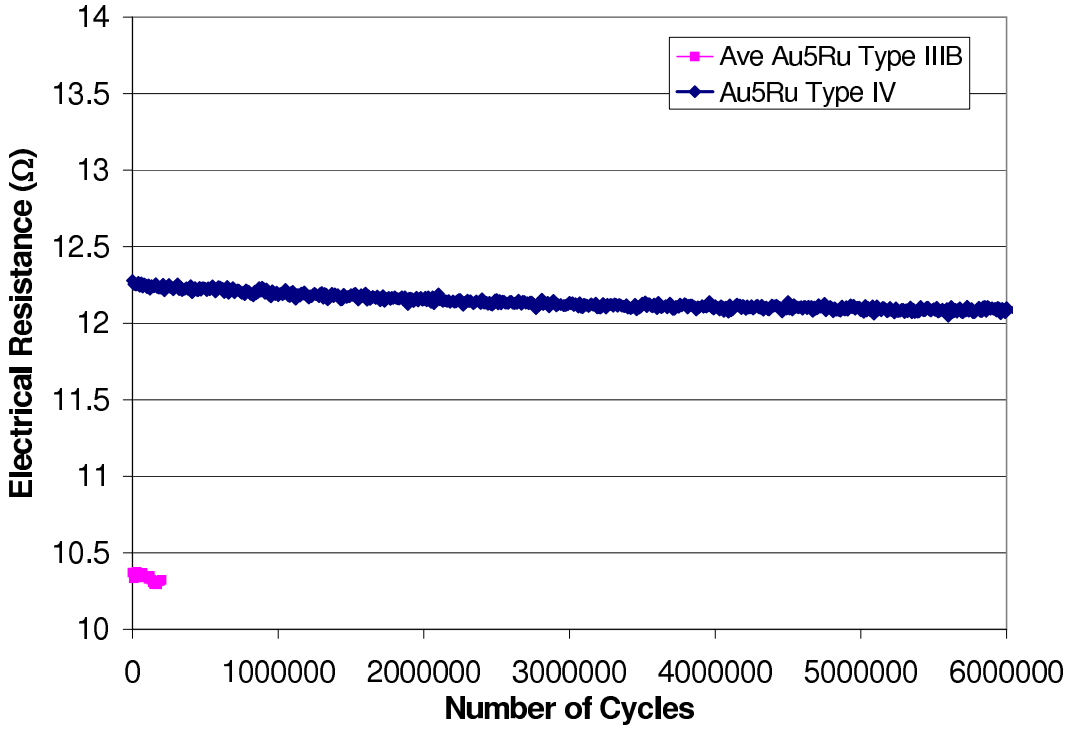

Figure 9.40: Contact Resistance comparison between lifetime failure categories. Note that the Type IIIB failure shows a lower measured contact resistance likely indicating lower levels of contact contamination.

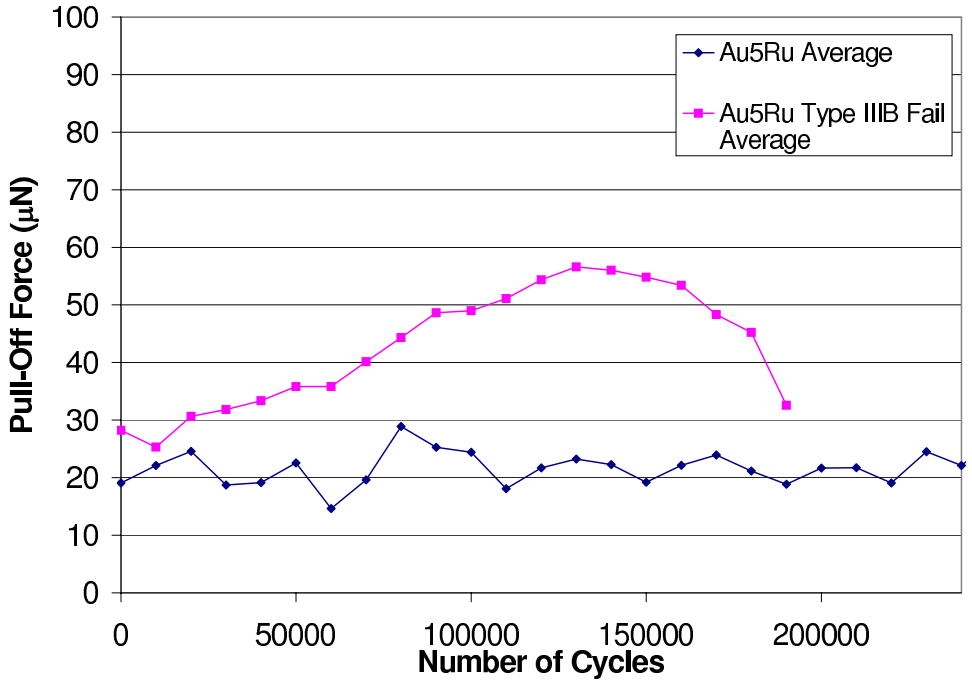

Figure 9.41: Average pull-off force results for Au5%Ru Type IIIB Failures. Note that the Type IIIB failure shows an average early pull-off force increase, while the average for all Au5%Ru results do not.

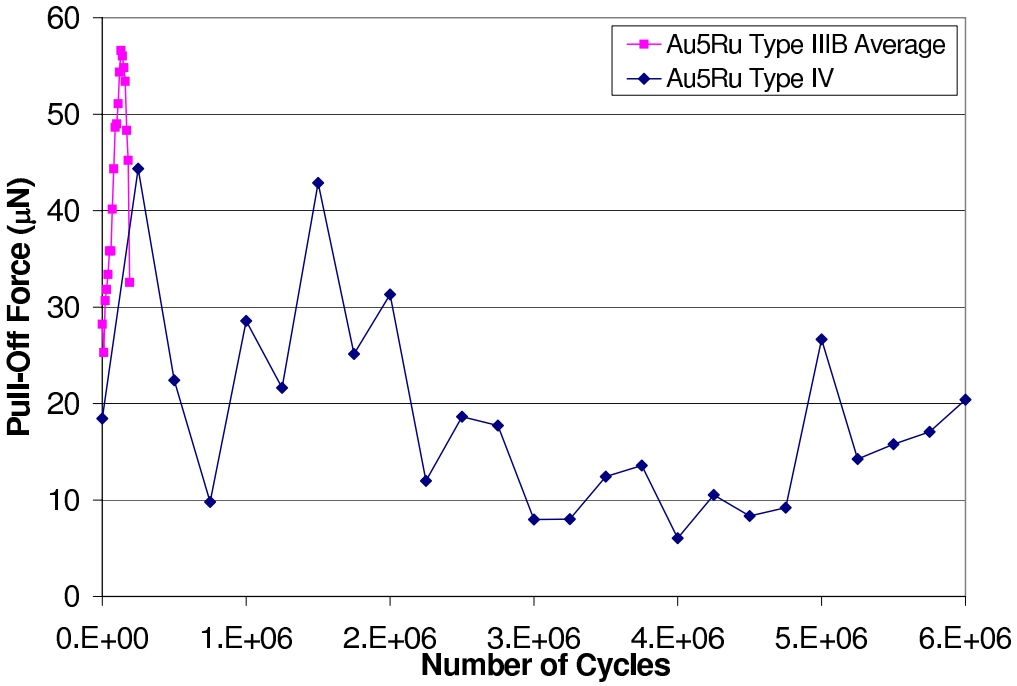

Figure 9.42: Pull-off force comparison between lifetime failure categories.

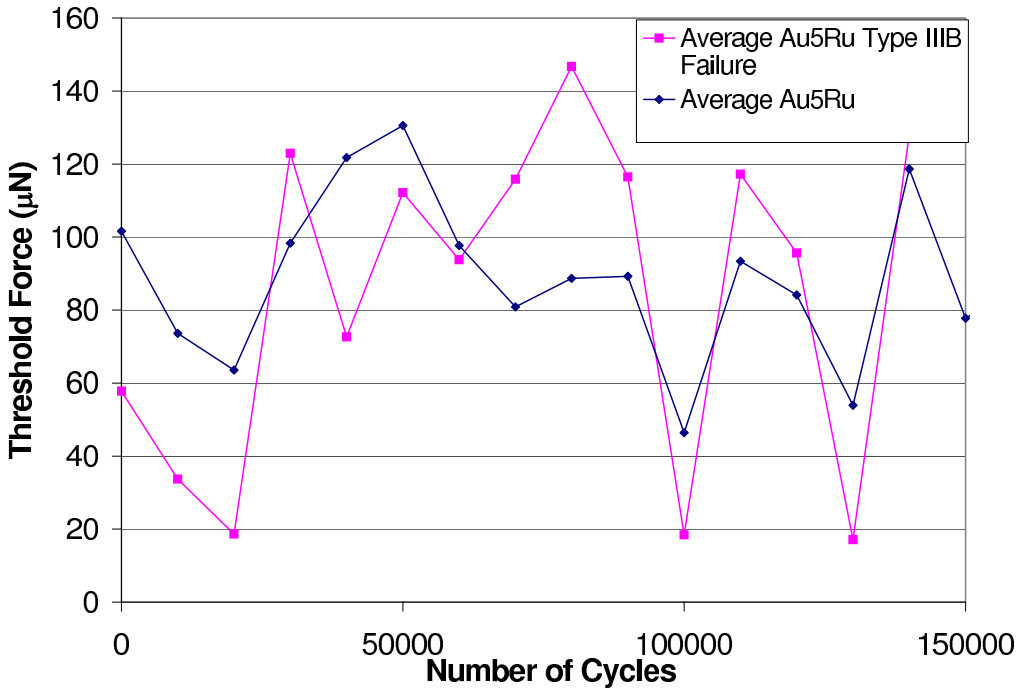

Figure 9.43: Average threshold force results for Au5%Ru Type IIIB Failures.

predicted in Section 9.11.1. The Au5%Ru average pull-off results show a constant level of pull-off force. The long-life Type IV example result shown in Figure 9.42 shows a variable pull-off force as the contact cycles. This may indicate changes occurring on the contact surface, including damage, changes to surface morphology and contamination creation or destruction. The peaks in pull-off force may correspond to the points in cycling where contact damage occurs. No large peak is seen at failure, but there is an increasing trend in the period leading up to failure. This indicates that the rise in adhesive force causing failure is sudden or occurs more quickly than the measurement interval is capable of measuring.

9.11.3 Threshold Force & Distance. Threshold force trends in Au5%Ru contacts are shown in Figures 9.43 and 9.44. The contacts exhibiting Type IIIB failure had a lower initial threshold force compared to the Au5%Ru contact test average, which quickly increased and required the same force as the longer life contacts to get into ohmic contact throughout the remainder of contact life. The wide variation in

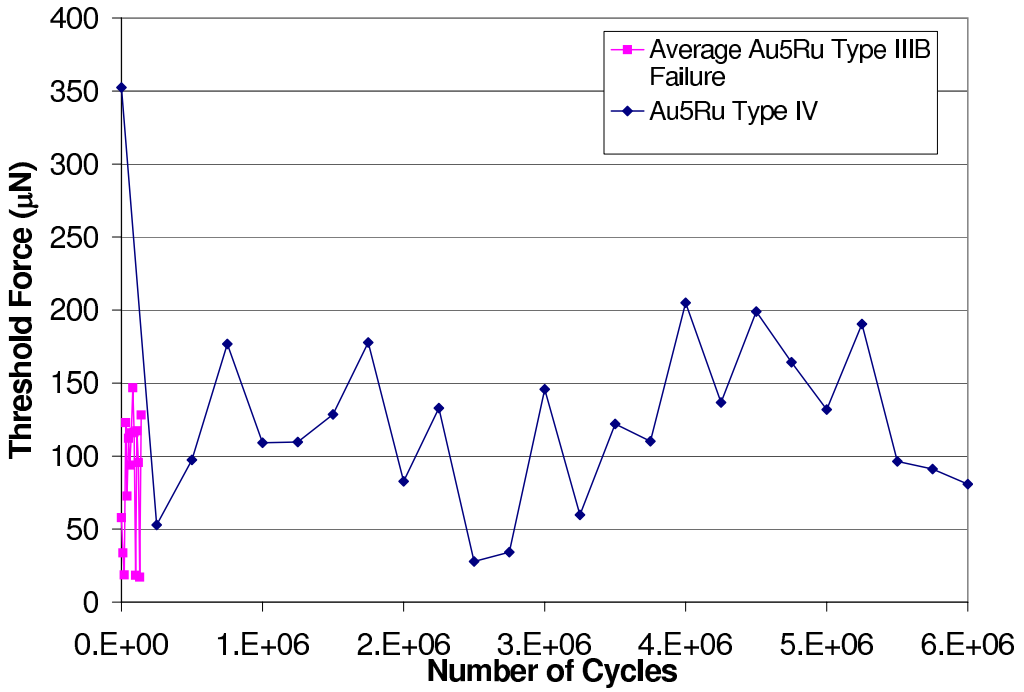

Figure 9.44: Threshold force comparison between lifetime failure categories. Note that threshold force for Type I early lifetime failure starts lower and is least value. Also, note that Type III longest lifetime shows high initial threshold force.

threshold force likely indicates changes in surface contamination conditions during cycling leading to a widely varying force needed for stable ohmic contact. This indicates that Type IIIB failures may start with a lower level of surface contamination and that the level of initial surface contamination and condition may have a large effect on contact life. The presence of surface contamination reduces adhesion, which could extend contact life by avoiding adhesive failure or slowing changes to surface morphology. The threshold force varies greatly between measurements indicating that there is likely a varying amount of contamination on the surface preventing consistent values of threshold force between measurement intervals. Note that longer life contacts, in general, have higher initial threshold force. This result is demonstrated in Figure 9.44 and is similar to the behavior seen in gold-gold contact testing and may indicate a higher level of initial contact contamination or higher initial surface roughness on contacts which demonstrate longer lifetimes.

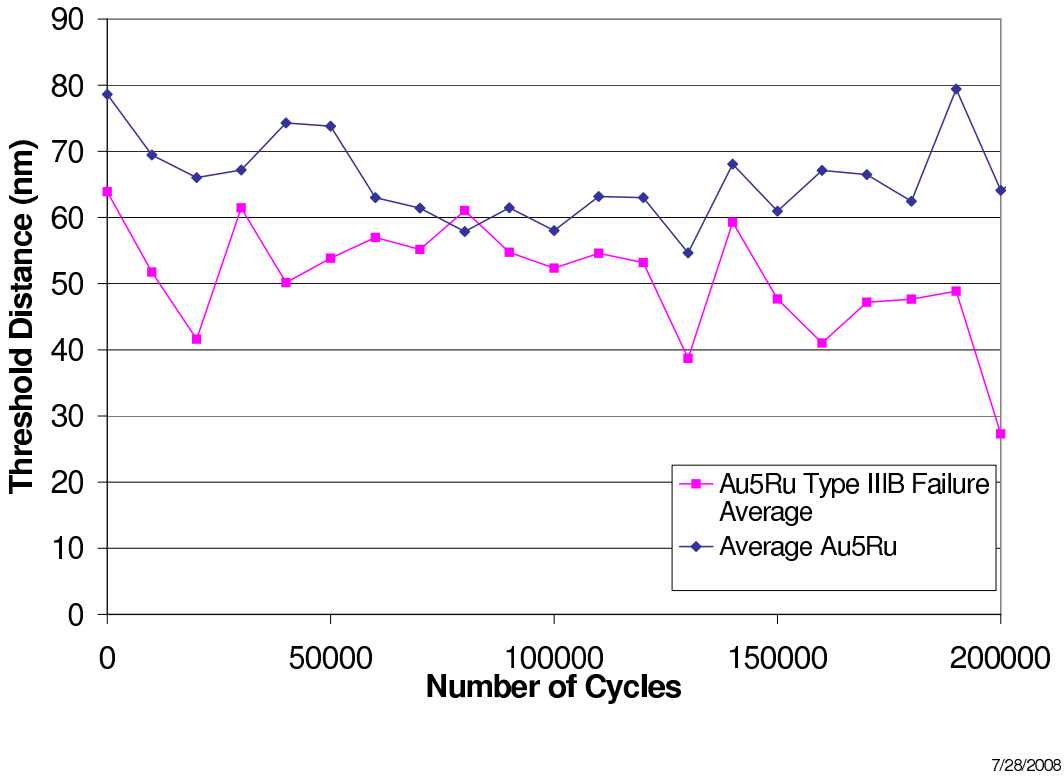

Figure 9.45: Average threshold distance results for Au5%Ru Type IIIB Failures.

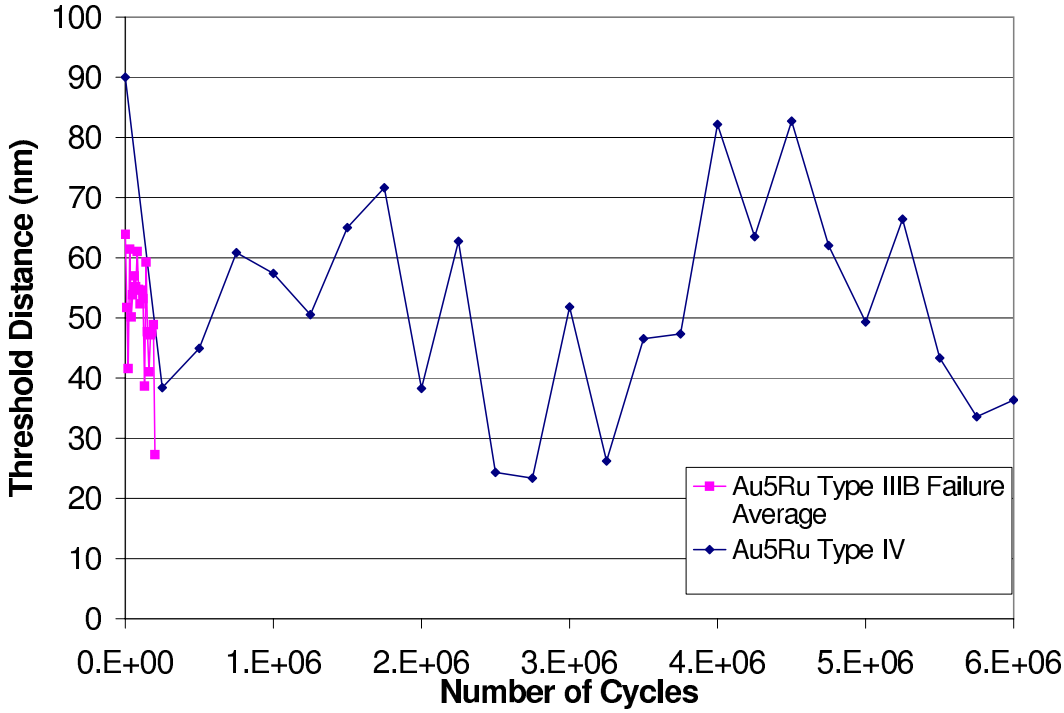

Figure 9.46: Threshold distance comparison between Au5%Ru lifetime failure categories.

An early difference in contact threshold distance required for Au5%Ru contacts was also demonstrated which may also indicate a higher level of initial surface contamination or a higher initial surface roughness. The Type IIIB shorter lifetime contacts required a lower threshold distance when compared to the average for all Au5%Ru contacts during the beginning of contact life (< 75,000 cycles), which can be seen in Figure 9.45. This indicates that that Type IIIB contacts may have had a different initial surface condition. Figure 9.46 shows the threshold distance behavior of a Type IV Au5%Ru contact surface as it cycles compared to the average results of the Type IIIB contacts. The threshold distance for the Type IV long-life contact becomes quite variable through the contact lifetime which may indicate creation and destruction of contamination on the contact surface or large changes to the surface morphology of the contact.

9.11.4 Contact Interference. Au5%Ru contacts demonstrated a slight difference in contact interference measurements when shorter and longer lifetime results were compared for less than 75,000 cycles which is shown in Figure 9.47. After 75,000 cycles, there is no difference between Type IIIB and average Au5%Ru contact interference. This indicates that a change is possibly occurring to the contact surface during the initial cycling. This could indicate that the Type IIIB contacts have lower initial contamination or are initially smoother than the average Au5%Ru contacts tested. Either factor could lead to earlier contact adhesive failure.

Figure 9.48 shows a comparison of contact interference between the average Type IIIB results compared to a representative Type IV long-life contact. This demonstrates that the interference increases slightly as the contact continues to cycle. This increase could be attributed to an accumulation of contact damage or softening of the contact, possibly due to contact heating.

9.11.5 Time Dependent Behavior. Au5%Ru shorter lifetime Type IIIB failures show similar time-dependent deformation when compared to the average for all tested Au5%Ru contacts as shown in Figure 9.49. Both sets of results show a decrease

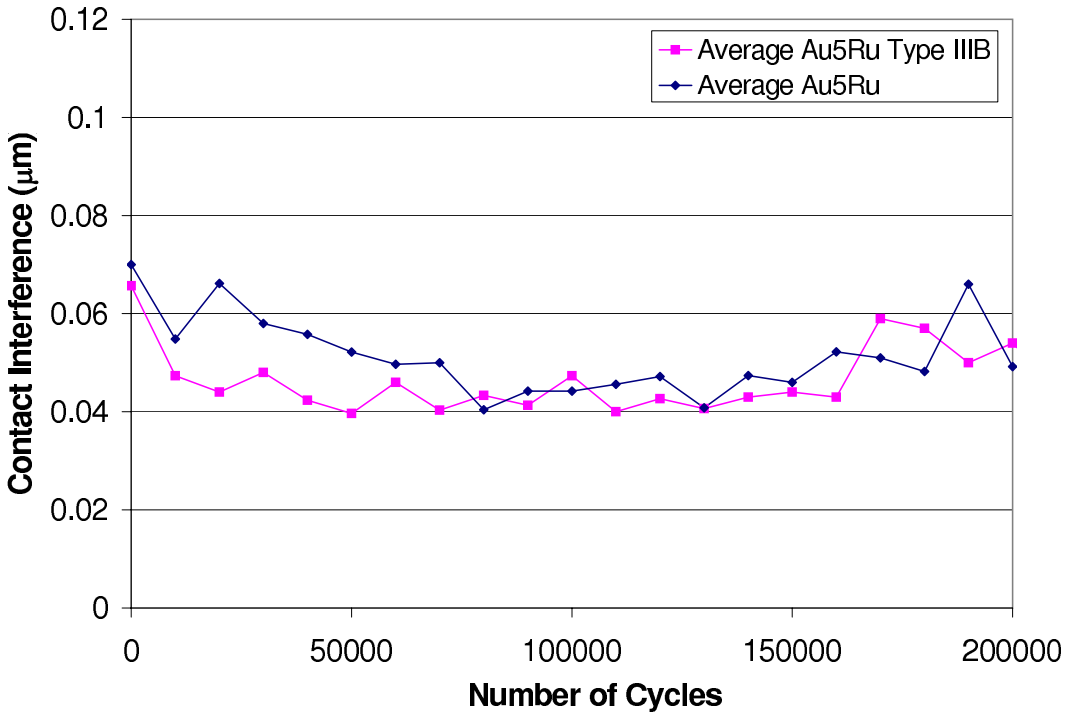

Figure 9.47: Average contact interference results for Au5%Ru Type IIIB Failures.

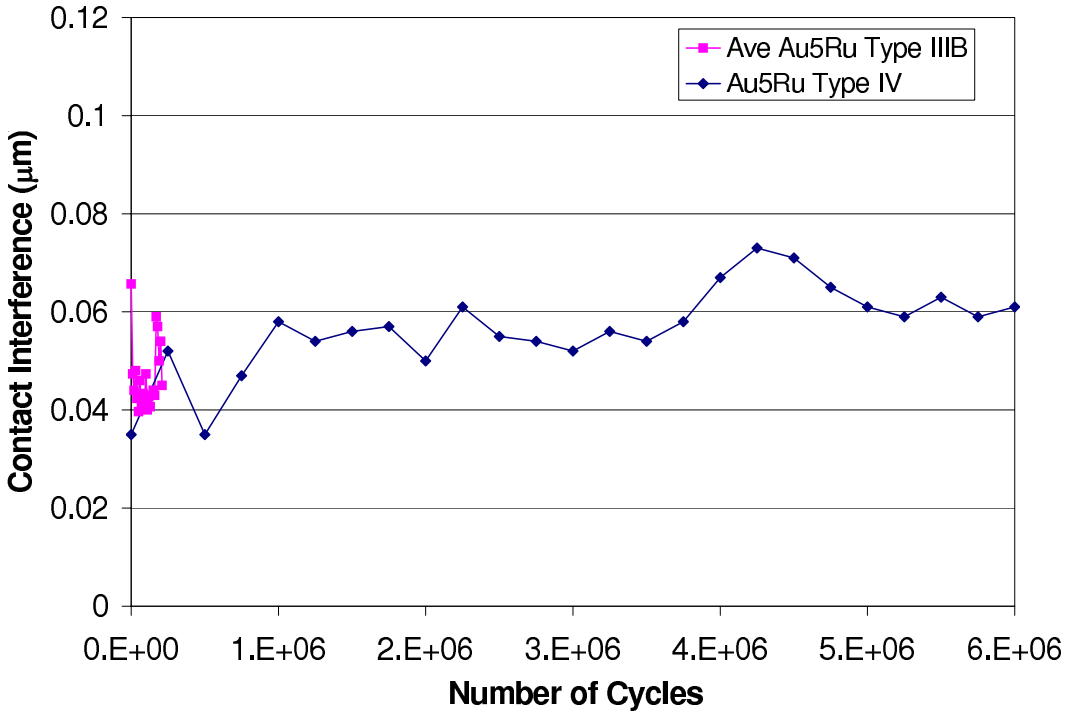

Figure 9.48: Contact Interference comparison between lifetime failure categories. Note that contact interference up to 75,000 cyles for Type IIIB early failure is slightly less than that for the Au5Ru contact average.

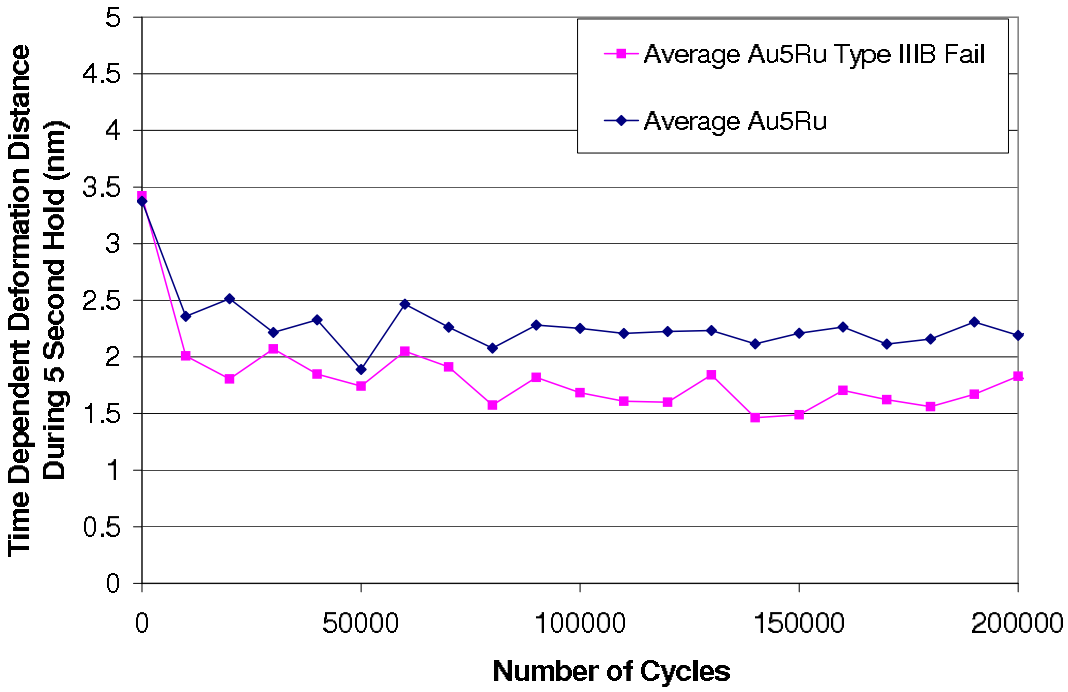

Figure 9.49: Average time-dependent deformation results for Au5%Ru Type IIIB Failures compared to average for all Au5%Ru contacts tested.

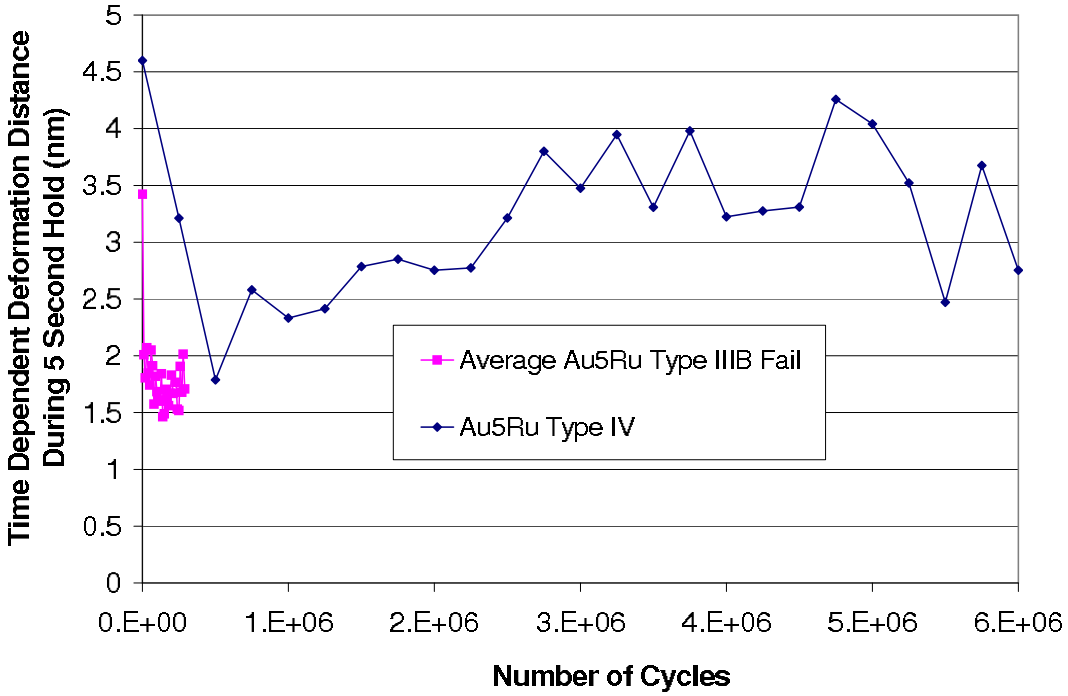

Figure 9.50: Time dependent deformation comparison between Type IIIB failures and a Type IV long-life contact.

in time dependent deformation as the contacts cycle and both show a relatively constant steady state deformation. However, the time-dependent deformation of the Type IIIB failed contacts is less than the average Au5Ru contacts by 0.5-1 nm up to 200,000 cycles. Note that the measurement resolution for displacement of the nanoindenter tip is given as ±0.01 nm by the manufacturer. The lower time-dependent deformation demonstrated by Type IIIB contacts may be due to lower initial surface roughness and therefore lower incidence of possible spot heating due to current flow through contact asperities. The lower initial time-dependent deformation in Type IIIB contacts may also indicate a difference in the thin film microstructure which reduces initial time-dependent deformation. This could be due to the existence or creation of more dislocation barriers and could also explain the slightly lower initial contact interference in Type IIIB contacts. Figure 9.50 also indicates that time-dependent deformation likely increases with cycling during the life of a long-life contact. This may point to contact heating and/or subsurface contact damage occurring during cycling.

9.11.6 Energy Absorbed. The energy absorbed by the contacts during a contact event is a measure of plastic deformation. The energy absorbed by the Type IIIB contacts decreases and remains constant followed by a slight increase as shown in Figure 9.51. The average result for all Au5%Ru contacts tested is higher initially and reaches a steady state value similar to the Type IIIB contacts. This may indicate smoothening occurring within the first 50,000 cycles on average in the Au5%Ru contacts which is not occurring in the Type IIIB contacts, possibly indicating that the Type IIIB contacts are initially smoother. This would explain the quicker growth in adhesive force and shorter lifetime of Type IIIB contacts and is similar to the behavior seen in long-life Type III gold contacts. This indicates that the processes involved in plastic deformation smoothing are similar between materials with differing properties.

The average plastic deformation for Type IIIB contacts is compared to a Type IV long-life contact in Figure 9.52. The long-life result shows increasing energy absorbed

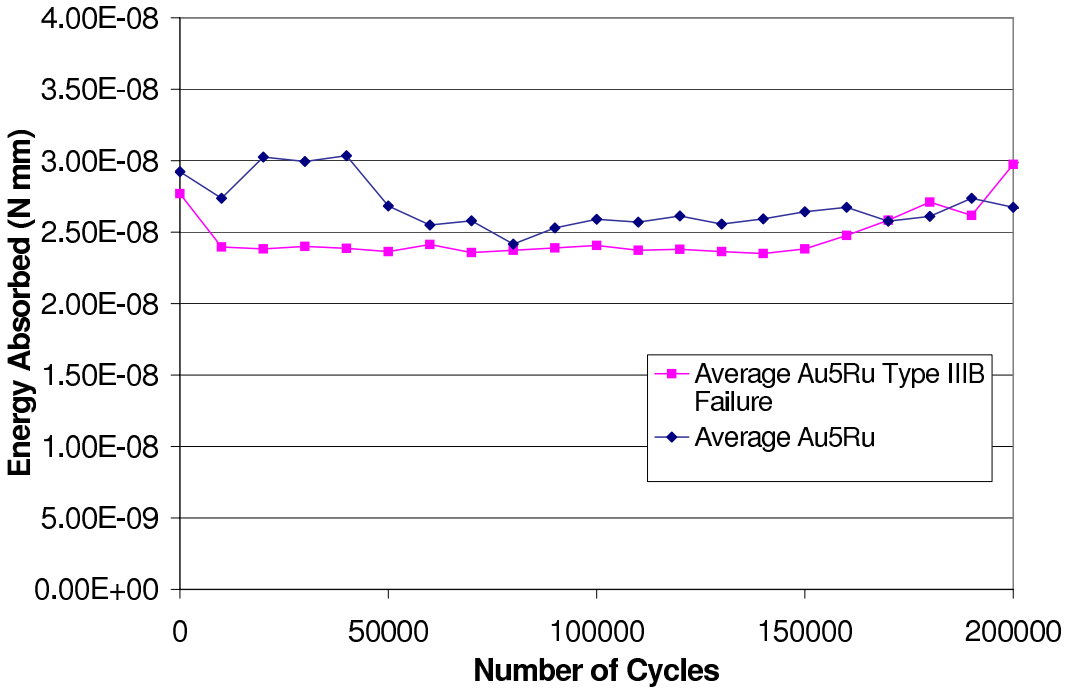

Figure 9.51: Average energy absorbed/plastic deformation results for Au5%Ru Type IIIB Failures.

and thus plastic deformation as the contact cycles. This matches the flattening effect seen in the contact surface examination which is shown in Figure 9.5. There appears to be more wear and plastic deformation in Au5%Ru long-life contacts when compared to gold. The gold long-term result, shown in Figure 8.35, does not show a long-term increase in plastic deformation. This is likely due to the more brittle nature of Au5%Ru when compared to gold which could cause surface fracture and removal of wear particles from the Au5%Ru surface and registers in the measurement of energy absorbed.

More work on these results and indicators will be required before they can be used as predictors of expected contact lifetime based on contact behavior. This work will need to include further measurement of contact behavior, such as is included in this study, and comparative analysis with measurements and images of failed MEMS switch contacts. This type of analysis does show promise and indicates trends in the failure characteristics of contacts of Au5%Ru contacts.

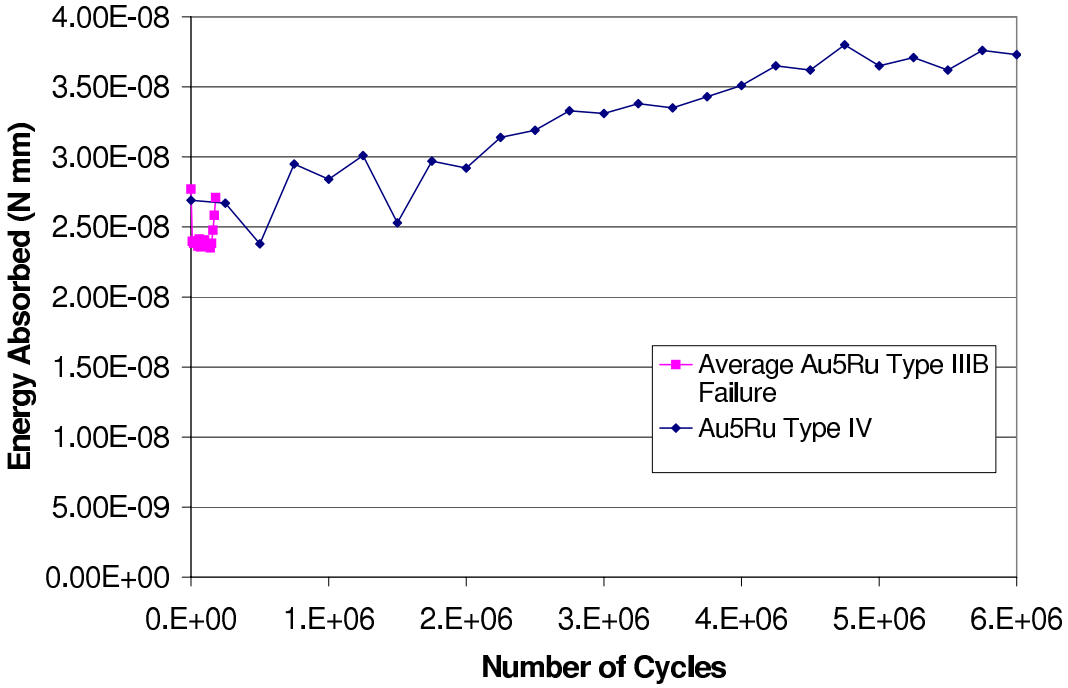

Figure 9.52: Energy absorbed comparison between lifetime failure categories in Au5%Ru contacts.

9.12 Summary of Gold-Ruthenium Alloy Results

The Au5%Ru contact material testing showed slightly different behavior when compared to gold-gold contact testing. Both materials were tested at the contact force of 400 μN, hot-switched with 0.5 mA current. The environment used during cycling was laboratory air, so contamination played a role in results. Note that humidity, temperature and trace gas components are uncontrolled in ambient air and may play a role in contact surface contamination. The Au5%Ru material lasted longer than gold but had a higher contact resistance which was expected due to the comparative material hardness and resistivities of the materials. The pull-off force, which is a measure of contact adhesion, for Au5%Ru contacts was less than gold due to the higher hardness and two-phase microstructure. This result contrasts with the analysis published in [132] and [202] which reports that higher hardness contact materials have higher adhesion. The threshold force for Au5%Ru was greater and was extremely variable between measurements. The higher required threshold force for Au5%Ru was due to its higher hardness when compared to gold. The variability in

the threshold force measurement was likely due to a greater presence of contamination on the Au5%Ru contacts. Threshold distance for Au5%Ru contacts was roughly the same as the distance required for gold. This result is reasonable, as the proximity of the two surfaces should be roughly the same in order to facilitate electron mobility between the contacts. There was no evidence of overall contact strain hardening throughout the testing of Au5%Ru contacts. However, an example Au5%Ru long-life test did show contact softening due to damage accumulation on the contact surface. This may have been accelerated by contact softening due to contact heating. The contact interference (or penetration) at maximum contact load was less for Au5%Ru than for gold. This is expected due to the higher hardness, and thus resistance to penetration, of Au5%Ru. The energy absorbed by the Au5%Ru contact during testing appeared to be very similar to that of gold. Both materials showed that the longer lifetime contacts had a higher plastic deformation early in cycling, which may be due to smoothening early in contact life. This may indicate that the shorter lifetime contacts in each case had lower initial surface roughness. It appeared that gold had a slightly higher initial plastic deformation when compared to Au5%Ru, but the amount of plastic deformation equalized and was comparable between gold-gold and Au5%Ru-Au5%Ru up to 250,000 cycles. This is attributed to the higher yield strength of Au5%Ru compared to gold. The contact surface evolution characteristics of Au5%Ru was different than the gold contacts tested. Analysis of failure surfaces showed that shorter-life Au5%Ru contacts commonly showed flattening or smoothing of the contact area, whereas short-life gold surfaces showed more instances of material transfer. This difference is attributed to brittle separation in the case of Au5%Ru contacts compared to ductile separation of gold contacts. There was no indication in the gold or Au5%Ru data sets that contact bump shape affected results in this study. However, more testing should be done to further investigate results of contact bump shape. Differences in contact behavior between shorter and longer lifetime results in Au5%Ru contacts were noted. Shorter lifetime contacts had slightly lower measured contact resistance, higher pull-off force, lower initial threshold force and

distance, lower initial contact interference, lower time dependent deformation and lower energy absorbed when compared to longer life Au5%Ru contacts. Most differences are attributed to smoother initial surfaces and less initial surface contamination on shorter-lifetime contacts. Early threshold distance differences between shorter-life contacts and the average for all Au5%Ru contacts indicated that differences in initial surface conditions may play a large role in contact lifetime. It is also possible that shorter-life contacts may have had more initial barriers to dislocation motion leading to less contact interference and time-dependent deformation.

The higher hardness of Au5%Ru contacts compared to gold led to lower adhesion and slower surface damage accumulation on contact surfaces. This testing showed that harder contact material is preferable to avoid early adhesive failure for longer lasting MEMS contacts.

X. Gold-Vanadium Oxide Alloy Contact Measurements

This chapter presents results of testing accomplished on gold-vanadium oxide (Au-4%V_2O_5) alloy contacts. The tests were run using the setup and method described in previous chapters. Custom fabricated cantilevers and strike plates were sent to Lehigh University for coating with Au-4%V_2O_5 contact material. Details of the material and coating process as well as some test data indicating that this dispersion strengthened material is a good candidate for use as a contact material in MEMS contact switches can be found in [8, 9]. The cantilevers were coated with 300 nm of contact material at Lehigh. Only six cantilevers coated with Au-V_2O_5 were available for testing, so the test measurement interval was increased when compared to most of the testing done on Au and Au5%Ru contacts to ensure tests continued to the end of contact life. Au-4%V_2O_5 is a dispersion strengthened conductive material with a modulus of elasticity of approximately 175 MPa as measured by nanoindentation at AFIT and a hardness of approximately 4 GPa and a resistivity of 17.7 $\mu\Omega$-cm as reported in [8]. Bannuru also estimates that the particle radius dispersed in the matrix is 2.2 nm [9]. Comparison of three material properties of interest for the three contact materials tested in this study is shown in Table 10.1.

10.1 Contact Lifetime

Six tests were performed using Au-4%V_2O_5 as a contact material. Two of the tests with this contact material ran for 8.0×10^6 cycles and 15.5×10^6 cycles without any failure, respectively. Two tests failed at 250,000 and 500,000 cycles due to adhesion and one test failed after 20,000 cycles when the thin film on the contact bump adhered

Table 10.1: Contact material properties comparison.

Contact Material	Modulus of Elasticity (MPa)	Hardness (GPa)	Resistivity ($\mu\Omega$-cm)
Gold	86	1.04	3.6
Au5%Ru	122	2.42	38.5
Au-4%V_2O_5	175	4	17.7

Table 10.2: Test summary of Au-4%V_2O_5 micro-contact testing. Note that two of the tests were stopped prior to failure.

Contact ID	Contact Material	Contact Force (μN)	Initial Contact Resistance (Ω)	Failure Type	Number of Cycles Tested (# Cycles)
B1011-1_5	Au-V_2O_5	400	7.8	High Resistance (film delaminated)	20,000
B1011-1_9	Au-V_2O_5	400	8.2	Adhesion	250,000
0602-3_4	Au-V_2O_5	400	9.5	Adhesion (film delaminated)	500,000
B1011-1_8	Au-V_2O_5	400	7.8	Overload (film delaminated)	1.63×10^6
0602-3_1	Au-V_2O_5	400	10.7	No Fail (partial film tear)	8.0×10^6
0210-2_11	Au-V_2O_5	400	8.8	No Fail	15.5×10^6

to the strike plate. The last test experienced an overload due to instrument error at 1.63×10^6 cycles and failed prematurely.

Table 10.2 shows an overview of lifetime test results for Au-4%V_2O_5. Not enough samples were tested to definitively categorize lifetime failures. However, these failures appear to fall in short-life, mid-life, and long-life categories similar to gold. The pre-cycling, post-cycling and bottom contact images for the short-life test which failed at 20,000 cycles are given in Figures 10.1, 10.2, 10.3 and 10.4 respectively. This contact failed in adhesion, as can be seen by the contact film which separated from the contact bump substrate and remained adhered to the strike plate at the bottom contact location. Note that the last in-contact resistance measurement of 79 Ω taken during this test indicated this as a high resistance failure, as seen in Figure 10.5, but SEM inspection of the failed contact showed that this was actually a contact adhesion failure. Relatively high levels of material transfer can be seen on the edge of the contact area in Figure 10.4. There also appears to have been contamination on the substrate surface before sputtering. This pre-existing contamination which is visible on the backside of the thin film contact shown in Figure 10.4 may have contributed to reduced adhesion between the thin film and substrate. This may have led to separation of the thin film from the substrate when contact adhesive forces increased. This failure, which could easily have been identified as a "contamination" failure due to the indication of high resistance at the end of life, shows that it is important to visually inspect failure surfaces when identifying the cause of failure.

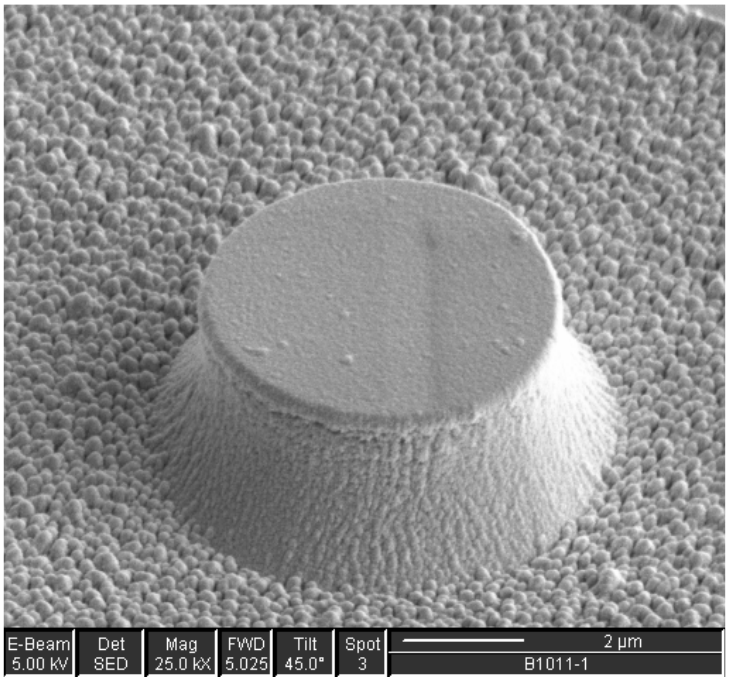

Figure 10.1: Au-4%V_2O_5 contact bump before testing. This contact failed in adhesion after 20,000 cycles due to the thin film separating from the contact bump.

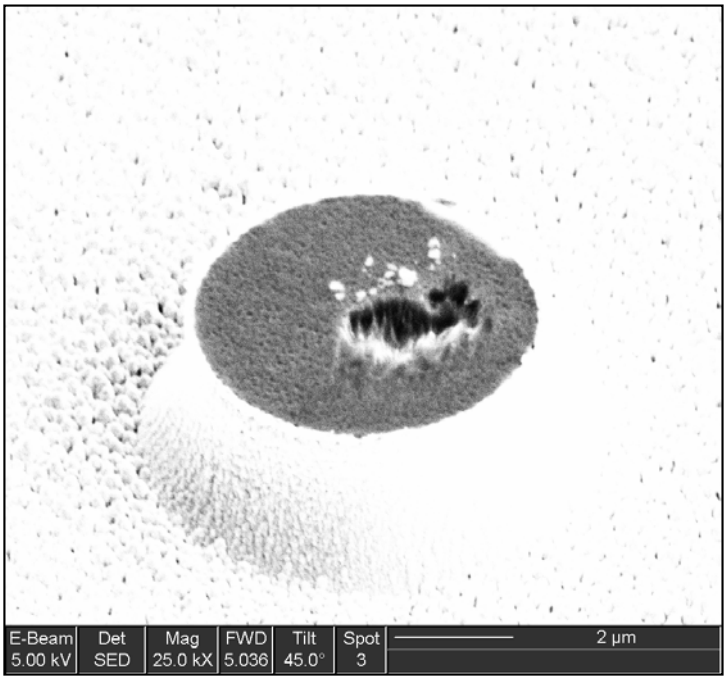

Figure 10.2: Au-4%V_2O_5 contact bump which failed in adhesion after 20,000 cycles. This contact failed in adhesion between 10,000 and 20,000 cycles due to the thin film separating from the contact bump. The contrast was adjusted in order to focus clearly on the contact bump surface.

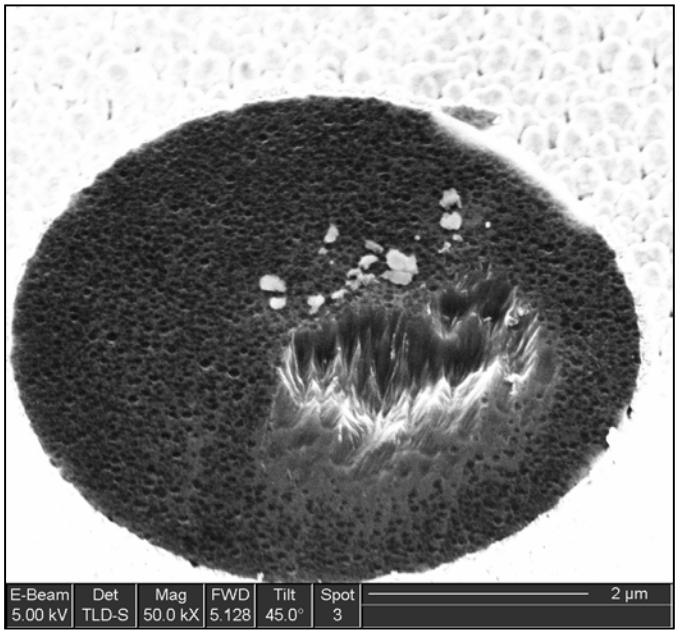

Figure 10.3: Closeup of Au-4%V_2O_5 contact bump which failed in adhesion after 20,000 cycles. This contact failed in adhesion between 10,000 and 20,000 cycles due to the thin film separating from the contact bump. The contrast was adjusted in order to focus clearly on the contact bump surface.

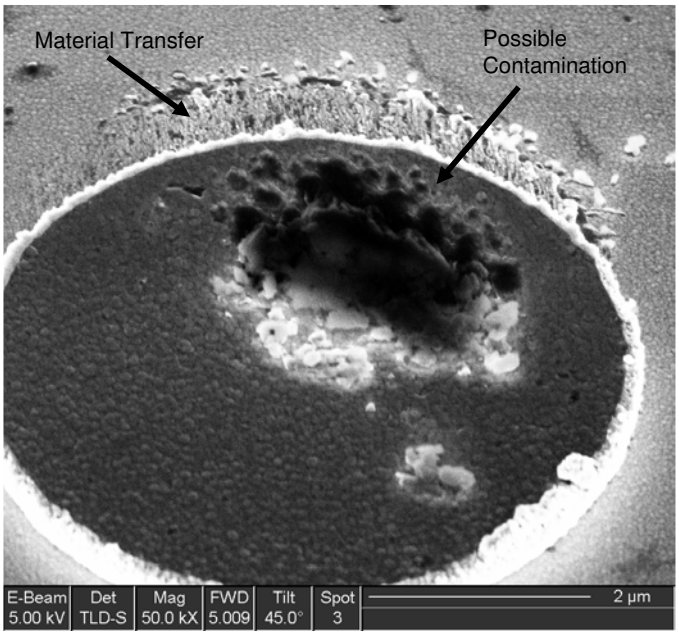

Figure 10.4: Au-4%V_2O_5 bottom contact location on strike plate which failed in adhesion between 10,000 and 20,000 cycles. This contact failed in adhesion when the thin film separated from the contact bump. The contact film can be seen here clearly adhering to the strike plate. There may have been contamination on the surface of the contact bump substrate leading to low adhesion of the thin film to the substrate.

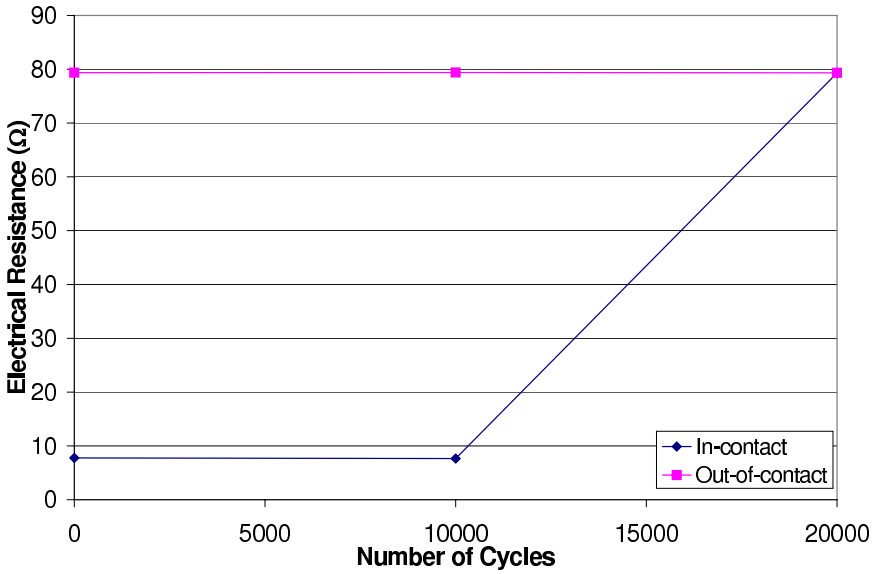

Figure 10.5: Resistance measurements on Au-4%V_2O_5 contact bump which failed between 10,000 and 20,000 cycles. Note that this measurement shows high resistance failure but this contact failed in adhesion between 10,000 and 20,000 cycles due to the thin film separating from the contact bump.

The mid-life adhesion failures (250,000-500,000 cycles) appear to be similar to the gold short-life (Type I) failures. However, there is some contamination present in the contact area of mid-life Au-V_2O_5 contacts while little to no contamination was visible on the short- or mid-life (Type I or II) gold contacts after cycling. Figure 10.6 shows a Au-4%V_2O_5 contact before testing and Figure 10.7 shows the same bump which failed in adhesion at 250,000 cycles. The contact appears to have experienced ductile separation and some debris is visible on the bottom contact surface which is shown in Figure 10.8. Figure 10.9 shows an example of a bump which experienced a thin film failure during cycling at 500,000 cycles and Figure 10.10 shows the corresponding strike plate after the thin film failure. Therefore, the Au-4%V_2O_5 contacts demonstrated both Type I and II failures, i.e. characteristic ductile failure surface and contact film failure respectively, but the failure types were not associated with lifetime groupings.

Two Au-4%V_2O_5 contact tests ran significantly longer without failure than all other tests accomplished during this study. Both of these long-running tests were

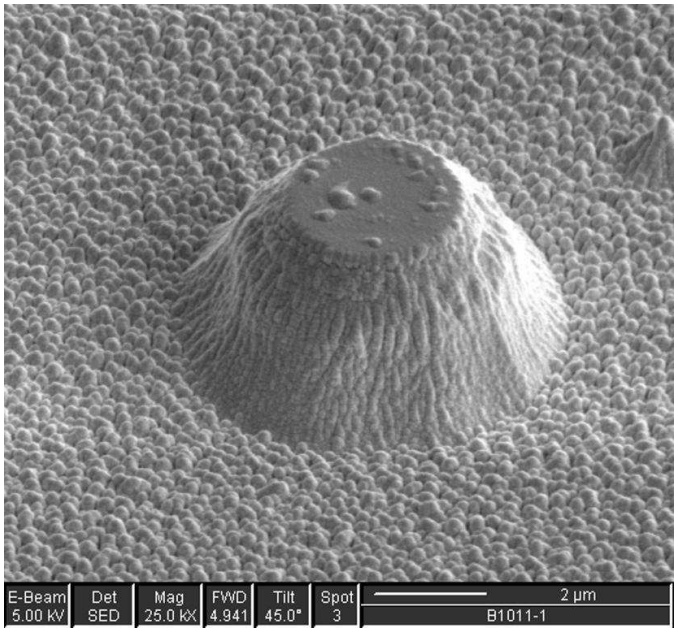

Figure 10.6: Au-4%V_2O_5 contact bump before testing. This contact failed in adhesion at 250,000 cycles.

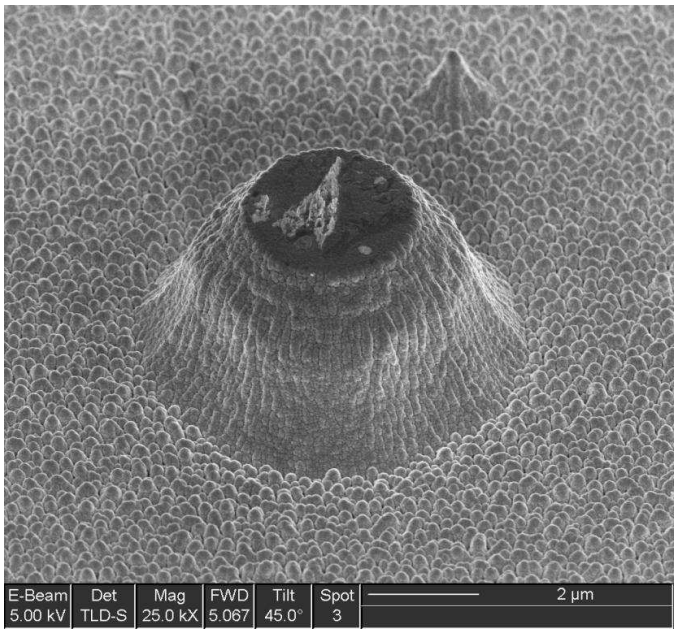

Figure 10.7: Au-4%V_2O_5 contact bump which failed in adhesion after 250,000 cycles. The resulting damage pattern is similar to the results for the short life gold contacts (Type I).

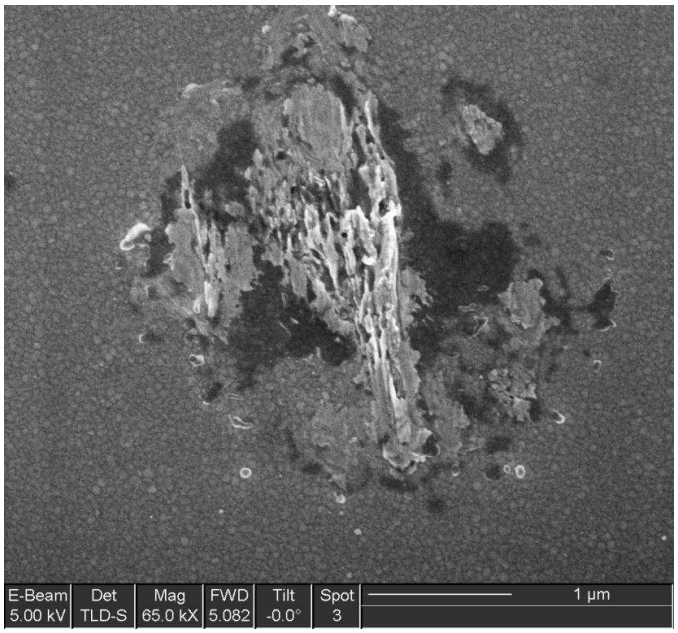

Figure 10.8: Au-4%V_2O_5 bottom contact location on strike plate which failed in adhesion after 250,000 cycles. The resulting damage pattern is similar to the results for the short life gold contacts (Type I).

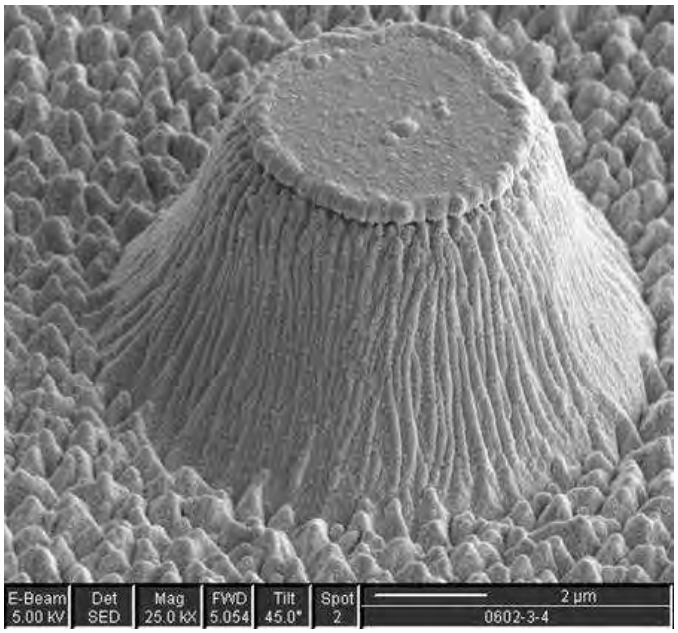

Figure 10.9: Pre-cycling image of Au-4%V_2O_5 coated contact bump which failed in adhesion causing the thin film to separate from the contact bump before 500,000 cycles (Type II).

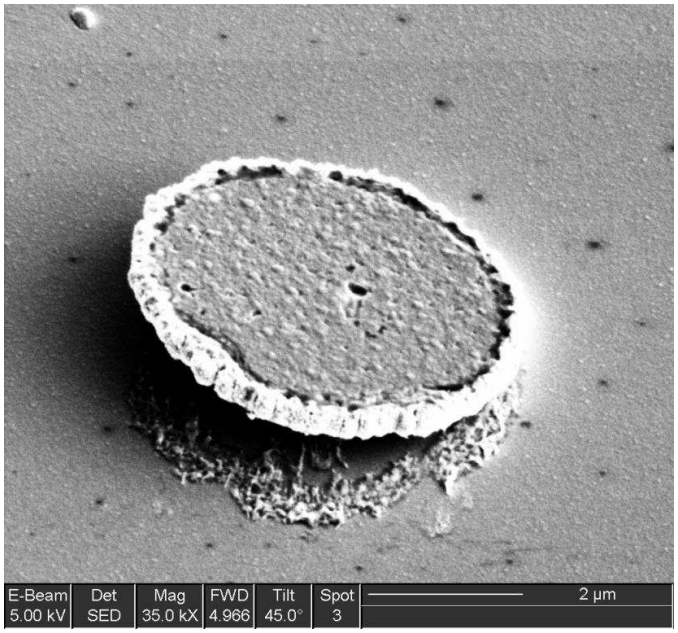

Figure 10.10: Au-4%V_2O_5 bottom contact location which failed in adhesion causing the thin film to separate from the contact bump after 500,000 cycles (Type II).

stopped prior to contact failure, one at 8×10^6 cycles and one at 15.5×10^6 cycles. The test which ran for 8×10^6 cycles had a large amount of damage on the contact due to part of the conductive contact film separating from the contact bump and remaining adhered to the strike plate. However, there was enough viable contact material remaining to continue cycling with measured contact resistance which met the criteria to continue testing. The before and after images of the contact which ran for 8×10^6 cycles are shown in Figures 10.11 and 10.12 respectively. The bottom contact location on the strike plate for this test is shown in Figure 10.13. This failure of the thin film likely occurred due to either a pre-existing flaw in the contact film or development of contact damage during cycling causing an initiation point for film failure. Note that the silicon cantilevers coated at Lehigh University were divided into two batches. The first batch was cleaned with a 10 minute piranha etch as previously described. However, that cleaning process destroyed several samples so the second batch of cantilevers was not cleaned prior to deposition. This may have led to poor adhesion between the Au-4%V_2O_5 film and the substrate in the second batch. Figure 10.13 shows some contamination under the edges of the adhered portion of the thin

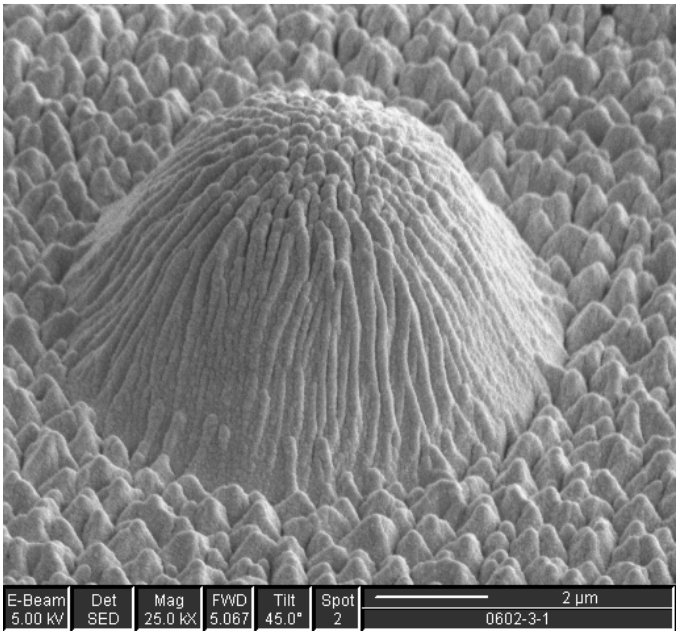

Figure 10.11: Au-4%V_2O_5 contact bump before 8×10^6 Cycles.

film which could have reduced adhesion between the contact bump and the strike plate over some part of the contact area.

The pre-cycling image of the Au-4%V_2O_5 contact bump which ran 15.5×10^6 cycles is shown in Figure 10.14. The failure surface on the contact bump shown in Figure 10.15 appears different than other failure surfaces developed during this study. There appears a smaller amount of material transfer than occurred in either gold or Au5%Ru contact tests. The surface also appears to show possible crack initiation points. Note that the bump features on the surface are artifacts from the fabrication process, likely during the RIE/ICP etch, and can be seen in Figure 10.16 which is an image of the contact bump after the fabrication etch before coating with Au-4%V_2O_5. These rough features can also be seen in Figure 10.14, although not as clearly. A topview image of the after-cycling surface is shown in Figure 10.17. The rough surface of the contact bump is visible, as are the evidence of material transfer and possible surface cracking. The bottom contact location on the strike plate is shown in Figure 10.18. There is indication of possible melting on the edge of the contact area. Recall that heat production rises sharply at the edge of circular electrical contact [85]. The

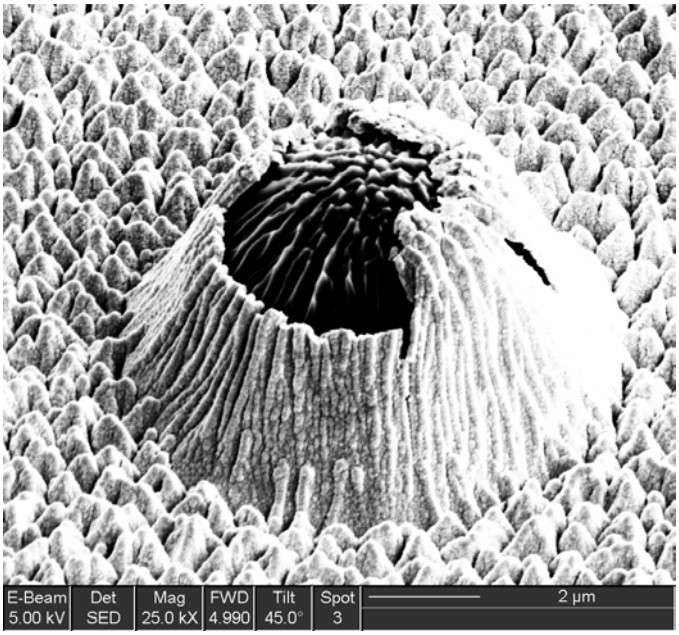

Figure 10.12: Au-4%V_2O_5 contact bump after 8×10^6 cycles. Note that part of contact film separated from contact bump substrate, but contact continued to cycle with low resistance.

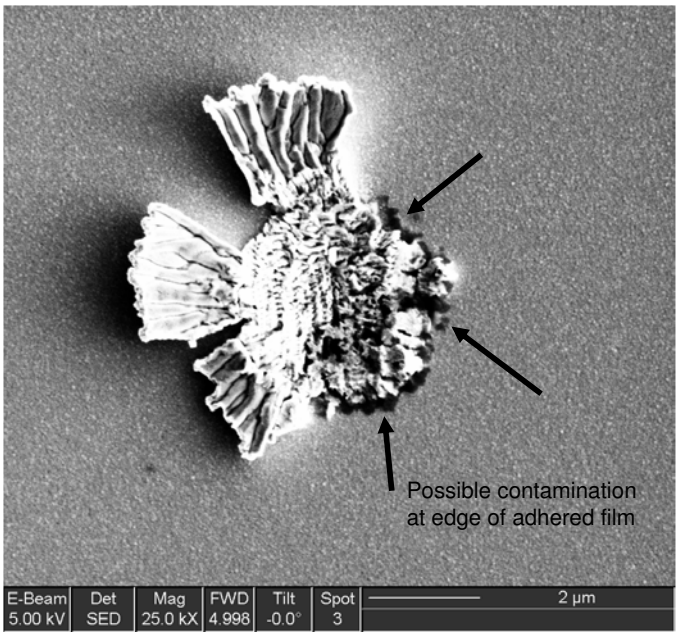

Figure 10.13: Au-4%V_2O_5 contact location on strike plate after 8×10^6 cycles. Note that part of contact film separated from contact bump substrate, but contact continued to cycle with low resistance.

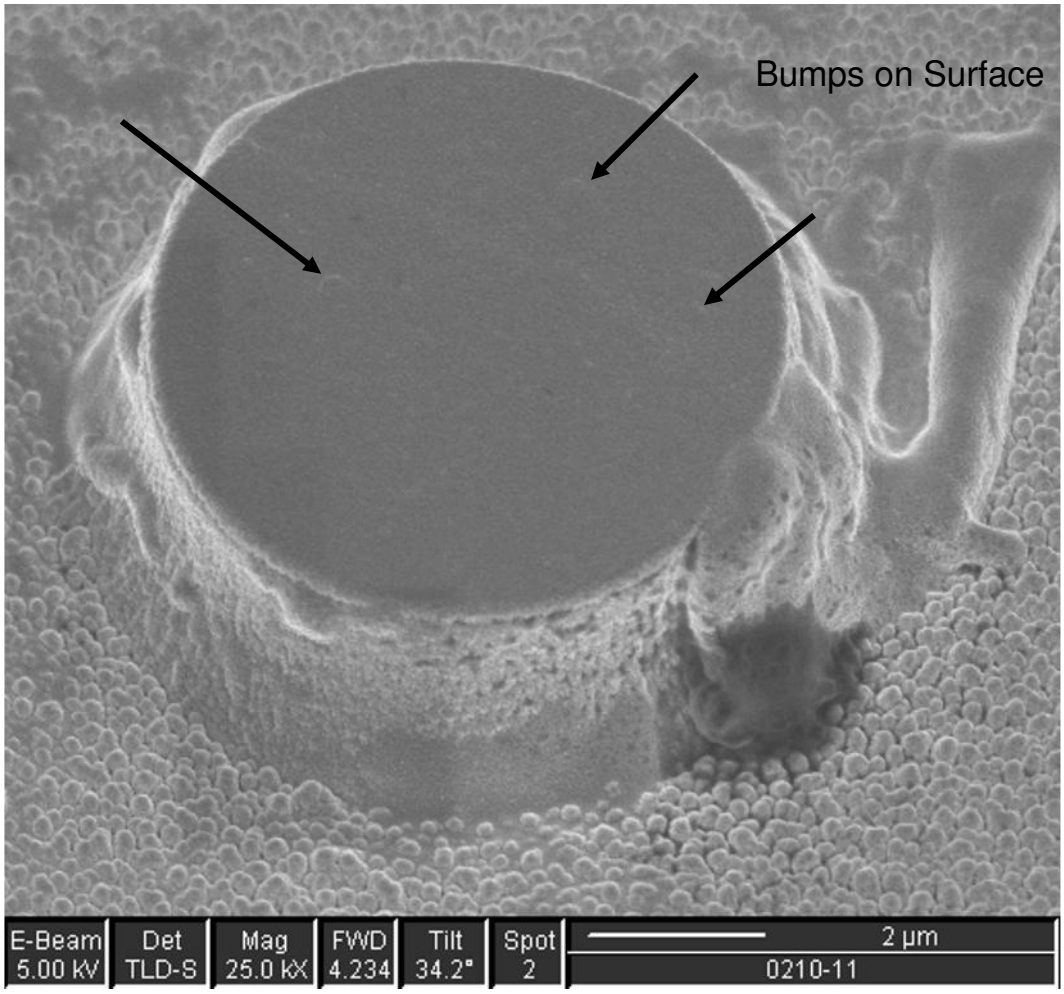

Figure 10.14: Au-4%V_2O_5 contact bump after coating before testing (0210-2_11). Note presence of bumps on surface (not all are marked with arrows).

contact was still providing good electrical contact and had not failed after 15.5×10^6 cycles. This contact lasted significantly longer than any of the other tests in this study. Surface cracking and damage is evident but no large ductile features or contamination is visible on the contact surface itself. More detailed images of the area of material transfer are shown in Figures 10.19 and 10.20.

This surface looks most like the gold Type III long-life failure surface shown in Figure 8.10. However, the lower contact surfaces do not appear similar. More contamination and possible heat damage appear on the Au-4%V_2O_5 surface when compared with the gold failure surface. This difference could partially be due to the

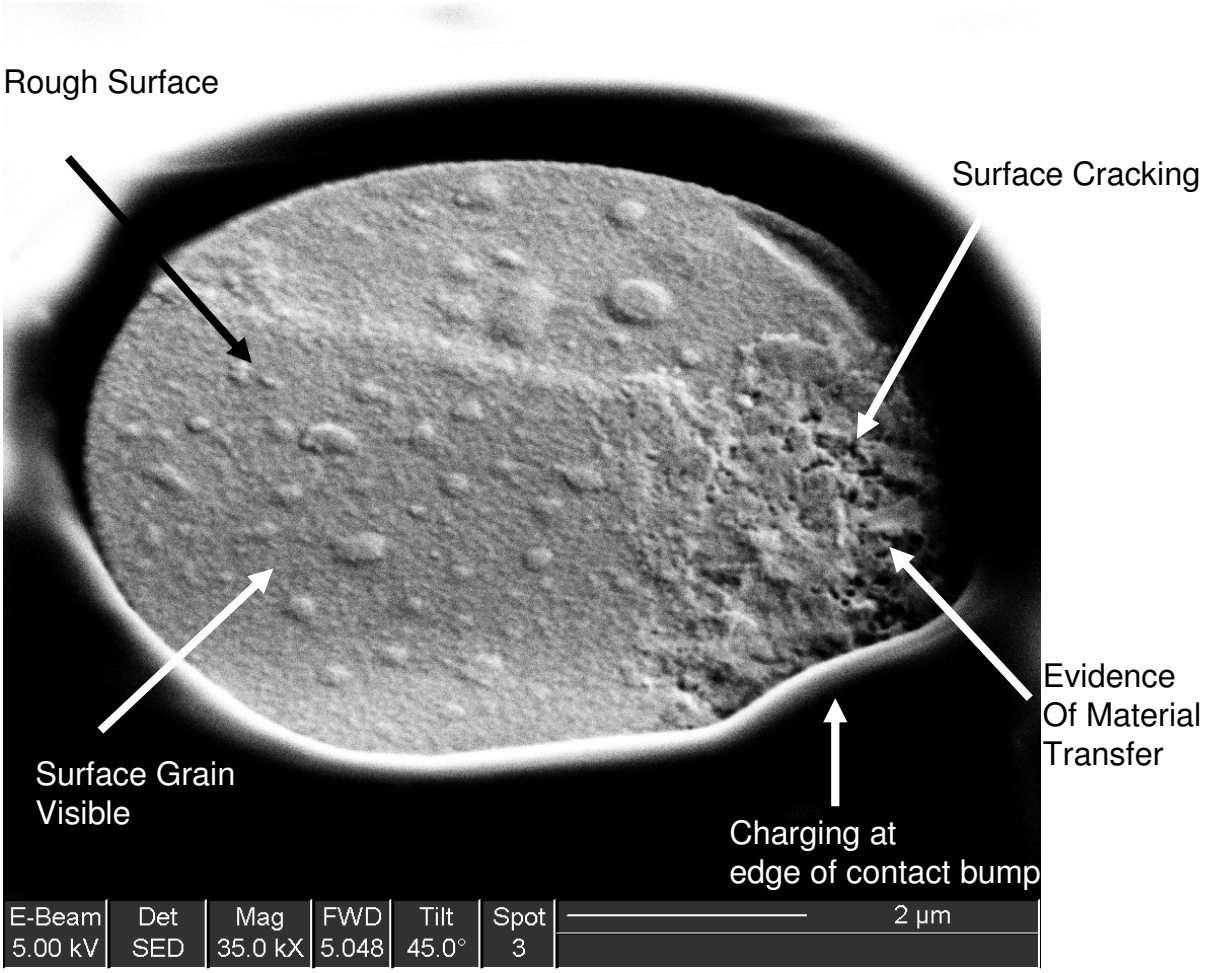

Figure 10.15: Au-4%V_2O_5 contact bump (0210-2_11) after 15.5×10^6 cycles. The contact did not fail and was the longest running test of any during this research. The resulting damage pattern appears to show cracking and material transfer on the contact surface. The white ring around the contact bump is likely contamination created during the cycling test.

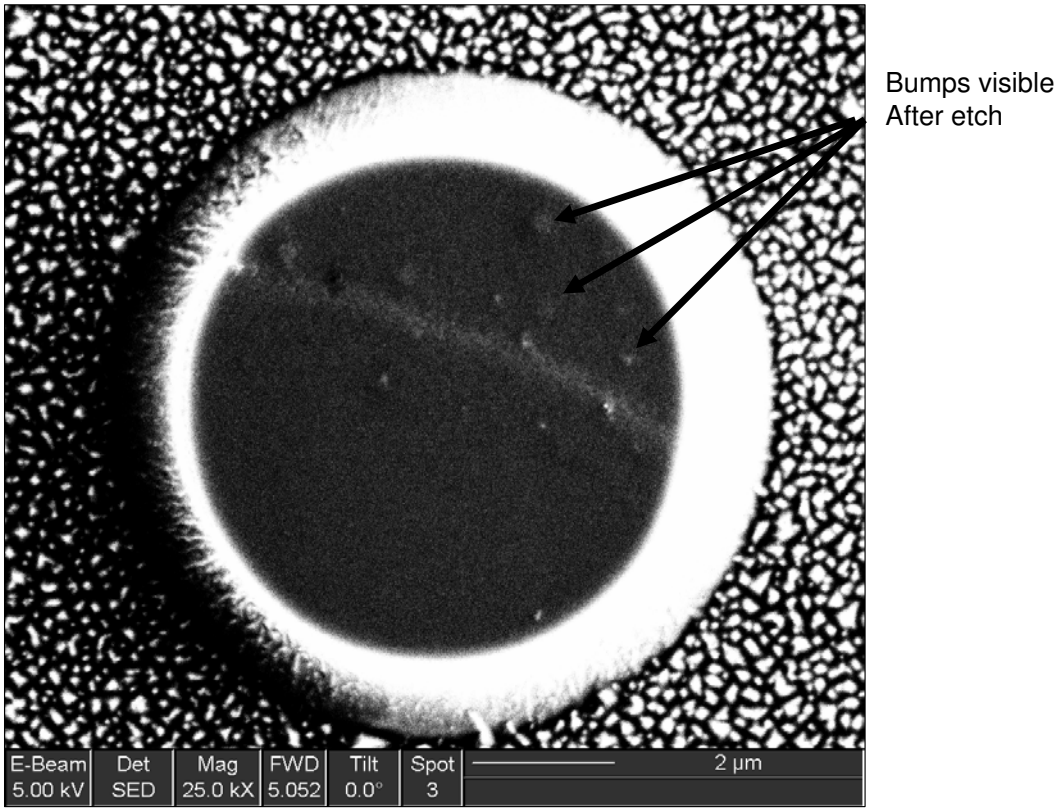

Figure 10.16: Au-4%V_2O_5 contact bump after bump etch but before coating (0210-2_11). Note existence of bump features on surface.

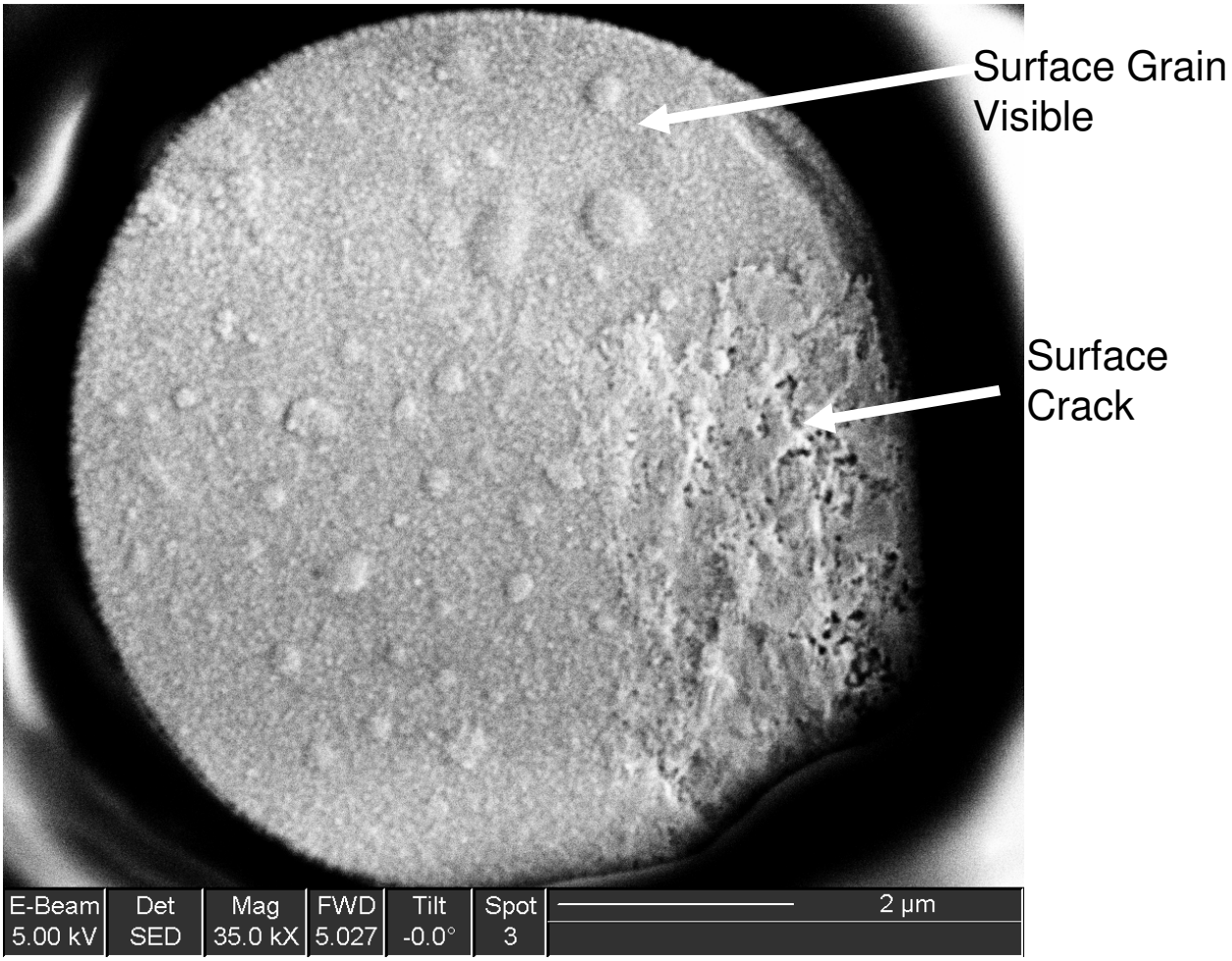

Figure 10.17: Au-4%V_2O_5 contact bump (0210-2_11) after 15.5×10^6 cycles topview. Topview of bump shown in Figure 10.15. Surface roughness is more clearly visible in this image. The small surface bumps pre-existed contact cycling.

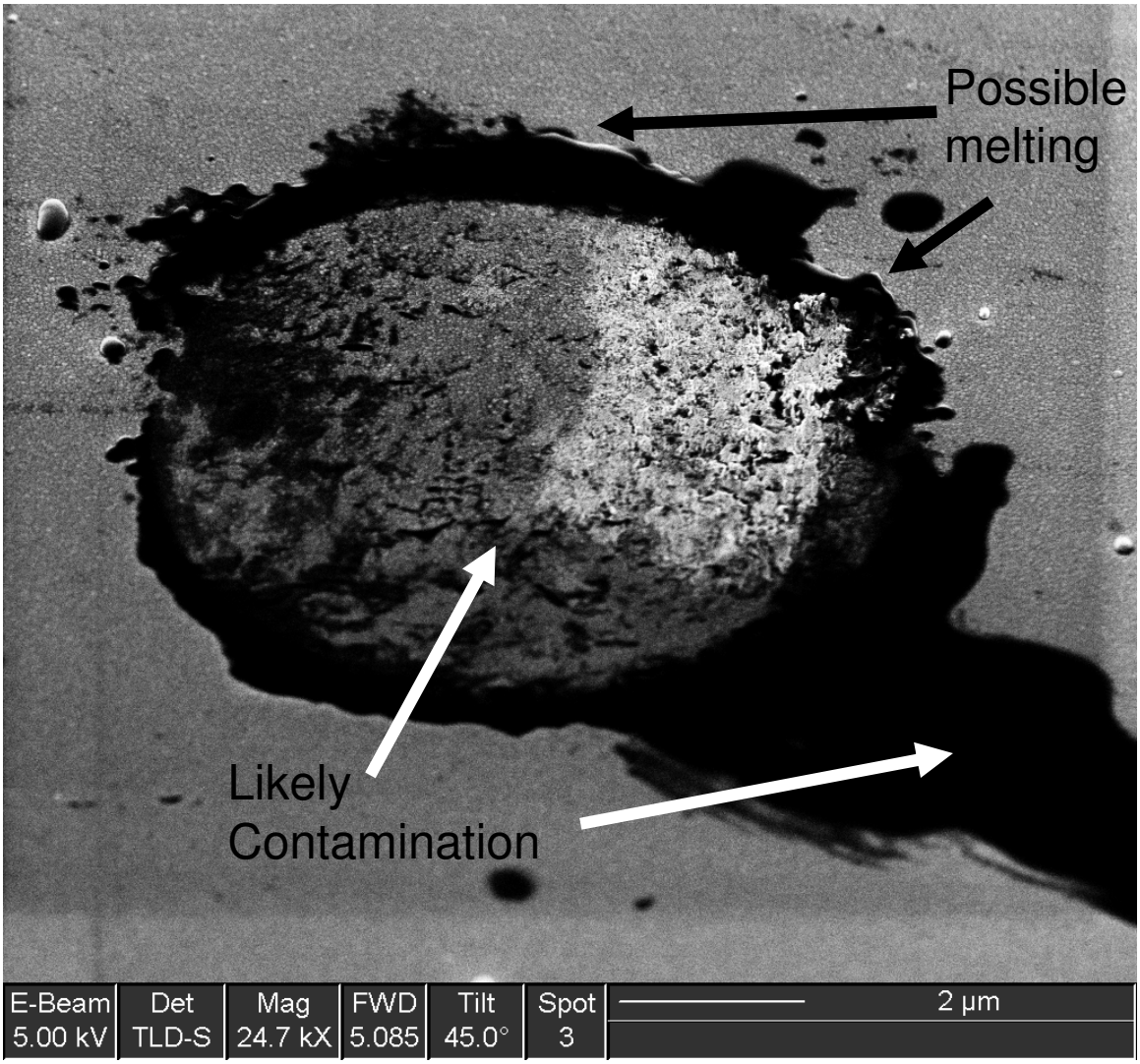

Figure 10.18: Au-4%V_2O_5 strike plate contact site after 15.5×10^6 cycles. The contact did not fail and was the longest running test of any during this research. The resulting wear pattern appears to show cracking and damage on the contact surface as well as indications of dark contamination.

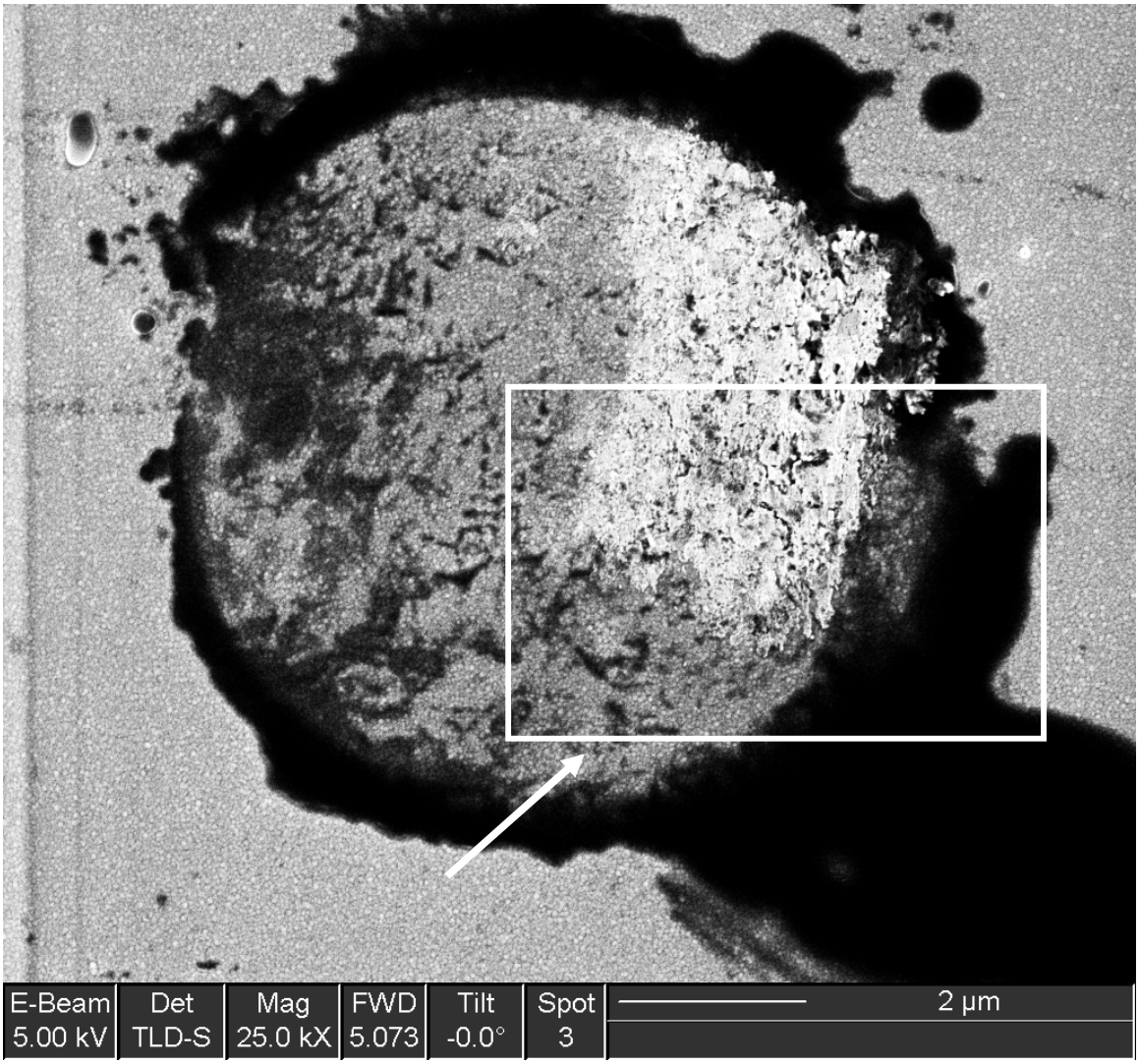

Figure 10.19: Au-4%V_2O_5 strike plate contact site showing area of closeup imaged in Figure 10.20

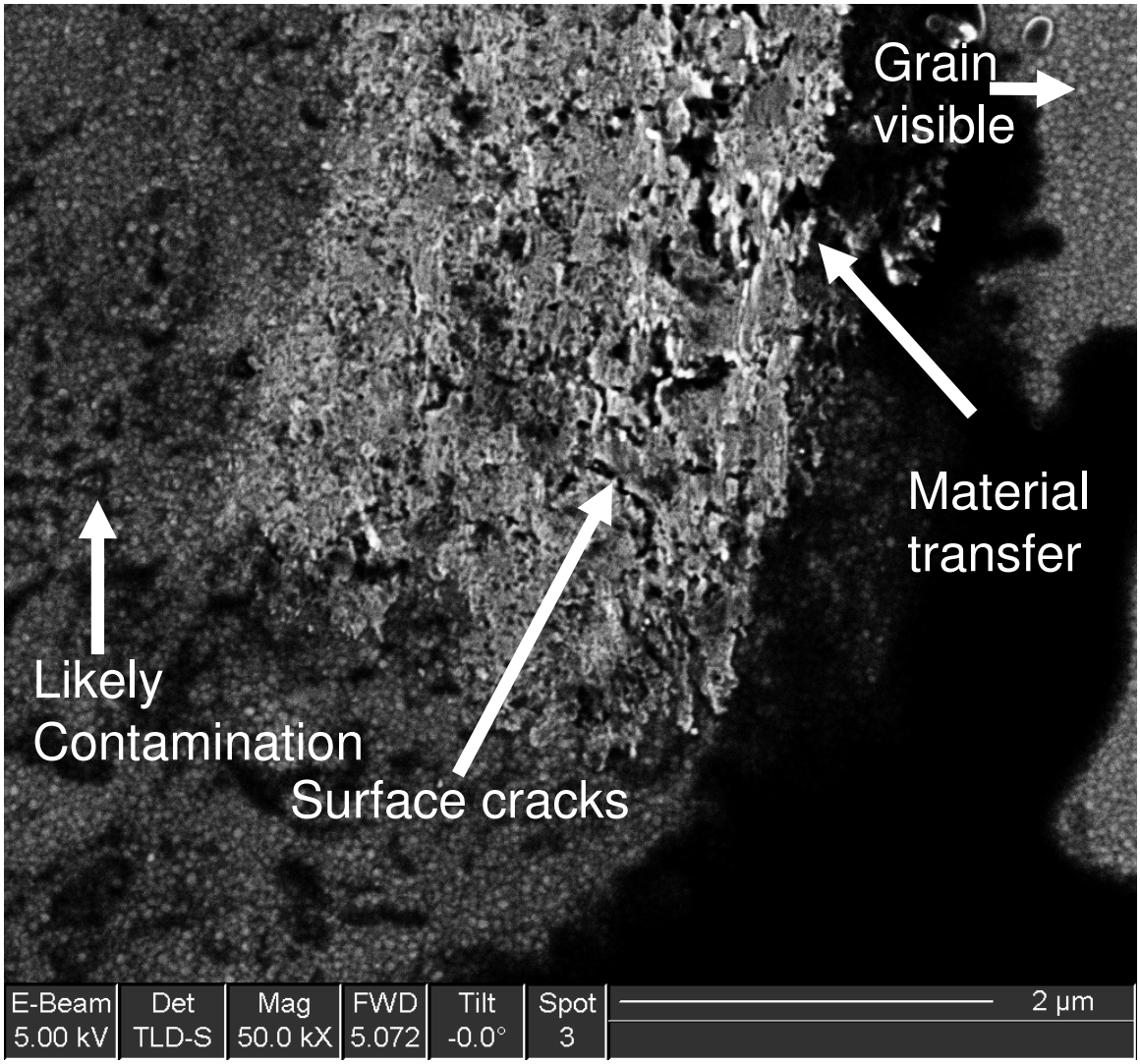

Figure 10.20: Au-4%V_2O_5 strike plate contact site after 15.5×10^6 cycles. High magnification image of portion of contact area on strike plate. Note surface grain is visible.

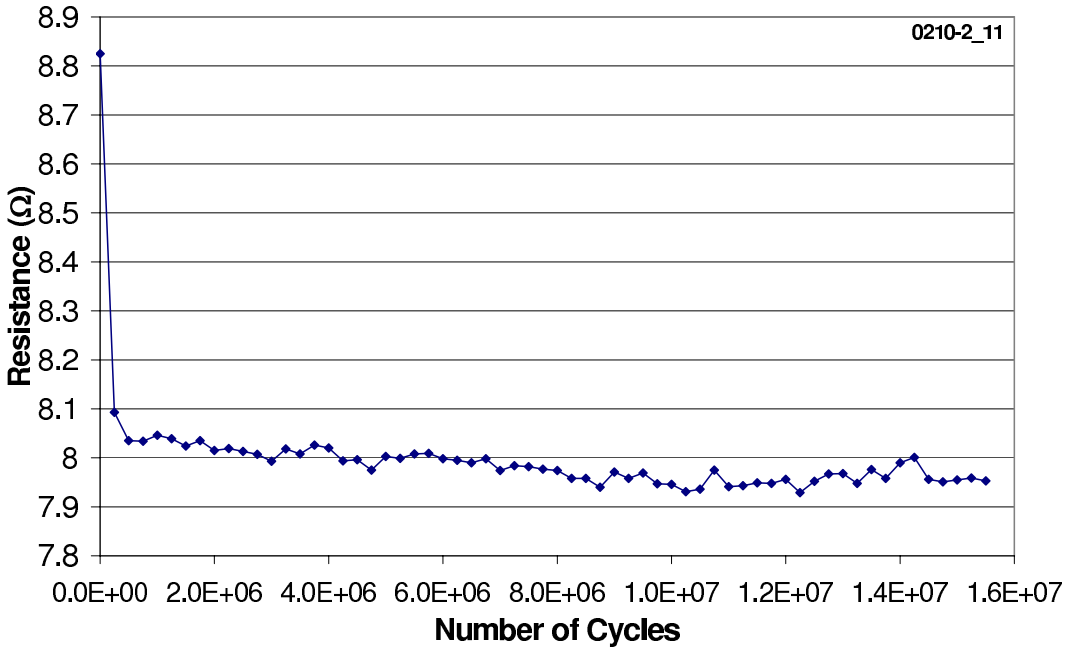

Figure 10.21: Contact resistance trend for longest running Au$-4\%V_2O_5$ contact test.

fact that the Au-$4\%V_2O_5$ surface had not yet failed. This difference is likely due to the extended amount of time over which the Au-$4\%V_2O_5$ experienced cycling and possible contact heating when compared to the gold.

Contamination created during cycling of Au-$4\%V_2O_5$ contacts appeared slightly different than that seen in either gold or Au5%Ru testing. Some contamination was located on the contact surface, but most was in an annular ring around the contact area. It also appears that there was some contact melting at the edge of the contact area. This is shown in Figure 10.18. The contact resistance during this long duration test stayed relatively constant, only decreasing slightly, at approximately 8.5 Ω. This result is shown in Figure 10.21 and indicates that the visible contamination on the strike plate contact surface did not affect the contact resistance.

There was, however, significant charging of the sample around the contact bump while under SEM investigation and is shown in Figures 10.15 and 10.22. This charging was attributed to contamination on the surface of the cantilever and around the contact bump. This contamination appeared bright in SEM imagery rather than dark

Table 10.3: Description of surface condition/failure types demonstrated and categorized for Au-4%V_2O_5. Thin film separation caused by contamination under thin film removed from list.

Failure Type	Description	Material Demonstrated	Lifetime (# Cycles)
I	Ductile characteristics	Au-4%V_2O_5	~250,000
II	Contact film failure	Au-4%V_2O_5	~500,000
III	Brittle separation, smoothed surfaces and contamination formation	Au-4%V_2O_5	$> 15.5 \times 10^6$

as was typical for contaminants observed on cantilevers and contacts in other tests accomplished during this study. XPS analysis accomplished at Lehigh University determined that the contaminant on the test cantilever appeared to be a hydrocarbon of some type [248]. XPS results are shown in Figures 10.23 and 10.24 for the contaminated contact and cleaner contact, respectively. The results show that the contaminated contact has approximately 4-times greater presence of carbon on the contact. This long-life sample (15.5×10^6 cycles) experienced a rigorous cleaning process at Lehigh prior to deposition, while the other Lehigh coated samples tested during this study were not cleaned prior to sputtering. The rigorous cleaning process used before coating at Lehigh damaged or destroyed multiple test devices so the decision was made to reduce the amount of cleaning done on remaining samples to ensure a higher yield of test ready devices. Only one sample tested survived the ten minute piranha etch rigorous cleaning process, and it was the only device which showed signs of significant contamination and charging during SEM examination after cycling. There was no noticeable change in contact resistance during the test due to the contamination. The long-term trend of contact resistance during the 15.5×10^6 cycle test is shown in Figure 10.21.

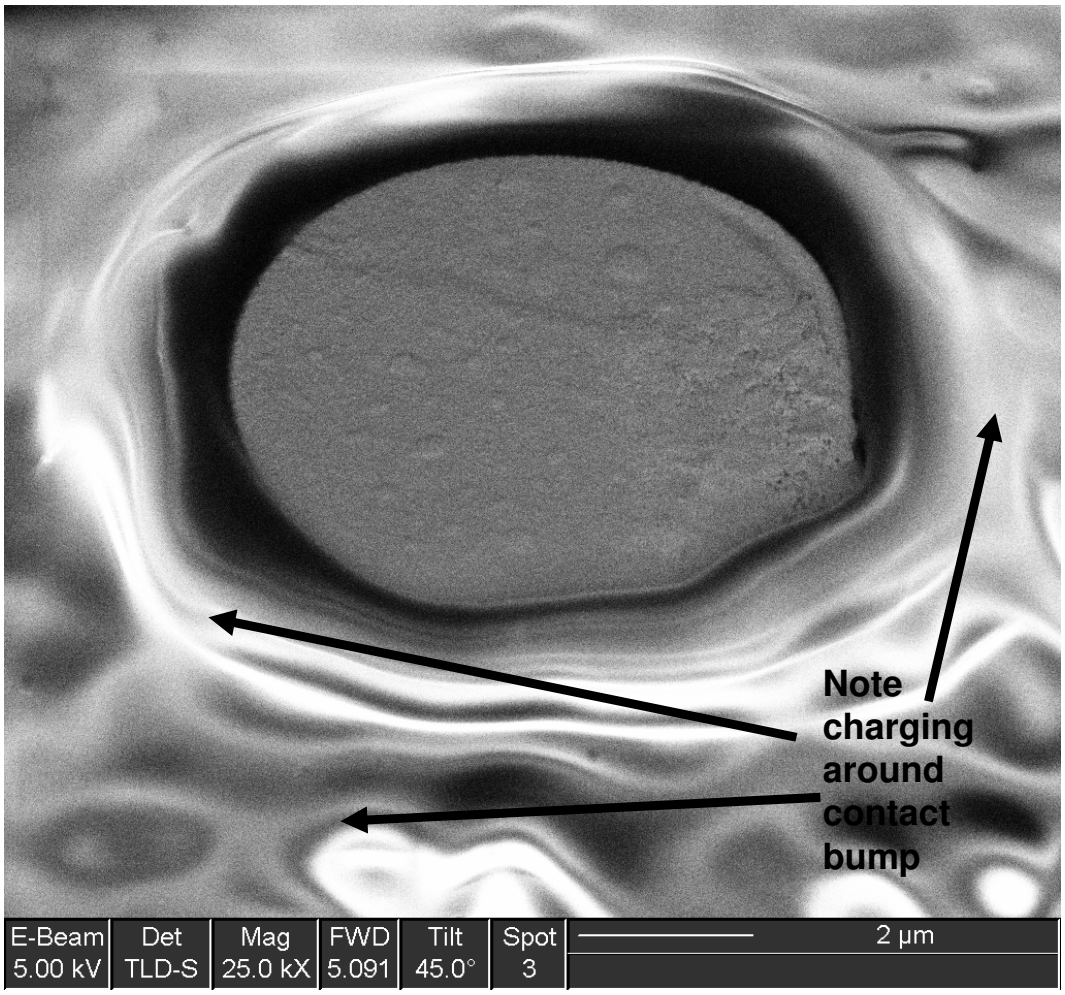

Figure 10.22: Au-4%V_2O_5 contact bump charging (0210-2_11) after 15.5×10^6 cycles. Bright areas around bump show charging during scanning electron microscope investigation. Possibly indicates contamination.

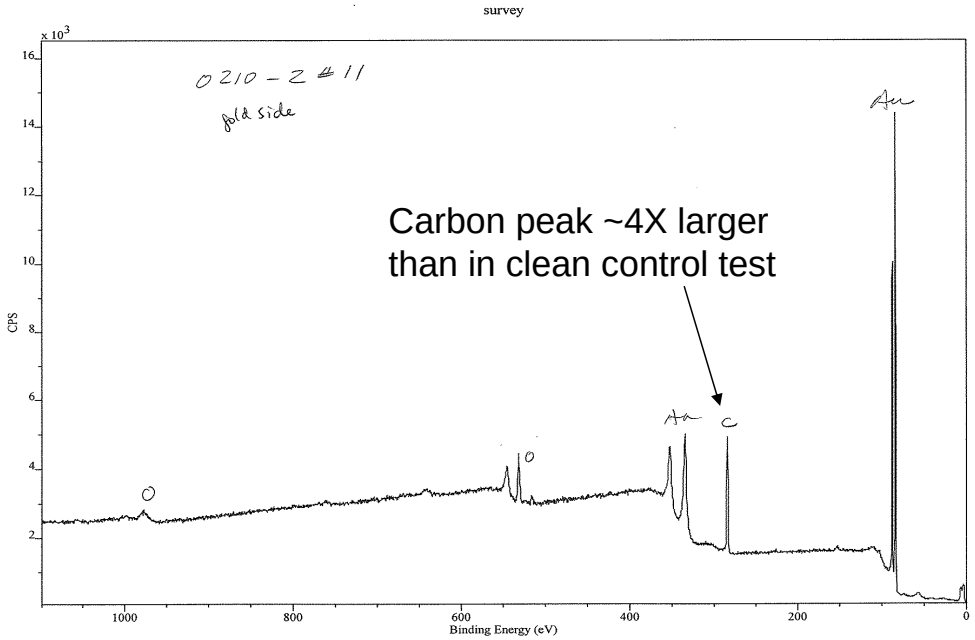

Figure 10.23: Lehigh University XPS Results on long-life (15.5×10^6 cycles) Au-$4\%V_2O_5$ contact shows carbon peak approximately 4-times larger than comparable visually clean contact whose result is shown in Figure 10.24. Contamination was evident in SEM image. [248].

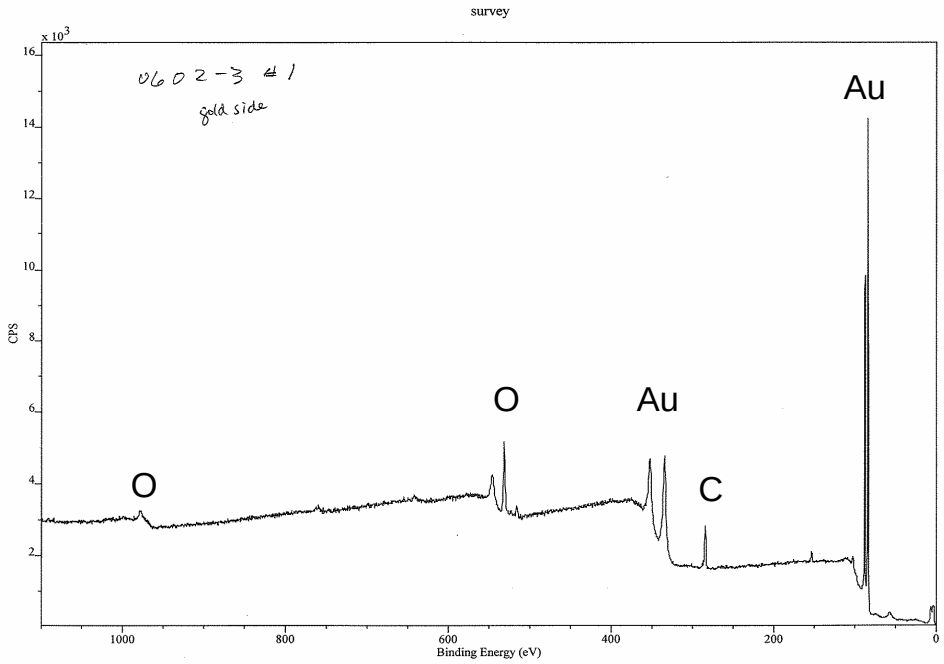

Figure 10.24: Lehigh University XPS Results on long-life (8×10^6 cycles) Au-$4\%V_2O_5$ contact shows smaller carbon peak when compared to result in Figure 10.23. No contamination was evident in SEM image of this contact [248].

10.2 Contact Resistance

The contact resistance of the Au$-4\%V_2O_5$ contacts during testing was slightly less than for Au%5Ru. The average contact resistance through all testing using the gold-vanadium oxide material was approximately 8.5 Ω with a range of values from 7.8-10.5 Ω. Contact resistance for this material was estimated at 5 Ω using the Holm equation (Equation 2.29) and a contact force of 400 μN. The difference is due to parasitic resistances in the experimental setup which were included in the resistance measurement (e.g. solder joints, terminal strip contacts, etc.) A comparison of average contact resistance between all three contact materials tested is shown in Figure 10.25 and long term examples of contact resistance for all three materials are shown in Figure 10.26. The error bars used in the figure show one standard deviation from the averaged values. Measurements of resistance over the life of the Au$-4\%V_2O_5$ contact given in Figure 10.21 show a similar downward trend during cycling that was demonstrated by the example given for Au5%Ru shown in Figure 9.17. This reduction in resistance effect is attributed to a small increase in contact area due to plastic deformation during cycling (e.g. [9]). This effect could also be caused by a temperature increase at the contact spot sufficient to cause annealing of dislocations in the contact material, thus reducing contact resistance through contact softening [115].

Detection of contact adhesion failure using in-contact and out-of-contact resistance was described in Section 7.3.5 and is shown graphically for a gold contact test in Figure 8.21 and a Au5%Ru contact test in Figure 9.18 and is shown here for a Au$-4\%V_2O_5$ contact test in Figure 10.27. The criteria used to detect contact adhesion failure is described in Section 6.2.5 and the ability of this test apparatus to automatically detect contact adhesion failure is described and demonstrated in Sections 7.2.1, 7.4.3, 8.3 and 9.3. All failed Au$-4\%V_2O_5$ contacts failed in adhesion.

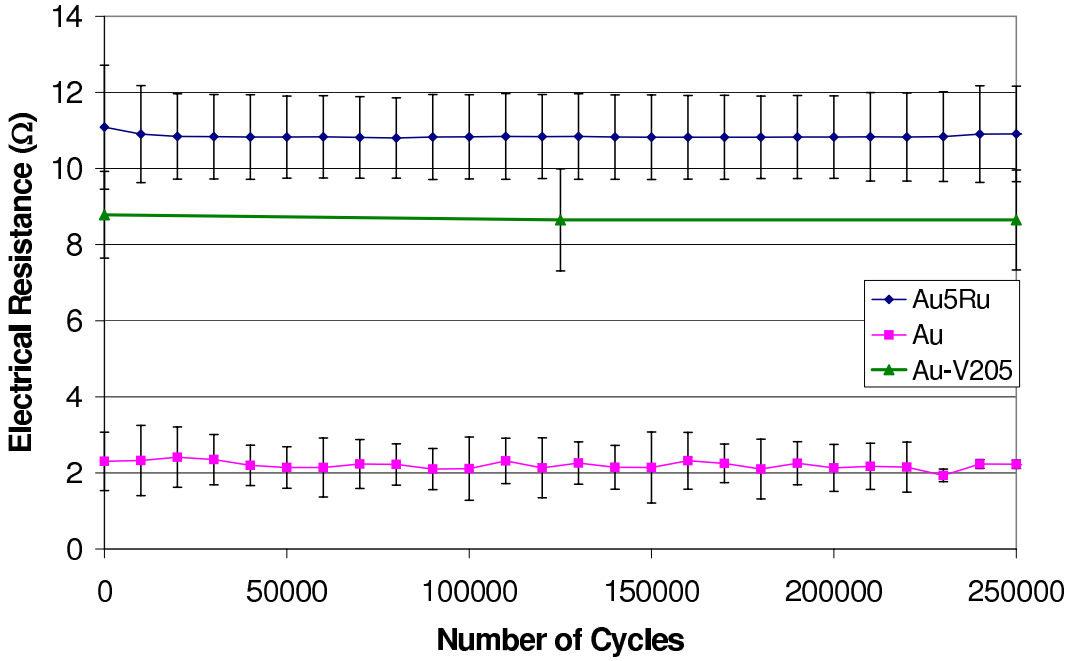

Figure 10.25: Average resistance measured during testing of Au-4%V_2O_5 contacts compared to average resistance of Au and Au5%Ru contacts.

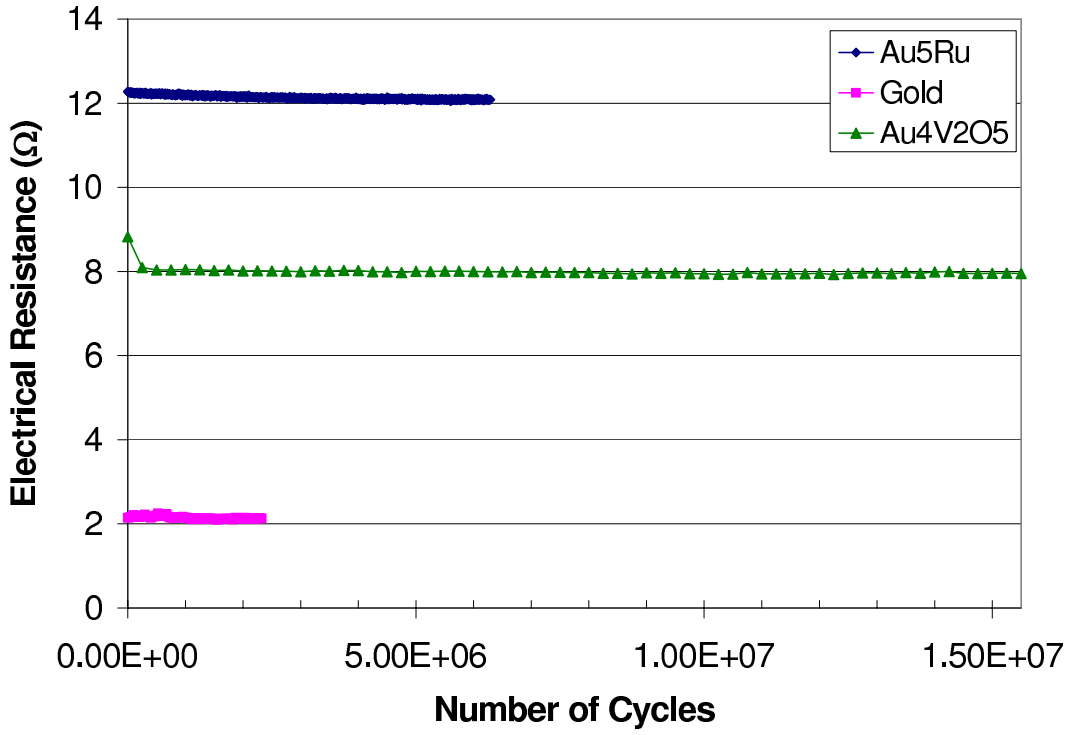

Figure 10.26: Sample long-term resistance measured during testing of contacts.

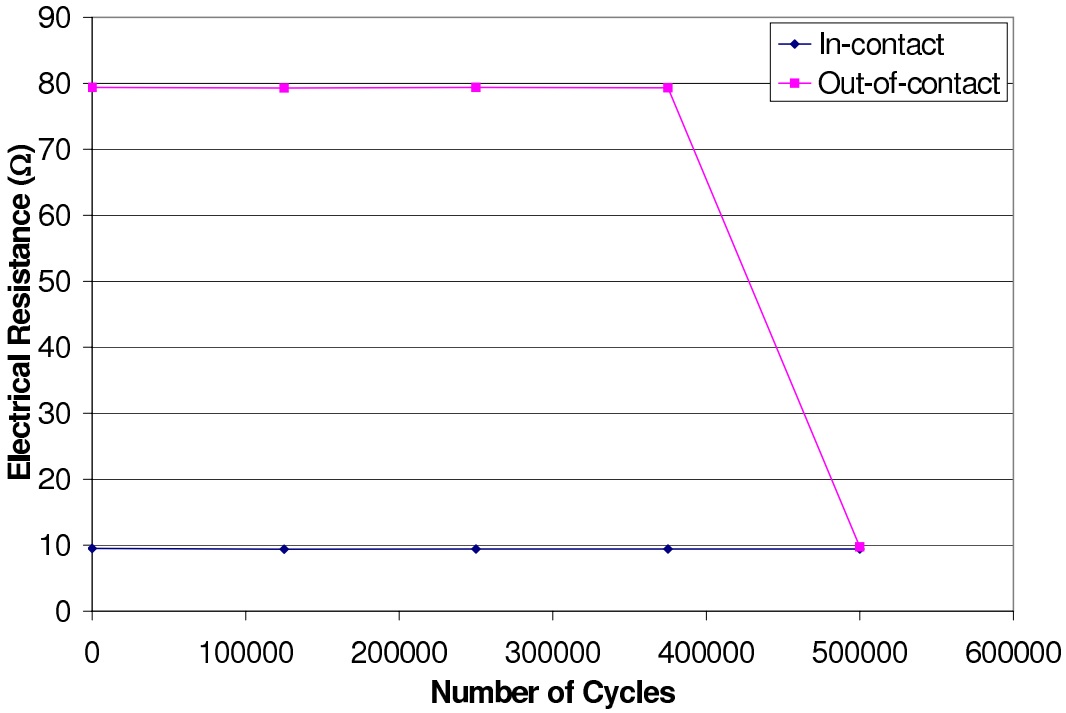

Figure 10.27: Contact resistance measurements used to indicate adhesion failure for Au$-4\%V_2O_5$ contact test.

10.3 Contact Adhesion

Pull-off results were used in this study as a measure of contact adhesion evolution in the devices under test. Figure 10.28 shows a comparison of average pull-off results from testing of Au-$4\%V_2O_5$ compared to the average results of gold and Au5%Ru testing during the first 250,000 cycles. The pull-off results from initial Au-$4\%V_2O_5$ tests indicate that the contact adhesion forces are comparable to the contact adhesion forces in similar gold-gold contacts and are slightly higher than the adhesion developed in Au5%Ru contacts. This result does not match predictions made based solely on contact material hardness. This difference may be due to differing surface energy between materials or different initial surface conditions at the start of testing. These differences could include initial levels of surface contamination or initial contact surface roughness. However, the results were within one standard deviation and only a few Au-$4\%V_2O_5$ contacts were tested so the difference may be within the measurement scatter band. Figure 10.29 shows the pull-off force measured over the entire span of

the longest running Au-4%V_2O_5 contact test which ran for 15.5 $\times 10^6$ cycles (shown in Figure 10.17). This is an example of the lifetime behavior of contact adhesion for microswitches using Au-4%V_2O_5 as a contact material. It shows a few spikes in adhesion force scattered through the life of the contact and a trend showing increasing pull-off force and then a drop just before the test was stopped. These spikes show that the adhesion in a contact can increase rapidly and likely depend on the contact contamination and surface roughness of the contact at the time of measurement.

The pull-off results for the second long-life Au-4%V_2O_5 contact which ran for 8 $\times 10^6$ cycles is shown compared to long-life examples of gold and Au5%Ru contacts in Figure 10.30. These Au-4%V_2O_5 results are for the contact shown in Figures 10.11, 10.12 and 10.13. The point where the Au-4%V_2O_5 contact film partially failed can be seen in Figure 10.30 as indicated. The tear occurred between 4.875×10^6 and 5×10^6 cycles, and can be seen in Figure 10.12. This demonstrates that large changes to the contact film can be seen through the use of the data gathered in this study. This long-term test result also shows that the pull-off force is variable during the test and shows relatively rapid increases and decreases in contact adhesion. These large changes may indicate that evolution of and contamination on the contact surface can affect contact adhesion. The long-term test comparison also shows that a long lasting contact material may generate relatively high pull-off forces but still last longer than a contact with a less damage tolerant contact material. The long-term Au-4%V_2O_5 test in Figure 10.30 appears to develop similar pull-off forces compared to the gold long-term test. This implies that the dispersion strengthening in Au-4%V_2O_5 tolerates contact damage and delays changes to the surface which cause contact adhesion failure in gold. This delay is possibly due to the dispersoids impeding dislocation motion. This may also indicate that brittle separation of Au-4%V_2O_5 contacts may show the same magnitude pull-off force, but not cause as much damage to the contact thus leading to a longer contact life.

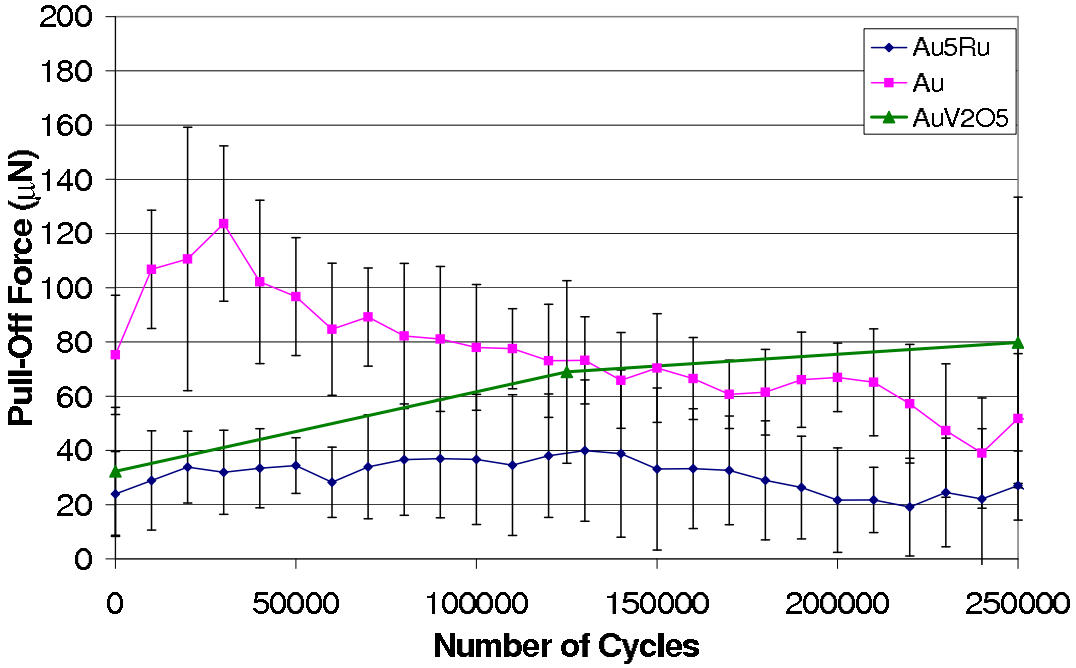

Figure 10.28: Average pull-off force measured during testing of Au-4%V_2O_5 contacts.

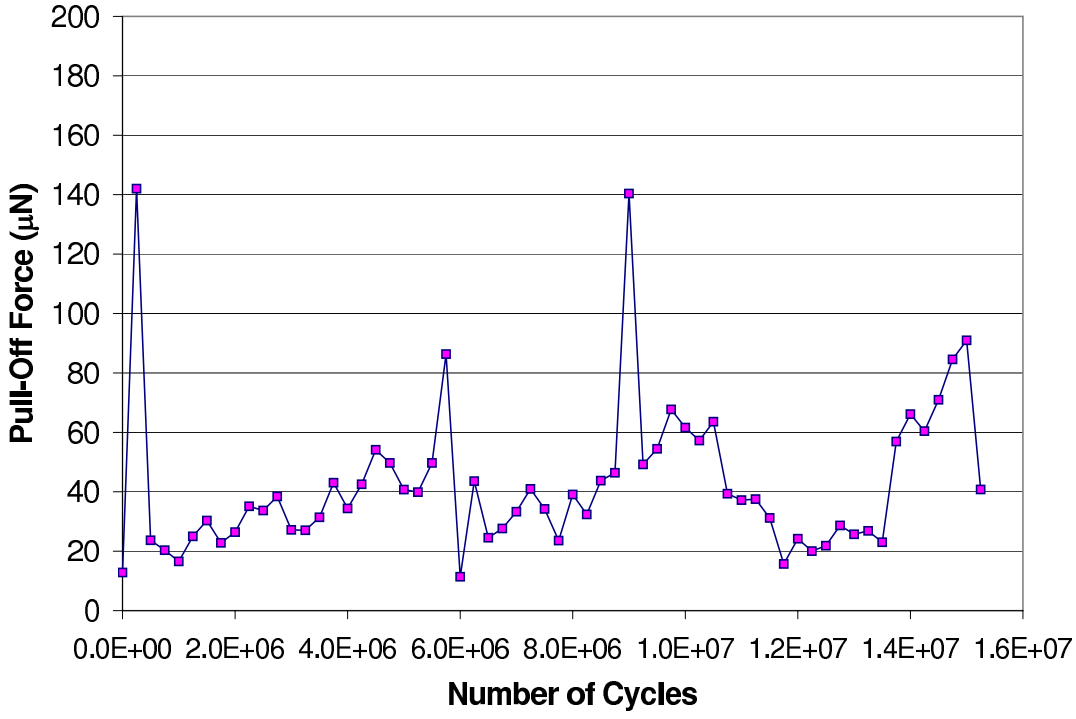

Figure 10.29: Pull-off force measured during longest running Au-4%V_2O_5 contact test (15.5 $\times 10^6$ cycles).

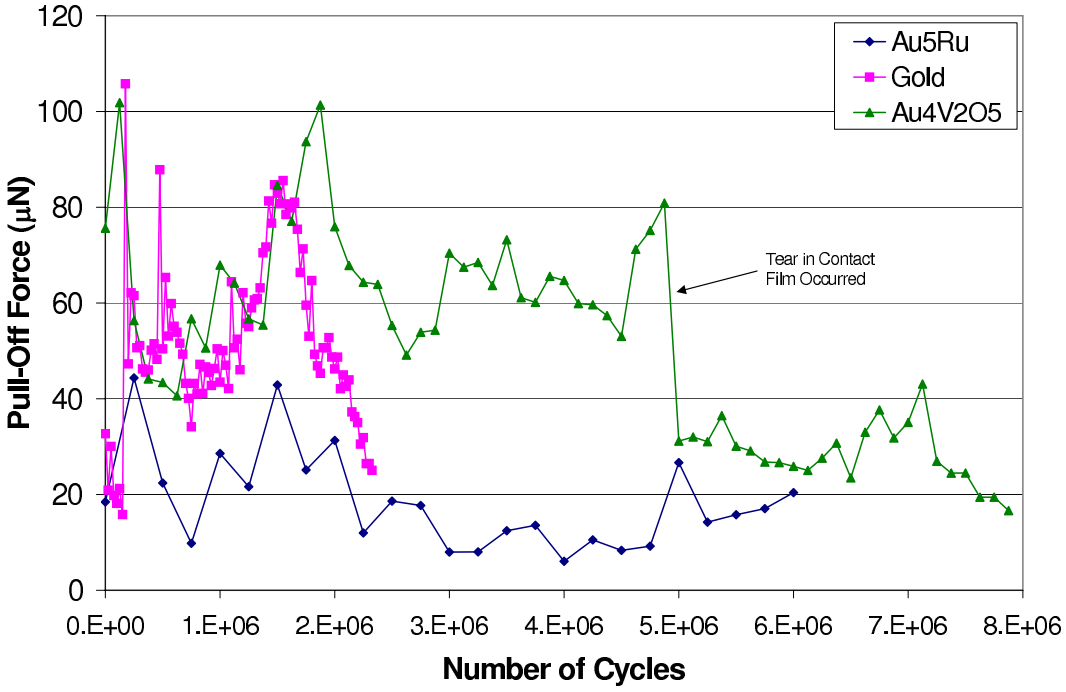

Figure 10.30: Pull-off force measured during long term Au-4%V_2O_5 contact test compared to other long-term tests in gold and Au5%Ru.

10.4 Threshold Force and Distance

The average threshold force necessary to bring Au-4%V_2O_5 contacts into contact compares very well with the average threshold force required for gold, and is less than the average threshold force required for ohmic contact in Au5%Ru contacts. The threshold force is relatively stable and is less than 25 μN after an initial burn-in period. A comparison of average threshold force results for the three materials tested up through 250,000 cycles is shown in Figure 10.31. A long-term example of Au-4%V_2O_5 threshold force compared to gold and Au5%Ru long-term tests is shown in Figure 10.32. These results indicate that there is likely less highly resistive contamination on Au-4%V_2O_5 when compared to Au5%Ru contacts in laboratory air and that Au-4%V_2O_5 does not require more contact force to ensure stable electrical contact than gold. Therefore, the hardness of the Au-4%V_2O_5 does not cause an increase in the design contact force required for a MEMS switch when compared to gold. This is a strong benefit of the Au-4%V_2O_5 material.

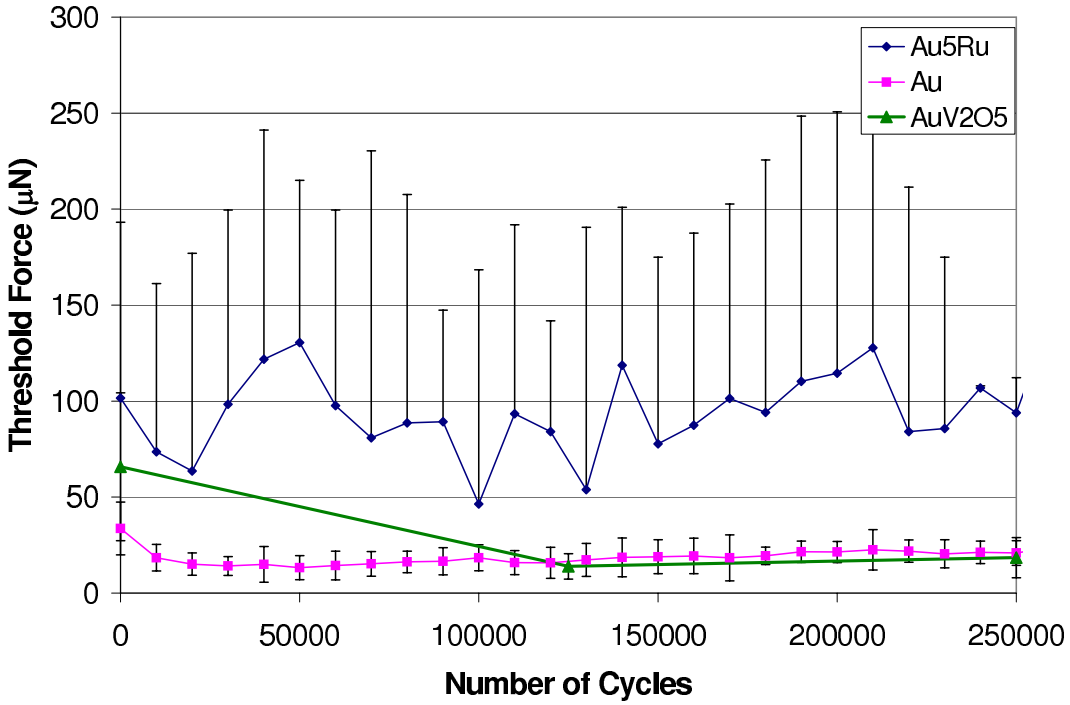

Figure 10.31: Average threshold force measured during testing of Au-4%V_2O_5 contacts.

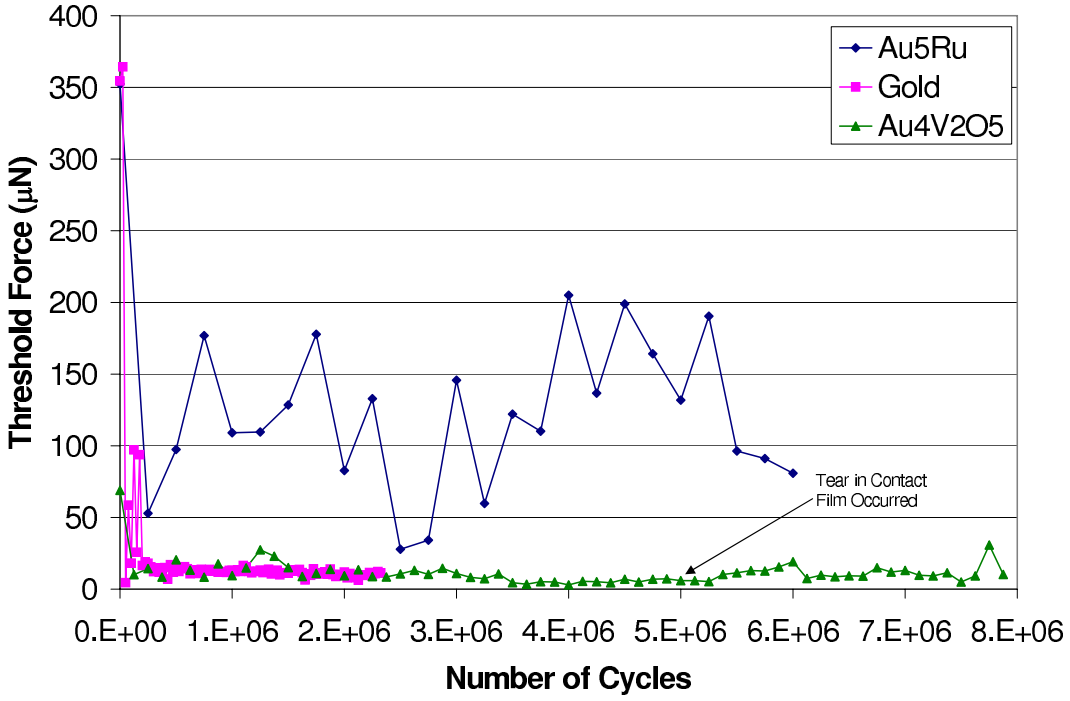

Figure 10.32: Threshold force measured during long term Au-4%V_2O_5 contact test.

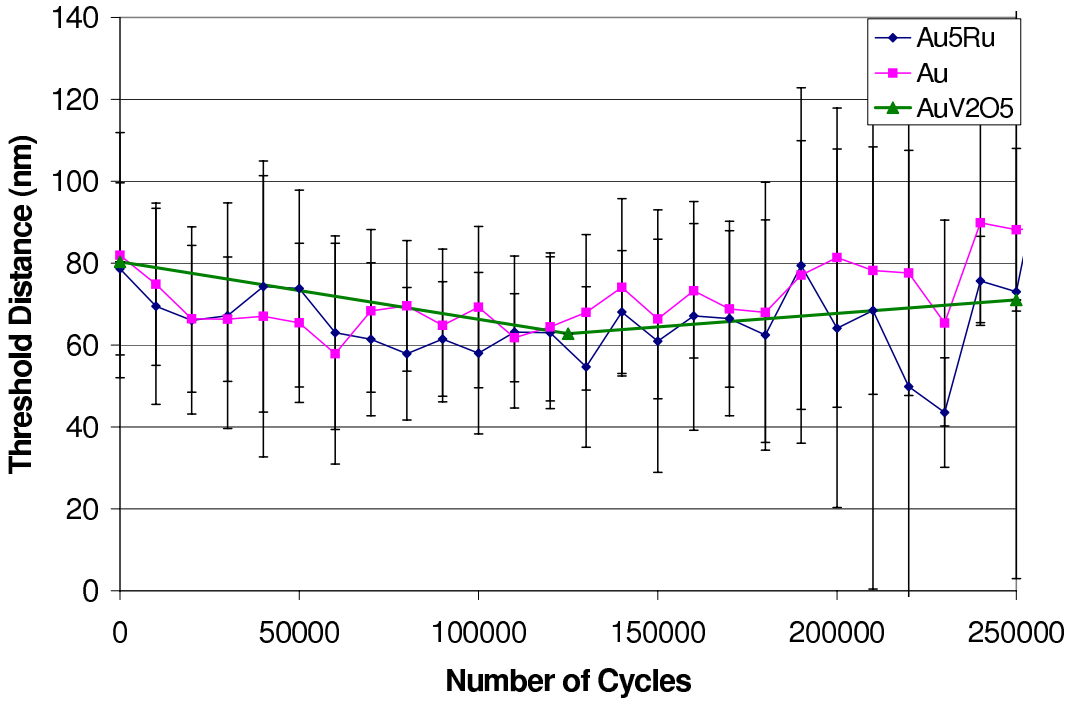

Figure 10.33: Average threshold distance measured during testing of Au-4%V_2O_5 contacts.

The threshold distance (or penetration) required for ohmic contact of Au-4%V_2O_5 contacts is the same as that required for gold and Au5%Ru contacts. The comparison of average threshold distance between all three materials tested can be seen in Figure 10.33. These results are consistent and indicate that the surface proximity required for stable electrical contact is initially the same for the contact materials tested. This result also suggests that the surface proximity required for all metals is the same. A comparison of long-term test examples for all three materials tested is shown in Figure 10.34. The threshold distance is constant in the beginning of the test, but shows variability starting around 3.5×10^6 cycles. This variability likely indicates the beginning of contact damage which led to the partial separation of the contact film from the contact bump. Variability in threshold distance could also be caused by buildup or destruction of surface contamination due to cycling.

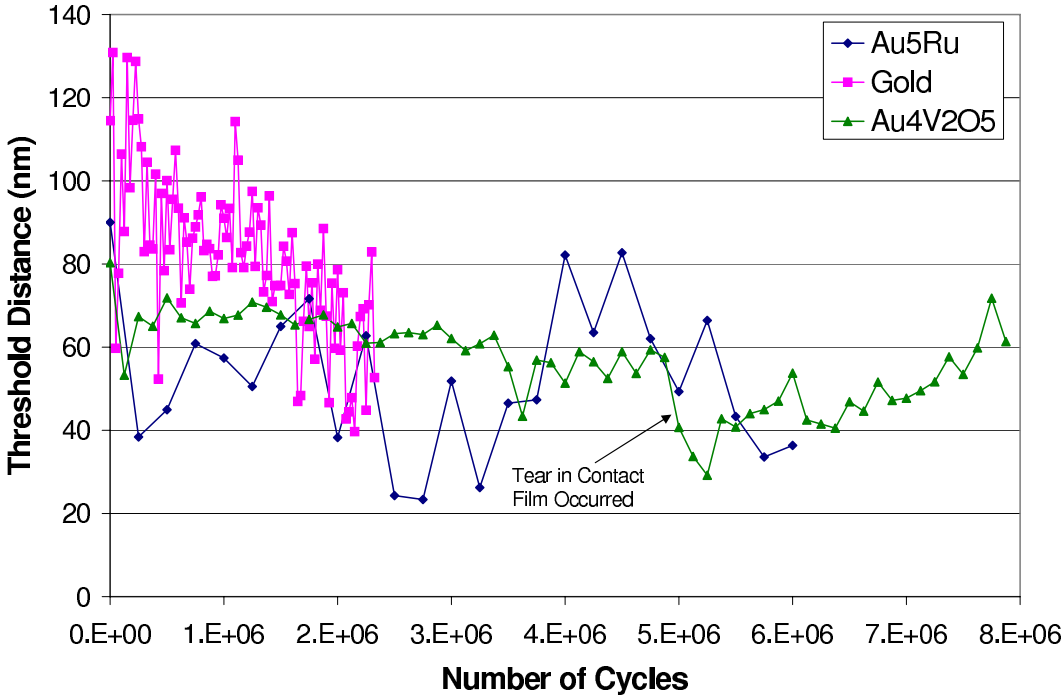

Figure 10.34: Threshold distance measured during long term Au-4%V_2O_5 contact test compared to long term tests of gold and Au5%Ru.

10.5 Contact Hardening

There is not enough data to conclusively determine whether the Au-4%V_2O_5 contacts strain harden during cycling. A comparison of average normalized contact unloading stiffness between all three contact materials tested in this study up to 250,000 is shown in Figure 10.35. The error bars are large so the trend is not conclusive. However, it does appear that Au$-4\%V_2O_5$ may show more of a propensity to strain harden early in cycling than the other materials. This may be due to the dispersion of the oxide with the contact material which would effectively hinder dislocation motion. A comparison of long term contact stiffness trend examples for the three contact metals is shown in Figure 10.36. This figure also indicates possible strain hardening of the Au$-4\%V_2O_5$ contact material up to the point of partial thin film failure. Strain hardening of the contact film may have led to its partial failure by reducing its ductility or the creation of a crack initiation point. Even though data is

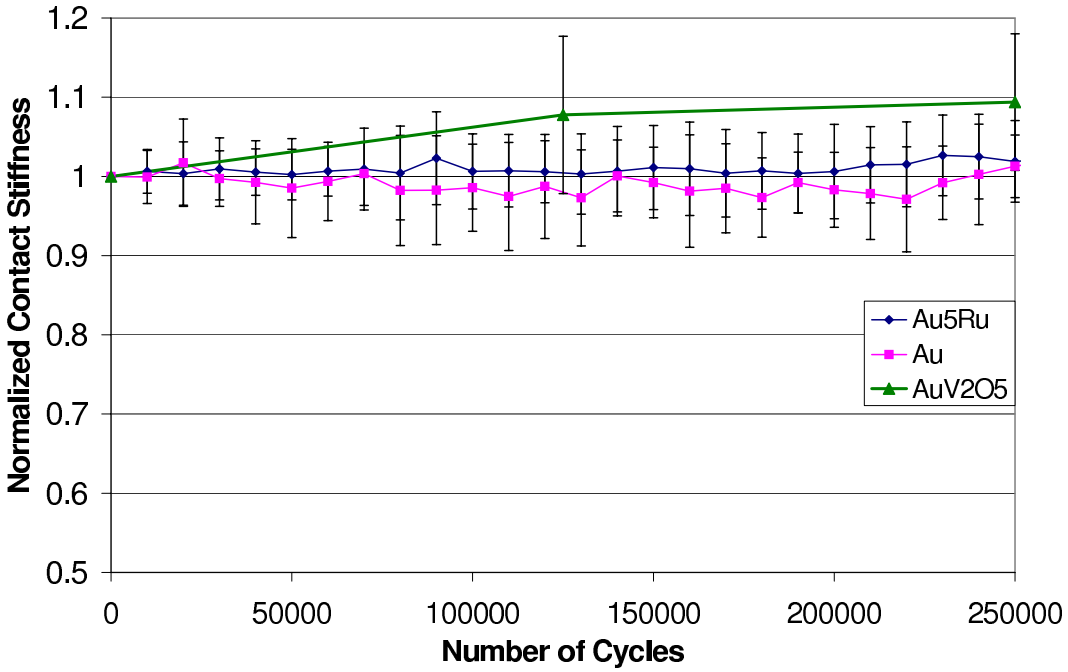

Figure 10.35: Average contact unloading stiffness measured during testing of Au-4%V_2O_5 contacts.

not absolutely conclusive, it appears that strain hardening may sometimes occur in the Au-4%V_2O_5 contact material.

10.6 Contact Interference

The contact interference (or penetration/deformation) at maximum contact load of the Au-4%V_2O_5 contacts is 0.07-0.09 μm and the averages of contact interference for all three materials are compared in Figure 10.37 with long-term examples compared in Figure 10.38. The error bars show one standard deviation based on the average for each material and demonstrate that the Au-4%V_2O_5 average result is between the interference values for the other two materials in Figure 10.37. The interference in the long-term example stayed relatively constant until the partial tear of the contact film occurred. The contact interference for the dispersion strengthened Au-4%V_2O_5 is higher than the interference of Au5%Ru contacts but slightly lower initially than the value found during gold testing. These results are unusual in that it would normally be expected that the interference would scale with hardness.

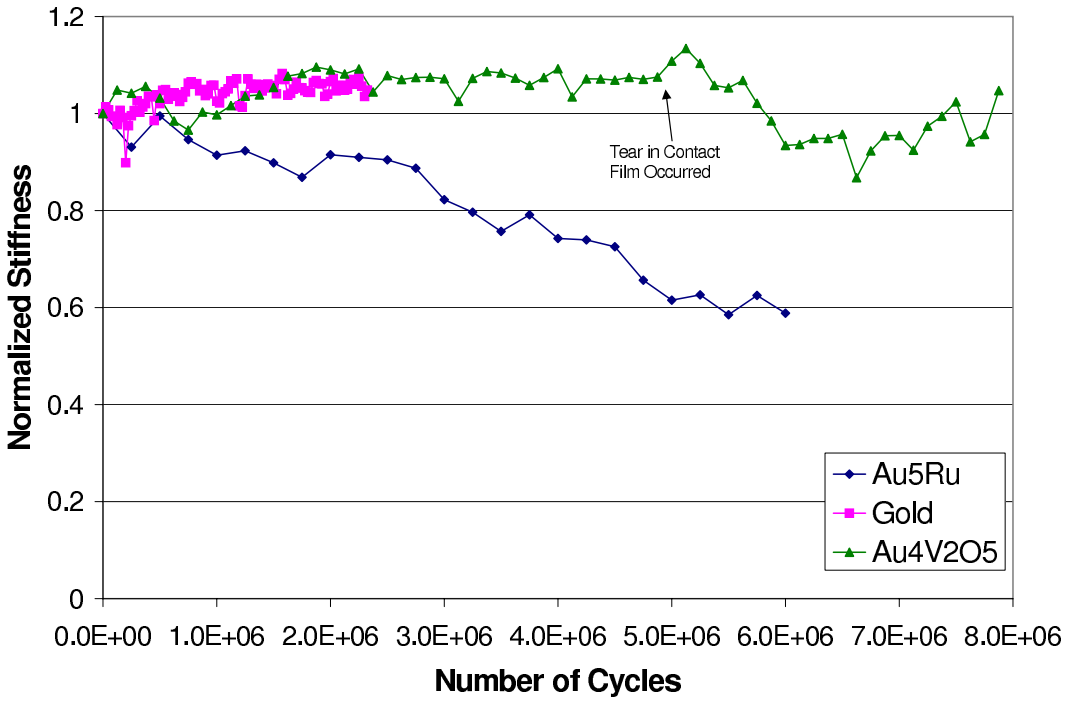

Figure 10.36: Normalized contact unloading stiffness measured during long term Au$-4\%V_2O_5$ contact test compared to gold and Au5%Ru long-term tests.

The increased interference may be an artifact of cracking occurring in or under the Au-$4\%V_2O_5$ contact surface or an increase in plastic deformation due to contact heating. Note that three of the six Au-$4\%V_2O_5$ contacts failed due to full or partial separation of the conductive film from the contact bump. This may indicate sub-surface damage occurring during cycling. The Au-$4\%V_2O_5$ material is harder than gold as evidenced by nanoindentation testing. However, the thermal characteristics of Au-$4\%V_2O_5$ thin films are not published but are likely very similar to the thermal properties of gold. It is possible that contact heating during microprobe actuation slightly softens the Au-$4\%V_2O_5$ material causing an increase in maximum contact interference.

10.7 Time Dependent Behavior

The time dependent behavior of Au-$4\%V_2O_5$ contacts during this test was comparable in magnitude to that shown in testing of the other two contact materials. A

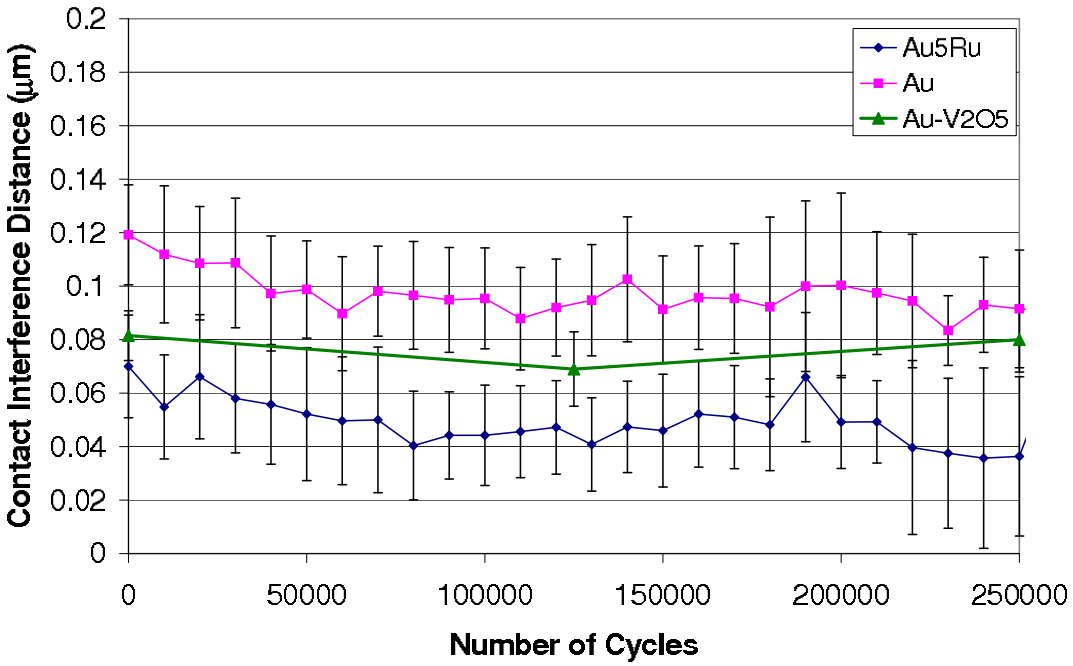

Figure 10.37: Average contact interference (or penetration/deformation) measured during testing of Au-4%V_2O_5 contacts.

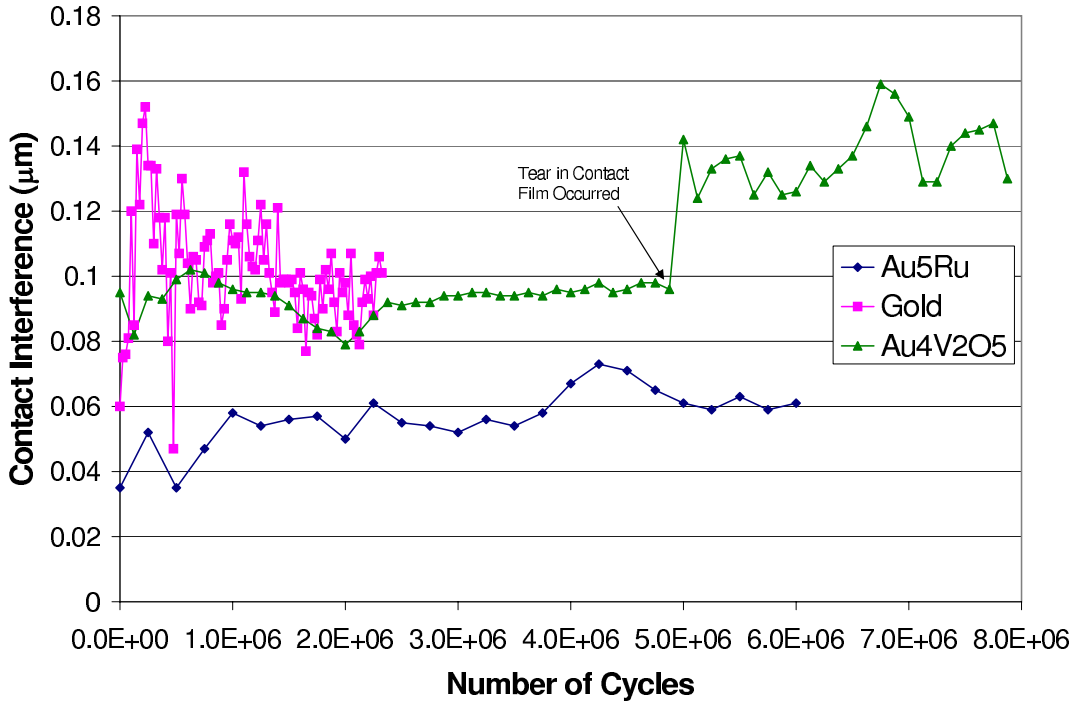

Figure 10.38: Contact interference measured during long term Au-4%V_2O_5 contact test compared to gold and Au5%Ru long term results.

comparison of the average time-dependent deformation during the five second load hold in the three contact materials tested is shown up to 250,000 cycles in Figure 10.39 with a comparison of long-term examples shown in Figure 10.40. The displacement under constant load of the Au-4%V_2O_5 contacts was slightly higher than the other materials, but appears to be within measurement scatter of the other results. Temperature increases in the thin film during cycling could cause the time dependent behavior in a similar manner to the other contact materials tested. The slight increase of time-dependent deformation in Au-4%V_2O_5 contacts when compared to gold and Au-5%Ru could be due to void nucleation at impurity/segregated regions of V_2O_5 particles which are activated during contact heating in the Au-4%V_2O_5 material. The long-term Au-4%V_2O_5 result shown in Figure 10.40 supports this hypothesis by showing a slow increase in time-dependent deformation through the test which possibly indicates elevating temperatures in the contact area during cycling. The increase in time-dependent deformation in the Au-4%V_2O_5 contact accelerates after the partial tearing of the contact film indicated on the graph, possibly due to a smaller effective contact area which increased contact heating due to more restricted current flow. It is also possible that elastic strain due to internal stress is present to a greater extent in the Au-4%V_2O_5 material and thus is converted to greater plastic strain when contact heating occurs. These measurements indicate that viscoelastic effects need to be included in any modeling of cyclic contact behavior.

10.8 Plastic Deformation

The average energy absorbed by the Au-4%V_2O_5 contacts during the first 250,000 cycles of testing was similar in value to the average energy absorbed by the other two materials tested in this study as seen in Figure 10.41. The energy absorbed by Au-4%V_2O_5 was well within one standard deviation of the measurements accomplished on the two other materials. There appears to be no reduction in energy absorbed up to 250,000 cycles, thus there does not appear to be more plastic deformation during initial cycling for this material. An example of the energy absorbed in long-term tests

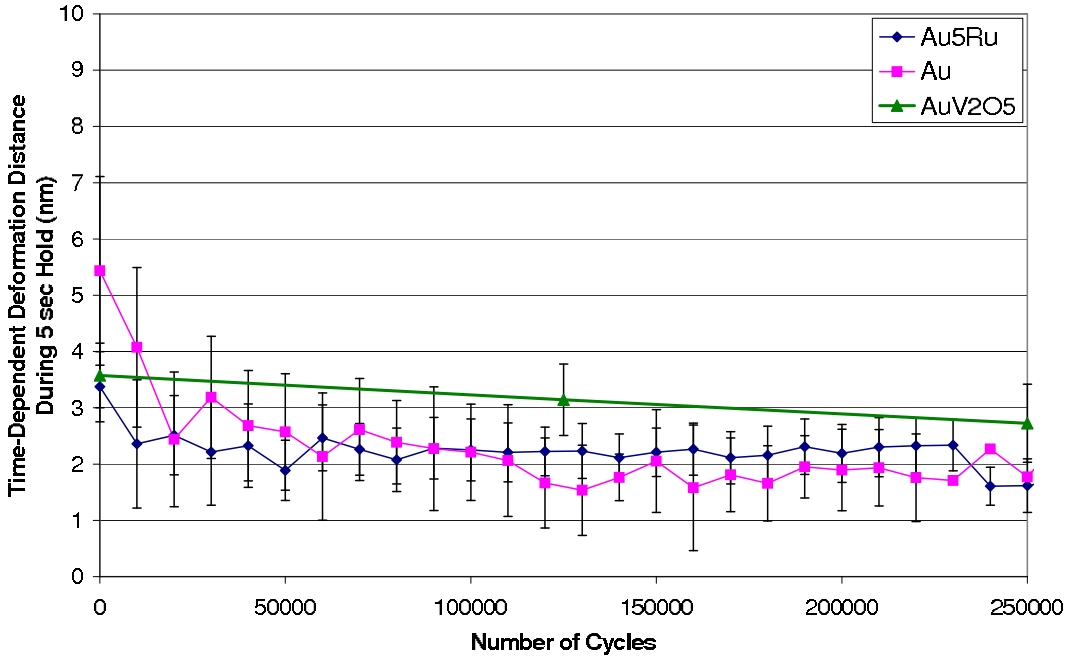

Figure 10.39: Average time dependent deformation during constant peak load measured during testing of Au-4%V_2O_5 contacts for the first 250,000 cycles.

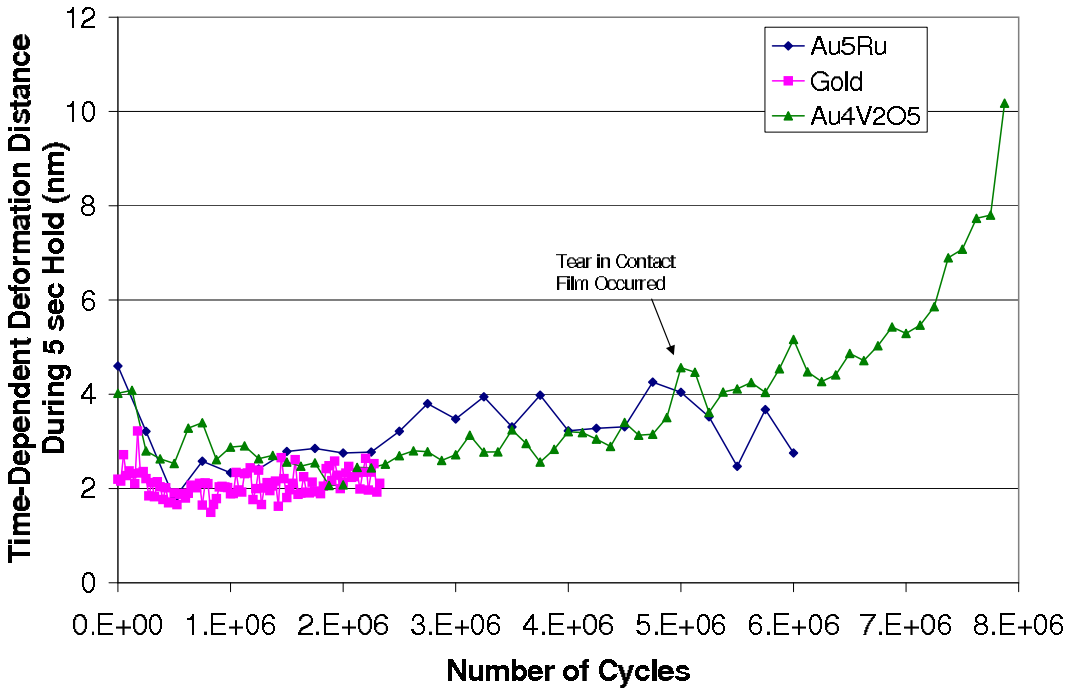

Figure 10.40: Time dependent deformation measured during long term Au-4%V_2O_5 contact test compared to long-term gold and Au5%Ru tests.

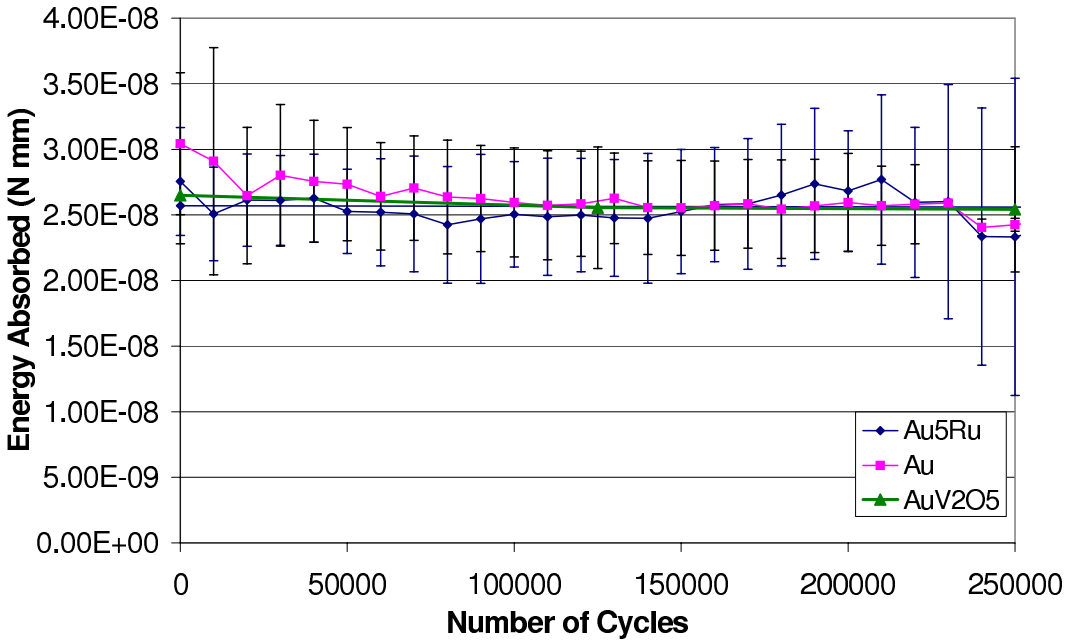

Figure 10.41: Average energy absorbed during contact measured during nanoindenter testing Au-4%V_2O_5 contacts for the first 250,000 cycles.

on all three materials tested is shown in Figure 10.42. The energy absorbed in the Au-4%V_2O_5 contact shows a local maximum at about 1 $\times 10^6$ cycles, then decreases to a local minimum at about 2 $\times 10^6$ cycles. This pattern is similar to the other two materials in that it shows a small increase in energy absorbed followed by a decrease. This pattern may indicate a process of strain hardening occurring early in the life of the contact. The increase shows plastic deformation contributing to the hardening, then the amount of plastic deformation slows because the newly hardened material resists further plastic deformation. This increase and decrease in the Au-4%V_2O_5 contact is followed by a slow increase starting at 2 $\times 10^6$ cycles. This indicates a slow increase in plastic deformation with cycling and may indicate a process of contact heating leading to more plastic deformation. The Au-4%V_2O_5 increases sharply after the contact film is partially ruptured at approximately 5 $\times 10^6$ cycles. The rate likely increases after the partial rupture of the contact film due to the smaller remaining contact material passing the same amount of current, thus increasing the contact heating and damage to the remaining contact material.

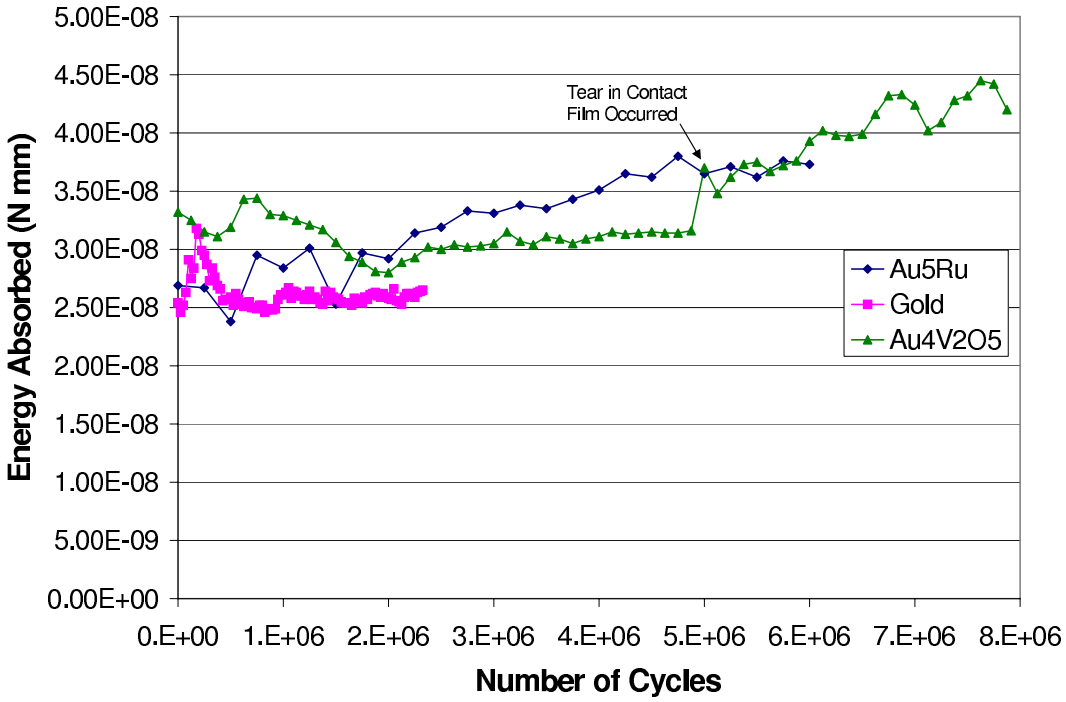

Figure 10.42: Energy Absorbed/Plastic deformation measured during long term Au-4%V_2O_5 contact test compared to gold and Au5%Ru tests.

10.9 Contact Shape

The shape of Au-4%V_2O_5 contacts did not appear to affect test results. This matches the result for gold and Au5%Ru contacts tested in this study. The diameter, height and shape of the Au-4%V_2O_5 contacts tested are given in Table 10.4. In fully plastic deformation, the real contact area does not depend on contact shape, therefore there should be little or no contact shape effect on contact test results. Note that both a rounded and flat contact each exhibited the longest lifetimes of any contacts demonstrated in this study. Note also that two contact bumps with virtually identical shapes exhibited very different contact lifetimes during testing: 20,000 cycles vs. failure at 1.625 $\times 10^6$ cycles due to microprobe overload. These results indicate that contact material may be more important to long contact life than contact bump shape. However, more testing should be accomplished to generate additional data on the possible effects of shape on microcontact lifecycle.

Table 10.4: Test summary of shapes and sizes of Au-4%V_2O_5 contacts tested to failure. Contact bumps described as "Flat" are flat-topped bumps.

Contact ID	Contact Shape	Contact Diameter (μm)	Contact Bump Height (μm)	Initial Contact Resistance (Ω)	Failure Type	Number of Cycles to Failure (# Cycles)
B1011-1_5	Flat	5.7	2.1	7.8	Adhesion (film torn)	20,000
B1011-1_9	Flat	3.0	2.4	8.2	Adhesion	250,000
0602-3_4	Flat	4.8	4.2	9.5	Adhesion (film torn)	500,000
B1011-1_8	Flat	5.8	2.1	7.8	Overload (film torn)	1.625×10^6
0602-3_1	Rounded	9.0	4.2	10.7	Did Not Fail	8.0×10^6
0210-2_11	Flat	6.5	1.9	8.8	Did Not Fail	15.5×10^6

Table 10.5: Qualitative comparison of results indicating initial differences in measurements between short and long-life in Au-4%V_2O_5 contacts. $\uparrow$ = higher initial value; $\downarrow$ = lower initial value

Measured Result	Long-Life	Short-Life
Resistance	Baseline	$\downarrow$
Pull-off Force	Baseline	$\uparrow$
Threshold Force	Baseline	$\downarrow$
Threshold Distance	Baseline	$\downarrow$
Interference	Baseline	$\downarrow$
Time-dependent deformation during 5 sec Hold	Baseline	$\downarrow$
Energy Absorbed	Baseline	$\downarrow$

10.10 Failure Type Categorization

Three tests run on Au-4%V_2O_5 were considered to be short-life results and the other three tests were considered to be long-life results. The measured data from these tests were averaged and compared in order to determine if any trends could be detected in performance measurements to distinguish the characteristics of longer lasting contacts from those which failed early. Table G.1 shows a qualitative overview of measured differences between the two categories of contacts. The long-life contacts were used as a baseline with arrows indicating whether the short life contacts exhibited higher or lower values for each measured result. Each area is described in detail in Appendix G. These results are consistent with the existence of a small amount of contamination on the long-lasting contact surfaces at the beginning of the tests.

10.11 Summary of Gold-Vanadium Oxide Alloy Results

The dispersion strengthened alloy of gold-vanadium oxide tested here is a very promising contact material for use in MEMS contact switches. Results indicate that it may last longer than either of the other two materials tested, and that it may have a higher resistance to contact damage as well as adhesion failure. The measured contact resistance was higher than gold, as expected, and was slightly lower than Au5%Ru. The measured pull-off force was between gold and Au5%Ru. The threshold force was comparable with that of gold. This result gives the benefits of the low contact force required for gold with less damage to the contact surface due to adhesion. The threshold distance, contact strain hardening, and energy absorbed during the testing were all comparable with both other materials. The contact interference did not follow the expected trend. Average contact interference was higher for Au-4%V_2O_5 than for Au5%Ru, whereas normally one would expect lower contact interference with harder contact material. This difference may indicate a higher potential for thermal effects with a temperature increase in Au-4%V_2O_5 contacts. The results for time-dependent deformation also indicate the possibility of more pronounced thermal effects in Au-4%V_2O_5 when compared to gold and Au5%Ru. Short-life Au-4%V_2O_5 contacts showed a higher increase in early pull-off force, lower initial threshold force and lower initial threshold distance when compared to Au-4%V_2O_5 long-life contacts. These trends match the results for gold and Au5%Ru contact testing conducted during this study and indicate possible higher surface contamination and roughness on the long-life contacts. Changes to the contact surface during cycling, including effects causing an increase in contamination and/or surface roughness may also be a factor. Gold-Vanadium Oxide (Au-4%V_2O_5) has the damage resistance benefits of harder material when compared to gold, without the commensurate requirement for a larger contact force. This appears to be a material with great potential as a contact material for MEMS switches. Dispersion strengthened materials should be further studied for possible use as MEMS contact materials.

XI. Summary

Significant interest exists in the design and manufacture of MEMS switches, especially those for use in RF devices. The characteristics of MEMS switches including low insertion loss, low power consumption and low weight offer significant advantages to future development of light weight spacecraft and airborne RF systems [82,95,202]. However, the issue of reliable longevity continues to hamper operational implementation of RF MEMS switches. The research reported here developed a new experimental method which is capable of comparing contact switch material performance and reliability. This study demonstrated the novel use of a nanoindenter and an experimental setup specially designed for characterizing micro-sized electrical contacts as they are cycled. This setup also provided data and a methodology which will prove useful to contact switch designers in their efforts to reliably extend RF MEMS contact switch lifetimes through better understanding of contact mechanics and behavior as well as characteristics of contact failure mechanisms. New microcontact performance data on gold, Au5%Ru, and Au-4%V_2O_5 was gathered and presented in this study. This test apparatus also captured changes in contact morphology due to wear, damage and contamination. The design and automation of this experimental setup and the data gathered contribute to the knowledge available to the MEMS contact switch design community and provided experimental data for use in understanding mechanics of MEMS switch contacts.

Most published MEMS switch designs use gold as the contact metal, e.g. [61, 62,107,115,140,161,163,173,189,190,252,253], due to its low resistivity and softness, meaning the contact force required for ohmic contact by the switch is low. However, gold has many problems in this application, including its susceptibility to damage and adhesive failure when the switch contact surfaces adhere and the switch no longer has enough opening force to pull the contacts apart. Other metals have been researched for use as contact metals (e.g. [36,216]) and a successful commercial switch design uses a "platinum group metal" [160]. However, little experimental measurement of contact

parameters has been reported, and no correlation of contact parameters to material properties has been accomplished. This study provided an experimental method where contact materials can be tested in a consistent manner without requiring a full switch redesign and fabrication process redevelopment. The apparatus as designed, built and integrated is unique and the capability provides the basis for a systematic method to develop new and useful information on RF MEMS contact performance under simulated operating conditions. This experimental technique could also be used to create an empirical method for use in selection and appropriate tradeoff of contact material properties.

This chapter summarizes the research accomplished and contributions made during this study. Future work in this area is also recommended. The experimental design and development will be summarized first, followed by a summary of the material testing accomplished. The contributions of this study will be presented followed by recommendations for future work and conclusions.

11.1 Experimental Design & Development

A novel nanoindenter-based testing apparatus was designed, fabricated, integrated and automated during the course of this study. The test apparatus allowed monitoring of the physical evolution of the contact over time and under cycling conditions, in addition to providing data on resistance, material property changes (e.g. strain hardening), and other changes in contact behavior. Directly measured data include displacement of the cantilever, contact force, resistance change as the simulated switch cycled, pull-off force, contact interference, time dependent deformation at maximum contact load, contact interference (or penetration) and energy absorbed by the contact which indicates plastic deformation during the life of the contact as a function of cycling. Threshold force and threshold distance were calculated based on the force vs. resistance curve developed during each measurement. The setup as designed and built allowed the contact material to be changed easily and the contact bump to be removed for analysis with minimal chance of contamination or damage

Table 11.1: Contact material properties comparison.

Contact Material	Modulus of Elasticity (MPa)	Hardness (GPa)	Resistivity ($\mu\Omega$-cm)
Gold	86	1.04	3.6
Au5%Ru	122	2.42	38.5
Au-4%V_2O_5	175	4	17.7

to the contact surface. These are significant concerns during contact removal from an enclosed MEMS switch.

The setup used MEMS sized silicon cantilever beams custom fabricated with contact bumps and cycled mechanically to simulate the action of a MEMS ohmic contact switch. These cantilever beams were designed during the study and required development of a non-planar fabrication process to create the contact bumps necessary for the study. Preliminary tests were performed on the set-up and cantilevers to ensure the apparatus adequately simulated the action of MEMS contact switches. Tests were then run on gold contacts as a baseline and further tests were accomplished on two other promising MEMS contact materials.

11.2 Material Testing Results

Gold, gold-ruthenium (Au5%Ru) and gold-vanadium oxide (Au-4%V_2O_5) contacts were tested during this study. Testing was done in laboratory air, with a current of 0.5 mA under hot-switched conditions using a contact force of 400 μN at a cycling frequency of 100 Hz. Table 11.1 repeats the comparison of material properties for the contact materials tested in this study. Table 11.2 shows a comparison of contact material performance parameters and Table 11.3 shows a comparison of average lifetime results from this study. The difference between predicted and measured resistance is due to parasitic resistances in the measurement path (e.g. solder joints, terminal strip)

Table 11.2: Comparison of contact material test results.

Measured Result	Gold	Au5%Ru	Au-4%V_2O_5
Predicted Resistance (Ω)	0.5	8.4	5
Measured Resistance (Ω)	2.1	10.8	8.5
Pull-off Force (μN)	50-125	10-40	25-60
Threshold Force (μN)	10-25	50-200	20-70
Threshold Distance (nm)	60-80	60-80	60-80
Interference (μm)	0.08-0.12	0.04-0.07	0.08-0.1
Deformation during 5s hold (nm)	1.5-2.5	1.75-4	2-5
Energy Absorbed (N·mm)	2.5×10^{-8}	2.5-3.75 $\times10^{-8}$	3-3.5 $\times10^{-8}$

Table 11.3: Comparison of average lifetime results from this study. Note that only complete lifetime tests were used in calculating these values.

Material	Average Lifetime (# Cycles)	Standard Deviation	Number Lifetime Tests	Total Number Tests Accomplished
Gold	414,000	596,000	19	26
Au5%Ru	2.18×10^6	3.17×10^6	7	12
Au-4%V_2O_5	$> 4.85\times10^6$	6.83×10^6	5	6

11.2.1 Gold. Gold contacts all failed in adhesion. Even the failures where a high resistance was measured showed that the contact film had adhered to the strike plate, thus the high-resistance failures were caused by increases in contact adhesion. Three failure types with differing characteristics were noted in gold contacts and categorized by lifetime. The short-lifetime (10,000-70,000 cycles) tests showed evidence of ductile separation while the long-life tests showed evidence of brittle separation. The brittle failure surfaces in gold appeared similar to the brittle failure surfaces seen in Au5%Ru contacts. The mid-life tests (190,000-500,000 cycles) showed a thin film failure where the contact film separated from the substrate. Small amounts of contamination were evident on the long-life contacts ($> 1 \times 10^6$ cycles). The differences between these failures was likely due to initial surface condition of the contact surfaces including initial surface contamination, surface roughness and existence of defects in the thin film. The rate of contact surface smoothening during cycling affected the contact lifetime. The smoothening of contact surfaces increased the likelihood of adhesive failure and soft gold surfaces were susceptible to smoothening due to cycling.

Note that very smooth surfaces such as atomically smooth mica produced by cleavage show very high friction [199] and that Majumder suggested gradual surface smoothing as a contributing factor to evolution of contact characteristics [162]. Noting also that, "The presence of adsorbed films containing water and other molecules derived from the air serves measurably to reduce the surface interaction of contacting materials" [199], it may be beneficial for contacts to have a small amount of non-resistive surface contamination in order to reduce adhesion and thereby adhesive failure.

Measurements of various parameters of gold contact performance were also performed. Threshold force of gold was determined to fall in the range of 15-25 μN. Threshold force is defined in this study as the applied contact force required for stable ohmic contact. Measured pull-off force for gold was approximately 50 μN which is higher than the predicted adhesive force of 20 μN based on JKR theory. This difference is likely due to the effects of surface roughness and other variables not accounted for in JKR theory. Contact interference was predicted based on the results given in [59] and compared to the contact interference measured in the test. Predicted interference in gold was 45-60 nm whereas measured interference was 85-100 nm. This comparison showed that the measured results were approximately double the predicted results. The difference can be attributed to additional plastic deformation occurring in the test which is not accounted for in the analysis.

Time-dependent deformation at maximum contact load was detected in all gold contact tests. Displacement was measured during the five second hold at maximum applied contact force. Initial analysis of gold contact testing indicated no dependence on contact lifetime due to contact bump shape, although further testing of contact shape impacts should be accomplished. A rounded gold bump and a flat-topped gold bump showed the same lifetime and similar failure characteristics.

11.2.2 Au5%Ru. The gold-ruthenium alloy tested was a two-phase material and all failures of this contact material were also adhesive in nature. The tests performed during this study contraindicate the conclusions made in [132] and [202]

that harder materials always generate higher adhesive forces in contact. Tests in this study showed that a harder material (Au5%Ru) develops lower adhesive forces due to contact when compared to a softer material (gold). Au5%Ru contacts also showed evidence of brittle separation. Brittle separation is desirable for contact lifetime extension, as it reduces damage to contact surfaces [37].

Contact surfaces of failed contacts were analyzed during the study. Shorter-lifetime Au5%Ru contacts commonly showed smoothening of the contact area indicating that smoothening rate affects contact lifetime. Small amounts of contamination were also visible on longer-life Au5%Ru contacts after failure. This indicates that initial surface roughness and initial contamination due to fabrication processes and handling may play a large role in contact lifetime. Also, a small amount of non-resistive contamination may delay adhesive failure and increase contact lifetime.

The Au5%Ru long-term test demonstrated contact softening. This reduction in the contact unloading stiffness was likely due to contact damage occurring during cycling, and was possibly accelerated by contact heating. Examination of the contact area of Au5%Ru contacts after cycling showed evidence of possible melting on the edge of the circular contact area. Time dependent deformation was also detected in Au5%Ru contacts. The magnitude of measured time dependent deformation was similar between gold and Au5%Ru. This indicates that similar processes caused the deformation under constant load.

There was no indication from Au5%Ru testing that contact bump shape affected contact measurements or lifetime. A set of tests showed that there was no difference in lifetime between a rounded and a flat contact bump. The damage pattern was the same between the two differently shaped contact bumps. More testing of contact shape affect on cycling parameters should be conducted.

11.2.3 Au-4%V_2O_5. Two Au-4%V_2O_5 contacts did not fail during testing. These two tests were stopped before failure to analyze the contact evolution after 8×10^6 and 15.5×10^6 cycles at 100 Hz cycling frequency, respectively. All failed Au-

4%V_2O_5 tests showed failure characteristics due to adhesion, either with the contact remaining stuck closed or thin film separation from the substrate.

The pull-off force results for Au-4%V_2O_5 showed that material hardness is not a direct indicator of adhesive force magnitude in a contact material. The pull-off force results were close to those of pure gold, and higher than the pull-off force results from Au5%Ru testing. The dispersant does not greatly affect the lattice in the gold matrix, thus adhesion due to lattice matching in the Au and Au-4%V_2O_5 was likely similar. These results also showed that adhesive force is also not necessarily directly indicative of damage occurring on the contact surface. The dispersant in the Au-4%V_2O_5 significantly delayed plastic deformation of the surface when compared with gold.

The threshold force measured for Au-4%V_2O_5 contacts ranged from 10-15 μN which is similar to the range of values measured for gold. Even though Au-4%V_2O_5 is harder than Au5%Ru, Au-4%V_2O_5 has a lower required threshold force. This indicated that there was less non-conductive contamination affecting contact when compared with Au5%Ru. Au-4%V_2O_5 also offers the benefit of better damage resistance than gold due to its dispersion hardening combined with a low threshold force comparable to gold. The Au-4%V_2O_5 dispersion strengthened alloy is better able to avoid plastic deformation and smoothening thus providing a longer-lasting contact material when compared to gold. Thus, Au-4%V_2O_5 offers some of the performance benefits of gold with improved damage resistance.

Contact surface analysis of Au-4%V_2O_5 contacts showed ductile separation, brittle separation and thin film failure. The brittle separation surface was on the longest-lasting Au-4%V_2O_5 contact tested. This surface appeared slightly different than the other brittle surfaces analyzed in this study, however it had not failed at 15.5 $\times 10^6$ cycles when examined. The surface showed evidence of a small amount of material transfer and possible surface cracking.

Testing also indicated that contact interference was greater than Au5%Ru and less than gold. Time dependent behavior in Au-4%V_2O_5 was greater than both gold and Au5%Ru. Analysis based solely on material hardness would predict that both contact interference and time-dependent deformation for the hardest material should be the least among the materials tested.

11.3 Discussion

The average number of cycles to failure based on lifetime tests of each material is given in Table 11.3. The standard deviation is very high for each material due to the spread of failure lifetimes and early lifetime failures for each of the materials. Note that the Au-4%V_2O_5 material lifetime likely should be greater as the two longest running tests in the study were halted before the contacts failed. The spread of lifetime values for each material is a representation of the wide variability in lifetimes of actual MEMS switches [65, 171, 239]. The preponderance of adhesive failures matches published results and analysis of the primary failure mechanisms on actual switches [121, 159, 239,241]. No method exists to predict the lifetime of a contact before it cycles. Further research into the specific behavior of contacts as they cycle is needed to understand the failure mechanisms in order to develop such a predictive capability. The study accomplished here is an initial step in the development of detailed information on contact material performance over cycling. Performance measurements of the three tested materials are compared next and the contact failure types are discussed.

11.3.1 Material Comparison. Results indicated, for the present test conditions, that the Au-4%V_2O_5 contacts were the most promising of the three tested. Further testing, especially in a dry noble gas environment, should be accomplished to develop more data on the contact performance of dispersion strengthened materials such as Au-4%V_2O_5. A qualitative summary of results is presented in Table 11.4. As expected, gold had the lowest measured contact resistance and the highest measured pull-off (adhesive) force. Gold had a lower threshold force when compared to Au5%Ru,

Table 11.4: Qualitative comparison of contact material test results.

Measured Result	Gold	Au5%Ru	Au-4%V_2O_5
Resistance (Ω)	Low	High	Mid
Pull-off Force (μN)	High	Low	Mid
Threshold Force (μN)	Low	High	Mid
Threshold Distance (nm)	=	=	=
Interference (μm)	High	Low	Mid
Time-dependent Deformation during 5 sec hold (nm)	Low	Mid	High

but gold and Au-4%V_2O_5 contacts had a similar threshold force. All three materials showed the same threshold distance which indicates the surface proximity needed for stable electrical contact is consistent between differing materials. No overall trends in contact stiffness change were detected. It is hypothesized that competing mechanisms of strain hardening and annealing due to contact heating were active in the contact materials during cycling. The contact interference (or penetration) at maximum load for Au5%Ru was lower than gold, as expected. However, the contact interference for Au-4%V_2O_5 was higher than expected. This could be due to thermal effects caused by an elevated temperature at the contact surface. Elevated contact temperature in the Au-4%V_2O_5 contacts also explains the higher level of time dependent deformation when compared to gold or Au5%Ru. However, the Au and Au5%Ru materials showed a decrease in time-dependent behavior after the first measurement, whereas the time-dependent displacement under maximum load was relatively constant for the Au-4%V_2O_5 contacts. The energy absorbed by all three materials early in their lifetimes was also similar. The Au and Au5%Ru materials showed a slight drop in energy absorbed (showing plastic deformation) just after the first measurement. The Au-4%V_2O_5 energy absorbed was constant over the same period.

The dispersion strengthened gold-vanadium oxide alloy showed significant promise as a contact material during this study. Tests showed higher resistance to contact damage and longer lifetimes in Au-4%V_2O_5 than in the other two materials tested. This is likely due to the nanoparticle-sized oxide dispersed in the gold matrix. The oxide particles are estimated to have a diameter of 4.4 nm [10]. The pull-off force

measured was more than Au5%Ru but less than gold. This indicates that material hardness is not a direct indicator of adhesive force magnitude in a contact material. It may also indicate that while the dispersed oxide strengthens the material, as seen in its increased resistance to damage, and because the dispersant does not change the crystal lattice, the adhesion due to lattice matching is not reduced. Note that, in general, HCP materials such as ruthenium exhibit less adhesion than FCC materials [199]. Therefore, the inclusion of ruthenium with gold may reduce adhesion more than the dispersion oxide in Au-4%V_2O_5. The goal of a switch designer is not necessarily merely to reduce contact adhesion, but to reduce the likelihood of changes to the contact surface which could lead to excessive smoothening and a large rapid increase in adhesive force. The dispersion strengthened Au-4%V_2O_5 appears to delay surface smoothening due to the characteristics of its micro-structure.

Time dependent deformation of the contact film was observed in all three materials tested. Displacement was measured during the five second hold at maximum microprobe applied contact force in every nanoindenter measurement. Previous researchers have studied room-temperature creep in thin film materials [147]. It has also been noted that the softening temperature of gold is lower at a micro-scale when compared to bulk softening temperature [115]. Bannuru reports that time-dependent plastic deformation in thin films is a cause of concern and that thin films are prone to creep even at room temperature and below the yield stress [9]. Gregori and Clarke suggested that creep in gold microcontacts occurs under load, and that creep is a factor in the development of adhesive forces between the contacts [92]. Current passing through the microcontact may also heat the contact, contributing to the time dependent deformation. Heating of the contact was indicated by several images of post-cycling contacts showing melting at the edge of the contact area in both Au5%Ru and Au-4%V_2O_5 contacts. Comparison of a gold contact tested without current to gold contacts tested with hot switching also implied heating effects due to current on the contact surface. Note that Greenwood and Williamson showed that the heat

production due to current passing through a contact rises sharply at the edge of the circle of contact [86].

While more testing of contact shape effects on lifetime and contact performance should be conducted, no dependence of lifetime or performance on contact bump shape was noted in test results. Rounded or flat-topped bumps did not appear to affect contact lifetime. Contact material choice seemed to be more important to contact lifetime than contact bump shape. Two cases of differently shaped bumps demonstrating similar performance and one case of similar contacts demonstrating very different performance were noted during the study. Gold contacts showed an example where a rounded and a flat-topped bump both demonstrated a short-life failure. Tests on Au5%Ru contacts showed an example where a rounded and a flat-topped bump both showed long-term lifetimes with very similar failure surfaces. Tests on Au-4%V_2O_5 contacts showed an example where virtually identically shaped contact bumps exhibited extremely different contact lifetimes. Further testing on effects of contact shape on microcontact performance should clearly be performed.

Contamination was evident on most contact surfaces analyzed. Gold contacts showed the least contamination, but in gold contacts contamination was most evident on long-life contacts. Contamination also appeared to be present on both gold and Au5%Ru contacts tested without electrical current, indicating that current is not necessary for the contact to become contaminated. Au5%Ru contacts showed more contamination than gold. Contamination often appeared as a dark annular ring around the edge of the contact area or in spots on the contact surface. Small amounts of contamination were visible on Au-4%V_2O_5 long-life contacts as well. This indicates that initial surface conditions including contamination levels are important to the lifetime of a contact. Two gold and one Au-4%V_2O_5 contact showed high resistance failure during tests but all three failed due to thin film separation from the contact bump substrate. This indicates that high resistance failures are not necessarily due to development of a highly resistive contaminant layer, but may be due to damage to the contact and indicate an adhesive failure. An example similar to this is given in [238]

Table 11.5: Description of failure types in this study. Lifetimes are given for each failure type in respective materials.

Failure Type	Description	Material	Lifetime (# Cycles)
I	Ductile characteristics	Au	10,000-70,000
		Au-4%V_2O_5	~250,000
II	Contact film failure	Au	200,000-500,000
		Au-4%V_2O_5	~500,000
III	Brittle separation, smoothed surfaces	Au	$> 10^6$
		Au5%Ru	130,000-210,000
		Au-4%V_2O_5	$> 15.5 \times 10^6$
IV	Worn down bump, wear fragments	Au5%Ru	$\sim 6 \times 10^6$

where severe damage to the contact bumps in a microswitch caused high resistance failures. The separation of the thin film from the substrate may be affected by the deposition quality including possible inclusion of subsurface flaws in the contact area or generation of subsurface damage during cycling.

11.3.2 Failure Comparison. The characteristic adhesive failures seen in this study were categorized into four basic types and are summarized with their descriptions, the material, and lifetime range in Table 11.5. These results indicate that similar processes are at work in varying microcontact materials and that basic studies of behavior and failure mechanisms should be undertaken to further define and explain microcontact adhesive behavior. The failure types which were analyzed and categorized during this study are Type I which exhibits ductile surface characteristics, Type II which shows a thin film failure, Type III which is identified by brittle separation characteristics, and Type IV which showed contacts with a worn surface.

Measurements of contact behavior were analyzed based on the type of failure exhibited in the tested contacts. A qualitative comparison of long-life to shorter-life contacts in each material tested is summarized and compared in Table 11.6. This table compares the indicators from long-lifetime contacts of each material to shorter lifetime contacts of the same contact material. This table shows commonality in the behavior of the pull-off force, threshold force and distance results, but different

Table 11.6: Qualitative comparison of shorter lifetime failures in contact materials gold and gold-ruthenium when compared to longer lifetime contacts in same material. $\uparrow$ = higher initial value; $\nearrow$ = slightly higher initial value; $\downarrow$ = lower initial value; $\searrow$ = slightly lower initial value; $\leftrightarrow$ = No Difference. The stars ($\star$) identify characteristics common to short-life contacts in all three materials.

Measured Result	Gold (Type I)			Au5%Ru (Type III)		Au-4%V_2O_5		Compare
	Long	Mid	Short	Long	Shorter	Long	Shorter	
Resistance (Ω)	Baseline	$\leftrightarrow$	$\leftrightarrow$	Baseline	$\downarrow$	Baseline	$\downarrow$	
Pull-off Force (μN)	Baseline	$\nearrow$	$\uparrow$	Baseline	$\uparrow$	Baseline	$\uparrow$	$\star$
Threshold Force (μN)	Baseline	$\downarrow$	$\downarrow$	Baseline	$\downarrow$	Baseline	$\downarrow$	$\star$
Threshold Distance (nm)	Baseline	$\searrow$	$\downarrow$	Baseline	$\downarrow$	Baseline	$\downarrow$	$\star$
Interference (μm)	Baseline	$\leftrightarrow$	$\leftrightarrow$	Baseline	$\downarrow$	Baseline	$\downarrow$	
Deformation during 5 sec hold (nm)	Baseline	$\uparrow$	$\uparrow$	Baseline	$\downarrow$	Baseline	$\downarrow$	
Energy Absorbed (N·mm)	Baseline	$\uparrow$	$\leftrightarrow$	Baseline	$\downarrow$	Baseline	$\downarrow$	

behaviors among the other measured quantities. This indicates that relatively higher initial pull-off force (or adhesion) in the contact is an indicator that the contact will likely exhibit a shorter life than average for that material. The lower initial threshold force and distance indicate that these shorter-life contacts may have less initial adsorbed contamination on the contact surfaces. This table shows that with further study, a method to sort contacts predicted to have a lower lifetime could be developed based on "burn-in" or initial screening testing. Further study could also quantitatively determine initial surface conditions associated with long contact life.

11.4 Contribution Highlights

This study created a novel experimental method to compare contact materials directly and developed contact performance data on three microcontact materials over their entire tested lifetimes. This study provided a basic experimental method to study microscale contact phenomena as they relate to MEMS contact switches as well as produced micro-scale contact data never before reported. These physical details of contact performance and analysis are unique in the literature. The categorization and analysis of failures is also unique. Further research into the details of failure mechanisms is necessary for the understanding of contact lifetime and the factors which affect contact failure. These are initial steps in understanding of microscale contact lifetime phenomena and development of a scientific, systematic method of comparing MEMS switch contact material lifetime performance and in understand-

ing microscale contact phenomena. The knowledge thus developed of microcontact mechanics will enable better MEMS contact material selection procedures. Note that this study did not provide the optimal contact material for use in a MEMS switch, but did demonstrate a methodology which could be used by future researchers to identify and compare high performing MEMS contact materials in an operational-like environment.

11.4.1 Novel Experimental Design & Capability. This study contributed a novel experimental capability which provides researchers a method to analyze the cycling behavior of micro-mechanical electrical contacts as well as new experimental data on micro-contact performance. The experiment employed precision piezo-electric devices in concert with a nanoindenter to measure characteristics of contact performance over time, including contact force and resistance data. No similar test setup integrating direct measurement capabilities and the ability to analyze the contact surfaces after testing has been reported. The study accomplished here is among the first experimental work to focus directly on mechanics of microcontacts as they evolve during cycling, and to provide data helpful to microcontact designers. This data and experimental setup was used to directly compare the performance of three contact metals. This type of data is necessary so designers can understand the tradeoffs they must make when designing and fabricating a MEMS switch. The setup can be used in all four steps of material selection in engineering design (See Section 3.1).

11.4.2 New Data on Microcontact Behavior. This project contributes knowledge of three contact metals and how they perform in MEMS scale contacts, and provides switch designers with information on failure mechanisms which can be used in improving switch design based on lifetime and reliability goals, switch force regime and intended use. Complete and integrated measurements showing a full description of microcontact behavior as it evolves over the lifetime of a contact was not previously reported. New data gathered include direct measurement of pull-off force, contact interference, time-dependent deformation of thin film contact material, energy absorbed

during contact as well as measurement of threshold force and distance and tracking of contact stiffness changes during cycling. Images of both contact surfaces at failure as well as evolving surfaces more complete and detailed than were previously reported are presented and analyzed. This study also provides the first reporting of the evolution of cycling characteristics on a MEMS scale for a dispersion strengthened contact material designed specifically for use in MEMS switches.

11.4.3 MEMS Contact Failure Analysis and Categorization. The study identified four adhesive failure types which were characterized by examination of the contact surfaces after failure. Differences in measurements of contact performance characteristics were also identified for the four failure categories. These different failure types may explain the widely varying cycles to adhesive failure seen both in actual MEMS switches and in the present study. This study shows that it may be possible to identify contacts at risk for early failure by various performance measurements on contacts during a "burn-in" phase. Note that Radant MEMS performs early testing on their microswitches for screening purposes [155]. Further study using this experimental design could determine criteria to be used for identification of contact switches susceptible to infant mortality or early adhesion failures.

11.5 Recommended Future Work

This research studied the impact of only a few contact variables while the test setup is capable of significantly more.

1. The effect of other contact forces as well as the cold-switching regime should be studied.
2. The effects of cycling speed and rate of pull-off should be investigated.
3. The effect of different levels of current through the contact should be analyzed.
4. An apparatus to ensure the cycling occurs in a noble gas/non-reactive environment should be designed and installed. The tests could be run in nitrogen

or argon to see how hydrocarbon contamination in laboratory air affects the results.

5. The ability to carefully analyze contacts after cycling should be used to develop a model of contact adhesion growth and wear on microcontact surfaces.
6. Further analysis of adhesion mechanisms and their relationship to contact lifetime should be performed. This could be used to identify leading indicators of imminent contact failure or contact susceptibility to shortened lifetime failure.
7. Other contact materials, including specific investigation of microstructure effects on adhesion, should be investigated.
8. The properties of thin films, especially methods to measure and calculate yield strength, should be further researched. A better knowledge of microcontact yield strength and relationship to micro-contact behavior would improve the design and performance of MEMS switches.
9. Investigation should be accomplished on MEMS switches experiencing "open" or high resistance failure to determine whether damage to surface or interposing high resistance contamination caused failure.
10. The thermal behavior of the contact materials at the micro scale should be investigated. The effect of heating in microcontacts should be studied and a method developed to directly measure temperature in cycling microcontacts. This would allow comparison of contact temperature between differing contact materials. Thermal characteristics of Au-4%V_2O_5 should be studied and compared to gold and Au5%Ru.
11. A method to measure the temperature of microcontacts during cycling should be developed.
12. The impact of thermal effects on contact lifetime should be further studied.
13. Surface energy of candidate contact materials should be analyzed to better determine predictive ability of surface energy to hardness ratio.

14. The effect of contact bump shape on micro-contact performance and lifetime should be further investigated.

11.6 Conclusions

Following are the major conclusions developed as a result of this study:

1. Experimental apparatus as designed and built is capable of simulating microswitches and comparing contact material performance.
2. High resistance failure (also sometimes called "open" failure) may sometimes be caused by damage to electrical contact surface.
3. Some minor contamination on contact surfaces may be beneficial in reducing contact adhesion.
4. Surface smoothening increases contact adhesion and should be delayed to extend contact lifetime. (Similar to result in [162])
5. No evidence found that contact shape affects lifetime results for fully plastic microcontact.
6. Lifetime performance of gold is improved by alloying with ruthenium. (Similar to result in [37])
7. Growth of contamination/resistive layers during cycling on ruthenium contacts is reduced by alloying with gold. (Similar to result in [37])
8. Adhesion force is greatest for softest metal tested, but does not scale with hardness.
9. Threshold force does not increase with cycling in the absence of an increase in highly-resistive contamination.
10. Dispersion strengthened materials offer great promise for MEMS contact switches.

Appendix A. Test Device Fabrication Development

This appendix describes the development required to process and fabricate silicon cantilevers with a contact bump. The preparation and etch of contact bumps onto custom SOIMUMPS die consisted of the following steps: (1) Mounting dies onto carrier wafers, (2) Processing mounted dies through photolithography, (3) Etching bumps into cantilevers using RIE/ICP, (4) Demounting dies from carrier wafers, and (5) Dicing cantilevers apart. Each of these steps and the problems solved enabling successful fabrication is described in this appendix. The first challenge was handling the die without destroying them during processing. This was accomplished by experimenting with methods to mount the dies to carrier wafers, the results of which are described in the next section.

A.1 Mounting of SOIMUMPS Die

MEMSCAP fabricated die were mounted on 50 mm silicon wafers to facilitate handling and processing during bump fabrication. The dies developed for this research were extremely unusual in that the center part of the die was etched away and the cantilevers were already released when they arrived, and thus the cantilevers extended over a large void. This made it impossible to process these die in the way normally done with POLYMUMPS or other continuous small die. Therefore, it was necessary to develop a method of mounting to allow processing and to protect the die during handling.

Several different methods were attempted, but the method ultimately found to be successful and repeatable was mounting the die on a 50 mm silicon wafer with the use of photoresist as a mounting medium/adhesive. Experimentation was required to develop the best possible mounting method. Photoresist is tacky and will hold when an item is pressed into it and baked. It will also come off when soaked for a period of time in solvent such as acetone or 1165. Carrier wafers were coated with 1818 photoresist at a relatively slow speed (3500 rpm) to ensure a thick coat of photoresist, then the die was pressed onto the tacky surface in the center of the wafer.

The mounted die was then baked for five minutes at 110°C, slightly below the curing temperature of 1818 (165°C) to ensure die adhesion to the wafer.

Demounting occasionally accidentally occurred when the die was not firmly adhered to the carrier wafer. This problem was solved by increasing the baking time to five minutes at the solvent cure temperature. Also, a step in the process flow was added to use the flat back of a swab to gently seat the die on the layer of photoresist by pushing down on opposite corners and sides of the die before baking the mounted carrier. After baking, the strength of the adhesion was checked by pressing gently on the sides of the die to determine if it adhered to the carrier wafer. If the die didn't slide during this check, it was strong enough to last through the rest of the processing steps.

A.2 Processing of Dies Mounted on Carrier Wafers

Development of the process for test device fabrication required solving several processing problems due to the nature of the devices needed for this experiment to simulate MEMS switches. Once the dies were mounted, they could be processed in a manner very similar to the standard processing steps of small wafers. The biggest difference was in the contact alignment and exposure step. The 350 μm thick die was mounted on top of a silicon carrier wafer with a similar thickness. This thickness is much larger than the thickness of the wafers or small die usually processed in the MJB3 mask aligner. Significant adjustment to the mask aligner was needed to ensure good contact and exposure. Manual stage height adjustment was required for solid contact and the vacuum chamber option available on the MJB3 was not usable due to the double thickness of the die on wafer combination and the gaps created around the edge of the wafer due to the height of the die.

One significant problem caused by processing of dies mounted on wafers was the problem of contamination caused by small drops of photoresist getting on the surface of the die during the mounting process. This was solved by flood exposing the die/wafer combination after the mounting process and then developing away all

photoresist which wasn't contributing to the adhesion of the die to the wafer by using straight 351 developer while the die/wafer combination was on a spinner. This step also helped to clean remaining impurities on the cantilever surfaces left over from SOIMUMPS processing.

The handle layer of the SOIMUMPS dies was 350 μm thick and the cantilevers as fabricated were already released when they were delivered. That means that the dies as mounted had a huge cavity underneath the cantilevers where photoresist could accumulate during the coating process.

A.2.1 Bump Fabrication Development. The starting point for the bump fabrication technique was the method used by Chen at Northeastern University [37]. The process used here, however, required significant development effort because the NEU process was performed on flat wafers before the cantilevers were etched out of the device layer. NEU cantilevers were optimized for use in the AFM test setup, so new cantilever design was needed at AFIT to enable the nanoindenter based setup developed during this study. AFIT test devices required coating and processing on non-planar surfaces in addition to development of a new etch recipe using a different tool. The process developed for coating photoresist, exposing, developing, and bump fabrication on the dies received from MEMSCAP is described in detail in the following sections. The development of the process for bump fabrication is described in Appendix B. The process follower developed by the author for this work is given in Appendix C. This is a unique process, generally photoresist is only spread on planar surfaces due to problems with edge beading and the need to create a smooth, even coat of photoresist. It was found during this study, that photoresist could be coated on non-planar surfaces and spread evenly when the non-planar dies were mounted on 50 mm carrier wafers.

Shipley 1818 was the initial photoresist attempted. However, the first RIE/ICP etch tests to create rounded bumps resulted in pyramidal shaped contact points. This was the indication that this process was unique and required etch recipe development

for the RIE/ICP tool available at AFRL. Next, SF-11 was chosen as a reasonable choice for use as a patterning photoresist because of its high viscosity and ability to coat silicon with a nominally 1.1 μm thick layer. It was hypothesized that the SF-11 photoresist would lead to thicker patterns on non-planar surfaces and that would result in thicker PR patterns.

The development of the etch recipe was accomplished patterning SF-11 dots on silicon wafer pieces and varying the parameters of the ICP/RIE etch. The process was patterned after the bump etch process used at NEU, as previously described. However, the ICP/RIE etch tool at AFRL was not able to maintain a chamber pressure of 100 mTorr which was used at NEU. This meant that the etch recipe required development. The process to create bumps on silicon was also unique to AFRL as standard AFRL etch recipes were formulated to have a strong selectivity of etch for the wafer but not the photoresist mask used, as is expected for standard processing in order to avoid etching through the photoresist mask. Standard processes etch trenches or other features into the sample of interest. There was no recipe available to provide a 1:1 (or similar) selectivity between photoresist and wafer, that is, to effectively etch the shape of the photoresist into the surface of the silicon. Development work was required to find the optimal etch recipe to etch the rounded, reflowed photoresist bump into the ends of the silicon cantilevers leaving a smooth silicon bump of the appropriate size. Appendix B contains a detailed description of the development work done to develop this recipe used to etch contact bumps into the silicon cantilevers.

SF-11 turned out not to be an optimal choice for non-planar processing of the mounted die, mostly because the hot plate bake on actual die to cure SF-11 caused black material to bubble up from under the mounted die. This contamination blocked the mask aligner from making good contact with the cantilevers. An attempt was made to solve this problem by filling in the cavity/void underneath the mounted die before the photoresist coating step.

A.2.2 Attempts to Fill Cavity in Die. When performing development while using SF-11, several dies were successfully processed forming bumps on the cantilevers. However, the repeatability of the process was very low due to air bubbles or solvent in photoresist trapped in the large cavity. Attempts were made to develop a method to fill the cavity under the cantilevers and avoid this processing problem.

The first method attempted was to shave small amounts of wax which was soluble in acetone and place it into the cavity using tweezers and a microscope. The plan was to put some wax into the cavity then place the mounted die/carrier wafer on a hot plate to melt the wax therefore causing even flow into all the crevices of the cavity underneath the die. However, the wax as placed in the cavity and melted did not flow evenly into all locations in the cavity. The cantilevers were also very fragile and would break if inadvertently touched by the end of a tweezer. This method was unsuccessful due to the inability to successfully fill the cavity. Spinning on photoresist over the partially filled cavity also was not successful.

The second method attempted was to use a compressed air precision liquid delivery system to fill the cavity stepwise with precise amounts of the photoresist in use and bake the solvent in the photoresist out with each step. The idea was to fill the cavity with a small amount of photoresist, bake out the solvent, then fill with a small amount more, therefore layering the photoresist and filling the cavity. The photoresist was to be placed with a small gauge needle using a microscope to view the work area and the reflow would smooth the photoresist and cover the bottom area of the cavity evenly. An EFD 2400 series liquid dispensing system available at AFRL Sensors Directorate was used to attempt cavity filling with SF-11 photoresist. SF-11 was placed in the reservoir of the system and a GP Clear 30 ga dispensing needle, the smallest available, was chosen. SF-11 was too viscous and would not flow from the 30 ga needle. The next larger dispensing needle was a GP Clear 27 ga needle which allowed SF-11 to flow. An operating pressure of 19 psi and pulse length of 0.05 sec was determined to be optimal for delivering a small drop of photoresist.

Attempts to fill the cavity using small drops from the needle also proved unsuccessful. At first, drops were applied to the corners of the cavity using a microscope to place the needle tip and drops of SF-11. However, it was extremely difficult to place drops in the locations necessary without touching and breaking cantilevers. Cantilevers were also buried by the photoresist. It was determined that drops should be placed in the center of the cavity. However, the photoresist placed in the center did not flow out to the sides and fill the corners of the cavity due to its viscosity. Attempts were made to bake out the solvent in the filler photoresist and to place photoresist in layers in the cavity. However, the photoresist did not planarize, even when left to sit overnight or for long periods of time (e.g. several days). When the dies were coated with photoresist and baked at the curing temperature, the solvent or air bubbles trapped during spinning still bubbled over and covered the working surface of the die enough to ruin contact in the mask aligner.

Another attempt was made to fill the cavity while mounting the die on a carrier wafer. This was done by placing a large amount of SF-11 on a carrier wafer on a spinner, then placing the die carefully on the spinner and pushing it down such that the photoresist came up through the cavity and covered the die. Then, the spinner was started. Initially, the die stuck to the carrier wafer and adhered solidly after baking. However, the process could not be successfully repeated because the die would often fly off the spinner due to a lack of adhesion from the SF-11. The die successfully mounted this way still had trouble with contamination bubbling up from below as well.

This problem of pattern repeatability was eventually solved by returning to 1818 as the photoresist, as the hotplate bake step for 1818 is done at a significantly lower temperature than the hotplate bake used for SF-11 (165°C vs. 270°C). The 1818 process was determined to be repeatable, and it was found that the recipe which worked the best for SF-11 patterns on silicon also worked the same way with 1818 bump patterns. The void did not cause a problem when 1818 was used as the patterning photoresist.

A.3 Photoresist Choice

Although the bump etch testing occurred using SF-11 as the patterning photoresist, 1818 was chosen as the appropriate material to use for bump patterning. This was due to the failure of attempts to fill the cavity and planarize the SF-11. A small number of die were processed successfully with SF-11 as the working photoresist, but the process was not repeatable.

A small number of test dies were mounted and the entire 1818 process was developed using cure and reflow temperatures appropriate to 1818. These temperatures are low enough such that no contamination emanates from below the die, and the surface of the die is cleaned extremely well using the new device fabrication process developed for this study. A few test wafers using 1818 as the photoresist were produced in order to test the ICP/RIE etch recipe determined for SF-11 patterns. These etch tests showed that the etch recipe developed for SF-11 on silicon worked in a very similar manner for 1818 on silicon.

A.4 Bump Etching

The working photoresist had to be changed back to 1818 due to factors described previously and in Section A.1. Tests on patterns on test wafers with 1818 were also accomplished, and bumps were patterned and etched on actual cantilever die as well. Typical results can be seen in Figures A.1 and A.2. These figures show that the shape of the bump can be determined by adjusting the etch time. It is possible to create either rounded or flat-topped bumps which are taller than the bumps created using SF-11. However, the flat-topped bumps are more repeatable and have a smoother contact surface. This is due to the fact that small variability in the process causes the photoresist dots on the end of each cantilever to be slightly different heights. The etching time/height goal needs to be 0.2 μm less than the height of the photoresist bump in order to etch a rounded final bump. Etch rate testing was performed on 1818 and silicon and the etch rate of the recipe was determined to be 800 Å/min for 1818 and 2600 Å/min for silicon. Flat-topped bumps fabricated using 1818 were used

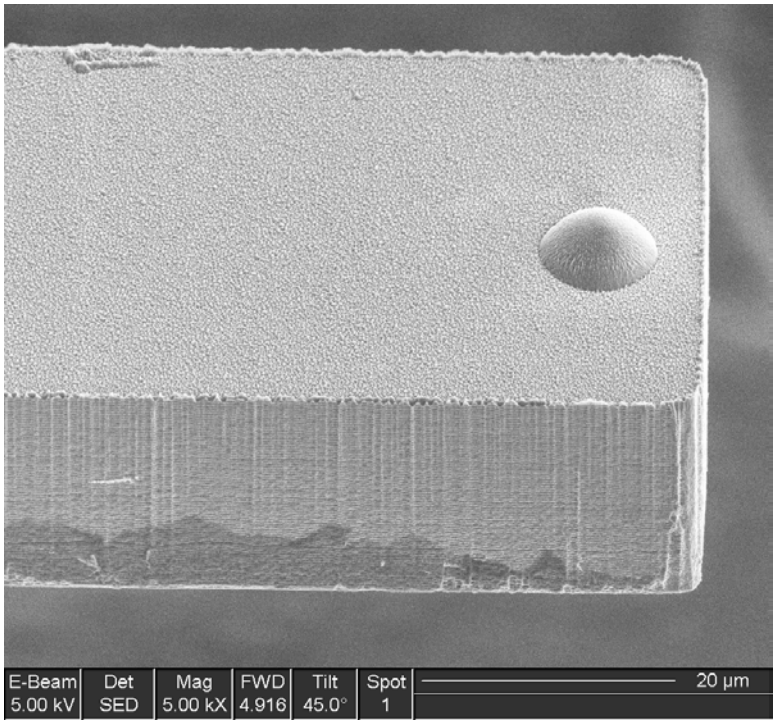

Figure A.1: Close-up SEM micrograph of a sample 7.5 μm diameter rounded contact bump fabricated using 1818 for these experiments.

for the majority of testing. The height of bumps can be measured in a Zygo fringe interferometer and the diameter and shape can be seen in an SEM. The processes developed for demounting and dicing the die are described in the next sections.

A.5 Die Removal from Carrier Wafer

Mounting the die also requires a process of de-mounting. 1818, the mounting medium used, is soluble in acetone, so soaking in acetone will release the die. However, acetone will not necessarily clean off the back of the die where it is possible that some of the photoresist is burned on due to the repeat baking required through this process. The best way to remove mounted die and ensure die and cantilever cleanliness was through 1165 solvent heated to 90°C. Five minutes in 1165 generally caused the die to slide easily off the carrier wafer. The die can be left in the solvent longer to ensure cleaning. The die also should be placed in an oxygen plasma asher for two to

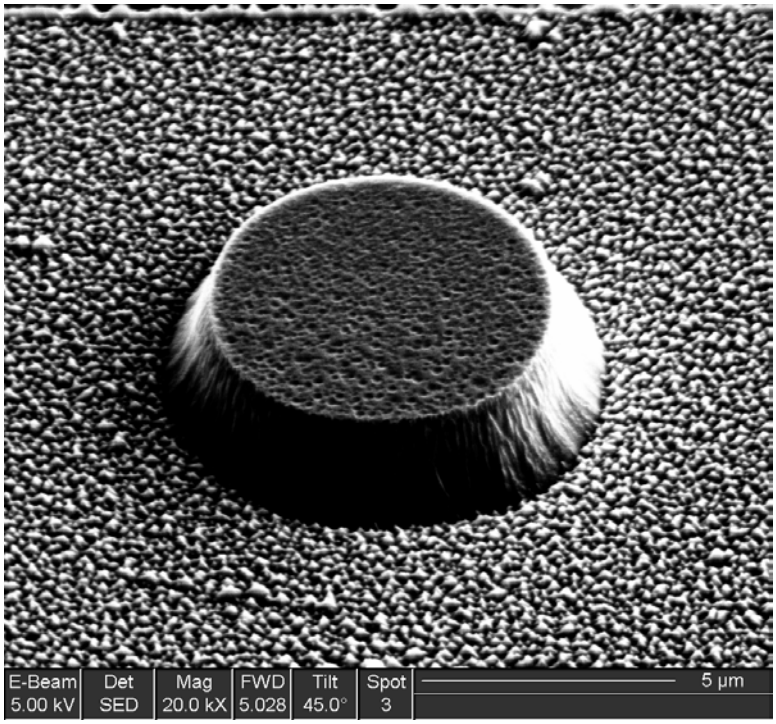

Figure A.2: Close-up SEM micrograph of a sample 7.5 μm diameter flat-topped contact bump fabricated using 1818 for these experiments.

four minutes to ensure any remaining residue is burned off so that metal coating can proceed after the die is cut and the cantilevers separated.

An extremely risky and possible single point of failure for the entire experimental design was in the ability (or inability) to dice the cantilevers as fabricated. This had never been accomplished and could not be attempted until die were received from MEMSCAP. This was a challenge because the cantilevers were released and unprotected. The next section describes the successful method developed to dice the fabricated and bulk-etched cantilevers.

A.6 Dicing

Each SOIMUMPS die was fabricated with 12 cantilevers. These required separation after bump fabrication and before contact material coating with a thin film of the appropriate test material. The cantilevers were extremely fragile and physically unprotected. Several methods were attempted before a successful method to separate

the cantilevers from the die was determined. The only way found to successfully split them apart was through the use of a precision high-speed diamond cutting saw. Water cools the working area and can be controlled enough such that the cantilevers are not harmed during the dicing process while keeping the process clean. The cutting was performed using a Micro-Ace 3 Load Point Limited Series 3 high-speed diamond saw at AFRL by a skilled technician. The first step was to mount the die to be diced upside down on blue tape. The tape with the attached die was placed in a mount ring and mounted in the diamond saw working area. The die was aligned with the blade and a cut was made through the thickness of the handle layer. The die was cleaned with water and dried with compressed air between cuts. A diamond coated nickel steel hubbed blade with cutting width of approximately 29 μm was used at 35,000 rpm to separate the cantilevers. The cantilevers generally survived this process, as long as nothing solid touched the ends of the cantilevers during the process. The cantilevers were then ready for cleaning and sputter coating with contact material.

Appendix B. Development of Bump Etching Technique

This appendix describes the process used to develop the etch recipe used to create contact bumps on test device cantilevers. This step in development was crucial to the success of the testing accomplished. A contact mask containing 5, 7.5, 10 and 15 μm dots corresponding to the proper location one diameter from the end of the cantilever was designed and procured. Test patterns of each dot size were created on silicon test wafers, the patterned dots were reflowed into hemispherical bumps and etch variables were adjusted to determine the best method to create useful contact bumps. The effort to develop a new etch recipe was necessary for this study because no existing recipe for the etch tool at AFRL was available to accomplish the type of etch needed to create contact bumps on the end of the test cantilevers.

After a recipe and etch times were determined, MEMSCAP dies were mounted on silicon wafers, coated with photoresist, and developed. The etch recipes were tested and bumps imaged to determine if the etch proceeded on the mounted non-planar dies with the same results as the test wafers. The following section will describe the work done to develop the ICP/RIE etch recipe appropriate for use with the test cantilevers. First the development and use of test wafers to simulate the silicon test cantilevers will be described. Results of various tests will be shown and the final etch recipe choice explained. Then, the efforts to mount and pattern actual cantilevers will be described.

In order to save expensive SOIMUMPS dies as much as possible, test wafers were used in developing the etch recipe and processes necessary for fabricating contact bumps on the ends of SOIMUMPS fabricated cantilevers. First, the photoresist coating of test wafers is described, then the exposures developed using the contact mask and Deep UV exposure is explained. Finally, the reflow used to create contact bumps is described and the ICP etch recipe developed specifically to cut the reflowed photoresist bump into silicon cantilevers is described.

The first step was to coat photoresist, then expose and develop wafers with multiple sets of cantilever dot patterns. Initially, this development was intended for

use with SF-11 photoresist so deep UV exposure was required. The bumps were reflowed to create a hemispherical shape, then the variables involved in RIE/ICP etching were varied to determine the effect of the variable changes on dump size, shape and surface roughness. Each of these steps in the experimental determination of the best recipe to use for the required test devices is described in detail in the following sections.

B.1 Photoresist Coating of Test Wafers

Test wafers were fabricated using a process similar to that envisioned for the final cantilever dies. A three-inch N-type mechanical silicon wafer (100) orientation doped with Arsenic was coated with three layers of SF-11. Each layer of SF-11 was spun on for 30 seconds at 4000 rpm with a ramp of 200, and then baked for two minutes at 270°C. This process created approximately a 3 μm height of SF-11. The wafer was then spin-coated with S1813 positive photoresist at 4000 rpm for 30 seconds and baked for 75 seconds at 110°C.

B.2 Contact Mask Exposure

The coated test wafer was inserted into the MJB3 with the contact mask containing the various size dots. The mask and wafer were brought into physical contact for exposure. The test wafer was exposed for 11.5 seconds in the MJB3 contact mask aligner. The 1813 layer was then spin developed using 351 Developer for 30 seconds at 500 rpm, with a 30 second de-ionized(DI) water rinse after development. The pattern is repeated several times on the contact mask, so several sets of dot patterns were created on the test wafer. The 1813 pattern developed is the mask for exposure and development of the SF-11.

B.3 Deep UV exposure and development

After development of the 1813, and a profilometer check showing the feature height was approximately 1.4 μm to ensure that the 1813 was developed completely,

the wafer was put under the deep UV lamp. The wafer was deep (UV) exposed for 200 seconds. After the first exposure, the wafer was spin developed for 60 seconds at 500 rpm using SAL-101 followed by a 30 second DI water rinse and Nitrogen dry.

Visual inspection showed that the SF-11 hadn't started to develop yet, so the wafer was exposed to deep UV for 200 more seconds. Then, the wafer was spin developed for 60 seconds at 500 rpm using SAL-101 for a second time. The SAL-101 was followed by 30 seconds of DI water rinse, and an N2 dry. Visual inspection showed multicolored fringes on the test wafer, and profilometer showed that the SF-11 development was underway. The wafer was then deep UV exposed for another 100 seconds. After this exposure, the wafer was spin-developed one more time for 60 seconds using SAL-101 followed by a 30 second DI water rinse and nitrogen dry.

The wafer was checked in the profilometer, showing the height of features was approximately 5 μm. This showed that the SF-11 was developed completely, as each layer of SF-11 was slightly more than 1 μm thick, and the 1813 was approximately 1.4 μm thick. The 1813 was then cleaned from the wafer using the acetone gun for 20 seconds at 500 rpm, followed by an acetone bottle rinse for 20 seconds. The wafer was then rinsed with Isopropanol for 30 seconds followed by 30 seconds of DI water. It is important to follow the acetone and isopropanol with DI water to ensure the SF-11 layers don't crack and fail due to cooling too quickly from the acetone and isopropanol.

The pattern was then checked again using the profilometer. The check verified that the feature heights remained at 3.5 μm showing that the three layer thickness of SF-11 was tall enough. However, the 5 μm dots were approximately 1 μm shorter at 2.5 μm. It is hypothesized that the small features develop away under the conditions required for completely developing the larger features. The pattern at this time was a set of various size dots, each in a cylindrical shape. The next step was to make them into a rounded shape.

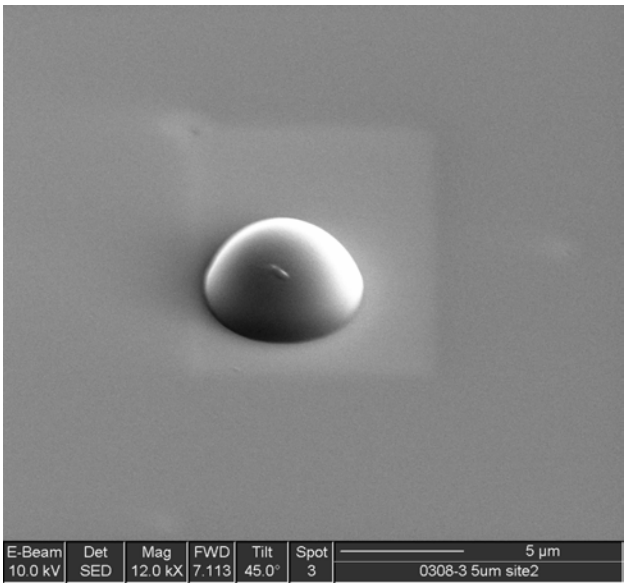

Figure B.1: Shape of the 5 μm SF-11 patterned bump after reflow. This is the desired shape of the final contact bump as it would be etched into silicon.

B.4 Reflow to create hemispherical photoresist bumps

In order to create a rounded shape, the test wafer was put into an oven for two minutes and thirty seconds at 260° C. This reflowed the dot pattern of SF-11 into rounded shapes, controlled by the surface tension of the softened SF-11. The success of this reflow can be seen in Figures B.1, B.2, B.3 and B.4 showing reflowed bumps of varying sizes on a piece of the test wafer flash coated with 100 Å of gold. The 15 μm bump did not reflow very well, as can be seen in Figure B.4. This bump size is too large to reflow nicely into a rounded shape. It is clearly still in the shape of a disc. The developed wafer was then cleaved in an attempt to create several pieces with multiple bump sizes for use in (ICP) etch tests.

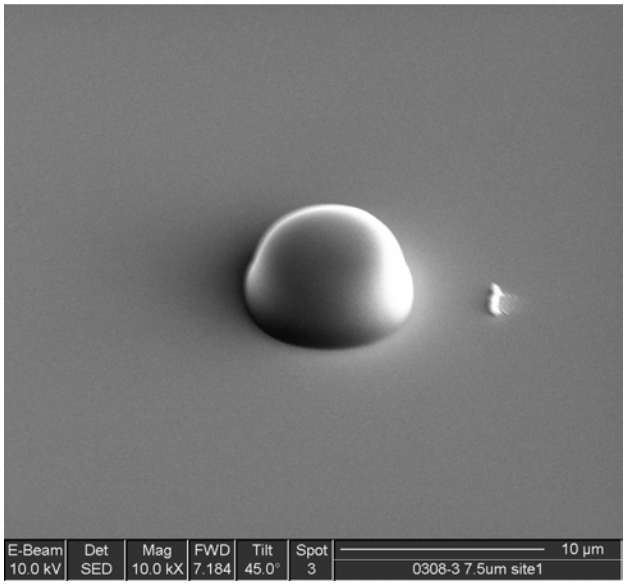

Figure B.2: Shape of the 7.5 μm SF-11 patterned bump after reflow. This is the desired shape of the final contact bump as it would be etched into silicon.

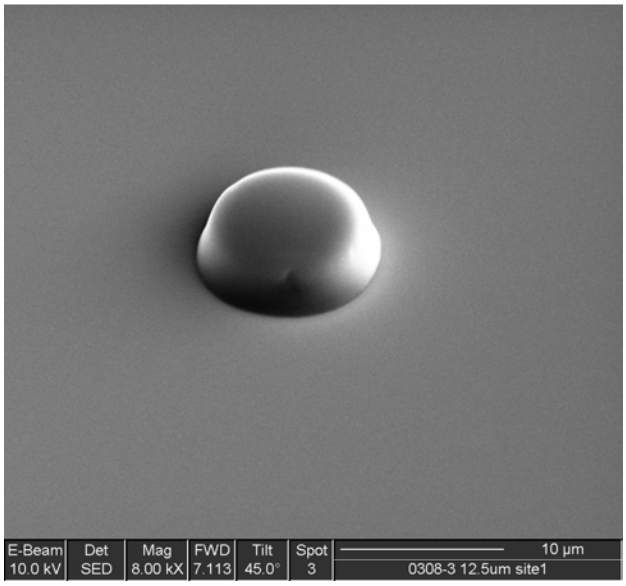

Figure B.3: Shape of the 10 μm SF-11 patterned bump after reflow. This is the desired shape of the final contact bump as it would be etched into silicon.

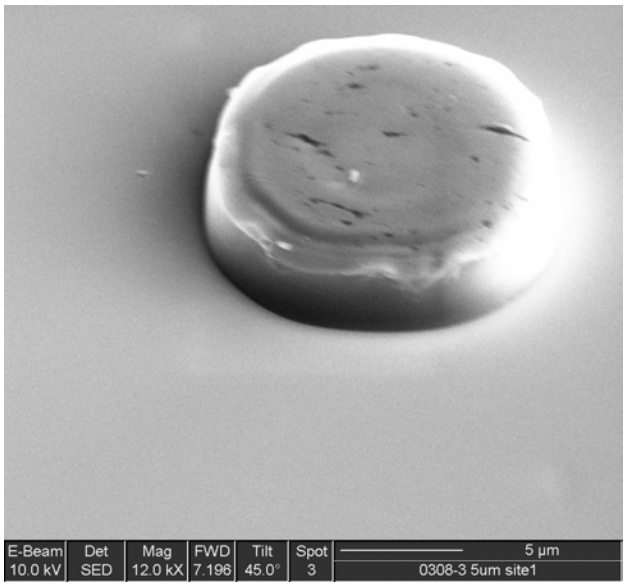

Figure B.4: Shape of the 15 μm SF-11 patterned bump after reflow. This bump is too large to reflow nicely into a rounded shape. As seen here, it is still disc shaped.

B.5 Development of ICP/RIE Etch Recipe

The recipe was intended to etch the resist and silicon equally with a ratio of 1:1. The etch should be a physical etch, with no selectivity between the silicon and the resist. This is unusual, as the mask in most ICP etches are intended to hold up during the etch. A similar etch was done by Chen at Northeastern University, using reflowed S1818 as the bump pattern [37]. These SF-11 bumps are intended to be taller than the 1818 bumps used by Chen in order to ensure contact in the AFIT experimental setup and the AFRL etch tool was not capable of the higher operating pressure used at NEU. This type of etch has many variables affecting etch rates and surface results, so it was necessary to perform testing to determine a recipe which would work for this application.

Several etch tests were conducted at AFRL/SN. SF_6 and Oxygen were used as the working plasma in the ICP tool. A Plasma-Therm SLR Series 700 RIE/ICP tool with shuttle-load lock was used for all etching. The tests and the variation of test parameters is shown in Table B.1. The chamber was pumped down to at least 5×10^{-6} Torr before the etch process was started. The RF power source is 13.56 MHz and the

Table B.1: Variables used in experimentation to develop a recipe for proper etching of a PMGI bump into silicon. Tests are shown in the order accomplished, and changes in parameters are shown.

Date	Sample	O_2 Flow Rate (sccm)	SF_6 Flow Rate (sccm)	Pressure (mTorr)	RIE Power (W)	ICP Power (W)	DC Bias (V)
28 Feb 07	1101-1	9	90	70	25	500	40
12 Mar 07	0308-1B	9	90	15	25	450	100
15 Mar 07	0308-1D	30	90	15	25	250	75
19 Mar 07	0308-2B	30	90	15	25	250	73
22 Mar 07	0308-2A	40	80	15	25	250	72
22 Mar 07	0308-2C	50	80	15	25	250	72
26 Mar 07	0308-1C	50	80	30	60	250	100
27 Mar 07	0319-1F	50	80	70	60	250	130
27 Mar 07	0319-1D	50	80	70	60	250	130
30 Mar 07	0319-1G	50	80	70	90	250	
3 Apr 07	0319-1B	50	50	70	90	250	195

ICP power source is 20 MHz. This combination produces a higher density plasma in the operating chamber.

An attempt was first made to etch bumps into cantilevers with an existing recipe. However, the recipe was a strong chemical etch and etched the silicon very preferentially and the bumps ended up in pyramidal shapes. An example is shown in Figure B.5. The first test on a silicon wafer was run at a very high pressure, and the high DC bias cooked the SF-11 bumps. The DC bias was reduced, and the flow rate of oxygen was increased in order to increase the etch rate of the PMGI. The results are shown in Figure B.6.

It was noted that the etch rate was not equivalent between the silicon and SF-11. For the shape of the bump to be rounded and hemispherical, the etch rate of the PMGI needed to be increased. This was accomplished by increasing the oxygen flow rate, and the issue of "cooking" the PMGI by overpowering was resolved by reducing the DC bias from 100 to 40 V. The results of this etch test are shown in Figure B.7. This bump clearly shows the effects of the increased oxygen and SF-11 etch rate. The etch was only run for a short time, so the remaining PMGI can be clearly seen on

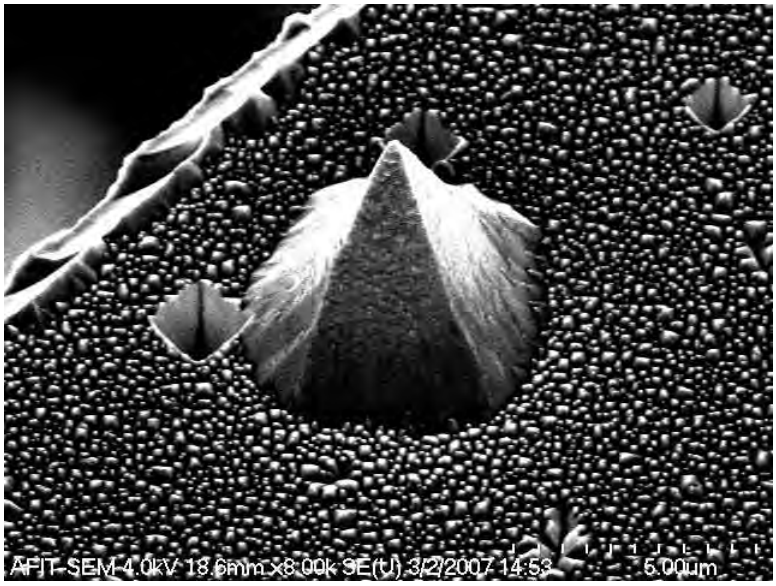

Figure B.5: Results of the first etch of a reflowed SF-11 bump patterned on a cantilever. It clearly shows preferential silicon etching.

the top of the bump. It is charging in the electron beam, so appears as bright white in the SEM image. Another test wafer was etched with the same recipe for a longer time. The results of this test are shown in Figure B.8 and B.9.

The surface in these 35 minute etch tests is extremely rough, showing that the recipe is running at a lower than ideal pressure. However, the straight sides of the bump also indicate that the selectivity of the etch is still off. The silicon is still being preferentially etched over the SF-11, and thus is not cutting the rounded shape of the bump into the silicon surface. The oxygen flow rate was increased for the next etch test.

Sample 0308-2A was etched next, and the results are shown in Figure B.10. The increased oxygen flow rate clearly increased the etch rate of the PMGI, bringing it much closer to the rate of silicon etch. This can clearly be seen by the rounded shape of the bumps. However, the black color on the cap of the bump is still PMGI, so the etch wasn't long enough to clear all the resist. A longer etch was tested, along with another increase in oxygen flow rate on sample 0308-2C. The results of this next test are shown in Figure B.11 and Figure B.12.

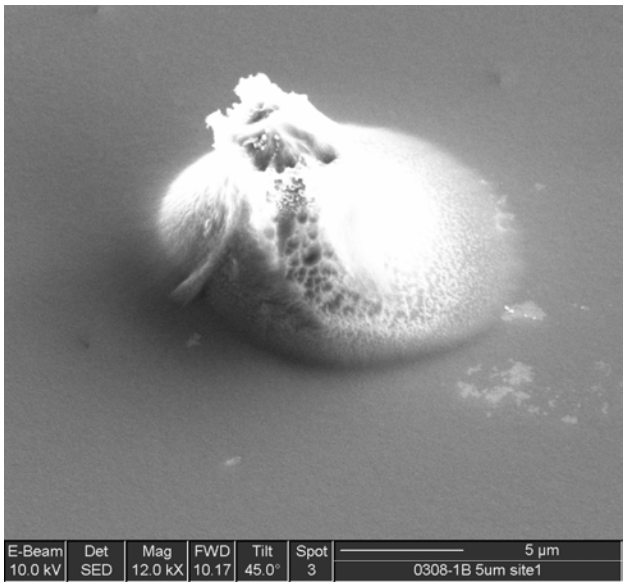

Figure B.6: Results of the first etch test of a reflowed SF-11 bump patterned on a wafer. It clearly shows damage done to the bump by the ICP.

This bump looks much more like the shape of interest, although after clearing the resist it clearly has a flat top due to the ICP not completely etching the resist away. Also, it has an extremely rough surface, both on the base silicon and the silicon that forms the bump. This indicates a higher operating pressure is needed. The next test was performed on sample 0308-1C doubling the working pressure from 15 mTorr to 30 mTorr, and increasing the RIE power from 25 to 60 Watts. An example of the results of this test etch on the patterned bumps is shown in Figure B.13

The next several etch tests were done on bare silicon wafers. The pressure was varied to see the effect on surface roughness and etch rate of the silicon. Table B.2 shows the variables set in these tests. An image at 150,000 X of the surface of the silicon at a 70 mTorr pressure etch is shown in Figure B.14.

The results of this test were used for the recipe on sample 0319-1F. This sample was etched for 12 minutes, and checking in an optical microscope. There was still evident PMGI on the bumps, so it was etched for another 12 minutes. This led to significant overetching. total etch as determined from measuring the protected area on the substrate silicon wafer the test piece was supported on was 5.4 μm. However,

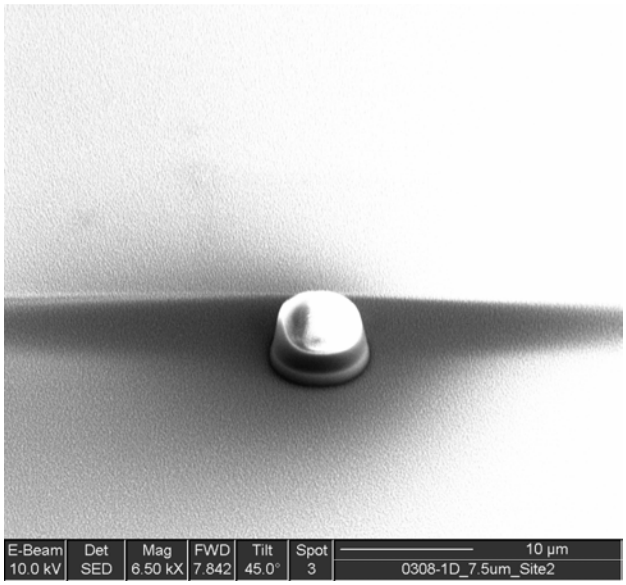

Figure B.7: Results of increased Oxygen flow on a a reflowed 7.5 μm diameter SF-11 bump patterned on a wafer. It clearly shows improvement in the etch rate, starting to show curved sides on the bump.

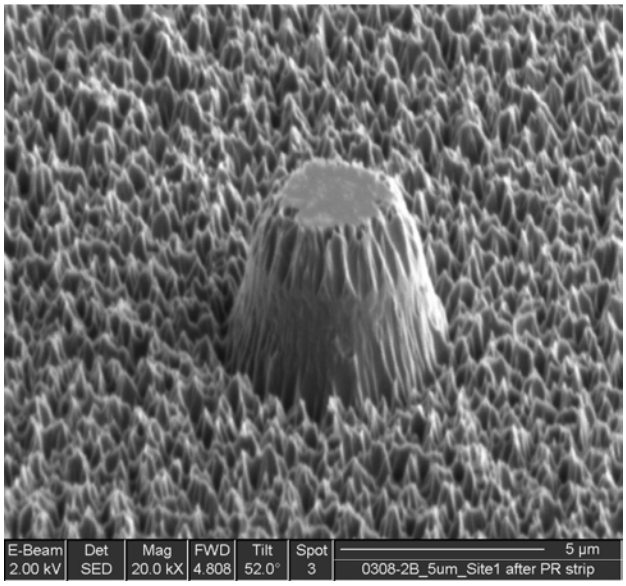

Figure B.8: Results of increased Oxygen flow on a a reflowed 5 μm diameter SF-11 bump patterned on a wafer after 35 minutes of etching, and after 1165 strip and oxygen plasma ash, removing all remaining PMGI. It clearly shows a very rough surface, and that the sides of the bump are not yet curved.

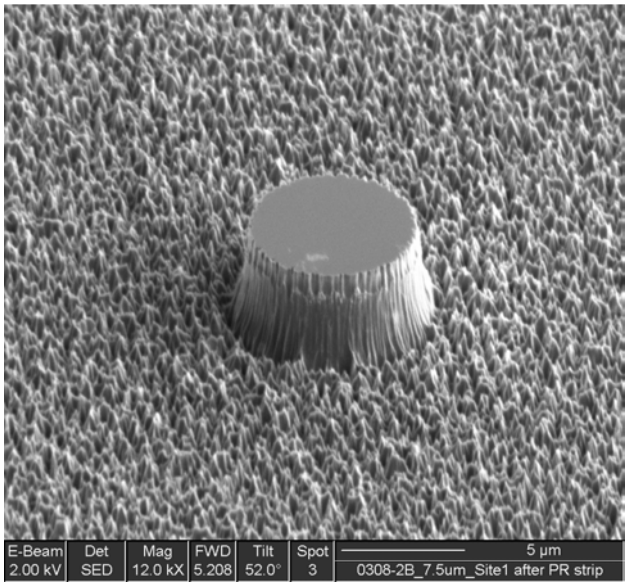

Figure B.9: Results of increased Oxygen flow on a a reflowed 7.5 μm diameter SF-11 bump patterned on a wafer after 35 minutes of etching, and after 1165 strip and oxygen plasma ash, removing all remaining PMGI. It clearly shows a very rough surface, and that the sides of the bump are not yet curved.

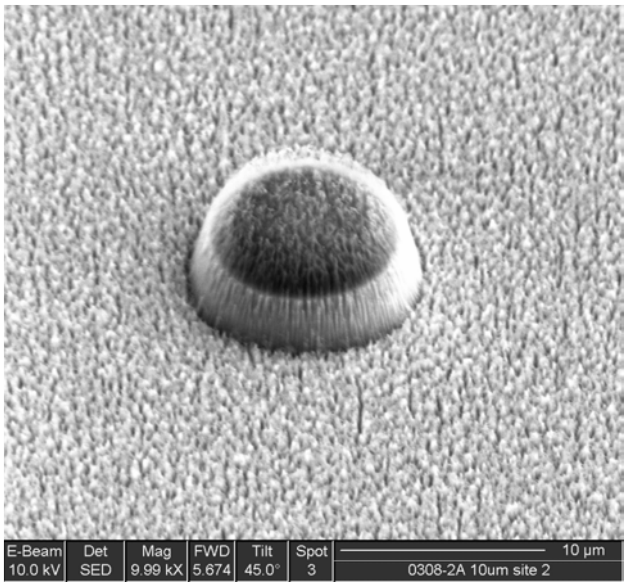

Figure B.10: Results of increased Oxygen flow on a 10 μm diameter SF-11 bump patterned on a wafer after 30 minutes of etching. The PMGI has not yet been stripped. The curved shape can clearly be seen.

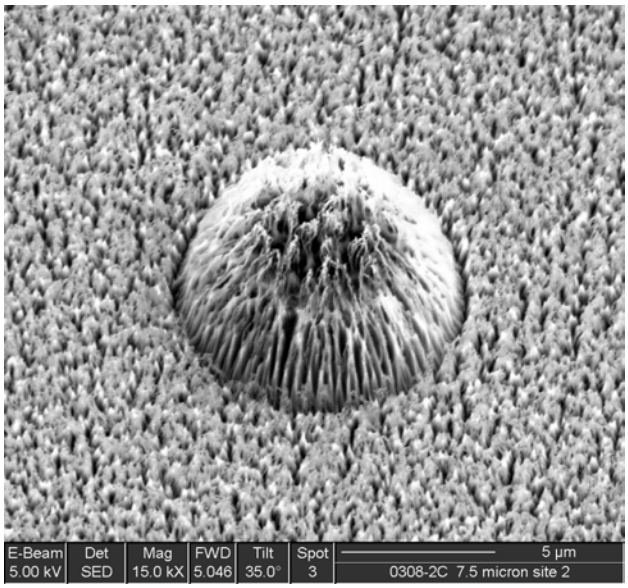

Figure B.11: Results of increased Oxygen flow on a 7.5 μm diameter SF-11 bump patterned on a wafer after 30 minutes of etching before clearing the photoresist. The curved shape can clearly be seen, as this is almost hemispherical.

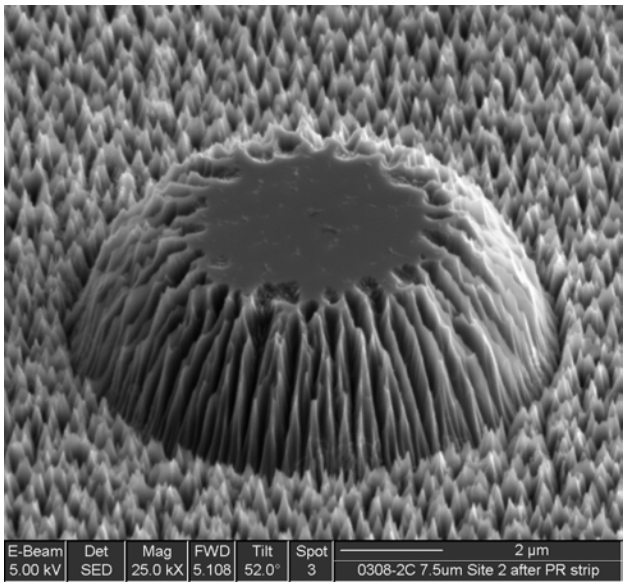

Figure B.12: Results of increased Oxygen flow on a 7.5 μm diameter SF-11 bump patterned on a wafer after 30 minutes of etching. The PMGI was stripped using 1165 and plasma ashing. The curved shape can clearly be seen.

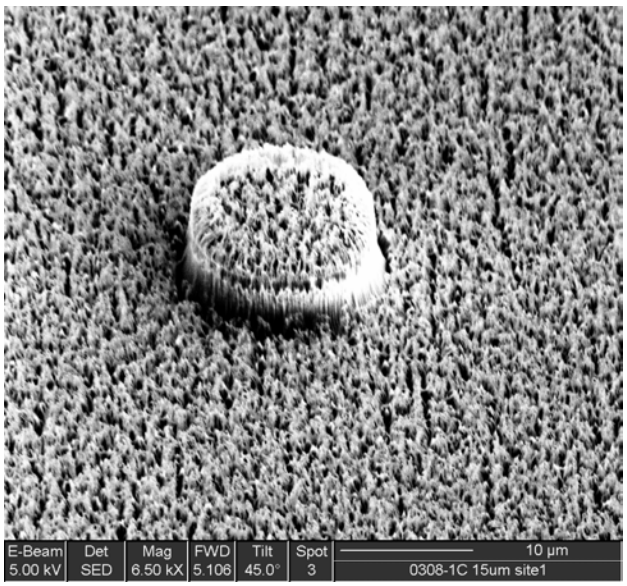

Figure B.13: Results of increased chamber pressure and increased RIE power on a 15 μm diameter SF-11 bump patterned on a wafer after 30 minutes of etching. The PMGI was not stripped. The curved shape can clearly be seen, and the surface is still rough.

Table B.2: Variables used in experimentation to determine effect of chamber pressure change on surface roughness of silicon. Tests were done on 26 Mar 07.

O_2 Flow Rate (sccm)	SF_6 Flow Rate (sccm)	Pressure (mTorr)	RIE Power (W)	ICP Power (W)	DC Bias (V)	Etch Time (min)	Etch Depth (μm)	Etch Rate (Å/min)
50	80	30	60	250	100	10	1.79	1790
50	80	50	60	250		10	1.58	1580
50	80	70	60	250	128	10	2.2	2200

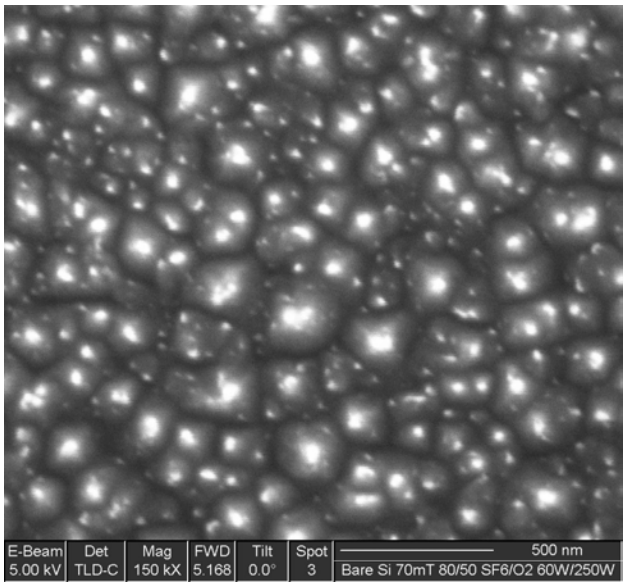

Figure B.14: Roughness after an etch test on bare silicon with the parameters: 70mTorr, 50 sccm O2, 80 sccm SF6, 60 W RIE, 250 W ICP, at 150kX magnification. The surface is clearly still rough.

the etch did not behave as expected as is shown in Figure B.16. The SEM image shows that the PMGI was cleared from the silicon, but the rounded hemisperical shape desired was not produced. Note the rough silicon on the top of the bump feature.

Sample 0319-1D was then etched for 18 minutes using the same recipe in an attempt to clear the PMGI without overetching. The depth of the etch was approximately 4 μm and the etch rate was 2222 Å/min determined from the silicon substrate on which the test piece was mounted during the etch. The results of this etch can be seen in Figure B.16. There still appears to be PMGI on the top of the feature, and the top surface looks slightly concave. The etch is clearly back to a more chemical etch, and not a physical etch as is desired for this case. However, note the 5 μm bump in Figure B.17. This clearly shows a rounded, albeit very rough, top with PMGI cleared.

Further tests were run on bare silicon wafers, varying the RIE power in an attempt to smooth the silicon surface. The results of this test are shown in Table B.3. These tests determined that 90 W RIE power was the best setting for a smoother

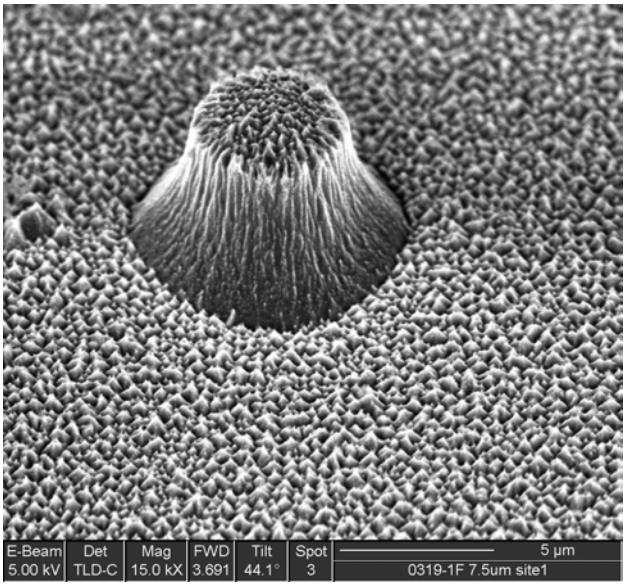

Figure B.15: Results of overetching on a 7.5 μm diameter SF-11 bump patterned on sample 0319-1D after 18 minutes of etching. The PMGI was not stripped. The surface is still rough, although it appears that all PMGI was cleared.

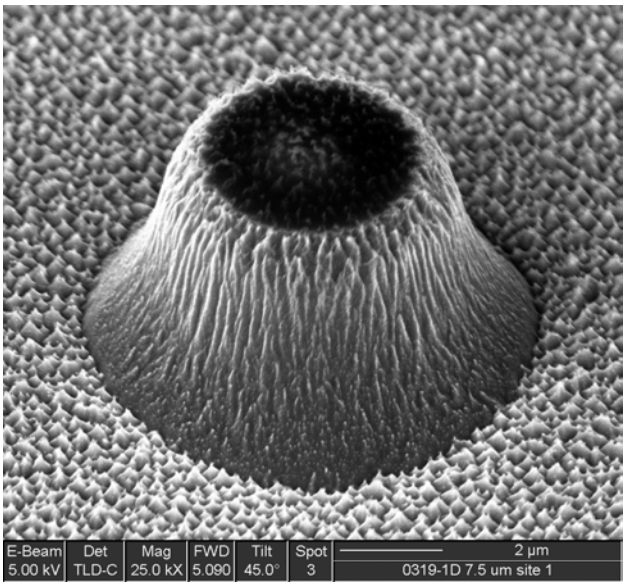

Figure B.16: Results of increased chamber pressure on a 5 μm diameter SF-11 bump patterned on sample 0319-1D after 18 minutes of etching. The PMGI was not stripped, and it appears that there still is some on the top of the feature. The chemical etch seems to be stronger and the surface is still rough.

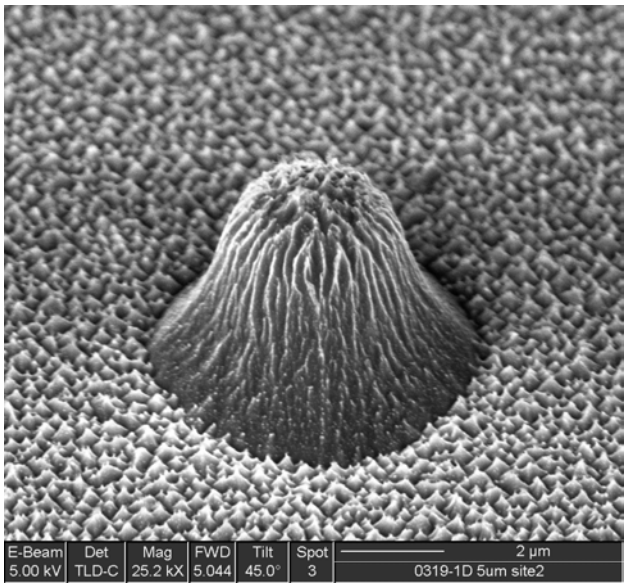

Figure B.17: Results of increased chamber pressure on a 7.5 μm diameter SF-11 bump patterned on sample 0319-1D after 18 minutes of etching. The PMGI was not stripped, and it appears that there still is some on the top of the feature. The chemical etch seems to be stronger and the surface is still rough.

Table B.3: Variables used in experimentation to determine effect of RIE power change on etch rate and surface roughness of silicon. Tests were done on 30 Mar 07.

O_2 Flow Rate (sccm)	SF_6 Flow Rate (sccm)	Pressure (mTorr)	RIE Power (W)	ICP Power (W)	DC Bias (V)	Etch Time (min)	Etch Depth (μm)	Etch Rate (Å/min)
50	80	70	80	250	165	10	3.25	3250
50	80	70	90	250	175	10	3.34	3340
50	80	70	100	250	198	10	3.8	3800

silicon surface. Surface roughness was measured with a TENCOR P-10 profilometer with a 2 μm radius tip. Surface roughness results are given in Table B.4. An example of what the surface looks like is shown in Figure B.14. This figure is an SEM image at 150,000X magnification and correlates to the etch recipe in line 1 of Table B.4.

B.5.1 Equalizing Etch Rates of PMGI and Silicon. In all of the etch tests thus far, the etch rate of silicon was higher than the etch rate of the PMGI, which led to the concave side-wall shapes. Test etches were performed reducing the flow rate of the SF_6 in an attempt to match etch rates of the mask and substrate. The recipe and

Table B.4: Effect of RIE power change on surface roughness of silicon. Tests were done on 26 & 30 Mar 07.

RIE Power (W)	DC Bias (V)	Etch Depth (μm)	R_a Rate (Å)	Max R_a (Å)	R_q (Å)	R_t (Å)
60	128	2.2	100.8	221.7	194.4	1926.7
80	165	3.25	92.1	71.1	119.5	626.6
90	175	3.34	65.6	65.1	91.2	632.9
100	198	3.8	112.8	155.5	142.8	1014.3

Table B.5: Variables used in experimentation to determine effect SF6 flow rate change on etch rate of silicon compared to PMGI. Tests were done on 3 Apr 07.

Material	O_2 Flow Rate (sccm)	SF_6 Flow Rate (sccm)	Pressure (mTorr)	RIE Power (W)	ICP Power (W)	DC Bias (V)	Etch Time (min)	Etch Depth (μm)	Etch Rate (Å/min)
Silicon	50	50	70	90	250	191	10	1.7	1700
PMGI	50	50	70	90	250	196	10	2.0	2000

etch depth rates achieved are shown in Table B.5. These were determined in separate tests, by placing Capton dots on each wafer for the etch test. The Capton dots were removed and the step height measured with the profilometer.

The test wafers appeared much smoother than previous test wafers, and also showed etch rates that were very close. Note that the etch rate of Silicon was also measured for the PMGI test, as the PMGI coated wafer piece was set on top of a silicon substrate. The step difference from the protected silicon beneath the PMGI sample and the etched silicon substrate was measured. This showed 2.2 μm etch over 10 minutes. This difference may have been due to a change in silicon wafers. Wafers for this test were selected from a new box, which had a different doping material (Arsenic vs. Antimony) and a different resistivity.

This etch recipe was used on test sample 0319-1B. It was etched for 13 minutes, which was the estimated etch time needed to leave approximately 1000 Åof PMGI pattern. A representative bump height was measured using the profilometer for each diameter present on the test sample. Then, the sample was cleaned in 1165 stripper for 5 minutes and oxygen plasma ashed for 10 minutes to remove any remaining

Table B.6: Bump heights before and after the ICP/RIE etch and how much PMGI was remaining after the etch.

Bump Diameter (μm)	After Reflow (μm)	After Etch (μm)	After Clean (μm)	Remaining PMGI (μm)
5	2.21	2.48	1.70	0.78
7.5	2.84	2.19	2.09	0.10
10	2.99	2.31	2.09	0.22
15	2.78	2.10	2.01	0.09

Table B.7: ICP/RIE etch variables used on the test etch of sample 1101-2 which was a MEMSCAP cantilever die mounted on a 1" diameter Silicon wafer.

Material	O_2 Flow Rate (sccm)	SF_6 Flow Rate (sccm)	Ar Flow Rate (sccm)	Pressure (mTorr)	RIE Power (W)	ICP Power (W)	DC Bias (V)	Etch Time (min)
Si Cantilever	50	65	10	70	90	250	188	6:05

PMGI. The bump heights after reflow, after etch, and after cleaning and the PMGI remaining after the etch are shown in Table B.6.

B.5.2 Patterning and Test Etching on Cantilever Die. The next step after finding a recipe which produced a rounded bump was to spread SF-11 on the MEMSCAP produced cantilever dies and to pattern dots on the end to test the recipe on the actual test devices. This process was accomplished on specimen 1101-2, and the etch using 50 SCCM O_2, 65 SCCM SF_6 and 10 SCCM Ar. The variables used in this etch are given in Table B.7.

The patterned bump heights were measured by a Zygo fringe interferometer. These heights were used to calculate the etch time based on the etch rates determined by silicon wafer etch testing. The silicon etch rate of this recipe was 2600 Åper minute while the PMGI etch rate was 1900 Åper minute as determined by test etching of a bare silicon wafer and a wafer covered with three layers of SF-11. The silicon roughness measured using the TENCOR profilometer after etch was R_a of 57 Å, R_q (or RMS) of 103.6 Å, Max R_a of 121.5 Å, and R_t of 1148.6 Å. This is much smoother than previous test etches. The PMGI etch rate was divided into the smallest bump height (1.15 μm) to ensure the smallest bumps weren't severely over-etched. The etch time calculated

Table B.8: Bump heights on the cantilevers before and after the ICP/RIE etch. All heights are in μm.

Cantilever ID	1	2	3	6	9	12
Pre-etch Height	1.18		1.3	1.35	1.15	1.15
After-etch Height	1.43	1.74	1.67	1.69	1.68	1.71

was 6 minutes and 5 seconds. Table B.8 shows the pre-etch PR bump heights and the post etch, post cleaning bump heights. The die was cleaned in 1165 stripper at 90 deg C for 5 minutes after etching, and then O_2 plasma ashed for 10 minutes to remove remaining PMGI before measurement of etched bump heights with the Zygo interferometer.

The bump as fabricated on test die 1101-2 is shown in Figure B.18. A closeup of the bump is shown in Figure B.19. The area around the bump is somewhat rough, and the surface of the bump is flat because the etching process did not clear the PMGI completely. Roughness measured using the TENCOR profilometer gave R_a of 49.4 Å, R_q (or RMS) of 77.4 Å, Max R_a of 109.1 Å, and R_t of 708.8 Å. This roughnesss compares extremely favorably with previous test etches. The sides are nicely rounded, and hemispherical in shape. The double hump shape is likely an artifact of the reflow, but won't affect contact morphology results in testing.

Bumps of this size and shape will be appropriate for the test devices needed for the experiment developed for this research. This fabrication process on silicon test wafers was repeatable. Attemps were made to fabricate consistent test devices for use with the apparatus designed and constructed for this study. However, the process of coating a non-planar mounted die was not repeatable using SF-11 as the photoresist. The SF-11 and/or trapped air bubbles in the void underneath the released cantilevers after baking at the SF-11 cure temperature made contact mask alignment and exposure impossible.

Thus, the working photoresist had to be changed back to 1818 due to these factors which are also described in Section A.1. Tests on patterns on test wafers with 1818 were also accomplished, and bumps were patterned and etched on actual

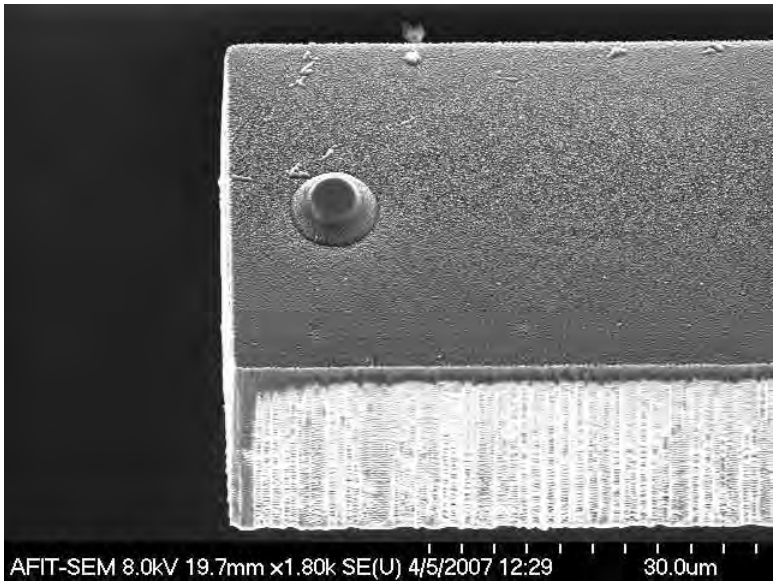

Figure B.18: Sample 7.5 μm diameter contact bump fabricated using SF-11 for these experiments showing its location on the cantilever. The height is approximately 1.8 μm.

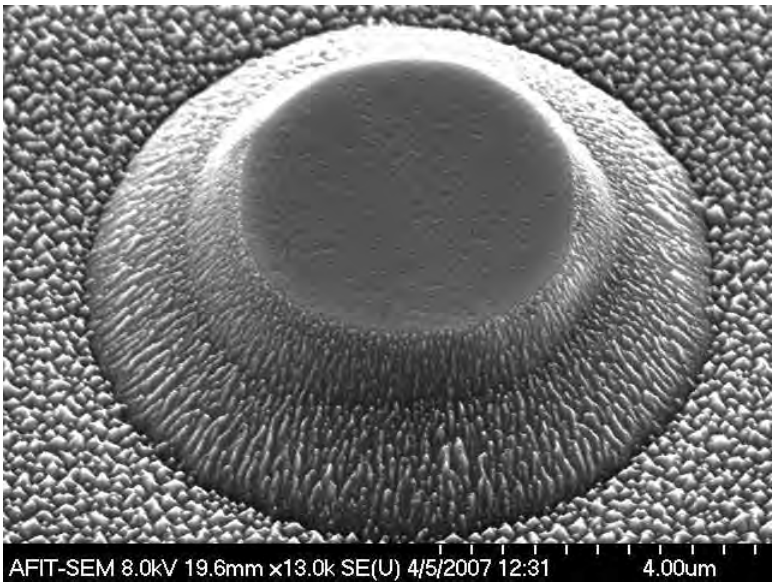

Figure B.19: Close-up SEM micrograph of a sample 7.5 μm diameter contact bump fabricated using SF-11 for these experiments. Note the surface finish.

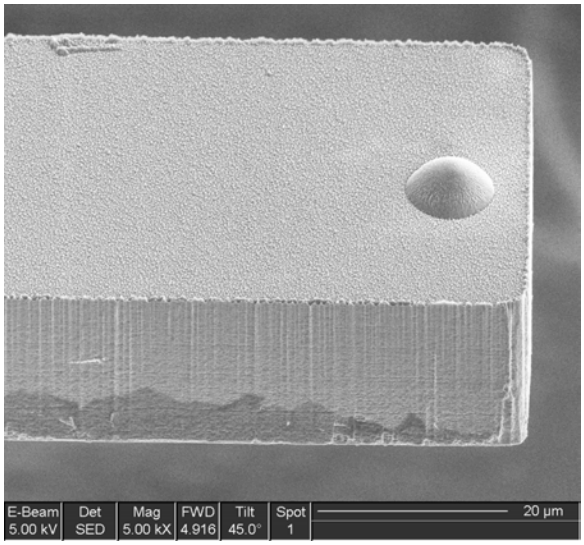

Figure B.20: Close-up SEM micrograph of a sample 7.5 μm diameter rounded contact bump fabricated using 1818 for these experiments. Note the surface finish.

cantilever die as well. Typical results can be seen in Figures B.20 and B.21. These figures show that the shape of the bump can be determined by adjusting the etch time. It is possible to create either rounded or flat-topped bumps which are taller than the bumps created using SF-11. However, the flat-topped bumps are more repeatable and have a smoother contact surface. than the height of the PR bump in order to etch a rounded final bump. Etch rate testing was performed on 1818 and silicon and the etch rate of the recipe was determined to be 800 Å/min for 1818 and 2600 Å/min in silicon. Flat-topped bumps fabricated using 1818 were used for the majority of testing. The height of bumps can be measured in a Zygo fringe interferometer and the diameter and shape can be seen in an SEM.

B.6 Summary

The patterning and etching of contact bumps onto the SOIMUMPS die with released cantilevers was an important step in this study. The appendix describes the process used to determine an appropriate etch recipe for use in this unusual process. The recipe for ICP/RIE etching using the available AFRL tool had multiple variables and therefore extensive testing was required in order to develop an appropriate fab-

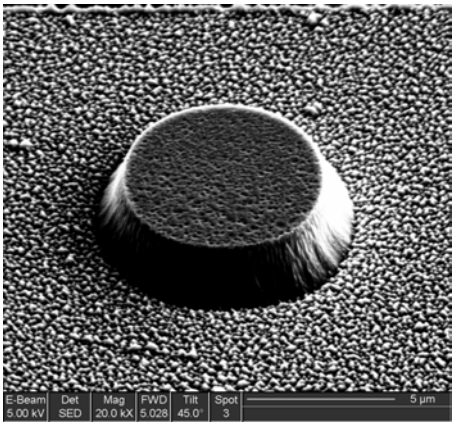

Figure B.21: Close-up SEM micrograph of a sample 7.5 μm diameter flat-topped contact bump fabricated using 1818 for these experiments. Note the surface finish.

Table B.9: ICP/RIE etch variables used for etching contact bumps into test cantilevers.

Material	O_2 Flow Rate (sccm)	SF_6 Flow Rate (sccm)	Ar Flow Rate (sccm)	Pressure (mTorr)	RIE Power (W)	ICP Power (W)	Etch Time (min)
Si Cantilever	50	65	10	70	90	250	6:05

rication method to locally and inexpensively produce MEMS-like test devices for use in this study. The final recipe developed is shown in Table B.9 and the fabrication processing is given in Appendix C.

Appendix C. Process Follower

Patterning & Developing Process Follower for creating hemispherical flat-topped bumps on released SOIMUMPS cantilevers

Start Date: **14 September, 2007**

Piece ID(*s*):

Etch Time:
Target height:
Carrier Wafer surface roughness after etch:

Rrms	
Ra	
Max Ra	
Pk to Valley	

Notes on Piece:

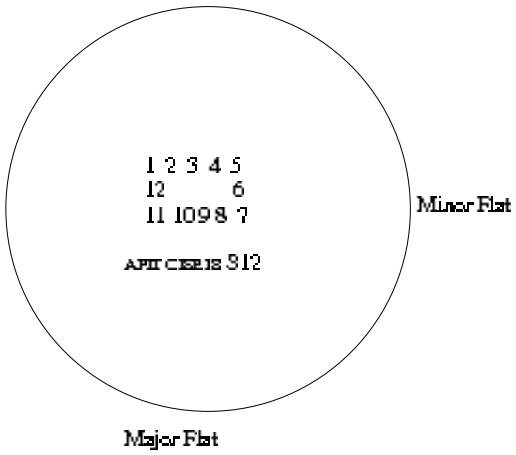

Cantilever	*Reflow Height (um)*	*Post-etch Height (um)*	*Shape*	*Flat diameter (um)*	*Bump Diameter (um)*	*Distance from Edge (um)*
1						
2						
3						
4						
5						
6						
7						
8						
9						
10						
11						
12						

1

Patterning Hemispherical Flat-topped contact bumps			
14 September, 2007		Piece ID:	
Date Time	Init.	Process	Notes
I. Die Removal & Cleaning and Carrier Wafer Cleaning			
		DIE ☐ Carefully cut tape around dies to be removed from ring ☐ Place dies on clean texwipe face down under Deep UV ☐ Deep UV Expose Tape & Dies for 100 seconds ☐ Carefully peel back tape. Adhesion should be significantly reduced ☐ Place removed dies in Petri dish, fill with Acetone, cover ☐ Let soak with intermittent agitation for 2-3 hours ☐ Rinse in fluoroware bucket with ISO ☐ Gently N2 dry ☐ O2 Plasma Ash – 10 minutes ☐ Check for cleanliness in Optical Microscope	
		CARRIER WAFERS ☐ Place 2" or 3" wafer on cleaning spinner ☐ Rinse using acetone gun 30 sec @ 500 rpm ☐ Rinse using acetone bottle 30 sec @ 500 rpm ☐ Rinse using Iso bottle 30 sec @ 500 rpm ☐ Dry with N2 gun ☐ Dehydrate bake 5 min @ 110°C (Both wafer and die)	
I. Die Mounting			
		Spin Adhesion layer of 1818 photoresist and mount die ☐ Set die and swabs on texwipe next to hotplate ☐ Set spinner at ramp=200; speed = 3500rpm; time=30sec ☐ Flood wafer with 1818 ☐ Spin 30 seconds ☐ Put wafer on texwipe ☐ Carefully place die on center of wafer with long edge parallel with main flat ☐ Gently press corners and sides of die into PR coat using swabs ☐ Gently put side pressure on die to check adhesion ☐ Hotplate bake at least 5 minutes at 110° C ☐ Let wafer cool on heatsink	
		Clean Wafer & Die using Flood Exposure & Development ☐ Place wafer in MJB3 ☐ Flood expose 20 seconds (no mask)	
		1818 Develop ☐ Fill graduated cylinder with ~50 mL 351 Developer ☐ 30 second Spin Develop with 351 @ 500 rpm, pouring cylinder onto wafer ☐ 30 second DIW rinse ☐ N_2 blow dry ☐ 5 min dehydrate bake at 110° C	
II. Bump Patterning and Developing			
		1818 Coat ☐ Set photoresist spinner ramp rate = 200; spin = 4000 rpm ☐ Flood wafer with 1818, ensuring die is covered ☐ Spin 30 seconds ☐ Remove edge bead on wafer ☐ Carefully use acetone dipped swab to remove edge bead on die ☐ 75 second Hot Plate Bake @ 110° C ☐ Cool on heatsink	

2

Patterning Hemispherical Flat-topped contact bumps			
14 September, 2007	**Piece ID:**		
Date Time	Init.	Process	Notes
		Verify Die is Ready and Mask is clean ☐ Inspect die to ensure 1818 coated on cantilevers and no barriers to good contact ☐ Inspect AFIT mask ☐ Clean with Acetone ☐ Rinse with IPA ☐ N_2 blow dry	
		Expose 1818 with dots aligned on ends of cantilevers ☐ Align on MJB3; ensure excellent contact with cantilevers by using vertical height adjustment (ensure dots centered on all cantilevers & equidistant from ends) ☐ Expose 20 seconds (405 nm, 7 mW/cm^2)	
		1818 Develop ☐ 15 second Spin Develop with 351: H_2O (1:5) @ 500 rpm ☐ 30 second DIW rinse ☐ N_2 blow dry	
		Inspect Lithography ☐ Examine wafer alignment ☐ Examine to ensure 1818 developed	
		Descum ☐ 2 minute LFE Descum @ 200W (Place in front of Asher, just behind door)	
		Bump Reflow ☐ 3 minute Hot Plate Bake at 165° C ☐ Visually Inspect at 100x	
		Bump Height Measurement in Zygo ☐ Use 50x or 100x magnification ☐ Enter reflowed heights in table on follower	
III. Etch PR Pattern into Cantilever (RIE/ICP)			
		Calculate Etch time needed ☐ Etch rate for ICP/RIE = _800_Å/min 1818 & _2600_Å/min Si (Calculate for 0.2 um shorter than Zygo height measurement) ☐ Bump flat diameter goal ~4-5 um or hemispherical	70 mTorr, SF6:O2:Ar 65:50:10 sccm RIE Power = 90 ICP Power = 250 TIME ETCHED : ETCH HT GOAL :
		RIE/ICP Etch ☐ Etch for calculated time ☐ Inspect in microscope at 100x	
		Wafer Clean ☐ Clean in 1165 for 5 minutes @ 90° C ☐ Descum 2 min in O2 plasma ☐ Inspect in microscope	
		Measure Bump Height in Zygo ☐ Measure heights of bumps in Zygo - 50x or 100x ☐ Enter Heights in table on follower	
		Image bumps in SEM ☐ Image all bumps in SEM – top view and 45° -- 1000x and 20000x ☐ Measure diameter of flat top	
		Dice Cantilevers ☐ Attempt to keep in order	
		Coat with contact metal ☐ Sputter coat contact metal - 3000 Å	
		SEM Image coated cantilevers ☐ Top View and 45° - 1000x and 20000x ☐ Measure diameter of flat top	

3

INSTRUCTIONS ON SETTING UP CANTILEVER CONTACT / MICRO-SWITCH SIMULATION TEST

BEFORE TEST: Make a note of room temperature & humidity Note "zero" position of PZT by copying down displayed voltage and displacement on front of E-665 controller.

1. Measure resistance through strike plate and mount plate using hand-held ohm-meter. Record on experimental data sheet

2. Attach strike plate to PZT using non-conductive fastener. Ensure rough positioning Z-stage (M-663) is pushed all the way down. Ensure strike plate is firmly attached. Do not over tighten or strike plate will crack.

3. Attach strike plate wires to appropriate terminal strip connectors.

4. Very carefully attach mount plate to stage. Beam should be facing down toward strike plate. Attach fasteners.

5. Attach mount plate wires to terminal strip.

6. Start MTS TestWorks.

7. Load appropriate test method when prompted by TestWorks.

8. Go to DEFINE page in Individual Mode, go to Configuration tab, click on the INPUT line.

9. Click on CURRENT INPUT on right hand side of screen under "Display Names". Change CURRENT INPUT to 0.500 mA in Default value block on bottom right of screen.

10. Go to TEST page. Ensure R_Meas4W is measuring the shunt resistor correctly.

11. Turn off current by setting CURRENT INPUT back to 0.000 mA and click over to TEST page.

12. Ensure locking pins are installed in indenter shaft

13. Bend wires down such that they do not extend above the guard rails on experimental sample tray.

13. Carefully place experimental sample tray onto XY-Stage. Check that nothing extends above the guard rails.

14. Attach new side rail to XY-stage. Carefully tighten at least two fasteners. Ensure experimental sample stage is firmly seated on XY-positioning stage.

15. Remove locking pins from indenter shaft.

16. In TestWorks, move stage to center position by moving at right angles being careful to stay away from indenter shaft. Left click

to target position for move, right click and select "Move to Target" to execute move.

17. Rt-Click -- Select Nano Video Handset to change to microscope view

18. Connect C-865 controller to power (M-663, Z rough positioning stage controller).

19. Start C-865 Quick Run. Icon is on desktop.

20. Select COM3 as the port and 9600 baud to connect to C-865.

21. Select Connect Stage -- connect to M663.465. Note: Do NOT perform Stage Reference.

22. Type RON 10 in Terminal Window. This turns the Reference Mode Off. (1=axis of motion, 0 = off)

23. Type MVR 11 in the terminal window.
This moves the Z-rough positioning stage up by 1mm. MVR = Move Relative. The user must be careful not to run the Z-stage down into the sample tray floor or up too far which could interfere or damage items in the working area inside the Nanoindenter.

24. Type MVR 10.5

25. Check for any light reflection in microscope. If so, move microscope view to edge of strike plate.

26. Focus microscope on edge of strike plate by raising/lowering Z-stage (M-663). The command POS? will return the current height of the stage. The focus position should be between 1.8-2.0 mm. DO NOT RAISE STAGE TOO MUCH.

27. Find Cantilever by moving stage clicking inside microscope window. Relative position can be determined by looking inside Nanoindenter working area.

28. Focus microscope on cantilever. Adjust light source as necessary.

29. Set user X-Y by right clicking in microscope window.

30. Click "up" in microscope screen to move microscope back toward strike plate. Use micrometer drive to move cantilever back into microscope view. Repeat process, stopping when both cantilever and strike plate are in view of microscope. Be careful not to drive cantilever into strike plate as both are at approximately the same height.

31. Focus microscope on strike plate by raising/lowering Z-rough positioning stage (M-663) as necessary. This step will ensure strike plate and cantilever are at the same height.

32. Use side microtranslation stage to fine ideal spot for cycling.

33. Pus cross hairs on spot approximately 80-100 um back from edge

of strike plate directly in line with cantilever.

34. Perform Microscope to Indenter Calibration by right clicking in microscope window and selecting option. This step will provide critical visual reference for finding bottom contact location in SEM as well as ensuring indenter contacts cantilever accurately. (choose ADVANCED to make sure 5 indents are performed, 10 um apart, and 2500 nm deep)

35. Rt click in microscope view -- select SAVE IMAGE.

36. Type MVR 1-0.075 to drop strike plate 50um below level of cantilever.

37. Use front micrometer drive stage to slide cantilever over user desired contact site.

38. Rt-Click and SAVE IMAGE of overlap site.

39. Focus on lower contact strike plate - Rt-Click and SAVE Image as overlap bottom focus.

40. Re-focus on cantilever

41. Hit "Batch Mode" Button

42. Change to DEFINE page

43. Go through batch programming steps by using "Next Step" button

at top of screen. It is long and thin and will step through each required input step.

44. Naming convention: Beam ID Number/Material/Contact Force/ContactFrequency/Measurement Interval/Date (e.g. 0210-3_8 Au5Ru 400 100 10k 18Dec07)

45. Verify inputs to make sure they are correct for test contemplated.
Approach Parameters: 5000 nm, 10%, 30 nm/s, 3000 nm

46. Choose contact location. Make microscope window bigger by extending both side and bottom window edges. Place red cross-hair at indent/load application point desired.

47. Click "Add test at this location" only once.

48. Go to NEXT STEP

49. Select "NO" when asked to add or edit another sample

50. Change to TEST Page

51. Check inside isolation chamber. Ensure nothing extends above protective guard rails on experiment sample tray. Ensure cables are supported by isolation table and are not putting any load on rough positioning Z-stage (M-663).

52. Close isolation chamber door.

53. Start test by pushing large green arrow button in middle of page.

54. Follow instructions on screen. Do not click OK until performing required actions.

55. To raise Z-rough positioning stage (M-663) into position:

    Type MVR 10.04 -- check to ensure R_Meas4W > 78

    Type MVR 10.005 -- check to ensure R_Meas4W > 78

    Type MVR 10.002 -- keep repeating until R < 15 Ohms

    If in contact, back off stage by MVR 1-0.002.

56. Use potentiometer on front of E-665 controller to raise PZT until contact is detected electrically. (<15 ohm) Determine if contact gap is at least 2 um by comparing to initial "zero" displacement noted at start of test.

57. Iterate dropping Z-rough positioning stage (using MVR 1-0.00x) until contact gap is determined to be 2 um by difference between displacement in contact and zero displacement as noted on E-665 controller. Write down contact PZT display voltage and displacement from E-665 display and resistance measured by TestWorks.

58. When gap is at least 2um, type POS? to get M-663 position at start of test, hit OK to start automatic contact location find

59. Write down Voltage At Contact, PZT displayed voltage, and displacement on E-665; Click OK

60. Write down Offset Voltage

61. Enter Offset Voltage into frequency generator; Click OK

62. Write down Resistance Just in Contact; click OK

63. Write down Resistance in Contact when Resistance in Contact is displayed in on-screen meter;

64. Write down PZTVoltage value (displayed in on-screen meter) when PZT is at +2um

65. Hit OK -- surface find will occur. Watch to ensure test runs properly.

Test Runs

AFTER TEST:

66. Write down final resistances (Resistance in contact & Resistance Out of -Contact) ;

- type POS? to get M-663 stage position at end of test. (compare to position at start of test)
- Click OK (after copying RESISTANCE OUT OF CONTACT)
- Click OK (after copying RESISTANCE IN CONTACT)

- Wait for processing/calculations to complete

67. Lower rough positioning Z-stage (M-663) 50 microns by typing MVR 1-0.050 when prompted. Click OK and stage will move back under microscope. Wait for processing and saving of sample.

68. Rt Click Screen -- SAVE IMAGE -- post cycling overlap

69. Slide cantilever back so that it is no longer above strike plate.

70. Raise Strike Plate 75um (MVR 10.075); ensure both cantilever and strike plate are in focus

71. Rt Click -- SAVE IMAGE -- post cycling showing bottom contact

72. Roll cantilever all the way back to starting position to prepare for removing stage from isolation chamber.

73. Rt click -- select Nano Handset

74. On Nano Handset page , move stage first to top of screen, then all the way to left corner.

75. Rt Click -- choose Load Sample Tray

76. Install locking pins when indenter head is parked

77. Carefully remove XY-stage side rail

78. Carefully place experimental sample tray on top of isolation box

79. Remove terminal strip from sample tray, attach to Velcro tab on top of isolation box

80. Disconnect wires from terminal strip

81. Stop all axes in M-663 (using PI C-865 Quick Run)

82. Disconnect M-663 stage (use drop down menu)

83. Exit PI C-865 Quick Run

84. Unplug M-663

85. Carefully remove Mount Plate. Carefully store in plastic case. Note number of cycles and date on case.

86. Carefully remove Strike Plate. Store in case. Note number of cycles, cantilever ID, date and type of failure on case.

87. Trim wires on strike plate -- leave approximately 1.5" on each side. Plate will be mounted as is in SEM

88. Turn on hot plate

89. Place carbon tape circle on SEM mount stub.

90. When hot plate is heated, carefully bend wires up so that mount plate may be placed on hotplate surface without wires touching and melting insulation.

91. Place mount plate on hotplate surface for a few seconds, with cantilever facing up.

92. Carefully grasp cantilever substrate with tweezers and remove from mount plate.

93. Carefully place test device in same orientation on carbon tape on SEM stub. This ensures that bump is facing up and can be imaged by SEM.

94. Save Sample in Test Works -- Copy Results folder to Flash Drive
    - Add sample number to folder name on flash drive

95. Exit TestWorks

96. Install new device/mount plate and strike plate and begin again.

RECOVERY FROM ERRORS:

If TestWorks crashes completely (error on screen/TW locked up or program no longer evident)

1. Restart TW -- follow instructions for Dr. Watson crash log

-- save log to flash drive.

2. Park Indenter head (under System, choose displacement and move indenter head to TOP)

3. Lower M-663 (Z-rough positioning stage) to bottom .

   - check position by typing POS?

   - lower stage by moving almost all the way down (stay 0.05 mm above ground) typing MVR 1-(distance to zero)

4. Install locking pins in indenter head (use long pins)

5. Initialize stage

If TestWorks is paused at a test segment and nothing is happening, but program is still running:

1. Check to see where indenter head is located (Raw Displacement and Displacement into Sample)

2. If at least 3 um above sample, and/or cycling won't crash plate into head, then hit ">>" button to move to next test segment.

3. Continue to monitor test until sure nothing else has failed, abort at first sign of problems.

Appendix E. Northeastern University Research

Research on MEMS switches has been ongoing at Northeastern University for a number of years [2, 36, 37, 39, 59, 96, 161–165, 170, 222, 263, 267]. Zavracky, et. al. reported on fabrication of MEMS switches [267]. Majumder studied contact behavior of a contact switch with gold-gold contacts [162]. Majumder, et. al. reported on adhesion and contact resistance behavior in MEMS microswitches [161, 165] as well as measurement and modeling of microswitches [164]. Yan, et. al. modeled thermal characteristics of microswitch operation [263]. Du, et. al. developed a finite element model of asperity contact including adhesion and plasticity effects [59]. McGruer, et. al. reported on mechanical, thermal and material influences on MEMS contact switch operation [170]. Recent work accomplished at Northeastern by Chen simulated the action of an ohmic contact switch using a micromachined silicon cantilever coated with a thin film of contact metal [36,37]. Test cantilevers were fabricated with varying sizes of contact bumps [37], which were coated by the thin conductive film. The cantilever was mounted in a Scanning Probe Microscope (SPM) and cycled mechanically using a PZT [37]. The laser detection system in the SPM was used to measure the tip motion of the cantilever with high accuracy [37]. The contact force applied to the cantilever was determined using the displacement of the cantilever tip multiplied by the stiffness of the cantilever (e.g. F=kx). A comparison between test parameters of Chen's study compared to the parameters used in this study is given in Table E.1.

E.1 Experimental Investigation using a Contact Test Station [37]

The focus of Chen's work [37] was on the evolution of contact in microswitches. He first analyzed adhesive failure in gold by looking at the difference between brittle and ductile separation modes. He also looked at rate-dependence of contact pull-off, size-dependence and material effects of pull-off forces. Larger contact bumps usually showed larger pull-off forces in his tests. His bumps ranged in radius from 4 μm to 50 μm (4, 15, 22, 50 μm). It is not shown whether bumps with a difference of just a few microns radius exhibit a clear difference in pull-off force. Differences in

Table E.1: Comparison of testing accomplished at Northeastern University to present study. Both used silicon cantilever beams to simulate the operation of MEMS contact switches. NEU data from [37]

	NEU	AFIT
Cantilever Stiffness	10^4 N/m	200 N/m
Measurement Equipment	Scanning Probe Microscope	Nanoindenter
Mechanical Cycling	PZT	PZT
Contact Force	200-250 μN	400 μN
Cantilever End Displacement	20 nm	2 μm
Current	200 μA, 1 mA	0.5 mA
Switching Type	Cold	Hot
Cycling Rate	0.5, 300 Hz	100 Hz
Materials	Au, Pt, Rh, Ru, alloys	Au, Au5%Ru, Au4%V_2O_5
Contact Diameter	3.0 - 80 μm	Nominal 7.5 μm
Contact Shape	Rounded, flat-topped	Rounded, flat-topped
Force Measured	Indirectly	Directly
Rate of Pull-off measurement	Unconstrained	50 μN/sec
Contacts Imaged	Bump	Bump & Flat
Force Measurement Resolution	12 μN	50 nN
Contact Sliding	Yes & No	Yes

bump shape were also not tested. He also reported on the differences in material effects on pull-off force. The contacts were parallel to each other for the pull-off evolution testing, so some contact sliding did occur. He reported that gold pull-off force varies from 50-200 μN and Au5%Ru pull-off force is in the range of 20-50 μN with a maximum loading of 200 μN. He reported large scatter in the magnitude of measured pull-off force. The slower pull-off rate used always showed a higher pull-off force in the Au5%Ru contact tests. Chen attributed the lower pull-off force in Au5%Ru contacts to alloy effects from Ru. He noted that the 5% Ru provided dislocation obstacles, therefore hardening the material and suggested the Ru disturbed the electron structures on the gold surface weakening the interfacial energy and leading to brittle separation. He also noted that the dominant separation mode can change during cycling as the contact evolves, and that the pull-off force can change quickly. It is interesting to note that he showed images of three different gold contact bumps, which had experienced the same number of test cycles (10^6), but all three showed different amounts of contact deformation and damage. Images presented did not

include the corresponding substrate contact location. Chen concluded that ductile separation should be avoided in MEMS switches.

Chen also analyzed the relation of contamination failure to contact evolution. His test results showed that Ru, Pt, and Rh are more susceptible to the growth of a contaminant film than Au. Chen determined that alloying these metals with gold reduces the contamination rate and makes the contacts less susceptible to contamination. 100% gold, Au5%Ru and Au10%Pt all lasted beyond 10^7 cycles without an increase in contact resistance. He showed that surface evolution does not change when the contacts are cycled in nitrogen when compared to lab air, thus he showed that nitrogen can slow down the contamination rate. Contact lifetime measurements were not included.

E.2 Summary

The study accomplished here used a similar experimental methodology to investigate the physics of microcontact behavior. However, the measurements made, results presented and main focus of the two studies were different. Table E.1 shows test parameter differences. Chen's research using a silicon cantilever coated with a contact metal at Northeastern was focused on adhesive force evolution in gold contacts, characteristics of ductile vs. brittle separation and the transition between them, and methods to reduce contact contamination via alloying. The study accomplished here was focused on measurement of multiple contact performance parameters, comparison of material contact behavior, and failure mode categorization.

Appendix F. Performance Measurement of RF Devices [84, 166]

This appendix gives an overview of the basic performance parameters of RF switches as they relate to the study accomplished here. RF devices are designed to transmit or receive high frequency signals. Measurement and characterization of RF devices differs from other microelectronic systems. In general, RF devices are described in terms of power rather than other signal parameters, such as voltage [84]. Also, the minimization of loss of voltage magnitude is not as important for RF devices as is matching impedance of components and transmission lines. When an RF signal experiences a discontinuity in transmission, some part of the signal is reflected, therefore causing loss of transmitted power. "The goal at RF is to transfer all the power to the load without loss" [84]. Most RF wireless transmission systems are designed at 50 Ω characteristic impedance in order to optimize power transfer [84]. Also, note that RF cables are coaxial in order to pass the high frequency signal and require more care in connection due to the importance of mismatch [84]. RF test systems are thus more complex than typical low frequency systems. The measurement of performance of RF systems is also more involved than typical low frequency circuits. Note that, "RF switches are precision-machined and designed to maintain a 50 Ω impedance through the switch" [84]. Insertion loss, isolation, and return loss are all important performance measures of RF switches. Measurements in RF systems are usually given in dB, based on power loss of the system [256]. Equation F.1 shows the calculation used to determine power loss in dBs [256].

$$dB = 10 \log \left[\frac{P_{out}}{P_{in}} \right] \tag{F.1}$$

F.1 Insertion Loss

Insertion loss is a measure of the power loss through a device such as a switch, cable connection, or other component [84,166]. Insertion loss is analogous to the closed resistance of a low frequency switch, and Hyman showed that the DC resistance of a MEMS switch is related to its insertion loss [108]. Insertion loss is the only measure

of RF performance that can be estimated based on simple DC resistance tests, such as those performed in this study.

F.2 Isolation

Isolation is a measure of switch performance when it is in the open state [166]. "Isolation is defined as the magnitude of a signal that gets coupled across an open circuit." [177]. This parameter is an indication of the amount of signal "leaked" when the switch should be passing no signal [177]. Isolation is also a measure of the insertion loss of the open switch [256]. A switch should have the lowest possible insertion loss and the highest possible isolation for performance in RF devices [256]. The minimum useful isolation in a switch is estimated to be about 20 dB [256]. Note that 20 dB refers to a power loss of 100x. This parameter can not be tested with DC current.

F.3 Return Loss

As previously discussed, impedance mismatch in cables and devices in an RF system cause some of the signal to be reflected. Return loss is a measure of the power of the reflected signal, and is a subset of insertion loss [84, 177]. There is no way to estimate this parameter with DC testing.

F.4 Skin Effect

RF signals, when passed by a conductor, are carried only on the surface of that conductor [256]. This is called "skin effect" [256] and is the reason that RF conductors can be effectively shielded by metal [81, 256]. The skin depth can be calculated by Equation F.2 where σ is the metal conductivity, $\mu_0 = 1.26 \times 10^{-6}$H/m [230] is the permeability of free space, μ_r is the relative permeability for the conductor (μ_r=1 for most metals), and f is the frequency of the signal [81]. Note that the skin depth is defined as the distance of penetration into the metal in order to decay by $e^{-1} = 0.368$ or 8.686 dB [81].

$$\delta_s = \frac{1}{\sqrt{\pi f \mu_0 \mu_r \sigma}} \tag{F.2}$$

Using this equation, and the resistivity (ρ=1/σ) of gold as 3.6×10^{-8} Ω·m, as used for thin gold films in this study, the resulting skin depths are presented in Table F.1.

Table F.1: Calculation of representative skin depth in gold at several signal frequencies.

Frequency (GHz)	1	2	5	10	40
Skin Depth (μm)	3.0	2.1	1.4	1.0	0.5

Thus, the contact film of 300 nm thickness used in this study would not be sufficient to pass all the current in a lower frequency signal, but it is on the order of the depth needed for higher frequencies. Note also that the field amplitude of an RF signal decays exponentially from its surface value according to Equation F.3, where x is the normal distance into the conductor measured from the surface [81].

$$A = e^{-x/\delta_s} \tag{F.3}$$

This behavior means that, "a poor conductor with a thin layer of high conductivity metal will exhibit the same RF conduction properties as a solid, high conductivity structure." [81] Thus, the behavior of a conductive thin film coating on a contact, even on a cantilever/substrate other than gold, can be a reasonable approximation for the behavior of a thin film coating on a gold cantilever beam as fabricated in a MEMS switch.

F.5 Summary

The factors which affect performance of an RF switch are impacted by the design and implementation of the switch. Insertion loss is directly related to DC contact resistance and thermal handling capability can be tested by DC current [38, 108].

See also Section 2.6. The purpose of this study was to investigate contact material performance and failure mechanisms, and used a similar methodology of simulating contact action of switches to that used by Chen at Northeastern [37, 38]. The use of DC current testing is therefore sufficient for the purposes of this study. Development of a test apparatus in the future which could simulate contact switch action and pass RF signals in order to analyze contact failure behavior using actual RF signals would be very useful in gathering further data on contact failure mechanisms.

Appendix G. Au-4%V_2O_5 Failure Type Categorization

Three tests run on Au-4%V_2O_5 were considered to be short-life results and the other three tests were considered to be long-life results. The measured data from these tests were averaged and compared in order to determine if any trends could be detected in performance measurements to distinguish the characteristics of longer lasting contacts from those which failed early. Table G.1 shows a qualitative overview of measured differences between the two categories of contacts. The long-life contacts were used as a baseline with arrows indicating whether the short life contacts exhibited higher or lower values for each measured result. Each area is described in detail in the next sections. These results are consistent with the existence of a small amount of contamination on the long-lasting contact surfaces at the beginning of the tests.

G.1 Contact Resistance

Figures G.1 and G.2 show the average contact resistance measured for long-life and short-life category Au-4%V_2O_5 contacts. Contact resistance was higher on average for the longer lasting contacts. This likely indicates higher levels of contamination on the longer lasting contacts, and is consistent with results from the other two materials tested in this study. Note that Figure G.1 includes the Au-4%V_2O_5 test case B1011-1_8 resistance in the average calculation while Figure G.2 does not. That test failed

Table G.1: Qualitative comparison of results indicating initial differences in measurements between short and long-life in Au-4%V_2O_5 contacts. $\uparrow$ = higher initial value; $\downarrow$ = lower initial value

Measured Result	Long-Life	Short-Life
Resistance	Baseline	$\downarrow$
Pull-off Force	Baseline	$\uparrow$
Threshold Force	Baseline	$\downarrow$
Threshold Distance	Baseline	$\downarrow$
Interference	Baseline	$\downarrow$
Time-dependent deformation during 5 sec Hold	Baseline	$\downarrow$
Energy Absorbed	Baseline	$\downarrow$

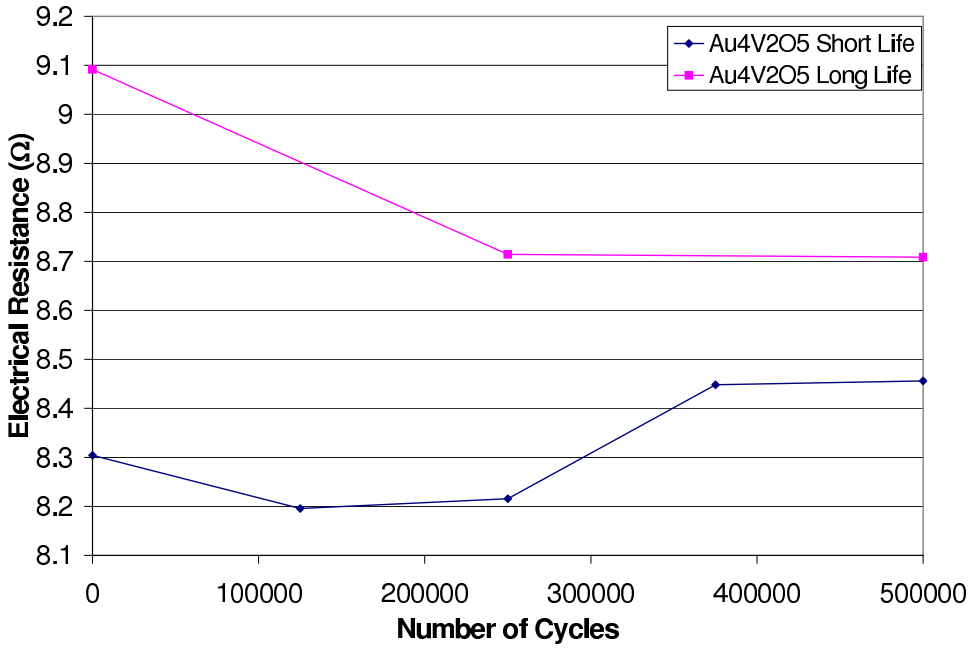

Figure G.1: Average contact resistance comparison between lifetime failure categories in Au-4%V_2O_5 contacts. Note that the short-lifetime contact average shows a lower measured contact resistance likely indicating lower levels of contact contamination.

due to an instrument problem at 1.625 $\times 10^6$ cycles, so it is unknown how long its lifetime would have been.

G.2 Pull-Off Force

Figures G.3 and G.4 show the average pull-off force for long-life and short-life category Au-4%V_2O_5 contacts. The pull off force for the longer lasting contacts started slightly higher initially, but the rise over the first few cycles was lower than that measured for the short-life Au-4%V_2O_5 contacts. This indicates that the adhesive force growth in the short-life contacts was faster and could have led to early contact failure. This could indicate surface conditions existing on the short-life contacts which were more conducive to development of adhesion including lower roughness or cleaner surfaces. The thin film failures possibly indicate subsurface damage or low adherence of the thin film to the contact substrate. Note that all but one of the short-life contacts failed in adhesion before cycle number 250,000.

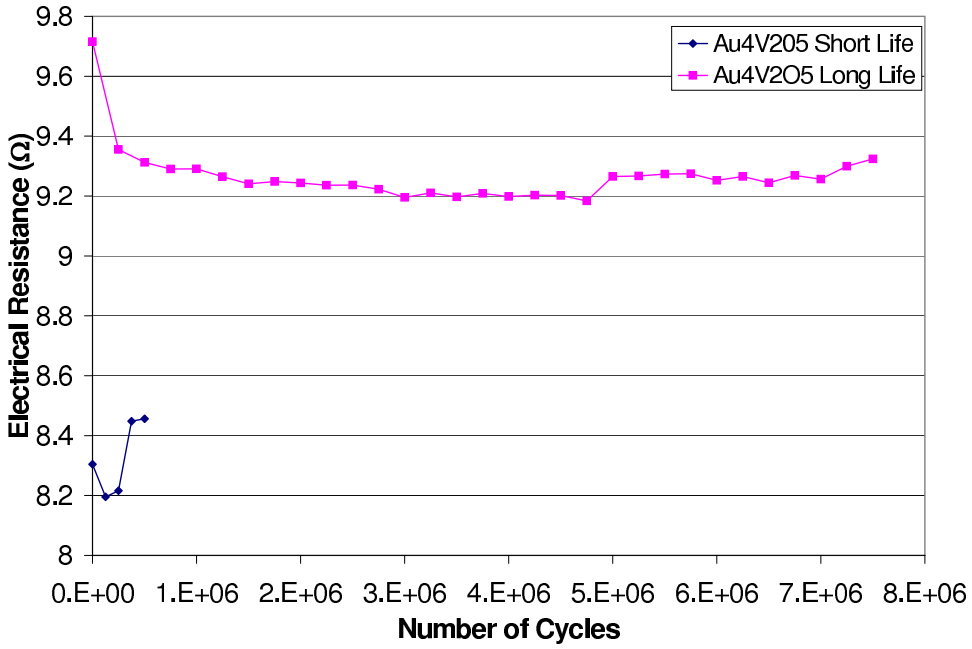

Figure G.2: Average long term contact resistance comparison between lifetime failure categories in Au-4%V_2O_5 contacts. Note that the short-lifetime contact average shows a lower measured contact resistance likely indicating lower levels of contact contamination.

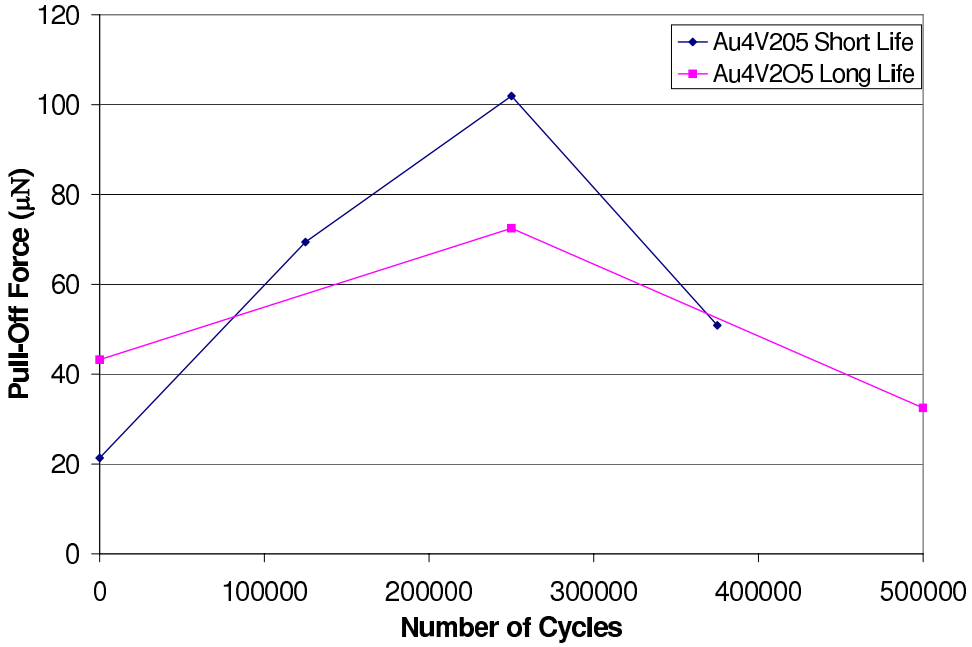

Figure G.3: Average pull-off force comparison between lifetime failure categories of Au-4%V_2O_5 contacts.

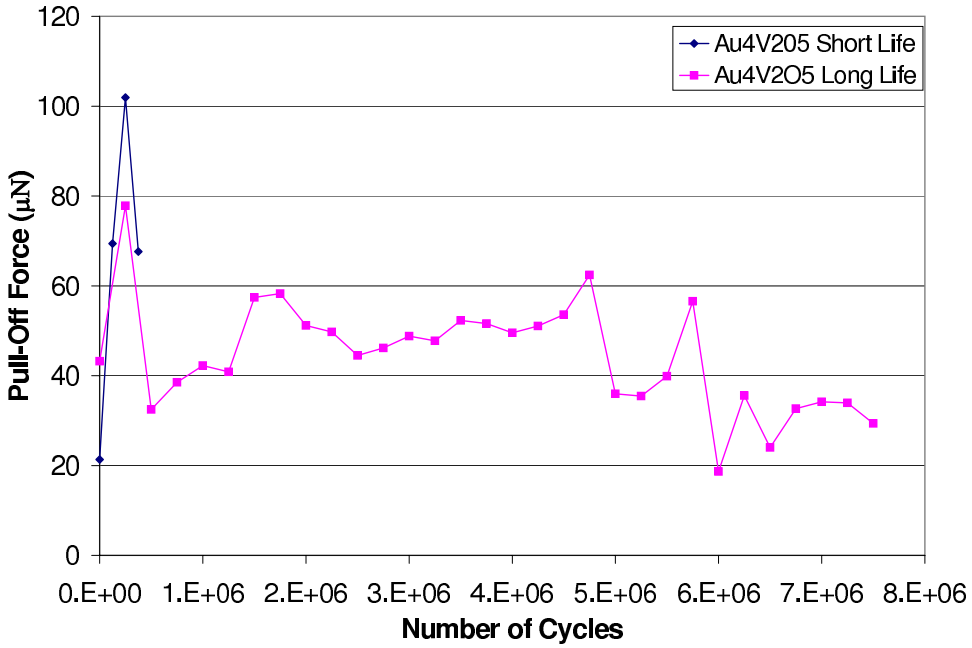

Figure G.4: Average long-term pull-off force comparison between lifetime failure categories of Au-4%V_2O_5 contacts.

G.3 Threshold Force & Distance

Figures G.5 and G.6 show a comparison of the average threshold force behavior for Au-4%V_2O_5 long-life contacts compared to Au-4%V_2O_5 short-life contacts. The initial threshold force for the longer life Au-4%V_2O_5 contacts is higher when compared to short life contacts. This trend is consistent with the other two materials tested and may indicate more initial surface contamination on the contact leading to a longer lifetime. The initial threshold distance in Au-4%V_2O_5 contacts is shown in Figures G.7 and G.8 also follows the same trend. The threshold distance equalized at approximately 70 nm after roughly 400,000 cycles and stayed constant until approximately 1.75 $\times 10^6$ cycles. Changes to surface morphology of the contacts may have begun at 1.75 $\times 10^6$ cycles as indicated by the threshold distance change after that point.

G.4 Contact Hardening

Figure G.9 shows the average normalized contact unloading stiffness change which occurred in Au-4%V_2O_5 contacts tested. There does not appear to be much

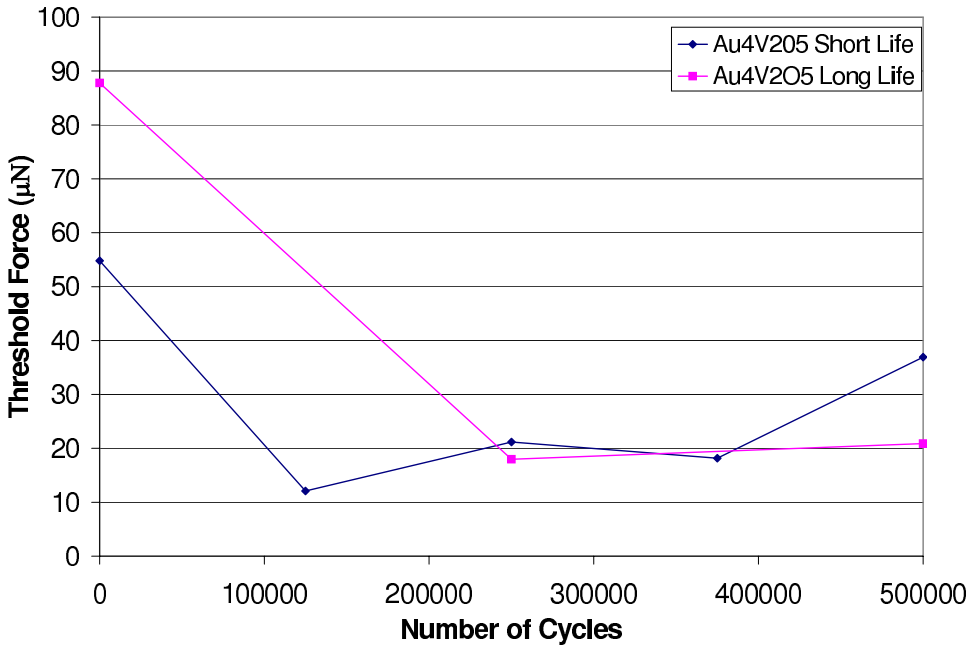

Figure G.5: Average threshold force comparison between lifetime failure categories of Au-4%V_2O_5 contacts. Note that the longest lifetime contact average shows high initial threshold force.

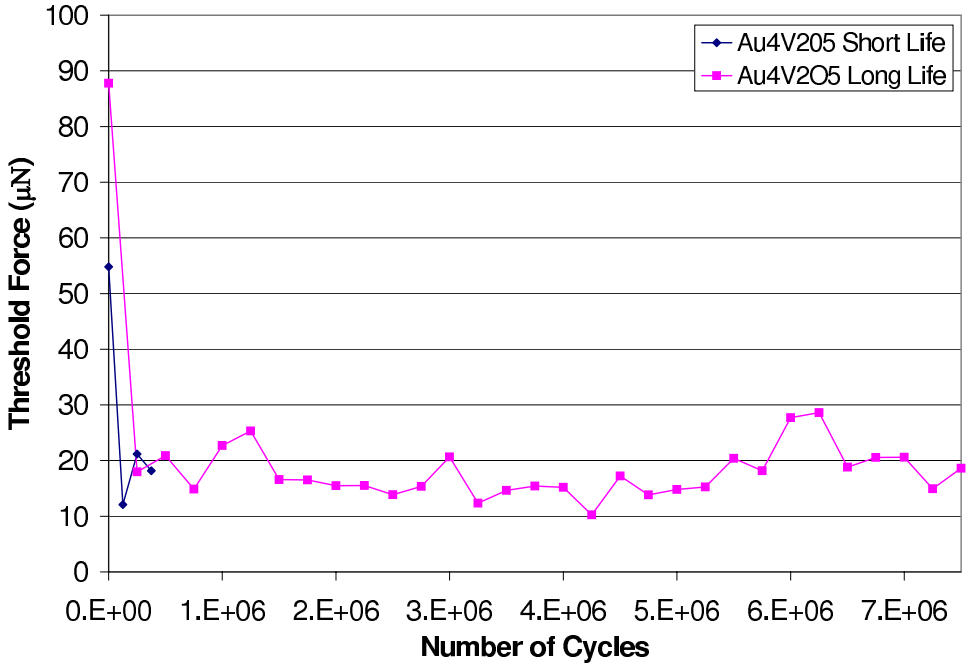

Figure G.6: Average long-term threshold force comparison between lifetime failure categories of Au-4%V_2O_5 contacts.

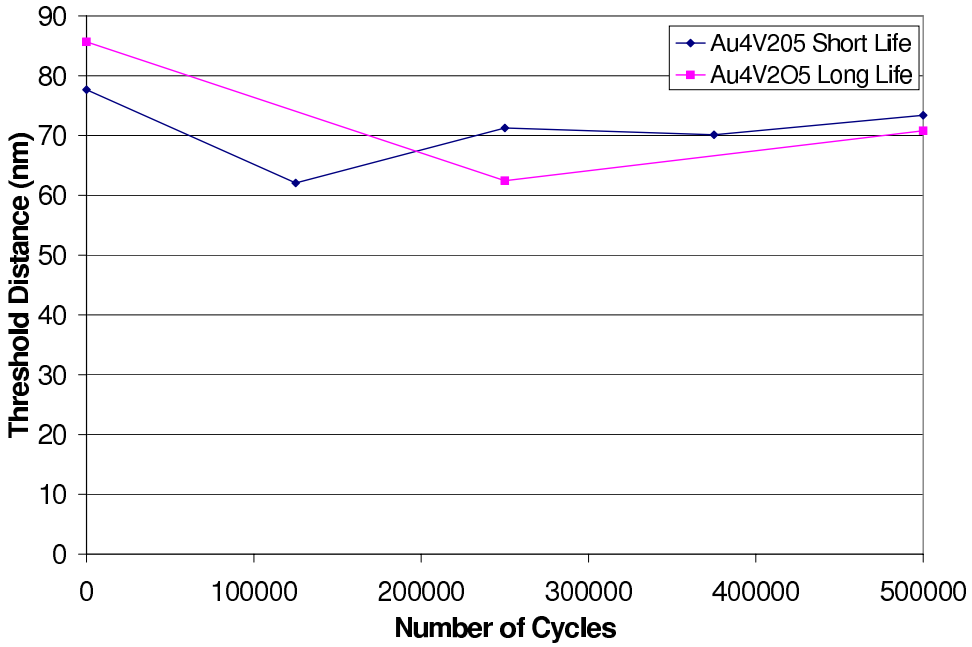

Figure G.7: Average threshold distance comparison between Au-4%V_2O_5 lifetime failure categories.

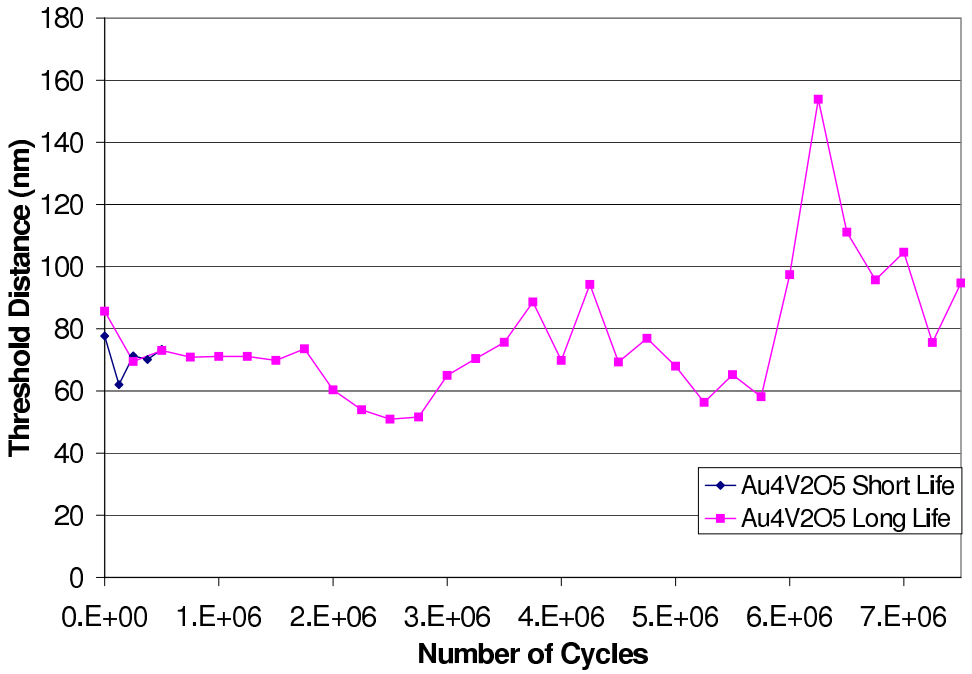

Figure G.8: Average long-term threshold distance comparison between Au-4%V_2O_5 lifetime failure categories.

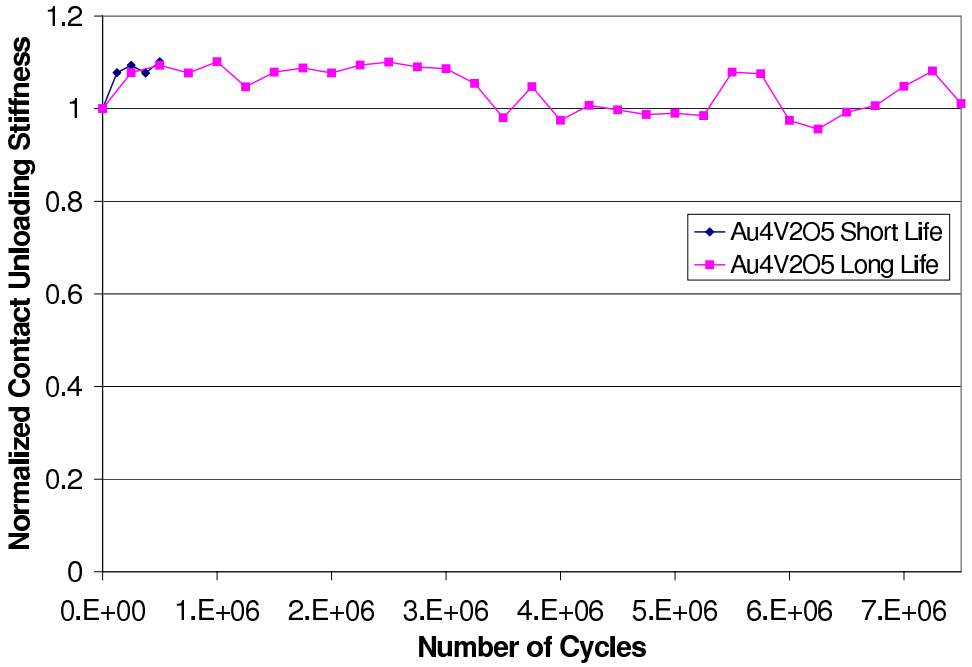

Figure G.9: Average long-term normalized contact stiffness change comparison between Au-4%V_2O_5 lifetime failure categories.

difference between the short-life contacts and the long-life contacts in this material. Both short and long-life contacts show some strain hardening during initial cycling before a tear in the contact film of one of the long-term contacts occurred at approximately 5×10^6 cycles. There are likely competing mechanisms of strain hardening and annealing due to contact heating occurring as indicated by the variation in average normalized contact stiffness later in the contact life.

G.5 Contact Interference

Figures G.10 and G.11 show the average contact interference of Au-4%V_2O_5 long-life contacts compared to the average result for Au-4%V_2O_5 short-life contacts. This shows slightly higher initial contact interference for the long-life contacts. The initial difference is consistent with more initial surface contamination on long-life contacts at the start of the tests. The late increase in contact interference likely indicates heating occurring in the contact as it cycles causing an increase in surface deformation under loading. The increase starts at approximately 3×10^6 cycles which

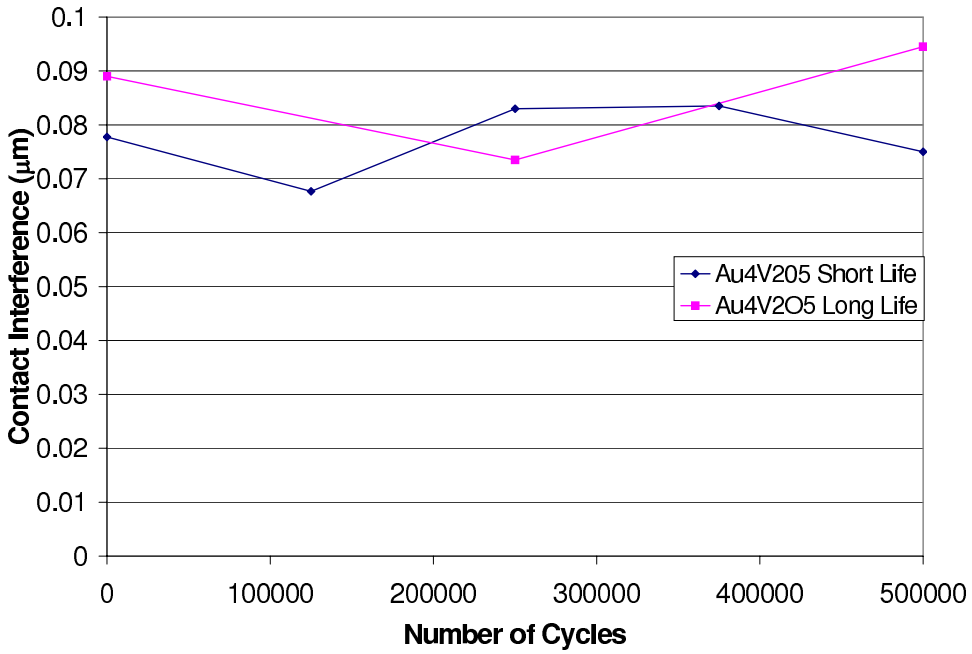

Figure G.10: Average contact interference comparison between lifetime failure categories of Au-4%V_2O_5 contacts.

matches the reduction in average contact unloading stiffness shown in Figure G.9. This likely indicates contact softening due to contact heating starting at 3 $\times 10^6$ cycles.

G.6 Time Dependent Behavior

Figures G.12 and G.13 show a comparison of the average time-dependent deformation for long-life Au-4%V_2O_5 contacts compared to the average time-dependent deformation seen in Au-4%V_2O_5 short-life contacts. This shows that the long-life contacts experience more time-dependent deformation during the first 500,000 cycles of testing. This result is consistent with increased initial surface contamination existing on long-life contacts. The average reduction in time-dependent deformation seen in short-life Au-4%V_2O_5 contacts is consistent with less initial surface contamination and contact hardening effects. The longer term increase in time-dependent deformation shown in Figure G.13 likely indicates increased contact temperature in the long-life Au-4%V_2O_5 contacts as they cycle.

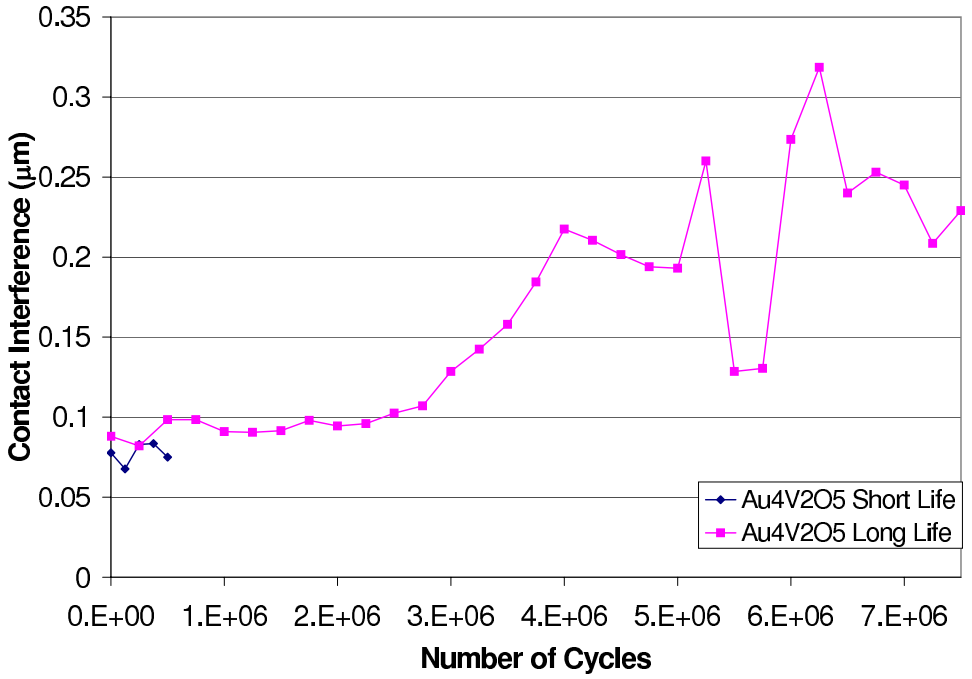

Figure G.11: Long-term average contact interference comparison between lifetime failure categories of Au-4%V_2O_5 contacts.

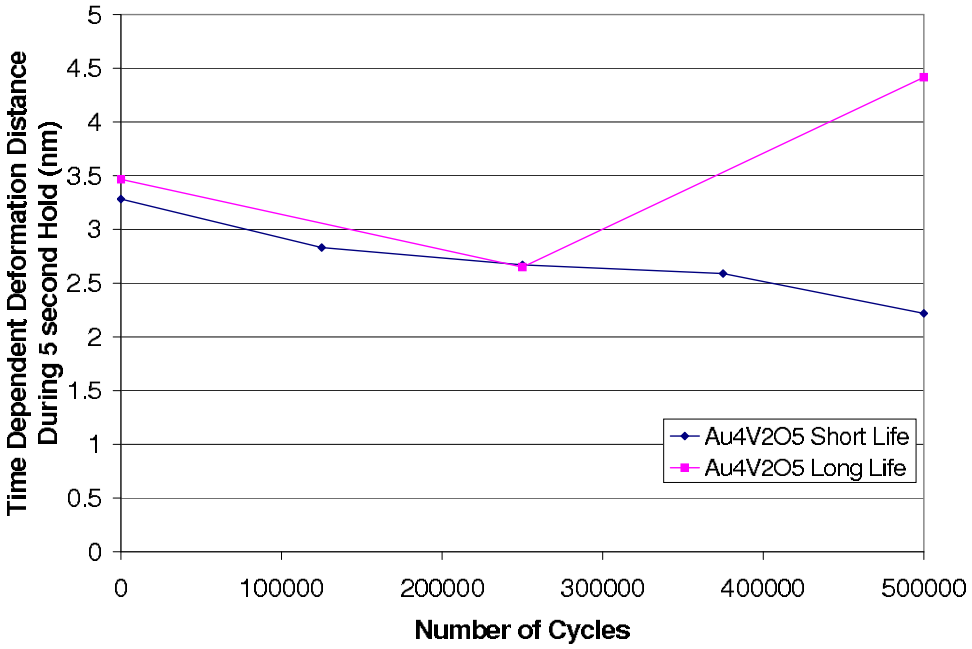

Figure G.12: Average time dependent deformation comparison between Au-4%V_2O_5 short-life and long-life failures.

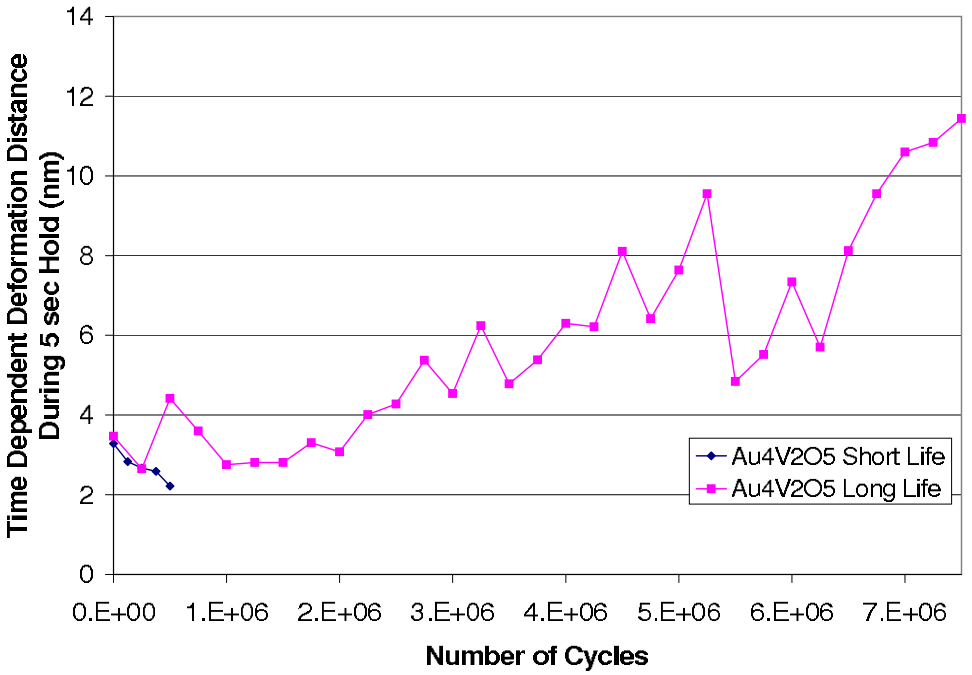

Figure G.13: Long-term average time dependent deformation comparison between Au-4%V_2O_5 short-life and long-life failures.

G.7 Energy Absorbed

Figures G.14 and G.15 show a comparison of the average energy absorbed for Au-4%V_2O_5 long-life contacts compared to the energy absorbed by Au-4%V_2O_5 short-life contacts. The long-life contacts show more initial energy absorbed and thus more initial plastic deformation occurring in the contact during cycling. This result is consistent with a thicker initial contamination layer being plastically deformed or more deformation occurring on larger contact asperities due to a rougher initial contact surface. While the thickness of initial contaminations on the contacts prior to cycling is unknown, the contacts were cycled in lab-air so the level of contamination and/or humidity could have been a factor. Surface roughnesses varied among tested contacts due to slight differences in processing. The increase in plastic deformation as the long-life contacts cycle also likely indicate a reduction in contact film yield stress due to contact heating. This increase in energy absorbed may also be attributable to damage due to surface fracture or a build up of subsurface damage in the contact film.

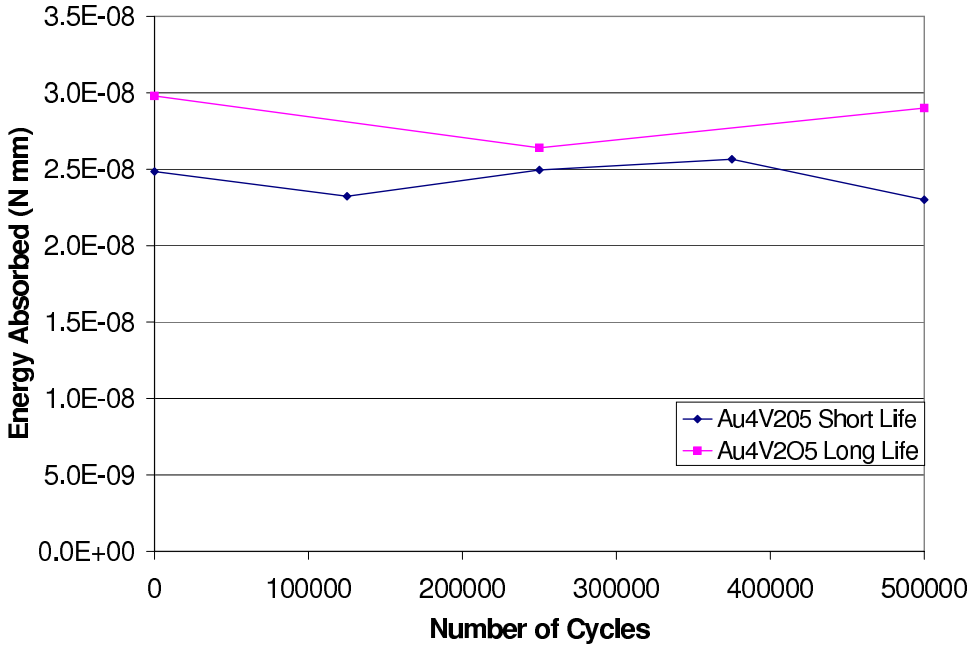

Figure G.14: Average energy absorbed comparison between lifetime failure categories of Au-4%V_2O_5 contacts.

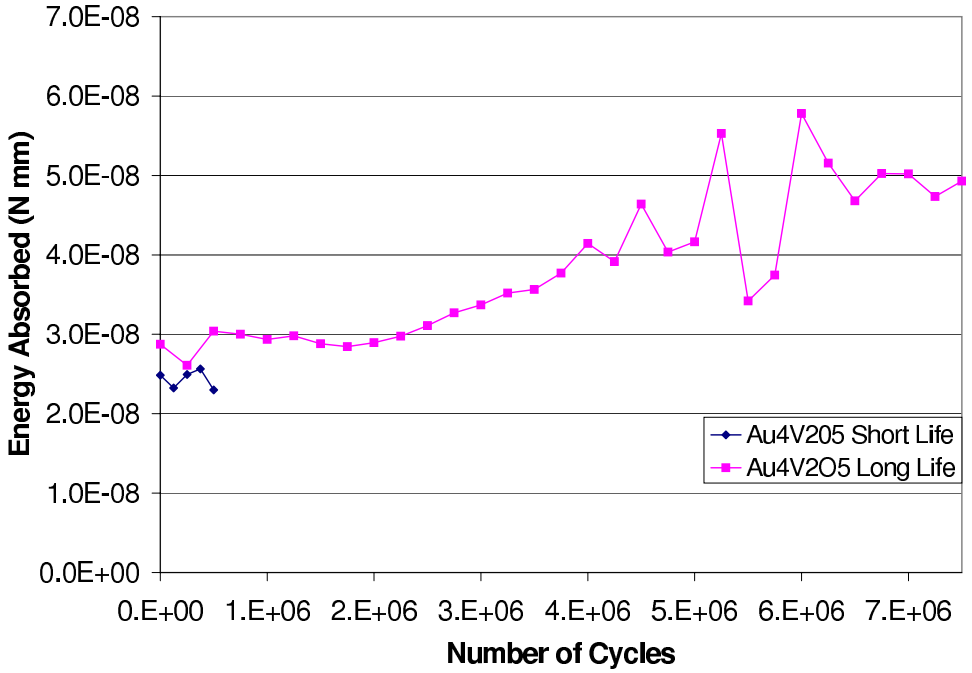

Figure G.15: Average long-term energy absorbed comparison between lifetime failure categories of Au-4%V_2O_5 contacts.

Appendix H. Test Method

Reproduced with Permission, Agilent Technologies, Inc.

```
Method Name : C:\Program Files\MTS
Systems\TestWorks\Methods\PZTControl_ Cycling_4-07-08_6000.msm Owner
: MTS Channels
    dVdt
        Internal Name : dVdt
        Units : V/s
        Formula : (_ACH0[CurrentIndex()]-_ACH0[CurrentIndex()-1])/(_Time[Current
        Index()]-_Time[CurrentIndex()-1])
        Description : Instantaneous change in Voltage measurement wrt time
        Places : 9
        Notation : Fixed
        Export Order : N/A
        Effect of Increasing Extension : Increases Value
        Invert Polarity : No
        Hidden : No
        Save Raw Data : No
        Recalculate Post-Test : No
        Calculate during Test : No
        Never Recalculate : No
        Advanced button : No
        Locked : No
        Discardable : No
    Time
        Internal Name : _Time
        Units : s
        Formula :
        Description : Time.
        Places : 3
        Notation : Fixed
        Export Order : N/A
        Effect of Increasing Extension : Increases Value
        Invert Polarity : No
        Hidden : No
        Save Raw Data : Yes
        Recalculate Post-Test : No
        Calculate during Test : No
        Never Recalculate : No
        Advanced button : No
        Locked : No
        Discardable : No
    dPdt
        Internal Name : dPdt
        Units : mN/s
```

```
        Formula : (_Load[CurrentIndex()]-_Load[CurrentIndex()-1])/(_Time[Current
        Index()]-_Time[CurrentIndex()-1])
        Description : Instantaneous change in Raw Load channel with respect to T
        ime.
        Places : 9
        Notation : Fixed
        Export Order : N/A
        Effect of Increasing Extension : Increases Value
        Invert Polarity : No
        Hidden : Yes
        Save Raw Data : No
        Recalculate Post-Test : No
        Calculate during Test : No
        Never Recalculate : No
        Advanced button : No
        Locked : No
        Discardable : No
    Harmonic Contact Stiffness
        Internal Name : Stiffness
        Units : N/m
        Formula : 1/(1/(_HarmonicStiffness)-1/ ( _HarmonicFrame+HarmonicFrameCor
        rection))
        Description : Harmonic stiffness of the contact, used directly in the ca
        lculation of contact area,
hardness, and reduced modulus.
        Places : 3
        Notation : Fixed
        Export Order : 4
        Effect of Increasing Extension : Increases Value
        Invert Polarity : No
        Hidden : No
        Save Raw Data : No
        Recalculate Post-Test : Yes
        Calculate during Test : No
        Never Recalculate : No
        Advanced button : No
        Locked : No
        Discardable : No
    Raw Load
        Internal Name : _Load
        Units : mN
        Formula :
        Description : Raw force applied electromagnetically to the indenter colu
        mn.
        Places : 6
        Notation : Fixed
```

```
    Export Order : 13
    Effect of Increasing Extension : Effect of Increasing Extension
    Invert Polarity : No
    Hidden : No
    Save Raw Data : Yes
    Recalculate Post-Test : No
    Calculate during Test : No
    Never Recalculate : No
    Advanced button : No
    Locked : No
    Discardable : No
Max Load
    Internal Name : MaxLoad
    Units : mN
    Formula : IF(SegmentType EQ UnloadFromPeak AND SegmentType[CurrentIndex(
    )-1] EQ Hold, LoadOnSample,InvalidDouble())
    Description : Load on the sample at the start of each unload.
    Places : 3
    Notation : Fixed
    Export Order : N/A
    Effect of Increasing Extension : Increases Value
    Invert Polarity : No
    Hidden : Yes
    Save Raw Data : No
    Recalculate Post-Test : Yes
    Calculate during Test : No
    Never Recalculate : No
    Advanced button : No
    Locked : No
    Discardable : No
(_ACH0)Voltage4WMeasured
    Internal Name : _ACH0
    Units : V
    Formula :
    Description :
    Places : 5
    Notation : Fixed
    Export Order : N/A
    Effect of Increasing Extension : Increases Value
    Invert Polarity : No
    Hidden : No
    Save Raw Data : Yes
    Recalculate Post-Test : No
    Calculate during Test : No
    Never Recalculate : No
    Advanced button : No
```

```
        Locked : No
        Discardable : No
    PerCycleDisplacementIntoContact
        Internal Name : PerCycleDisplacementIntoContact
        Units : um
        Formula : _Displacement - _Displacement[PerCyclePlateContactMarker] - (1
        .0*(_Load-_Load[PerCyclePlateContactMarker] )/(_Frame + FrameStiffn
        essCorrection))
        Description : Penetration into the test surface as measured from the poi
        nt at which the
indenter first touches the sample.  This value has been corrected
for th ermal drift and for any deflection in the instrument frame.
        Places : 3
        Notation : Fixed
        Export Order : 2
        Effect of Increasing Extension : Increases Value
        Invert Polarity : No
        Hidden : No
        Save Raw Data : No
        Recalculate Post-Test : Yes
        Calculate during Test : No
        Never Recalculate : No
        Advanced button : No
        Locked : No
        Discardable : No
    Segment Number
        Internal Name : SegmentIndex
        Units :
        Formula : IF(CurrentIndex() eq 0, 0, SegmentIndex)
        Description : Identifies segment number (sequentially indexed).
        Places : 0
        Notation : Fixed
        Export Order : N/A
        Effect of Increasing Extension : Increases Value
        Invert Polarity : No
        Hidden : Yes
        Save Raw Data : Yes
        Recalculate Post-Test : No
        Calculate during Test : No
        Never Recalculate : Yes
        Advanced button : No
        Locked : No
        Discardable : No
    PerCycleDisplacementIntoSurface
        Internal Name : PerCycleDisplacementIntoSurface
        Units : um
```

```
        Formula : _Displacement - _Displacement[PerCycleSurfaceMarker] - (1.0*(_
        Load-_Load[PerCycleSurfaceMarker] )/(_Frame + FrameStiffnessCorrect
        ion))
        Description : Penetration into the test surface as measured from the poi
        nt at which the
indenter first touches the sample.  This value has been corrected
for th ermal drift and for any deflection in the instrument frame.
        Places : 3
        Notation : Fixed
        Export Order : 3
        Effect of Increasing Extension : Increases Value
        Invert Polarity : No
        Hidden : No
        Save Raw Data : No
        Recalculate Post-Test : Yes
        Calculate during Test : No
        Never Recalculate : No
        Advanced button : No
        Locked : No
        Discardable : No
    Y Position
        Internal Name : _YPosition
        Units : mm
        Formula :
        Description : The y-position of the sample stage.
        Places : 3
        Notation : Fixed
        Export Order : N/A
        Effect of Increasing Extension : Increases Value
        Invert Polarity : No
        Hidden : Yes
        Save Raw Data : Yes
        Recalculate Post-Test : No
        Calculate during Test : No
        Never Recalculate : No
        Advanced button : No
        Locked : No
        Discardable : No
    X Position
        Internal Name : _XPosition
        Units : mm
        Formula :
        Description : The x-position of the sample stage.
        Places : 3
        Notation : Fixed
        Export Order : N/A
```

```
        Effect of Increasing Extension : Increases Value
        Invert Polarity : No
        Hidden : Yes
        Save Raw Data : Yes
        Recalculate Post-Test : No
        Calculate during Test : No
        Never Recalculate : No
        Advanced button : No
        Locked : No
        Discardable : No
    Frame Stiffness
        Internal Name : _Frame
        Units : N/m
        Formula :
        Description : Stiffness used to account for slight deformation in the te
        st frame that
occurs when applying load to a sample.
        Places : 0
        Notation : Fixed
        Export Order : N/A
        Effect of Increasing Extension : Increases Value
        Invert Polarity : No
        Hidden : Yes
        Save Raw Data : Yes
        Recalculate Post-Test : No
        Calculate during Test : No
        Never Recalculate : No
        Advanced button : No
        Locked : No
        Discardable : No
    _HarmonicLoad
        Internal Name : _HarmonicLoad
        Units : uN
        Formula :
        Description :
        Places : 3
        Notation : Fixed
        Export Order : N/A
        Effect of Increasing Extension : Increases Value
        Invert Polarity : No
        Hidden : No
        Save Raw Data : Yes
        Recalculate Post-Test : No
        Calculate during Test : No
        Never Recalculate : No
        Advanced button : No
```

```
        Locked : No
        Discardable : No
    Segment Type
        Internal Name : SegmentType
        Units :
        Formula : IF(CurrentIndex() eq 0, 0, SegmentType)
        Description : Identifies segment type (approach, load, unload, etc.) for
         post-test analysis.
Set using "Segment Type" test segments.
        Places : 0
        Notation : Fixed
        Export Order : N/A
        Effect of Increasing Extension : Increases Value
        Invert Polarity : No
        Hidden : Yes
        Save Raw Data : Yes
        Recalculate Post-Test : No
        Calculate during Test : No
        Never Recalculate : Yes
        Advanced button : No
        Locked : No
        Discardable : No
    Raw Displacement
        Internal Name : _Displacement
        Units : nm
        Formula :
        Description : Absolute position of the indenter shaft relative to the ce
        nter of its full range
of travel.
        Places : 3
        Notation : Fixed
        Export Order : 12
        Effect of Increasing Extension : Effect of Increasing Extension
        Invert Polarity : No
        Hidden : No
        Save Raw Data : Yes
        Recalculate Post-Test : No
        Calculate during Test : No
        Never Recalculate : No
        Advanced button : No
        Locked : No
        Discardable : No
    Load vs Disp Slope
        Internal Name : _ContactStiffness
        Units : N/m
        Formula :
```

```
        Description : Instantaneous and continuous slope of load with respect to
         displacement.
Used for the in-situ determination of surface contact.
        Places : 3
        Notation : Fixed
        Export Order : N/A
        Effect of Increasing Extension : Increases Value
        Invert Polarity : No
        Hidden : No
        Save Raw Data : Yes
        Recalculate Post-Test : No
        Calculate during Test : No
        Never Recalculate : No
        Advanced button : No
        Locked : No
        Discardable : No
    _HarmonicDamping
        Internal Name : _HarmonicDamping
        Units : N/m
        Formula :
        Description :
        Places : 3
        Notation : Fixed
        Export Order : N/A
        Effect of Increasing Extension : Increases Value
        Invert Polarity : No
        Hidden : Yes
        Save Raw Data : Yes
        Recalculate Post-Test : No
        Calculate during Test : No
        Never Recalculate : No
        Advanced button : No
        Locked : No
        Discardable : No
    CurrentSupplied
        Internal Name : CurrentSupplied
        Units : mA
        Formula : Current
        Description :
        Places : 3
        Notation : Fixed
        Export Order : N/A
        Effect of Increasing Extension : Increases Value
        Invert Polarity : No
        Hidden : No
        Save Raw Data : Yes
```

```
    Recalculate Post-Test : No
    Calculate during Test : No
    Never Recalculate : Yes
    Advanced button : No
    Locked : No
    Discardable : No
_HarmonicFrame
    Internal Name : _HarmonicFrame
    Units : N/m
    Formula :
    Description :
    Places : 3
    Notation : Fixed
    Export Order : N/A
    Effect of Increasing Extension : Increases Value
    Invert Polarity : No
    Hidden : Yes
    Save Raw Data : Yes
    Recalculate Post-Test : No
    Calculate during Test : No
    Never Recalculate : No
    Advanced button : No
    Locked : No
    Discardable : No
Support Spring Stiffness
    Internal Name : _Column
    Units : N/m
    Formula :
    Description : Stiffness of the springs which support the indenter column
    .
    Places : 3
    Notation : Fixed
    Export Order : N/A
    Effect of Increasing Extension : Increases Value
    Invert Polarity : No
    Hidden : Yes
    Save Raw Data : Yes
    Recalculate Post-Test : No
    Calculate during Test : No
    Never Recalculate : No
    Advanced button : No
    Locked : No
    Discardable : No
_HarmonicFrequency
    Internal Name : _HarmonicFrequency
    Units : Hz
```

```
        Formula :
        Description :
        Places : 3
        Notation : Fixed
        Export Order : N/A
        Effect of Increasing Extension : Increases Value
        Invert Polarity : No
        Hidden : Yes
        Save Raw Data : Yes
        Recalculate Post-Test : No
        Calculate during Test : No
        Never Recalculate : No
        Advanced button : No
        Locked : No
        Discardable : No
    PerCyclePullOffLoadOnContact
        Internal Name : PerCyclePullOffLoadOnContact
        Units : uN
        Formula : IF(AbsValdVdt > VoltageTolerance AND AbsValdVdt[CurrentIndex()
        -1]<VoltageTolerance AND SegmentType EQ UnloadFromPeak AND FAbs(Per
        CycleLoadOnContact)<MaximumContactForce/2, Fabs(PerCycleLoadOnConta
        ct[CurrentIndex()-1]),InvalidDouble())
        Description : Load on the sample, "zeroed" when the indenter first conta
        cts the surface.
This value has been corrected for the force imposed by the springs
suppo rting the indenter shaft.
        Places : 6
        Notation : Fixed
        Export Order : 6
        Effect of Increasing Extension : Increases Value
        Invert Polarity : No
        Hidden : No
        Save Raw Data : No
        Recalculate Post-Test : Yes
        Calculate during Test : No
        Never Recalculate : No
        Advanced button : No
        Locked : No
        Discardable : No
    _HarmonicDisplacement
        Internal Name : _HarmonicDisplacement
        Units : nm
        Formula :
        Description :
        Places : 3
        Notation : Fixed
```

```
        Export Order : N/A
        Effect of Increasing Extension : Increases Value
        Invert Polarity : No
        Hidden : No
        Save Raw Data : Yes
        Recalculate Post-Test : No
        Calculate during Test : No
        Never Recalculate : No
        Advanced button : No
        Locked : No
        Discardable : No
    PerCycleThresholdContactLoad
        Internal Name : PerCycleThresholdContactLoad
        Units : uN
        Formula : IF(CurrentIndex()>PerCyclePlateContactMarker AND CurrentIndex(
        )<PerCycleEndOfLoadingMarker AND PeakValue (ResistanceMeasured4W, C
        urrentIndex()-20, CurrentIndex())<ResistanceTriggerThresholdCalc AN
        D ResistanceMeasured4W[CurrentIndex()-21]>ResistanceTriggerThreshol
        dCalc, PerCycleLoadOnContact[CurrentIndex()-20], InvalidDouble() )
        Description : Load on the sample, "zeroed" when the indenter first conta
        cts the surface.
This value has been corrected for the force imposed by the springs
suppo rting the indenter shaft.
        Places : 6
        Notation : Fixed
        Export Order : 7
        Effect of Increasing Extension : Increases Value
        Invert Polarity : No
        Hidden : No
        Save Raw Data : No
        Recalculate Post-Test : Yes
        Calculate during Test : No
        Never Recalculate : No
        Advanced button : No
        Locked : No
        Discardable : No
    Load On Sample
        Internal Name : LoadOnSample
        Units : uN
        Formula : _Load-_Load[SurfaceMarker] -(_Displacement-_Displacement[Surfa
        ceMarker] )*_Column
        Description : Load on the sample, "zeroed" when the indenter first conta
        cts the surface.
This value has been corrected for the force imposed by the springs
suppo rting the indenter shaft.
        Places : 6
```

```
        Notation : Fixed
        Export Order : 8
        Effect of Increasing Extension : Increases Value
        Invert Polarity : No
        Hidden : No
        Save Raw Data : No
        Recalculate Post-Test : Yes
        Calculate during Test : No
        Never Recalculate : No
        Advanced button : No
        Locked : No
        Discardable : No
    _HarmonicStiffness
        Internal Name : _HarmonicStiffness
        Units : N/m
        Formula :
        Description :
        Places : 3
        Notation : Fixed
        Export Order : N/A
        Effect of Increasing Extension : Increases Value
        Invert Polarity : No
        Hidden : No
        Save Raw Data : Yes
        Recalculate Post-Test : No
        Calculate during Test : No
        Never Recalculate : No
        Advanced button : No
        Locked : No
        Discardable : No
    R_Meas4W
        Internal Name : ResistanceMeasured4W
        Units : Ohm
        Formula : _ACH0/100.0/(CurrentSupplied/1000.0)
        Description : ACH0 must be divided by 2 when using 5v analog input modul
        e to account for gain of 2.
ACH0 must be divided by 10 when using 1v analog input module to
account for gain of 10 ACH0 must be divided by 200 when using 50mV
analog input module to accou nt for gain of 200
        Places : 3
        Notation : Fixed
        Export Order : 11
        Effect of Increasing Extension : Increases Value
        Invert Polarity : No
        Hidden : No
        Save Raw Data : No
```

```
        Recalculate Post-Test : Yes
        Calculate during Test : No
        Never Recalculate : No
        Advanced button : No
        Locked : No
        Discardable : No
    Digital IO (_PA0)
        Internal Name : _PA0
        Units :
        Formula : RelaySwitch
        Description :
        Places : 3
        Notation : Fixed
        Export Order : N/A
        Effect of Increasing Extension : Increases Value
        Invert Polarity : No
        Hidden : No
        Save Raw Data : No
        Recalculate Post-Test : No
        Calculate during Test : No
        Never Recalculate : No
        Advanced button : No
        Locked : No
        Discardable : No
    Per Cycle Load On Contact
        Internal Name : PerCycleLoadOnContact
        Units : uN
        Formula : _Load-_Load[PerCyclePlateContactMarker] -(DisplacementIntoSurf
        ace-DisplacementIntoSurface[PerCyclePlateContactMarker])*_Column
        Description : Load on the sample, "zeroed" when the indenter first conta
        cts the surface.
This value has been corrected for the force imposed by the springs
suppo rting the indenter shaft.
        Places : 6
        Notation : Fixed
        Export Order : 9
        Effect of Increasing Extension : Increases Value
        Invert Polarity : No
        Hidden : No
        Save Raw Data : No
        Recalculate Post-Test : Yes
        Calculate during Test : No
        Never Recalculate : No
        Advanced button : No
        Locked : No
        Discardable : No
```

```
    Time On Sample
        Internal Name : TimeOnSample
        Units : s
        Formula : _Time-_Time[SurfaceMarker]
        Description : Time, "zeroed" when the indenter first contacts the surfac
        e.
        Places : 6
        Notation : Fixed
        Export Order : 0
        Effect of Increasing Extension : Increases Value
        Invert Polarity : No
        Hidden : No
        Save Raw Data : No
        Recalculate Post-Test : Yes
        Calculate during Test : No
        Never Recalculate : No
        Advanced button : No
        Locked : No
        Discardable : No
    Per Cycle Load On Sample
        Internal Name : PerCycleLoadOnSample
        Units : uN
        Formula : _Load-_Load[PerCycleSurfaceMarker] -(DisplacementIntoSurface-D
        isplacementIntoSurface[PerCycleSurfaceMarker])*_Column
        Description : Load on the sample, "zeroed" when the indenter first conta
        cts the surface.
This value has been corrected for the force imposed by the springs
suppo rting the indenter shaft.
        Places : 6
        Notation : Fixed
        Export Order : 10
        Effect of Increasing Extension : Increases Value
        Invert Polarity : No
        Hidden : No
        Save Raw Data : No
        Recalculate Post-Test : Yes
        Calculate during Test : No
        Never Recalculate : No
        Advanced button : No
        Locked : No
        Discardable : No
    _HarmonicSystemDamping
        Internal Name : _HarmonicSystemDamping
        Units : N/m
        Formula :
        Description :
```

```
    Places : 3
    Notation : Fixed
    Export Order : N/A
    Effect of Increasing Extension : Increases Value
    Invert Polarity : No
    Hidden : Yes
    Save Raw Data : Yes
    Recalculate Post-Test : No
    Calculate during Test : No
    Never Recalculate : No
    Advanced button : No
    Locked : No
    Discardable : No
Abs Val dPdt
    Internal Name : AbsValdPdt
    Units : mN/s
    Formula : IF(dPdt <0, -1*dPdt, dPdt)
    Description : Absolute value of dPdt channel.
    Places : 9
    Notation : Fixed
    Export Order : N/A
    Effect of Increasing Extension : Increases Value
    Invert Polarity : No
    Hidden : Yes
    Save Raw Data : No
    Recalculate Post-Test : No
    Calculate during Test : No
    Never Recalculate : No
    Advanced button : No
    Locked : No
    Discardable : No
CSM Status
    Internal Name : _CSM
    Units :
    Formula :
    Description :
    Places : 0
    Notation : Fixed
    Export Order : N/A
    Effect of Increasing Extension : Increases Value
    Invert Polarity : No
    Hidden : Yes
    Save Raw Data : Yes
    Recalculate Post-Test : No
    Calculate during Test : No
    Never Recalculate : No
```

```
    Advanced button : No
    Locked : No
    Discardable : No
AbsValdVdt
    Internal Name : AbsValdVdt
    Units : V/s
    Formula : IF(dVdt<0, -1*dVdt, dVdt)
    Description : Absolute value of dPdt channel.
    Places : 9
    Notation : Fixed
    Export Order : N/A
    Effect of Increasing Extension : Increases Value
    Invert Polarity : No
    Hidden : No
    Save Raw Data : No
    Recalculate Post-Test : No
    Calculate during Test : No
    Never Recalculate : No
    Advanced button : No
    Locked : No
    Discardable : No
_XForce
    Internal Name : _XForce
    Units : N
    Formula :
    Description :
    Places : 3
    Notation : Fixed
    Export Order : N/A
    Effect of Increasing Extension : Increases Value
    Invert Polarity : No
    Hidden : Yes
    Save Raw Data : Yes
    Recalculate Post-Test : No
    Calculate during Test : No
    Never Recalculate : No
    Advanced button : No
    Locked : No
    Discardable : No
_YForce
    Internal Name : _YForce
    Units : N
    Formula :
    Description :
    Places : 3
    Notation : Fixed
```

```
    Export Order : N/A
    Effect of Increasing Extension : Increases Value
    Invert Polarity : No
    Hidden : Yes
    Save Raw Data : Yes
    Recalculate Post-Test : No
    Calculate during Test : No
    Never Recalculate : No
    Advanced button : No
    Locked : No
    Discardable : No
_PhaseAngle
    Internal Name : _PhaseAngle
    Units : deg
    Formula :
    Description :
    Places : 3
    Notation : Fixed
    Export Order : N/A
    Effect of Increasing Extension : Increases Value
    Invert Polarity : No
    Hidden : Yes
    Save Raw Data : Yes
    Recalculate Post-Test : No
    Calculate during Test : No
    Never Recalculate : No
    Advanced button : No
    Locked : No
    Discardable : No
Points In Stiffness Fit
    Internal Name : PointsInStiffnessFit
    Units :
    Formula : IF(dPdt < -Tol AND AbsValdPdt[CurrentIndex()-1]<Tol, Floor(Per
    centUnloadInStiffnessCalc*(ChannelIndex (SegmentIndex, Double(Segme
    ntIndex[CurrentIndex()]+1), CurrentIndex())-CurrentIndex())), -1)
    Description : Number of points included in the linear regression fit to
    calculate stiffness.
    Places : 0
    Notation : Fixed
    Export Order : N/A
    Effect of Increasing Extension : Increases Value
    Invert Polarity : No
    Hidden : Yes
    Save Raw Data : No
    Recalculate Post-Test : Yes
    Calculate during Test : No
```

```
    Never Recalculate : No
    Advanced button : No
    Locked : No
    Discardable : No
PZTConstantVoltage (_DAC0OUT)
    Internal Name : _DAC0OUT
    Units : V
    Formula : PZTVoltage
    Description :
    Places : 3
    Notation : Fixed
    Export Order : N/A
    Effect of Increasing Extension : Increases Value
    Invert Polarity : No
    Hidden : No
    Save Raw Data : No
    Recalculate Post-Test : No
    Calculate during Test : No
    Never Recalculate : No
    Advanced button : No
    Locked : No
    Discardable : No
Current4WOutput (_DAC1OUT)
    Internal Name : _DAC1OUT
    Units : V
    Formula : CurrentSupplied*0.05
    Description : Voltage = Current*500 if units are correct...error in Amps
     in TW (mA used as base unit)
    Places : 3
    Notation : Fixed
    Export Order : N/A
    Effect of Increasing Extension : Increases Value
    Invert Polarity : No
    Hidden : No
    Save Raw Data : No
    Recalculate Post-Test : No
    Calculate during Test : No
    Never Recalculate : No
    Advanced button : No
    Locked : No
    Discardable : No
Displacement Into Surface
    Internal Name : DisplacementIntoSurface
    Units : um
    Formula : _Displacement - _Displacement[SurfaceMarker] - (1.0*(_Load-_Lo
    ad[SurfaceMarker] )/(_Frame + FrameStiffnessCorrection))
```

```
        Description : Penetration into the test surface as measured from the poi
        nt at which the
indenter first touches the sample.  This value has been corrected
for th ermal drift and for any deflection in the instrument frame.
        Places : 3
        Notation : Fixed
        Export Order : 1
        Effect of Increasing Extension : Increases Value
        Invert Polarity : No
        Hidden : No
        Save Raw Data : No
        Recalculate Post-Test : Yes
        Calculate during Test : No
        Never Recalculate : No
        Advanced button : No
        Locked : No
        Discardable : No
    _HarmonicSystemStiffness
        Internal Name : _HarmonicSystemStiffness
        Units : N/m
        Formula :
        Description :
        Places : 3
        Notation : Fixed
        Export Order : N/A
        Effect of Increasing Extension : Increases Value
        Invert Polarity : No
        Hidden : Yes
        Save Raw Data : Yes
        Recalculate Post-Test : No
        Calculate during Test : No
        Never Recalculate : No
        Advanced button : No
        Locked : No
        Discardable : No
Inputs
    Batch Inputs
        1 Second Delay Time
            Internal Name : OneSecondDelayTime
            Default Value : 1.000  s
            Description : Time over which the force on the indenter is held at a sma
            ll, constant value.
Data acquired during this time are used to determine thermal drift.
            Source : Keyboard Only
            Statistics Type : None
            Number of Readings : 1
```

```
    When : Pre-Test
    Minimum : No
    Maximum : No
    Places : 3
    Notation : Fixed
    Hidden : No
    Display Only : No
    Editable Post-Test : No
    Input Required : No
    Locked : No
    Result : No
    Reporting Order : N/A
    Panel Input : No
    Sample Level : Yes
    Reset To Default Values : Yes
    Choice List : No
    Only Allow Choice : No
    Input Order : N/A
10 Hz Data Rate
    Internal Name : TenHzDataRate
    Default Value : 10.000  Hz
    Description : Data acquisition rate
    Source : Keyboard Only
    Statistics Type : None
    Number of Readings : 1
    When : Pre-Test
    Minimum : No
    Maximum : No
    Places : 3
    Notation : Fixed
    Hidden : No
    Display Only : No
    Editable Post-Test : No
    Input Required : No
    Locked : No
    Result : No
    Reporting Order : N/A
    Panel Input : No
    Sample Level : Yes
    Reset To Default Values : Yes
    Choice List : No
    Only Allow Choice : No
    Input Order : N/A
100 Point Buffer Size
    Internal Name : OneHundredPtBufferSize
    Default Value : 100
```

```
    Description :
    Source : Keyboard Only
    Statistics Type : None
    Number of Readings : 1
    When : Pre-Test
    Minimum : No
    Maximum : No
    Places : 0
    Notation : Fixed
    Hidden : No
    Display Only : No
    Editable Post-Test : No
    Input Required : No
    Locked : No
    Result : No
    Reporting Order : N/A
    Panel Input : No
    Sample Level : Yes
    Reset To Default Values : No
    Choice List : No
    Only Allow Choice : No
    Input Order : N/A
200 HzDataRate
    Internal Name : TwoHundredHzDataRate
    Default Value : 200.000  Hz
    Description : Data acquisition rate
    Source : Keyboard Only
    Statistics Type : None
    Number of Readings : 1
    When : Pre-Test
    Minimum : No
    Maximum : No
    Places : 3
    Notation : Fixed
    Hidden : No
    Display Only : No
    Editable Post-Test : No
    Input Required : No
    Locked : No
    Result : No
    Reporting Order : N/A
    Panel Input : No
    Sample Level : Yes
    Reset To Default Values : Yes
    Choice List : No
    Only Allow Choice : No
```

```
    Input Order : N/A
25 Hz Data Rate
    Internal Name : TwentyFiveHzDataRate
    Default Value : 25.000  Hz
    Description : Data acquisition rate
    Source : Keyboard Only
    Statistics Type : None
    Number of Readings : 1
    When : Pre-Test
    Minimum : No
    Maximum : No
    Places : 3
    Notation : Fixed
    Hidden : No
    Display Only : No
    Editable Post-Test : No
    Input Required : No
    Locked : No
    Result : No
    Reporting Order : N/A
    Panel Input : No
    Sample Level : Yes
    Reset To Default Values : Yes
    Choice List : No
    Only Allow Choice : No
    Input Order : N/A
25 Point Buffer Size
    Internal Name : TwentyFivePtBufferSize
    Default Value : 25
    Description :
    Source : Keyboard Only
    Statistics Type : None
    Number of Readings : 1
    When : Pre-Test
    Minimum : No
    Maximum : No
    Places : 0
    Notation : Fixed
    Hidden : No
    Display Only : No
    Editable Post-Test : No
    Input Required : No
    Locked : No
    Result : No
    Reporting Order : N/A
    Panel Input : No
```

```
    Sample Level : Yes
    Reset To Default Values : No
    Choice List : No
    Only Allow Choice : No
    Input Order : N/A
2HzDataRate
    Internal Name : TwoHzDataRate
    Default Value : 2.000  Hz
    Description : Data acquisition rate
    Source : Keyboard Only
    Statistics Type : None
    Number of Readings : 1
    When : Pre-Test
    Minimum : No
    Maximum : No
    Places : 3
    Notation : Fixed
    Hidden : No
    Display Only : No
    Editable Post-Test : No
    Input Required : No
    Locked : No
    Result : No
    Reporting Order : N/A
    Panel Input : No
    Sample Level : Yes
    Reset To Default Values : Yes
    Choice List : No
    Only Allow Choice : No
    Input Order : N/A
300 Hz Data Rate
    Internal Name : ThreeHundredHzDataRate
    Default Value : 300.000  Hz
    Description : Data acquisition rate
    Source : Keyboard Only
    Statistics Type : None
    Number of Readings : 1
    When : Pre-Test
    Minimum : No
    Maximum : No
    Places : 3
    Notation : Fixed
    Hidden : No
    Display Only : No
    Editable Post-Test : No
    Input Required : No
```

```
            Locked : No
            Result : No
            Reporting Order : N/A
            Panel Input : No
            Sample Level : Yes
            Reset To Default Values : Yes
            Choice List : No
            Only Allow Choice : No
            Input Order : N/A
        300 Point Buffer Size
            Internal Name : ThreeHundredPtBufferSize
            Default Value : 300
            Description :
            Source : Keyboard Only
            Statistics Type : None
            Number of Readings : 1
            When : Pre-Test
            Minimum : No
            Maximum : No
            Places : 0
            Notation : Fixed
            Hidden : No
            Display Only : No
            Editable Post-Test : No
            Input Required : No
            Locked : No
            Result : No
            Reporting Order : N/A
            Panel Input : No
            Sample Level : Yes
            Reset To Default Values : No
            Choice List : No
            Only Allow Choice : No
            Input Order : N/A
        4000 Nanometers
            Internal Name : FourThousandNanometers
            Default Value : 5000.000  nm
            Description : This is the distance to use the slow data rate during in c
            ycle surface approach.
Changed to 5000 nm
            Source : Keyboard Only
            Statistics Type : None
            Number of Readings : 1
            When : Pre-Test
            Minimum : No
            Maximum : No
```

```
    Places : 3
    Notation : Fixed
    Hidden : No
    Display Only : No
    Editable Post-Test : No
    Input Required : No
    Locked : No
    Result : No
    Reporting Order : N/A
    Panel Input : No
    Sample Level : No
    Reset To Default Values : No
    Choice List : No
    Only Allow Choice : No
    Input Order : N/A
5 Point Buffer Size
    Internal Name : FivePtBufferSize
    Default Value : 5
    Description :
    Source : Keyboard Only
    Statistics Type : None
    Number of Readings : 1
    When : Pre-Test
    Minimum : No
    Maximum : No
    Places : 0
    Notation : Fixed
    Hidden : No
    Display Only : No
    Editable Post-Test : No
    Input Required : No
    Locked : No
    Result : No
    Reporting Order : N/A
    Panel Input : No
    Sample Level : Yes
    Reset To Default Values : No
    Choice List : No
    Only Allow Choice : No
    Input Order : N/A
50 Hz DataRate
    Internal Name : FiftyHzDataRate
    Default Value : 50.000  Hz
    Description : Data acquisition rate
    Source : Keyboard Only
    Statistics Type : None
```

```
    Number of Readings : 1
    When : Pre-Test
    Minimum : No
    Maximum : No
    Places : 3
    Notation : Fixed
    Hidden : No
    Display Only : No
    Editable Post-Test : No
    Input Required : No
    Locked : No
    Result : No
    Reporting Order : N/A
    Panel Input : No
    Sample Level : Yes
    Reset To Default Values : Yes
    Choice List : No
    Only Allow Choice : No
    Input Order : N/A
50 Nanometers
    Internal Name : FiftyNanometers
    Default Value : 50.000  nm
    Description :
    Source : Keyboard Only
    Statistics Type : None
    Number of Readings : 1
    When : Pre-Test
    Minimum : No
    Maximum : No
    Places : 3
    Notation : Fixed
    Hidden : No
    Display Only : No
    Editable Post-Test : No
    Input Required : No
    Locked : No
    Result : No
    Reporting Order : N/A
    Panel Input : No
    Sample Level : No
    Reset To Default Values : No
    Choice List : No
    Only Allow Choice : No
    Input Order : N/A
50 Point Buffer Size
    Internal Name : FiftyPtBufferSize
```

```
    Default Value : 50
    Description :
    Source : Keyboard Only
    Statistics Type : None
    Number of Readings : 1
    When : Pre-Test
    Minimum : No
    Maximum : No
    Places : 0
    Notation : Fixed
    Hidden : No
    Display Only : No
    Editable Post-Test : No
    Input Required : No
    Locked : No
    Result : No
    Reporting Order : N/A
    Panel Input : No
    Sample Level : Yes
    Reset To Default Values : No
    Choice List : No
    Only Allow Choice : No
    Input Order : N/A
5um Per Second Speed
    Internal Name : 5umPerSecond
    Default Value : 5.000  um/s
    Description : Fast speed used during the surface find
    Source : Keyboard Only
    Statistics Type : None
    Number of Readings : 1
    When : Pre-Test
    Minimum : No
    Maximum : No
    Places : 3
    Notation : Fixed
    Hidden : No
    Display Only : No
    Editable Post-Test : No
    Input Required : No
    Locked : No
    Result : No
    Reporting Order : N/A
    Panel Input : No
    Sample Level : Yes
    Reset To Default Values : Yes
    Choice List : No
```

```
    Only Allow Choice : No
    Input Order : N/A
Approach Distance To Store
    Internal Name : _ApproachDistanceToSave
    Default Value : 3000.000  nm
    Description : Distance within the approach segment over which data is ac
    quired and recorded.
    Source : Keyboard Only
    Statistics Type : None
    Number of Readings : 1
    When : Pre-Test
    Minimum : No
    Maximum : No
    Places : 3
    Notation : Fixed
    Hidden : No
    Display Only : No
    Editable Post-Test : No
    Input Required : Yes
    Locked : No
    Result : No
    Reporting Order : N/A
    Panel Input : No
    Sample Level : Yes
    Reset To Default Values : Yes
    Choice List : No
    Only Allow Choice : No
    Input Order : N/A
ApproachSegment1BufferSize
    Internal Name : ApproachSegment1BufferSize
    Default Value : 100
    Description :
    Source : Keyboard Only
    Statistics Type : None
    Number of Readings : 1
    When : Pre-Test
    Minimum : No
    Maximum : No
    Places : 0
    Notation : Fixed
    Hidden : No
    Display Only : No
    Editable Post-Test : No
    Input Required : No
    Locked : No
    Result : No
```

```
    Reporting Order : N/A
    Panel Input : No
    Sample Level : Yes
    Reset To Default Values : No
    Choice List : No
    Only Allow Choice : No
    Input Order : N/A
ApproachSegment2Buffer
    Internal Name : ApproachSegment2Buffer
    Default Value : 250
    Description :
    Source : Keyboard Only
    Statistics Type : None
    Number of Readings : 1
    When : Pre-Test
    Minimum : No
    Maximum : No
    Places : 0
    Notation : Fixed
    Hidden : No
    Display Only : No
    Editable Post-Test : No
    Input Required : No
    Locked : No
    Result : No
    Reporting Order : N/A
    Panel Input : No
    Sample Level : Yes
    Reset To Default Values : No
    Choice List : No
    Only Allow Choice : No
    Input Order : N/A
Author
    Internal Name : Author
    Default Value : Kevin Gilbert
    Description : Author of the method
    Source : Keyboard Only
    Statistics Type : None
    Number of Readings : 1
    When : Pre-Test
    Minimum : No
    Maximum : No
    Places : 0
    Notation : Fixed
    Hidden : No
    Display Only : No
```

```
    Editable Post-Test : No
    Input Required : No
    Locked : No
    Result : No
    Reporting Order : N/A
    Panel Input : No
    Sample Level : Yes
    Reset To Default Values : No
    Choice List : No
    Only Allow Choice : No
    Input Order : N/A
BufferCantileverBend
    Internal Name : BufferCantileverBend
    Default Value : 200
    Description :
    Source : Keyboard Only
    Statistics Type : None
    Number of Readings : 1
    When : Pre-Test
    Minimum : No
    Maximum : No
    Places : 0
    Notation : Fixed
    Hidden : No
    Display Only : No
    Editable Post-Test : No
    Input Required : No
    Locked : No
    Result : No
    Reporting Order : N/A
    Panel Input : No
    Sample Level : Yes
    Reset To Default Values : No
    Choice List : No
    Only Allow Choice : No
    Input Order : N/A
BufferSizePlateLoading
    Internal Name : BufferSizePlateLoading
    Default Value : 800
    Description :
    Source : Keyboard Only
    Statistics Type : None
    Number of Readings : 1
    When : Pre-Test
    Minimum : No
    Maximum : No
```

```
    Places : 0
    Notation : Fixed
    Hidden : No
    Display Only : No
    Editable Post-Test : No
    Input Required : No
    Locked : No
    Result : No
    Reporting Order : N/A
    Panel Input : No
    Sample Level : Yes
    Reset To Default Values : No
    Choice List : No
    Only Allow Choice : No
    Input Order : N/A
Contact Load Multiplier
    Internal Name : ContactLoadMultiplier
    Default Value : 3.000
    Description :
    Source : Keyboard Only
    Statistics Type : None
    Number of Readings : 1
    When : Pre-Test
    Minimum : No
    Maximum : No
    Places : 3
    Notation : Fixed
    Hidden : No
    Display Only : No
    Editable Post-Test : No
    Input Required : Yes
    Locked : No
    Result : No
    Reporting Order : N/A
    Panel Input : No
    Sample Level : Yes
    Reset To Default Values : No
    Choice List : No
    Only Allow Choice : No
    Input Order : N/A
Current Input
    Internal Name : Current
    Default Value : 0.000  mA
    Description : Input Current to run through switch
    Source : Keyboard Only
    Statistics Type : None
```

```
    Number of Readings : 1
    When : Pre-Test
    Minimum : 0.000
    Maximum : 20.000
    Places : 3
    Notation : Fixed
    Hidden : No
    Display Only : No
    Editable Post-Test : No
    Input Required : No
    Locked : No
    Result : No
    Reporting Order : N/A
    Panel Input : No
    Sample Level : Yes
    Reset To Default Values : No
    Choice List : No
    Only Allow Choice : No
    Input Order : N/A
Current Used in Test
    Internal Name : TestCurrent
    Default Value : 0.500  mA
    Description : Test Current to run through switch
    Source : Keyboard Only
    Statistics Type : None
    Number of Readings : 1
    When : Pre-Test
    Minimum : 0.000
    Maximum : 20.000
    Places : 3
    Notation : Fixed
    Hidden : No
    Display Only : No
    Editable Post-Test : No
    Input Required : No
    Locked : No
    Result : No
    Reporting Order : N/A
    Panel Input : No
    Sample Level : Yes
    Reset To Default Values : No
    Choice List : No
    Only Allow Choice : No
    Input Order : N/A
Delta X For Finding Surface
    Internal Name : _DeltaXForFindingSurface
```

```
            Default Value : 0.000  um
            Description : Instrument uses a 'practice' indent to locate the test sur
            face.
This is the distance in the x-direction of the practice indent from
the first prescribed indent on the sample.
            Source : Keyboard Only
            Statistics Type : None
            Number of Readings : 1
            When : Pre-Test
            Minimum : No
            Maximum : No
            Places : 3
            Notation : Fixed
            Hidden : No
            Display Only : No
            Editable Post-Test : No
            Input Required : Yes
            Locked : No
            Result : No
            Reporting Order : N/A
            Panel Input : No
            Sample Level : Yes
            Reset To Default Values : Yes
            Choice List : No
            Only Allow Choice : No
            Input Order : N/A
        Delta Y For Finding Surface
            Internal Name : _DeltaYForFindingSurface
            Default Value : 0.000  um
            Description : Instrument uses a 'practice' indent to locate the test sur
            face.
This is the distance in the y-direction of the practice indent from
the first prescribed indent on the sample.
            Source : Keyboard Only
            Statistics Type : None
            Number of Readings : 1
            When : Pre-Test
            Minimum : No
            Maximum : No
            Places : 3
            Notation : Fixed
            Hidden : No
            Display Only : No
            Editable Post-Test : No
            Input Required : Yes
            Locked : No
```

```
    Result : No
    Reporting Order : N/A
    Panel Input : No
    Sample Level : Yes
    Reset To Default Values : Yes
    Choice List : No
    Only Allow Choice : No
    Input Order : N/A
Displacement Gain (0-7)
    Internal Name : DisplacementGain
    Default Value : 5
    Description :
    Source : Keyboard Only
    Statistics Type : None
    Number of Readings : 1
    When : Pre-Test
    Minimum : No
    Maximum : No
    Places : 0
    Notation : Fixed
    Hidden : No
    Display Only : No
    Editable Post-Test : No
    Input Required : No
    Locked : No
    Result : No
    Reporting Order : N/A
    Panel Input : No
    Sample Level : Yes
    Reset To Default Values : Yes
    Choice List : No
    Only Allow Choice : No
    Input Order : N/A
FastApproachRate
    Internal Name : FastApproachRate
    Default Value : 1.000  um/s
    Description : Fast speed used during the surface find
    Source : Keyboard Only
    Statistics Type : None
    Number of Readings : 1
    When : Pre-Test
    Minimum : No
    Maximum : No
    Places : 3
    Notation : Fixed
    Hidden : No
```

```
    Display Only : No
    Editable Post-Test : No
    Input Required : No
    Locked : No
    Result : No
    Reporting Order : N/A
    Panel Input : No
    Sample Level : Yes
    Reset To Default Values : Yes
    Choice List : No
    Only Allow Choice : No
    Input Order : N/A
FastApproachSpeed
    Internal Name : FastApproachSpeed
    Default Value : 10.000  um/s
    Description : Fast speed used during the surface find
    Source : Keyboard Only
    Statistics Type : None
    Number of Readings : 1
    When : Pre-Test
    Minimum : No
    Maximum : No
    Places : 3
    Notation : Fixed
    Hidden : No
    Display Only : No
    Editable Post-Test : No
    Input Required : No
    Locked : No
    Result : No
    Reporting Order : N/A
    Panel Input : No
    Sample Level : Yes
    Reset To Default Values : Yes
    Choice List : No
    Only Allow Choice : No
    Input Order : N/A
Harmonic Displacement Target
    Internal Name : HarmonicDisplacementTarget
    Default Value : 50.000  nm
    Description : Target (set point) for amplitude of displacement oscillati
    on.
    Source : Keyboard Only
    Statistics Type : None
    Number of Readings : 1
    When : Pre-Test
```

```
            Minimum : No
            Maximum : No
            Places : 3
            Notation : Fixed
            Hidden : No
            Display Only : No
            Editable Post-Test : No
            Input Required : Yes
            Locked : No
            Result : No
            Reporting Order : N/A
            Panel Input : No
            Sample Level : Yes
            Reset To Default Values : Yes
            Choice List : No
            Only Allow Choice : No
            Input Order : N/A
        Harmonic Frame Correction
            Internal Name : HarmonicFrameCorrection
            Default Value : 0.000  N/m
            Description : Correction applied to the Harmonic Frame Stiffness.  This
            correction is added
directly to the Harmonic Frame Stiffness (i.e. compliances are NOT
summe d). Correction might be needed if the sample is mounted in
such a way that a ffects the frame stiffness.
            Source : Keyboard Only
            Statistics Type : None
            Number of Readings : 1
            When : Pre-Test
            Minimum : No
            Maximum : No
            Places : 3
            Notation : Fixed
            Hidden : No
            Display Only : No
            Editable Post-Test : No
            Input Required : No
            Locked : No
            Result : No
            Reporting Order : N/A
            Panel Input : No
            Sample Level : Yes
            Reset To Default Values : Yes
            Choice List : No
            Only Allow Choice : No
            Input Order : N/A
```

```
Harmonic Frequency Target
    Internal Name : FrequencySetPoint
    Default Value : 45.000  Hz
    Description : Target (set point) for harmonic frequency.
    Source : Keyboard Only
    Statistics Type : None
    Number of Readings : 1
    When : Pre-Test
    Minimum : No
    Maximum : No
    Places : 3
    Notation : Fixed
    Hidden : No
    Display Only : No
    Editable Post-Test : No
    Input Required : Yes
    Locked : No
    Result : No
    Reporting Order : N/A
    Panel Input : No
    Sample Level : Yes
    Reset To Default Values : Yes
    Choice List : No
    Only Allow Choice : No
    Input Order : N/A
HarmonicContactTrigger
    Internal Name : HarmonicContactTrigger
    Default Value : 100.000  N/m
    Description : Value used to detect contact between the cantilever and th
    e plate.
    Source : Keyboard Only
    Statistics Type : None
    Number of Readings : 1
    When : Pre-Test
    Minimum : No
    Maximum : No
    Places : 3
    Notation : Fixed
    Hidden : No
    Display Only : No
    Editable Post-Test : No
    Input Required : Yes
    Locked : No
    Result : No
    Reporting Order : N/A
    Panel Input : No
```

```
    Sample Level : Yes
    Reset To Default Values : Yes
    Choice List : No
    Only Allow Choice : No
    Input Order : N/A
HarmonicContactTriggerCantilever
    Internal Name : HarmonicContactTriggerCantilever
    Default Value : 50.000  N/m
    Description : Value used to detect contact between the cantilever and th
    e plate.
    Source : Keyboard Only
    Statistics Type : None
    Number of Readings : 1
    When : Pre-Test
    Minimum : No
    Maximum : No
    Places : 3
    Notation : Fixed
    Hidden : No
    Display Only : No
    Editable Post-Test : No
    Input Required : Yes
    Locked : No
    Result : No
    Reporting Order : N/A
    Panel Input : No
    Sample Level : Yes
    Reset To Default Values : Yes
    Choice List : No
    Only Allow Choice : No
    Input Order : N/A
HarmonicDisplacementTolerance
    Internal Name : HarmonicDisplacementTolerance
    Default Value : 3.000  nm
    Description : The tolerance for the harmonic displacement during the set
    tel time for the approach.
    Source : Keyboard Only
    Statistics Type : None
    Number of Readings : 1
    When : Pre-Test
    Minimum : No
    Maximum : No
    Places : 3
    Notation : Fixed
    Hidden : No
    Display Only : No
```

```
            Editable Post-Test : No
            Input Required : No
            Locked : No
            Result : No
            Reporting Order : N/A
            Panel Input : No
            Sample Level : Yes
            Reset To Default Values : Yes
            Choice List : No
            Only Allow Choice : No
            Input Order : N/A
        Level Crossing Resistance Change
            Internal Name : LevelCrossingResistanceChange
            Default Value : 0.500  Ohm
            Description : Data Rate to collect when resistance changes by X ohms
            Source : Keyboard Only
            Statistics Type : None
            Number of Readings : 1
            When : Pre-Test
            Minimum : No
            Maximum : No
            Places : 3
            Notation : Fixed
            Hidden : No
            Display Only : No
            Editable Post-Test : No
            Input Required : Yes
            Locked : No
            Result : No
            Reporting Order : N/A
            Panel Input : No
            Sample Level : Yes
            Reset To Default Values : Yes
            Choice List : No
            Only Allow Choice : No
            Input Order : N/A
        LevelCrossingMeasuredVoltageChange
            Internal Name : LevelCrossingMeasuredVoltageChange
            Default Value : 0.0005  V
            Description : Measured voltage change which corresponds to 1 Ohm measure
            d resistance
change.  Should be equal to current (in amps)
            Source : Keyboard Only
            Statistics Type : None
            Number of Readings : 1
            When : Pre-Test
```

```
            Minimum : No
            Maximum : No
            Places : 4
            Notation : Fixed
            Hidden : No
            Display Only : No
            Editable Post-Test : No
            Input Required : No
            Locked : No
            Result : No
            Reporting Order : N/A
            Panel Input : No
            Sample Level : Yes
            Reset To Default Values : Yes
            Choice List : No
            Only Allow Choice : No
            Input Order : N/A
        LevelCrossingMeasuredVoltageDelta
            Internal Name : LevelCrossingMeasuredVoltageDelta
            Default Value : 0.0005  V
            Description : Measured voltage change which corresponds to 1 Ohm measure
            d resistance
change.  Should be equal to current (in amps)
            Source : Keyboard Only
            Statistics Type : None
            Number of Readings : 1
            When : Pre-Test
            Minimum : No
            Maximum : No
            Places : 4
            Notation : Fixed
            Hidden : No
            Display Only : No
            Editable Post-Test : No
            Input Required : No
            Locked : No
            Result : No
            Reporting Order : N/A
            Panel Input : No
            Sample Level : Yes
            Reset To Default Values : Yes
            Choice List : No
            Only Allow Choice : No
            Input Order : N/A
        Loading Rate After Plate Contact
            Internal Name : LoadingRateAfterPlateContact
```

```
    Default Value : 50.000  uN/s
    Description :
    Source : Keyboard Only
    Statistics Type : None
    Number of Readings : 1
    When : Pre-Test
    Minimum : No
    Maximum : No
    Places : 3
    Notation : Fixed
    Hidden : No
    Display Only : No
    Editable Post-Test : No
    Input Required : Yes
    Locked : No
    Result : No
    Reporting Order : N/A
    Panel Input : No
    Sample Level : Yes
    Reset To Default Values : Yes
    Choice List : No
    Only Allow Choice : No
    Input Order : N/A
LoadingRate
    Internal Name : LoadingRate
    Default Value : 25.000  uN/s
    Description :
    Source : Keyboard Only
    Statistics Type : None
    Number of Readings : 1
    When : Pre-Sample
    Minimum : No
    Maximum : No
    Places : 3
    Notation : Fixed
    Hidden : No
    Display Only : No
    Editable Post-Test : No
    Input Required : Yes
    Locked : No
    Result : No
    Reporting Order : N/A
    Panel Input : No
    Sample Level : Yes
    Reset To Default Values : Yes
    Choice List : No
```

```
    Only Allow Choice : No
    Input Order : N/A
MaximumContactForce
    Internal Name : MaximumContactForce
    Default Value : 400.000  uN
    Description : Max Force for plate contact
    Source : Keyboard Only
    Statistics Type : None
    Number of Readings : 1
    When : Pre-Test
    Minimum : No
    Maximum : No
    Places : 3
    Notation : Fixed
    Hidden : No
    Display Only : No
    Editable Post-Test : No
    Input Required : Yes
    Locked : No
    Result : No
    Reporting Order : N/A
    Panel Input : No
    Sample Level : Yes
    Reset To Default Values : Yes
    Choice List : No
    Only Allow Choice : No
    Input Order : N/A
MaximumContactForceXtwo
    Internal Name : MaximumContactForceXtwo
    Default Value : 600.000  uN
    Description : 2 x Max Force for plate contact
    Source : Keyboard Only
    Statistics Type : None
    Number of Readings : 1
    When : Pre-Test
    Minimum : No
    Maximum : No
    Places : 3
    Notation : Fixed
    Hidden : No
    Display Only : No
    Editable Post-Test : No
    Input Required : Yes
    Locked : No
    Result : No
    Reporting Order : N/A
```

```
    Panel Input : No
    Sample Level : Yes
    Reset To Default Values : Yes
    Choice List : No
    Only Allow Choice : No
    Input Order : N/A
MaxsUnloadContactSegmentTime
    Internal Name : MaxsUnloadContactSegmentTime
    Default Value : 100.000  s
    Description : Maximum allowable time for a single segment.
    Source : Keyboard Only
    Statistics Type : None
    Number of Readings : 1
    When : Pre-Test
    Minimum : No
    Maximum : No
    Places : 3
    Notation : Fixed
    Hidden : No
    Display Only : No
    Editable Post-Test : No
    Input Required : No
    Locked : No
    Result : No
    Reporting Order : N/A
    Panel Input : No
    Sample Level : Yes
    Reset To Default Values : Yes
    Choice List : No
    Only Allow Choice : No
    Input Order : N/A
Memo
    Internal Name : _Memo
    Default Value :
    Description : This input is used to hold the sample memo.
    Source : Keyboard Only
    Statistics Type : None
    Number of Readings : 1
    When : Pre-Test
    Minimum : No
    Maximum : No
    Places : 0
    Notation : Fixed
    Hidden : Yes
    Display Only : No
    Editable Post-Test : No
```

```
            Input Required : No
            Locked : No
            Result : No
            Reporting Order : N/A
            Panel Input : No
            Sample Level : Yes
            Reset To Default Values : Yes
            Choice List : No
            Only Allow Choice : No
            Input Order : N/A
        Number of Tests in this Sample
            Internal Name : _MaxSpecimens
            Default Value : 0.000
            Description : Used for batch mode.  Do not modify or delete.
            Source : Keyboard Only
            Statistics Type : None
            Number of Readings : 1
            When : Pre-Test
            Minimum : No
            Maximum : No
            Places : 3
            Notation : Fixed
            Hidden : Yes
            Display Only : No
            Editable Post-Test : No
            Input Required : No
            Locked : No
            Result : No
            Reporting Order : N/A
            Panel Input : No
            Sample Level : Yes
            Reset To Default Values : No
            Choice List : No
            Only Allow Choice : No
            Input Order : N/A
        Part Number and Version
            Internal Name : PartNumberandVersion
            Default Value : see description field
            Description : Part number:  XPF-11435
Version: 1 For Version Control history, consult the documentation
for this method.
            Source : Keyboard Only
            Statistics Type : None
            Number of Readings : 1
            When : Pre-Test
            Minimum : No
```

```
            Maximum : No
            Places : 0
            Notation : Fixed
            Hidden : No
            Display Only : No
            Editable Post-Test : No
            Input Required : No
            Locked : No
            Result : No
            Reporting Order : N/A
            Panel Input : No
            Sample Level : Yes
            Reset To Default Values : No
            Choice List : No
            Only Allow Choice : No
            Input Order : N/A
        PZTCalSlopeVoltsperMicron
            Internal Name : PZTCalSlopeVoltsperMicron
            Default Value : 0.787  V
            Description : Control Voltage calibrated for open loop P-841 operation
0.812 V/um is linearly interpolated for 0-3V travel Changes to Freq
Generator: Amp = 2*V/um Offset = V/um
            Source : Keyboard Only
            Statistics Type : None
            Number of Readings : 1
            When : Pre-Test
            Minimum : No
            Maximum : No
            Places : 3
            Notation : Fixed
            Hidden : No
            Display Only : No
            Editable Post-Test : No
            Input Required : No
            Locked : No
            Result : No
            Reporting Order : N/A
            Panel Input : No
            Sample Level : Yes
            Reset To Default Values : No
            Choice List : No
            Only Allow Choice : No
            Input Order : N/A
        PZTVoltage
            Internal Name : PZTVoltage
            Default Value : 0.000  V
```

```
    Description : Voltage used for setting DACOUT0. This input is set in for
    mulas.
    Source : Keyboard Only
    Statistics Type : None
    Number of Readings : 1
    When : In Test Segment
    Minimum : 0.000
    Maximum : 10.000
    Places : 3
    Notation : Fixed
    Hidden : No
    Display Only : No
    Editable Post-Test : No
    Input Required : No
    Locked : No
    Result : No
    Reporting Order : N/A
    Panel Input : No
    Sample Level : Yes
    Reset To Default Values : Yes
    Choice List : No
    Only Allow Choice : No
    Input Order : N/A
PZTVoltageLoadingRate
    Internal Name : PZTVoltageLoadingRate
    Default Value : 250.000  mV/s
    Description :
    Source : Keyboard Only
    Statistics Type : None
    Number of Readings : 1
    When : Pre-Test
    Minimum : No
    Maximum : No
    Places : 3
    Notation : Fixed
    Hidden : No
    Display Only : No
    Editable Post-Test : No
    Input Required : No
    Locked : No
    Result : No
    Reporting Order : N/A
    Panel Input : No
    Sample Level : Yes
    Reset To Default Values : No
    Choice List : No
```

```
    Only Allow Choice : No
    Input Order : N/A
Ramp Condition Ignored Time
    Internal Name : RampConditionIgnoredTime
    Default Value : 2.000  s
    Description :
    Source : Keyboard Only
    Statistics Type : None
    Number of Readings : 1
    When : Pre-Test
    Minimum : No
    Maximum : No
    Places : 3
    Notation : Fixed
    Hidden : No
    Display Only : No
    Editable Post-Test : No
    Input Required : No
    Locked : No
    Result : No
    Reporting Order : N/A
    Panel Input : No
    Sample Level : Yes
    Reset To Default Values : Yes
    Choice List : No
    Only Allow Choice : No
    Input Order : N/A
RelaySwitch
    Internal Name : RelaySwitch
    Default Value : 0
    Description :
    Source : Keyboard Only
    Statistics Type : None
    Number of Readings : 1
    When : In Test Segment
    Minimum : No
    Maximum : No
    Places : 0
    Notation : Fixed
    Hidden : No
    Display Only : No
    Editable Post-Test : No
    Input Required : No
    Locked : No
    Result : No
    Reporting Order : N/A
```

```
    Panel Input : No
    Sample Level : Yes
    Reset To Default Values : Yes
    Choice List : No
    Only Allow Choice : No
    Input Order : N/A
Resistance Trigger
    Internal Name : ResistanceTrigger
    Default Value : 30.000  Ohm
    Description : Trigger that indicates a closed switch during loading of t
    he contact.
    Source : Keyboard Only
    Statistics Type : None
    Number of Readings : 1
    When : Pre-Test
    Minimum : No
    Maximum : No
    Places : 3
    Notation : Fixed
    Hidden : No
    Display Only : No
    Editable Post-Test : No
    Input Required : Yes
    Locked : No
    Result : No
    Reporting Order : N/A
    Panel Input : No
    Sample Level : Yes
    Reset To Default Values : Yes
    Choice List : No
    Only Allow Choice : No
    Input Order : N/A
ResistanceTriggerThresholdCalc
    Internal Name : ResistanceTriggerThresholdCalc
    Default Value : 13.000  Ohm
    Description : Trigger that indicates a closed switch during loading of t
    he contact.
    Source : Keyboard Only
    Statistics Type : None
    Number of Readings : 1
    When : Pre-Test
    Minimum : No
    Maximum : No
    Places : 3
    Notation : Fixed
    Hidden : No
```

```
            Display Only : No
            Editable Post-Test : No
            Input Required : Yes
            Locked : No
            Result : No
            Reporting Order : N/A
            Panel Input : No
            Sample Level : Yes
            Reset To Default Values : Yes
            Choice List : No
            Only Allow Choice : No
            Input Order : N/A
        SlowApproachRate
            Internal Name : SlowApproachRate
            Default Value : 0.300  um/s
            Description : Fast speed used during the surface find
            Source : Keyboard Only
            Statistics Type : None
            Number of Readings : 1
            When : Pre-Test
            Minimum : No
            Maximum : No
            Places : 3
            Notation : Fixed
            Hidden : No
            Display Only : No
            Editable Post-Test : No
            Input Required : No
            Locked : No
            Result : No
            Reporting Order : N/A
            Panel Input : No
            Sample Level : Yes
            Reset To Default Values : Yes
            Choice List : No
            Only Allow Choice : No
            Input Order : N/A
        SlowLevelCrossingMeasuredVoltageChange
            Internal Name : SlowLevelCrossingMeasuredVoltageChange
            Default Value : 0.003  V
            Description : Measured voltage change which corresponds to 1 Ohm measure
            d resistance
change.  Should be equal to current (in amps)
            Source : Keyboard Only
            Statistics Type : None
            Number of Readings : 1
```

```
            When : Pre-Test
            Minimum : No
            Maximum : No
            Places : 3
            Notation : Fixed
            Hidden : No
            Display Only : No
            Editable Post-Test : No
            Input Required : No
            Locked : No
            Result : No
            Reporting Order : N/A
            Panel Input : No
            Sample Level : Yes
            Reset To Default Values : Yes
            Choice List : No
            Only Allow Choice : No
            Input Order : N/A
        Surface Approach Distance
            Internal Name : _SurfaceApproachDistance
            Default Value : 6000.000  nm
            Description : The indenter begins 'looking' for the test surface at this
             (estimated) distance
above the surface.
            Source : Keyboard Only
            Statistics Type : None
            Number of Readings : 1
            When : Pre-Test
            Minimum : No
            Maximum : No
            Places : 3
            Notation : Fixed
            Hidden : No
            Display Only : No
            Editable Post-Test : No
            Input Required : Yes
            Locked : No
            Result : No
            Reporting Order : N/A
            Panel Input : No
            Sample Level : Yes
            Reset To Default Values : Yes
            Choice List : No
            Only Allow Choice : No
            Input Order : N/A
        Surface Approach Sensitivity
```

```
            Internal Name : _SurfaceApproachSensitivity
            Default Value : 10.000  %
            Description : This value sets the criteria that the indenter uses to dec
            ide whether it has
contacted the test surface.  A lower value causes more sensitive
surface
 detection,
but increases the likelihood of false detection (and vice versa).
            Source : Keyboard Only
            Statistics Type : None
            Number of Readings : 1
            When : Pre-Sample
            Minimum : No
            Maximum : No
            Places : 3
            Notation : Fixed
            Hidden : No
            Display Only : No
            Editable Post-Test : No
            Input Required : Yes
            Locked : No
            Result : No
            Reporting Order : N/A
            Panel Input : No
            Sample Level : Yes
            Reset To Default Values : Yes
            Choice List : No
            Only Allow Choice : No
            Input Order : N/A
        Surface Approach Velocity
            Internal Name : _SurfaceApproachVelocity
            Default Value : 30.000  nm/s
            Description : Speed with which the indenter approaches the test surface.

            Source : Keyboard Only
            Statistics Type : None
            Number of Readings : 1
            When : Pre-Sample
            Minimum : No
            Maximum : No
            Places : 3
            Notation : Fixed
            Hidden : No
            Display Only : No
            Editable Post-Test : No
            Input Required : Yes
```

```
            Locked : No
            Result : No
            Reporting Order : N/A
            Panel Input : No
            Sample Level : Yes
            Reset To Default Values : Yes
            Choice List : No
            Only Allow Choice : No
            Input Order : N/A
        SurfaceApproachDistance3rdSurfFind
            Internal Name : SurfaceApproachDistance3rdSurfFind
            Default Value : 4000.000  nm
            Description : The indenter begins 'looking' for the test surface at this
             (estimated) distance
above the surface.
            Source : Keyboard Only
            Statistics Type : None
            Number of Readings : 1
            When : Pre-Test
            Minimum : No
            Maximum : No
            Places : 3
            Notation : Fixed
            Hidden : No
            Display Only : No
            Editable Post-Test : No
            Input Required : Yes
            Locked : No
            Result : No
            Reporting Order : N/A
            Panel Input : No
            Sample Level : Yes
            Reset To Default Values : Yes
            Choice List : No
            Only Allow Choice : No
            Input Order : N/A
        Tol
            Internal Name : Tol
            Default Value : 0.010  mN/s
            Description : Tolerance for defining the start of unload.  See formula f
            or Stiffness channel.
            Source : Keyboard Only
            Statistics Type : None
            Number of Readings : 1
            When : Pre-Sample
            Minimum : No
```

```
    Maximum : No
    Places : 3
    Notation : Fixed
    Hidden : Yes
    Display Only : No
    Editable Post-Test : No
    Input Required : No
    Locked : No
    Result : No
    Reporting Order : N/A
    Panel Input : No
    Sample Level : Yes
    Reset To Default Values : Yes
    Choice List : No
    Only Allow Choice : No
    Input Order : N/A
VoltageTolerance
    Internal Name : VoltageTolerance
    Default Value : 2.300  V/s
    Description : Tolerance for rate of voltage change to trigger pull off f
    orce calc
    Source : Keyboard Only
    Statistics Type : None
    Number of Readings : 1
    When : Pre-Sample
    Minimum : No
    Maximum : No
    Places : 3
    Notation : Fixed
    Hidden : Yes
    Display Only : No
    Editable Post-Test : Yes
    Input Required : No
    Locked : No
    Result : No
    Reporting Order : N/A
    Panel Input : No
    Sample Level : Yes
    Reset To Default Values : Yes
    Choice List : No
    Only Allow Choice : No
    Input Order : N/A
X Test Position
    Internal Name : _XLocation
    Default Value : ****  um
    Description : The x coordinate of the desired test position.
```

```
    Source : Keyboard Only
    Statistics Type : None
    Number of Readings : 1
    When : Pre-Test
    Minimum : No
    Maximum : No
    Places : 3
    Notation : Fixed
    Hidden : No
    Display Only : No
    Editable Post-Test : No
    Input Required : No
    Locked : No
    Result : No
    Reporting Order : N/A
    Panel Input : Yes
    Sample Level : No
    Reset To Default Values : Yes
    Choice List : No
    Only Allow Choice : No
    Input Order : N/A
X Y Table Speed
    Internal Name : XYTableSpeed
    Default Value : 1.000  mm/s
    Description : Velocity of stages.
    Source : Keyboard Only
    Statistics Type : None
    Number of Readings : 1
    When : Pre-Test
    Minimum : No
    Maximum : No
    Places : 3
    Notation : Fixed
    Hidden : No
    Display Only : No
    Editable Post-Test : No
    Input Required : No
    Locked : No
    Result : No
    Reporting Order : N/A
    Panel Input : No
    Sample Level : Yes
    Reset To Default Values : Yes
    Choice List : No
    Only Allow Choice : No
    Input Order : N/A
```

```
Y Test Position
    Internal Name : _YLocation
    Default Value : ****  um
    Description : The y coordinate of the desired test position.
    Source : Keyboard Only
    Statistics Type : None
    Number of Readings : 1
    When : Pre-Test
    Minimum : No
    Maximum : No
    Places : 3
    Notation : Fixed
    Hidden : No
    Display Only : No
    Editable Post-Test : No
    Input Required : No
    Locked : No
    Result : No
    Reporting Order : N/A
    Panel Input : Yes
    Sample Level : No
    Reset To Default Values : Yes
    Choice List : No
    Only Allow Choice : No
    Input Order : N/A
ZeroDisplacement
    Internal Name : ZeroDisplacement
    Default Value : 0.000  um
    Description : Zero Displacement used durignt the surface find test segme
    nt.
    Source : Keyboard Only
    Statistics Type : None
    Number of Readings : 1
    When : Pre-Test
    Minimum : No
    Maximum : No
    Places : 3
    Notation : Fixed
    Hidden : No
    Display Only : No
    Editable Post-Test : No
    Input Required : No
    Locked : No
    Result : No
    Reporting Order : N/A
    Panel Input : No
```

```
        Sample Level : Yes
        Reset To Default Values : Yes
        Choice List : No
        Only Allow Choice : No
        Input Order : N/A
    ZeroForceAmp
        Internal Name : ZeroForceAmp
        Default Value : 0.000  mN
        Description : Used to zero harmonic oscillation at the start of unload.
        Source : Keyboard Only
        Statistics Type : None
        Number of Readings : 1
        When : Pre-Test
        Minimum : No
        Maximum : No
        Places : 3
        Notation : Fixed
        Hidden : No
        Display Only : No
        Editable Post-Test : No
        Input Required : No
        Locked : No
        Result : No
        Reporting Order : N/A
        Panel Input : No
        Sample Level : Yes
        Reset To Default Values : Yes
        Choice List : No
        Only Allow Choice : No
        Input Order : N/A
Internal Use
    Load Counter
        Internal Name : LoadCounter
        Default Value : 1
        Description : Initial value
        Source : Keyboard Only
        Statistics Type : None
        Number of Readings : 1
        When : Pre-Test
        Minimum : No
        Maximum : No
        Places : 0
        Notation : Fixed
        Hidden : No
        Display Only : No
        Editable Post-Test : No
```

```
    Input Required : No
    Locked : No
    Result : No
    Reporting Order : N/A
    Panel Input : No
    Sample Level : No
    Reset To Default Values : Yes
    Choice List : No
    Only Allow Choice : No
    Input Order : N/A
Max Segment Time
    Internal Name : MaxSegmentTime
    Default Value : 1000.000  s
    Description : Maximum allowable time for a single segment.
    Source : Keyboard Only
    Statistics Type : None
    Number of Readings : 1
    When : Pre-Test
    Minimum : No
    Maximum : No
    Places : 3
    Notation : Fixed
    Hidden : No
    Display Only : No
    Editable Post-Test : No
    Input Required : No
    Locked : No
    Result : No
    Reporting Order : N/A
    Panel Input : No
    Sample Level : Yes
    Reset To Default Values : Yes
    Choice List : No
    Only Allow Choice : No
    Input Order : N/A
Newtons Per Meter
    Internal Name : NewtonsPerMeter
    Default Value : 1.000  N/m
    Description : Used for clarification of dimensions in various calculatio
    ns.
    Source : Keyboard Only
    Statistics Type : None
    Number of Readings : 1
    When : Pre-Test
    Minimum : No
    Maximum : No
```

```
            Places : 3
            Notation : Fixed
            Hidden : Yes
            Display Only : No
            Editable Post-Test : No
            Input Required : No
            Locked : No
            Result : No
            Reporting Order : N/A
            Panel Input : No
            Sample Level : Yes
            Reset To Default Values : Yes
            Choice List : No
            Only Allow Choice : No
            Input Order : N/A
        Surface Displacement
            Internal Name : _SurfaceDisplacement
            Default Value : 100.000  mm
            Description : Used by several test segments to keep track of the current
             displacement
value at the surface of the sample.  Do not delete.
            Source : Keyboard Only
            Statistics Type : None
            Number of Readings : 1
            When : Pre-Sample
            Minimum : No
            Maximum : No
            Places : 3
            Notation : Fixed
            Hidden : No
            Display Only : No
            Editable Post-Test : No
            Input Required : No
            Locked : No
            Result : No
            Reporting Order : N/A
            Panel Input : No
            Sample Level : Yes
            Reset To Default Values : Yes
            Choice List : No
            Only Allow Choice : No
            Input Order : N/A
    Hold Segment Inputs
        Drift Determination Time
            Internal Name : DriftDeterminationTime
            Default Value : 10.000  s
```

```
            Description : Time over which the force on the indenter is held at a sma
            ll, constant value.
Data acquired during this time are used to determine thermal drift.
            Source : Keyboard Only
            Statistics Type : None
            Number of Readings : 1
            When : Pre-Test
            Minimum : No
            Maximum : No
            Places : 3
            Notation : Fixed
            Hidden : No
            Display Only : No
            Editable Post-Test : No
            Input Required : No
            Locked : No
            Result : No
            Reporting Order : N/A
            Panel Input : No
            Sample Level : Yes
            Reset To Default Values : Yes
            Choice List : No
            Only Allow Choice : No
            Input Order : N/A
        Settle Time
            Internal Name : SettleTime
            Default Value : 5.000  s
            Description : Settling time before hold for thermal drift calculation.
            Source : Keyboard Only
            Statistics Type : None
            Number of Readings : 1
            When : Pre-Test
            Minimum : No
            Maximum : No
            Places : 3
            Notation : Fixed
            Hidden : No
            Display Only : No
            Editable Post-Test : No
            Input Required : No
            Locked : No
            Result : No
            Reporting Order : N/A
            Panel Input : No
            Sample Level : Yes
            Reset To Default Values : Yes
```

```
        Choice List : No
        Only Allow Choice : No
        Input Order : N/A
Data Acquistion Inputs
    Data Acquisition Rate
        Internal Name : DataRate
        Default Value : 5.000  Hz
        Description : Data acquisition rate
        Source : Keyboard Only
        Statistics Type : None
        Number of Readings : 1
        When : Pre-Test
        Minimum : No
        Maximum : No
        Places : 3
        Notation : Fixed
        Hidden : No
        Display Only : No
        Editable Post-Test : No
        Input Required : No
        Locked : No
        Result : No
        Reporting Order : N/A
        Panel Input : No
        Sample Level : Yes
        Reset To Default Values : Yes
        Choice List : No
        Only Allow Choice : No
        Input Order : N/A
    Drift Determination Acquisition Rate
        Internal Name : DriftDeterminationAcquisitionRate
        Default Value : 0.500  Hz
        Description : Data acquisition rate during hold for thermal drift correc
        tion.
        Source : Keyboard Only
        Statistics Type : None
        Number of Readings : 1
        When : Pre-Sample
        Minimum : No
        Maximum : No
        Places : 3
        Notation : Fixed
        Hidden : No
        Display Only : No
        Editable Post-Test : No
        Input Required : No
```

```
            Locked : No
            Result : No
            Reporting Order : N/A
            Panel Input : No
            Sample Level : Yes
            Reset To Default Values : Yes
            Choice List : No
            Only Allow Choice : No
            Input Order : N/A
        Outer Loop Rate
            Internal Name : _OuterLoopRate
            Default Value : 100.000  Hz
            Description : Data acquisition rate.  Do not delete.
            Source : Keyboard Only
            Statistics Type : None
            Number of Readings : 1
            When : Pre-Test
            Minimum : No
            Maximum : No
            Places : 3
            Notation : Fixed
            Hidden : No
            Display Only : No
            Editable Post-Test : No
            Input Required : No
            Locked : No
            Result : No
            Reporting Order : N/A
            Panel Input : No
            Sample Level : Yes
            Reset To Default Values : Yes
            Choice List : No
            Only Allow Choice : No
            Input Order : N/A
    Oliver & Pharr Constants
        Beta
            Internal Name : Beta
            Default Value : 1.034
            Description : Factor which allows one to apply the axisymmetric Sneddon
            contact solution to
indentation with pyramids.
            Source : Keyboard Only
            Statistics Type : None
            Number of Readings : 1
            When : Pre-Sample
            Minimum : No
```

```
    Maximum : No
    Places : 3
    Notation : Fixed
    Hidden : No
    Display Only : No
    Editable Post-Test : No
    Input Required : No
    Locked : No
    Result : No
    Reporting Order : N/A
    Panel Input : No
    Sample Level : Yes
    Reset To Default Values : Yes
    Choice List : Yes
    Only Allow Choice : No
    Input Order : N/A
Epsilon
    Internal Name : Epsilon
    Default Value : 0.750
    Description : Geometric factor used in the calculation of contact depth.

    Source : Keyboard Only
    Statistics Type : None
    Number of Readings : 1
    When : Pre-Test
    Minimum : No
    Maximum : No
    Places : 3
    Notation : Fixed
    Hidden : No
    Display Only : No
    Editable Post-Test : No
    Input Required : No
    Locked : No
    Result : No
    Reporting Order : N/A
    Panel Input : No
    Sample Level : Yes
    Reset To Default Values : Yes
    Choice List : No
    Only Allow Choice : No
    Input Order : N/A
Indenter Poissons Ratio
    Internal Name : IndenterTipPoissonsRatio
    Default Value : 0.070
    Description : Poisson ratio for indenter material.  Default is for diamo
```

```
        nd.
        Source : Keyboard Only
        Statistics Type : None
        Number of Readings : 1
        When : Pre-Sample
        Minimum : No
        Maximum : No
        Places : 3
        Notation : Fixed
        Hidden : No
        Display Only : No
        Editable Post-Test : No
        Input Required : No
        Locked : No
        Result : No
        Reporting Order : N/A
        Panel Input : No
        Sample Level : Yes
        Reset To Default Values : Yes
        Choice List : No
        Only Allow Choice : No
        Input Order : N/A
Segment Types
    CyclingSegment
        Internal Name : CyclingSegment
        Default Value : 800
        Description :
        Source : Keyboard Only
        Statistics Type : None
        Number of Readings : 1
        When : Pre-Test
        Minimum : No
        Maximum : No
        Places : 0
        Notation : Fixed
        Hidden : No
        Display Only : No
        Editable Post-Test : No
        Input Required : No
        Locked : No
        Result : No
        Reporting Order : N/A
        Panel Input : No
        Sample Level : Yes
        Reset To Default Values : No
        Choice List : No
```

```
    Only Allow Choice : No
    Input Order : N/A
Hold Segment Type
    Internal Name : Hold
    Default Value : 300
    Description : Integer used to designate a test segment as a specific seg
    ment type.
    Source : Keyboard Only
    Statistics Type : None
    Number of Readings : 1
    When : Pre-Test
    Minimum : No
    Maximum : No
    Places : 0
    Notation : Fixed
    Hidden : No
    Display Only : No
    Editable Post-Test : No
    Input Required : No
    Locked : No
    Result : No
    Reporting Order : N/A
    Panel Input : No
    Sample Level : Yes
    Reset To Default Values : Yes
    Choice List : No
    Only Allow Choice : No
    Input Order : N/A
Load Segment Type
    Internal Name : Load
    Default Value : 0
    Description : Integer used to designate a test segment as a specific seg
    ment type.
    Source : Keyboard Only
    Statistics Type : None
    Number of Readings : 1
    When : Pre-Test
    Minimum : No
    Maximum : No
    Places : 0
    Notation : Fixed
    Hidden : No
    Display Only : No
    Editable Post-Test : No
    Input Required : No
    Locked : No
```

```
    Result : No
    Reporting Order : N/A
    Panel Input : No
    Sample Level : Yes
    Reset To Default Values : Yes
    Choice List : No
    Only Allow Choice : No
    Input Order : N/A
LoadContact Segment Type
    Internal Name : LoadContact
    Default Value : 700
    Description :
    Source : Keyboard Only
    Statistics Type : None
    Number of Readings : 1
    When : Pre-Test
    Minimum : No
    Maximum : No
    Places : 0
    Notation : Fixed
    Hidden : No
    Display Only : No
    Editable Post-Test : No
    Input Required : No
    Locked : No
    Result : No
    Reporting Order : N/A
    Panel Input : No
    Sample Level : Yes
    Reset To Default Values : No
    Choice List : No
    Only Allow Choice : No
    Input Order : N/A
Thermal Drift Hold Segment Type
    Internal Name : ThermalDriftHold
    Default Value : 400
    Description : Integer used to designate a test segment as a specific seg
    ment type.
    Source : Keyboard Only
    Statistics Type : None
    Number of Readings : 1
    When : Pre-Test
    Minimum : No
    Maximum : No
    Places : 0
    Notation : Fixed
```

```
    Hidden : No
    Display Only : No
    Editable Post-Test : No
    Input Required : No
    Locked : No
    Result : No
    Reporting Order : N/A
    Panel Input : No
    Sample Level : Yes
    Reset To Default Values : Yes
    Choice List : No
    Only Allow Choice : No
    Input Order : N/A
Unload From Peak Segment Type
    Internal Name : UnloadFromPeak
    Default Value : 600
    Description : Integer used to designate a test segment as a specific seg
    ment type.
    Source : Keyboard Only
    Statistics Type : None
    Number of Readings : 1
    When : Pre-Test
    Minimum : No
    Maximum : No
    Places : 0
    Notation : Fixed
    Hidden : No
    Display Only : No
    Editable Post-Test : No
    Input Required : No
    Locked : No
    Result : No
    Reporting Order : N/A
    Panel Input : No
    Sample Level : Yes
    Reset To Default Values : Yes
    Choice List : No
    Only Allow Choice : No
    Input Order : N/A
Unload Segment Type
    Internal Name : Unload
    Default Value : 500
    Description : Integer used to designate a test segment as a specific seg
    ment type.
    Source : Keyboard Only
    Statistics Type : None
```

```
            Number of Readings : 1
            When : Pre-Test
            Minimum : No
            Maximum : No
            Places : 0
            Notation : Fixed
            Hidden : No
            Display Only : No
            Editable Post-Test : No
            Input Required : No
            Locked : No
            Result : No
            Reporting Order : N/A
            Panel Input : No
            Sample Level : Yes
            Reset To Default Values : Yes
            Choice List : No
            Only Allow Choice : No
            Input Order : N/A
    Reported Calculation Inputs
        Frame Stiffness Correction
            Internal Name : FrameStiffnessCorrection
            Default Value : 0.000  N/m
            Description : Correction applied to the Frame Stiffness.  This correctio
            n is added directly
to the Frame Stiffness (i.e. compliances are NOT summed).
Correction mi ght be needed if the sample is mounted in such a way
that affects the frame stiffness.
            Source : Keyboard Only
            Statistics Type : None
            Number of Readings : 1
            When : Pre-Test
            Minimum : No
            Maximum : No
            Places : 3
            Notation : Fixed
            Hidden : No
            Display Only : No
            Editable Post-Test : Yes
            Input Required : No
            Locked : No
            Result : No
            Reporting Order : N/A
            Panel Input : No
            Sample Level : Yes
            Reset To Default Values : Yes
```

```
            Choice List : No
            Only Allow Choice : No
            Input Order : N/A
        Percent Unload In Stiffness Calculation
            Internal Name : PercentUnloadInStiffnessCalc
            Default Value : 50.000  %
            Description : Percent of unloading curve used in the calculation of stif
            fness from unload.
            Source : Keyboard Only
            Statistics Type : None
            Number of Readings : 1
            When : Pre-Test
            Minimum : No
            Maximum : No
            Places : 3
            Notation : Fixed
            Hidden : No
            Display Only : No
            Editable Post-Test : Yes
            Input Required : No
            Locked : No
            Result : No
            Reporting Order : N/A
            Panel Input : No
            Sample Level : Yes
            Reset To Default Values : Yes
            Choice List : No
            Only Allow Choice : No
            Input Order : N/A
        Perform Drift Correction
            Internal Name : PerformDriftCorrection
            Default Value : 1
            Description : Flag that determines whether the displacement data are cor
            rected for
thermal expansion/contraction of the test material and/or equipment.
 A value of unity means that the correction will be performed.  Note: thi
 s
input should be set to zero when testing polymers or metals that
creep.
            Source : Keyboard Only
            Statistics Type : None
            Number of Readings : 1
            When : Pre-Test
            Minimum : No
            Maximum : No
            Places : 0
```

```
            Notation : Fixed
            Hidden : No
            Display Only : No
            Editable Post-Test : Yes
            Input Required : No
            Locked : No
            Result : No
            Reporting Order : N/A
            Panel Input : No
            Sample Level : Yes
            Reset To Default Values : No
            Choice List : Yes
            Only Allow Choice : Yes
            Input Order : N/A
    Reported Test Inputs
        Allowable Drift Rate
            Internal Name : _AllowableDriftRate
            Default Value : 8.000  nm/s
            Description : Thermal stability criteria for initiating tests on a sampl
            e.   While the indenter is in
contact with the test surface under a small constant force, the time
rat e of change in the displacement must be less than this value.
The lower the value, the longer the instrument will wait before
initiating testing on a sample.
            Source : Keyboard Only
            Statistics Type : None
            Number of Readings : 1
            When : Pre-Sample
            Minimum : No
            Maximum : No
            Places : 3
            Notation : Fixed
            Hidden : No
            Display Only : No
            Editable Post-Test : No
            Input Required : Yes
            Locked : No
            Result : No
            Reporting Order : N/A
            Panel Input : No
            Sample Level : Yes
            Reset To Default Values : Yes
            Choice List : No
            Only Allow Choice : No
            Input Order : N/A
        Load Rate Multiple For Unload Rate
```

```
    Internal Name : LoadRateMultipleForUnloadRate
    Default Value : 1
    Description : This number is multiplied by the last loading rate to get
    the unloading rate.
    Source : Keyboard Only
    Statistics Type : None
    Number of Readings : 1
    When : Pre-Test
    Minimum : No
    Maximum : No
    Places : 0
    Notation : Fixed
    Hidden : No
    Display Only : No
    Editable Post-Test : No
    Input Required : Yes
    Locked : No
    Result : No
    Reporting Order : N/A
    Panel Input : No
    Sample Level : Yes
    Reset To Default Values : Yes
    Choice List : No
    Only Allow Choice : No
    Input Order : N/A
Maximum Load
    Internal Name : MaximumLoad
    Default Value : 10.000  mN
    Description : Peak load for the final loading cycle.
    Source : Keyboard Only
    Statistics Type : None
    Number of Readings : 1
    When : Pre-Test
    Minimum : No
    Maximum : No
    Places : 3
    Notation : Fixed
    Hidden : No
    Display Only : No
    Editable Post-Test : No
    Input Required : No
    Locked : No
    Result : No
    Reporting Order : N/A
    Panel Input : No
    Sample Level : Yes
```

```
            Reset To Default Values : Yes
            Choice List : No
            Only Allow Choice : No
            Input Order : N/A
        Peak Hold Time
            Internal Name : PeakHoldTime
            Default Value : 5.000  s
            Description : Time over which load is held constant immediately before e
            ach unload.
            Source : Keyboard Only
            Statistics Type : None
            Number of Readings : 1
            When : Pre-Test
            Minimum : No
            Maximum : No
            Places : 3
            Notation : Fixed
            Hidden : No
            Display Only : No
            Editable Post-Test : No
            Input Required : Yes
            Locked : No
            Result : No
            Reporting Order : N/A
            Panel Input : No
            Sample Level : Yes
            Reset To Default Values : Yes
            Choice List : No
            Only Allow Choice : No
            Input Order : N/A
    Switch Inputs
        Beam Cycle Frequency
            Internal Name : BeamCycleFrequency
            Default Value : 1.000  kHz
            Description : This is the input for the rate of the high frequency switc
            hing from the
frequency generator.
            Source : Keyboard Only
            Statistics Type : None
            Number of Readings : 1
            When : Pre-Test
            Minimum : 0.000
            Maximum : 0.000
            Places : 3
            Notation : Fixed
            Hidden : No
```

```
            Display Only : No
            Editable Post-Test : No
            Input Required : Yes
            Locked : No
            Result : No
            Reporting Order : N/A
            Panel Input : No
            Sample Level : Yes
            Reset To Default Values : No
            Choice List : No
            Only Allow Choice : No
            Input Order : N/A
        MaxSwitchResistance
            Internal Name : MaxSwitchResistance
            Default Value : 40.000  Ohm
            Description : This input is the maximum switch resistance used to stop t
            he test. The test will stop
when the switch measures a resistance of this input value.
            Source : Keyboard Only
            Statistics Type : None
            Number of Readings : 1
            When : Pre-Test
            Minimum : 0.000
            Maximum : 0.000
            Places : 3
            Notation : Fixed
            Hidden : No
            Display Only : No
            Editable Post-Test : No
            Input Required : Yes
            Locked : No
            Result : No
            Reporting Order : N/A
            Panel Input : No
            Sample Level : Yes
            Reset To Default Values : No
            Choice List : No
            Only Allow Choice : No
            Input Order : N/A
        Number Of Beam Cycles
            Internal Name : NumberOfBeamCycles
            Default Value : 125000.000
            Description : This is the input for the desired number of contact cycles
             during the high frequency
switching segment.
            Source : Keyboard Only
```

```
        Statistics Type : None
        Number of Readings : 1
        When : Pre-Test
        Minimum : 0.000
        Maximum : 0.000
        Places : 3
        Notation : Fixed
        Hidden : No
        Display Only : No
        Editable Post-Test : No
        Input Required : Yes
        Locked : No
        Result : No
        Reporting Order : N/A
        Panel Input : No
        Sample Level : Yes
        Reset To Default Values : No
        Choice List : No
        Only Allow Choice : No
        Input Order : N/A
Cycle Inputs
    _Cycle
        Internal Name : _Cycle
        Default Value : 0
        Description : Used for cycling
        Source : Keyboard Only
        Statistics Type : None
        Number of Readings : 1
        When : Pre-Test
        Minimum : No
        Maximum : No
        Places : 0
        Notation : Fixed
        Hidden : No
        Display Only : No
        Editable Post-Test : No
        Input Required : No
        Locked : No
        Result : No
        Reporting Order : N/A
        Panel Input : No
        Sample Level : Yes
        Reset To Default Values : Yes
        Choice List : No
        Only Allow Choice : No
        Input Order : N/A
```

```
Formulas
    Batch Formulas
        Approach Distance For Second Surface Find
            Internal Name : ApproachDistanceForSecondSurfaceFind
            Units : nm
            Formula : _Displacement-_SurfaceApproachDistance
            Description :
            Default Value :
            When : In Test Segment
            Notation : Fixed
            Places : 3
            Marker : No
            Moveable Marker : No
            Symbol :
            Color : White
            Hidden : No
            Locked : No
            Result : Yes
            Reporting Order : 18
            Recalculate Post-Test : No
            Never Recalculate : Yes
            Sample Level : No
            Reset To Default Values : No
            Advanced button : Yes
        ApproachDistanceNoDataCollection
            Internal Name : ApproachDistanceNoDataCollection
            Units : nm
            Formula : ApproachDistanceForSecondSurfaceFind+SurfaceApproachDistance3r
            dSurfFind
            Description : Distance to travel toward cantilever in While loop without
             taking data.  Set to start
data collection 500nm before anticipated surface contact.
            Default Value :
            When : In Test Segment
            Notation : Fixed
            Places : 3
            Marker : No
            Moveable Marker : No
            Symbol :
            Color : White
            Hidden : No
            Locked : No
            Result : No
            Reporting Order : N/A
            Recalculate Post-Test : No
            Never Recalculate : Yes
```

```
            Sample Level : No
            Reset To Default Values : No
            Advanced button : Yes
        AverageBeamStiffness : [ Disabled ]
        AverageDynamicBeamStiffness : [ Disabled ]
        Batch Name
            Internal Name : _BatchName
            Units :
            Formula : concat(CurrentDate("yyyy-MM-dd")," Batch #")
            Description : Creates the name of the batch.
TestWorks stores the information for a batch in a directory.  The
direct ory contains the batch file, sample files, and other
information stored abou t the batch.
            Default Value :
            When : Post-Test
            Notation : Fixed
            Places : 0
            Marker : No
            Moveable Marker : No
            Symbol :
            Color : White
            Hidden : No
            Locked : No
            Result : No
            Reporting Order : N/A
            Recalculate Post-Test : Yes
            Never Recalculate : No
            Sample Level : Yes
            Reset To Default Values : Yes
            Advanced button : No
        Beam Cycle Time
            Internal Name : BeamCycleTime
            Units : s
            Formula : NumberOfBeamCycles/BeamCycleFrequency
            Description : Time to cycle the PZT calculated from the following inputs
            : Beam Cycle Frequency
and Number of Beam Cycles.
            Default Value :
            When : Pre-Test
            Notation : Fixed
            Places : 1
            Marker : No
            Moveable Marker : No
            Symbol :
            Color : White
            Hidden : No
```

```
            Locked : No
            Result : No
            Reporting Order : N/A
            Recalculate Post-Test : No
            Never Recalculate : Yes
            Sample Level : No
            Reset To Default Values : No
            Advanced button : Yes
        BeamStiffness
            Internal Name : BeamStiffness
            Units : N/m
            Formula : AverageValue (_HarmonicStiffness, SurfaceMarker+10, SurfaceMar
            ker+40) -AverageValue (_HarmonicStiffness, SurfaceMarker-50, Surfac
            eMarker-20)
            Description : This is the stiffness of the beam during the loading measu
            red dynamically. This beam
stiffness is used to determine the load on the contact during the
test.
            Default Value :
            When : In Test Segment
            Notation : Fixed
            Places : 3
            Marker : No
            Moveable Marker : No
            Symbol :
            Color : White
            Hidden : No
            Locked : No
            Result : No
            Reporting Order : N/A
            Recalculate Post-Test : No
            Never Recalculate : Yes
            Sample Level : No
            Reset To Default Values : No
            Advanced button : Yes
        ComplianceResistance
            Internal Name : ComplianceResistance
            Units : Ohm
            Formula : ResistanceOutOfContact
            Description : Resistance of the drain resistors
            Default Value :
            When : In Test Segment
            Notation : Fixed
            Places : 3
            Marker : No
            Moveable Marker : No
```

```
            Symbol :
            Color : White
            Hidden : No
            Locked : No
            Result : Yes
            Reporting Order : 21
            Recalculate Post-Test : No
            Never Recalculate : Yes
            Sample Level : No
            Reset To Default Values : Yes
            Advanced button : Yes
        ContactGap
            Internal Name : ContactGap
            Units : um
            Formula : _Displacement[PlateContactMarker]-_Displacement[SurfaceMarker]

            Description : Contact GAp
            Default Value :
            When : Every Cycle
            Notation : Fixed
            Places : 3
            Marker : No
            Moveable Marker : No
            Symbol :
            Color : White
            Hidden : No
            Locked : No
            Result : No
            Reporting Order : N/A
            Recalculate Post-Test : Yes
            Never Recalculate : No
            Sample Level : No
            Reset To Default Values : No
            Advanced button : Yes
        ContactUnloadingStiffness
            Internal Name : ContactUnloadingStiffness
            Units : N/m
            Formula : SlopeValue (PerCycleLoadOnContact, PerCycleDisplacementIntoSur
            face, PerCycleStartContStiffCalc, PerCycleEndContStiffCalc)
            Description : Relative Stiffness of Contact to be compared as contact cy
            cles for any change.
OLD Formula: SlopeValue (PerCycleLoadOnContact,
PerCycleDisplacementIntoSurface, PerC ycleUnloadingMarker+5,
PerCycleUnloadingMarker+30)
            Default Value :
            When : Every Cycle
```

```
    Notation : Fixed
    Places : 3
    Marker : No
    Moveable Marker : No
    Symbol :
    Color : White
    Hidden : No
    Locked : No
    Result : Yes
    Reporting Order : 5
    Recalculate Post-Test : Yes
    Never Recalculate : No
    Sample Level : No
    Reset To Default Values : No
    Advanced button : Yes
CurrentOff
    Internal Name : CurrentOff
    Units : mA
    Formula : Current=0.0
    Description : Turns Current Off -- used at end of test
    Default Value :
    When : In Test Segment
    Notation : Fixed
    Places : 3
    Marker : No
    Moveable Marker : No
    Symbol :
    Color : White
    Hidden : No
    Locked : No
    Result : No
    Reporting Order : N/A
    Recalculate Post-Test : No
    Never Recalculate : Yes
    Sample Level : No
    Reset To Default Values : No
    Advanced button : Yes
CurrentOn
    Internal Name : CurrentOn
    Units : mA
    Formula : Current=TestCurrent
    Description : Turns Current On -- Testing Level
    Default Value :
    When : In Test Segment
    Notation : Fixed
    Places : 3
```

```
    Marker : No
    Moveable Marker : No
    Symbol :
    Color : White
    Hidden : No
    Locked : No
    Result : No
    Reporting Order : N/A
    Recalculate Post-Test : No
    Never Recalculate : Yes
    Sample Level : No
    Reset To Default Values : No
    Advanced button : Yes
Dynamic Beam Stiffness
    Internal Name : DynamicBeamStiffness
    Units : N/m
    Formula : AverageValue (_HarmonicStiffness, PerCycleSurfaceMarker+10, Pe
    rCycleSurfaceMarker+40) -AverageValue (_HarmonicStiffness, PerCycle
    SurfaceMarker-30, PerCycleSurfaceMarker-5)
    Description : This is the stiffness of the beam during the loading measu
    red dynamically.
    Default Value :
    When : Every Cycle
    Notation : Fixed
    Places : 3
    Marker : No
    Moveable Marker : No
    Symbol :
    Color : White
    Hidden : No
    Locked : No
    Result : Yes
    Reporting Order : 12
    Recalculate Post-Test : Yes
    Never Recalculate : No
    Sample Level : No
    Reset To Default Values : No
    Advanced button : Yes
DynamicBeamStiffnessCOV : [ Disabled ]
DynamicBeamStiffnessSTD : [ Disabled ]
End Of Mechanical Deflection Test
    Internal Name : EndOfMechanicalDeflectionTest
    Units :
    Formula : CurrentIndex()
    Description : Marks the end of the loading cycle - real time.
    Default Value :
```

```
    When : In Test Segment
    Notation : Fixed
    Places : 0
    Marker : Yes
    Moveable Marker : No
    Symbol : M
    Color : Magenta
    Hidden : No
    Locked : No
    Result : No
    Reporting Order : N/A
    Recalculate Post-Test : No
    Never Recalculate : Yes
    Sample Level : No
    Reset To Default Values : Yes
    Advanced button : Yes
EndOfLoadingMarker
    Internal Name : EndOfLoadingMarker
    Units :
    Formula : CurrentIndex()
    Description : Marks the end of the loading cycle - real time.
    Default Value :
    When : In Test Segment
    Notation : Fixed
    Places : 0
    Marker : Yes
    Moveable Marker : No
    Symbol : EL
    Color : Magenta
    Hidden : No
    Locked : No
    Result : No
    Reporting Order : N/A
    Recalculate Post-Test : No
    Never Recalculate : Yes
    Sample Level : No
    Reset To Default Values : Yes
    Advanced button : Yes
Fast Surface Approach Loading Rate
    Internal Name : FastSurfaceApproachLoadingRate
    Units : uN/s
    Formula : FastApproachSpeed/2.0*_Column
    Description : Loading Rate for the fast surface find
    Default Value :
    When : In Test Segment
    Notation : Fixed
```

```
            Places : 3
            Marker : No
            Moveable Marker : No
            Symbol :
            Color : White
            Hidden : No
            Locked : No
            Result : No
            Reporting Order : N/A
            Recalculate Post-Test : No
            Never Recalculate : Yes
            Sample Level : No
            Reset To Default Values : Yes
            Advanced button : Yes
        Hardness At Max Load : [ Disabled ]
        LevelCrossingVoltageChange
            Internal Name : LevelCrossingVoltageChange
            Units : V
            Formula : LevelCrossingMeasuredVoltageChange=LevelCrossingResistanceChan
            ge*Current
            Description : Change in the input voltage across the switch to correspon
            d to a change in the
contact resistance.
            Default Value :
            When : Pre-Test
            Notation : Fixed
            Places : 3
            Marker : No
            Moveable Marker : No
            Symbol :
            Color : White
            Hidden : No
            Locked : No
            Result : No
            Reporting Order : N/A
            Recalculate Post-Test : No
            Never Recalculate : Yes
            Sample Level : No
            Reset To Default Values : No
            Advanced button : Yes
        Limit Detection Load On Contact
            Internal Name : LimitDetectionLoadOnCOntact
            Units : mN
            Formula : RawLoadAtPlateContact * ContactLoadMultiplier
            Description : Raw load when the cantilever makes plate contact. This for
            mula is
```

used to stop the loading oft he contact.
Default Value :
When : In Test Segment
Notation : Fixed
Places : 3
Marker : No
Moveable Marker : No
Symbol :
Color : White
Hidden : No
Locked : No
Result : No
Reporting Order : N/A
Recalculate Post-Test : Yes
Never Recalculate : No
Sample Level : No
Reset To Default Values : Yes
Advanced button : No
Load At Resistance Contact Trigger
Internal Name : LoadAtResistanceContactTrigger
Units : uN
Formula : LoadOnSample
Description :
Default Value :
When : In Test Segment
Notation : Fixed
Places : 3
Marker : No
Moveable Marker : No
Symbol :
Color : White
Hidden : No
Locked : No
Result : No
Reporting Order : N/A
Recalculate Post-Test : No
Never Recalculate : Yes
Sample Level : No
Reset To Default Values : No
Advanced button : Yes
Max Raw Load on Contact
Internal Name : RawLoadAtPlateContact
Units : uN
Formula : _Load+MaximumContactForce
Description : Raw load when the cantilever makes plate contact. This for
mula is

```
used to stop the loading of  the contact.
            Default Value :
            When : In Test Segment
            Notation : Fixed
            Places : 3
            Marker : No
            Moveable Marker : No
            Symbol :
            Color : White
            Hidden : No
            Locked : No
            Result : No
            Reporting Order : N/A
            Recalculate Post-Test : Yes
            Never Recalculate : No
            Sample Level : No
            Reset To Default Values : Yes
            Advanced button : No
        OffsetVoltage
            Internal Name : OffsetVoltage
            Units : V
            Formula : (VoltageAtContact-2*PZTCalSlopeVoltsperMicron)/2.0 + PZTCalSlo
            peVoltsperMicron
            Description : Offset Voltage to plug into Freq Generator
OLD:  (VoltageAtContact-1.333)/2.0 + 0.667 POSSIBLE:
(VoltageAtContact-2.0*0.643)/2.0 + 0.643
            Default Value :
            When : In Test Segment
            Notation : Fixed
            Places : 3
            Marker : No
            Moveable Marker : No
            Symbol :
            Color : White
            Hidden : No
            Locked : No
            Result : Yes
            Reporting Order : 19
            Recalculate Post-Test : No
            Never Recalculate : Yes
            Sample Level : No
            Reset To Default Values : No
            Advanced button : Yes
        Out of Contact Hold Distance
            Internal Name : OutofContactHoldDistance
            Units : nm
```

```
    Formula : _Displacement[SurfaceMarker]-_SurfaceApproachDistance
    Description : Distance to pull off indenter head while holding before cy
    cling PZT (Switch)
    Default Value :
    When : Every Cycle
    Notation : Fixed
    Places : 3
    Marker : No
    Moveable Marker : No
    Symbol :
    Color : White
    Hidden : No
    Locked : No
    Result : Yes
    Reporting Order : 25
    Recalculate Post-Test : No
    Never Recalculate : Yes
    Sample Level : No
    Reset To Default Values : No
    Advanced button : Yes
ParkDisplacement
    Internal Name : ParkDisplacement
    Units : nm
    Formula : _Displacement
    Description : Location of the indenter in the parked position.
    Default Value :
    When : Every Cycle
    Notation : Fixed
    Places : 3
    Marker : No
    Moveable Marker : No
    Symbol :
    Color : White
    Hidden : No
    Locked : No
    Result : No
    Reporting Order : N/A
    Recalculate Post-Test : Yes
    Never Recalculate : No
    Sample Level : No
    Reset To Default Values : No
    Advanced button : Yes
PerCycle Contact Resistance
    Internal Name : PerCycleResistanceOfContact
    Units : Ohm
    Formula : ResistanceOfContact
```

```
    Description : Resistance for each cycle
    Default Value :
    When : Every Cycle
    Notation : Fixed
    Places : 3
    Marker : No
    Moveable Marker : No
    Symbol :
    Color : White
    Hidden : No
    Locked : No
    Result : Yes
    Reporting Order : 1
    Recalculate Post-Test : No
    Never Recalculate : Yes
    Sample Level : No
    Reset To Default Values : Yes
    Advanced button : Yes
PerCycle ContactGap
    Internal Name : PerCycleContactGap
    Units : um
    Formula : _Displacement[PerCyclePlateContactMarker]-_Displacement[PerCyc
    leSurfaceMarker]
    Description : Contact GAp
    Default Value :
    When : Every Cycle
    Notation : Fixed
    Places : 3
    Marker : No
    Moveable Marker : No
    Symbol :
    Color : White
    Hidden : No
    Locked : No
    Result : Yes
    Reporting Order : 10
    Recalculate Post-Test : Yes
    Never Recalculate : No
    Sample Level : No
    Reset To Default Values : No
    Advanced button : Yes
PerCycle End Of Mechanical Deflection Test
    Internal Name : PerCycleEndOfMechanicalDeflectionTest
    Units :
    Formula : EndOfMechanicalDeflectionTest
    Description : Marks the end of the mechanical deflection test.
```

```
    Default Value :
    When : Every Cycle
    Notation : Fixed
    Places : 0
    Marker : Yes
    Moveable Marker : Yes
    Symbol : M2
    Color : Black
    Hidden : No
    Locked : No
    Result : No
    Reporting Order : N/A
    Recalculate Post-Test : No
    Never Recalculate : Yes
    Sample Level : No
    Reset To Default Values : Yes
    Advanced button : Yes
PerCycle Resistance Out Of Contact
    Internal Name : PerCycleResistanceOutOfContact
    Units : Ohm
    Formula : ResistanceOutOfContact
    Description :
    Default Value :
    When : Every Cycle
    Notation : Fixed
    Places : 3
    Marker : No
    Moveable Marker : No
    Symbol :
    Color : White
    Hidden : No
    Locked : No
    Result : Yes
    Reporting Order : 14
    Recalculate Post-Test : No
    Never Recalculate : Yes
    Sample Level : No
    Reset To Default Values : Yes
    Advanced button : Yes
PerCycleAdhesiveForce : [ Disabled ]
PerCycleBeamContactPt
    Internal Name : PerCycleBeamContactPt
    Units : nm
    Formula : _Displacement[PerCycleSurfaceMarker]
    Description :
    Default Value :
```

```
    When : Every Cycle
    Notation : Fixed
    Places : 3
    Marker : No
    Moveable Marker : No
    Symbol :
    Color : White
    Hidden : No
    Locked : No
    Result : Yes
    Reporting Order : 16
    Recalculate Post-Test : Yes
    Never Recalculate : No
    Sample Level : No
    Reset To Default Values : No
    Advanced button : Yes
PerCycleEndContStiffCalc
    Internal Name : PerCycleEndContStiffCalc
    Units :
    Formula : PerCycleUnloadingMarker+10
    Description : Marks the start of the unloading cycle - real time.
    Default Value :
    When : Every Cycle
    Notation : Fixed
    Places : 0
    Marker : Yes
    Moveable Marker : Yes
    Symbol : 5
    Color : Red
    Hidden : No
    Locked : No
    Result : No
    Reporting Order : N/A
    Recalculate Post-Test : Yes
    Never Recalculate : No
    Sample Level : No
    Reset To Default Values : Yes
    Advanced button : Yes
PerCycleEnergyValue
    Internal Name : PerCycleEnergyValue
    Units : N*mm
    Formula : EnergyValue (PerCycleLoadOnContact, PerCycleDisplacementIntoCo
    ntact, PerCyclePlateContactMarker, PerCycleUnloadingMarker) - Energ
    yValue (PerCycleLoadOnContact, PerCycleDisplacementIntoContact, Per
    CycleUnloadingMarker, ChannelIndex (PerCycleLoadOnContact, 0.0, Per
    CycleUnloadingMarker,CycleEndIndex()))
```

```
            Description :
            Default Value :
            When : Every Cycle
            Notation : Scientific
            Places : 3
            Marker : No
            Moveable Marker : No
            Symbol :
            Color : White
            Hidden : No
            Locked : No
            Result : Yes
            Reporting Order : 13
            Recalculate Post-Test : Yes
            Never Recalculate : No
            Sample Level : No
            Reset To Default Values : No
            Advanced button : Yes
        PerCycleIndentCreep
            Internal Name : PerCycleIndentCreep
            Units : um
            Formula : _Displacement[PerCycleUnloadingMarker]-_Displacement[PerCycleE
            ndOfLoadingMarker]
            Description : Per Cycle Contact Interference
uses percycle unloading marker, but could use end of loading marker
to a void
 drift into sample
            Default Value :
            When : Every Cycle
            Notation : Fixed
            Places : 3
            Marker : No
            Moveable Marker : No
            Symbol :
            Color : White
            Hidden : No
            Locked : No
            Result : Yes
            Reporting Order : 8
            Recalculate Post-Test : Yes
            Never Recalculate : No
            Sample Level : No
            Reset To Default Values : No
            Advanced button : Yes
        PerCycleIndentCreepnm
            Internal Name : PerCycleIndentCreepnm
```

```
            Units : nm
            Formula : _Displacement[PerCycleUnloadingMarker]-_Displacement[PerCycleE
            ndOfLoadingMarker]
            Description : Per Cycle Contact Interference
uses percycle unloading marker, but could use end of loading marker
to a void
 drift into sample
            Default Value :
            When : Every Cycle
            Notation : Fixed
            Places : 3
            Marker : No
            Moveable Marker : No
            Symbol :
            Color : White
            Hidden : No
            Locked : No
            Result : Yes
            Reporting Order : 9
            Recalculate Post-Test : Yes
            Never Recalculate : No
            Sample Level : No
            Reset To Default Values : No
            Advanced button : Yes
        PerCycleInterference
            Internal Name : PerCycleInterference
            Units : um
            Formula : _Displacement[PerCycleUnloadingMarker]-_Displacement[PerCycleP
            lateContactMarker]
            Description : Per Cycle Contact Interference
uses percycle unloading marker, but could use end of loading marker
to a void
 drift into sample
            Default Value :
            When : Every Cycle
            Notation : Fixed
            Places : 3
            Marker : No
            Moveable Marker : No
            Symbol :
            Color : White
            Hidden : No
            Locked : No
            Result : Yes
            Reporting Order : 6
            Recalculate Post-Test : Yes
```

```
            Never Recalculate : No
            Sample Level : No
            Reset To Default Values : No
            Advanced button : Yes
        PerCycleInterferenceEndLoad
            Internal Name : PerCycleInterferenceEndLoad
            Units : um
            Formula : _Displacement[PerCycleEndOfLoadingMarker]-_Displacement[PerCyc
            lePlateContactMarker]
            Description : Per Cycle Contact Interference
uses percycle unloading marker, but could use end of loading marker
to a void
 drift into sample
            Default Value :
            When : Every Cycle
            Notation : Fixed
            Places : 3
            Marker : No
            Moveable Marker : No
            Symbol :
            Color : White
            Hidden : No
            Locked : No
            Result : Yes
            Reporting Order : 7
            Recalculate Post-Test : Yes
            Never Recalculate : No
            Sample Level : No
            Reset To Default Values : No
            Advanced button : Yes
        PerCycleMaxContactLoad
            Internal Name : PerCycleMaxContactLoad
            Units : uN
            Formula : PeakValue(PerCycleLoadOnContact,PerCyclePlateContactMarker,Cyc
            leEndIndex())
            Description :
            Default Value :
            When : Every Cycle
            Notation : Fixed
            Places : 3
            Marker : No
            Moveable Marker : No
            Symbol :
            Color : White
            Hidden : No
            Locked : No
```

```
    Result : Yes
    Reporting Order : 11
    Recalculate Post-Test : Yes
    Never Recalculate : No
    Sample Level : No
    Reset To Default Values : No
    Advanced button : Yes
PerCyclePlateContactPt
    Internal Name : PerCyclePlateContactPt
    Units : nm
    Formula : _Displacement[PerCyclePlateContactMarker]
    Description :
    Default Value :
    When : Every Cycle
    Notation : Fixed
    Places : 3
    Marker : No
    Moveable Marker : No
    Symbol :
    Color : White
    Hidden : No
    Locked : No
    Result : Yes
    Reporting Order : 17
    Recalculate Post-Test : Yes
    Never Recalculate : No
    Sample Level : No
    Reset To Default Values : No
    Advanced button : Yes
PerCyclePullOffMarker
    Internal Name : PerCyclePullOffMarker
    Units :
    Formula : PeakIndex(PerCyclePullOffLoadOnContact,CycleStartIndex(),Cycle
    EndIndex())
    Description : Index for the data point corresponding to surface contact
    - Per Cycle.
    Default Value :
    When : Every Cycle
    Notation : Fixed
    Places : 0
    Marker : Yes
    Moveable Marker : Yes
    Symbol : 6
    Color : DarkMagenta
    Hidden : No
    Locked : No
```

```
    Result : No
    Reporting Order : N/A
    Recalculate Post-Test : Yes
    Never Recalculate : No
    Sample Level : No
    Reset To Default Values : Yes
    Advanced button : Yes
PerCyclePullOffResults
    Internal Name : PerCyclePullOffResults
    Units : uN
    Formula : -1*PerCycleLoadOnContact[PerCyclePullOffMarker]
    Description :
    Default Value :
    When : Every Cycle
    Notation : Fixed
    Places : 3
    Marker : No
    Moveable Marker : No
    Symbol :
    Color : White
    Hidden : No
    Locked : No
    Result : Yes
    Reporting Order : 2
    Recalculate Post-Test : Yes
    Never Recalculate : No
    Sample Level : No
    Reset To Default Values : No
    Advanced button : Yes
PerCycleStartContStiffCalc
    Internal Name : PerCycleStartContStiffCalc
    Units :
    Formula : PerCycleUnloadingMarker+3
    Description : Marks the start of the unloading cycle - real time.
    Default Value :
    When : Every Cycle
    Notation : Fixed
    Places : 0
    Marker : Yes
    Moveable Marker : Yes
    Symbol : 4
    Color : Red
    Hidden : No
    Locked : No
    Result : No
    Reporting Order : N/A
```

```
    Recalculate Post-Test : Yes
    Never Recalculate : No
    Sample Level : No
    Reset To Default Values : Yes
    Advanced button : Yes
PerCycleThresholdDisplacement
    Internal Name : PerCycleThresholdDisplacement
    Units : nm
    Formula : PerCycleDisplacementIntoContact[PerCycleThresholdMarker]
    Description :
    Default Value :
    When : Every Cycle
    Notation : Fixed
    Places : 3
    Marker : No
    Moveable Marker : No
    Symbol :
    Color : White
    Hidden : No
    Locked : No
    Result : Yes
    Reporting Order : 4
    Recalculate Post-Test : Yes
    Never Recalculate : No
    Sample Level : No
    Reset To Default Values : No
    Advanced button : Yes
PerCycleThresholdMarker
    Internal Name : PerCycleThresholdMarker
    Units :
    Formula : PeakIndex(PerCycleThresholdContactLoad,CycleStartIndex(),Cycle
    EndIndex())-20
    Description : Threshold contact point
    Default Value :
    When : Every Cycle
    Notation : Fixed
    Places : 0
    Marker : Yes
    Moveable Marker : Yes
    Symbol : T
    Color : Green
    Hidden : No
    Locked : No
    Result : No
    Reporting Order : N/A
    Recalculate Post-Test : Yes
```

```
    Never Recalculate : No
    Sample Level : No
    Reset To Default Values : Yes
    Advanced button : Yes
PerCycleThresholdResults
    Internal Name : PerCycleThresholdResults
    Units : uN
    Formula : PerCycleLoadOnContact[PerCycleThresholdMarker]
    Description :
    Default Value :
    When : Every Cycle
    Notation : Fixed
    Places : 3
    Marker : No
    Moveable Marker : No
    Symbol :
    Color : White
    Hidden : No
    Locked : No
    Result : Yes
    Reporting Order : 3
    Recalculate Post-Test : Yes
    Never Recalculate : No
    Sample Level : No
    Reset To Default Values : No
    Advanced button : Yes
PZTInContactMinusOne
    Internal Name : PZTInContactMinusOne
    Units : V
    Formula : PZTVoltage=VoltageAtContact - 2.0/3.0
    Description :
    Default Value :
    When : In Test Segment
    Notation : Fixed
    Places : 3
    Marker : No
    Moveable Marker : No
    Symbol :
    Color : White
    Hidden : No
    Locked : No
    Result : No
    Reporting Order : N/A
    Recalculate Post-Test : No
    Never Recalculate : Yes
    Sample Level : No
```

```
            Reset To Default Values : Yes
            Advanced button : Yes
        PZTInContactMinusTwo
            Internal Name : PZTInContactMinusTwo
            Units : V
            Formula : PZTVoltage=VoltageAtContact - 2*PZTCalSlopeVoltsperMicron
            Description : PZTVoltage=VoltageAtContact - 2.0*0.643  (too low...0-10V
            linear interp)
0.724 too low -- 0-5V interp OLD:   PZTVoltage=VoltageAtContact -
4.0/3.0
            Default Value :
            When : In Test Segment
            Notation : Fixed
            Places : 3
            Marker : No
            Moveable Marker : No
            Symbol :
            Color : White
            Hidden : No
            Locked : No
            Result : No
            Reporting Order : N/A
            Recalculate Post-Test : No
            Never Recalculate : Yes
            Sample Level : No
            Reset To Default Values : Yes
            Advanced button : Yes
        PZTInContactPlusTwo
            Internal Name : PZTInContactPlusTwo
            Units : V
            Formula : PZTVoltage=VoltageAtContact + 2*PZTCalSlopeVoltsperMicron
            Description : OLD:  PZTVoltage=VoltageAtContact + 4.0/3.0
            Default Value :
            When : In Test Segment
            Notation : Fixed
            Places : 3
            Marker : No
            Moveable Marker : No
            Symbol :
            Color : White
            Hidden : No
            Locked : No
            Result : No
            Reporting Order : N/A
            Recalculate Post-Test : No
            Never Recalculate : Yes
```

```
            Sample Level : No
            Reset To Default Values : Yes
            Advanced button : Yes
        Resistance Just In Contact
            Internal Name : ResistanceJustInContact
            Units : Ohm
            Formula : AverageValue (ResistanceMeasured4W, CurrentIndex()-15, Current
            Index())
            Description : Resistance at the contact just after the plate has come in
            to contact with the
cantilever.
            Default Value :
            When : In Test Segment
            Notation : Fixed
            Places : 3
            Marker : No
            Moveable Marker : No
            Symbol :
            Color : White
            Hidden : No
            Locked : No
            Result : Yes
            Reporting Order : 22
            Recalculate Post-Test : No
            Never Recalculate : Yes
            Sample Level : No
            Reset To Default Values : Yes
            Advanced button : Yes
        Resistance Of Initial Contact
            Internal Name : ResistanceOfInitialContact
            Units : Ohm
            Formula : AverageValue (ResistanceMeasured4W, CurrentIndex()-15, Current
            Index())
            Description :
            Default Value :
            When : In Test Segment
            Notation : Fixed
            Places : 3
            Marker : No
            Moveable Marker : No
            Symbol :
            Color : White
            Hidden : No
            Locked : No
            Result : Yes
            Reporting Order : 23
```

```
    Recalculate Post-Test : No
    Never Recalculate : Yes
    Sample Level : No
    Reset To Default Values : Yes
    Advanced button : Yes
ResistanceOutOfContact
    Internal Name : ResistanceOutOfContact
    Units : Ohm
    Formula : AverageValue (ResistanceMeasured4W, CurrentIndex()-10, Current
    Index())
    Description : Changed from R_MEas4W to AVerageMeasuredR4W
    Default Value :
    When : In Test Segment
    Notation : Fixed
    Places : 3
    Marker : No
    Moveable Marker : No
    Symbol :
    Color : White
    Hidden : No
    Locked : No
    Result : No
    Reporting Order : N/A
    Recalculate Post-Test : No
    Never Recalculate : Yes
    Sample Level : No
    Reset To Default Values : Yes
    Advanced button : Yes
ResistanceOutOfContactInitial
    Internal Name : ResistanceOutOfContactInitial
    Units : Ohm
    Formula : AverageValue (ResistanceMeasured4W, CurrentIndex()-10, Current
    Index())
    Description :
    Default Value :
    When : In Test Segment
    Notation : Fixed
    Places : 3
    Marker : No
    Moveable Marker : No
    Symbol :
    Color : White
    Hidden : No
    Locked : No
    Result : No
    Reporting Order : N/A
```

```
    Recalculate Post-Test : No
    Never Recalculate : Yes
    Sample Level : No
    Reset To Default Values : Yes
    Advanced button : Yes
ResistanceSetforTestControl
    Internal Name : ResistanceSetforTestControl
    Units : Ohm
    Formula : ResistanceOfContact=ResistanceOfInitialContact
    Description :
    Default Value :
    When : In Test Segment
    Notation : Fixed
    Places : 3
    Marker : No
    Moveable Marker : No
    Symbol :
    Color : White
    Hidden : No
    Locked : No
    Result : No
    Reporting Order : N/A
    Recalculate Post-Test : No
    Never Recalculate : Yes
    Sample Level : No
    Reset To Default Values : Yes
    Advanced button : Yes
SetSurfaceDisplacement
    Internal Name : SetSurfaceDisplacement
    Units :
    Formula : _SurfaceDisplacement=_Displacement
    Description : Raw displacement of the surface
    Default Value :
    When : In Test Segment
    Notation : Fixed
    Places : 0
    Marker : No
    Moveable Marker : Yes
    Symbol : S
    Color : White
    Hidden : No
    Locked : No
    Result : No
    Reporting Order : N/A
    Recalculate Post-Test : No
    Never Recalculate : Yes
```

```
    Sample Level : No
    Reset To Default Values : Yes
    Advanced button : Yes
Test File Name For Export
    Internal Name : _ExportFileName
    Units :
    Formula : IF((NumberOfSpecimens (1)+1) GT 99, Concat("Test",IToA((Number
    OfSpecimens (1)+1) ) ), IF((NumberOfSpecimens (1)+1) GT 9, Concat("
    Test0",IToA((NumberOfSpecimens (1)+1) ) ),Concat("Test00",IToA(Numb
    erOfSpecimens (1)+1 ) )))
    Description : File Name to be used when the test is exported.
    Default Value :
    When : Pre-Test
    Notation : Fixed
    Places : 0
    Marker : No
    Moveable Marker : No
    Symbol :
    Color : White
    Hidden : No
    Locked : No
    Result : No
    Reporting Order : N/A
    Recalculate Post-Test : No
    Never Recalculate : Yes
    Sample Level : No
    Reset To Default Values : No
    Advanced button : Yes
Unloading Rate
    Internal Name : UnloadingRate
    Units : uN/s
    Formula : LoadRateMultipleForUnloadRate*LoadingRateAfterPlateContact
    Description : Prescribed unloading rate for the current cycle
    Default Value :
    When : Pre-Test
    Notation : Fixed
    Places : 3
    Marker : No
    Moveable Marker : No
    Symbol :
    Color : White
    Hidden : No
    Locked : No
    Result : No
    Reporting Order : N/A
    Recalculate Post-Test : No
```

```
            Never Recalculate : Yes
            Sample Level : No
            Reset To Default Values : Yes
            Advanced button : Yes
        UnloadResistanceMeasurementThreshold
            Internal Name : UnloadResistanceMeasurementThreshold
            Units : Ohm
            Formula : 0.9*ResistanceOutOfContact
            Description : Resistance value to determine that the cantilever is no lo
            nger in contact with the
bottom plate. Calculated as 90% of the out of contact resistance measure
d at the start of the test.
            Default Value :
            When : Every Cycle
            Notation : Fixed
            Places : 3
            Marker : No
            Moveable Marker : No
            Symbol :
            Color : White
            Hidden : No
            Locked : No
            Result : No
            Reporting Order : N/A
            Recalculate Post-Test : No
            Never Recalculate : No
            Sample Level : No
            Reset To Default Values : Yes
            Advanced button : Yes
    Approach Formulas
        Surface Stiffness Increase
            Internal Name : SurfaceStiffnessIncrease
            Units : N/m
            Formula : 500.0*NewtonsPerMeter*_SurfaceApproachSensitivity
            Description : In situ, surface contact is determined to be the point at
            which the change in
load with respect to displacement reaches this value.  When this
criteri a is met, the approach is terminated and the prescribed
loading algorithm begins.
            Default Value :
            When : Pre-Sample
            Notation : Fixed
            Places : 3
            Marker : No
            Moveable Marker : No
            Symbol :
```

```
        Color : White
        Hidden : No
        Locked : No
        Result : No
        Reporting Order : N/A
        Recalculate Post-Test : No
        Never Recalculate : Yes
        Sample Level : Yes
        Reset To Default Values : No
        Advanced button : Yes
Hold Segment Formulas
    Drift Correction : [ Disabled ]
Oliver & Pharr Calculations
    Area Coefficient 1 : [ Disabled ]
    Area Coefficient 2 : [ Disabled ]
    Modulus At Max Load : [ Disabled ]
    Tip Name : [ Disabled ]
Data Acquisition Formulas
    Approach Points To Save
        Internal Name : ApproachPointsToSave
        Units :
        Formula : _ApproachDistanceToSave/_SurfaceApproachVelocity * DataRate
        Description : The number of approach points to save.
        Default Value :
        When : Pre-Sample
        Notation : Fixed
        Places : 0
        Marker : No
        Moveable Marker : No
        Symbol :
        Color : White
        Hidden : No
        Locked : No
        Result : No
        Reporting Order : N/A
        Recalculate Post-Test : No
        Never Recalculate : No
        Sample Level : Yes
        Reset To Default Values : Yes
        Advanced button : Yes
Switch Formulas
    Number Of Switch Cycles
        Internal Name : NumberOfSwitchCycles
        Units :
        Formula : (_CycleNumber)*NumberOfBeamCycles
        Description : Number of switching cycles performed.
```

```
    Default Value :
    When : Every Cycle
    Notation : Fixed
    Places : 3
    Marker : No
    Moveable Marker : No
    Symbol :
    Color : White
    Hidden : No
    Locked : No
    Result : Yes
    Reporting Order : 0
    Recalculate Post-Test : No
    Never Recalculate : Yes
    Sample Level : No
    Reset To Default Values : No
    Advanced button : Yes
PZTInContact
    Internal Name : PZTInContact
    Units : V
    Formula : PZTVoltage=VoltageAtContact
    Description :
    Default Value :
    When : In Test Segment
    Notation : Fixed
    Places : 3
    Marker : No
    Moveable Marker : No
    Symbol :
    Color : White
    Hidden : No
    Locked : No
    Result : No
    Reporting Order : N/A
    Recalculate Post-Test : No
    Never Recalculate : Yes
    Sample Level : No
    Reset To Default Values : Yes
    Advanced button : Yes
PZTOneMicronDrop
    Internal Name : PZTOneMicronDrop
    Units : V
    Formula : PZTVoltage=PZTVoltage-2.0/3.0
    Description :
    Default Value :
    When : In Test Segment
```

```
    Notation : Fixed
    Places : 3
    Marker : No
    Moveable Marker : No
    Symbol :
    Color : White
    Hidden : No
    Locked : No
    Result : No
    Reporting Order : N/A
    Recalculate Post-Test : No
    Never Recalculate : Yes
    Sample Level : No
    Reset To Default Values : Yes
    Advanced button : Yes
PZTTwoMicronDrop
    Internal Name : PZTTwoMicronDrop
    Units : V
    Formula : PZTVoltage=PZTVoltage-4.0/3.0
    Description :
    Default Value :
    When : In Test Segment
    Notation : Fixed
    Places : 3
    Marker : No
    Moveable Marker : No
    Symbol :
    Color : White
    Hidden : No
    Locked : No
    Result : No
    Reporting Order : N/A
    Recalculate Post-Test : No
    Never Recalculate : Yes
    Sample Level : No
    Reset To Default Values : Yes
    Advanced button : Yes
PZTVoltageIncrement
    Internal Name : PZTVoltageIncrement
    Units : V
    Formula : PZTVoltage=PZTVoltage+0.001
    Description :
    Default Value :
    When : In Test Segment
    Notation : Fixed
    Places : 3
```

```
    Marker : No
    Moveable Marker : No
    Symbol :
    Color : White
    Hidden : No
    Locked : No
    Result : No
    Reporting Order : N/A
    Recalculate Post-Test : No
    Never Recalculate : Yes
    Sample Level : No
    Reset To Default Values : Yes
    Advanced button : Yes
PZTZero
    Internal Name : PZTZero
    Units : V
    Formula : PZTVoltage = 0.0
    Description :
    Default Value :
    When : In Test Segment
    Notation : Fixed
    Places : 3
    Marker : No
    Moveable Marker : No
    Symbol :
    Color : White
    Hidden : No
    Locked : No
    Result : No
    Reporting Order : N/A
    Recalculate Post-Test : No
    Never Recalculate : No
    Sample Level : No
    Reset To Default Values : Yes
    Advanced button : Yes
RelaySwitchOFF
    Internal Name : RelaySwitchOFF
    Units :
    Formula : RelaySwitch=0
    Description :
    Default Value :
    When : In Test Segment
    Notation : Fixed
    Places : 0
    Marker : No
    Moveable Marker : No
```

```
    Symbol :
    Color : White
    Hidden : No
    Locked : No
    Result : No
    Reporting Order : N/A
    Recalculate Post-Test : No
    Never Recalculate : No
    Sample Level : Yes
    Reset To Default Values : Yes
    Advanced button : Yes
RelaySwitchON
    Internal Name : RelaySwitchON
    Units :
    Formula : RelaySwitch=1
    Description :
    Default Value :
    When : In Test Segment
    Notation : Fixed
    Places : 0
    Marker : No
    Moveable Marker : No
    Symbol :
    Color : White
    Hidden : No
    Locked : No
    Result : No
    Reporting Order : N/A
    Recalculate Post-Test : No
    Never Recalculate : No
    Sample Level : Yes
    Reset To Default Values : Yes
    Advanced button : Yes
Resistance in Contact
    Internal Name : ResistanceOfContact
    Units : Ohm
    Formula : AverageValue (ResistanceMeasured4W, CurrentIndex()-15, Current
    Index())
    Description : Changed from RMEas_4W to averaged Resistance 17Sep07
    Default Value :
    When : In Test Segment
    Notation : Fixed
    Places : 3
    Marker : No
    Moveable Marker : No
    Symbol :
```

```
        Color : White
        Hidden : No
        Locked : No
        Result : No
        Reporting Order : N/A
        Recalculate Post-Test : No
        Never Recalculate : Yes
        Sample Level : No
        Reset To Default Values : Yes
        Advanced button : Yes
    Voltage At Contact
        Internal Name : VoltageAtContact
        Units : V
        Formula : _DAC0OUT
        Description :
        Default Value :
        When : In Test Segment
        Notation : Fixed
        Places : 3
        Marker : No
        Moveable Marker : No
        Symbol :
        Color : White
        Hidden : No
        Locked : No
        Result : Yes
        Reporting Order : 20
        Recalculate Post-Test : No
        Never Recalculate : Yes
        Sample Level : No
        Reset To Default Values : No
        Advanced button : Yes
Test Markers
    _CycleMarker
        Internal Name : _CycleMarker
        Units :
        Formula : 0
        Description :
        Default Value :
        When : Every Cycle
        Notation : Fixed
        Places : 0
        Marker : Yes
        Moveable Marker : No
        Symbol : X
        Color : White
```

```
    Hidden : Yes
    Locked : No
    Result : No
    Reporting Order : N/A
    Recalculate Post-Test : No
    Never Recalculate : Yes
    Sample Level : No
    Reset To Default Values : Yes
    Advanced button : Yes
PerCycleEndOfLoadingMarker
    Internal Name : PerCycleEndOfLoadingMarker
    Units :
    Formula : EndOfLoadingMarker
    Description : Marks the end of the loading cycle for each cycle.
    Default Value :
    When : Every Cycle
    Notation : Fixed
    Places : 0
    Marker : Yes
    Moveable Marker : No
    Symbol : NL
    Color : Magenta
    Hidden : No
    Locked : No
    Result : No
    Reporting Order : N/A
    Recalculate Post-Test : No
    Never Recalculate : Yes
    Sample Level : No
    Reset To Default Values : Yes
    Advanced button : Yes
PerCyclePlateContactMarker
    Internal Name : PerCyclePlateContactMarker
    Units :
    Formula : PlateContactMarker
    Description : Marks the end of the loading cycle for each cycle.
    Default Value :
    When : Every Cycle
    Notation : Fixed
    Places : 0
    Marker : Yes
    Moveable Marker : Yes
    Symbol : 2
    Color : Cyan
    Hidden : No
    Locked : No
```

```
    Result : No
    Reporting Order : N/A
    Recalculate Post-Test : No
    Never Recalculate : Yes
    Sample Level : No
    Reset To Default Values : Yes
    Advanced button : Yes
PerCycleSurfaceMarker
    Internal Name : PerCycleSurfaceMarker
    Units :
    Formula : SurfaceMarker
    Description : Index for the data point corresponding to surface contact
    - Per Cycle.
    Default Value :
    When : Every Cycle
    Notation : Fixed
    Places : 0
    Marker : Yes
    Moveable Marker : Yes
    Symbol : 1
    Color : DarkBlue
    Hidden : No
    Locked : No
    Result : No
    Reporting Order : N/A
    Recalculate Post-Test : No
    Never Recalculate : Yes
    Sample Level : No
    Reset To Default Values : Yes
    Advanced button : Yes
PerCycleUnloadingMarker
    Internal Name : PerCycleUnloadingMarker
    Units :
    Formula : UnloadingMarker
    Description : Marks the start of the unloading cycle - real time.
    Default Value :
    When : Every Cycle
    Notation : Fixed
    Places : 0
    Marker : Yes
    Moveable Marker : No
    Symbol : UL
    Color : Red
    Hidden : No
    Locked : No
    Result : No
```

```
    Reporting Order : N/A
    Recalculate Post-Test : No
    Never Recalculate : Yes
    Sample Level : No
    Reset To Default Values : Yes
    Advanced button : Yes
PlateContactMarker
    Internal Name : PlateContactMarker
    Units :
    Formula : CurrentIndex()
    Description : Marks the end of the loading cycle - real time.
    Default Value :
    When : In Test Segment
    Notation : Fixed
    Places : 0
    Marker : Yes
    Moveable Marker : No
    Symbol : P
    Color : Magenta
    Hidden : No
    Locked : No
    Result : No
    Reporting Order : N/A
    Recalculate Post-Test : No
    Never Recalculate : Yes
    Sample Level : No
    Reset To Default Values : Yes
    Advanced button : Yes
Surface Marker
    Internal Name : SurfaceMarker
    Units :
    Formula : CurrentIndex()
    Description : Index for the data point corresponding to surface contact
    - real time.
    Default Value :
    When : In Test Segment
    Notation : Fixed
    Places : 0
    Marker : Yes
    Moveable Marker : Yes
    Symbol : S
    Color : White
    Hidden : No
    Locked : No
    Result : No
    Reporting Order : N/A
```

```
        Recalculate Post-Test : No
        Never Recalculate : Yes
        Sample Level : No
        Reset To Default Values : Yes
        Advanced button : Yes
    UnloadingMarker
        Internal Name : UnloadingMarker
        Units :
        Formula : CurrentIndex()
        Description : Marks the start of the unloading cycle - real time.
        Default Value :
        When : In Test Segment
        Notation : Fixed
        Places : 0
        Marker : Yes
        Moveable Marker : Yes
        Symbol : U
        Color : Red
        Hidden : No
        Locked : No
        Result : No
        Reporting Order : N/A
        Recalculate Post-Test : No
        Never Recalculate : Yes
        Sample Level : No
        Reset To Default Values : Yes
        Advanced button : Yes
Cycle Formulas
    _CycleNumber
        Internal Name : _CycleNumber
        Units :
        Formula : _CycleNumber
        Description :
        Default Value :
        When : Every Cycle
        Notation : Fixed
        Places : 0
        Marker : No
        Moveable Marker : No
        Symbol :
        Color : White
        Hidden : No
        Locked : No
        Result : No
        Reporting Order : N/A
        Recalculate Post-Test : No
```

```
    Never Recalculate : Yes
    Sample Level : No
    Reset To Default Values : Yes
    Advanced button : Yes
Beam Loading Stiffness : [ Disabled ]
Disp at Max Load
    Internal Name : DisplacementAtMaxLoad
    Units : nm
    Formula : DisplacementIntoSurface[PeakIndex(Stiffness, CycleStartIndex()
    ,CycleEndIndex())]
    Description : Penetration into the test surface at the maximum load.
    Default Value :
    When : Every Cycle
    Notation : Fixed
    Places : 3
    Marker : No
    Moveable Marker : No
    Symbol :
    Color : White
    Hidden : No
    Locked : No
    Result : No
    Reporting Order : N/A
    Recalculate Post-Test : Yes
    Never Recalculate : No
    Sample Level : No
    Reset To Default Values : No
    Advanced button : Yes
Load At Max Load
    Internal Name : LoadAtMaxLoad
    Units : mN
    Formula : LoadOnSample[PeakIndex(Stiffness,CycleStartIndex(),CycleEndInd
    ex())]
    Description : Maximum load on the sample
    Default Value :
    When : Every Cycle
    Notation : Fixed
    Places : 3
    Marker : No
    Moveable Marker : No
    Symbol :
    Color : White
    Hidden : No
    Locked : No
    Result : No
    Reporting Order : N/A
```

```
    Recalculate Post-Test : Yes
    Never Recalculate : No
    Sample Level : No
    Reset To Default Values : No
    Advanced button : Yes
Per Cycle Time At Start Of Approach
    Internal Name : PerCycleTimeAtStartOfApproach
    Units :
    Formula : TimeAtStartOfApproach
    Description : Clock reading off the PC, recorded just before starting th
    e approach.
    Default Value :
    When : Every Cycle
    Notation : Fixed
    Places : 0
    Marker : No
    Moveable Marker : No
    Symbol :
    Color : White
    Hidden : No
    Locked : No
    Result : Yes
    Reporting Order : 15
    Recalculate Post-Test : No
    Never Recalculate : Yes
    Sample Level : No
    Reset To Default Values : No
    Advanced button : Yes
Time At Start Of Approach
    Internal Name : TimeAtStartOfApproach
    Units :
    Formula : CurrentTime("hh:mm:ss tt")
    Description : Clock reading off the PC, recorded just before starting th
    e approach.
    Default Value :
    When : In Test Segment
    Notation : Fixed
    Places : 0
    Marker : No
    Moveable Marker : No
    Symbol :
    Color : White
    Hidden : No
    Locked : No
    Result : Yes
    Reporting Order : 24
```

```
            Recalculate Post-Test : No
            Never Recalculate : Yes
            Sample Level : No
            Reset To Default Values : No
            Advanced button : Yes
        Unload Limit
            Internal Name : UnloadLimit
            Units : uN
            Formula : LoadOnSample[EndOfLoadingMarker]*0.1
            Description : Load at which to stop the unload.
            Default Value :
            When : In Test Segment
            Notation : Fixed
            Places : 3
            Marker : No
            Moveable Marker : No
            Symbol :
            Color : White
            Hidden : No
            Locked : No
            Result : No
            Reporting Order : N/A
            Recalculate Post-Test : No
            Never Recalculate : Yes
            Sample Level : No
            Reset To Default Values : No
            Advanced button : Yes
Configuration Objects
    Indenter Tip
        CurrentTipName
            TipName : B1824kwg
            FunctionType : 0
            Modulus : 1.1635e+005
            Parameters
                Label0 : m0   Value : 2.4585e+001
                Label1 : m1   Value : 2.7590e+002
                Label2 : m2   Value : -3.7730e+002
                Label3 : m3   Value : -5.5900e+001
                Label4 : m4   Value : 2.3040e+002
                Label5 : m5   Value : 0.0000e+000
                Label6 : m6   Value : 0.0000e+000
                Label7 : m7   Value : 0.0000e+000
                Label8 : m8   Value : 0.0000e+000
        OriginalTipName
            TipName : B1824kwg
            FunctionType : 0
```

```
        Modulus : 116349.6199
        Parameters
            Label0 : m0   Value : 2.4585e+001
            Label1 : m1   Value : 2.7590e+002
            Label2 : m2   Value : -3.7730e+002
            Label3 : m3   Value : -5.5900e+001
            Label4 : m4   Value : 2.3040e+002
            Label5 : m5   Value : 0.0000e+000
            Label6 : m6   Value : 0.0000e+000
            Label7 : m7   Value : 0.0000e+000
            Label8 : m8   Value : 0.0000e+000
Units
    Category : SI
Sample Report
    Report Template : %system%\MTS Nano Standard Sample Report.rtf
    Options
        Report Header
        Test Results
        Statistics
        Modulus vs. Displacement Into Surface
        Hardness vs. Displacement Into Surface
        Tip Information
        Calculation Inputs
        Test Inputs
Hardware Status
    Maximum Displacement Limit : [ Disabled ]
    Minimum Displacement Limit : [ Disabled ]
    Crosshead Stopped : [ Disabled ]
    Positive Device Overload : [ Disabled ]
    Hardware Communication Error : [ Disabled ]
    Negative Device Overload : [ Disabled ]
    Amp Fault : [ Disabled ]
    Lost Frame Communication : [ Disabled ]
    Emergency Stop : [ Disabled ]
    Z Stage Upper Limit : [ Disabled ]
    Lower Auxiliary Limit Active : [ Disabled ]
Limit Detection
Miscellaneous
    Method Access Level : 0
    Raw Data : Save Raw Data
    Automatically Save Every Test : No
    Master Flag : No
    Switch to Review after test : No
    Enable Next Test Segment button : Yes
    Disable Jog buttons during test : Yes
    Method Description : XP Basic Hardness, Modulus, and Tip Calibration to
```

```
        a Series of Loads
Current Tip: "{_TipName}"
    Tag Limits
    Excel Output Configuration
Test Segments
    Idle
        Data Collection : [ Disabled ]

    Review Sample Names
        Run-Time Message :
        Data Collection : [ Disabled ]

    Review First Location
        Run-Time Message :
        Data Collection : [ Disabled ]

    Delay before Running Batch
        Use Default Start Time
        Default Start Time : 8:37:PM
        Run-Time Message : Waiting to Start Batch
        Data Collection : [ Disabled ]

    Formulas
        Calculation Time : Pre-Sample
        Run-Time Message :
        Data Collection : [ Disabled ]

    Formulas
        Calculation Time : Pre-Test
        Run-Time Message :
        Data Collection : [ Disabled ]

    Tare Time
        Data Collection : [ Disabled ]

    One-Time Formula - CurrentOff
        Data Collection : [ Disabled ]

    One-Time Formula - PZTZero
        Data Collection : [ Disabled ]

    One-Time Formula - RelaySwitchOFF
        Data Collection : [ Disabled ]

    XY Goto Test Segment
        Speed : X Y Table Speed
```

```
        X Position : X Test Position
        Y Position : Y Test Position
        Run-Time Message : Moving Table to Indent Location
        Data Collection : [ Disabled ]

    One-Time Formula - CurrentOn
        Data Collection : [ Disabled ]

    Test Message
        Message : RAISE Z (ROUGH POSITIONING) STAGE TILL CANTILEVER IN CONTACT.
BACK OFF CONTACT GAP DISTANCE.
        Dialog Type : OK Dialog
        Run-Time Message :
        Data Collection : [ Disabled ]

    Test Message : [ Disabled ]
    WHILE ResistanceMeasured4W>ResistanceTrigger
        Data Collection : [ Disabled ]

    One-Time Formula - PZTVoltageIncrement
        Data Collection : [ Disabled ]

    EndWHILE
        Data Collection : [ Disabled ]

    Hold
        Channel : Raw Load
        Hold Current Value : Yes
        Enable Stopping Conditions : Yes
            Channel : Time
            Comparison : Increases by
            Value : Settle Time
        Run-Time Message : Holding to stabilize Resistance Measurement
        PID Parameters
            Always use Outer Loop Control : No
            Show PID dialog during test : No
            Use Multiplier : No
        Data Collection :
            Acquisition Type 1 : Rate
            Channel 1 : Time
            Rate Value Input 1 : Data Acquisition Rate
            Buffer : -1
            Buffer Full Action : Fold and Reduce Data Rate
            Take Data on Pause : Yes
            Preserve last data point : No
```

```
    WHILE ResistanceMeasured4W>ResistanceTrigger
        Data Collection : [ Disabled ]

    One-Time Formula - PZTVoltageIncrement
        Data Collection : [ Disabled ]

    EndWHILE
        Data Collection : [ Disabled ]

    One-Time Formula - Voltage At Contact
        Data Collection : [ Disabled ]

    IF VoltageAtContact<2*PZTCalSlopeVoltsperMicron OR VoltageAtContact>(10-
    2*PZTCalSlopeVoltsperMicron)
        Data Collection : [ Disabled ]

    One-Time Formula - CurrentOff : [ Disabled ]
    One-Time Formula - PZTZero
        Data Collection : [ Disabled ]

    Show Results
        Variables :
Voltage At Contact
        Additional Message : Voltage At Contact Either too high or too low for P
        ZT operation.  Adjust Z-stage up or down to locate base plate withi
        n reach of PZT.  < 1.574 or >8.426 out of range of PZT.
        Dialog Type : Dialog Type
        Run-Time Message :
        Data Collection : [ Disabled ]

    One-Time Formula - CurrentOn
        Data Collection : [ Disabled ]

    Test Message
        Message : SECOND TEST OF CONTACT GAP.  READY TO RAISE PZT INTO CONTACT.
         Adjust Vertical Stage again now.
        Dialog Type : OK Dialog
        Run-Time Message :
        Data Collection : [ Disabled ]

    WHILE ResistanceMeasured4W>ResistanceTrigger
        Data Collection : [ Disabled ]

    One-Time Formula - PZTVoltageIncrement
        Data Collection : [ Disabled ]
```

```
    EndWHILE
        Data Collection : [ Disabled ]

    One-Time Formula - Voltage At Contact
        Data Collection : [ Disabled ]

    EndIF
        Data Collection : [ Disabled ]

    One-Time Formula - CurrentOff : [ Disabled ]
    Show Results
        Variables :
Voltage At Contact
        Additional Message : This is to check value of PZT control Voltage At Co
        ntact (Must be > 1.574 V and < 8.426)
        Dialog Type : Dialog Type
        Run-Time Message :
        Data Collection : [ Disabled ]

    One-Time Formula - OffsetVoltage
        Data Collection : [ Disabled ]

    Show Results
        Variables :
OffsetVoltage
        Additional Message : Offset Voltage to enter into frequency generator
        Dialog Type : Dialog Type
        Run-Time Message : Offset Voltage
        Data Collection : [ Disabled ]

    One-Time Formula - PZTInContact
        Data Collection : [ Disabled ]

    One-Time Formula - CurrentOn
        Data Collection : [ Disabled ]

    Hold
        Channel : Raw Load
        Hold Current Value : Yes
        Enable Stopping Conditions : Yes
            Channel : Time
            Comparison : Increases by
            Value : Settle Time
        Run-Time Message : Holding to make a resistance measurement.
        PID Parameters
            Always use Outer Loop Control : No
```

```
            Show PID dialog during test : No
            Use Multiplier : No
        Data Collection :
            Acquisition Type 1 : Rate
            Channel 1 : Time
            Rate Value Input 1 : Data Acquisition Rate
            Buffer : -1
            Buffer Full Action : Fold and Reduce Data Rate
            Take Data on Pause : Yes
            Preserve last data point : No

    One-Time Formula - Resistance Just In Contact
        Data Collection :
            Acquisition Type 1 : Rate
            Channel 1 : Time
            Rate Value Input 1 : Data Acquisition Rate
            Buffer : -1
            Buffer Full Action : Fold and Reduce Data Rate
            Take Data on Pause : Yes
            Preserve last data point : No

    Show Results
        Variables :
Resistance Just In Contact
        Additional Message : Checking Resistance in Contact Default
        Dialog Type : Dialog Type
        Run-Time Message :
        Data Collection : [ Disabled ]

    One-Time Formula - PZTInContactPlusTwo
        Data Collection : [ Disabled ]

    Hold
        Channel : Raw Load
        Hold Current Value : Yes
        Enable Stopping Conditions : Yes
            Channel : Time
            Comparison : Increases by
            Value : Settle Time
        Run-Time Message : Measuring Contact Resistance.
        PID Parameters
            Always use Outer Loop Control : No
            Show PID dialog during test : No
            Use Multiplier : No
        Data Collection :
            Acquisition Type 1 : Rate
```

```
            Channel 1 : Time
            Rate Value Input 1 : Data Acquisition Rate
            Buffer : -1
            Buffer Full Action : Fold and Reduce Data Rate
            Take Data on Pause : Yes
            Preserve last data point : No

    One-Time Formula - Resistance Of Initial Contact
        Data Collection :
            Acquisition Type 1 : Rate
            Channel 1 : Time
            Rate Value Input 1 : Data Acquisition Rate
            Buffer : -1
            Buffer Full Action : Fold and Reduce Data Rate
            Take Data on Pause : Yes
            Preserve last data point : No

    One-Time Formula - ResistanceSetforTestControl
        Data Collection : [ Disabled ]

    Test Message : [ Disabled ]
    Show Results
        Variables :
Resistance in Contact
        Additional Message : Initial Contact Resistance
Note this value on Data Sheet
        Dialog Type : Dialog Type
        Run-Time Message :
        Data Collection : [ Disabled ]

    One-Time Formula - PZTInContactMinusTwo
        Data Collection : [ Disabled ]

    One-Time Formula - PZTInContactMinusOne : [ Disabled ]
    Hold
        Channel : Raw Load
        Hold Current Value : Yes
        Enable Stopping Conditions : Yes
            Channel : Time
            Comparison : Increases by
            Value : Settle Time
        Run-Time Message : Measuring Contact Resistance out of contact.
        PID Parameters
            Always use Outer Loop Control : No
            Show PID dialog during test : No
            Use Multiplier : No
```

```
        Data Collection :
            Acquisition Type 1 : Rate
            Channel 1 : Time
            Rate Value Input 1 : Data Acquisition Rate
            Buffer : -1
            Buffer Full Action : Fold and Reduce Data Rate
            Take Data on Pause : Yes
            Preserve last data point : No

    One-Time Formula - ResistanceOutOfContact
        Data Collection :
            Acquisition Type 1 : Rate
            Channel 1 : Time
            Rate Value Input 1 : Data Acquisition Rate
            Buffer : -1
            Buffer Full Action : Fold and Reduce Data Rate
            Take Data on Pause : Yes
            Preserve last data point : No

    Show Results
        Variables :
ResistanceOutOfContact
        Additional Message : Resistance Out of Contact
        Dialog Type : Dialog Type
        Run-Time Message : Showing Resistance Out of Contact
        Data Collection : [ Disabled ]

    One-Time Formula - ComplianceResistance
        Data Collection : [ Disabled ]

    Test Message : [ Disabled ]
    CSM Test Segment
        Send Command to CSM controller.
        Send Command   : REFP. -3.0
        Run-Time Message : CSM Phase Test Segment
        Data Collection : [ Disabled ]

    CSM Test Segment
        CSM Channel : _HarmonicFrequency
        Value : Harmonic Frequency Target
        Run-Time Message : Set Harmonic Frequency
        Data Collection : [ Disabled ]

    CSM Test Segment
        Send Command to CSM controller.
        Send Command   : TC 10
```

```
    Run-Time Message :
    Data Collection : [ Disabled ]

CSM Test Segment
    CSM Channel : _HarmonicDisplacement
    Value : Harmonic Displacement Target
    Run-Time Message : Set Harmonic Displacement
    Data Collection : [ Disabled ]

One-Time Formula - ParkDisplacement : [ Disabled ]
Hold
    Channel : Raw Displacement
    Hold Current Value : Yes
    Enable Stopping Conditions : Yes
        Channel : _HarmonicDisplacement
        Comparison : Becomes Equal and Stabile
        Value : Harmonic Displacement Target
    Run-Time Message : Holding for Harmonic stability (Before First Surface
    Find)
    PID Parameters
        Always use Outer Loop Control : No
        Show PID dialog during test : No
        Use Multiplier : No
    Data Collection :
        Acquisition Type 1 : Rate
        Channel 1 : Time
        Rate Value Input 1 : Data Acquisition Rate
        Buffer : -1
        Buffer Full Action : Fold and Reduce Data Rate
        Take Data on Pause : Yes
        Preserve last data point : No

IF _SurfaceDisplacement >= 2.0
    Data Collection : [ Disabled ]

Hold
    Channel : Raw Load
    Hold Current Value : Yes
    Enable Stopping Conditions : Yes
        Channel : _HarmonicDisplacement
        Comparison : Becomes Equal and Stabile
        Value : Harmonic Displacement Target
    Run-Time Message : Holding for Harmonic Stability (_HarmonicDisplacement
     stabilizes to +/- 3nm tolerance)
    PID Parameters
        Always use Outer Loop Control : No
```

```
        Show PID dialog during test : No
        Use Multiplier : No
    Data Collection :
        Acquisition Type 1 : Rate
        Channel 1 : Time
        Rate Value Input 1 : Data Acquisition Rate
        Buffer : -1
        Buffer Full Action : Fold and Reduce Data Rate
        Take Data on Pause : Yes
        Preserve last data point : No

One-Time Formula - Fast Surface Approach Loading Rate
    Data Collection : [ Disabled ]

        Load vs Disp Slope
            Comparison : >
            Variable :
            Action : Next Test Segment
GoTo
    Rate Channel : Raw Load
    Rate Unit Class : Force Rate
    Direction : Loading
    Rate Value : Fast Surface Approach Loading Rate
    Enable Stopping Conditions : Yes
        Stop Channel : Raw Displacement
        Comparison : Exceeds
        Stop Value : ZeroDisplacement
        Ramping Time (Stopping Conditions Ignored) : Ramp Condition Ignored Time

        End Action : Stop
    Run-Time Message : Moving to Surface find position (0 displacement)
    PID Parameters
        Always use Outer Loop Control : Yes
        Show PID dialog during test : No
        Use Multiplier : No
    Data Collection : [ Disabled ]

Hold
    Channel : Raw Load
    Hold Current Value : Yes
    Enable Stopping Conditions : Yes
        Channel : Time
        Comparison : Increases by
        Value : Drift Determination Time
    Run-Time Message : Holding
    PID Parameters
```

```
        Always use Outer Loop Control : No
        Show PID dialog during test : No
        Use Multiplier : No
    Data Collection : [ Disabled ]

GoTo
    Rate Channel : Raw Displacement
    Rate Unit Class : Speed
    Direction : Loading
    Rate Value : FastApproachRate
    Enable Stopping Conditions : Yes
        Stop Channel : _HarmonicStiffness
        Comparison : Exceeds
        Stop Value : Surface Stiffness Increase
        Ramping Time (Stopping Conditions Ignored) : Ramp Condition Ignored Time

        End Action : Stop
    Run-Time Message : Fast Surface Find
    PID Parameters
        Always use Outer Loop Control : Yes
        Show PID dialog during test : No
        Use Multiplier : No
    Data Collection : [ Disabled ]

One-Time Formula - SetSurfaceDisplacement
    Data Collection : [ Disabled ]

        R_Meas4W : [ Disabled ]
            Comparison : <
            Variable :
            Action : Next Test Segment
One-Time Formula - Approach Distance For Second Surface Find
    Data Collection : [ Disabled ]

        R_Meas4W : [ Disabled ]
            Comparison : <
            Variable :
            Action : Next Test Segment
GoTo
    Rate Channel : Raw Displacement
    Rate Unit Class : Speed
    Direction : UnLoading
    Rate Value : FastApproachRate
    Enable Stopping Conditions : Yes
        Stop Channel : Raw Displacement
        Comparison : Becomes less than
```

```
        Stop Value : Approach Distance For Second Surface Find
        Ramping Time (Stopping Conditions Ignored) : [ Disabled ]
        End Action : Stop
    Run-Time Message : Unloading for second Surface find
    PID Parameters
        Always use Outer Loop Control : Yes
        Show PID dialog during test : No
        Use Multiplier : No
    Data Collection : [ Disabled ]

        R_Meas4W : [ Disabled ]
            Comparison : <
            Variable :
            Action : Next Test Segment
Hold
    Channel : Raw Load
    Hold Current Value : Yes
    Enable Stopping Conditions : Yes
        Channel : Time
        Comparison : Increases by
        Value : Drift Determination Time
    Run-Time Message : Holding for Harmonic Stability (Time increases by Dri
    ft Det Time)
    PID Parameters
        Always use Outer Loop Control : No
        Show PID dialog during test : No
        Use Multiplier : No
    Data Collection :
        Acquisition Type 1 : Rate
        Channel 1 : Time
        Rate Value Input 1 : Data Acquisition Rate
        Buffer : -1
        Buffer Full Action : Fold and Reduce Data Rate
        Take Data on Pause : Yes
        Preserve last data point : No

        R_Meas4W : [ Disabled ]
            Comparison : <
            Variable :
            Action : Next Test Segment
GoTo
    Rate Channel : Raw Displacement
    Rate Unit Class : Speed
    Direction : Loading
    Rate Value : SlowApproachRate
    Enable Stopping Conditions : Yes
```

```
        Stop Channel : _HarmonicStiffness
        Comparison : Exceeds
        Stop Value : Surface Stiffness Increase
        Ramping Time (Stopping Conditions Ignored) : Ramp Condition Ignored Time

        End Action : Stop
    Run-Time Message : Slow Surface Find
    PID Parameters
        Always use Outer Loop Control : Yes
        Show PID dialog during test : No
        Use Multiplier : No
    Data Collection : [ Disabled ]

        R_Meas4W : [ Disabled ]
            Comparison : <
            Variable :
            Action : Next Test Segment
One-Time Formula - Surface Marker
    Data Collection : [ Disabled ]

        R_Meas4W : [ Disabled ]
            Comparison : <
            Variable :
            Action : Next Test Segment
One-Time Formula - SetSurfaceDisplacement
    Data Collection : [ Disabled ]

        R_Meas4W : [ Disabled ]
            Comparison : <
            Variable :
            Action : Next Test Segment
One-Time Formula - Approach Distance For Second Surface Find
    Data Collection : [ Disabled ]

        R_Meas4W : [ Disabled ]
            Comparison : <
            Variable :
            Action : Next Test Segment
Hold
    Channel : Raw Load
    Hold Current Value : Yes
    Enable Stopping Conditions : Yes
        Channel : Time
        Comparison : Increases by
        Value : Settle Time
    Run-Time Message : Holding during second surface find
```

```
    PID Parameters
        Always use Outer Loop Control : No
        Show PID dialog during test : No
        Use Multiplier : No
    Data Collection :
        Acquisition Type 1 : Rate
        Channel 1 : Time
        Rate Value Input 1 : Data Acquisition Rate
        Buffer : -1
        Buffer Full Action : Fold and Reduce Data Rate
        Take Data on Pause : Yes
        Preserve last data point : No

        R_Meas4W
            Comparison : <
            Variable :
            Action : Post-Specimen
GoTo
    Rate Channel : Raw Displacement
    Rate Unit Class : Speed
    Direction : UnLoading
    Rate Value : FastApproachRate
    Enable Stopping Conditions : Yes
        Stop Channel : Raw Displacement
        Comparison : Becomes less than
        Stop Value : Approach Distance For Second Surface Find
        Ramping Time (Stopping Conditions Ignored) : [ Disabled ]
        End Action : Stop
    Run-Time Message : Unloading after second Surface find
    PID Parameters
        Always use Outer Loop Control : Yes
        Show PID dialog during test : No
        Use Multiplier : No
    Data Collection : [ Disabled ]

        R_Meas4W
            Comparison : <
            Variable :
            Action : Post-Specimen
Surface Find : [ Disabled ]
EndIF
    Data Collection : [ Disabled ]

Hold
    Channel : Raw Displacement
    Hold Current Value : No
```

```
    Value : Approach Distance For Second Surface Find
    Enable Stopping Conditions : Yes
        Channel : Time
        Comparison : Increases by
        Value : Peak Hold Time
    Run-Time Message : Displacement to Approach Dist for 2nd Surf find - Pea
    k Hold Time
    PID Parameters
        Always use Outer Loop Control : No
        Show PID dialog during test : No
        Use Multiplier : No
    Data Collection :
        Acquisition Type 1 : Rate
        Channel 1 : Time
        Rate Value Input 1 : Data Acquisition Rate
        Buffer : -1
        Buffer Full Action : Fold and Reduce Data Rate
        Take Data on Pause : Yes
        Preserve last data point : No

Nano Configuration Test Segment
    Find Offset : Yes
    Set Offset : No
    Set Gain : Yes
    Set Gain to : Displacement Gain (0-7)
    Run-Time Message : Setting Instrument Gains.
    Data Collection : [ Disabled ]

Tare Time : [ Disabled ]
Test Message : [ Disabled ]
One-Time Formula - CurrentOn
    Data Collection : [ Disabled ]

WHILE ResistanceOfContact < MaxSwitchResistance AND ResistanceOutOfConta
ct>40
    Data Collection : [ Disabled ]

CSM Test Segment
    CSM Channel : _HarmonicDisplacement
    Value : Harmonic Displacement Target
    Run-Time Message : Set Harmonic Displacement
    Data Collection : [ Disabled ]

Hold
    Channel : Raw Displacement
    Hold Current Value : No
```

```
    Value : Approach Distance For Second Surface Find
    Enable Stopping Conditions : Yes
        Channel : _HarmonicDisplacement
        Comparison : Becomes Equal and Stabile
        Value : Harmonic Displacement Target
    Run-Time Message : Holding for Harmonic stability - Equal and Stable to
    harmonic displacement target
    PID Parameters
        Always use Outer Loop Control : No
        Show PID dialog during test : No
        Use Multiplier : No
    Data Collection :
        Acquisition Type 1 : Rate
        Channel 1 : Time
        Rate Value Input 1 : Drift Determination Acquisition Rate
        Buffer : -1
        Buffer Full Action : Remove Initial Data Points
        Take Data on Pause : Yes
        Preserve last data point : Yes

One-Time Formula - Time At Start Of Approach
    Data Collection : [ Disabled ]

Segment Type Test Segment
    New Segment Type : Load Segment Type
    Segment Type Channel : Segment Type
    Segment Index Channel : Segment Number
    Run-Time Message : Setting Segment type
    Data Collection : [ Disabled ]

One-Time Formula - Time At Start Of Approach : [ Disabled ]
Approach Surface : [ Disabled ]
GoTo
    Rate Channel : Raw Displacement
    Rate Unit Class : Speed
    Direction : Loading
    Rate Value : Surface Approach Velocity
    Enable Stopping Conditions : Yes
        Stop Channel : Raw Displacement
        Comparison : Increases by
        Stop Value : 4000 Nanometers
        Ramping Time (Stopping Conditions Ignored) : Ramp Condition Ignored Time

        End Action : Continue
    Run-Time Message : Cycle Cantilever Surface Find (0.5 Hz data collection
    )
```

```
    PID Parameters
        Always use Outer Loop Control : Yes
        Show PID dialog during test : No
        Use Multiplier : No
    Data Collection :
        Acquisition Type 1 : Rate
        Channel 1 : Time
        Rate Value Input 1 : Drift Determination Acquisition Rate
        Buffer : -1
        Buffer Full Action : Remove Initial Data Points
        Take Data on Pause : Yes
        Preserve last data point : Yes

        _HarmonicStiffness
            Comparison : Increases By
            Variable : HarmonicContactTriggerCantilever
            Action : Next Test Segment
GoTo
    Rate Channel : Raw Displacement
    Rate Unit Class : Speed
    Direction : Loading
    Rate Value : Surface Approach Velocity
    Enable Stopping Conditions : Yes
        Stop Channel : _HarmonicStiffness
        Comparison : Increases by
        Stop Value : HarmonicContactTriggerCantilever
        Ramping Time (Stopping Conditions Ignored) : [ Disabled ]
        End Action : Stop
    Run-Time Message : Cycle Cantilever Surface Find (2Hz data acq rate)
    PID Parameters
        Always use Outer Loop Control : Yes
        Show PID dialog during test : No
        Use Multiplier : No
    Data Collection :
        Acquisition Type 1 : Rate
        Channel 1 : Time
        Rate Value Input 1 : 2HzDataRate
        Buffer : -1
        Buffer Full Action : Remove Initial Data Points
        Take Data on Pause : Yes
        Preserve last data point : Yes

One-Time Formula - SetSurfaceDisplacement
    Data Collection : [ Disabled ]

One-Time Formula - Surface Marker
```

```
    Data Collection :
        Acquisition Type 1 : Rate
        Channel 1 : Time
        Rate Value Input 1 : Data Acquisition Rate
        Buffer : -1
        Buffer Full Action : Fold and Reduce Data Rate
        Take Data on Pause : Yes
        Preserve last data point : Yes

One-Time Formula : [ Disabled ]
Segment Type Test Segment : [ Disabled ]
Test Message : [ Disabled ]
GoTo
    Rate Channel : Raw Load
    Rate Unit Class : Force Rate
    Direction : Loading
    Rate Value : LoadingRate
    Enable Stopping Conditions : Yes
        Stop Channel : Time
        Comparison : Increases by
        Stop Value : Ramp Condition Ignored Time
        Ramping Time (Stopping Conditions Ignored) : [ Disabled ]
        End Action : Continue
    Run-Time Message : Indenter Head loading (1) to bring cantilever into el
    ectrical contact
    PID Parameters
        Always use Outer Loop Control : Yes
        Show PID dialog during test : Yes
        Save updated parameters : Yes
        kP : 0
        kI : 0
        kD : 1
        Maximum Integral (mN/s) : 5000.00
        Derivative Interval (s) : 1
        Maximum Speed (mN/s) : 5000.00
        Minimum Speed (mN/s) : 0.00
        Use Multiplier : No
    Data Collection :
        Acquisition Type 1 : Rate
        Channel 1 : Time
        Rate Value Input 1 : Data Acquisition Rate
        Buffer : -1
        Buffer Full Action : Fold and Reduce Data Rate
        Take Data on Pause : Yes
        Preserve last data point : Yes
```

```
        Time : [ Disabled ]
            Comparison : >
            Variable : Max Segment Time
            Action : Post-Specimen
GoTo
    Rate Channel : Raw Load
    Rate Unit Class : Force Rate
    Direction : Loading
    Rate Value : LoadingRate
    Enable Stopping Conditions : Yes
        Stop Channel : _HarmonicStiffness
        Comparison : Increases by
        Stop Value : HarmonicContactTrigger
        Ramping Time (Stopping Conditions Ignored) : [ Disabled ]
        End Action : Stop
    Run-Time Message : Indenter Head loading (2) to bring cantilever into el
    ectrical contact
    PID Parameters
        Always use Outer Loop Control : Yes
        Show PID dialog during test : Yes
        Save updated parameters : Yes
        kP : 0
        kI : 0
        kD : 1
        Maximum Integral (mN/s) : 5000.00
        Derivative Interval (s) : 1
        Maximum Speed (mN/s) : 5000.00
        Minimum Speed (mN/s) : 0.00
        Use Multiplier : No
    Data Collection :
        Acquisition Type 1 : Rate
        Channel 1 : Time
        Rate Value Input 1 : 10 Hz Data Rate
        Acquisition Type 2 : Level Crossing
        Channel 2 : (_ACH0)Voltage4WMeasured
        Delta Input 2 : LevelCrossingVoltageChange
        Buffer : -1
        Buffer Full Action : Fold and Reduce Data Rate
        Take Data on Pause : Yes
        Preserve last data point : Yes

        Time : [ Disabled ]
            Comparison : Increases By
            Variable : Max Segment Time
            Action : Post-Specimen
CSM Test Segment
```

```
    CSM Channel : _HarmonicLoad
    Value : ZeroForceAmp
    Run-Time Message : Set CSM Harmonic load to zero
    Data Collection :
        Acquisition Type 1 : Rate
        Channel 1 : Time
        Rate Value Input 1 : Data Acquisition Rate
        Buffer : -1
        Buffer Full Action : Fold and Reduce Data Rate
        Take Data on Pause : Yes
        Preserve last data point : Yes

        Time : [ Disabled ]
            Comparison : >
            Variable : Max Segment Time
            Action : Post-Specimen
Segment Type Test Segment
    New Segment Type : LoadContact Segment Type
    Segment Type Channel : Segment Type
    Segment Index Channel : Segment Number
    Run-Time Message : Set LoadContact Segment Type
    Data Collection :
        Acquisition Type 1 : Rate
        Channel 1 : Time
        Rate Value Input 1 : Data Acquisition Rate
        Buffer : -1
        Buffer Full Action : Fold and Reduce Data Rate
        Take Data on Pause : Yes
        Preserve last data point : Yes

One-Time Formula - PlateContactMarker
    Data Collection :
        Acquisition Type 1 : Rate
        Channel 1 : Time
        Rate Value Input 1 : Data Acquisition Rate
        Buffer : -1
        Buffer Full Action : Fold and Reduce Data Rate
        Take Data on Pause : Yes
        Preserve last data point : Yes

One-Time Formula - BeamStiffness
    Data Collection :
        Acquisition Type 1 : Rate
        Channel 1 : Time
        Rate Value Input 1 : Data Acquisition Rate
        Buffer : -1
```

```
        Buffer Full Action : Fold and Reduce Data Rate
        Take Data on Pause : Yes
        Preserve last data point : Yes

One-Time Formula - Max Raw Load on Contact
    Data Collection :
        Acquisition Type 1 : Rate
        Channel 1 : Time
        Rate Value Input 1 : Data Acquisition Rate
        Buffer : -1
        Buffer Full Action : Fold and Reduce Data Rate
        Take Data on Pause : Yes
        Preserve last data point : Yes

One-Time Formula - Limit Detection Load On Contact
    Data Collection :
        Acquisition Type 1 : Rate
        Channel 1 : Time
        Rate Value Input 1 : Data Acquisition Rate
        Buffer : -1
        Buffer Full Action : Fold and Reduce Data Rate
        Take Data on Pause : Yes
        Preserve last data point : Yes

        Raw Load
            Comparison : >
            Variable :
            Action : Next Test Segment
GoTo
    Rate Channel : Raw Load
    Rate Unit Class : Force Rate
    Direction : Loading
    Rate Value : Loading Rate After Plate Contact
    Enable Stopping Conditions : Yes
        Stop Channel : R_Meas4W
        Comparison : Becomes less than
        Stop Value : Resistance Trigger
        Ramping Time (Stopping Conditions Ignored) : 1 Second Delay Time
        End Action : Continue
    Run-Time Message : Loading the contact (until R_Meas4W drops below Resis
    tance Trigger)
    PID Parameters
        Always use Outer Loop Control : Yes
        Show PID dialog during test : No
        Use Multiplier : No
    Data Collection :
```

```
        Acquisition Type 1 : Rate
        Channel 1 : Time
        Rate Value Input 1 : 25 Hz Data Rate
        Acquisition Type 2 : Level Crossing
        Channel 2 : (_ACH0)Voltage4WMeasured
        Delta Input 2 : LevelCrossingVoltageChange
        Buffer : -1
        Buffer Full Action : Fold and Reduce Data Rate
        Take Data on Pause : Yes
        Preserve last data point : Yes

        Raw Load
            Comparison : >
            Variable :
            Action : Next Test Segment
GoTo
    Rate Channel : Raw Load
    Rate Unit Class : Force Rate
    Direction : Loading
    Rate Value : Loading Rate After Plate Contact
    Enable Stopping Conditions : Yes
        Stop Channel : Raw Load
        Comparison : Exceeds
        Stop Value : Max Raw Load on Contact
        Ramping Time (Stopping Conditions Ignored) : [ Disabled ]
        End Action : Stop
    Run-Time Message : Loading contact up to maximum contact force
    PID Parameters
        Always use Outer Loop Control : Yes
        Show PID dialog during test : No
        Use Multiplier : No
    Data Collection :
        Acquisition Type 1 : Rate
        Channel 1 : Time
        Rate Value Input 1 : 25 Hz Data Rate
        Acquisition Type 2 : Level Crossing
        Channel 2 : (_ACH0)Voltage4WMeasured
        Delta Input 2 : LevelCrossingVoltageChange
        Buffer : -1
        Buffer Full Action : Fold and Reduce Data Rate
        Take Data on Pause : Yes
        Preserve last data point : Yes

One-Time Formula - EndOfLoadingMarker
    Data Collection :
        Acquisition Type 1 : Rate
```

```
        Channel 1 : Time
        Rate Value Input 1 : Data Acquisition Rate
        Buffer : -1
        Buffer Full Action : Fold and Reduce Data Rate
        Take Data on Pause : Yes
        Preserve last data point : Yes

Segment Type Test Segment
    New Segment Type : Hold Segment Type
    Segment Type Channel : Segment Type
    Segment Index Channel : Segment Number
    Run-Time Message : Set hold segment type
    Data Collection :
        Acquisition Type 1 : Rate
        Channel 1 : Time
        Rate Value Input 1 : Data Acquisition Rate
        Buffer : -1
        Buffer Full Action : Fold and Reduce Data Rate
        Take Data on Pause : Yes
        Preserve last data point : Yes

Hold
    Channel : Raw Load
    Hold Current Value : Yes
    Enable Stopping Conditions : Yes
        Channel : Time
        Comparison : Increases by
        Value : Peak Hold Time
    Run-Time Message : Hold Peak Value
    PID Parameters
        Always use Outer Loop Control : No
        Show PID dialog during test : No
        Use Multiplier : No
    Data Collection :
        Acquisition Type 1 : Rate
        Channel 1 : Time
        Rate Value Input 1 : Data Acquisition Rate
        Acquisition Type 2 : Level Crossing
        Channel 2 : (_ACH0)Voltage4WMeasured
        Delta Input 2 : LevelCrossingVoltageChange
        Buffer : -1
        Buffer Full Action : Fold and Reduce Data Rate
        Take Data on Pause : Yes
        Preserve last data point : Yes

Segment Type Test Segment
```

```
    New Segment Type : Unload From Peak Segment Type
    Segment Type Channel : Segment Type
    Segment Index Channel : Segment Number
    Run-Time Message : Unloading
    Data Collection :
        Acquisition Type 1 : Rate
        Channel 1 : Time
        Rate Value Input 1 : Data Acquisition Rate
        Buffer : -1
        Buffer Full Action : Fold and Reduce Data Rate
        Take Data on Pause : Yes
        Preserve last data point : Yes

One-Time Formula - UnloadResistanceMeasurementThreshold : [ Disabled ]
One-Time Formula - UnloadingMarker
    Data Collection :
        Acquisition Type 1 : Rate
        Channel 1 : Time
        Rate Value Input 1 : Data Acquisition Rate
        Buffer : -1
        Buffer Full Action : Fold and Reduce Data Rate
        Take Data on Pause : Yes
        Preserve last data point : Yes

        Time
            Comparison : Increases By
            Variable : MaxsUnloadContactSegmentTime
            Action : Next Test Segment
GoTo
    Rate Channel : Raw Load
    Rate Unit Class : Force Rate
    Direction : UnLoading
    Rate Value : Unloading Rate
    Enable Stopping Conditions : Yes
        Stop Channel : Raw Load
        Comparison : Decreases by
        Stop Value : MaximumContactForceXtwo
        Ramping Time (Stopping Conditions Ignored) : [ Disabled ]
        End Action : Stop
    Run-Time Message : Unloading
    PID Parameters
        Always use Outer Loop Control : Yes
        Show PID dialog during test : No
        Use Multiplier : No
    Data Collection :
        Acquisition Type 1 : Rate
```

```
        Channel 1 : Time
        Rate Value Input 1 : Data Acquisition Rate
        Acquisition Type 2 : Level Crossing
        Channel 2 : (_ACH0)Voltage4WMeasured
        Delta Input 2 : LevelCrossingVoltageChange
        Buffer : -1
        Buffer Full Action : Fold and Reduce Data Rate
        Take Data on Pause : Yes
        Preserve last data point : Yes

Test Message : [ Disabled ]
One-Time Formula - End Of Mechanical Deflection Test
    Data Collection :
        Acquisition Type 1 : Rate
        Channel 1 : Time
        Rate Value Input 1 : Data Acquisition Rate
        Buffer : -1
        Buffer Full Action : Fold and Reduce Data Rate
        Take Data on Pause : Yes
        Preserve last data point : Yes

GoTo
    Rate Channel : Raw Displacement
    Rate Unit Class : Speed
    Direction : UnLoading
    Rate Value : FastApproachRate
    Enable Stopping Conditions : Yes
        Stop Channel : Raw Displacement
        Comparison : Becomes less than
        Stop Value : Approach Distance For Second Surface Find
        Ramping Time (Stopping Conditions Ignored) : [ Disabled ]
        End Action : Stop
    Run-Time Message : Pulling Indenter Head Back
    PID Parameters
        Always use Outer Loop Control : Yes
        Show PID dialog during test : No
        Use Multiplier : No
    Data Collection :
        Acquisition Type 1 : Rate
        Channel 1 : Time
        Rate Value Input 1 : Drift Determination Acquisition Rate
        Buffer : -1
        Buffer Full Action : Fold and Reduce Data Rate
        Take Data on Pause : Yes
        Preserve last data point : Yes
```

```
        Time
            Comparison : Increases By
            Variable : Drift Determination Time
            Action : Next Test Segment
Hold
    Channel : Raw Displacement
    Hold Current Value : No
    Value : Approach Distance For Second Surface Find
    Enable Stopping Conditions : Yes
        Channel : Time
        Comparison : Increases by
        Value : Settle Time
    Run-Time Message : Settling time delay at out of contact hold distance (
    approach dist for 2nd Surf Find for 5 sec)
    PID Parameters
        Always use Outer Loop Control : No
        Show PID dialog during test : No
        Use Multiplier : No
    Data Collection :
        Acquisition Type 1 : Rate
        Channel 1 : Time
        Rate Value Input 1 : Drift Determination Acquisition Rate
        Buffer : -1
        Buffer Full Action : Fold and Reduce Data Rate
        Take Data on Pause : Yes
        Preserve last data point : Yes

        Time
            Comparison : Increases By
            Variable : Drift Determination Time
            Action : Next Test Segment
Segment Type Test Segment
    New Segment Type : CyclingSegment
    Segment Type Channel : Segment Type
    Segment Index Channel : Segment Number
    Run-Time Message : Cycling Segment
    Data Collection : [ Disabled ]

Test Message : [ Disabled ]
One-Time Formula - RelaySwitchON
    Data Collection : [ Disabled ]

Hold
    Channel : Raw Displacement
    Hold Current Value : No
    Value : Approach Distance For Second Surface Find
```

```
    Enable Stopping Conditions : Yes
        Channel : Time
        Comparison : Increases by
        Value : Beam Cycle Time
    Run-Time Message : Cycling PZT / Simulated Switch
    PID Parameters
        Always use Outer Loop Control : No
        Show PID dialog during test : No
        Use Multiplier : No
    Data Collection : [ Disabled ]

Test Message : [ Disabled ]
One-Time Formula - RelaySwitchOFF
    Data Collection : [ Disabled ]

One-Time Formula - PZTInContactMinusTwo : [ Disabled ]
GoTo
    Rate Channel : Raw Displacement
    Rate Unit Class : Speed
    Direction : UnLoading
    Rate Value : FastApproachRate
    Enable Stopping Conditions : Yes
        Stop Channel : Raw Displacement
        Comparison : Becomes less than
        Stop Value : Approach Distance For Second Surface Find
        Ramping Time (Stopping Conditions Ignored) : [ Disabled ]
        End Action : Stop
    Run-Time Message : Pulling Indenter Head Back
    PID Parameters
        Always use Outer Loop Control : Yes
        Show PID dialog during test : No
        Use Multiplier : No
    Data Collection : [ Disabled ]

Hold
    Channel : Raw Displacement
    Hold Current Value : No
    Value : Approach Distance For Second Surface Find
    Enable Stopping Conditions : Yes
        Channel : Time
        Comparison : Increases by
        Value : Ramp Condition Ignored Time
    Run-Time Message : Pausing for indenter pull-back/placement
    PID Parameters
        Always use Outer Loop Control : No
        Show PID dialog during test : No
```

```
        Use Multiplier : No
    Data Collection : [ Disabled ]

One-Time Formula - PZTInContactPlusTwo
    Data Collection : [ Disabled ]

Hold
    Channel : Raw Displacement
    Hold Current Value : No
    Value : Approach Distance For Second Surface Find
    Enable Stopping Conditions : Yes
        Channel : Time
        Comparison : Increases by
        Value : Settle Time
    Run-Time Message : Measuring Contact Resistance in Contact.
    PID Parameters
        Always use Outer Loop Control : No
        Show PID dialog during test : No
        Use Multiplier : No
    Data Collection :
        Acquisition Type 1 : Rate
        Channel 1 : Time
        Rate Value Input 1 : Data Acquisition Rate
        Buffer : -1
        Buffer Full Action : Fold and Reduce Data Rate
        Take Data on Pause : Yes
        Preserve last data point : Yes

One-Time Formula - Resistance in Contact
    Data Collection :
        Acquisition Type 1 : Rate
        Channel 1 : Time
        Rate Value Input 1 : Data Acquisition Rate
        Buffer : -1
        Buffer Full Action : Fold and Reduce Data Rate
        Take Data on Pause : Yes
        Preserve last data point : Yes

Test Message : [ Disabled ]
One-Time Formula - PZTInContactMinusTwo
    Data Collection : [ Disabled ]

One-Time Formula - PZTInContactMinusOne : [ Disabled ]
GoTo
    Rate Channel : Raw Displacement
    Rate Unit Class : Speed
```

```
    Direction : UnLoading
    Rate Value : FastApproachRate
    Enable Stopping Conditions : Yes
        Stop Channel : Raw Displacement
        Comparison : Becomes less than
        Stop Value : Approach Distance For Second Surface Find
        Ramping Time (Stopping Conditions Ignored) : [ Disabled ]
        End Action : Stop
    Run-Time Message : Pulling Indenter Head Back
    PID Parameters
        Always use Outer Loop Control : Yes
        Show PID dialog during test : No
        Use Multiplier : No
    Data Collection : [ Disabled ]

Hold
    Channel : Raw Displacement
    Hold Current Value : No
    Value : Approach Distance For Second Surface Find
    Enable Stopping Conditions : Yes
        Channel : Time
        Comparison : Increases by
        Value : Settle Time
    Run-Time Message : Measuring Out of Contact Resistance.
    PID Parameters
        Always use Outer Loop Control : No
        Show PID dialog during test : No
        Use Multiplier : No
    Data Collection :
        Acquisition Type 1 : Rate
        Channel 1 : Time
        Rate Value Input 1 : Data Acquisition Rate
        Buffer : -1
        Buffer Full Action : Fold and Reduce Data Rate
        Take Data on Pause : Yes
        Preserve last data point : Yes

One-Time Formula - ResistanceOutOfContact
    Data Collection :
        Acquisition Type 1 : Rate
        Channel 1 : Time
        Rate Value Input 1 : Data Acquisition Rate
        Buffer : -1
        Buffer Full Action : Fold and Reduce Data Rate
        Take Data on Pause : Yes
        Preserve last data point : Yes
```

```
    Increment Cycle
        Data Collection : [ Disabled ]

    IF Mod(_CycleNumber,3) EQ 0 : [ Disabled ]
    Save Sample : [ Disabled ]
    EndIF : [ Disabled ]
    EndWHILE
        Data Collection : [ Disabled ]

    Test Message : [ Disabled ]
    One-Time Formula - RelaySwitchOFF
        Data Collection : [ Disabled ]

    One-Time Formula - PZTZero
        Data Collection : [ Disabled ]

    One-Time Formula - CurrentOff
        Data Collection : [ Disabled ]

    Show Results
        Variables :
ResistanceOutOfContact
        Additional Message : Showing Last Resistance Out of Contact Measurement.

Should be > 40 (using 80 ohm shunt resistor), otherwise showing
contact stiction
        Dialog Type : Dialog Type
        Run-Time Message :
        Data Collection : [ Disabled ]

    Show Results
        Variables :
Resistance in Contact
        Additional Message : Showing last in Contact Resistance Measurement
        Dialog Type : Dialog Type
        Run-Time Message :
        Data Collection : [ Disabled ]

    One-Time Formula - CurrentOff
        Data Collection : [ Disabled ]

    One-Time Formula - PZTZero
        Data Collection : [ Disabled ]

    One-Time Formula - RelaySwitchOFF
```

```
    Data Collection : [ Disabled ]

Save Sample
    Data Collection : [ Disabled ]

Recalculate Test
    Data Collection : [ Disabled ]

Test Message
    Message : Write down POS? of Z-Stage to ensure no drift during test
    Dialog Type : OK Dialog
    Run-Time Message : Pausing for user data transcription
    Data Collection : [ Disabled ]

Test Message
    Message : LOWER Z ROUGH POSITIONING STAGE FOR TABLE MOVEMENT.
    Dialog Type : OK Dialog
    Run-Time Message :
    Data Collection : [ Disabled ]
```

Bibliography

1. Abys, Joseph A. "Palladium Plating," *Plating & Surface Finishing*, 29–30, August 2004.

2. Adams, George G., Sinan Müftü, and Nazif Mohd Azar. "A Scale-Dependent Model for Multi-Asperity Contact and Friction," *ASME Journal of Tribology*, 125:700–708, 2003.

3. Agrait, Nicolas, Alfredo Levy Yeyati, and Jan M. van Ruitenbeek. "Quantum properties of atomic-sized conductors," *Physics Reports*, 377:81–279, 2003.

4. Almeida, L., R. Ramadoss, R. Jackson, K. Ishikawa, and Q. Yu. "Study of the electrical contact resistance of multi-contact MEMS relays fabricated using the MetalMUMPS process," *Journal of Micromechanics and Microengineering*, 16:1189–1194, 2006.

5. Ashby, Michael F. *Materials Selection in Mechanical Design*. Butterworth Heinemann, Oxford, 1999.

6. *ASM Handbook, Volume 18: Friction, Lubrication, and Wear Technology*. ASM International, New York, 1992.

7. Automation Creations, Inc. "MATWEB: The Online Materials Database," www.matweb.com.

8. Bannuru, T., S. Narksitipan, W.L. Brown, and R.P. Vinci. "Effects of V additions on the mechanical behavior of Au thin films for MEMS contact switches." Allyson L. Hartzell (editor), *Proceedings of SPIE, Reliability, Packaging, Testing, and Characterization of MEMS/MOEMS VI*, volume 6463. SPIE, 2007.

9. Bannuru, Thirumalesh. *Effects of Alloying on Mechanical Behavior of Noble Metal Thin Films for Micro-electronic and MEMS/NEMS Applications*. Ph.D. dissertation, Lehigh University, Bethlehem, PA, January 2008.

10. Bannuru, Thirumalesh, Walter L. Brown, Suparut Narksitipan, and Richard P. Vinci. "The electrical and mechanical properties of Au-V and Au-V_2O_5 thin films for wear-resistant RF MEMS switches," *Journal of Applied Physics*, 103:083522–(1–6), 2008.

11. Barker, N. Scott and Gabriel M. Rebeiz. "Distributed MEMS True-Time Delay Phase Shifters and Wide-Band Switches," *IEEE Transactions on Microwave Theory and Techniques*, 46(11):1881–1890, 1998.

12. Bayer, R.G. (editor). *Symposium on Selection and Use of Wear Tests for Metals*. American Society for Testing and Materials, MRS, New Orleans, LA, 17-21 Nov 1975.

13. Beale, John and R. Fabian Pease. "Limits of High-Density, Low-Force Pressure Contacts," *IEEE Transactions on Components, Packaging, and Manufacturing Technology-Part A*, 17(2):257–262, 1994.

14. Beale, J.P. and R.F.W. Pease. "Apparatus for Studying Ultrasmall Contacts." *Proceedings of the 38th IEEE Holm Conference on Electrical Contacts*, 45–49. IEEE, Philadelphia, PA, October 18-21 1992.

15. Becher, David, Richard Chan, Michael Hattendorf, and Milton Feng. "Reliability Study of Low-Voltage RF MEMS Switches." *Proceedings of 2002 GaAs-MANTECH Conference*, 54–57. San Diego, CA, 8-11 April 2002.

16. Beck, Paul A. *Electronic Structure and Alloy Chemistry of the Transition Elements*. Interscience Publishers a division of John Wiley & Sons, New York, NY, 1963.

17. Bhushan, Bharat. "Contact mechanics of rough surfaces in tribology: multiple asperity contact," *Tribology Letters*, 4:1–35, 1998.

18. Bhushan, Bharat (editor). *Handbook of Micro/Nano Tribology, Second edition*. CRC Press, Boca Raton, 1999.

19. Bhushan, Bharat. *Introduction to Tribology*. John Wiley & Sons, Inc., New York, 2002.

20. Bhushan, Bharat. "Nanotribology and nanomechanics," *Wear*, 259:1507–1531, 2005.

21. Bhushan, Bharat. "Nanotribology and nanomechanics of MEMS/NEMS and BioMEMS/BioNEMS materials and devices," *Microelectronic Engineering*, 2006.

22. Bhushan, Bharat (editor). *Handbook of Nanotechnology, 2nd edition*. Springer, Boston, 2007.

23. Bowden, F.P. and J.B.P. Williamson. "Electrical conduction in solids I. Influence of the passage of current on the contact between solids," *Proceedings of the Royal Society of London, Series A, Mathematical and Physical Sciences*, 246(1244):1–12, July 22 1958.

24. Brady, George S. and Henry R. Clauser. *Materials Handbook, 12th Ed.* McGraw-Hill Book Company, New York, 1986.

25. Briggs, David and John T. Grant (editors). *Surface Analysis by Auger and X-Ray Photoelectron Spectroscopy*. Surface Spectra and IM Publications, Trowbridge, UK, 2003.

26. Brinckmann, Steffen, Ju-Young Kim, and Julia R. Greer. "Fundamental Differences in Mechanical Behavior between Two Types of Crystals at the Nanoscale," *Physical Review Letters*, 100:155502, 1–4, 2008.

27. Brown, Chris, III Arthur S. Morris, Angus I. Kingon, and Jacqueline Krim.

28. Buckley, Donald H. "The Metal-to-Metal Interface and Its Effect on Adhesion and Friction," *Journal of Colloid and Interface Science*, 58(1):36–53, January 1977.

29. Carton, Andrew. *Investigating the Lifetime of RF MEMS Ohmic Switches Using a Lifetime Test Station.* Master's Thesis, The University of New Mexico, Albuquerque, New Mexico, July 2006.

30. Cass, Stephen. "MEMS in Space," *IEEE Spectrum*, 56–61, July 2001.

31. Chan, M.L., Francis E.H. Tay, Logeeswaran VJ, K.Y. Zeng, Lu Shen, and F.S. Chau. "Experimental Determination of Micromachined Discrete and Continuous Device Spring Constants using Nanoindentation Method." *Proceedings of SPIE, Design, Test, Integration, and Packaging of MEMS/MOEMS 2002*, volume 4755, 726–735. SPIE, 2002.

32. Chan, Richard, Robert Lesnick, David Becher, and Milton Feng. "Low-Actuation Voltage RF MEMS Shunt Switch With Cold Switching Lifetime of Seven Billion Cycles," *Journal of Microelectromechanical Systems*, 12(5):713–719, October 2003.

33. Chang, Wen-Ruey. *Contact, Adhesion, and Static Friction of Metallic Rough Surfaces.* Ph.D. dissertation, Graduate Division, University of California, Berkeley, 1986.

34. Chang, Wen-Ruey. "An elastic-plastic contact model for a rough surface with an ion-plated soft metallic coating," *Wear*, 212:229–237, 1997.

35. Chang, W.R., I. Etsion, and D.B. Bogy. "An Elastic-Plastic Model for the Contact of Rough Surfaces," *Journal of Tribology*, 109:257–263, April 1987.

36. Chen, L., H. Lee, Z.J. Guo, K.W. Gilbert, S. Mall, K.D. Leedy, N.E. McGruer, and G.G. Adams. "Contact resistance study of noble metals and alloy films using a scanning probe microscope test station," *Journal of Applied Physics*, 102(7), 2007.

37. Chen, Lei. *Physics of Microcontacts for MEMS Relays.* Ph.D. dissertation, Northeastern University, Department of Electrical and Computer Engineering, Boston, MA, August 2007.

38. Chen, Lei. "Personal Communication," 2008.

39. Chen, Lei, Nicol E. McGruer, and George G. Adams. "AFM-Based Testing and Measurements of Contact and Stiction in a Micromechanical Switch." *Proceedings of 2004 ASME/STLE International Joint Tribology Conference*, 65–68. ASME/STLE, ASME, Long Beach, California USA, October 24-27 2004.

40. Collins, Jack A. *Failure of Materials in Mechanical Design.* Wiley Inter-Science, New York, 1993.

41. Constantine A. Balanis, ed. *Modern Antenna Handbook*. John Wiley & Sons, Inc., New York, 2008.

42. Courtney, Thomas H. *Mechanical Behavior of Materials*. McGraw-Hill Publishing Company, New York, 1990.

43. Coutu, R.A., P.E. Kladitis, R. Cortez, R.E. Strawser, and R.L. Crane. "Microswitches with Sputtered Au, AuPd, Au-on-AuPt, and AuPtCu Alloy Electric Contacts." *IEEE Holm Conference on Electrical Contacts*, 214–221. IEEE, 2004.

44. Coutu, R.A., Jr., P.E. Kladitis, L.A. Starman, and J.R. Reid. "A Comparison of Micro-switch Analytic, Finite Element, and Experimental Results," *Sensors and Actuators A*, 2(A115):252–258, 21 September 2004.

45. Coutu, Ronald A., James R. Reid, Rebecca Cortez, Richard E. Strawser, and Paul E. Kladitis. "Microswitches with Sputtered Au, AuPd, Au-on-AuPt, and AuPtCu Alloy Electric Contacts," *IEEE Transactions on Components and Packaging Technologies*, 29(2):341–349, 2006.

46. Coutu, Ronald A., Jr. *Electrostatic Radio Frequency (RF) Microelectromechanical Systems (MEMS) Switches with Metal Alloy Electric Contacts*. Ph.D. dissertation, Graduate School of Engineering, Air Force Institute of Technology (AETC), Wright-Patterson AFB OH, September 2004. AFIT//DS//ENG//04-05.

47. Coutu, Ronald A., Jr., Paul E. Kladitis, Kevin D. Leedy, and Robert L. Crane. "Selecting Metal Alloy Electric Contact Materials for MEMS Switches," *Journal of Micromechanics and Microengineering*, 14:1157–1164, 2004.

48. DeBoer, M.P., J.A. Knapp, T.A. Michalske, U. Srinivasan, and R. Maboudian. "Adhesion Hysteresis of Silane Coated Microcantilevers," *Acta Material*, 48:4531–4541, 2000.

49. DelRio, Frank W., Maarten P. de Boer, James A. Knapp, Jr. E. David Reedy, Peggy J. Clews, and Martin L. Dunn. "The role of van der Waals forces in adhesion of micromachined surfaces," *Nature Materials*, 4:629–634, August 2005.

50. DeNatale, Jeffrey and Robert Mihailovich. "RF MEMS Reliability." *Proceedings of the 12th International Conference on Solid State Sensors, Actuators and Microsystems, Transducers '03*, 943–946. IEEE, IEEE, Boston, June 8-12 2003.

51. DeNatale, Jeffrey, Robert Mihailovich, and James Waldrop. "Techniques for Reliability Analysis of MEMS RF Switch." *40th Annual International Reliability Physics Symposium*, 116–117. IEEE, IEEE, Dallas, Texas, 2002.

52. DeWolf, Ingrid. "Instrumentation and Methodology for MEMS Testing, Reliability Assessment and Failure Analysis." *Proceedings 24th International Conference on Microelectronics (MIEL 2004)*, 57–63. IEEE, IEEE, Serbia and Montenegro, 16-19 May 2004.

53. Dhariwal, R.S., J.-M. Torres, and M.P.Y. Desmulliez. "Electric field breakdown at micrometre separations in air and nitrogen at atmospheric pressure," *IEEE Proc.-Sci. Meas. Technol.*, 147(5):261–265, September 2000.

54. Dickrell III, Daniel J. and Michael T. Dugger. "The Degradation of Electrical Contact Resistance of Metal Films at Low Contact Force." *Proceedings of 2004 ASME/STLE International Joint Tribology Conference*, 9–15. ASME/STLE, ASME, Long Beach, California USA, October 24-27 2004.

55. Dickrell III, Daniel J. and Michael T. Dugger. "The Effects of Surface Contamination on Resistance Degradation of Hot-Switched Low-Force MEMS Electrical Contacts." *51st IEEE Holm Conference on Electrical Contacts*, 255–258. IEEE, IEEE, 26-28 September 2005.

56. Dieter, George E. *Mechanical Metallurgy, Third Edition*. McGraw Hill, Boston, 1986.

57. Dieter, George E. *Engineering Design: A Materials and Processing Approach*. McGraw-Hill, Boston,MA, 1991.

58. Du, Yan, George G. Adams, Nicol E. McGruer, and Izhak Etsion. "A parameter study of separation modes of adhering microcontacts," *Journal of Applied Physics*, 103:064902:1–9, 2008.

59. Du, Yan, Lei Chen, Nicol E. McGruer, George G. Adams, and Itzak Etsion. "A Finite Element Model of Asperity Contact With Adhesion and Plasticity." *Proceedings of STLE/ASME International Joint Tribology Conference*, 1–8. STLE/ASME, ASME, San Antonio, Texas, October 22-25 2006. IJTC2006-12295.

60. Du, Yan, Lei Chen, Nicol E. McGruer, George G. Adams, and Izhak Etsion. "A finite element model of loading and unloading of an asperity contact with adhesion and plasticity," *Journal of Colloid and Interface Science*, 312:522–528, 2007.

61. Dyck, et. al., Christopher W. "A Compact MMIC-Compatible RF MEMS Switch." *MEMS Components and Applications for Industry, Automobiles, Aerospace and Communication II*, volume 4981, 222–229. SPIE, 2003.

62. Dyck, et. al., Christopher W. "Fabrication and Characterization of Ohmic Contacting RF MEMS Switches." *MEMS/MOEMS Components and Their Applications*, volume 5344, 79–88. SPIE, 2004.

63. Ebel, John L. "Personal Communication,".

64. Ebel, John L. "SEM Micrographs," February 2007. Briefing material.

65. Ebel, John L., Daniel J. Hyman, and Harvey S. Newman. "RF-MEMS Testing-Beyond the S-Parameters," *IEEE Microwave Magazine*, 8(6):56–60, December 2007.

66. Espinosa, Horacio D., M. Fischer, Erik Herbert, and Warren Oliver. "Identification of Residual Stress State in an RF-MEMS Device," MTS White Paper, 2000.

67. Espinoza, H.D., Y. Zhu, M. Fischer, and J. Hutchinson. "An Experimental/Computational Approach to Identify Moduli and Residual Stress in MEMS Radio-Frequency Switches," *Experimental Mechanics*, 43(3):309–316, September 2003.

68. Feng, Gang, William D. Nix, Youngki Yoon, and Cheol Jin Lee. "A study of the mechanical properties of nanowires using nanoindentation," *Journal of Applied Physics*, 99(074304):1–10, 2006.

69. Ferrante, John, John R. Smith, and James H. Rose. "Universal Binding Energy Relations in Metallic Adhesion," *NASA Technical Memorandum 86889*, 1984. Prepared for the 1984 Materials Research Society Annual Meeting, Boston, MA, November 27-29, 1984.

70. Fischer-Cripps, Anthony C. *Introduction to Contact Mechanics*. Springer, New York, 2000.

71. Flinn, Richard A. and Paul K. Trojan. *Engineering Materials and Their Applications, 4th ed.* Houghton Mifflin Company, Boston, MA, 1990.

72. Fortescue, Peter, John Stark, and Graham Swinderd. *Spacecraft Systems Engineering, Third Edition*. John Wiley & Sons, Inc., London, 2003.

73. Fuller, K.N.G. and D. Tabor. "The effect of surface roughness on the adhesion of elastic solids," *Proceedings of the Royal Society of London, Series A, Mathematical and Physical Sciences*, 345:327–342, 1975.

74. Gally, Brian J., C. Cameron Abnet, and Stuart Brown. "Investigation of Wear of Microelectromechanical Contacts." *Mat. Res. Soc. Symp Proc, Materials Science of Microelectromechanical Systems (MEMS) Devices II*, volume 605, 117–122. Materials Research Society, MRS, Boston, MA, Nov 29 - Dec 1 1999.

75. Gammel, Peter, Georg Fischer, and Jeremie Bouchaud. "RF MEMS and NEMS Technology, Devices, and Applications," *Bell Labs Technical Journal*, 10(3):29–59, 2005.

76. Gerberich, William and William Mook. "Nanomechanics: A new picture of plasticity," *Nature Materials*, 4:577–578, 2005.

77. Germer, L.H. "Physical Processes in Contact Erosion," *Journal of Applied Physics*, 29(7):1067–1082, July 1958.

78. Germer, L.H. and J.L. Smith. "Activation of Electrical Contacts by Organic Vapors," *The Bell System Technical Journal*, 769–812, May 1957.

79. Goins, David A., Richard D. Nelson, and John S. McKillop. "Design of a 20 GHz Low Loss Ohmic Contact RF MEMS Switch." *Proceedings of 2007 IEEE/MTT-S International Microwave Symposium*, 311–374. IEEE, Honolulu, HI, June 2007.

80. Goldsmith, Chuck, John Maciel, and John McKillop. "Demonstrating Reliability," *IEEE Microwave Magazine*, 8(6):56–60, December 2007.

81. Golio, Mike (editor). *RF and Microwave Semiconductor Device Handbook*. CRC Press, Boca Raton, 2003.

82. Grant, P.D., M.W. Denhoff, and R.R. Mansour. "A Comparison Between RF MEMS Switches and Semiconductor Switches." *Proceedings of teh 2004 International Conference on MEMS, NANO and Smart Systems (ICMENS'04)*. IEEE, 2004.

83. Greeley, Jeff and Jens K. Nørskov. "A general scheme for the estimation of oxygen binding energies on binary transition metal surface alloys," *Surface Science*, 592:104–111, 2005.

84. Green, Robert. "RF Measurement Basics for the Non-RF Test Engineer," Keithley Instruments, Inc. Application Note, January 2007.

85. Greenwood, J.A. and J.B.P. Williamson. "Electrical conduction in solids II. Theory of temperature-dependent conductors," *Proceedings of the Royal Society of London, Series A, Mathematical and Physical Sciences*, 246(1244):13–31, July 22 1958.

86. Greenwood, J.A. and J.B.P. Williamson. "Contact of nominally flat surfaces," *Proceedings of the Royal Society of London, Series A, Mathematical and Physical Sciences*, 295(1442):300–319, December 06 1966.

87. Greer, Julia R. "Bridging the Gap Between Computational and Experimental Length Scales: A Review on Nano-scale Plasticity," *Reviews on Advanced Materials Science*, 13(1):59–70, 2006.

88. Greer, Julia R. and William D. Nix. "Size dependence of mechanical properties of gold at the sub-micron scale," *Applied Physics A*, 80:1625–1629, 2005.

89. Greer, Julia R. and William D. Nix. "Nanoscale gold pillars strengthened through dislocation starvation," *Physical Review B*, 73(245410):1–6, 2006.

90. Greer, Julia R. and William D. Nix. "Erratum: Size dependence of mechanical properties of gold at the sub-micron scale," *Applied Physics A*, 90:203, 2008.

91. Greer, Julia R., Warren C. Oliver, and William D. Nix. "Size dependence of mechanical properties of gold at the micron scale in the absence of strain gradients," *Acta Materialia*, 53:1821–1830, 2005.

92. Gregori, G. and D.R. Clarke. "Mechanical creep as a life-limiting factor of radio frequency microswitches," *Applied Physics Letters*, 87:154101 (1–3), 2005.

93. Gregori, G., R.E. Mihailovich, J.F. DeNatale, and D.R. Clarke. "Development of Adhesive Contact of MEMS-Switches Upon Actuation Cycling." *18th IEEE Conference on Micro Electro Mechanical Systems. MEMS 2005*, 439–442. IEEE, 30 Jan - 3 Feb 2005.

94. Gregori, Giuliano and David R. Clarke. "The interrelation between adhesion, contact creep, and roughness on the life of gold contacts in radio-frequency microswitches," *Journal of Applied Physics*, 100(094904):1–10, 2006.

95. Gronland, Tor-Arne, Pelle Rangsten, Martin Nese, and Martin Lang. "Miniaturization of components and systems for space using MEMS-technology," *Acta Astronautica*, 61:228–233, 2007.

96. Guo, Z.J., N.E. McGruer, and G.G. Adams. "Modeling, simulation and measurement of the dynamic performance of an ohmic contact, electrostatically actuated RF MEMS switch," *Journal of Micromechanics and Microengineering*, 17:1899–1909, 2007.

97. Hannoe, S. and H. Hosaka. "Electrical characteristics of micro-mechanical contacts," *Microsystem Technologies*, 3(1):31–35, 1996.

98. Haque, M.A. and M.T.A. Saif. "Thermo-mechanical properties of nano-scale freestanding aluminum films," *Thin Solid Films*, 484:364–368, 2005.

99. Harman, George G. *Reliability and Yield Problems of Wire Bonding in Microelectronics: The Application of Materials and Interface Science.* National Institute of Standards and Technology, Reston, VA, 1989.

100. Hemker, Kevin J. and William D. Nix. "Nanoscale Deformation: Seeing is believing," *Nature Materials*, 7:97–98, February 2008.

101. Hermance, H.W. and T.F. Egan. "Organic Deposits on Precious Metal Contacts," *The Bell System Technical Journal*, 739–776, May 1958.

102. Hinohara, Kunio. "Tribology in Electrical Contacts," *Japanese Journal of Tribology*, 36(5):583–588, 1994.

103. Holm, Ragnar. *Electric Contacts: Theory and Application, 4th ed.* Springer-Verlag, Berlin/Heidelberg/New York, 1967.

104. Hong, S., T.P. Weihs, J.C. Bravman, and W.D. Nix. "The determination of mechanical parameters and residual stresses for thin films using micro-cantilever beams." *Materials Research Society Symposium Proceedings*, volume 130, 93–98. MRS, Pittsburgh, PA, 1989.

105. Hosaka, Hiroshi, Hiroki Kuwano, and Keiichi Yanagisawa. "Electromagnetic Microrelays: Concepts and Fundamental Characteristics." *Proceedings of IEEE Microelectromechanical Systems*, 12–17. IEEE, 1993.

106. Hyman, Daniel, Juan Lam, Brett Warneke, Adele Schmitz, T.Y. Hsu, Julia Brown, James Schaffner, Andy Walston, Robert Y. Loo, Mehran Mehregany, and Jae Lee. "Surface-Micromachined RF MEMs Switches on GaAs Substrates," *International Journal of RF and Computer Aided Engineering*, 9(4):348–361, 1999.

107. Hyman, Daniel and Mehran Mehregany. "Contact Physics of Gold Microcontacts for MEMS Switches," *IEEE Transactions on Components and Packaging Technology*, 22(3):357–364, September 1999.

108. Hyman, Daniel John. *Physics of Microcontacts for MEMS Relays*. Ph.D. dissertation, Department of Electrical Engineering and Applied Physics, Case Western Reserve University, May 2000.

109. Hyun, Seungmin, Oliver Kraft, and Richard P. Vinci. "Mechanical behavior of Pt and Pt-Ru solid solution alloy thin films," *Acta Materialia*, 52:4199–4211, 2004.

110. Iliuc, Ivan. *Tribology of Thin Layers*. Elsevier Scientific Publishing Company, Amsterdam, 1980.

111. Jaeger, Richard C. *Introduction to Microelectronic Fabrication, 2nd Ed.* Prentice Hall, Upper Saddle River, New Jersey, 2002.

112. Janson, Siegfried W. "Micro/Nanotechnology for Micro/Nano/Picosatellites." *Proceedings of AIAA Space 2003*, 2003-6269, 1–11. American Institute of Aeronautics and Astronautics, AIAA, Long Beach, California USA, 23-25 September 2003.

113. Jensen, B.D., L.W. Chow, R.F. Webbink, K. Saitou, J.L. Volakis, and K. Kurabayashi. "Force Dependence of RF MEMS Switch Contact Heating." *Proceedings of 33rd European Microwave Conference*, 137–140. 2004.

114. Jensen, Brian D. *Multi-Physics Modeling and Experimental Investigation of Low-Force MEMS Switch Contact Behavior*. Ph.D. dissertation, Department of Mechanical Engineering, University of Michigan, 2004.

115. Jensen, Brian D., Linda L.-W. Chow, Kuangwei Huang, Kazuhiro Sautou, John. L. Volakis, and Katsuo Kurabayashi. "Effect of Nanoscale Heating on Electrical Transport in RF MEMS Switch Contacts," *Journal of Microelectromechanical Systems*, 14(5):935–946, October 2005.

116. Jensen, Brian D., Kuangwei Huang, Linda Chow, Kazuhiro Sautou, John. L. Volakis, and Katsuo Kurabayashi. "Asperity Heating for Repair of Metal Contact RF MEMS Switches." *IEEE MTT-S Digest*, 1939–1942. 2004.

117. Jensen, Brian D., Kuangwei Huang, Linda L.-W. Chow, and Katsuo Kurabayashi. "Adhesion effects on contact opening dynamics in micromachined switches," *Journal of Applied Physics*, 97(103535):1–9, 16 May 2005.

118. Jensen, Brian D., Kuangwei Huang, Linda L.-W. Chow, and Katsuo Kurabayashi. "Low-force contact heating and softening using micromechanical switches in diffusive-ballistic electron-transport transition," *Applied Physics Letters*, 86(023507):1–3, 2005.

119. Johnson, K.L. *Contact Mechanics*. Cambridge University Press, Cambridge, 1985.

120. Jones, Edward E., Matthew R. Begley, and Kevin D. Murphy. "Adhesion of Micro-Cantilevers Subjected to Mechanical Point Loading: Modeling and Experiments," *Journal of Mechanics and Physics of Solids*, 51:1601–1622, 2003.

121. Jones, Refugio and Mark Chapman. "RF MEMS in mobile phones," *RF Design*, 20–26, September 2005.

122. Kading, Glen A. *Micro-Electromechanical Switches for Micro-Satellite Power Transfer*. Master's Thesis, Graduate School of Engineering and Management, Air Force Institute of Technology, Wright-Patterson AFB, OH, December 1997. AFIT//GCS//ENG//97D-11.

123. Keefer, H.J. and R.H. Gumley. "Relay Contact Behavior Under Non-Eroding Circuit Conditions," *The Bell System Technical Journal*, 777–814, May 1958.

124. Khan, Akhtar S., Babak Farrokh, and Laszlo Takacs. "Compressive properties of Cu with different grain sizes: sub-micron to nanometer realm," *Journal of Material Science*, 43:3305–3313, 2008.

125. Kim, Jong-Man, Sanghyo Lee, Chang-Wook Baek, Youngwoo Kwon, and Yong-Kweon Kim. "Cold- and hot-switching lifetime characterizations of ohmic-contact RF-MEMS switches," *IEICE Electronics Express*, 5(11):418–423, 2008.

126. Kim, M., J.B. Hacker, R.E. Mihailovich, and J.F. DeNatale. "A DC-to-40 GHz Four-Bit RF MEMS True-Time Delay Network," *IEEE Microwave and Wireless Components Letters*, 11(2):56–58, February 2001.

127. Knapp, James A. and Maarten P. de Boer. "Mechanics of Microcantilever Beams Subject to Combined Electrostatic and Adhesive Forces," *Journal of Microelectromechanical Systems*, 11(6):754–764, December 2002.

128. Kobayashi, Atsuto, Satoshi Takano, and Takayoshi Kubono. "Measuring equipment and measurements of adhesive force between gold electrical contacts," *IEEE Transactions on Components, Packaging, and Manufacturing Technology - Part A*, 21(1):46–53, 1998.

129. Kogut, L. and I. Etsion. "Elastic-Plastic Contact Analysis of a Sphere and Rigid Flat," *Journal of Applied Mechanics*, 69:657–662, September 2002.

130. Kogut, Lior and Izhak Etsion. "Adhesion in elastic-plastic spherical microcontact," *Journal of Colloid and Interface Science*, 261:372–378, 2003.

131. Komvopoulos, K. "Adhesion and friction forces in microelectromechanical systems: mechanisms, measurement, surface modification techniques, and adhesion theory," *Journal of Adhesion Science and Technology*, 17(4):477–517, 2003.

132. Kruglick, Ezekiel John Joseph. *Microrelay design, performance, and systems*. Ph.D. dissertation, Department of Electrical Engineering and Computer Science, University of California, Berkeley, Spring 1999.

133. Kucko, Jay F. *Insulator Charging in RF MEMS Capacitive Switches*. Ph.D. dissertation, Air Force Institute of Technology, Wright-Patterson AFB, OH, 2005.

134. Kucko, Jay F., James C. Petrosky, J. Robert Reid, and Yung Kee Yeo. "Non-Charge Related Mechanism Affecting Capacitive MEMS Switch Lifetime," *IEEE Microwave and Wireless Components Letters*, 16(3), March 2006.

135. Kudrle, Thomas David. *Design and Fabrication of High Performance RF MEMS Devices*. Ph.D. dissertation, Graduate School, Cornell University, 2000.

136. Kwiatkowski, Regina, Mihai Vladimirescu, Andre Zyburna, and Jelena Bradic. "High Contact Resistance Readings on Clean Microwave Mobile Contacts." *Proceedings of IEEE Holm Conference on Electrical Contacts*, 160–167. IEEE, 2004.

137. Kwon, Hyouk, Dong-June Choi, Jae-Hyoung Park, Hee-Chul Lee, Yong-Hee Park, Yong-Dae Kim, Hyo-Jin Nam, Young-Chang Joo, and Jong-Uk Bu. "Contact Materials and Reliability for High Power RF-MEMS Switches." *Proceedings of 20th International Conference on Micro Electro Mechanical Systems (MEMS 2007)*, 231–234. IEEE, Kobe, Japan, 21-25 January 2007.

138. Lafontan, Xavier, Francis Pressecq, Guy Perez, Christian Dufaza, and Jean-Michel Karam. "Physical and Reliability Issues in MEMS Micro-Relays with Gold Contacts." *Proceedings of SPIE, Reliability, Testing, and Characterization of MEMS/MOEMS*, volume 4558, 11–21. SPIE, SPIE, 2001.

139. Lampen, J., S. Majumder, R. Morrison, A. Chaudry, and J. Maciel. "A Wafer-Capped, High-Lifetime Ohmic MEMS RF Switch," *International Journal of RF and Microwave Computer-Aided Engineering*, 14(4):338–344, July 2004.

140. Lee, Hee-Chul, Jae-Yeong Park, and Jong-Uk Bu. "Piezoelectrically Actuated RF MEMS DC Contact Switches With Low Voltage Operation," *IEEE Microwave and Wireless Components Letters*, 15(4):202–204, April 2005.

141. Lee, Hsin-Yi, Yung-Wei Hsieh, C.-H. Hsu, and K.S. Liang. "Characteristics of sputter-deposited Ru thin films on Si substrates," *Materials Chemistry and Physics*, 82:984–990, 2003.

142. Lee, Hyukjae, Ronald A. Coutu, Shankar Mall, and Kevin D. Leedy. "Characterization of metal and metal alloy films as contact materials in MEMS switches," *Journal of Micromechanics and Microengineering*, 16:557–563, 2006.

143. Lee, Hyukjae, Ronald A. Coutu Jr, Shankar Mall, and Paul E. Kladitis. "Nanoindentation Technique for Characterizing Cantilever Beam Style RF Microelectromechanical Systems (MEMS) Switches," *Journal of Micromechanics and Microengineering*, 15:1230–1235, 2005.

144. Leedy, K.D., R. Cortez, J.L. Ebel, R.E. Strawser, A.P. Walker, G.C. DeSalvo, and R.M. Young. "Metallization schemes for radio frequency microelectromechanical system switches," *Journal of Vacuum Science and Technology A*, 21(4):1172–1177, Jul/Aug 2003.

145. Leedy, Kevin D. May 2007. Personal Communication.

146. Leedy, Kevin D., Richard E. Strawser, Rebecca Cortez, and John L. (Jack) Ebel. "Thin-Film Encapsulated RF MEMS Switches," *Journal of Microelectromechanical Systems*, 16(2):304–309, April 2007.

147. Leseman, Zayd Chad. *A Novel Method for Testing Freestanding Nanofilms using a Custom MEMS Load Cell*. Ph.D. dissertation, University of Illinois Urbana-Champaign, Urbana-Champaign, IL, April 2006.

148. Li, Xiaodong and Bharat Bhushan. "Fatigue Studies of Nanoscale Structures for MEMS/NEMS Applications using Nanoindentation Techniques," *Surface and Coatings Technology*, 163-164:521–526, 2003.

149. Lide, David R. (editor). *CRC Handbook of Chemistry and Physics, 2005-2006, 86th Ed.* CRC Press, Boca Raton, FL, 2005.

150. Lilleodden, E.T. and W.D. Nix. "Microstructural length-scale effects in the nanoindentation behavior of thin gold films," *Acta Materialia*, 54:1583–1593, 2006.

151. Lin, Ming-Tzer, Richard R. Chromik, Nicholas Barbosa III, Paul El-Deiry, Seungmin Hyun, Walter L. Brown, Richard P. Vinci, and Terry J. Delph. "The influence of vanadium alloying on the elevated-temperature mechanical properties of thin gold films," *Thin Solid Films*, 515:7919–7925, 2007.

152. Lin, Ming-Tzer, Paul El-Deiry, Richard R. Chromik, Nicholas Barbosa, Walter L. Brown, Terry J. Delph, and Richard P. Vinci. "Temperature-dependent microtensile testing of thin film materials for application to microelectromechanical system," *Microsystem Technology*, 12:1045–1051, 2006.

153. Llewellyn Jones, Frank. *The Physics of Electrical Contacts*. Clarendon Press, Oxford, 1957.

154. Losee, Ferril A. *RF Systems, Components, and Circuits Handbook*. Artech House, Boston, MA, 2005.

155. Maciel, John. "Briefing," September 2008.

156. Maciel, John, Sumit Majumder, Richard Morrison, and James Lampen. "Lifetime Characteristics of Ohmic MEMS Switches." *Proceedings of SPIE, Reliablity, Testing, and Characterization of MEMS/MOEMS III*, volume 5343, 9–14. SPIE - The International Society for Optical Engineering, SPIE, San Jose, CA, 26-28 January 2004.

157. Maciel, John J., John F. Slocum, John K. Smith, and John Turtle. "MEMS Electronically Steerable Antennas for Fire Control Radars." *Proceedings of 2007 IEEE Radar Conference*, 677–682. IEEE, Waltham, MA, November 2007.

158. Majumdar, B.S., Bing Ye, D.A. Lavan, and S.V. Prasad. "Contact and Adhesion of Curved Rough Surfaces with Application to MEMS." *Proceedings of*

WTC2005 World Tribology Congress III. ASME, Washington DC, September 12-16 2005.

159. Majumder, S., J. Lampen, R. Morrison, and J. Maciel. "MEMS Switches," *IEEE Instrumentation & Measurement Magazine*, 12–15, March 2003.

160. Majumder, S., J. Lampen, R. Morrison, and J. Maciel. "A Packaged, High-Lifetime Ohmic MEMS RF Switch." *Microwave Symposium Digest, 2003 IEEE MTT-S International*, 1935–1938. IEEE, IEEE, 8-13 June 2003.

161. Majumder, S., N.E. McGruer, and G.G. Adams. "Adhesion and Contact Resistance in an Electrostatic MEMS Microswitch," *18th IEEE International Conference on Micro Electro Mechanical Systems (MEMS 2005)*, 215–218, 2005.

162. Majumder, Sumit. *Contact Properties of a Micromechanical Switch with Gold-on-Gold Contacts*. Ph.D. dissertation, Department of Electrical and Computer Engineering, Northeastern University, 2003.

163. Majumder, Sumit, N.E. McGruer, George G. Adams, P.M. Zavracky, Richard H. Morrison, and Jacqueline Krim. "Study of contacts in an electrostatically actuated microswitch," *Sensors and Actuators A*, 93:19–26, 2001.

164. Majumder, Sumit, N.E. McGruer, P.M. Zavracky, G. G. Adams, R. H. Morrison, and J. Krim. "Measurement and modeling of surface micromachined electrostatically actuated microswitches." *Proceedings of International Conference on Solid-State Sensors and Actuators(Transducers 97)*, 1145–1148. IEEE, Chicago, IL, June 1997.

165. Majumder, Sumit, Nicol McGruer, and George G. Adams. "Contact Resistance and Adhesion in a MEMS Microswitch." *Proceedings of 2003 ASME/STLE Joint International Tribology Conference*, 79–84. ASME/STLE, ASME, Ponte Vedra Beach, Florida USA, October 26-29 2003.

166. Marsh, Eric D. *Thin Film Encapsulation of Radio Frequency (RF) Microelectromechanical Systems (MEMS) Switches*. Master's Thesis, Graduate School of Engineering and Management, Air Force Institute of Technology, Wright-Patterson AFB, OH, March 2004. AFIT//GE//ENG//04-16.

167. Mastrangelo, C.H. and C.H. Hsu. "A Simple Experimental Technique for the Measurement of the Work of Adhesion of Microstructures." *Proceedings of IEEE MEMS 1992*, 208–212. Hilton Head, 1992.

168. Maugis, D. *Contact, Adhesion and Rupture of Elastic Solids*. Springer, Berlin, 2000.

169. Maugis, D. and H.M. Pollock. "Surface Forces, Deformation and Adherence at Metal Microcontacts," *Acta Metall.*, 32(9):1323–1334, 1984.

170. McGruer, N.E., G.G. Adams, L. Chen, Z.J. Guo, and Y. Du. "Mechanical, Thermal, and Material Influences on Ohmic-Contact-Type MEMS Switch Op-

eration." *MEMS 2006*, 230–233. IEEE, IEEE, Istanbul, Turkey, 22-26 January 2006 2006.

171. McKillop, John. "RF MEMS: Ready for Prime Time," *Microwave Journal*, February 2007. TeraVicta Technologies Inc., Austin, TX.

172. Meng, Hsien-Chung. *Wear Modeling: Evaluation and Categorization of Wear Models*. Ph.D. dissertation, Department of Mechanical Engineering, The University of Michigan, 1994.

173. Mercado, Lei L., Shun-Meen Kuo, Tien-Yu Tom Lee, and Lianjun Liu. "Mechanics-Based Solutions to RF MEMS Switch Stiction Problem," *IEEE Transactions on Components and Packaging Technology*, 27(3):357–364, September 2004.

174. Mihailovich, R.E. and J.F. DeNatale. "A Model for the Electrical Degradation of Metal Microcontacts During Many Cycle Operation." *Proceedings of 2004 ASME/STLE International Joint Tribology Conference*, 1–4. ASME/STLE, ASME, Long Beach, California USA, October 24-27 2004.

175. Mihailovich, R.E., M. Kim, J.B. Hacker, E.A. Sovero, J. Studer, J.A. Higgins, and J.F. DeNatale. "MEM Relay for Reconfigurable RF Circuits," *IEEE Microwave and Wireless Components Letters*, 11(2):53–55, February 2001.

176. Miller, Keith, Allen Cowan, Greg Hames, and Busbee Hardy. *SOIMUMPS Design Handbook, Rev. 4.0*. MEMScAP, 2004.

177. National Instruments Corporation. *Guide to Selecting an RF Switch*, 2006.

178. Neufeld, Christian N. and Werner F. Rieder. "Influence of Organic Vapors on Contact Reliability." *Proceedings of the 17th International Conference on Electric Contacts*, 135–144. Mano R&D Tech Center, Nagoya, Japan, July 1994.

179. Neufeld, Christian N. and Werner F. Rieder. "Carbon Contamination of Contacts Due to Organic Vapors," *IEEE Transactions on Components, Packaging, and Manufacturing Technology, Part A*, 18(2):399–404, June 1995.

180. Neufeld, Christian N. and Werner F. Rieder. "Electrical Characteristics of Various Contact Contaminations," *IEEE Transactions on Components, Packaging, and Manufacturing Technology, Part A*, 18(2):369–374, June 1995.

181. Newman, Harvey S., John L. Ebel, Daniel Judy, and John Maciel. "Lifetime Measurements on a High-Reliability RF-MEMS Contact Switch," *IEEE Microwave and Wireless Components Letters*, 2008.

182. Nix, William D., Julia R. Greer, Gang Feng, and Erica T. Lilleodden. "Deformation at the nanometer and micrometer length scales: Effects of strain gradients and dislocation starvation," *Thin Solid Films*, 515:3152–3157, 2007.

183. Oberhammer, Joachim and Göran Stemme. "Active Opening Force and Passive Contact Force Electrostatic Switches for Soft Metal Contact Materials," *Journal of Microelectromechanical Systems*, 15(5):1235–1242, October 2006.

184. O'Hern, Michael. "Dedicated MEMS Testers Becoming Available," *R&D Magazine*, 38–40, December 2000.

185. Oliver, W.C. and G.M. Pharr. "Measurement of hardness and elastic modulus by instrumented indentation: Advances in understanding and refinements to methodology," *Journal of Materials Research*, 19(1):3–20, January 2004.

186. Ono, Takahito, Dong Youn Sim, and Masayoshi Esashi. "Micro-discharge and electric breakdown in a micro-gap," *Journal of Micromechanics and Microengineering*, 10:445–451, 2000.

187. Pacheco, Sergio P., Linda P.B. Katehi, and Clark T.-C. Nguyen. "Design of Low Actuation Voltage RF MEMS Switch." *Microwave Symposium Digest, 2000 IEEE MTT-S International*, 165–168. IEEE, 2000.

188. Patton, S.T. and J.S. Zabinski. "Failure mechanisms of capacitive MEMS RF switch contacts," *Tribology Letters*, 19(4):265–272, August 2005.

189. Patton, S.T. and J.S. Zabinski. "Fundamental studies of Au contacts in MEMS RF switches," *Tribology Letters*, 18(2):215–230, February 2005.

190. Patton, Steven T., Kalathil C. Eapen, and Jeffrey S. Zabinski. "Micro/Nanotribology of RF MEMS Switches." *Proceedings of 2004 ASME/STLE International Joint Tribology Conference*, 1–3. ASME/STLE, Long Beach, California USA, October 24-27 2004.

191. Patton, Steven T., Kalathil C. Eapen, Jeffrey S. Zabinski, Jeffrey H. Sanders, and Andrey A. Voevodin. "Lubrication of microelectromechanical systems radio frequency switch contacts using self-assembled monolayers," *Journal of Applied Physics*, 102:024903–(1–5), 2007.

192. Patton, Steven T., Joseph M. Slocik, Angela Campbell, Jianjun Hu, Rajesh R. Naik, and Andrey A. Voevodin. "Bimetallic nanoparticles for surface modification and lubrication of MEMS switch contacts," *Nanotechnology*, 19:405705, 2008.

193. Patton, Steven T. and Andrey A. Voevodin. "Tribological challenges in MEMS/NEMS devices." *Proceedings of 2007 ASME/STLE International Joint Tribology Conference*, 1–3. ASME/STLE, San Diego, California USA, October 22-24 2007.

194. Patton, Steven T. and Jeffrey S. Zabinski. "Failure mechanisms of DC and capacitive RF MEMS switches." Danelle M. Tanner and Rajeshuni Ramesham (editors), *Proceedings of SPIE: Reliability, Packaging, Testing and Characterization of MEMS/MOEMS V*, 61110E 1–20. SPIE, 2006.

195. Pauling, Linus. *General Chemistry*. Dover Publications, Inc., New York, 1988.

196. Petersen, Kurt E. and C.R. Guarnieri. "Young's modulus measurements of thin films using micromechanics," *Journal of Applied Physics*, 50(11):6761–6766, November 1979.

197. Pharr, G.M. and W.C. Oliver. "Measurement of Thin Film Mechanical Properties Using Nanoindentation," *MRS Bulletin*, 17(7):28–33, July 1992.

198. Pruitt, Beth L. and Thomas W. Kenny. "Piezoresistive cantilevers and measurement system for characterizing low force electrical contacts," *Sensors and Actuators A*, 104:68–77, 2003.

199. Rabinowicz, Ernest. *Friction and Wear of Materials, Second edition*. John Wiley & Sons, Inc., New York, 1995.

200. Radant Technologies, Inc. "World's First Demonstration of Microelectromechanical Systems Based X-Band Radar," www.radantmems.com/radantmems/04-06-06.html, April 2006.

201. Randall, Nicholas X. and Richard A.J. Soden. "Characterisation of MEMS mechanical properties using nanoscale techniques." *Proceedings of SPIE, Reliability, Testing, and Characterization of MEMS/MOEMS*, volume 4558, 287–294. SPIE, SPIE, 2001.

202. Rebeiz, Gabriel M. *RF MEMS Theory, Design, and Technology*. John Wiley & Sons, Hoboken, NJ, 2003.

203. Rebeiz, Gabriel M. and Jeremy B. Muldavin. "RF MEMS Switches and Switch Circuits," *IEEE Microwave Magazine*, 59–71, December 2001.

204. *Reference Data for Radio Engineers*. Howard W. Sams & Co., Inc., Indianapolis, 1977.

205. Rezvanian, O., C. Brown, M.A. Zikry, A.I. Kingon, J. Krim, D.L. Irving, and D.W. Brenner. "The role of creep in the time-dependent resistance of Ohmic gold contacts in radio frequency microelectromechanical system devices," *Journal of Applied Physics*, 104:024513, 2008.

206. Rezvanian, O. and M.A. Zikry. "Inelastic Contact Behavior of Crystalline Asperities in rf MEMS Devices," *Journal of Engineering Materials and Technology*, 131:011002 1–10, January 2009.

207. Rezvanian, O., M.A. Zikry, C. Brown, and J. Krim. "RF MEMS Behavior, Surface Roughness and Asperity Contact." *Material Research Society Symposium*, volume 1052, 135–140. MRS, Boston, November 26-28 2007.

208. Rezvanian, O., M.A. Zikry, C. Brown, and J. Krim. "Surface roughness, asperity contact and gold RF MEMS switch behavior," *Journal of Micromechanics and Microengineering*, 17:2006–2015, 2007.

209. Rice, Stephen L., Steven F. Wayne, and Hans Nowotny. "Material transport phenomena in the impact wear of titanium alloys," *Wear*, 65:215–226, 1980.

210. Rieder, Werner F. and Thomas W. Strof. "Relay Life Tests with Contact Resistance Measurement After Each Operation," *IEEE Transactions on Components, Hybrids, and Manufacturing Technology*, 14(1):109–112, March 1991.

211. R.L. Peek, Jr. and H.N. Wagar. *Switching Relay Design.* D. Van Nostrand Company, Inc., Princeton, New Jersey, 1955.

212. Rubio-Bollinger, G., P. Joyez, and N. Agräit. "Metallic Adhesion in Atomic-Size Junctions," *Physical Review Letters*, 93(11):116803:1–4, 2004.

213. Savitskii, E.M. and A. Prince. *Handbook of Precious Metals.* Hemisphere Publishing Corporation, New York, 1989.

214. SB962-069, SBIR/STTR. "Microelectromechanical Systems (MEMS) Demonstration Radar System," 2006. Small Business Innovative Research Innovation Story.

215. Schauwecker, Bernd, Karl M. Strohm, Winfried Simon, Torsten Mack, and Johann-Friedrich Luy. "A Very Compact RF MEMS Switch for Frequencies up to 50 GHz." *Proceedings of 33rd European Microwave Conference*, 655–658. Munich, Germany, 2003.

216. Schimkat, J. "Contact measurements providing basic design data for microrelay actuators," *Sensors and Actuators A*, 73:138–143, 1999.

217. Schimkat, Joachim. "Contact Materials for Microrelays." *Proceedings of the Eleventh Annual International Workshop on Micro Electro Mechanical Systems, MEMS 98*, 190–194. IEEE, IEEE, Heidelberg, Germany, January 25-29 1998.

218. Schröder, Klaus (editor). *Handbook of Electrical Resistivities of Binary Metallic Alloys.* CRC Press, Inc., Boca Raton, 1983.

219. Schuh, C.A., J.K. Mason, and A.C. Lund. "Quantitative insight into dislocation nucleation from high-temperature nanoindentation experiments," *Nature Materials*, 4:617–621, 2005.

220. Schweitz, Jan-Ake. "Mechanical Characterization of Thin Films by Micromechanical Techniques," *MRS Bulletin*, 17(7):34–45, July 1992.

221. Seguineau, Cedric, Adrien Broue, Fabienne Pennec, Jeremie Dhennin, Jean-Michel Desmarres, Arnaud Pothier, Xavier Lafontan, and Michel Ignat. "New experimental approach for measuring electrical contact resistance with accurate mechanical actuation, evaluation of the performance of gold micro-switches." *Materials Research Society Symposium Proceedings - Microelectromechanical Systems-Materials and Devices*, volume 1052, 235–240. MRS, Nov 26-28, 2007 2008.

222. Sergici, A. Onur, George G. Adams, and Sinan Müftü. "Adhesion in the contact of a spherical indenter with a layered elastic half-space," *Journal of the Mechanics and Physics of Solids*, 54:1843–1861, 2006.

223. Sextro, Walter. *Dynamical Contact Problems with Friction.* Springer, Berlin, 2002.

224. Sharma, S.P. "Adhesion of Electrical Contacts." *Proceedings of 3rd International-22nd Annual National Relay Conference*. IEEE, Oklahoma State University, Stillwater, Oklahoma, April 1974.

225. Sharma, S.P. "Adhesion coefficients of plated contact materials," *Journal of Applied Physics*, 47(8):3573–3576, 1976.

226. Shi, Yong and Sang-Gook Kim. "A lateral, self-cleaning, direct contact MEMS switch." *Proceedings of 18th IEEE International Conference on Micro Electro Mechanical Systems*, 195–198. Miami Beach, FL, 30 Jan - 3 Feb 2005.

227. Shigley, Joseph Edward and Charles R. Mischke. *Mechanical Engineering Design, Fifth Edition*. McGraw-Hill Publishing Company, New York, 1989.

228. Shim, Sanghoon, Jae il Jang, and G.M. Pharr. "Extraction of flow properties of single-crystal silicon carbide by nanoindentation and finite-element simulation," *Acta Materialia*, doi:10.1016j.actamat.2008.04.013, 2008.

229. Sinha, Anil Kumar. *Physical Metallurgy Handbook*. McGraw-Hill, New York, 2003.

230. Slade, Paul G. *Electrical Contacts: Principles and Applications*. CRC Press, New York, NY, 1999.

231. Smith, John K., Francis W. Hopwood, and Kevin A. Leahy. "MEM Switch Technology in Radar." *Proceedings of 2000 IEEE International Radar Conference*, 193–198. IEEE, 2000.

232. Soboyejo, Winston O. (editor). *Advanced Structural Materials: Properties, Design Optimization, and Applications*. CRC Press, Boca Raton, 2007.

233. Song, J. and D.J. Srolovitz. "Adhesion effects in material transfer in mechanical contacts," *Acta Materialia*, 54:5305–5312, 2006.

234. Strong, Fabian W., Jack L. Skinner, Paul M. Dentinger, and Norman C. Tien. "Electrical Breakdown across Micron Scale Gaps in MEMS Structures." Danelle M. Tanner (editor), *Reliability, Packaging, Testing, and Characterization of MEMS/MOEMS V*, volume 6111 of *Proceedings of SPIE*, 611103 1–9. SPIE, 1996.

235. Sun, Ming, Michael G. Pecht, Marjorie Ann E. Natishan, and Rodney I. Martens. "Lifetime Resistance Model of Bare Metal Electrical Contacts," *IEEE Transactions on Advanced Packaging*, 22(1):60–66, February 1999.

236. Tabor, David. *The Hardness of Metals*. Oxford University Press, London, 1951.

237. Tazzoli, A., V. Peretti, R. Gaddi, A. Gnudi, E. Zanoni, and G. Meneghesso. "Reliability issues in RF-MEMS switches submitted to cycling and ESD test." *Proceedings of IEEE International Reliability Physics Symposium*, 410–415. March 2006.

238. Tazzoli, Augusto, Vanni Peretti, Enrico Autizi, and Gaudenzio Meneghesso. "Suspensions Shape Impact on the Reliability of Ohmic RF-MEMS Redundancy Switches." *Proceedings of 46th IEEE International Reliability Physics Symposium*, 510–515. 2008.

239. Tazzoli, Augusto, Vanni Peretti, and Gaudenzio Meneghesso. "Electrostatic Discharge and Cycling Effects on Ohmic and Capacitive RF-MEMS Switches," *IEEE Transactions on Device and Meterials Reliability*, 7(3):429–437, March 2007.

240. TENCOR Corporation. *P-10 Profilometer Reference Manual, Rev A*, 1998.

241. Tilmans, H.A.C. "Switches," www.amicom.info/OpenPlatform/index.php/Switches, December 2003.

242. Tilmans, Harrie A.C., Walter De Raedt, and Eric Beyne. "MEMS for wireless communications: 'from RF-MEMS components to RF-MEMS-SiP'," *Journal of Micromechanics and Microengineering*, 13:S139–S163, 2003.

243. Timoshenko, S.P. and J.N. Goodier. *Theory of Elasticiy, 3rd Ed.* McGraw-Hill Book Company, New York, 1970.

244. Torres, J.-M. and R.S. Dhariwal. "Electric field breakdown at micrometre separations," *Nanotechnology*, 10:102–107, 1999.

245. Tringe, Joseph, Warren Wilson, and Jack Houston. "Conduction properties of microscopic gold contact surfaces." *Proceedings of SPIE, Reliability, Testing, and Characterization of MEMS/MOEMS*, volume 4558, 151–158. SPIE, SPIE, 2001.

246. Tyson, W.R. "Surface energies of solid metals," *Canadian Metallurgical Quarterly*, 14(4):307–314, 1975.

247. Varadan, Vijay K., K.J. Vinoy, and K.A. Jose. *RF MEMS and Their Applications*. John Wiley & Sons, Ltd, West Sussex, England, 2003.

248. Vinci, Richard P. "Personal Communication," 2008.

249. Vinci, R.P. and J.C. Bravman. "Mechanical Testing of Thin Films." *Digest of Technical Papers, International Conference on Solid-State Sensors and Actuators, TRANSDUCERS 91*. IEEE, San Francisco, CA, 24-27 June 1991.

250. Walraven, Jeremy A. "Future Challenges for MEMS Failure Analysis." *ITC International Test Conference*, 850–855. IEEE, 2003.

251. Walraven, Jeremy A., Jr. Edward I. Cole, Lynn R. Sloan, Susan Hietala, Chris P. Tigges, and Christopher W. Dyck. "Failure Analysis of Radio Frequency (RF) Microelectromechanical Systems (MEMS)." Rajeshuni Ramesham (editor), *Proceedings of SPIE, Reliability, Testing, and Characterization of MEMS/MOEMS*, volume 4558, 254–259. SPIE, SPIE, 2001.

252. Wang, Ling, Zeng Cui, Jia-Sheng Hong, Eamon P. McErlean, Robert B. Greed, and Daniel C. Voyce. "Fabrication of high power RF MEMS switches," *Microelectronic Engineering*, 83:1418–1420, 2006.

253. Wang, Zhongde, Brian D. Jensen, Linda L. Chow, John L. Volakis, Kazuhiro Saitou, and Katsuo Kurabayashi. "Full-wave electromagnetic and thermal modeling for the prediction of heat-dissipation-induced RF-MEMS Switch Failure," *Journal of Micromechanics and Microengineering*, 16:157–164, 2006.

254. Weihs, T.P., S. Hong, J.C. Bravman, and W.D. Nix. "Mechanical deflection of cantilever microbeams: A new technique for testing the mechanical properties of thin films," *Journal of Materials Research*, 3(5):931–942, Sep/Oct 1988.

255. Weihs, T.P., S. Hong, J.C. Bravman, and W.D. Nix. "Measuring the strength and stiffness of thin film materials by mechanically deflecting cantilever microbeams." *Materials Research Society Symposium Proceedings*, volume 130, 87–92. MRS, Pittsburgh, PA, 1989.

256. Weisman, Carl J. *The Essential Guide to RF and Wireless, Second Edition.* Prentice Hall PTR, Upper Saddle River, NJ, 2002.

257. Wikipedia http://en.wikipedia.org/wiki/Switch.

258. Williams, Jesse R. and David R. Clarke. "Strengthening gold thin films with zirconia nanoparticles for MEMS electrical contacts," *Acta Materialia*, 56:1813–1819, 2008.

259. Williamson, J.B.P. "The Microworld of the Contact Spot." *Proceedings of the 27th Holm Conference on Electrical Contacts*, 1–10. IEEE, 1981.

260. Winter, Mark. "WebElements, the periodic table on the world wide web," www.webelements.com. Chemistry Dept, Univ of Sheffield, England.

261. Witvrouw, A., H.A.C. Tilmans, and I. De Wolf. "Materials issues in the processing, the operation and the reliability of MEMS," *Microelectronic Engineering*, 76:245–257, 2004.

262. Yan, W. and K. Komvopoulos. "Contact analysis of elastic-plastic fractal surfaces," *Journal of Applied Physics*, 84(7):3617–3624, 1998.

263. Yan, Xiaomin, N.E. McGruer, G.G. Adams, and S. Majumder. "Finite Element Analysis of the Thermal Characteristics of MEMS Switches." *Proceedings of the 12th International Conference on Solid State Sensors, Actuators and Microsystems, Transducers '03*, 412–415. IEEE, Boston, June 8-12 2003.

264. Yang, Z, D Lichtenwalner, A Morris, S Menzel, C Nauenheim, A Gruverman, J Krim, and A I Kingon. "A new test facility for efficient evaluation of MEMS contact materials," *Journal of Micromechanics and Microengineering*, 17:1788–1795, 2007.

265. Yang, Zhenyin, Daniel J. Lichtenwalner, III Arthur S. Morris, Jacqueline Krim, and Angus I. Kingon. "Comparison of Au and Au-Ni Alloys as Contact Materials for MEMS Switches," *Journal of Microelectromechanical Systems*, 2009.

266. Young, Warren C. and Richard G. Budynas. *Roark's Formulas for Stress and Strain, 7th ed.* McGraw-Hill, New York, 2002.

267. Zavracky, Paul M., Sumit Majumder, and Nicol E. McGruer. "Micromechanical Switches Fabricated Using Nickel Surface Micromachining," *Journal of Microelectromechanical Systems*, 6(1):3–9, March 1997.

268. Ziad, Hocine, Kris Baert, and Harrie A.C. Tilmans. "Design considerations of the electrical contacts in (micro)relays." *Micromachined devices & components II, Proceedings of the Conference*, volume 2882, 210–217. SPIE, 1996.

269. Zygo Corporation, Middlefield, Connecticut. *MetroPro Reference Guide, Version 7.6.1*, 2001.

270. Zygo Corporation, Middlefield, Connecticut. *MetroPro Surface Texture Parameters*, 2002.

REPORT DOCUMENTATION PAGE

Form Approved
OMB No. 0704–0188

1. REPORT DATE *(DD–MM–YYYY)*	2. REPORT TYPE	3. DATES COVERED *(From — To)*
24–11–2009	Doctoral Dissertation	Aug 2004 — Sep 2009

4. TITLE AND SUBTITLE

Investigation into Contact Resistance
And Damage of Metal Contacts
Used in RF-MEMS Switches

5a. CONTRACT NUMBER

5b. GRANT NUMBER

5c. PROGRAM ELEMENT NUMBER

6. AUTHOR(S)

Kevin W. Gilbert, Lt Col, USAF

5d. PROJECT NUMBER

5e. TASK NUMBER

5f. WORK UNIT NUMBER

7. PERFORMING ORGANIZATION NAME(S) AND ADDRESS(ES)

Air Force Institute of Technology
Graduate School of Engineering and Management
Department of Aeronautics & Astronautics
2950 Hobson Way
WPAFB OH 45433-7765

8. PERFORMING ORGANIZATION REPORT NUMBER

AFIT/DS/ENY/09-J03

9. SPONSORING / MONITORING AGENCY NAME(S) AND ADDRESS(ES)

Sensors Directorate
Air Force Research Laboratory
AFRL/RYDD, Bldg 620
2241 Avionics Circle
Wright-Patterson AFB, OH 45433-7322
Attn: Dr. Kevin D. Leedy

10. SPONSOR/MONITOR'S ACRONYM(S)

11. SPONSOR/MONITOR'S REPORT NUMBER(S)

12. DISTRIBUTION / AVAILABILITY STATEMENT

Approval for public release; distribution is unlimited.

13. SUPPLEMENTARY NOTES

14. ABSTRACT This research examines the physical and electrical processes involved in lifecycle failure of Microelectromechanical (MEMS) Radio-Frequency (RF) cantilever beam ohmic contact switches. Failures of these switches generally occur at the contact, but complete details of performance of microcontacts are difficult to measure and have not been previously reported. This study investigated the mechanics of microcontact behavior by designing and constructing a novel experimental setup. Three representative contact materials of varying microstructure (Au, Au5%Ru, Au4%V2O5) were tested and parameters of contact during cycling were measured. The Au4%V2O5, a dispersion strengthened material developed at Lehigh University, showed the most promise of the materials tested with the longest-life contact lasting more than 15.5x106 cycles. Evidence of time-dependent deformation and contact heating during cycling was noted in all materials tested. Material hardness was not proportional to contact lifetime or adhesive forces measured during testing. Surfaces of post-cycling contact surfaces were evaluated and failures were categorized by ductile or brittle separation characteristics. Separation characteristics were correlated by contact lifetime.

15. SUBJECT TERMS

RF-MEMS switches, micro-contact mechanics, electrical contact materials

16. SECURITY CLASSIFICATION OF:			17. LIMITATION OF ABSTRACT	18. NUMBER OF PAGES	19a. NAME OF RESPONSIBLE PERSON
a. REPORT	b. ABSTRACT	c. THIS PAGE			Dr. Shankar Mall
U	U	U	UU	578	19b. TELEPHONE NUMBER *(include area code)* (937) 255–3636, ext 4587